ICCC 2023 - Guidelines for citation and reuse



Please cite the conference proceedings as following:
Thailand Concrete Association, Ed. *Further Reduction of CO2 -Emissions and Circularity in the Cement and Concrete Industry, 16th International Congress on the Chemistry of Cement 2023 - ICCC2023* (Bangkok 18.-22.09.2023). Bangkok, 2023. Available at: https://www.iccc-online.org/archive/

Please cite individual papers as following:
Author. Title. In: Thailand Concrete Association, Ed. *Further Reduction of CO2 -Emissions and Circularity in the Cement and Concrete Industry, 16th International Congress on the Chemistry of Cement 2023 - ICCC2023* (Bangkok 18.-22.09.2023). Bangkok, 2023. Available at: https://www.iccc-online.org/archive/

All papers in the 2023 conference proceedings are published under the license CC-BY-ND 4.0.
(https://creativecommons.org/licenses/by-nd/4.0/legalcode)

Organized by

TCA
สมาคมคอนกรีตแห่งประเทศไทย
Thailand Concrete Association

THE 16TH INTERNATIONAL CONGRESS ON THE CHEMISTRY OF CEMENT
ICCC 2023
BANGKOK THAILAND



CONGRESS PROCCEDING VOLUME II

Further reduction of CO_2-emission and circularity in the cement and concrete industry

SEPTEMBER 18-22, 2023

CENTARA GRAND & BANGKOK CONVENTION CENTRE @CENTRALWORLD

Co-Sponsor by

aci American Concrete Institute · SEADMA · gcca · ASTM INTERNATIONAL

Contact infomation :
Email: iccc2023.tca@gmail.com
Website : https://www.iccc2023.org/

PREFACE

The International Congress on the Chemistry of Cement (ICCC) is the renowned global platform that summarizes the state of the art of cement chemistry as well as major trends in cement application. Since the first International Congress on the Chemistry of Cement started in London in 1918, it has provided a strong and fruitful link between the academic world and the cement industry. It has always stimulated scientific exchanges and discussions between researchers, students, and those who have already gained working experience in many fields of chemistry relevant to cement production and its use in concrete and mortar. The ICCC is the venue to present cement and environmental development together with meeting worldwide and renowned experts from all over the world who come to present their works at the congress.

This proceeding collects the papers submitted to the 16th International Congress on the Chemistry of Cement (ICCC 2023), which was held in Bangkok, Thailand between September 18-22, 2023, and organized by Thailand Concrete Association on the theme of "further reduction of CO2-emission and circularity in the cement and concrete industry". The ICCC 2023 attracted more than 565 papers and more than 800 delegates and students from 49 countries.

The scientific program covers the topics of the newest and the most important research and development describing the new dimensions in clinker production, advances in hydration chemistry, enhancing clinker substitution and supplementary cementitious materials, advances in characterization methods and modelling, new low carbon cement and carbonatable binders, new findings in admixture & rheology, new technology for quality concrete, durability & reactive transport, sustainability, circular economy, waste processing and recycling, and standardization of cement and concrete.

The Organizing Committee and the Scientific Committee believe that our participants will be most satisfied with the congress and will gain the knowledge to improve their professional works in the future.



Prof.Thanakorn Pheeraphan
Chairman of the Organizing Committee



Prof.Somnuk Tangtermsirikul
Chairman of the Scientific Committee

Steering Committee Members

The Steering Committee is comprised of 26 members.

1. Prof. Dr. Mark G. Alexander, University of Cape Town, South Africa
2. Prof. Dr. Alexandra Bertron, INSA Toulouse, France
3. Prof. Dr. Shashank Bishnoi; Indian Institute of Technology Delhi, India
4. Prof. Dr. Leon Black, University of Leeds, United Kingdom
5. Dr. Cesar Constantino; Titan America LLC, USA
6. Jesper Sand Damtoft, Aalborg Portland A/S, Denmark
7. Prof. Dr. Jan Deja; Stowarzyszenie Producentów Cementu – PCA, Poland
8. Dr. Wolfgang Dienemann, HeidelbergCement AG, Germany
9. Daniel Duque, Cementos Argos S.A., Columbia
10. Ing. Jan Gemrich, Czech Cement Association, Czech Republic
11. Prof. Dr. Frederik Paul Glasser, University of Aberdeen, Scotland
12. Prof. Dr. R. Doug Hooton, University of Toronto, Canada
13. Prof. Dr. Vanderley M. John, Escola Politécnica da USP, Brasil
14. Prof. Dr. Kimberly Kurtis, Georgia Institute of Technology, USA
15. Christophe Levy, Lafarge Holcim Innovation Center (Chairman), France
16. Prof. Dr. Ippei Maruyama, Nagoya University Furocho, Japan
17. Dr. Bibekananda Mohapatra, Director General of the National Council for Cement and Building Materials, India
18. Dr. Marta Palacios, Instituto Eduardo Torroja, Spain
19. Prof. Dr. Angel Palomo, Instituto Eduardo Torroja, Spain
20. Prof. Dr. Thanakorn Pheeraphan, Thailand Concrete Association (Deputy-Chairman), Thailand
21. Prof. Dr. Martin Schneider, VDZ e.V., Research Institute, Germany
22. Prof. Dr. Karen Scrivener, École Polytechnique Fédérale de Lausanne – EPFL, Switzerland
23. Prof. Dr. Caijun Shi, Hunan University, China
24. Prof. Dr. Sui Tongbo, Sinoma International Engineering Co., Ltd., China
25. Prof. Dr. Jannie S. J. Van Deventer, Zeobond Pty Ltd, Australia
26. Dr. Kazuo Yamada, National Institute for Environmental Studies, Japan

Dr. Joerg Rickert, VDZ (Permanent Secretariat of ICCC), Germany - (Without the right to vote)

Organizing Committee Members

Advisory committee members

1. Dr. Wonchalerm Chalodhorn, Siam City Cement Co. Ltd.
2. Prof.Dr. Chai Jaturapitakkul, King Mongkut's University of Technology Thonburi
3. Prof.Dr. Parinya Jindaprasert, KhonKaen University
4. Mr. Ferdinand Leopolder, The South East Asia Drymix Mortar Association SEADMA,
5. Assoc.Prof.Dr. Pichai Nimityongskul , 1st President of Thailand Concrete Association
6. Mr. Chakporn Oonjitt, Construction Institute of Thailand
7. Mr. Wanchai Phanomchai, Thai Industrial Standards Institute
8. Mr. Chana Poomee, Thai Cement Manufacturers Association
9. Dr. Phirun Saiyasitpanich, Office of Natural Resources and Environmental Policy and Planning
10. Mr. Manasit Sarigaphuti, The Siam Cement Group Public Company Limited
11. Assoc.Prof. Anek Siripanichgorn, Engineering Institute of Thailand
12. Prof.Dr. Boonchai Stitmannaithum, Chulalongkorn University
13. Prof.Dr. Piti Sukontasukkul, King Mongkut's University of Technology North Bangkok
14. Mr. Sumate Surabotsopon, Italian-Thai Development Public Company Limited
15. Prof.Dr. Somnuk Tantermsirikul, Sirindhorn International Institute of Technology
16. Dr. Saranyu Viriyavejakul, Neighboring Countries Economic Development Cooperation Agencies
17. Prof.Dr. Pennung Warnitchai, Asian Institute of Technology
18. Mr. Boonyanit Wongrukmit, Electricity Generating Authority of Thailand

Organizing Committee members

1. Prof.Dr. Thanakorn Pheeraphan, Thailand Concrete Association and NavamindaKasatriyadhiraj Royal Air Force Academy (Chairman)
2. Asst.Prof. Dr. Chuchai Sujivorakul, King Mongkut's University of Technology Thonburi (Deputy Chairman)
3. Mr. Boonrawd Kuptitanhi, The Concrete Products and Aggregate Co., Ltd. (Treasurer)
4. Asst.Prof.Dr. Nattapong Magaratat , King Mongkut's University of Technology North Bangkok (Secretariat)
5. Dr. Praveen Chompreda, K.C.S. & ASSOCIATES. Co., Ltd.
6. Assoc.Prof.Dr. Phongthorn Julphunthong, Naresuan University
7. Miss Sunkamol Khongsawatvorakul, Saint-Gobain Thailand.
8. Mr. Sumet Kiatmetha, Hilti (Thailand) Ltd.
9. Gp.Capt. Nuth Limsuwan, Office of Civil Engineering Royal Thai Armed Forces.
10. Dr. Nontapat Nimityongskul, Asia Cement Public Company Limited.
11. Assoc.Prof. Panuwat Joykad, Srinakharinwirote University
12. Dr. Yut Panitanwong, Concrete Product and Aggregate Co.,Ltd.
13. Mr. Suwatchai Puwapattanachat, SIKA (Thailand) Ltd.
14. Mr. Narin Sayanwisuttikam, KAO Industrial (Thailand) Co., Ltd.
15. Dr. Kritsada Sisomphon, The Siam Cement Group Public Company Limited.
16. Mr. Chalermwut Snguanyat, The Siam Cement Group Public Company Limited.
17. Mr. Pakorn Sutthiwaree, Siam City Cement Public Company Limited.
18. Assoc.Prof.Dr. Weerachart Tangchirapat, King Mongkut's University of Technology Thonburi
19. Asst. Prof. Dr. WarangkanaSaengsoy, Construction and Maintenance Technology Research Center, SIIT
20. Prof.Dr. Wanchai Yodsudjai, Kasetsart University

Scientific Committee Members

1. Prof.Mark Alexander, South Africa
2. Prof.Carmen Andrade, Spain
3. Prof.Sergio Angulo, Brazil
4. Dr.Mohsen Ben Haha, Germany
5. Prof.Susan Bernal Lopez, UK
6. Prof.Alexandra Bertron, France
7. Prof.Shashank Bishnoi, India
8. Prof.Maria Blanco, Spain
9. Prof.Jeff Bullard, USA
10. Prof.Maria Alba Cincotto, Brazil
11. Prof.Jan Deja, Poland
12. Prof.Donguk Choi, South Korea
13. Prof.Josee Duchesne, Canada
14. Mr.Wilmar Echeverri, Colombia
15. Prof.Ivan Escalante, Mexico
16. Dr.Duncan Herfort, Denmark
17. Prof.Bruno Huet, France
18. Prof.Jason Ideker, USA
19. Prof.Edgardo Irassar, Argentinia
20. Prof.Zhengwu Jiang, China
21. Prof.Maria Juenger, USA
22. Dr.Marios Katsiotis, Greece
23. Prof.Shiho Kawashima, USA
24. Prof.Paula Kirchheim, Brazil
25. Prof.Jiaping Liu, China
26. Mr.Federico Lopez, Mexico
27. Prof.Barbara Lothenbach, Switzerland
28. Prof.Horst Ludwig, Germany
29. Prof.Ippei Maruyama, Japan
30. Prof.Thomas Matschei, Germany
31. Mr.Mike McDonald, South Africa
32. Dr.Sean Monkman, Canada
33. Prof.Paulo Monteiro, USA
34. Mr.Carlos Orozco, Colombia
35. Dr.Marta Palacios, Spain
36. Prof.Martin Palou, Slovakia
37. Dr.César Pedrajas, Spain
38. Prof.Rafael Pileggi, Brazil
39. Prof.Kedsarin Pimraksa, Thailand
40. Prof.John Provis, UK
41. Prof.Francisca Puertas, Spain

Scientific Committee Members

42.Prof.Jueshi Qian, China
43.Prof.Aleksandra Radlinska, USA
44.Dr.Nailia Rakhimova, Russia
45.Prof.Matteo Romano, Italy
46.Prof.Nicolas Roussel, France
47.Dr.Kwesi Sagoe-Crentsil, Australia
48.Prof.Manu Sanathanam, India
49.Prof.Miguel Sanjuán, Spain
50.Prof.Caijun Shi, China
51.Dr.Denise Silva, USA
52.Prof.Somnuk Tangtermsirikul, Thailand (Chairman)
53.Dr.Theodor Staněk, CZ
54.Prof.Arezki Tagnit-Hamou, Canada
55.Mr.Antonio Telesca, Italy
56.Dr.Paul Tennis, USA
57.Prof.Michael Thomas, Canada
58.Prof.Jorge Tobon, Canada
59.Prof.Sandro Torres, Brazil
60.Prof.Matthieu Vandamme, France
61.Dr.Yury Villagrán Zaccardi, Argentina
62.Prof.Fazhou Wang, China
63.Prof.Zhang Wensheng, China
64.Prof.Claire White, USA
65.Dr.Frank Winnefeld, Switzerland
66.Dr.Hong Wong, UK
67.Dr.Kazuo Yamada, Japan
68.Prof.Cheng Yu, China
69.Prof.Doug Hooton, Canada
70.Peter Kruspan, Switzerland

Contents

	Topics	Page
	Preface	i
	Committees	
	- Steering Committee Members	ii
	- Organizing Committee Members	iii
	- Scientific Committee Members	v
	Papers	
PF0002	Effects of Magnesium Ion on Retardation Mechanism of Noncalcium Metakaolin Geopolymer	1
PF0004	Effect of further water curing on properties of carbonated reactive MgO cement	5
PF0007	Lightweight reactive magnesia cement (RMC) and biochar-based CO_2-reducing composites	9
PF0008	Processing and hydration activation of limestone calcined clay belite-rich cements	14
PF0010	Effect of relative humidity on carbonation of hardened cement paste particles under atmospheric CO_2 concentration	18
PF0011	Optimizing calcined clay geopolymer production	23
PF0013	Physical properties and CO_2 fixation of concrete using carbonated cement slurry	27
PF0014	Cement and Synthetic SCM with Low-CO_2 Footprint	
PF0015	Influence of elevated heating temperature on the mechanical performance of carbonated belite pastes	31
PF0016	Fresh Properties and Compressive Strength of Alkali Activated Mortar with Different Powder Composition	35
PF0019	Formation and stability of magnesium silicate hydrate and hydromagnesite	39
PF0020	The modification of ultra fines on the rheological properties of alkali-activated ternary paste	43
PF0021	Strength development and CO_2 sequestration by carbonation curing of mortar using blast furnace slag fine powder and γ-C_2S	48
PF0023	Microstructure of MgO-Al_2O_3-SiO_2 binders	52
PF0024	Development of Carbonation-cured Low-carbon Precast Concrete Products and Evaluation of Avoided CO_2 Emissions	56
PF0025	Experimental study on synergy between CO_2 mineralized steel slag and carbonation-cured steel slag-cement paste	61
PF0026	Hydration of cementitious binders based on magnesium oxide / hydromagnesite blends	65

Contents

	Topics	Page
	PAPERS	
PF0028	Carbonation of iron (Fe)-rich materials for cement/concrete matrices: where are we now?	69
PF0029	Enhancement of the properties of recycled concrete aggregates in different mediums	75
PF0030	Reaction Kinetics and Mechanical Properties of Alkali-Activated Metakaolin-Limestone Cements	79
PF0032	Microstructure of Alkali-activated Slag Paste Modified by Superabsorbent Polymers	83
PF0034	Utilization of carbonated steel slag powder in cementitious materials	87
PF0036	Insights into the Role of Carbonation Curing on Calcium Leaching Behavior of Cement Paste	91
PF0039	Mechanical properties of Hardened Cement Paste Containing Amines	95
PF0041	Further Carbon Capture by Semi-Carbonated Concrete Waste Fines through Wet Carbonation Process	99
PF0042	Fracture properties of in-situ polymerization modified cementitious materials	104
PF0044	Hydration and Shrinkage Behavior of Copper Slag Activated by Sodium Silicate at Different Na_2O Equivalents	108
PF0047	Low CO_2 footprint and high circular cementitious binders based on mineralized RCF and LF steel slags under synergistic approach.	112
PF0048	Understanding the role of carbon nanotubes in low-caron concrete: from experiment to molecular dynamics	116
PF0050	Accelerated Carbonation of Brucite Recovered from Desalination Reject Brine for Construction Applications	120
PF0052	Enhancing Carbonation of Reactive Magnesium Oxide Cement (RMC)-Based Composites with Cenospheres	125
PF0054	Shrinkage in carbonatable binders: Are the cementitious standards applicable for non-hydraulic lime-cement systems?	130
PF0055	Compressive strength, pore structure and hydration of alkali activated slag-waste ceramic powder-silica fume ternary system	134
PF0057	Hydration, microstructure and macro-properties of high belite MgO expansive cement	138

Contents

	Topics	Page
	PAPERS	
PF0058	Development of Magnesium Silicate Hydrates from Brucite and Silica Fume	142
PF0059	Spatial and Temporal Analysis of Carbonation Depth via Raman Spectroscopy and Imaging	147
PF0060	Carbon Dioxide Absorption by Amine Mediated Calcium-Silicate-Hydrate (C-S-H)	151
PF0063	Enzymatic Carbon Sequestration in Cementitious Materials	155
PF0064	Role of Mixing Temperature on CO_2 Mineralization of Cement-based Materials	159
PF0068	Experience of a real precast and site-cast application of alkali-activated GGBS based binder concrete	163
PF0069	Promoting Carbonization of Hardened Cement Paste by Wet-Dry Cycle	167
PF0070	Global Warming and its Consequences for the Construction Industry	172
PF0071	Investigating the influence of addition of γ-C_2S and Carbon Dioxide on concrete performance and CO_2 absorption	178
PF0075	Investigating Carbonation and Hydration of Reactive Magnesia Cement using Advanced Characterization Methods	182
PF0076	Quantitative analysis of carbon dioxide bound by carbonation of belite	186
PF0079	Early hydration of low-energy cements from clinkers doped with combination of dopants	191
PF0080	Alkali activated cements based on natural and designed blends of clay and calcium carbonate sources	195
PF0081	Evaluation of iron ore tailing in alkali-activated cement	199
PF0085	An alkali-activated cement factory in Brazil: quantification of CO_2 emissions for a class of cements	203
PF0086	Effect of CO_2 concentration on amount of carbonation in Mortar	207
PF0088	Fundamental understanding of carbonation mechanism of aluminosilicate based material: A state-of-the art review	211
PF0091	Preservation of α' Dicalcium Silicate (C_2S) under SO_2-Containing Atmosphere	216

Contents

	Topics	Page
	PAPERS	
PF0092	Chloride Diffusion and Migration into Concrete Made with Ternary Cements (Clinker, Blast-furnace Slag and Coal Fly Ash)	220
PF0093	The study of relationship between capability of CO_2 absorption and strength and pore structure using blast furnace slag cement	224
PF0095	Effect of Low Temperature Calcination on Pozzolanic Activity of Volcanic Powder	229
PF0098	Development of plaster-like materials from magnesium carbonates	233
PF0102	Suitability of Low purity Limestone for Limestone Calcined Clay Cement (LC^3) Production	237
PF0103	Influence of acetate on the carbonation of brucite ($Mg(OH)_2$)	241
PF0105	Synthesis of Calcium Sulfoaluminate-Belite Cement from Lignite Bottom Ash Using Clinkerization and Hydrothermal-Calcination	246
PF0106	CO_2 mineralization of silicate minerals and the potential inhibiting effect of amorphous silica-rich surface layers	250
PF0107	Two-Step Synthesis of Low-Lime Cement and its Hydration	254
PF0108	The optimal water conditions for the accelerated carbonation curing of cement-based materials incorporating dicalcium silicate	258
PF0112	Leaching-Induced Mass Loss Characterisation of Calcium Sulfoaluminate Binders Using Acid Titrimetry	262
PF0113	Reactivity of novel artificial precursors for alkali-activated materials made from industrial residues	266
PF0114	Belitic calcium sulphoaluminate (BCSA) cements and the current durability standards: What are we testing?	270
PF0115	Early-Age Hydration Characteristics of Ye'elimite in the Presence of Calcium Sulfate and Alkalis	274
PF0116	'A Tale of Two Cations': the influence of interlayer chemistry on the behaviour of montmorillonite clay alkali-activated cements	278
PF0122	Understanding Reaction Mechanisms, Kinetics, and Structural Evolution in Alkali-Activated Slag Cements	282
PF0123	Optimization of Hybrid Portland Cement – Metakaolin Binders	286

Contents

	Topics	Page
	PAPERS	
PF0127	Evaluation of the properties of completely recyclable mortar	290
PF0130	Synthesis, characterization and solubility of sodium aluminosilicate hydrate (N-A-S-H) gel	294
PF0136	Investigation of the effects of supplementary cementitious materials in mitigating alkali-silica reaction using thermodynamic modelling	298
PF0138	Utilization of Dolomitic Limestone Waste for manufacturing of Limestone Calcined Clay Cement	302
PF0139	High-efficient Solidification and Stabilization by Low Carbon Supersulfated Cement	306
PF0145	Comparison of set retarders in CSA and blended CSA/OPC systems	310
PF0146	CO_2 mineralization in the limestone calcined clay cement	314
PF0151	Influence of slaked lime on hydration kinetics of Portland cement	318

The 16th International Congress on the Chemistry of Cement 2023 (ICCC2023)
"Further Reduction of CO_2 -Emissions and Circularity in the Cement and Concrete Industry"
September 18–22, 2023, Bangkok, Thailand

Effects of Magnesium Ion on Retardation Mechanism of Non-calcium Metakaolin Geopolymer

S.B. Wang[1], S.S. Zhang[2], and X. Chen[3*]

[1] *School of Civil and Hydraulic Engineering, Huazhong University of Science and Technology, Wuhan, China*
Email: shuaibin_wang@hust.edu.cn
[2] *School of Civil and Hydraulic Engineering, Huazhong University of Science and Technology, Wuhan, China*
Email: shishun@hust.edu.cn
[3] *School of Civil and Hydraulic Engineering, Huazhong University of Science and Technology, Wuhan, China*
Email: xuchen@hust.edu.cn

ABSTRACT

Seawater-based geopolymers exhibit potential to substantially reduce water usage and carbon emissions. While many seawater-bearing ions (e.g., Ca^{2+}, Na^{+}, and Cl^{-}) have been widely investigated in the geopolymer system, the study on magnesium (Mg) ion-induced changes in properties/structures has so far been very limited. The present study aims to understand the effects of Mg^{2+} on the setting of non-calcium geopolymers. It was confirmed that magnesium chloride could retard the setting of sodium silicate-activated metakaolin through the Vicat penetration, as also evidenced by the delayed dissolution of metakaolin via chemical extractions. Through FTIR and composition analyses, it was found that such retardation was mainly due to the Mg^{2+}-caused consumption of OH^{-} in the activating solution, and thus decelerated the process of dissolution and condensation during geopolymerization. All these findings well verify the tailorability of setting by Mg^{2+} and therefore pave the way to develop the low-carbon geopolymers using marine resources.

KEYWORDS: *magnesium, geopolymer, setting, retardation*

1. Introduction

While geopolymer is being developed as a low-carbon alternative to the ordinary Portland cement, the use of seawater for mixing shows promise to address water shortages (Shi and Yao (2019)). To develop seawater-based geopolymers, the magnesium ions (Mg^{2+}) could react with the alkali-activating solutions and thus potentially affect the hardening process of geopolymers (Shi and Yao (2019), Ren and Sun (2021)). In this study, the hardening process of Mg^{2+}-dosed geopolymers was monitored using Vicat penetration. To understand the effects of Mg^{2+}, the alkali-activating solution was measured via Fourier transform infrared spectroscopy (FTIR), and the corresponding metakaolin geopolymers were examined via FTIR aided with chemical extractions to examine the structure evolution.

2. Materials and methods

2.1 Materials and sample preparation

Geopolymer mixtures were synthesized using metakaolin as the precursor. Sodium hydroxide (NaOH) and fumed silica powder were used to prepare the sodium silicate-activating solution. Anhydrous magnesium chloride ($MgCl_2$) was used to study the effects of Mg^{2+} on the geopolymer setting. The molar ratio (expressed as $MgCl_2$:Na_2O:Al_2O_3:SiO_2:H_2O) was 0.05:1:1:4:11 for the $MgCl_2$ mixture (named as "GP_Mg") and was 0:1:1:4:11 for the non-$MgCl_2$ mixture ("GP_control"), the latter of which was also used in our previous study (Chen and Sutrisno (2017)). $MgCl_2$ was added to the sodium silicate solution and kept stirring for 24h before further mixing with metakaolin. During the synthesis, 1 min of manual

mixing was followed by a mechanical mixing at 800 rpm for 4 min. Immediately after mixing, the mixtures were wrapped by plastic films to prevent water evaporation and then placed in a curing box (20 ± 1℃) until further testing.

2.2 Testing procedure

The setting time was measured in accordance with ASTM C191 (ASTM (2019)) using a Vicat needle apparatus. Each measurement was repeated three times to ensure the accuracy. Meanwhile, according to the Chinese standard of GB/T 17671 (GB/T 17671 (2021)), each six specimens (40 mm cube) were tested at different ages (3, 5 and 28 days) for each mixture. The effects of Mg^{2+} on the silicate polymerization of the activating solutions were examined using an attenuated total reflectance (ATR) Fourier transform infrared (FTIR, Vertex 70, Bruker, Germany) instrument. The spectra were recorded in the range of 4000 - 600 cm^{-1} with a resolution of 2 cm^{-1}. Furthermore, the degree of reaction at various ages was estimated by removing the geopolymer gel (or sodium aluminosilicate hydrate, abbreviated as N-A-S-H) from the geopolymer mixture via hydrochloric acid (HCl) extractions (Chen and Sutrisno (2017)). The residue before and after the extraction was weighed and measured via FTIR with the same manner as described above.

3. Results and discussion

3.1 Effects of Mg^{2+} on the hardening behavior

As shown in Figure 1(a), the curves of penetration depth for "GP_Mg" obviously shifted to the right compared with the "GP_control", indicating the setting of geopolymer was considerably prolonged when Mg^{2+} was present. According to the ASTM C191 (ASTM (2019)), the initial setting time for "GP_Mg" was about 18 hours, being delayed by 4 hours compared to "GP_control". Meanwhile, as shown in Figure1(b), the "GP_Mg" exhibited a significantly lower compressive strength than "GP_control" when cured for 3 days. Such a difference however gradually disappeared as curing days increased. The 28-day compressive strength of the two mixtures (i.e., with and without Mg^{2+}) did not exhibit much difference (about 55 MPa). Such an early-age retardation combined with a slight difference at the later age indicates the feasibility of Mg^{2+} to tailor the setting of geopolymers while keeping their longer-term performance.

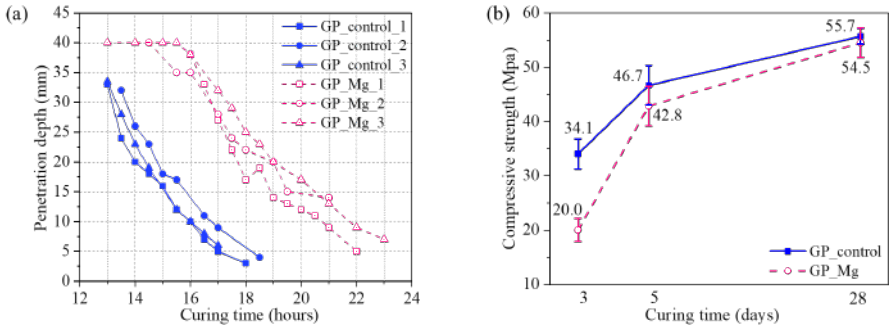


Figure 1 Effects of Mg^{2+} on the hardening process: (a) Vicat penetration curves (b) compressive strength development with curing time

3.2 Mechanism of the retardation

Normally, a main chemical reaction of Mg^{2+} with the activating solution would be the consupmtion of the hydroxyl groups as depicted below:

$$MgCl_2 + 2NaOH \longrightarrow Mg(OH)_2 + 2NaCl \quad (1)$$

The resulting reduction in alkalinity could (a) alter the silicate polymerization of the activating solutions and (b) reduce the metakaolin dissolution, as examined in the following sections.

3.2.1 Extent of silicate polymerization in the activating solution

The sodium silicate solution with and without Mg^{2+} was prepared and characterized to study the effects of Mg^{2+}. While the pH value decreased from 13.65 to 13.41 as the Mg^{2+} was introduced, the silicate species became more polymerized (Figure 2). Specifically, the main band (Q^1 and Q^2: dimer and trimer) shifted from 973 to 976 cm^{-1}, while the peak intensity at 1100 cm^{-1} (Q^3: tetrameric silicate anions) increased as the peak intensity at 875 cm^{-1} (Q^0: monomer) decreased. Though these changes are not substantial, such change towards a higher extent of polymierzation is generally seen to retard the condensation reaction between the silicate and aluminate species at early ages (Gharzouni and Joussein (2015)), thus likely having caused the retardation effects (see Fig. 1).

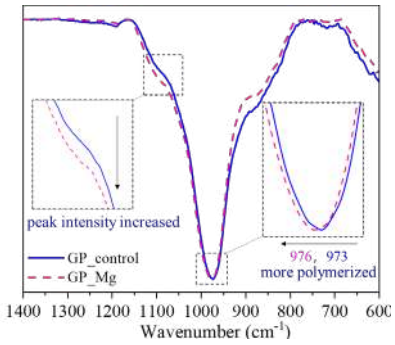


Figure 2 Effects of Mg^{2+} on the silicate polymerization of sodium silicate solutions

3.2.2 Dissolution rate of metakaolin

Besides the condensation process, the change in alkalinity caused by Mg^{2+} could also influence the dissolution rate of metakaolin. As shown in Figure 3, the proportion of the unreacted metakaolin at the various ages for "GP_control" and "GP_Mg" was determined via HCl extraction. While the amount of unreacted metakaolin for all the mixtures exhibited a decreasing trend with time, the amount of unreacted metakaolin for "GP_Mg" at each early age clearly increased compared with "GP_control", indicating that the introduction of Mg^{2+} reduced the dissolution rate of metakaolin. Notably, the proportion of unreacted metakaolin at 28 days was comparable to each other, again supporting the introduction of Mg^{2+} has little influence on the later-age performance.

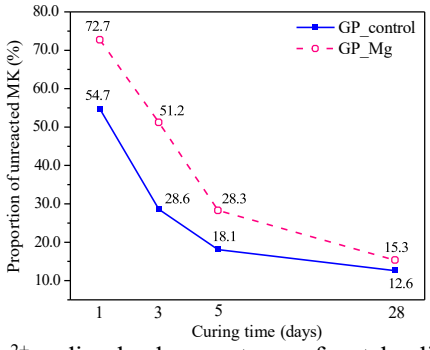


Figure 3 Effects of Mg^{2+}on dissolved percentages of metakaolin at 1 to 28 days

Such Mg^{2+}-induced hinderance in dissolution could also be seen from the direct characterization of the geopolymer mixtures via FTIR (Figure 4). With the addition of Mg^{2+}, the main peak shifted to a higher wavenumber from the "GP_control" to the "GP_Mg", specifically, from 1024 to 1048 cm^{-1} at 1 day, from 998 to 1017 cm^{-1} at 3 days, and from 987 to 999 cm^{-1} at 5 days (Figure 4(a-c)). Generally, a higher FTIR wavenumber is correlated with either a higher percent of metakaolin (Chen and Meawad (2014)) or a higher Si/Al ratio of the gel (Zhang and Wang (2012)). While the higher percent metakaolin is in line with the Mg^{2+}-induced hindrance of dissolution (Figure 3), the higher Si/Al ratio also indicates a less percent of Al was converted from the metakaolin particle to the three-dimensional structure of geopolymer gel. Similarly, no obvious difference were observed in peak positions and intensities at 28 days (Figure 4d), which was consistent with the HCl extraction results.

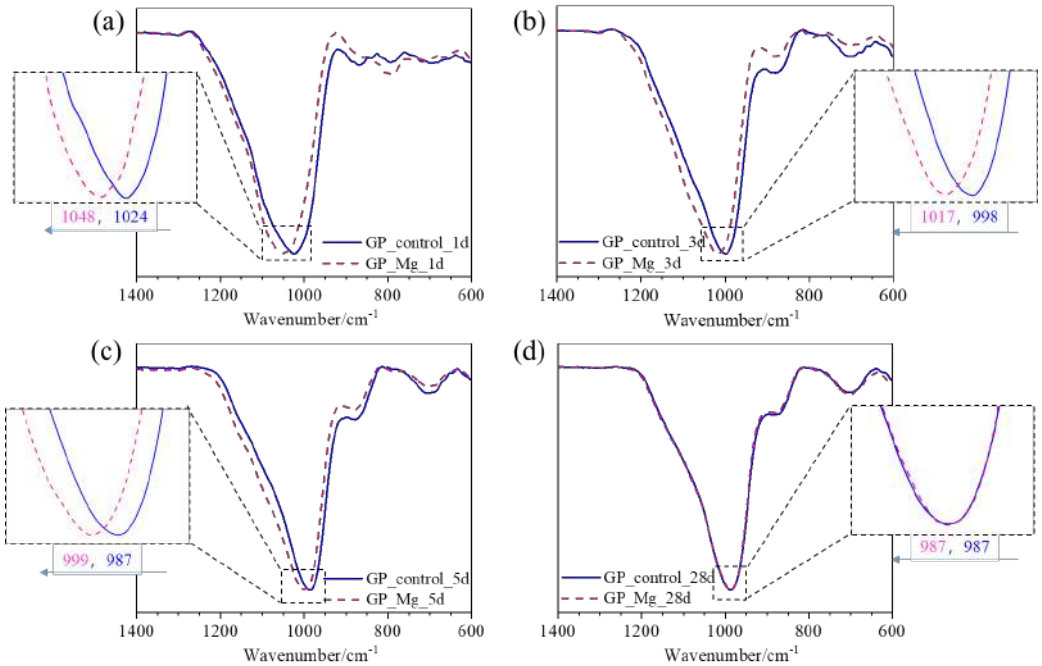


Figure 4 FTIR spectra of metakaolin geopolymers with and without Mg^{2+} at 1 to 28 days

4. Conclusions

In this study, the mechansim by which Mg^{2+} retards the reaction of metakaolin-based geopolymers was elucidated. The main conclusions are as follows:

(1) A significant delay in the initial setting of the metakaolin geopolymer occurred when the Mg^{2+} was present, specifically, by a 4-hour delay with the introduction of Mg^{2+} at 5 mol% relative to the Na_2O. Notably, the addition of Mg^{2+} exhibited negligible effects on the long-term strength (i.e., at 1-month age).

(2) To understand this retardation, the polymerization degree of the sodium silicate solutions and the reaction extent of the metakaolin were investigated via FTIR and HCl extraction. The decreased alkalinity caused by the interaction of Mg^{2+} and OH^- in the activating solution was found to promote the polymerization of silicates in the solution and to hinder the dissolution of metakaolin, thus decelerating the reaction of geopolymerization.

References

ASTM C191 (2019) "Standard Test Methods for Time of Setting of Hydraulic Cement by Vicat Needle", ASTM International, West Conshohocken, United States.

Chen, Meawad and Struble. (2014) "Method to stop geopolymer reaction", *Journal of the American Ceramic Society*, 97(10): 3270-3275

Chen, Sutrisno and Struble. (2018) "Effects of calcium on setting mechanism of metakaolin-based geopolymer", *Journal of the American Ceramic Society*, 101: 957-968

GB/T17671 (2021) Test method of cement mortar strength (ISO method). GB/T 17671-2021, State Bureau of Quality and Technical Supervision, Standards Press of China, Beijing, China.

Gharzouni, Joussein, Samet, Baklouti, Sobrados, Sanz and Rossignol. (2015) "The effect of an activation solution with siliceous species on the chemical reactivity and mechanical properties of geopolymers", *Journal of Sol-Gel Science and Technology,* 73: 250–259

Ren, Sun, Cao, Ren, Zhou, Wu and Xing. (2021) "Effects of natural seawater mixing on the properties of alkali-activated slag binders", *Construction and Building Materials*, 294: 123601

Shi, Yao, Ye and Zhang. (2019) "Effects of seawater on mechanical properties, mineralogy and microstructure of calcium silicate slag-based alkali-activated materials", *Construction and Building Materials*, 212: 569-577

Zhang, Wang, Provis, Bullen, Reid and Zhu. (2012) "Quantitative kinetic and structural analysis of geopolymers. Part 1. The activation of metakaolin with sodium hydroxide", *Thermochimica Acta*, 539:23-33

The 16th International Congress on the Chemistry of Cement 2023 (ICCC2023)
"Further Reduction of CO_2 -Emissions and Circularity in the Cement and Concrete Industry"
September 18–22, 2023, Bangkok, Thailand

Effect of further water curing on properties of carbonated reactive MgO cement

Zhen Li, Jueshi Qian*

College of Materials Science and Engineering, Chongqing University, Chongqing 400045, China

Email: 690490526@qq.com (Z. Li)
qianjueshi@163.com (J. Qian)

ABSTRACT

Reactive MgO cement (RMC) has attracted much attention because of its ability to gain strength through permanently sequestrating CO_2. However, there are risks of delayed expansion caused by further hydration of residue MgO. Meanwhile, the water stability of carbonation products in RMC is still unclear. In this study, carbonated RMCs with different carbonation degrees were prepared by changing the water-to-cement ratio and curing duration. Then, their performance development under further water curing was investigated. The compressive strength, dimensional changes and phase evolutions were characterized before and after water immersion. The results showed that strength increased after long-term soaking degradation of carbonated RMC was only found in specimens with high carbonation degree at early immersion stage due to the dissolution of nesquehonite. By contrast, carbonated RMC with low carbonation degree exhibited continuous strength development but large expansion above 0.12% caused by residue MgO hydration. The reaction of nesquehonite with MgO results in the formation of amorphous hydrated magnesium carbonate with a network structure, resulting in densified microstructure, reduced shrinkage, improved strength and an almost unchanged CO_2 absorption rate. An appropriate amount of MgO residue is beneficial to the water stability of carbonated RMC.

KEYWORDS: *Reactive MgO cement, Water stability, Strength development, Expansion*

1. Introduction

Reactive MgO cement (RMC) is being investigated due to its lower calcination temperature compared with PC (700~1000 °C vs. 1450 °C), and ability to gain strength through CO_2 mineralization (Unluer and Al-Tabbaa (2013)). The strength development of RMC depends on two mechanisms: a) hydration; and b) carbonation. The hydration product $Mg(OH)_2$ reacts with CO_2 and H_2O to form a series of hydrated magnesium carbonates (HMCs) such as nesquehonite ($MgCO_3 \cdot 3H_2O$), hydromagnesite ($4MgCO_3 \cdot Mg(OH)_2 \cdot 5H_2O$), dypingite ($4MgCO_3 \cdot Mg(OH)_2 \cdot 4H_2O$) and artinite ($MgCO_3 \cdot Mg(OH)_2 \cdot 3H_2O$) (Dung et al (2019)). The hydration and carbonation reactions together determine the amount of HMCs and further strength development of RMC (Gardeh et al (2022)).

The hydration of MgO is a dissolution-precipitation process and is controlled by the dissolution of MgO. The formation and coating of HMCs and $Mg(OH)_2$ on the surface of MgO particles inhibit its further hydration, and there is usually 25~60% residual MgO present in hardened RMC (Wang et al (2020), Dung and Unluer (2019)). Under air condition, the residual MgO would not hydrate due to the coating of $Mg(OH)_2$ and HMCs. Unfortunately, the HMCs are not all water stable. It is reported that only hydromagnesite is the most stable product at room temperature, while nesquehonite is unstable, slowly releasing CO_2 and water at room temperature and pressure (Xiong et al (2008)). More importantly, the solubility of HMCs is much greater than that of $Mg(OH)_2$. The water solubility of nesquehonite, hydromagnesite and $Mg(OH)_2$ is 0.295, 0.038 and 0.007 g/L at 25 °C, respectively, calculated from solubility product constant (Winnefeld et al (2019)). Once these HMCs dissolves in water, a deterioration on the performance of the hardened RMC might occurred. Moreover, the dissolution of HMCs brings the internal residual MgO into contact with water and further hydrates, which may lead to volume stability

problems. However, at present, few researches has focused on the properties changes of RMC cured in water.

The objective of this work is to investigate the properties of carbonated RMC further cured in water. The effect of w/b ratio and carbonation curing time on compressive strength and dimensional changes were investigated. Furthermore, the phase evolution of the carbonated RMC was examined before and after soaking.

2. Materials and methods

2.1 Raw materials and sample preparation

Magnesia used in this study is obtained from calcining magnesite (Taida magnesium, China) at 900 °C for 4 h, and the MgO content measured from X-ray fluorescence is above 92%.

The RMC pastes were prepared using w/b ratios of 0.5, 0.6 and 0.7. All specimens were demoulded 1 d after casting and then placed in an accelerated carbonation environment: 20 ℃, 70% RH and 20% CO_2. The carbonated reactive MgO cement (CRMC) with different carbonation degree was obtained after accelerated carbonation for 1 d, 3 d, 7 d or 28 d. Then, the CRMC specimens were immersed in deionized water for another 90 days.

For convenience of description, the specimen was abbreviated as x-ACy, where x is the w/b ratio and y is the curing ages of specimen under accelerated carbonation. For example, 0.5-AC1 is the specimens with a w/b ratio of 0.5 after 1 day of carbonation curing.

2.2 Testing methods

The compressive strength was measured using a universal testing machine (TYE-300B, Wuxi Jianyi Instrument and Machinery Co. LTD, China) at a loading rate of 0.5 kN/s. Each strength data was the average value of 6 specimens (25 mm × 25 mm × 25 mm). The dimensional changes of CRMC in water at different ages was studied by measuring the length of specimens (20 mm × 20 mm × 170 mm).

The fragments after strength test were soaked in ethanol for 48 h to terminate hydration, and vacuum dried for another 48 h. Then the fragments were ground to pass through a 75 μm sieve for XRD test. XRD was tested using a powder X-ray diffractometer (Panalytical X'pert, Netherlands) with Cu-Kα X-ray tube with a step size of 0.026 ° 2θ at a scanning angle of 5–65 ° 2θ.

3. Results and discussion

3.1 Compressive strength

The compressive strength development of CRMC with different curing ages and w/c ratios under further water curing is shown in **Fig. 1**. Before soaking in water, the strength of all specimens increased with the increasing CO_2 curing age, and decreased with the increasing w/b ratio. However, these specimens showed different strength development after are soaking in water. The strength of 0.5-AC1, 0.6-AC1 and 0.7-AC1 specimens continued to increase up to 90 d. For specimens with longer carbonation curing times, their strength first decreased and then increased after soaking in water, and the 90 d strength was still far higher than that of specimens before soaking. For 0.5-AC28 specimen, the strength was 50.8 MPa before soaking in water, and the value decreased 17.7% to 41.8 MPa after 3 d of soaking. Then the 90 d strength increased 24.8% to 63.4 MPa. Generally, the strength of hardened cement depends on the amounts of cementing products, and the decrease in strength in water could be attributed to the decrease amounts of reaction products. The strength increase of CRMC in water indicating the continuous formation of new reaction products.

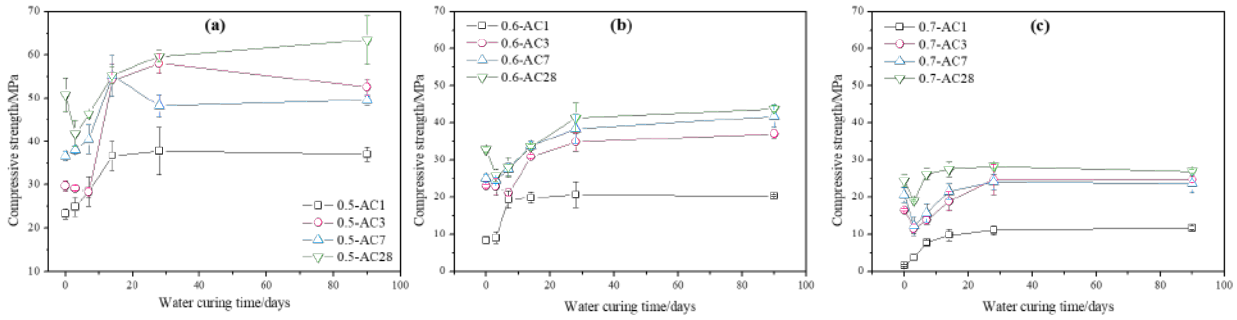


Fig. 1. Compressive strength of CRMCs subjected to further water curing: (a) w/b=0.5, (b) w/b=0.6 and (c) w/b=0.7.

3.2 Dimensional changes

The dimensional changes of CRMC under further water curing are shown in **Fig. 2**. It is observed that almost all specimens expanded after soaking in water, which was caused by the continuous hydration of MgO. The expansion value of 0.5-AC1, 0.6-AC1 and 0.7-AC1 even reached above 1200 μm/m after being soaking in water for 90 days, and the value increased with the increasing w/b ratio. This is attributed to relatively high carbonation degree of low w/b ratio specimens at early stage, and the formation of carbonation products prevents the further hydration of MgO, thus reducing the expansion. Moreover, the expansion of specimens decreased with the increasing carbonation curing time, indicating that the formation of carbonation products is helpful to reduce the expansion of CRMC in water. All specimens carbonated for 3 days or longer time exhibited expansion values less than 600 μm/m at 90 d after soaking, which is a relatively low level. This could be partially attributed to less amount of residue MgO in high carbonated specimens. On the other hand, the formation and coating of the carbonation products on surface of the MgO particles prevent further hydration.

It is worth noting that partial CRMC specimen with longer carbonation curing time (i.e. 3 d, 7 d and 28 d) first expanded rapidly in early age of soaking due to the swelling. Then, the specimens showed obvious shrinkage, which might be attributed to the reaction of HMCs and MgO. Finally, the sepcimens showed continuous expansion up to 90 d.

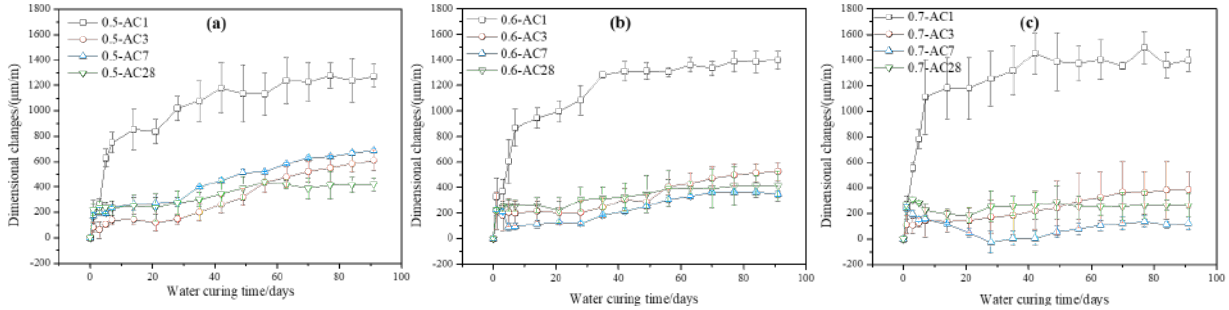


Fig. 2. Dimensional changes of CRMC subjected to further water curing: (a) w/b=0.5, (b) w/b=0.6 and (c) w/b=0.7.

3.3 XRD

XRD was used to identify the phase changes of CRMC with a w/b ratio of 0.5 further cured in water (**Fig. 3**). As shown in **Fig. 3**(a), the prominent peaks are brucite at 18.5 ° and 39.0 ° and periclase at 42.9 ° for all specimens. The peaks corresponding to nesquehonite could also be found in specimens after 3 d, 7 d, and 28 d carbonation curing. Meanwhile, the peak intensities of periclase decreased after soaking, indicating continuous reaction of MgO in water. It is also observed from Fig. 3b and c that the peak intensity of nesquehonite decreased or even disappeared after 90 days of soaking, indicating a decrease of nesquehonite in water. It is worth noting that the AC3 samples showed weak peak at about 20 ° and broadening peak at 35~40 ° after 90 d of soaking, indicating formation of amorphous products. Combined with the results of dimensional changes results (Fig. 2), the shrinkage of CRMC in water could be attributed to the reaction of MgO and nesquehonite to form amorphous products.

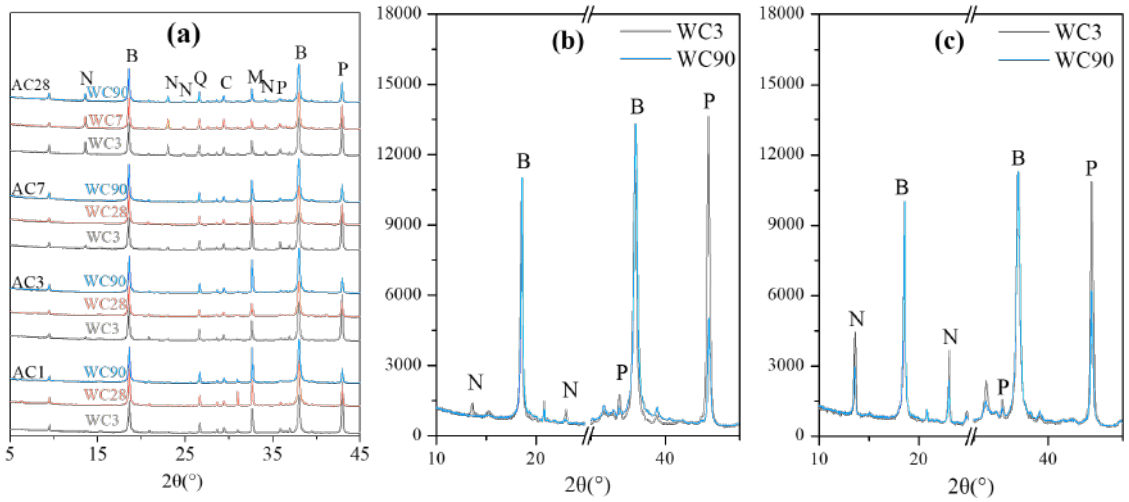


Fig. 3. XRD patterns of the CRMC with a w/b ratio of 0.5: (a) full scans of 0.5-AC1, 0.5-AC3, 0.5-AC7 and 0.5-AC28 samples at water curing for 3d, 7d and 28d; (b) comparison of AC3 samples after 3 and 90 days of water curing; (c) comparison of AC28 samples after 3 and 90 days of water curing (P-Periclase; B-Brucite; N-Nesquehonite; Q-Quartz; M-Magnesite; C-Calcite).

3. Conclusions

RMC is a promising cementitious material due to its ability to gain strength through permanently sequestrating CO_2. However, the performance changes of RMC in water are rarely reported, which is likely to be encountered in its application. In this study, the properties of CRMC with different carbonation degree further soaking in water were studied. The results showed that the strength of CRMC pastes after long-term soaking is higher than that before soaking. The strength reduction caused by dissolution of nesquehonite only occurred in specimens with high carbonation degree at early stage of soaking, and then the strength developed due to the reaction between residue MgO and nesquehonite. The strength of CRMC with low carbonation degree increased continuously but showed high expansion value of above 1200 μm/m. The reaction of MgO with nesquehonite results in the formation of new amorphous phase, leading to shrinkage and inhibiting further hydration of MgO.

Acknowledgements

This study was supported by the National Natural Science Foundation of China (No. 51461135003).

References

Dung, N.T., Lesimple, A., Hay, R., et al., (2019) "Formation of carbonate phases and their effect on the performance of reactive MgO cement formulations" *Cement and Concrete Research,* 125: 105894.

Dung, N.T. and Unluer, C. (2019) "Performance of reactive MgO concrete under increased CO2 disolution" *Cement and Concrete Research*, 118: 92-101

Gardeh, M.G., Kistanov, A.A., Nguyen, H., et al., Kinnunen, P. (2022) "Exploring mechanisms of hydration and carbonation of MgO and $Mg(OH)_2$ in reactive magnesium oxide-based cements" *Journal of Physical Chemistry C*, 126(14): 6196-6206

Unluer, C., Al-Tabbaa, A. (2013) "Impact of hydrated magnesium carbonate additives on the carbonation of reactive MgO cements", *Cement and Concrete Research*, 54: 89-97.

Wang, L., Chen, L. Provis, J.L., Tsang, D.C.W. and Poon, C.S. (2020) "Accelerated carbonation of reactive MgO and Portland cement blends under flowing CO2 gas" *Cement and Concrete Composites*, 106: 103489

Winnefeld, F., Epifania, E., Montagnaro, F., Gartner, E.M., (2019) "Further studies of the hydration of MgO-hydromagnesite blends" *Cement and Concrete Research*, 126: 105912

Xiong, Y. and Lord, A.S., (2008) "Experimental investigation of the reaction path in the MgO-CO_2-H_2O system in solutons with various ionic strengths, and their applications to nuclear waste isolation" *Applied Geochemistry,* 23(6): 1634-1659

The 16th International Congress on the Chemistry of Cement 2023 (ICCC2023)
"Further Reduction of CO_2 -Emissions and Circularity in the Cement and Concrete Industry"
September 18–22, 2023, Bangkok, Thailand

Lightweight reactive magnesia cement (RMC) and biochar-based CO_2-reducing composites

Y. Tang[1*], J. Qiu[1]

[1] *Department of Civil and Environmental Engineering, The Hong Kong University of Science and Technology, Clear Water Bay, Hong Kong, China*
Email: ytangck@connect.ust.hk

ABSTRACT

The hydrates of reactive magnesia cement (RMC) are carbonated to sequestrate massive CO_2; theoretically, 1 kg RMC could sequestrate approximately 1 kg CO_2. However, in real buildings, the majority of its CO_2 capacity would not be utilized for two reasons. First, a considerable fraction of RMC cannot hydrate because of the low solubility of $Mg(OH)_2$; second, CO_2 can only penetrate in by a few millimeters because of the dense microstructure of hydrates. Biochar is a group of highly porous material that is recycled from pyrolyzed bio-waste (S_{BET}=20-545 m^2/g). It can physically adsorb CO_2 with its ultra-large surface area. In this study, we present the effect of mixing these two ingredients to make concrete – the biochar particles introduce connected pores that have a larger size than the mean free path of CO_2 (45 nm), so the sequestrated CO_2 and carbonation degree in RMC matrix is enlarged; the biochar embedded in cured RMC matrix provide a larger specific surface area for CO_2 adsorption, so the CO_2 regulation ability has been improved. Specifically, the chemical compositions of the CO_2-cured RMC-biochar matrix of different biochar-RMC mix design are examined with acid digestion method to determine its CO_2 sequestration capacity; the porosity and pore size distribution after CO_2 curing are analyzed by Brunauer–Emmett–Teller(BET) method; the CO_2 adsorption capacity under ambient CO_2 level and relatively humidity is measured in a customized testing chamber, where the ambient conditions can be controlled.

KEYWORDS: *Reactive magnesia cement, biochar, carbonation, adsorption, porous microstructure*

1. Introduction

RMC has widely attracted research attentions as a promising green binder due to its low calcination temperature (700-900℃ vs 1450℃ for Portland cement) and potential to significantly absorb CO_2 during its service life (Walling and Provis (2016), Mehta and Monteiro (2014)). However, the insufficient carbonation degree of RMC is still a concern. Since the dense microstructure of surface hydrated magnesium carbonates (several millimetres) delays the CO_2 diffusion and decrease the carbonation degree inside the RMC matrix. Hollow natural fiber (HNF) had been successfully proven to provide CO_2 with gas pathway to enhance the carbonation degree of matrix (Wu and Qiu (2022a), Wu and Qiu (2022b)). Despite the rarity of related research, the potential for biochar to create connected pores in the RMC matrix and increase the carbonation degree by allowing deeper CO_2 penetration is compelling, highlighting the urgent need for further investigation.

Biochar can also physically adsorb CO_2 on its ultra-large non-polar surface area, and desorb when heating, degassing, or dehumidifying etc. In such case, specific surface area (S_{BET}) and porosity volume (V_p) of biochar are two main factors to affect its adsorption ability (Leng et al (2021), Zhao et al (2013)).

Chen et al (2022) and Wang et al (2021) aim to increase hydration/and carbonation degree of matrix by internal curing effect with limited biochar dosage. Kua and Choo (2019) used biochar-coated plaster for indoor carbon dioxide sequestration. However, present work reported the mixing of large quantity of biochar and RMC to enhance CO_2 sequestration ability of RMC matrix as well as maintain CO_2 adsorption ability of embedded biochar in RMC matrix at the same time. This combination of materials provides insight to fabricate the lightweight masonry wall material for indoor air regulation in the future.

2. Materials and methods

2.1 Raw materials, mix design, and specimen preparation

RMC was used as binder and sodium hexametaphosphate ($Na(PO_3)_6$) was used as dispersion agent for the fresh RMC paste. Silica sands with a mean diameter of 150μm were used as fine aggregates. Biochar particles with particle size less than 1mm were used as a lightweight CO_2-adsorbing aggregate. Shale

particles (S_{BET}=0.025 m^2/g) with particle size less than 0.2mm were used as a lightweight aggregate with ignorable CO_2-adsorbing capability.

Table 1 summarizes the mix proportions and the testing plan of this work. From B0 to B160, the biochar-to-RMC ratio increased from 0 to 1.6; the group S had the same RMC content as B100 and was used as a control group. All the groups had a free water-to-cement ratio of 0.79.

Table 1 Mix proportions and testing plan in this work

Group	Mix proportions (kg/m^3)							Testing method			
	MgO	Biochar/ shale	Silica sand	Absorbed water	Free Water	$Na(PO_3)_6$	Total	f_c (MPa)	Dry density (kg/m^3)	Carbonation, porosity	CO_2 adsorption
B0	815	0	326	0	644	32.2	1817	55.9±2.63	1591.9±9.3	√	
B60	541	325	216	237	427	21.4	1767	11.88±0.55	1263.5±8.1	√	
B100	442	442	177	323	349	26.6	1760	8.8±0.3	1140.1±6.3	√	√
B160	347	555	139	405	274	48.6	1769	5.48±0.14	1046.6±8.4	√	
S	442	1349	117	337	349	17.5	2612	-	-		√

The lightweight composites listed above were mixed and cast according to Wu and Qiu (2022b), and the fresh mixture was cast into 40×40×40 mm^3 cubes for dry density measurement and compressive test; it was cast into R50×H100 mm^3 cylinders for carbonation degree measurement and subsequent porosity characterization; it was cast into 15×250×250 mm^3 thin plates for in-situ CO_2 adsorption test. After 48 hours curing in ambient air, the specimens were demolded. After demolding, the side and bottom of cylindrical specimens were sealed with paraffin, while the upper face left open to allow one-way CO_2 diffusion. Then all the cube, cylinder and plate specimens were cured in an CO_2 environmental chamber (30℃, 85% relative humidity,10 vol.% CO_2 concentration) for RMC carbonation.

2.2 Testing procedures

Unconfined uniaxial compressive tests were conducted to the 28-day CO_2 cured cubes with the loading rate of 0.05 mm/s; The oven-dry density was calculated by oven-dried mass of specimen divided by the sample volume obtained by Archimedes method.

The porosity and pore size distribution of samples were characterized by surface area and pore size distribution analyzer (Microtrac BEL, Belsorp Mini X). Powder samples were degassed at 180℃ for 6 hours before N_2 adsorption-desorption process. S_{BET} of samples were analyzed by BET theory, the pore size and pore distribution of samples were analyzed by Barrett-Joyner-Halenda (BJH) method.

Acid digestion method was applied to quantitatively detect carbonation degree of composites. After 14-day CO_2 curing, the specimens were cut accordingly from surface, middle and bottom, each layer has thickness of 10mm. The slices from same depth were collected and crushed into powder. Diluted 600ml 5 vol.% sulfuric acid solution with excess H_2SO_4 (30ml, 95-97%) were prepared for testing. The procedure for acid digestion is as follows: 1) weight the beaker with mixture W_0; 2) mix the solution gently with magnetic stirrer for 2 minutes; 3) add about 30g power (W_1) into mixture then stirring for about 5 minutes at a speed of 850 rpm; 4) weight the resultant mixture with breaker W_2; the control group without adding samples was also carried out to calculate the weight loss due to water evaporation (ΔWc). So, the decreased mass(ΔW) of samples and digestion ratio(α) can be calculated.

$$\Delta w = w_! + w_" - w_\# - \Delta w_\$ \quad (1)$$

$$\alpha = \frac{\%\&}{\blacksquare} \times 100\% \quad (2)$$

The carbonation degree(β) could be approximately calculated by amount of sequestrated carbon dioxide(mol) divided by amount of magnesium ion(mol) in the samples. If the biochar to RMC ratio is x, then the derived carbonation degree can be expressed as follow:

$$\beta = \frac{(\times *! \times (". *-.)}{**} \quad (3)$$

The chemical reaction of CO_2 and hydrated RMC can largely sequestrate CO_2, but it takes much longer time than physically adsorption process by biochar, which dominated by CO_2 diffusion rate. In-situ CO_2 adsorption test set up is shown in figure 1, CO_2 level in chamber is controlled as between 500-1500 ppm (mean value is 1000ppm, which is the upper limit of indoor CO_2 level in Hong Kong). The chamber size is 600mm×600mm×600mm. In this set up, a gas valve connected with an environmental controller were used to control the CO_2 level in the chamber. The test was conducted at about 25℃, and saturated potassium bromide solution was used to maintain about 75% R.H. in chamber. The chamber was tightly sealed. Real-time CO_2 concentration, R.H. and temperature were recorded simultaneously by datalogger every 3 minutes and lasting for 48 hours for each test.

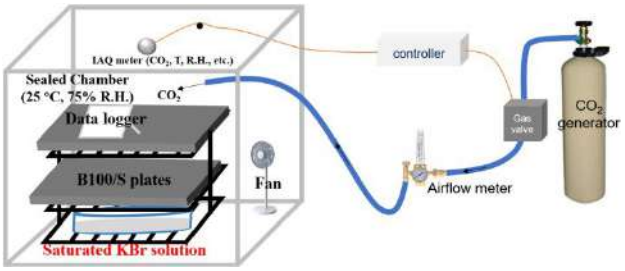


Fig. 1 Schematic diagram of self-designed chamber

3. Results and discussions

3.1 Compressive strength and oven-dry density

The compressive strength and over-dry density are shown in the table 1 above, the mean value with standard deviation of triplicate samples for each group was reported.

3.2 S_{BET}, porosity and pore size distribution

Fig. 2 below indicates the pore size distribution of biochar and biochar-based RMC composites after 28-day CO_2 curing. For pristine biochar, most of pores were distributed within 10 nm, there are two peaks located at 1.1903 and 1.4952 nm respectively. Besides, S_{BET}, V_p and peak aperture ($d_{p,peak}$) of biochar and biochar-incorporated RMC composites were listed in the table 3. For biochar-incorporated RMC composites, the pores within the matrix were introduced by both the biochar and RMC composites after hydration and carbonation. Despite the relatively low S_{BET} (only 6.224 m^2/g) of hydrated and carbonated RMC matrix after 28-d CO_2 curing, Table 3 demonstrates that the incorporation of biochar increases the S_{BET} of the composites from 20.543m^2/g, 29.351m^2/g to 39.902m^2/g, depending on the biochar dosage. This increase in S_{BET} indicates that the available adsorption sites on the surface of biochar were not largely occupied by hydrates and carbonates, thereby preserving the CO_2 adsorption potential of embedded biochar in the 28-day cured RMC matrix.

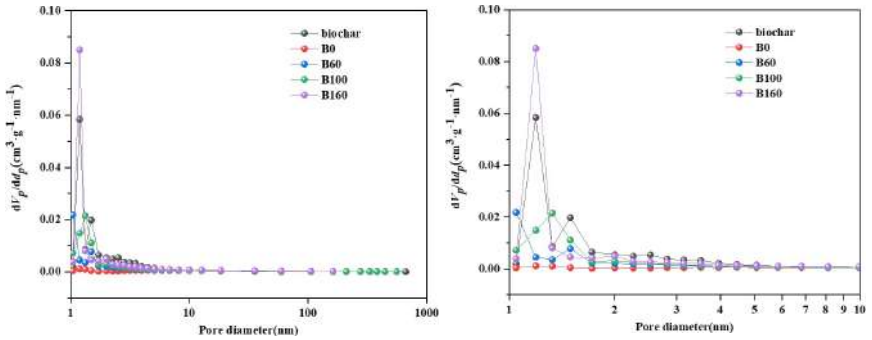


Fig.2 Pore size distribution of biochar and 28-day cured biochar-based RMC composites

Table 3 S_{BET} and V_p of 28-day cured biochar-based RMC composites

Groups	$S_{BET}(m^2/g)$	$V_p(cm^3/g)$	$d_{p,peak}$(nm)
biochar	64.225	0.037	1.1903
B0	6.224	0.0472	1.1903
B60	20.543	0.0643	1.0454
B100	29.351	0.0867	1.3261
B160	39.902	0.0671	1.1903

3.2 Acid digestion ratio and carbonation degree

Table 4 Acid digestion ratio and carbonation degree of 14-day cured biochar-based RMC composites

Groups	Acid digestion ratio (%)	Carbonation degree (%)
B0	5.84	7.43
B60	8.54	15.33
B100	8.07	17.59
B160	7.41	20.21

The acid digestion ratio and carbonation degree of the 14-day cured samples are presented in Table 4. The B0 group exhibited the lowest acid digestion ratio (only 5.84%), indicating that it produced the least hydrated magnesium carbonates after 14-day CO_2 curing. Nevertheless, all three biochar-incorporated RMC composites demonstrated enhanced CO_2 sequestration ability of composites, as evidenced by an increasing amount of digestion ratio compared to B0.

Observably, the carbonation degree of the biochar-incorporated group increased significantly, when compared to that of the B0 group, which also indicated by Table 4. Furthermore, the carbonation degree of all biochar-incorporated groups increased proportionately to the biochar to RMC mass ratio, ranging from 15.33% (B60) and 17.59% (B100) to 20.21% (B160). This suggests that the diffusion path of CO_2 is no longer hindered by dense matrix on the surface, and the connected pores within biochar provide an additional pathway for CO_2 to penetrate deeper into the matrix, resulting in a higher amount of sequestrated CO_2 inside compared with B0 group. As the dosage of biochar increases, so does the penetration of CO, resulting in a higher amount of sequestered CO_2 during curing.

3.3 In-situ CO_2 adsorption capacity

Fig. 3 displays the CO_2 concentration changes in a self-designed chamber for 0-day and 28-day cured B100 and S groups. 0-day CO_2 curing revealed that B100 and S group have a significant CO_2 reducing ability, as shown by the approximately 25 and 24 cycles, respectively, in Fig. 3a. After 28 days of CO_2 curing, the cycles reduced to only 4 and 3 for B100 and S groups, respectively, indicating a slower CO_2 reducing ability of the RMC matrix compared to the uncured groups. This is primarily due to the RMC matrix's reduced chemical absorption ability. In Fig. 3b, the slope of the curve in the first few cycles is significantly steeper for B100 compared to S group. As the cycle time increases, t_i in B100 group also increases, while this trend is not as pronounced for S group. This suggests that C_i in the first few cycles is due to both biochar adsorption and RMC matrix absorption effects, with the adsorption ability of biochar becoming exhausted after the first 1-3 cycles, leaving only chemical absorption of RMC to reduce CO_2, thereby S and B100 groups show similar CO_2-reducing trend during the later cycles.

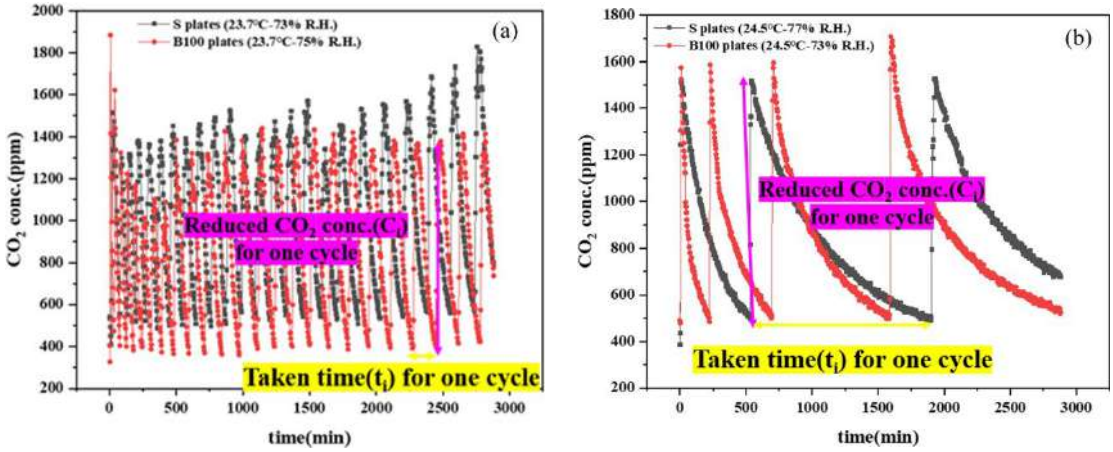


Fig. 3 the CO_2 concentration changes in a self-designed chamber for 0-day (a) and 28-day (b) CO_2 cured B100 and S plates

The total C_i was calculated by adding up all the individual C_i values for 48 hours. In Fig. 3a, the difference in total C_i between B100 and S groups was 2124 ppm, indicating a biochar adsorption ability of 1.03 mg (CO_2)/g within 48 hours. In Fig. 3b, the adsorption ability of embedded biochar was 0.76 mg (CO_2)/g, which might be attributed to the formation of a denser microstructure on the surface. This denser microstructure slows down the diffusion rate of CO_2 into the embedded biochar and prolongs the CO_2 adsorption process.

4. Conclusion

This work presents the combined effects of large biochar dosage and RMC mixing for the first time to create lightweight composites. The combination of biochar and RMC enhances the sequestered CO_2 amount while maintaining the CO_2 adsorption ability of embedded biochar in the RMC matrix. The conclusions can be summarized as follows:

1) With biochar dosage increases from 0% to 160% of cement quantity, 28-d compressive strength of biochar-incorporated composites dropped from 55.9, 11.88, 8.8 to 5.48 MPa;
2) Hydrates and carbonates do not significantly occupy the surface of the embedded biochar in RMC matrix after 28 days of CO_2 curing;
3) The incorporation of biochar results in a maximum carbonation degree that is over 270% higher than that of the group without biochar;
4) CO_2 adsorption ability of embedded biochar in RMC matrix slightly decreased after 28-d CO_2 curing.

References

Walling, S.A. and Provis, J.L. (2016) “Magnesia-based cements: a journey of 150 years, and cements for the future?”, Chemical reviews, 116(7):4170-4204

Mehta, P.K. and Monteiro, P.J., (2014) Concrete: microstructure, properties, and materials. McGraw-Hill Education.

Khalil, A. and Celik, K., (2019) “Optimizing reactivity of light-burned magnesia through mechanical milling”, Ceramics International, 45(17): 22821-22828

Dung, N.T. and Unluer, C., (2016) “Improving the performance of reactive MgO cement-based concrete mixes”, Construction and Building Materials, 126: 747-758

Unluer, C. and Al-Tabbaa, A., (2013) “Impact of hydrated magnesium carbonate additives on the carbonation of reactive MgO cements”, Cement and Concrete Research, 54: 87-97

Wu, B. and Qiu, J., (2022a) “Incorporating hollow natural fiber (HNF) to enhance CO2 sequestration and mechanical properties of reactive magnesia cement (RMC)-based composites: Feasibility study”, Journal of CO2 Utilization, 57:101874

Wu, B. and Qiu, J., (2022b) “High-performance Reactive Magnesium Cement Incorporating Hollow Natural Fiber and Silica Sand”, In MATEC Web of Conferences (Vol. 364). EDP Sciences

Leng, L., Xiong, Q., Yang, L., Li, H., Zhou, Y., Zhang, W., Jiang, S., Li, H. and Huang, H., (2021) “An overview on engineering the surface area and porosity of biochar”, Science of the total Environment, 763:144204

Zhao, L., Cao, X., Mašek, O. and Zimmerman, A., (2013) “Heterogeneity of biochar properties as a function of feedstock sources and production temperatures”, Journal of hazardous materials, 256: 1-9

Chen, L., Zhang, Y., Wang, L., Ruan, S., Chen, J., Li, H., Yang, J., Mechtcherine, V. and Tsang, D.C., (2022) “Biochar-augmented carbon-negative concrete”, Chemical Engineering Journal, 431: 133946

Wang, L., Chen, L., Poon, C.S., Wang, C.H., Ok, Y.S., Mechtcherine, V. and Tsang, D.C., (2021) “Roles of biochar and CO2 curing in sustainable magnesia cement-based composites”, ACS Sustainable Chemistry & Engineering, 9(25): 8603-8610

Kua, H.W. and Choo, S.Y.G., (2019) “The Use of Biochar-Coated Lime Plaster Pellets for Indoor Carbon Dioxide Sequestration”, In Biochar from Biomass and Waste (pp. 305-317). Elsevier.

The 16th International Congress on the Chemistry of Cement 2023 (ICCC2023)
"Further Reduction of CO_2 -Emissions and Circularity in the Cement and Concrete Industry"
September 18–22, 2023, Bangkok, Thailand

Processing and hydration activation of limestone calcined clay belite-rich cements

C. Redondo-Soto[1*], N. Fernández-Pérez[1], A. Cuesta[1], I. Santacruz[1], D. Gastaldi[2], F. Canonico[2], and M.A.G. Aranda[1]

[1] *Departamento de Química Inorgánica, Cristalografía y Mineralogía, Universidad de Málaga, Málaga, Spain*
Email: cinthyars@uma.es, noe.fernandez98@uma.es, a_cuesta@uma.es, isantacruz@uma.es, g_aranda@uma.es
[2] *BUILT – Buzzi Unicem Innovation Lab and Technology, Vercelli, Italy*
Email: dgastaldi@buzziunicem.it, fcanonico@buzziunicem.it

ABSTRACT

Belite-rich limestone calcined clay cements, BR-LC^3, could be an alternative for low carbon binders with potentially very good durability properties, given the high amount of C-S-H gel from the cement hydration with additional C-(A)-S-H from the pozzolanic reaction. Nevertheless, BR-LC^3 phase hydration rates at early ages are slow and they must be enhanced, for instance by using C-S-H nucleation seeding admixtures. In this work, a BR-LC^3 binder was prepared using a clinker-activated Belite-rich cement, BC (58 wt%), kaolinitic calcined clay (26 wt%), limestone (13 wt%) and gypsum (3 wt%). Pastes were prepared with a water-to-binder (w/b) ratio of 0.40 and superplasticizer. Mortars were prepared with the w/b=0.40 and having a target slump self-flow of 210±20 mm. Paste hydration characterization was carried out by thermal analysis, Rietveld quantitative phase analysis and mercury intrusion porosimetry. The compressive strengths of the mortars were also determined. Remarkable compressive strength improvements at 7 and 28 days are shown by using a C-S-H seeding admixture. The improvement of mechanical strengths is not related to belite phase hydration acceleration but mainly to lower porosity.

KEYWORDS: *low-carbon cement, calcined clay, chemical admixture, pozzolanic reaction*

1. Introduction

Clinker replacement by the combination of limestone and kaolinite-containing calcined clays is one of the foremost approaches for minimizing cement CO_2 emissions because of its wide availability and the resulting mechanical strength performances at 3 days or later, Scrivener et al (2019). These materials benefit from the pozzolanic reaction, i.e. the chemical reaction of metakaolin, and related amorphous alumina-silicate(s), with portlandite (CH) to yield calcium silicate aluminate hydrate (C-A-S-H) gel which has very good cementing and pore-refining properties. Moreover, lower limestone demand cements, such as BCs, present advantages for developing low-carbon binders and possibly extending infrastructure service lives, Cuesta et al (2021). However, BCs have slow strength development at early ages that can be enhanced with admixtures.

One possibility, which does not compromise durability performances, is the use of C-S-H nucleation seeding admixtures. These admixtures behave according to two principal mechanisms in cement hydration: i) modifying the pore solution ion contents, and ii) supplying additional nucleation sites. These features lead to an enhancement of the hydration of Belite-rich cements, Morales-Cantero et al (2022a, 2022b). Moreover, two BR-LC^3 binders have been prepared very recently and accelerated with a C-S-H seeding admixture, Redondo-Soto et al (2023). The aim of the present project is to complement that previous work by employing a different admixture, Master X-Seed STE53, which is tailored for strength enhancement of low-carbon cements. BR-LC^3 mortars have been prepared with similar self-flow slump values and hence very similar rheological features.

2. Materials and Methods

2.1 Materials. The employed BC was a CEM I 42.5 N-like, provided by Buzzi Unicem SpA with the following mineralogical composition: 28.4wt% of C_3S, 50.6wt% of ᵞ-C_2S, 11.6wt% of C_4AF, 2.3wt% of

C_3A, 2.2wt% of $C_4A_3\underline{S}$, 1.6wt% of MgO, 1.5wt% of C$\underline{C}$ and 1.8wt% of C$\underline{S}$. The key textural features are: $D_{v,50}$=12.8 μm and a Blaine value of 502 m^2/kg. The remaining materials were: i) a 80 wt% kaolinitic clay from Caolines de Vimianzo; ii) an 96 wt% limestone (LS) by Omya; and iii) a 96 wt% gypsum (Gy) by Fábrica de yesos y escayolas La Maruxiña. The raw clay was calcined at 860ºC to yield the calcined clay (CC). Additionally, a polycarboxylate superplasticizer based on poly(ethylene glycol) polyacrylate ether sodium salt (PCE) from Master Builders Solutions was employed to obtain the slump target for mortars. The C-S-H seeding admixture was Master X-Seed STE-53 (STE53) provided by Master Builders Solutions. Further information and characterization of these materials have been previously reported, Redondo-Soto et al (2023) and Morales-Cantero et al (2022b).

2.2 Pastes and mortars preparation. BR-LC^3-42 binder was prepared using 58 wt% of BC, 26 wt% of CC, 13 wt% of LS and 3 wt% of Gy. Mortars were prepared using sand-to-binder (s/b) ratio of 1.78 and w/b ratio of 0.40. The steps were as follows: i) homogenization of the binder with sand, in a plastic bag, and addition of the 80 wt% of the water mixing at 140 rpm for 60 s; ii) addition of the PCE with a syringe and of the residual 20 wt% of the water; and iii) stirring at 285 rpm for 180 s. When using STE53, the water is added in three stages: a) addition of SP and 80 wt% of the water followed by stirring at 140 rpm for 60 s; b) addition of the PCE with a syringe and 10 wt% of the water and then mixing at 285 rpm during 60 s; and finally, c) addition of STE53 with a syringe and 10 wt% of the water, stirring at 285 rpm for 120 s. The amount of PCE for each sample was optimized to yield a free-flow value of 210±20 mm. 2 wt% of STE53 was added, when required. The amounts of both admixtures are referred to the binder amount, correspond to the as-received products, and their water contents were considered for w/b calculations. The same mixing procedure was carried out for the cement pastes.

2.3 Analytical techniques. Hydrated pastes characterization was carried out at 2, 7 and 28 days by thermal analysis (TA) and laboratory X-ray powder diffraction (LXRPD) with Rietveld quantitative phase analysis (RQPA). Moreover, some microstructural features were characterized by mercury intrusion porosimetry (MIP). Resulting mortars properties were studied by compressive strength measurements. More details related to the employed analytical techniques are given in Redondo-Soto et al (2023). Slump free-flow measurements were performed pouring the mortar in the cone, UNE-EN 1015–3 standard, previously moistened, in two steps: i) filling it up to 80 % of its volume and removing the air bubbles with a glass rod: 15 vertical punctures and then, ii) filling the cone completely and making another 15 vertical punctures. Once the cone was leveled using a spatula, it was gently lifted, and the diameter of the mortar after flowing was measured in two perpendicular directions. The free-flow values were obtained for BC-ref, BR-LC^3-42, and BR-LC^3-42-STE53 by adding 0.27, 0.76 and 0.81 wt% of PCE, respectively. The weight percentage of PCE used for each sample will not be detailed next for sake of simplification.

3. Results and discussion

3.1. Calorimetry study of the pastes. The heat development of the pastes is shown in Figure 1. The BC is used as reference, and it develops a cumulative heat of hydration of 208 J/g at 7 d. This value is much smaller than those of typical PC 42.5 at that age, about 300 J/g. The maximum of the heat flow trace for BC, see Fig. 1, is located at ~24 h. As it can be seen, and as expected, BR-LC^3-42 develops less heat, 172 J/g-of-binder at 7 d. This lower heat is undoubtedly due to the dilution of the belite cement by the mixture of limestone and calcined clay. However, it must be noted that the induction period is largely reduced for the BR-LC^3 binder, see Fig. 1. This is likely due to the filler effect because the fine particle sizes of the employed calcined clay and limestone. As the developed heat was low, binder activation was carried out with STE53 as previously reported for neat PC and BC by Morales-Cantero et al (2022b). The heat of hydration for BR-LC^3-42-STE53 was 181 J/g-of-binder at 7 d. The admixture addition moved the maximum of the aluminate peak from 25 to 19 h, it becomes more intense and sharper. The maximum of alite peak, located at ~10 h, was not influenced by the STE53 addition, see Fig. 1. Hence, the acceleration/activation of the hydration of this BR-LC^3 binder is demonstrated and it mainly involved the aluminate-rich phase(s).

3.2. Phase evolution with hydration for the studied pastes. Paste hydration characterization was carried out by RQPA to obtain the degree of hydration (DoH) of the main cement phases. Additionally, TA was performed to follow the pozzolanic reactivity by measuring the portlandite contents. Table 1

shows the most important results from both techniques. From the inspection of Table 1, the following conclusions concerning the DoHs can be drawn. i) Alite hydration rates are very high and similar for the three samples. ii) Belite phase, which was activated at the clinkering stage, reacts faster than in PC but its hydration rate does not increase when STE53 admixture is employed. iii) The DoH of C_4AF is larger and it clearly increases with C-S-H seeding. Focusing on TA result, the Portlandite (CH) content increases with time for BC-ref, but it is very small and it decreases in BR-LC^3-42 seeded and unseeded pastes. These results are a proof of the pozzolanic reaction and they are in full agreement with our previous report for related samples, Redondo-Soto et al (2023).

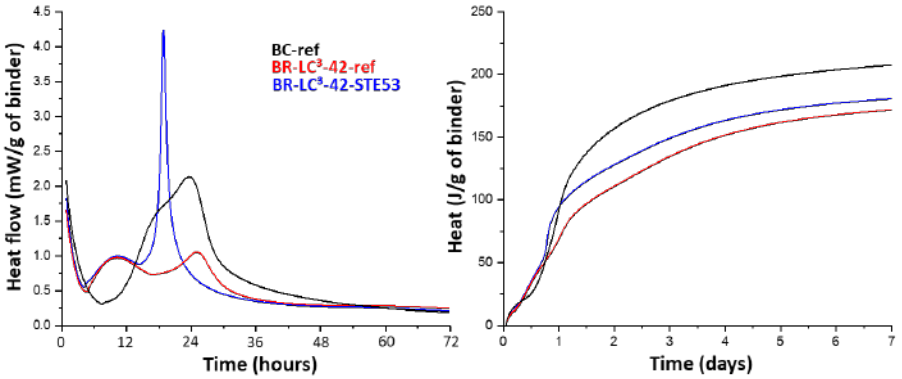


Figure 1. Calorimetric study for BR-LC^3-42 pastes, w/b=0.40. Left: Heat flow curves shown up to 3 days for better visualization. Right: Cumulative heat traces. Both plots contain the data for neat BC as reference.

Table 1. DoH (%) of the most important cement phases as determined by Rietveld quantitative phase analyses. The CH contents (wt% referred to 100 g of paste) determined by TA are also shown.

	Degree of hydration (%) from LXRPD-RQPA			CH (wt%) from TA
	C_3S-M3	β-C_2S	C_4AF	
	2 – 7 – 28 /d	2 – 7 – 28 /d	2 – 7 – 28 /d	2 – 7 – 28 /d
BC-ref	89 – 94 – 94	3 – 37 – 46	44 – 86 – 86	4.1 – 4.7 – 5.4
BR-LC^3-42-ref	92 – 94 – 95	22 – 37 – 42	76 – 86 – 88	1.0 – 0.8 – 0.0
BR-LC^3-42-STE53	91 – 95 – 96	23 – 27 – 43	96 – 96 – 98	1.3 – 0.8 – 0.0

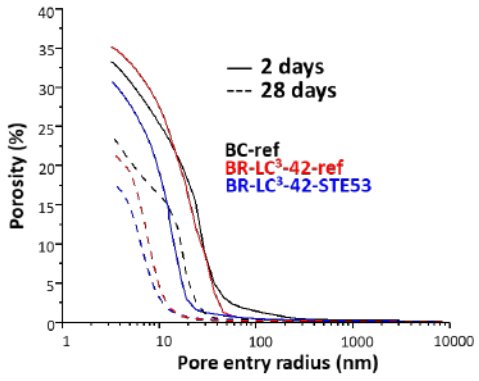


Figure 2. Mercury intrusion porosimetry results for the pastes at 2 and 28 days.

3.3 Microstructural evolution from MIP. MIP traces are given in Figure 2. At early ages, i.e. 2 d, the overall porosity of BR-LC^3-42 is slightly larger than that of BC-ref reflecting the lower amount of cement and the reduced rate of pozzolanic reaction. Interestingly, BR-LC^3-42-STE53 paste at 2 d showed smaller pore entry size threshold value and lower overall porosities. This clearly shows the benefits of C-S-H nucleation seeding by refining the porosities. At later ages, i.e. 28 days, the overall porosities of BC-ref and BR-LC^3-42 are similar but the pore entry threshold value for BR-LC^3-42 is smaller, which is a signature of the pozzolanic reaction. BR-LC^3-42-STE53 showed the lowest overall porosities showing the benefits of C-S-H seeding.

3.4 Mechanical strength investigation for the mortars. To compare the mechanical strength performances, mortars with very similar viscosity have been prepared. The workability is also an important parameter. Therefore, these values were determined here. The free-flow values for BC were 224(3), 169(2) and 164(1) mm at mixing time (t_0), 30 and 60 min, respectively. For BR-LC^3-42, these values were 202(1), 172(1) and 162(1) mm at t_0, 30 and 60 min, respectively. The corresponding results for BR-LC^3-42-STE53 were 210(2), 191(1) and 178(1) mm, respectively. These values reflect a small slump retention loss but much less severe than those observed in Portland-based LC^3 using the same type of PCE. The values in parenthesis are the standard deviation of the slump measurements.

Compressive strength results are shown in Figure 3. For the BR-LC^3-42 binder, the compressive strength at 2 d was low, 14 MPa, reflecting the slow hydration rate of belite and that the contribution of pozzolanic reaction is not important at this age. This is a 46 % decrease respect to BC-ref, a consequence of the 42 wt% cement replacement. At 7 d, the compressive strength was 28 MPa, 26 % lower than the value for BC-ref. At this age, the pozzolanic reaction is contributing. Finally, at 28 d, the corresponding value for BR-LC^3-42 was 53 MPa, just 12 % less than that of BC-ref. Thus, the contribution of the pozzolanic reaction at this age is relatively more important. In any case, the compressive strengths for BR-LC^3-42 were low and therefore, strength enhancement by C-S-H nucleation seeding was attempted as described above. For BR-LC^3-42-STE53, the compressive strength value at 2 d was the same than that of the unseeded LC^3 mortar within the variability of the measurements. Therefore, it is concluded that if a hydration acceleration has taken place, its effect on the mechanical strength is only shown at ages earlier than 2 days.

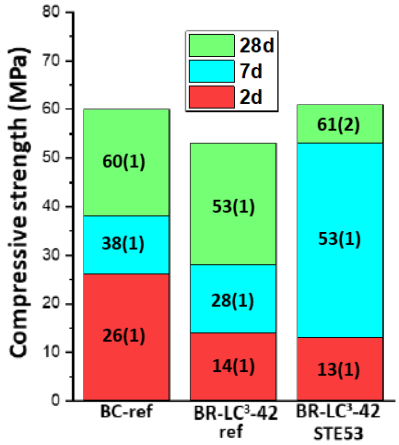


Figure 3. Compressive strength data for the studied mortars at 2, 7 and 28 days.

Conversely, the consequences of C-S-H nucleation seeding is remarkable at 7 d. This C-S-H seeded low-carbon binder develops 53 MPa at 7 d, a 39 % increase over BC-ref despite containing 42 wt% less cement. Moreover, the compressive strength increase compared to the unseeded binder, BR-LC^3-42, was 89 %. Clearly, the pozzolanic reaction is already significantly contributing at this age, and C-S-H seeding is enhancing it, likely through a more homogenous distribution of the hydrates in agreement with MIP results. However, spatially resolved techniques is required to firmly establish this key point. The mechanical strength for BR-LC^3-42-STE53 at 28 d was 61 MPa, presenting the same value as BC-ref, within the variability of the measurements. BR-LC^3-42-STE53 performs better than the unseeded binder by 8 MPa, which indicates the long-term benefits of C-S-H seeding.

3. Conclusions

Belite-rich limestone calcined clay cement binders have been prepared with similar fresh properties. The compressive strengths were measured at 2, 7 and 28 days of hydration. The use of STE53, a C-S-H nucleation seeding admixture, highly improves the compressive strength at 7 days. An 89% enhancement respect to the unseeded binder was measured. An improvement, relatively lower, is also measured at 28 days. Thermal and Rietveld analyses have been employed to determine the degree of reactions. This study indicates that the improvement in the performances, when using STE53, does no relate to belite phase hydration acceleration but partly due to accelerated C_4AF hydration and likely to a more homogenous hydration product arrangement within the matrix. Mercury intrusion porosimetry clearly shows lower porosities for the C-S-H seeded pastes.

Acknowledgements

Financial support from PID2020-114650RB-I00 research grant, co-funded by FEDER, is acknowledged.

References

Cuesta, A., Ayuela, A., Aranda, M.A.G. (2021) “Belite Cement and their Activation”, *Cement and Concrete Research,* 140: 106319

Morales-Cantero, A., Cuesta, A., De la Torre, A.G., Santacruz, I., Mazanec, O., Borralleras, P., Weldert, K.S., Gastaldi, D., Canonico, F., Aranda, M.A.G. (2022a) "C-S-H seeding activation of Portland and Belite Cements: an enlightening in situ synchrotron powder diffraction study", *Cem. Concr. Res.* 161: 106946.

Morales-Cantero, A., Cuesta, A., Torre, A.G.D. la, Mazanec, O., Borralleras, P., Weldert, K.S., Gastaldi, D., Canonico, F., Aranda, M.A.G. (2022b) "Portland and Belite Cement Hydration Acceleration by C-S-H Seeds with Variable w/c Ratios", *Materials* 15: 3553.

Redondo-Soto, C., Morales-Cantero, A., Cuesta, A., Santacruz, I., Gastaldi, D., Canonico, F., Aranda, M.A.G. (2023) “Limestone Calcined Clay Binders Based on a Belite-rich Cement”, *Cement and Concrete Research*, 163: 107018.

Scrivener, K. L., Avet, F., Maraghechi, H., Zunino, F., Ston, J., Hanpongpun, W., Favier, A. (2019) “Impacting Factors and Properties of Limestone Calcined Clay Cements (LC^3)”, *Green Materials*, 7: 3-14.

The 16th International Congress on the Chemistry of Cement 2023 (ICCC2023)
"Further Reduction of CO_2 -Emissions and Circularity in the Cement and Concrete Industry"
September 18–22, 2023, Bangkok, Thailand

Effect of relative humidity on carbonation of hardened cement paste particles under atmospheric CO_2 concentration

N. Saeki[1]*, L. Cheng[1], and I. Maruyama[1, 2]

[1] *The University of Tokyo, Graduate School of Engineering, Department of Architecture, Tokyo, Japan*
Email: n.saeki@bme.arch.t.u-tokyo.ac.jp
Email: chengluge@g.ecc.u-tokyo.ac.jp
[2] *Nagoya University, Department of Environmental Engineering and Architecture, Nagoya, Japan*
Email: i.maruyama@bme.arch.t.u-tokyo.ac.jp

ABSTRACT

Understanding of carbonation reactions is necessary to accurately assess the uptake of carbon dioxide in cementitious structures. In this paper, we investigated the effect of varying relative humidity (RH) from 23% to 95% on the progress of carbonation reactions in cement pastes ground under 75 μm. The experiment was done under atmospheric CO_2 concentration. Calcium carbonate (CC) formation and calcium hydroxide (CH) dissolution as well as the precipitated CC phases were quantitatively examined by TGA and XRD. Additionally, C-S-H decalcification and decomposition were measured qualitatively by ATR-FTIR. The results showed more CC was produced with increasing RH. CH kept dissolving at RH 75% or above but stopped dissolving midway at RH 58% or below. C-S-H decalcification was detected at RH45% or above, especially at RH 75% or above its decomposition to silica gel was clearly seen from FTIR spectra. It was also proven that precipitated CC phases depended on RH, which were only calcite at RH75% or above, while all three polymorphs coexisted at RH 33%, 45% and 58%.

KEYWORDS: *Atmospheric carbonation, relative humidity, reaction rate, C-S-H, CC polymorphs*

1. Introduction

Cement clinker inevitably emits CO_2 due to the calcination of limestone in its manufacturing process, but cementitious structures also have the ability to immobilize CO_2 in their lifetime, which is known as carbonation. So far, the assessment of CO_2 uptake has a large predictive range (Hyodo et al. (2020)), thus it is necessary to understand the mechanism of carbonation to evaluate the environmental load correctly. In this paper, the carbonation reaction was focused and the effect of relative humidity (RH) was investigated. To minimize the CO_2 diffusion effect, finely ground hardened cement paste (hcp) was used. Similar experiments have been already done, but those data were taken per single ingredient (Steiner et al (2020), Boumaaza et al. (2020)) or for shorter experimental duration (Zajac et al. (2020)). Additionally, they were conducted in higher CO_2 concentration than atmospheric to shorten the duration, which may be different from real situation. Therefore, the reaction at atmospheric CO_2 concentration was investigated.

2. Experiment

The hcp was prepared by mixing Ordinary Portland Cement (OPC) with tap water at w/c = 0.5. The composition of the OPC used is shown in Table 1 and Table 2. A Hobart mixer was used for mixing. After mixing at low speed for 60 seconds, the mixture was paused for 30 seconds, and then mixed again at high speed for 90 seconds. Then it was periodically mixed to minimize the segregation, cast into cylindrical moulds (5 x 10 cm) in two layers and cured in water at 20°C for 38 weeks. After curing, samples were dried at 105 °C for 7 days. The dried samples were coarsely crushed to under 300 μm by a jaw crusher, and then ground to under 75 μm by a planetary ball mill in a nitrogen atmosphere. After grinding, they were stored in a vacuum desiccator.

Table 1 Chemical Composition of OPC

	CaO	SiO_2	Al_2O_3	Fe_2O_3	SO_3	MgO	TiO_2	K_2O	Na_2O	SUM
Chemical Composition [mass %]	64.7	20.7	5.0	2.7	2.6	1.2	0.3	0.3	0.2	97.7

Table 2 Mineral Composition of OPC

	C3S	C2S	C3A	C4AF	Calcite	Bassanite	Periclase	Gypsum	SUM
Mineral Composition [mass %]	51.3	22.7	9.1	7.9	5.8	2.3	0.5	0.4	99.9

Carbonation experiment was conducted in desiccators into which ambient air constantly pumped at 4 L/min by the air pump. The ambient air was constantly monitored, and confirmed the temperature was at 20 ± 1 °C and CO_2 concentration was 500 ~ 1000ppm. The air was bubbled through saturated solution to reach the target RH. The salts used were CH_3COOK (Theoretical RH 23% at 20 °C), $MgCl_2$ (33%), K_2CO_3 (45%), NaBr (58%), NaCl (75%), KCl (85%) and KNO_3 (95%). About 500 mg of the sample was prepared in each 20 ml plastic container, and subjected to carbonation for 1, 3, 7, 14 days. After target carbonation periods, the sample was stored to vacuum desiccator to prevent further carbonation.

Thermogravimetric Analysis (TGA) was performed with Netzsch STA-449 under N_2 flow for 70 ml/min. The heating rate was 10 K/min. The amount of calcium hydroxide (CH) and calcium carbonate (CC) were determined by tangential method (Scrivener et al. (2017)). Powder X-ray Diffraction (XRD) was carried out using PANalytical EMPEREAN with the follwing settings: Cu-Kα X-ray source, 45 kV tube voltage, 40 mA tube current, 2θ = 5 to 70◦ scanning range, 0.026◦ step width and total scanning time of 51 min. Rietveld analysis was also done with TOPAS 6.0 to quantify the amount of calcium carbonate polymorphs. i.e., calcite, aragonite and vaterite. Here, total amount of CC was calculated by TGA, then it was distributed based on the ratio of CC polymorphs. FTIR was performed with ATR method with Bruker ALPHA II. Specta from 400 to 4000 cm^{-1} were taken with resolution of 2 cm^{-1}, and the average of 128 scans were used.

3. Results and Discussion

TGA result is shown in Fig. 1. The precipitated CC increased more at higher RH. This is contrary to the reaction rate of the real structures that RH 60 to 80% is the optimal, where the whole reaction rate is governed by CO_2 transport and too high RH slows down the rate. However, required time for CO_2 transport is almost negligible when discussing tens of micrometer order like the present research (Georget et al. (2020)). The maximum CC amount when all CaO turns to CC is about 1.16 g/g_cement in this cement composition, thus all the samples did not reach the theoretical maximum at 14 days of carbonation.

CH dissolution proceeded continuously at RH 75% or above, and it completely disappeared at RH 95%. At RH 58% or below, however, its dissolution stopped midway. At 14 days at those RHs, about 0.12 g/g_cement of CH remained in the samples. This was presumably due to the formation of CC on the surface of the CH, which protected CH inside and hindered its dissolution (Steiner et al (2020)). Although CH dissolution stopped midway, the amount of CC increased at the same period at RH 45% and 58%, meaning this CC was not derived from CH. Considering that other calcium hydrate products were relatively scarce, the CC increase after 3 days came from carbonation of C-S-H. At RH 33% or below, especially at RH 23%, the CC increase slowed down with the end of the CH dissolution, meaning that C-

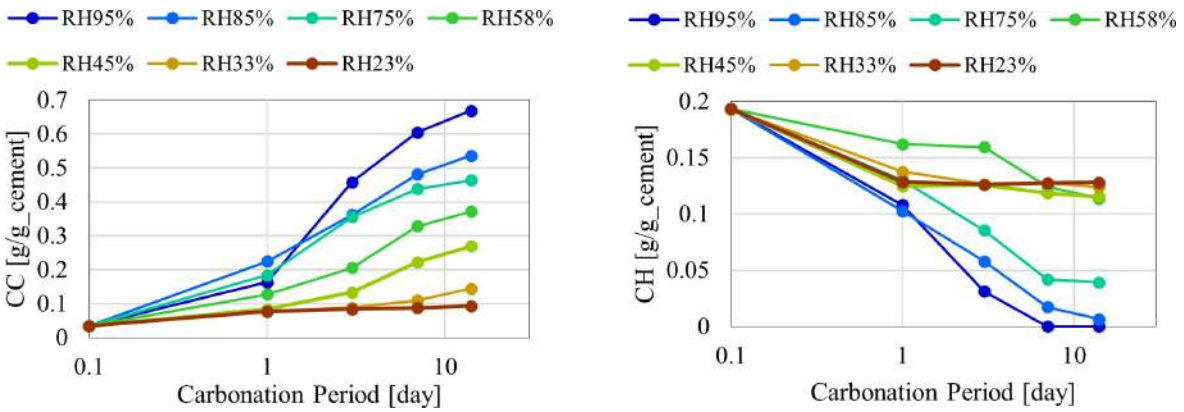


Fig. 1 The amount of calcium carbonate (CC, left) and calcium hydroxide (CH, right) from TGA.

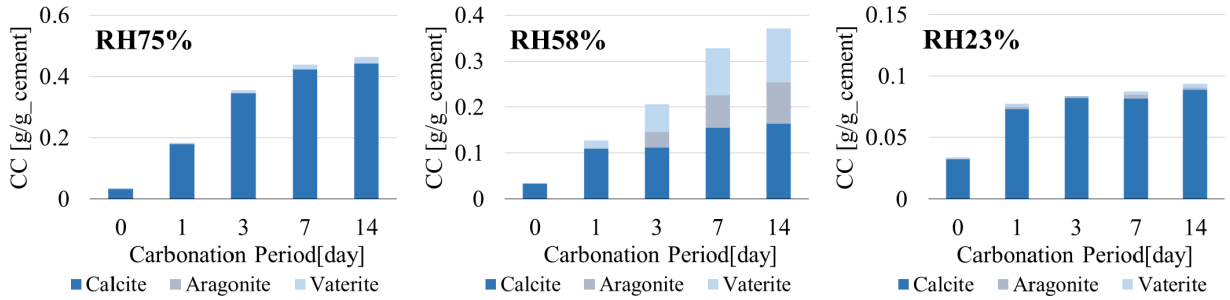


Fig. 2 Evolution of the amount of calcium carbonate polymorphs at RH 75%, 58% and 23%.

S-H at those RHs did not convert to CC, which will be discussed later with FTIR data.

Rietveld analysis results based on XRD spectra are shown in Fig.2. Due to the limitations of the page, only characteristic results are present in this paper. Only calcite was the precipitated product at RH 75% or above. At RH 58%, calcite increased after 1 day of carbonation, later however, the increase in calcite stalled and aragonite and vaterite started to increase at the same time. Considering that the amount of CH did not change significantly at that time (Fig. 1), those precipitated aragonite and vaterite were derived from C-S-H carbonation. At RH45% and 33% (not shown) also had the same CC polymorph trends. The precipitated phase was consistent with the report by Black et al (2007) who observed aragonite and vaterite formation from C-S-H condition in ambient condition. At RH 23%, only calcite was detected.

FTIR spectra of the samples with carbonation duration of 14 days and uncarbonated hcp are shown in Fig.3. ATR method depends on how the sample covers the diamond crystal, thus the result cannot be discussed quantitatively. Wavenumber range of 800 to 1200 cm^{-1} indicates the stretching vibrations of Si-O bonds (Yu et al (1999)). The peak at around 960 to 970 cm^{-1} corresponds to Q^2 peak in the C-S-H, and this peak position is known to shift to higher wavenumber with the decrease of Ca/Si ratio. Fig.3 shows that uncarbonated hcp had the peak at 957 cm^{-1}, whilst that peak shifted to ~970 cm^{-1} at RH45% or above. At RH33% or below, however, the peak position was lower than 970 cm^{-1}, which suggested C/S ratio of these samples were higher than those above RH45% due to less severe carbonation. Additionally, new Si-O stretching peak appeared at range above 1050cm^{-1} at higher RHs. The hump around 1060 cm^{-1} was from the Q^3 and Q^4 peak, i.e., amorphous silica gel (Wu and Ye (2016)). The humps around 1080 cm^{-1} and 1130 cm^{-1} were also considered to be Q^3 and Q^4, respectively (García Lodeiro et al (2009)). At RH 75% or above these humps can be clearly recognized. They can be seen slightly at RH 58% and 45%, but not detected at RH 33% or below.

When amorphous silica was detected (i.e., at RH45% or above), the Q^2 peak shifted to ~970 cm^{-1}. It was reported by Sevelsted and Skibsted (2015) that C-S-H carbonation progressed in two steps; first Ca ion in interlayer dissolves and Ca/Si in C-S-H drops to ~0.67 (decalcification), then Ca in main layer dissolves and silica gel generates (decomposition). Steiner et al (2020) also observed the Q^2 peak shift first and C/S lowered to 0.7, then amorphous silica gel peak emerged later. Taking these into consideration, the followings can be guessed; 1) At RH75% or above, decomposition as well as decalcification occurred. 2) At RH 58% and 45%, C-S-H decalcified but not decomposed heavily (Q^3 and Q^4 peaks were very small). 3) At RH 33% and 23%, decalcification was not finished completely. These speculations should be confirmed by measuring Ca/Si ratio or the ratio among Q^1 to Q^4 in future experiments.

FTIR spectra also give information about CC polymorphs in their *v2* (out-of-plane bending, ~850 cm^{-1}), *v3* (asymmetric stretching, 700 to 750 cm^{-1}) and *v4* (in-plane bending, 1300 to 1600 cm^{-1}) region. Only calcite was detected at RH 75% or above, while at RH 33 to 58% aragonite and vaterite were also detected. The peak of hydroxy group in CH was seen in the region of ~3640 cm^{-1}, which gradually decreased at higher RH and completely disappeared at RH 75% or above. These match XRD results.

4. Conclusions

Effect of RH on carbonation reaction was investigated. Data at wide range of RH (from 23% to 95%) under atmospheric CO_2 concentration has not been thoroughly investigated so far. We were able to minimize the effect of CO_2 transport and focus on the reaction itself using the finely ground cement paste. The samples were measured with TGA, XRD and FTIR, and conclusions obtained were as follows.

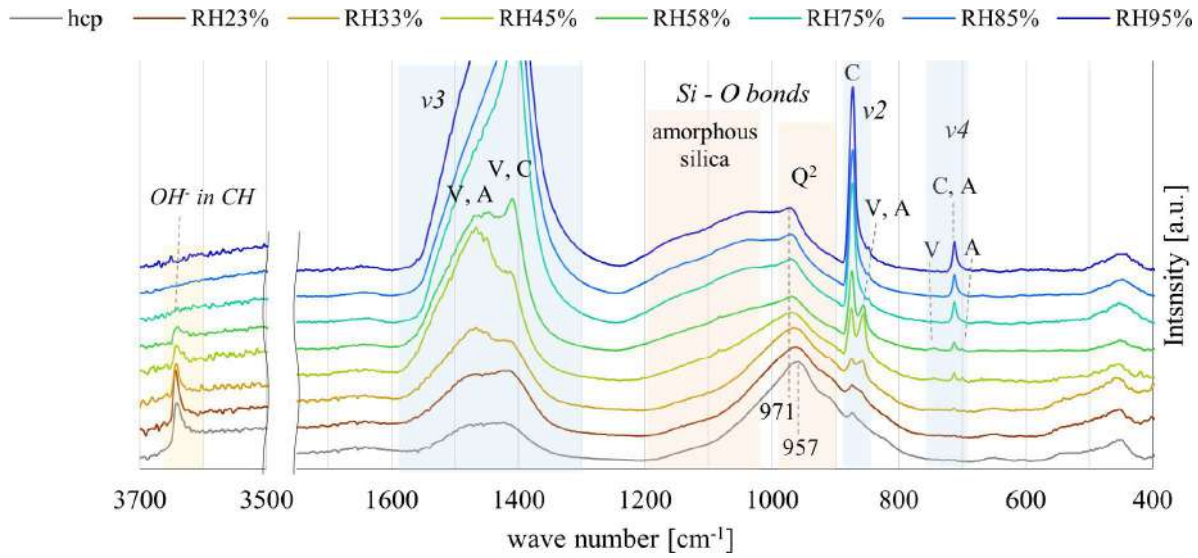


Fig.3 FTIR spectra after 14 days of carbonation. C = Calcite, A = Aragonite, V = Vaterite.

- Higher RH condition promoted more CC precipitation, because CO_2 transport was not rate-controlling step due to the small particle size.
- At RH 75% or above, CH continued to dissolve through the experiment and C-S-H experienced both decalcification and decomposition. Produced CC phase was only calcite.
- At RH 58% and 45%, CC amount kept increasing, while CH dissolution stopped midway possibly due to the formation of CC on its surface. The peak shift in FTIR spectra showed decalcification of C-S-H, but it did not decompose severely. All calcite, aragonite and vaterite were detected.
- At RH 33% and 23%, CH dissolved similar amount to RH 58% and 45%, but CC did not increase compared to those RHs. C-S-H did not decalcify completely.

It would be possible to link the reaction rate obtained to the local RH state inside the materials when considering carbonation degree of cementitious structures.

Acknowledgements

This paper is based on results obtained from a project, JPNP21023, commissioned by the New Energy and Industrial Technology Development Organization (NEDO).

References

Black, L. et al. (2007) 'Structural features of C-S-H(I) and its carbonation in air-A Raman spectroscopic study. Part II: Carbonated phases.' Journal of the American Ceramic Society, 90, 908–917

Boumaaza, M. et al. (2020) "The CO2-binding capacity of synthetic anhydrous and hydrates: Validation of a test method based on the instantaneous reaction rate," Cement and Concrete Research, 135, 106113

Hyodo, H. et al. (2022) 'A STUDY ON CALCULATING CO_2 UPTAKE DUE TO CARBONATION DURING CONCRETE LIFE-CYCLE', Cement Science and Concrete Technology, 74: 333-340 (in Japanese)

García Lodeiro, I. et al. (2009) 'Effect of alkalis on fresh C–S–H gels. FTIR analysis' Cement and Concrete Research, 39(3): 147–153.

Georget, F. et al. (2020) 'Characteristic lengths of the carbonation front in naturally carbonated cement pastes: Implications for reactive transport models' Cement and Concrete Research 134, 106080

Scrivener, K., Snellings, R. and Lothenbach, B. (eds) (2017) 'A Practical Guide to Microstructural Analysis of Cementitious Materials', CRC Press

Sevelsted, T.F. and Skibsted, J. (2015) 'Carbonation of C–S–H and C–A–S–H samples studied by 13 C, 27 Al and 29 Si MAS NMR spectroscopy', Cement and Concrete Research, 71: 56–6

Steiner, S. Et al. (2020). "Effect of relative humidity on the carbonation rate of portlandite, calcium silicate hydrates and ettringite." Cement and Concrete Research, 135, 106116.

Wu, B. and Ye, G. (2016) 'CARBONATION MECHANISM OF DIFFERENT KINDS OF C-S-H: RATE AND PRODUCTS'., RILEM Proceedings Pro 113, Lyngby, Denmark: 276-285

Yu, P., Kirkpatrick et al. (1999) ‘Structure of Calcium Silicate Hydrate (C-S-H): Near-, Mid-, and Far-Infrared Spectroscopy’, Journal of the American Ceramic Society 82, 742–748
Zajac, M. et al. (2022) ‘Semi-dry carbonation of recycled concrete paste’, Journal of CO2 Utilization, 63, 102111

The 16th International Congress on the Chemistry of Cement 2023 (ICCC2023)
"Further Reduction of CO_2 -Emissions and Circularity in the Cement and Concrete Industry"
September 18–22, 2023, Bangkok, Thailand

Optimizing calcined clay geopolymer production

I.P. Segura[1*], P.A. Jensen[1], A.J. Damø[1], M. Canut[2], and L.S. Jensen[2]

[1] *Technical University of Denmark, Copenhagen, Denmark*
**Email: isapol@kt.dtu.dk, ajp@kt.dtu.dk, paj@kt.dtu.dk*

[2] *FLSmidth, Copenhagen, Denmark*
Email: Mariana.Canut@FLSmidth.com, lasj@FLSmidth.com

ABSTRACT

Clay minerals are gaining attention as geopolymer precursors due to their aluminosilicate composition and global availability. This study focuses on optimizing calcined clay geopolymer production, aiming for acceptable setting and compressive strength, as well as evaluating its practical feasibility in the construction industry. This work compares an identical high-grade metakaolin geopolymer mix synthesized by two methods: 1) an alkali activator is added as a liquid (two-part mix) and 2) as a solid powder (one-part mix). The results show that one-part metakaolin geopolymers require a high-water demand (water-to-solids ratio of 0.69), have a slower setting time than two-part mix and the 28-day compressive strength was 17.2 MPa for the one-part mix, and 21.1 MPa for the two-part mix. In addition, since metakaolin is already widely used in the paper, ceramics, and paint industry, this study also evaluates the suitability of other abundant calcined clays (e.g. halloysite and montmorillonite) besides metakaolin as two-part geopolymer precursors. Calcined halloysite two-part mix had a fast setting and reached a 28-day compressive strength of 17 MPa, whereas the calcined montmorillonite two-part mix had a slow final setting and reached 13 MPa. From these results, it is recommended that other pre-treatments beyond calcination are explored as an attempt to increase the 28-day compressive strength (>32.5 MPa).

KEYWORDS: *Geopolymers, calcined clays, one-part mix, two-part mix*

1. Introduction

The cement industry needs to reduce its CO_2 emissions while satisfying the increasing cement demand from the global economy. Alternative binders such as geopolymers are a plausible solution to reduce carbon emissions. Nevertheless, geopolymers have limitations that constrain their widespread use. This includes high prices of some raw materials, handling of hazardous alkaline components in the production process, and uncertainties on which mix designs lead to acceptable settings and strengths by cement standards and regulations. In addition, mineral clays are typical geopolymer precursors, rich in silica and alumina, and constitute 2/3's of the Earth crust. Generally, they need to be calcined to enhance their reactivity (Dewi et al (2018)).

Most current research and applications of geopolymers are based on a two-part mix, which results from the reaction of a concentrated alkali aqueous solution and a solid precursor (Provis et al. (2014)). Their large-scale utilization is probably limited by the handling of hazardous alkaline solutions, especially for in-situ applications. Meanwhile, one-part mix is formed by mixing dry-form alkali activators with the solid precursor and water, quite similarly to how Portland cement paste is produced. Though there is significant amount of research published on the mechanical properties and mix design options of one-part synthesis (Ma et al (2019)), there is a lack of documentation on the differences between one- and two-part geopolymer using identical mix designs. Thus, this work investigates how the setting time and compressive strength of metakaolin geopolymers are influenced by the production method. Furthermore, since metakaolin is rather expensive and with low availability, the potential of using other calcined clays (halloysite and montmorillonite) in a two-part mix geopolymer production is also going to be investigated in this study.

2. Materials and methods

The used clay-based precursors and their elemental compositions measured by X-ray Fluorescence (XRF) are shown in Table 1. As commercial alkali activators, sodium hydroxide (NaOH) powder was obtained from Sigma Aldrich (97% purity), and solid sodium silicate (Na_2SiO_3) was purchased from VWR with a chemical composition of 50.4% Na_2O and 46.15% SiO_2.

Table 1. Chemical oxide composition (wt.%) of each clay precursor measured by XRF.

Clay	SiO_2	Al_2O_3	Na_2O	K_2O	TiO_2	Fe_2O_3	CaO	MgO	P_2O_5	SO_3	LOI
Metakaolin	53.0	43.8	0.23	0.19	1.70	0.43	0.02	0.03	0.03	0.03	0.46
Kaolinite	49.27	36.98	0.03	1.82	0.57	0.77	0.07	0.28	0.07	0.03	10.11
Halloysite	44.77	37.91	0.01	0.04	0.04	0.58	0.10	0.05	1.15	0.18	15.03
Montmorillonite	74.21	13.39	0.34	1.69	0.56	2.40	0.34	1.13	0.04	0.03	5.4

Two different approaches have been considered to optimize the production of calcined clay geopolymers:

1. Comparison of one-part and two-part mix production using metakaolin as the precursor and identical mix designs. The selected mix formulation (Table 2) is based on previously reported ratios (Liew et al (2017)), except that the water-to-solids (w/s) ratio was set quite higher than that from optimal values (w/s≈0.5) due to the poor workability of one-part metakaolin at lower w/s ratios.

Table 2. Mix design of one-part and two-part metakaolin geopolymer.

Metakaolin (g)	NaOH (g)	Solid-Na_2SiO_3 (g)	Water (g)	w/s (-)
400	22	46	325	0.69

2. Use of other clay types as two-part geopolymer precursors. Kaolinite and halloysite were calcined at 750ºC for 0.5h, whereas montmorillonite was calcined at 850ºC for 0.5h. Commercial metakaolin was used as the calcined clay reference (REF). All calcinations were performed in a lab-scale muffle furnace. Thereafter, two-part geopolymers were synthesized with a w/s ratio set at 0.52 and the mix proportions shown in Table 3.

Table 3. Mix design of two-part calcined clay geopolymers.

Clay (g)	NaOH (g)	Solid-Na_2SiO_3 (g)	Water (g)	w/s (-)
400	53	181	329	0.52

The sample preparation for one-part geopolymers consisted in mixing the dry activators (NaOH and Na_2SiO_3) with the solid precursor for 2 min at low speed. Then, water was added to the bowl and mixing continued for another 4 min. Whereas the two-part geopolymers were prepared by dissolving NaOH in half the total amount of water and the Na_2SiO_3 in the other half. Each solution was then left to cool down to room temperature for 2 h, while continuous stirring. Thereafter, the solid precursor and the solutions of NaOH and Na_2SiO_3 were mixed for 4 min.

The setting time was tested using an automatic Vicat apparatus with continuous penetration at ambient conditions (E044-03N), following EN196-3 standard. The fresh homogenous mixtures were cast into 50 mm cubes and vibrated for 30 seconds to remove any trapped air bubbles. The samples were then cured at 21°C ± 2 °C and 80% relative humidity (RH). They were demolded after 24 hours and left in the curing chamber until testing. Compressive strength tests were carried out using a Digitec E160-01D testing machine with a constant loading rate set at 0.75 MPa/s. Tests were performed after 3, 7, and 28 days. The reported values correspond to the average of three measurements.

3. Results and discussion

3.1 Comparison of one-part and two-part metakaolin geopolymers

Despite having the same mix design and complying with the setting EN196-3 requirement (initial setting > 45 min, and final setting < 600min), a clear difference between the setting times of each mixing method can be observed (Table 4). The one-part mixture has a slower initial and final setting time with respect to the two-part mixture. The final set of one-part metakaolin has a delay of 15% when compared to two-part.

This is likely due to the mixing of alkali activator powder with the dry precursor before dissolved in water, which can delay the dissolution of the precursors as well as the following gelation and condensation reactions.

Table 4. Initial and final setting time of one- and two-part metakaolin (MK) geopolymers.

Geopolymer	Initial setting (min)	Final setting (min)
MK two-part	47±1	105±2
MK one-part	74±5	121±4

Figure 1 shows that both mixes present a rapid strength development up to 3 days, and then the two-part mix reaches higher compressive strengths. Specifically, at 28 days, the one-part metakaolin reaches 17.2 MPa, and two-part metakaolin reaches 21.1 MPa. This strength difference could be explained by the delayed dissolution of the precursors in the alkali solution in one-part mix (Zhang et al (2021)). Both mixes are below the required strength at 28 days by the EN197-1 standard (≥32.5 MPa). This is probably due to the high w/s ratio used, which was given from the high-water demand in the metakaolin one-part mix.

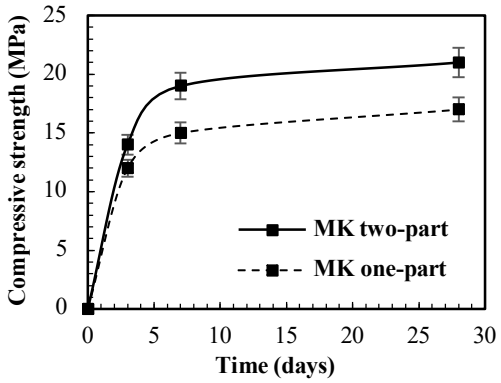


Figure 1. Compressive strength development of two-part and one-part metakaolin (MK) geopolymer.

3.2 Other calcined clays as two-part geopolymer precursors

Table 5 shows that metakaolin, calcined kaolinite, and calcined montmorillonite lead to geopolymers that set within the EN196-3 requirements. In contrast, calcined halloysite geopolymer sets extremely fast, not complying with the standards.

The setting time of the pastes is directly related to the composition and structure of the clays. In particular, halloysite has the lowest content of soluble SiO_2 (see Table 1), and this tends to accelerate setting times since there is a low amount of silica for the reaction, and the geopolymerization takes less time to complete its major portion of the reaction. Moreover, the nano-tubular structures characteristic of halloysite clay might require a higher water demand than the one used in the present mix design, and the water might be consumed in the reaction and evaporated faster. In addition, it has been previously observed that calcined halloysite geopolymers set faster than metakaolin geopolymers (Kaze et al (2021)).

Finally, at SiO_2/Al_2O_3 ratios above 4, there is probably a lack of soluble aluminum that can stabilize the aluminosilicate gel (Chindaprasirt et al (2012)), and there is an excess of silica dissolution; delaying the setting time and decreasing the rate of polymerization. This is likely the case for montmorillonite, in which the longest initial and final setting time are observed.

Table 5. Initial and final setting time of two-part calcined geopolymers

Geopolymer	Initial setting (min)	Final setting (min)
Commercial Metakaolin (REF)	95±1	129±4
Calcined 750 ℃ Kaolin	122±2	169±3
Calcined 750 ℃ Halloysite	30±1	48±2
Calcined 850 ℃ Montmorillonite	144±5	508±6

Similarly to the setting time trends, the compressive strength is directly influenced by the soluble content of SiO_2, Al_2O_3 and Na_2O. As shown in Figure 2, it is very likely that montmorillonite-based geopolymer

was not properly activated, as there is no early-strength gain, and after 28 days only an average of 13 MPa has been reached. Calcined kaolin in a muffle furnace at 750℃ for 0.5h does not seem to be as reactive as commercial metakaolin, leading to 24 and 36 MPa compressive strength, respectively. Nonetheless, from the tested clays, those having a 1:1 layer structure (kaolinite and halloysite) could become potential aluminosilicate precursors. This is because they are rich in SiO_2 and Al_2O_3, require lower calcination temperatures than montmorillonite, and can achieve 28-day compressive strengths ≥17 MPa, which is sufficient for non-structural applications (>15MPa) in developing countries (Rodsin et al (2020)). Further calcination conditions or pre-treatments (e.g. mechanical, chemical or a combination) should be explored to increase the clays reactivity and optimize the compressive strength of the clay-based geopolymers.

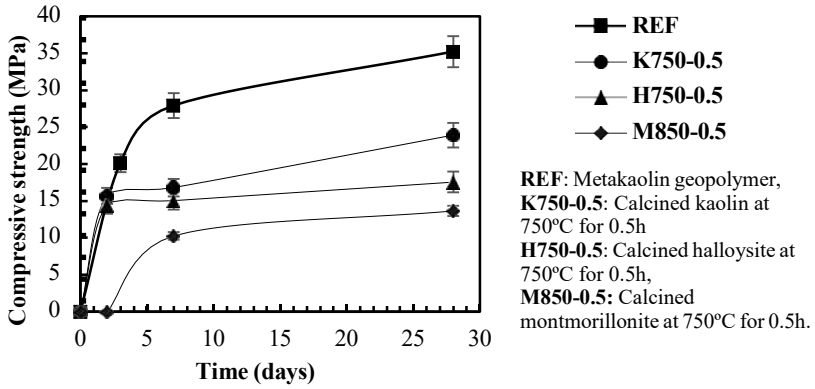


Figure 2. Compressive strength development of two-part calcined clay geopolymers.

4. Conclusions

Two-part metakaolin geopolymers have shown to reach higher compressive strength and faster setting time than when produced as one-part geopolymer. This is probably due to the delayed dissolution of the precursors in one-part mix. Two-part mixes are suitable for pre-cast applications, where high-volume hazardous solutions can be handled in a controlled environment. However, one-part mixes would be a more convenient manufacturing method since it would be an easier and safer approach for in-situ casting. Thus, further investigations on optimizing the water demand in one-part mixes are recommended. In addition, since metakaolin has a low availability and high price, other calcined clays such as halloysite and montmorillonite have been considered as geopolymer precursors. For the tested samples, their average 28-day compressive strength was below 20MPa. Thus, further activation methods (e.g. mechanical or chemical) beyond calcination shall be explored to enhance especially non-kaolinite mineral clays.

References

Dewi, R., Agusnar, H., and Alfian, Z. (2018) "Characterization of technical kaolin using XRF, SEM, XRD, FTIR and its potentials as industrial raw materials", *Journal of Physics: Conference Series*,Vol. 1116, No. 4, p. 042010.

Provis, J. L. and Bernal S.A. (2014) "Geopolymers and related alkali-activated materials", *Annual Review of Materials Research*, 44: 299-327.

Ma, C., Zhao, B., Guo, S., Long, G., and Xie, Y. (2019) "Properties and characterization of green one-part geopolymer activated by composite activators", *Journal of Cleaner Production*, 220, 188-199.

Liew, Y. M., Heah, C. Y., and Kamarudin, H. (2016) "Structure and properties of clay-based geopolymer cements: A review", *Progress in Materials Science*, 83, 595-629.

Zhang, H. Y., Liu, J. C., & Wu, B. (2021). Mechanical properties and reaction mechanism of one-part geopolymer mortars. *Construction and Building Materials*, *273*, 121973.

Kaze, C. R., Adesina, A., Alomayri, T., Assaedi, H., Kamseu, E., Melo, U. C., and Leonelli, C. (2021) "Characterization, reactivity and rheological behaviour of metakaolin and Meta-halloysite based geopolymer binders", *Cleaner Materials*, 2, 100025.

Chindaprasirt, P., De Silva, P., Sagoe-Crentsil, K., and Hanjitsuwan, S. (2012) "Effect of SiO2 and Al2O3 on the setting and hardening of high calcium fly ash-based geopolymer systems", *Journal of Materials Science*, 47(12): 4876-4883.

Rodsin, K., Hussain, Q., Suparp, S., & Nawaz, A. (2020) "Compressive behavior of extremely low strength concrete confined with low-cost glass FRP composites", *Case Studies in Construction Materials*, 13, e00452.

The 16th International Congress on the Chemistry of Cement 2023 (ICCC2023)
"Further Reduction of CO_2 -Emissions and Circularity in the Cement and Concrete Industry"
September 18–22, 2023, Bangkok, Thailand

Physical properties and CO_2 fixation of concrete using carbonated cement slurry

T. Hayakawa[1*], T. Anno[2], T. Nozaki[3] and T. Noguchi[4]

[1] *Central Research Laboratory, Taiheiyo Cement Corporation, Chiba, Japan*
Email: Takayuki_Hayakawa@taiheiyo-cement.co.jp
[2] *Central Research Laboratory, Taiheiyo Cement Corporation, Chiba, Japan*
Email: Toshinari_Anno@taiheiyo-cement.co.jp
[3] *Environmental Business Development Department, Taiheiyo Cement Corporation, Tokyo, Japan*
Email: Takahito_Nozaki@taiheiyo-cement.co.jp
[4] *Department of Architecture, Graduate School of Engineering, The University of Tokyo, Tokyo, Japan*
Email: noguchi@bme.arch.t.u-tokyo.ac.jp

ABSTRACT

In this study, we immobilized 335 kg/t-cem of CO_2 in cement slurry and mixed them properly in concrete to immobilize the CO_2. Fine calcite and hydrate were formed in the cement slurry after the carbonation reaction, and their morphology varied depending on the temperature conditions and the fluidity of the cement paste. Concrete tests using carbonated cement slurry were conducted at a ready-mixed concrete plant. The results showed that the amount of water-reducing agent added to obtain the target slump and the slump loss with elapsed time were smaller in the 10°C environment than in the 20°C environment. This phenomenon was considered to be related to the morphology of calcite formed in the carbonated slurry, although the difference in environmental temperature was also a factor. Concrete with carbonated cement slurry had shorter setting time and much less bleeding than that without carbonated cement slurry. The compressive strength of the concrete with the carbonated slurry was higher than that without. Furthermore, an increase in strength from 28 to 91 days of age was also observed.

KEYWORDS: *Carbonated cement slurry, Calcium Carbonate, Compressive strength, CO_2 fixation, CCU*

1. Introduction

In recent years, the reduction of greenhouse gases such as CO_2 is a pressing issue from the viewpoint of global warming control, and various efforts are being made. Concrete, which is mainly composed of cement, has the property of absorbing and fixing CO_2. Monkman et al (2016) investigated the use of dry ice as an admixture to accelerate setting of concrete. However, much of the dry ice is easily dissipated into the atmosphere by sublimation. On the other hand, Monkman and Meyer (2022) reported that carbon dioxide treatment of wash water generated as a by-product of the ready-mixed concrete production process can mineralize 28 mass% of CO_2 in the treated solids, and that using them as mixing water improves compressive strength more than using untreated wash water. In this study, we investigated the efficient addition and mixing of carbonated cement slurry (hereafter referred to as carbonated slurry) to fresh concrete and evaluated the basic performance and CO_2 fixation of the concrete.

2. Study of conditions for production of carbonated slurry

A schematic of the equipment used to produce the carbonated slurry we studied is shown in figure 1. Cement slurry with a water-cement ratio of 300% was circulated in a reaction tank filled with CO_2 and reacted with CO_2. The relationship among the amount of CO_2 injected during the CO_2 injection process, the pH of the cement slurry, and the amount of CO_2 fixed is shown in figure 2. The amount of CO_2 immobilized in the carbonation slurry was determined by calculating the amount of calcination of solids

at 550-800°C. The amount of CO_2 immobilized was 335 kg/t-cem at a CO_2 injection rate of 360 kg/t-cem. In other words, this method was capable of immobilizing 93% of the injected CO_2 in cement slurry. The specific surface area of the solids was 13810 cm^2/g, approximately four times that of ordinary Portland cement (3360 cm^2/g). The particle size distribution of the solids is shown in figure 3. The solids have a peak at approximately 7 μm, indicating that a large amount of fine calcium carbonate particles were produced.

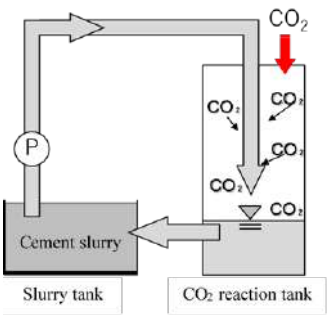


Figure 1. Carbonated slurry equipment

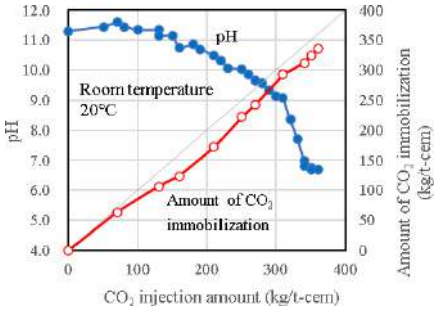


Figure 2. Amount of CO_2 fixation

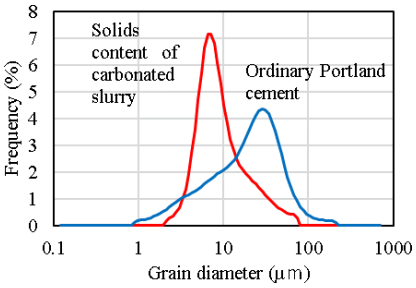


Figure 3. Particle distribution of solids

Subsequently, we investigated the morphology of calcium carbonate and cement hydrates formed when CO_2 is blown into cement slurries at different temperatures. Reflected electron images of solids dried after blowing CO_2 into cement slurry at 10°C and 30°C are shown in figure 4. CO_2 was blown into the cement slurry until the amount fixed in the cement slurry was 270 kg/t-cem. Flow test results for a paste with 15% replacement of solids with cement are shown in figure 5. Fine calcite and hydrates were formed in the solids, and their morphology depended on the temperature conditions: at 10°C, independent cubic calcite crystals were dispersed mostly outside the cement clinker particles; at 20°C and 30°C, spindle-shaped calcite crystals were formed covering the clinker particles. The solids at 20 and 30°C showed a significant decrease in the calcium-silica ratio of the clinker particles, indicating that they may have been transformed into silica gel. Flow tests of cement paste mixed with these solids showed that the solids with CO_2 blown in at 10°C had better flowability than those at 20°C and 30°C.

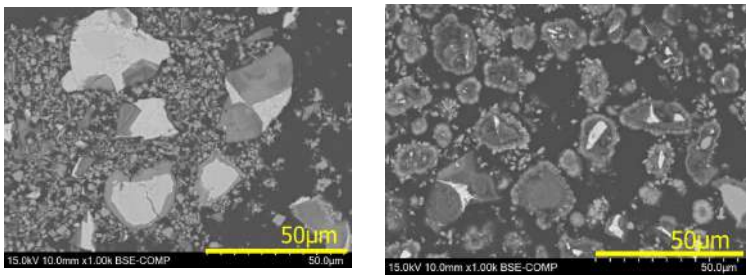


Figure 4. Reflected electron images of solids (L:10℃ R:30℃)

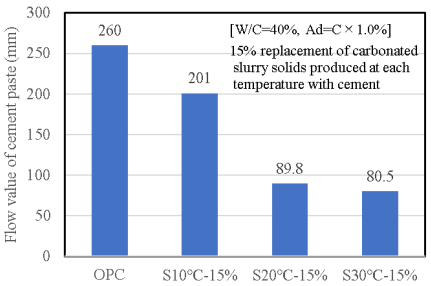


Figure 5. Cement paste flow

3. Evaluation of concrete mixed with carbonated slurry

Carbonated slurry production and concrete tests were conducted at a ready-mixed concrete plant under the average (approx. 20°C) and cold (approx. 10°C) temperature seasons.

3.1 Concrete mix design and mixing methods

Regarding the materials used, the carbonation slurry fixed approximately 20 mass% of CO_2 in the solids was prepared in this experiment. Assuming that the total amount was fixed as calcium carbonate, that amount corresponds to about 46 mass% of the carbonation slurry solids. The secondary electron image of the solid is shown in figure 6. The solids were agglomerated rhombohedral calcium carbonate, forming particles of 5 to 10 μm in size. Figure 7 shows a conceptual diagram of mix design for concrete using carbonated slurry. Ws and Cs were calculated by measuring the liquid-solid ratio using an infrared moisture meter. The standard product without carbonation slurry was designated PL-C, and the concrete mixed with carbonation slurry was designated CO_2-C. Table 1 shows the concrete mixes used in the

concrete tests. The cement was ordinary Portland cement, the fine aggregate (S1-S3) was crushed sand, and the coarse aggregate was crushed limestone. The target slump was set at 18 ± 2.5 cm and the target air content at 4.5 ± 1.5%, and the admixture type and its addition rate were selected. In addition, a two-step mixing method was adopted for CO_2-C to ensure fluidity.Table 2 shows the concrete mixing method.

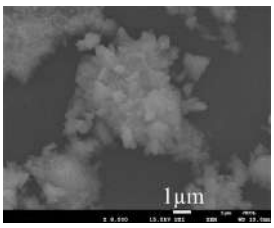


Figure.6. Secondary election image of solids

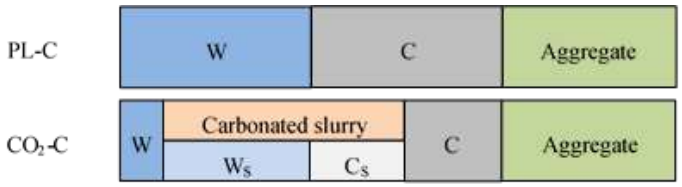


Figure 7. Concept of carbonated slurry in concrete

Table 1. Mix proportion of concrete

Type of specimen	W/C (%)	s/a (%)	Unit weight (kg/m³)								Ad (C×%)	SP (C×%)
			W		C		S1	S2	S3	G		
			Ws	W	Cs	C						
PL-C	54.8	48.2	183		334		294	126	421	948	1.0	—
CO_2-C			75	108	43	291					—	1.0

Table 2. Method of concrete mixture

PL-C	(W+C+S+G+Ad) → Mixing [1min]→ Discharging
CO_2-C	(C+S+G+Carbonated slurry) → Mixing [1min]→ (W+SP) → Mixing[1min]→ Discharging

3.2 Test result

The slump and air content of CO_2-C were within the target range by utilizing a superplasticizer and the two-step mixing method. Figure 8 shows the slump of the concrete. The temperature behavior of the specimens is shown in figure 9, and the results of bleeding tests conducted at 20°C are shown in figure 10. Slump loss was lower at 10°C than at 20°C. This could be due to the effect of differences in ambient and concrete temperatures on the hydration reaction rate. On the other hand, an effect due to the morphology of solids formed in the carbonation slurry at different temperatures was also considered. The specimen temperature of CO_2-C showed an earlier appearance of the second peak than that of PL-C in both the 10°C and 20°C environments, and the maximum temperature was about 2 to 3°C higher. In addition, the amount of bleeding was significantly reduced in CO_2-C compared to PL-C, and the setting time was also shortened by 2 to 3 hours. Japan Cement Association (2001) stated that the substitution of calcium carbonate powder with a specific surface area exceeding 7100 cm^2/g in cement increases the rate of hydration exothermicity. Tokumitsu et al (2001) also stated that the presence of anions, which can increase the solubility of calcium, is effective in improving the hydration reaction rate. In the present study, CO_2-C is considered to have promoted hydration of cement by fine calcium carbonate particles of less than 1 μm dispersed in the carbonation slurry and carbonate ions in the liquid phase. Bleeding is also thought to have been reduced by the increase in bound water due to the calcium carbonate particles.

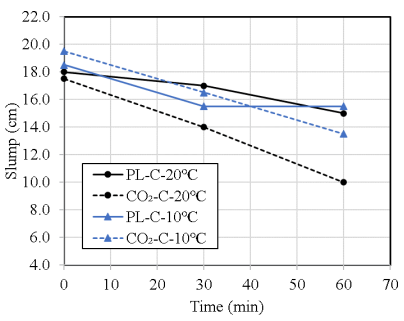


Figure 8. Slump test results

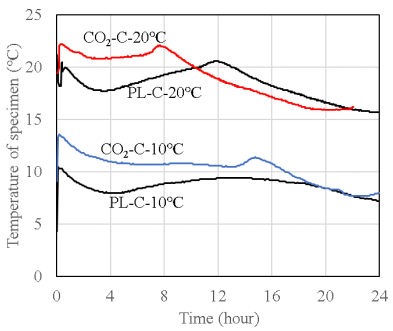


Figure 9. Temperature of specimen

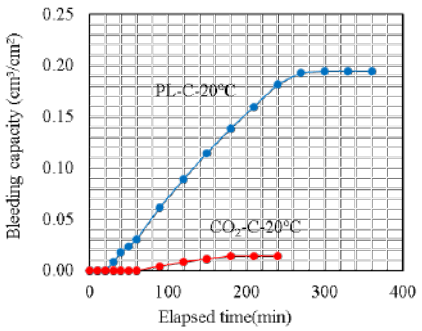


Figure 10. Bleeding test results

The results of compressive strength tests are shown in figure 11. The compressive strength of CO_2-C was equal to or greater than that of PL-C at all ages. In addition, the strength increase from 28 to 91 days of

age was slightly greater than that of PL-C. Lagerblad (2005) reported that during the carbonation process of the cement hydrate phase, calcium carbonate and silica gel containing a certain amount of CaO are formed. It is also possible that these may have undergone the pozzolanic reaction, but further study is needed to clarify the detailed mechanism. Table 3 shows the measurement results of CO_2 immobilized in concrete. The amount of CO_2 fixed in concrete by CO_2-C-10℃ was 7.7 kg/m^3. Secondary electron images of the split surface of the CO_2-C-10℃ specimen are shown in figure 12. As a result of the observation, cubic calcite of several hundred nm in size was observed. These are calcite formed in the carbonation slurry, and some of them may have been formed by the reaction of carbonate ions in the carbonation slurry with calcium ions in the concrete.

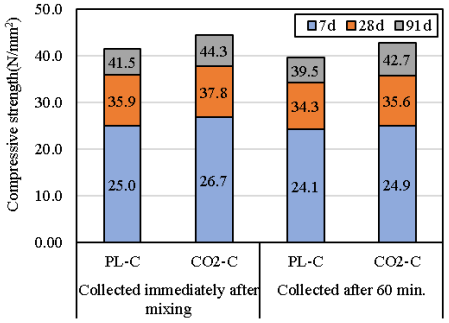


Figure 11. Compressive strength

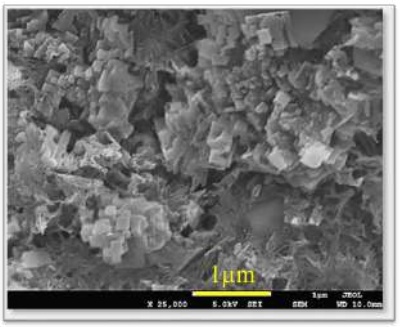


Figure 12. Secondary election image (CO_2-C-10℃)

Table 3. CO_2 fixation amount of concrete

	Ratio of CO_2 (mass%)	Decarbonization per m^3 of concrete(kg)	CO_2 fixation per m^3 of concrete(kg)
PL-C-10℃	3.26	44.3	-
CO_2-C-10℃	3.83	52.0	7.7

4. Conclusions

We evaluated the fundamental properties and CO_2 fixation of concrete produced using carbonated slurry.

- The amount of CO_2 fixed in the carbonation slurry was 335 kg/t-cem, and the fixation ratio was 93%.
- The solids in the carbonation slurry were cubic calcite dispersed outside the cement clinker at 10°C and spindle-shaped calcite covering the cement clinker at 20°C and 30°C.
- The flowability of concrete mixed with carbonated slurry differed between 10°C and 20°C environments, suggesting a relationship with the morphology of solids in the carbonated slurry as well as differences in the hydration reaction due to temperature.
- Concrete mixed with carbonated slurry showed slightly greater initial heat of hydration, shorter setting time, and less bleeding than that without.
- Concrete mixed with carbonated slurry was equal to or better than that without, with a slightly greater strength gain from 28 to 91 days of age.
- The amount of CO_2 fixed in concrete mixed with carbonated slurry was about 7.7 kg/m^3.
- The concrete mixed with the carbonated cement slurry prepared under appropriate temperature can even immobilize CO_2, and also ensure the fluidity and the strength development.

5. References

Lagerblad, B. (2005) "Carbon dioxide uptake during concrete life cycle–State of the art", *Swedish Cement and Concrete Research Institute. CBI Report 2,* :11

Monkman, S., MacDonald, M., Hooton, R.D. and Sandberg, P. (2016) "Properties and durability of concrete produced using CO_2 as an accelerating admixture", *Cement and Concreate Composites*, (74):218-224

Monkman, S. and Meyer, V. (2022) "Sustainable concrete production with recycled concrete wash water beneficiated with CO_2", *Acta Polytechnica CTU Proceedings*, 33:377-382

"Report of committee on properties and microstructure of hardened cement (2001)", *Japan cement. Association*, :67-68

Tokumitsu, N., Kanari, A. and Nakayama, C. (2001) "Effect of Admixtures on Hydration Rate of Blast Furnace Slag",*Research reports of Akita National College of Technology*, 36:44-48

The 16th International Congress on the Chemistry of Cement 2023 (ICCC2023)
"Further Reduction of CO_2 -Emissions and Circularity in the Cement and Concrete Industry"
September 18–22, 2023, Bangkok, Thailand

Influence of elevated heating temperature on the mechanical performance of carbonated belite pastes

J. Ou[1], Y. Wang [2], F. Zeng[3], Z. Luo[4], Y. Li[5], G. Ye[6], and Y. Mu[7*]

[1] *School of Materials Science and Engineering, Zhengzhou University, Zhengzhou, China*
Email: 980670097@163.com
[2] *School of Materials Science and Engineering, Zhengzhou University, Zhengzhou, China*
Email: 15538003738@163.com
[3] *China Construction Seventh Engineering Division Corp. LTD, Zhengzhou, China*
Email: 315853911@qq.com
[4] *School of Materials Science and Engineering, Zhengzhou University, Zhengzhou, China*
Email: luozhongtao@128.com
[5] *Jiangsu Jingxin New Materials Co., Ltd, Yangzhou, China*
Email: qispruce@163.com
[6] *School of Materials Science and Engineering, Zhengzhou University, Zhengzhou, China*
Email: gtye@zzu.edu.cn
[7] *School of Materials Science and Engineering, Zhengzhou University, Zhengzhou, China*
Email: myd1228@zzu.edu.cn

ABSTRACT

Carbonation curing endows calcium silicate pastes with accelerated strength increase and substantial carbon dioxide sequestration. The carbonation products, including calcium carbonate and silica-rich gel, are quite different from the hydration products of calcium silicate, which might lead to the different heat resistance properties between carbonated and hydrated paste. This study investigates the mechanical strength, phase composition and microstructure evolution of the carbonated belite pastes subjected to elevated temperatures of heating treatment. The results indicate that the compressive strength of the carbonated pastes increases with the heating temperature rising to 400 °C. The compressive strength after heating at 400 °C is 50% higher than that without heating. However, heating at 500 °C leads to 20% of decrease of compressive strength of the pastes, compared to the un-heated pastes. Then the strength continues to decline with the temperature increase to 600 °C and 700 °C, and heating at temperature higher than 800 °C causes the loss of strength of the pastes. The XRD result indicates that the metastable aragonite would gradually convert to stable calcite. Moreover, the heating at temperature lower than 500 °C facilitates the growth of crystallinity of calcite which favors the strength enhancement, but heating at 500 °C and above gradually decomposes the carbonation products and deteriorates the mechanical property of the pastes. As a result, the highest compressive strength occurs at the heating temperature of 400 °C.

KEYWORDS: *Belite; Carbonation; Heating temperature; Compressive strength; Crystallinity*

1. Introduction

Concrete is one of the most successful building materials in the world, which has made great contributions to the development and progress of the human society. However, the manufacturing of huge amount of cement and concrete is accompanied with emission of massive carbon dioxide (CO_2). Global warming caused by CO_2 and other greenhouse gases has believed as one of the most crucial problems that threaten the living of mankind. Therefore, reducing the CO_2 emission during the production of cement and concrete is drawing much research attention in the recent decades (Hasanbeigi, Price et al. 2012).

Among the several approaches of reducing CO_2 emission, carbonatable binder is regarded as one of the potential low-carbon building material, since it produces binding capability with an extra advantage of CO_2 absorption (Ashraf 2016). Carbonatable binder is usually composed of calcium silicate minerals which could react with CO_2 at the presence of water film (Gartner and Sui 2018). The carbonation reaction products include various crystal forms of calcium carbonates and silica-rich gel. The structural analysis indicates that the silica-rich gel covers the unreacted calcium silicate particles and the calcium

carbonate assembles the network skeleton, which is much different from the structure of Portland cement stone (Mu, Liu et al. 2019).

The discrepancy in the components and structures of carbonated binder and hydrated binder would definitely lead to dissimilar service performances. As one of the service performances, heat resistance evaluates the property deterioration degree of the concrete of subjected to fire. Related researches have demonstrated that the hydration products of Portland cement gradually decompose with the heating temperature rising, including the disintegration of ettringite at about 80 °C, the calcium-silicate-hydrate gel between 100 °C and 450 °C, and calcium hydroxide from 400 °C to 500 °C (Memon, Shah et al. 2019). However, there is still lack of study on the effect of elevated heating temperature on the phase transformation and property evolution of carbonatable calcium silicate binders.

Our previous research indicated different calcium silicate minerals show different carbonation characters and properties. For instance, γ-dicalcium silicate (γ-C_2S) is non-hydraulic but it could absorb CO_2 in a relatively high rate; monocalcium silicate (CS) has the lowest Ca/Si ratio and poor carbonation reactivity; β-dicalcium silicate (β-C_2S, belite) has a moderate carbonation reactivity but gains the highest compressive strength (Mu, Liu et al. 2019). This paper investigates the influence of heating on the phase conversion and strength development of carbonated belite, to evaluate the fire resistance of carbonatable calcium silicate cement.

2. Materials and methods

Chemically pure calcium hydroxide ($Ca(OH)_2$) and silica (SiO_2) agents were respectively chosen as the calcium source and silicon source of belite, and boracic acid (H_3BO_3) agent was employed as the crystal form stabilizer. Stoichiometric ratio of $Ca(OH)_2$ and SiO_2 together with 0.5 wt.% of H_3BO_3 was mixed and pressed into tablets. Then the tablets were fired at 1450 °C for 3 h and cooled down fast by forced air. The belite clinkers were ground to powders with particle size less than 75 μm. 10 g of belite powder and 1.5 g of deionized water were mixed and pressed into cylindric compacts with diameter of 20 mm and height of 20 mm. The compacts were placed in the chamber full of CO_2 with partial pressure of 0.3 MPa for 24 h carbonation curing. The carbonated samples were then heated at various target temperatures (300, 400, 500, 600, 700 and 800 °C) for 1 h and cooled down to the ambient temperature.

The thermal gravity analysis of the carbonated belite sample was conducted using TA Q600 analyser with heating rate of 20 °C/min from 50 to 1000 °C to detect the thermal decomposition of the carbonation products. The compressive strength of the heated samples was tested via using an electronic testing machine (CMT6103) with loading rate of 0.5 mm/min. The final strength result was the average value of 5 samples. The phase components of the heated and unheated samples were detected by X-ray diffraction (XRD, Rigaku SmartLab SE), with scanning rate of 2 °/min from 20 to 50 °. Specifically, 10 wt.% of well-crystallized corundum was dosed into the powders as the internal standard, so that the exact phases proportion could be calculated.

3. Results and discussions

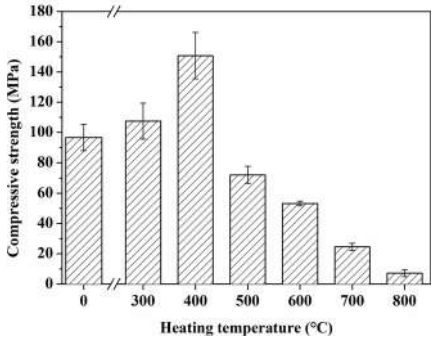


Fig. 1. Compressive strength of the carbonated belite samples subjected to different heating temperatures.

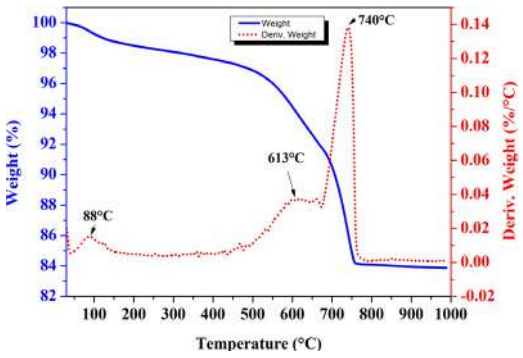


Fig. 2. TG-DTG curves of carbonated belite sample

The compressive strength of the carbonated belite samples subjected to different heating temperatures was illustrated in **Fig. 1**. It can be seen that after carbonation curing for 24 h, the belite sample could achieve the compressive strength of 96 MPa, indicating that carbonation endows belite binder with extremely high early strength. After heating at 300 °C for 1 h, the compressive strength of the carbonated sample reaches 108 MPa, which is a bit higher than that of the unheated sample. As the temperature rises to 400 °C, the compressive strength increases to 151 MPa, which is almost 57 % higher than the unheated

group. However, there is a sharp decrease of compressive strength when the heating temperature is further elevated to 500 °C, at which the strength is 71 MPa, less than half of the strength at 400 °C. And the strength keeps decrease with the increasing of heating temperature. After heating at 800 °C for 1 h, the residual strength is only 6 MPa, indicating the failure of the carbonate structure.

The development of the compressive strength of carbonated belite paste sample subjected to thermal treatment is similar to findings in some researches on hydrated cement paste (Heikal, El-Didamony et al. 2013). There is also a strength increase at around 400 °C of Portland cement which is believed to be attributed to the internal autoclaving effect that the hydration reaction is further enhanced (Memon, Shah et al. 2019). However, the water content in the compacted paste is much lower, thus the porosity of the paste is much higher than the normal cement paste. Therefore, the autoclaving effect should be weak in the heating of carbonated sample. Additionally, the strength increase is much sharper than ordinary cement paste, there should be some other factors that influencing the compressive strength of the heated carbonated belite samples.

The mass loss during the heating process is evaluated to characterize the decomposition of the carbonated belite paste sample, as shown in **Fig. 2**. From the TG curve it can be observed that the weight of the sample is keeping decreasing during heating before 750 °C, and the sample weight is almost constant after heating at temperature higher than 750 °C. The DTG curve indicates that there are three typical decomposition points located at around 88 °C, 613 °C and 740 °C. The decomposition at 88 °C corresponds to the release of free water. The mass loss at 613 °C and 740 °C should be caused by the decomposition of poorly crystallized carbonate and decomposition of crystal calcium carbonate, respectively. Combining the TG and DTG results, it can be estimated that the percentage of free water in the sample is about 1 wt.%, and 13 wt.% of the sample equals to the absorbed CO_2. It should be noted that the decomposition of calcium carbonate begins from heating temperature of 500 °C which is in accordance with the temperature where the compressive strength begins to decrease. Therefore, it can be deduced that the declination of the compressive strength of carbonated belite paste samples owes to the gradual decomposition of calcium carbonate, as the carbonates formed the skeleton of the structure. However, there is still no explanation for the compressive strength increase after heating at 400 °C.

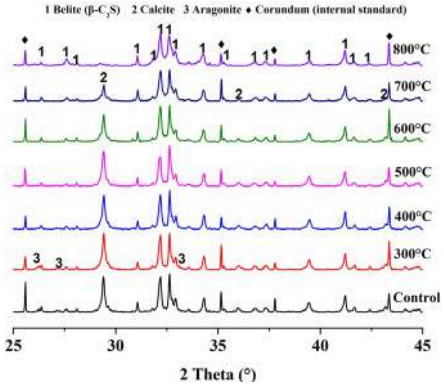


Fig. 3. XRD patterns of the carbonated belite samples subjected to different heating temperatures.

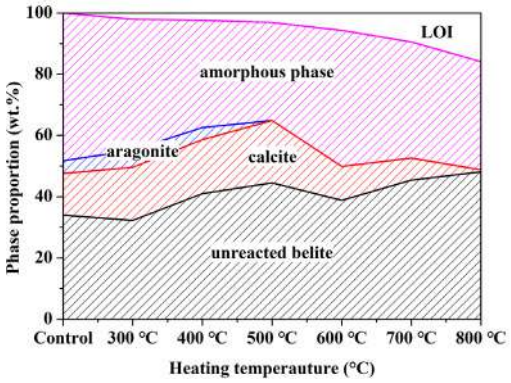


Fig. 4. Phase proportion evolution of carbonated belite sample after heating at different temperatures.

Although the TG-DTG result demonstrates the decomposition of calcium carbonates, it is still uncertain whether there are conversions between the different crystal forms of calcium carbonate, i.e. calcite, aragonite, vaterite and poorly crystallized calcium carbonate. Therefore, the mineral phases of the carbonated belite after heating at different temperatures were detected via XRD. As the XRD patterns illustrate in **Fig. 3**, the carbonation curing of belite paste samples induces the generation of two forms of calcium carbonate: calcite as the major product and aragonite as the minor product. When the samples were heated at 500 °C, the peaks of aragonite vanish. As the heating temperature rises to 600 °C and above, the peak height of calcite begins to decline. And the peaks of calcite disappear when the heating temperature increases to 800 °C, which agrees with the results of TG-DTG.

In order to exhibit the evolution of phases assemblage of the carbonated belite paste during the heating treatment, the weight percentage of each phase was calculated based on Rietveld method with the help of 10 wt. % corundum as the internal standard, which is illustrated in **Fig. 4**. The loss on ignition (LOI) corresponds to the TG result. The amorphous phase in **Fig. 4** includes not only the silica-rich gel but also the poorly crystallized belite and calcium carbonate. With the heating temperature rising to 500 °C, the content of aragonite gradually decreases. The vanish of aragonite does not indicate that aragonite is

decomposed, because of the slight increase of calcite content at 500 °C. Actually, aragonite is a metastable calcium carbonate mineral which would convert to stable calcite during heating. From the phase content analysis, it is speculated that the compressive strength increase might related to the transformation from aragonite to calcite. As reported in the literature (Silva, Bucea et al. 2006), the crystallinity also has significant influence on the structure's mechanical property. Therefore, the crystalline degree of calcite, which is the principal support of the structure of the carbonated belite, was evaluated by the full width at half maximum (FWHM) of the top peak of calcite in the XRD patterns.

Table 1 FWHM of the top peak of calcite in XRD patterns.

Heating temperature	FWHM	Heating temperature	FWHM
No heating	0.217	600 °C	0.219
300 °C	0.221	700 °C	0.224
400 °C	0.213	800 °C	0.218
500 °C	0.211		

As shown in **Table 1**, the FWHM of the top peak of calcite exhibits a slight decrease when the heating temperature increases to 500 °C, indicating that the crystallinity of calcite is improved. It has been demonstrated that the higher crystallinity is conducive to the higher mechanical property. The low FWHM value at 400 °C and 500 °C reveals the high crystal degree of calcite, suggesting that the calcite skeleton in carbonated belite samples is stronger than the others. However, as proved in the TG results, a small proportion of calcium carbonate was decomposed during the heating at 500 °C, which damages the carbonated structure. Therefore, although the FWHM of 500 °C is slightly lower than that of 400 °C, the compressive strength of 400 °C is much higher than that of 500 °C.

4. Conclusion

The influence of thermal treatment on the performance of carbonated belite paste samples was evaluated by investigating the compressive strength and phase component development of the samples subjected to various heating temperatures.

It is concluded that heating at 400 °C significantly enhances the compressive strength of the carbonated belite pastes. However, when heated at 500 °C and above, the compressive strength of the carbonated paste decreases sharply. Calcining at 800 °C would lead to the structure failure of the carbonated paste.

The phase analysis indicates that the metastable aragonite would gradually convert to stable calcite with the heating temperature increases to 500 °C. Meanwhile, the crystallinity of calcite, which assembles the skeleton of the carbonated structure, increases with the temperature elevated to 500 °C according to the FWHM calculation, which should account for the strength improvement of the carbonated belite paste. However, as firing at 500 °C is proved to partially disintegrate the calcium carbonate products which would deteriorate the structure of carbonated belite paste, the highest compressive strength is achieved after heating at 400 °C. Additionally, the calcium carbonate products have been thoroughly decomposed before 800 °C, thus the compressive strength of the carbonated paste after firing at 800 °C is negligible.

Acknowledgements

This work was supported by the National Natural Science Foundation of China [grant number 52108258].

References

Ashraf, W. (2016). "Carbonation of cement-based materials: Challenges and opportunities." *Construction and Building Materials* **120**: 558-570.

Gartner, E. and T. Sui (2018). "Alternative cement clinkers." *Cement and Concrete Research* **114**: 27-39.

Hasanbeigi, A., L. Price and E. Lin (2012). "Emerging energy-efficiency and CO2 emission-reduction technologies for cement and concrete production: A technical review." *Renewable & Sustainable Energy Reviews* **16**(8): 6220-6238.

Heikal, M., H. El-Didamony, T. M. Sokkary and I. A. Ahmed (2013). "Behavior of composite cement pastes containing microsilica and fly ash at elevated temperature." *Construction and Building Materials* **38**: 1180-1190.

Memon, S. A., S. F. A. Shah, R. A. Khushnood and W. L. Baloch (2019). "Durability of sustainable concrete subjected to elevated temperature – A review." *Construction and Building Materials* **199**: 435-455.

Mu, Y., Z. Liu and F. Wang (2019). "Comparative Study on the Carbonation-Activated Calcium Silicates as Sustainable Binders: Reactivity, Mechanical Performance, and Microstructure." *ACS Sustainable Chemistry & Engineering* **7**(7): 7058-7070.

Silva, P. D., L. Bucea, D. R. Moorehead and V. Sirivivatnanon (2006). "Carbonate binders: Reaction kinetics, strength and microstructure." *Cement & Concrete Composites* **28**(7): 613-620.

The 16th International Congress on the Chemistry of Cement 2023 (ICCC2023)
"Further Reduction of CO_2 -Emissions and Circularity in the Cement and Concrete Industry"
September 18–22, 2023, Bangkok, Thailand

Fresh Properties and Compressive Strength of Alkali Activated Mortar with Different Powder Composition

B. Kipkemboi[1,4*], N. Aoyagi[1], S. Miyazawa[2], M. Hata[3] and H. Igawa[3]

[1] *Graduate School of Engineering, Ashikaga University, Ashikaga, 326-8558 Japan*
Email: kipkemboibenson@yahoo.com , Email: g22701@g.ashikaga.ac.jp
[2] *Department of Civil & Environmental Engineering, Ashikaga University, Ashikaga, 326-8558 Japan*
Email: miyazawa.shingo@g.ashikaga.ac.jp
[3] *Nippon Hume Corporation, 3300 Magechi, Kumagaya, 360-0161 Japan*
Email: m-hata@nipponhume.co.jp , Email: h-igawa@nipponhume.co.jp
[4] *Kenya Industrial Research & Development Institute, P.O Box 30650 – 00100 Nairobi, Kenya*

ABSTRACT

The purpose of this study is to analyze fresh properties of alkali activated mortar using primarily industrial by-product materials as fly-ash (FA), ground granulated blast-furnace slag (BFS) and silica fume (SF) without including OPC. Calcium hydroxide (CH) was used as an activator. In order to find out the effect of combination and blend ratio of these powders on flowability and strength of mortar, a series of tests were done by varying the following parameters one at a time; Partial replacement of silica fume, ratio variation of BFS to fly ash ratio and usage of BFS with different Blaine fineness. Flowability of the fresh mortar was measured. To simulate the actual curing condition in the production of precast concrete members, steam curing method was used at a maximum temperature of 65°C. Compressive strength of the specimen was tested at the age of 14 days. The optimum blend ratio of the powders to obtain good flowability and strength was determined from these experimental results.

KEYWORDS: *Steam curing, Alkali activated binder, Viscosity, Compressive Strength*

1.0 Introduction

Ordinary Portland cement-based mortar and concrete is the most widely used construction material in the world. Production of ordinary portland cement is associated with significant CO_2 emissions making up approximately 2.4% of global CO_2 emissions Marland and Dennis (2021). Gradual decrease in human labour force and increased demand for high quality, durable and construction effecient concrete works has led to increased demand for precast concrete. Effective solutions to this problem include reductions in the amount of cement used and the use of industrial by-products materials as binders in mortar and concrete mixes. The concept of alkali activated material as an alternative to OPC has been studied by many researchers since at least 1908 Provis and Jannie (2014). Previous research indicate that concrete products from alkali activated materials have demonstrated sufficient durability comparable to conventional concrete. It is also reported that steam curing method generally applied to coventional precast concrete products is also effective in early strength development of alkali-activated concrete product materials Hata et al (2022). Based on this background, the study focuses to analyze the fresh properties of alkali-activated mortar materials using user friendly powder combination that can be used by simply adding water and mixing.

2.0 Experiment

2.1 Materials properties

In this study, powder materials used are mainly industrial by products materials (IBPM) without any ordinary Portland cement (OPC). These powders were composed of fly-ash (FA), ground granulated blast

furnace slag (BFS) with different Blaine fineness (4,550 & 6530 cm^2/g), silica fume (SF) and calcium hydroxide (CH) as an activator. Standard sand with density (2.64g/cm^3), absorption rate (0.42%) and fineness modulus (2.83) according to JIS A 5005 was used as fine aggregates. The chemical composition and physical properties of powder materials used are shown in **Table 1 & Table 2**.

Table 1: Chemical composition of each powder used

IBPM Material	Ig. Loss (%)	Chemical composition (%)									
		SiO_2	Al_2O_3	FeO_3	CaO	MgO	SO_3	Na_2O_3	K_2O	TiO_2	P_2O_5
FA	2.63	52.78	29.05	4.12	3.79	1.90	0.26	0.50	1.09	1.59	0.41
BFS	0.08	34.03	14.69	0.41	42.90	6.01	3.4	0.22	0.32	0.55	0.01
SF	3.71	92.97	-	-	-	0.37	0.65	-	-	-	-
CH	24.76	0.19	0.11	0.12	73.82	0.77	0.07	-	0.01	0.02	0.03

Table 2: Physical properties of each powder used

IBPM Material	Density (g/cm^3)	Blaine fineness (cm^2/g)	Activity index at 28 days (%)
FA	2.20	3,480	81
BFS	2.91	4,550	92
SF	2.30	191,000	110
CH	2.32	150,000	-

Polycarboxylate type high range water reducing admixture (SP) commonly used in pre-cast concrete works and de-airing agent (DA) was used to improve on workability and reduce entrained air respectively. The range of air content was 0.7 - 2.9%.

2.2 Mix proportion of Mortar

Each mix series was developed based on BFS and FA ratios which are the major components of the powder mix. The dosage of SF in each mix was varied from 0% to 10%. To enable easy comparison, a constant water binder ratio (W/B) ratio of 21.0% sufficient for adequate 14-day compressive strength was used Hata et al (2022), sand to paste volume ratio and chemical admixture dosage were kept constant at 48.0% and 1.15% SP respectively. The content of calcium hydroxide (CH) in IBPM was maintained at 4% by weight in all mixes. Experiment mix proportions are shown in **Table 3**.

Table 3: Mix proportions of Mortar

Series	W/B (%)	BFS: FA (%)	SF (%)	Unit Content (kg/m^3)						Admix (%)
				Water	IBPM				Sand	
				W	BFS	FA	SF	CH	S	SP
I	21.0	25:75	0.0	171.4	195.9	587.8	0.0	32.7	1267.2	1.15
			5.0	171.3	185.6	556.8	40.8	32.6		
			10.0	171.2	175.3	525.9	81.5	32.6		
II	21.0	50:50	0.0	178.9	408.9	408.9	0.0	34.1		
			5.0	178.4	386.5	386.5	42.5	34.0		
			10.0	177.9	364.2	364.2	84.7	33.9		
III	21.0	75:25	0.0	187.1	641.4	213.8	0.0	35.6		
			5.0	186.1	604.7	201.6	44.3	35.4		
			10.0	185.1	568.4	189.5	88.1	35.2		
IV	21.0	100:0	0.0	196.0	896.0	0.0	0.0	37.3		
			5.0	194.4	842.4	0.0	46.3	37.0		
			10.0	192.8	789.8	0.0	91.8	36.7		

2.3 Experimental methods

For each mix proportion, flow table test according to ASTM C 1437-07 and air content test according to ASTM C 185 – 02 was done. To analyze viscosity and yield value properties assuming a Bingham body, Mortar flow rate through a J-shaped circular plastic pipe was measured under varying pressure and depths versus corresponding time recorded using an automatic laser (KEYENCE LK-G500A) tool kit. See **Fig. 1**

for the experiment set-up according to Yamamoto et al (1996). Assuming a Bingham fluid model, shear stress (P) and shear rate (V) relationship is given by equation (1). Shear stress (P) and shear rate (V) is calculated from the experimental data using equations (2) and (3) respectively.

$$P = l \bullet V + g \quad \text{.....(1)}$$

$$P = (\Delta P \bullet R)/(2L) = [\{\rho\ (h_{i-1} + h_i)/2\}/\{C_L + ((h_{i-1} + h_i)/2\}] \bullet [R/2] \quad \text{.....(2)}$$

$$V = [4Q/\pi R^3] = [4(h_{i-1} - h_i) / (t_i \times R)] \quad \text{.....(3)}$$

Where: **ΔP** is pressure difference, **L** is length of the U portion of the J – shaped plastic pipe (24.3cm), **ρ** is the density of mortar (g/cm^3), **R** is the radius of the plastic pipe (2.5cm), **Q** is mortar flow rate / discharge (liters/sec), $\mathbf{C_L}$ is the total length of the J – shaped plastic pipe (400+ $\mathbf{L}$) in cm and $\mathbf{h_i}$ mortar depth (cm) at time t (sec). The reciprocal of the trendline slope given by relationship in equation (1) gives the viscosity (l) while the horizontal X – axis intercept gives the yield value (g). To simulate the actual curing condition in the production of precast concrete members, steam curing method was used. After casting, specimens were sealed and placed in the chamber at 20°C for precuring time of 24hr±2hrs. According to research by (Hata et.al), the effect of precuring time under 6hrs on compressive strength is adverse therefore this experiment adopted 24hrs to minimize these effects. Chamber temperature was then raised steadily to 65°C at a rate of 20°C/hr. for 2hr 15min. The temperature was then kept constant at 65°C for 4hrs and then decreased at a rate of -3.75°C/hr. for 12hrs to 20°C. The relative humidity of the chamber was kept constant at 80%. Specimens were then stored in a room at 20 °C and 60% relative humidity. Compressive strength of the specimens was tested at the age of 14 days.

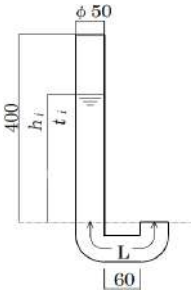


Figure -1: J-Flow experiment set-up

3.0 Results and discussions

3.1 J-Flow Experiment and Flow Value

From the graph in **Fig. 2**, it can be seen that the mortar mixtures can be analyzed as a Bingham body fluid. Therefore, viscosity and yield values can be computed according to **Eqn. (1) – (3)**. Proportions with BFS:FA ratio of 75:25 and 100:0 indicates zero yield value and low viscosity compared with BFS:FA ratio of 50:50 which has high yield value and viscosity. Graph in **Fig. 3** indicates that increasing the ratio of BFS drastically reduces the yield value while flow value increases making mortar highly flowable.

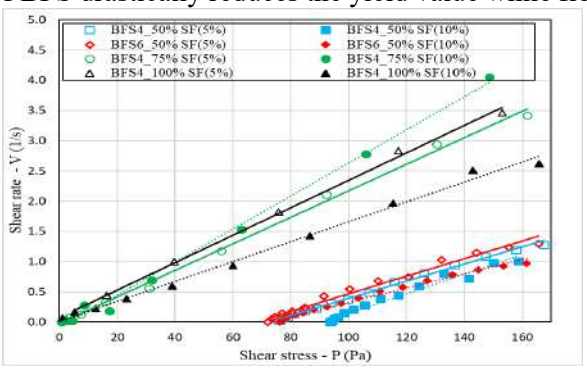


Figure -2: Shear rate and shear stress relationship of the different mix proportions

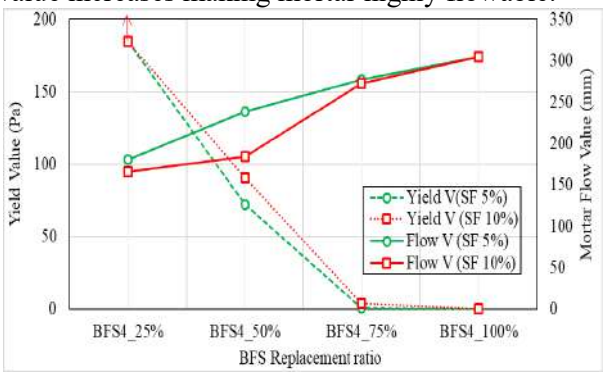


Figure -3: Yield and Flow value relationship with BFS replacement ratios

Mortar flow results in **Fig. 4** indicate that for each ratio of BFS:FA, good flow is achieved at 5% SF dosage. It was observed that mortar without FA (BFS: FA is 100:0) was very sticky yet highly flowable – high dilatancy Maruoka et al. (2016). Even without any tapping, the flow was over 300mm. Despite good flow, slight dilatancy was observed with BFS4_75%. When dosage of silica fume is increased to 10%, BFS6_50% & BFS4_75% still exhibited good flow while BF4_50% flow value decreases. Yield value of BFS4_75% & BFS4_100% at 5% SF dosage is almost 0. When SF is increased to 10% the yield value does not change significantly while BFS4_50% has considerably high yield value **72.45Pa** at SF 5% and increases to **90.76Pa** when SF is increased to 10%. Graph in **Fig.5** shows a relationship of mortar viscosity with BFS replacement ratio. When BFS ratio is increased from 50% to 75%, there is a drastic

decrease in viscosity for both 5% & 10% SF dosage. However, when BFS replacement ratio is increased to 100% (No FA), viscosity increases for SF 10% dosage and almost constant for SF 5% dosage.

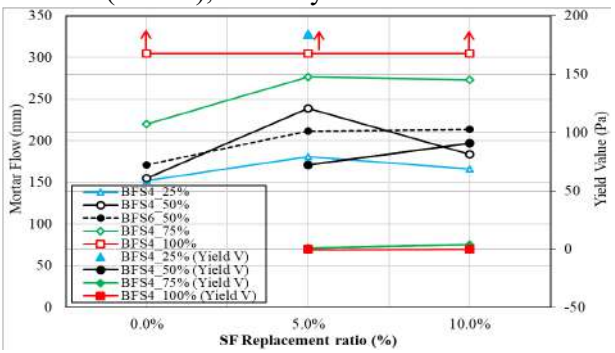


Figure -4: Flow value of mortar after 25 tapping & Yield value relationship with SF dosage

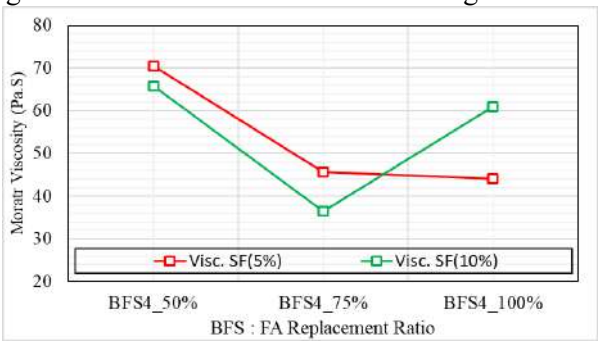


Figure -5: Mortar Viscosity relationship with BFS Replacement Ratio

3.2 Compressive strength of steam cured mortar

As shown in **Fig. 6**, Steam curing method as generally applied to conventional precast concrete products is also effective in early strength development of alkali-activated concrete product materials Hata et al (2022). High temperature catalyzes C-H-S reaction to quickly harden which would have otherwise taken long. The results in **Fig. 7** indicates that increasing the proportion of BFS and the dosage of SF increases compressive strength. This is due to increased availability of high calcium which plays an important role in C-H-S hydration reaction.

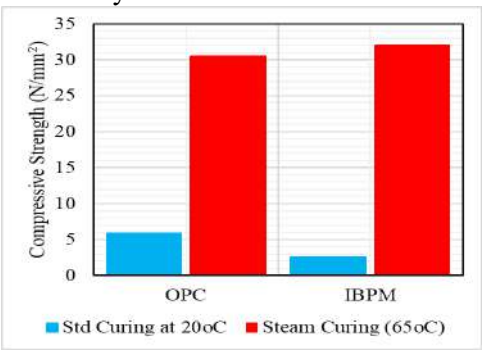


Figure -6: 1-day Compressive strength

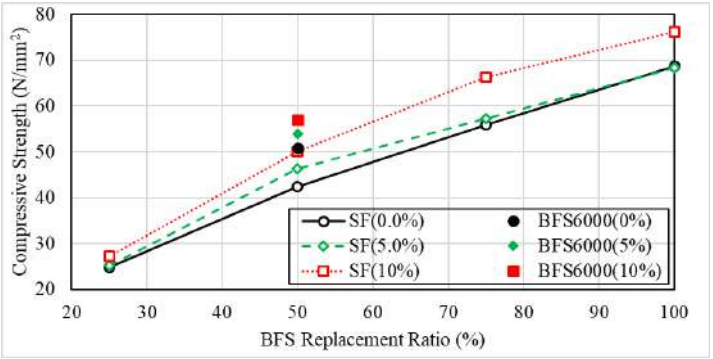


Figure -7: 14 days Compressive strength

4.0 Conclusions

1) Silica fume dosage of 5% exhibits good workability for 50% BFS replacement ratio.
2) Yield value decreases with an increase in BFS replacemnent ratio.
3) Increased proportions of SF (0-10%) and BFS (25-100%) increases 14-day compressive strength.

References

Hata M., Sato M., & Miyazawa S. (2022). Experimental Study on the Application of Cementless Material with Industrial By-Products to Steam-Cured Precast Concrete Products. *Materials*.

Marland G.& Dennis G. (2021). CDIAC-FF: Global and National CO2 Emissions from Fossil Fuel Combustion and Cement Manufacture: 1751–2017. *ESSD, 13*(4).

Maruoka M., Fujiwara H., Sugawara T. and Kawato T (2016). Study on Improvement of the Properties of Environment Load-Reduce High Strength Concrete, *Cement Science and Concrete Technology*, Vol.70, pp.328-335

Provis L. John, & Jannie S.J Van Deventer. (2014). *Alkali Activated Materials - State of the Art Report RILEM TC 224-AAM.* Dordrecht Heidelberg New York London: Springer.

Yamamoto Y., Homma A. & Kitsutaka Y (1996). " Study on the Testing Method of the Rheological Characteristic of High-Fluidity Concrete." *Journal of Structural & Construction Engineering* Tokyo: *Architectural Institute of Japan*. P. 9 - 16.

The 16th International Congress on the Chemistry of Cement 2023 (ICCC2023)
"Further Reduction of CO_2 -Emissions and Circularity in the Cement and Concrete Industry"
September 18–22, 2023, Bangkok, Thailand

Formation and stability of magnesium silicate hydrate and hydromagnesite

E. Bernard[1*], B. Lothenbach[1], H. Nguyen[2], R. Kuhn[1], F. Winnefeld[1]

[1] *Empa, Laboratory for Concrete and Asphalt, 8600 Dübendorf, Switzerland*

[2] *Fibre and Particle Engineering Research Unit, University of Oulu, Pentti Kaiteran katu 1, 90014 Oulu, Finland*

*Email: *ellina.bernard@empa.ch; barbara.lothenbach@empa.ch; raphael.kuhn@empa.ch; hoang.nguyen@oulu.fi; frank.winnefeld@empa.ch*

ABSTRACT

The effect of carbonate on the magnesium silicate hydrate (M-S-H) formation was studied at high Mg/Si molar ratio of 1.5. M-S-H pastes were synthesized from silica fume and MgO or MgO plus hydromagnesite in a Na_2CO_3 containing solution. X-ray diffraction data and thermogravimetric analysis indicated that brucite is destabilized and M-S-H phases formed much faster in the presence of carbonates. Additionally, in the system containing hydromagnesite, the hydromagnesite reacted to form M-S-H. In a third experiment, the carbonation of M-S-H with Mg/Si=1.5 in a suspension was investigated. While a reference suspension of M-S-H with Mg/Si=1.5 kept under inert atmosphere still contained brucite and a pH about 10.1, the forced carbonation of M-S-H decreased the pH to 7.3 and destabilized the brucite. No evidence of the formation of crystalline or amorphous hydrated magnesium (hydroxy)carbonate phases was observed.

KEYWORDS: *Magnesium silicate hydrate; hydrated magnesium carbonates; low-CO_2 cement, thermodynamic modelling*

1. Introduction

Binders based on Mg chemistries are one option to substitute Portland cement, because they can have a low or even negative carbon footprint when the MgO source comes from non-carbonate Mg-based minerals. The hydration of MgO in the presence of carbonates results in brucite potentially together with hydrated magnesium carbonate (HMC) phases, which provide relatively good mechanical properties (20 MPa to 50 MPa after 28 days). The hydration of reactive MgO-SiO_2 cements in the absence of carbonates results in precipitation of a magnesium silicate hydrate phase (M-S-H) as the primary reaction product, which can generate high compressive strength up to 50-80 MPa after 28 days. Thus, the combination of HMC and M-S-H in the hydrate assemblage seems promising to obtain a binder with both very low carbon footprint and optimized performance. However, the stability of M-S-H versus the stability of HMC is not yet understood. In this study three different experiments to tackle this issue are presented: i) the potential co-precipitation of M-S-H and HMC, ii) the formation of M-S-H in the presence of hydromagnesite and, iii) the carbonation of M-S-H.

2. Materials and methods

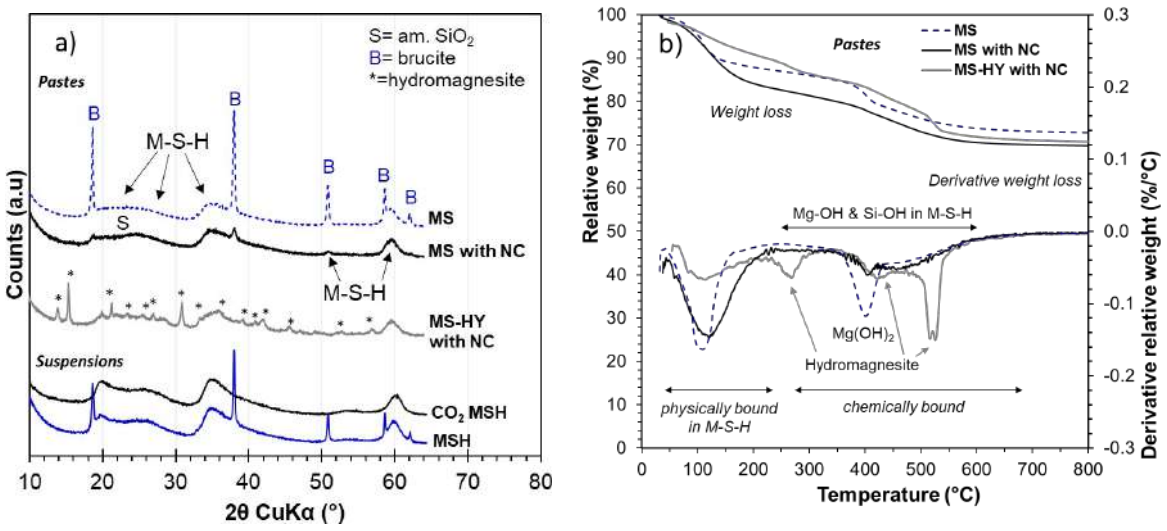
The co-precipitation of M-S-H and HMC was carried out using reactive SiO_2, MgO, and Na_2CO_3 as the source of carbonate as reported in Bernard et al (2022). The amount of MgO was chosen corresponding to an atomic ratio Mg/Si of 1.5. In literature generally M-S-H with a lower Mg/Si (1.2 to 1.3) has been

reported in Bernard et al (2017) such that hydration of the remaining MgO should therefore result in brucite ($Mg(OH)_2$), and the added carbonate could lead to the additional formation of HMC.
In a similar second experiment, half of the MgO was replaced by reactive as hydromagnesite has been proven to help in the formation of a poorly crystalline amorphous hydrate or other HMC phases (details can be found in Winnefeld et al (2019) and Dung et al (2017)).
In a third experiment, 100% CO_2 (flow of 100 cm^3/min) was bubbled through a suspension of an 8-year-old M-S-H with Mg/Si = 1.5 prepared as in Bernard et al (2017)for 2 days.

After the experiments, the samples were analysed by X-ray diffraction (XRD) and thermogravimetry (TGA), after 28 days for the co-precipitation samples of the first two experiments, and after 2 days for the carbonation of the M-S-H suspension. pH values of the samples were either measured when in suspension as in Bernard et al (2017) or measured by a leaching experiment. For the latter, more details can be found in Bernard et al (2022).
XRD data were collected using a PANalytical X'Pert Pro MPD diffractometer operating at 45 mV and 40 mA applying CuKα radiation (λ=1.54 Å), and equipped with a rotating sample stage, a fixed divergence slit and an anti-scattering slit on the incident beam side of 0.5° and 1°, respectively. The samples were scanned between 10° and 75° 2Θ with an X'Celerator detector. TGA measurements were carried out using a Netzsch STA 449 F3 Jupiter TGA apparatus coupled with a Bruker Fourier-transform infrared (FT-IR) spectrometer for the analysis of the exhaust gases. Approximately 40 mg of each sample was heated from 30 to 980 °C with a heating rate of 10 or 20 K/min in 150 µL alumina crucibles.

3. Results

Figure 1 displays the XRD and the TGA data of the pastes and suspensions. M-S-H is the main product in all samples. While the MS paste contains still a large amount of brucite after 28 days, the MS paste synthesised with Na_2CO_3 shows only traces of brucite (< 1 mass-%). M-S-H forms faster when sodium carbonate is present as Mg and carbonate ions form complexes which destabilizes brucite as detailed in Bernard et al (2022). However, the formation of crystalline or amorphous hydrated magnesium phases is not observed by XRD and TGA.



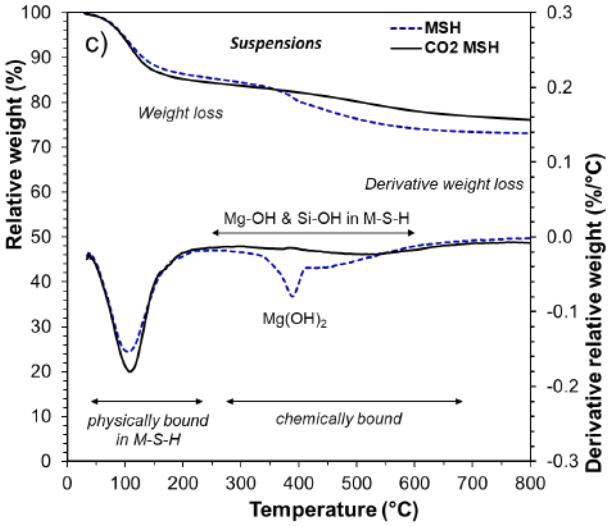
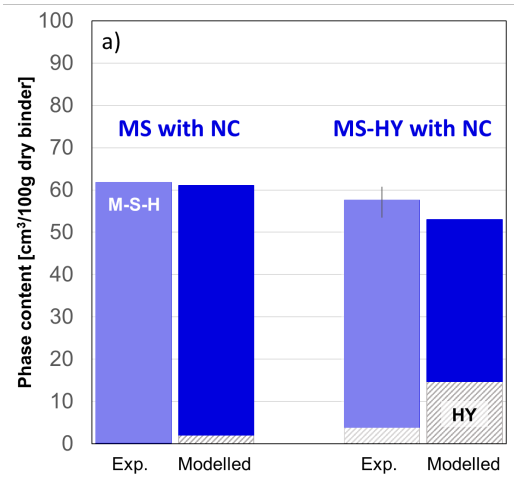


Figure 1: a) XRD data of magnesium silicate pastes without (MS) and with Na_2CO_3 (MS with NC), magnesium silicate paste with hydromagnesite and Na_2CO_3 (MS-HY with NC) after 28 days, and M-S-H suspension before (MSH) and after 2 days of interaction with 100% CO_2 (CO_2 MSH); TGA data of b) of MS, MS with Na_2CO_3, MS-HY with Na_2CO_3 pastes after 28 days, and of c) MSH and CO_2 MSH suspensions.

XRD and TGA data of the MS-HY paste synthesised with Na_2CO_3 indicates the presence of unreacted hydromagnesite in addition to M-S-H. Figure 2a shows the phase contents observed in the experiments after 6 months and the thermodynamically predicted phase assemblage, consisting simply of M-S-H and unreacted hydromagnesite. However, experimentally the amount of hydromagnesite strongly decreased as detailed Bernard et al (2022), indicating an apparent contradiction between thermodynamic prediction and experiments as detailed in Bernard et al (2022), pointing either towards an incomplete thermodynamic dataset and/or the presence of an additional not identified solid phase.



b)	pH (23°C)
MS*	9.1
MS with Na_2CO_3 (Bernard et al. 2022)	9.8
MS-HY with Na_2CO_3 (Bernard et al. 2022)	9.7
MSH	10.1
CO_2 MSH	7.4

* Data measured in the suspension instead of leaching of the paste

Figure 2: a) Phase assemblages estimated from the experimental results and thermodynamic modelling for the MS with Na_2CO_3, MS-HY with Na_2CO_3 pastes, adapted from Bernard et al (2022) and b) pH of the different samples measured at room temperature.

The suspension of M-S-H with Mg/Si=1.5 kept in inert atmosphere still contains brucite after 8 years (XRD and TGA data in Figure 1). The pH value has slightly decreased from 10.4 after 2 years (Bernard et al. 2017) to 10.1 after 8 years (Figure 2b), probably due to carbonation of the solution over time by CO_2 from the atmosphere. While the formation of M-S-H with Mg/Si=1.5 in the presence of carbonates was

fast (brucite had completely reacted within 1 month as shown in Figure 1), the presence of silicate seems to kinetically hinder the dissolution of the brucite in the absence of carbonates.
The forced carbonation of a M-S-H suspension, aged for 8 years, significantly decreases the pH from 10.1 to 7.3 (Figure 2b) and destabilizes the brucite (XRD and TGA data in Figure 1). Carbonation, however, does not decrease the amount of M-S-H present, indicating in agreement with the studies above, a high resistance of M-S-H towards carbonation. The magnesium originally presence in brucite seems to be in solution and/or used to form additional M-S-H, as there is no clear evidence for the formation of crystalline or amorphous hydrated magnesium (hydroxy)carbonate phases.

4. Conclusions

Na_2CO_3 accelerates the formation of M-S-H with a Mg/Si = 1.5 as the presence of carbonates destabilizes the brucite initially formed. However, the presence of crystalline or amorphous Mg-carbonate phases could not be confirmed. The hydration of a blend of MgO-SiO_2 and hydromagnesite (one of the HMC phases) results mainly in M-S-H, as also the hydromagnesite partially reacts to M-S-H. The bubbling of 100% CO_2 through a suspension of an 8-year-old M-S-H with Mg/Si= 1.5, presenting a pH value of 10.1, leads to a lower pH and the release Mg ions from brucite. Even under these harsh carbonation conditions, no Mg-carbonate phases could be observed, indicating that the formation of HMC from the carbonation of M-S-H is unlikely. In the three investigated cases, i.e. i) the co-precipitation of M-S-H and HMC, ii) the formation of M-S-H in presence of hydromagnesite and iii) the carbonation of M-S-H, M-S-H seems to be more stable than hydromagnesite, while crystalline HMC did not form or even were destabilized to form M-S-H. These observations are in contradiction with thermodynamic modeling results using the most recent data for Mg-phases, which predict the precipitation of HMC phases in addition to M-S-H, when dissolved CO_3^{2-}/HCO_3^- is present in concentrations of above 80 mmol/L. This discrepancy between experiments and thermodynamic modelling needs further investigations. Nevertheless, the high stability of the strength-forming M-S-H phase in the presence of CO_2/carbonates seems promising regarding the future application of such cements.

Acknowledgements

We would like to thanks Alexander German and Daniel Rentsch for the discussions. The financial support of the Swiss National Science Foundation (SNSF) for Ellina Bernard's Ambizione Fellowship under the grant n◦ PZ00P2_201697 is gratefully acknowledged.

References

Bernard, E., B. Lothenbach, D. Rentsch, I. Pochard, and A. Dauzères. (2017). 'Formation of magnesium silicate hydrates (M-S-H)', Physics and Chemistry of the Earth, Parts A/B/C, 99, 142-57.

Bernard, Ellina, Barbara Lothenbach, Daniel Rentsch, Alexander German, and Frank Winnefeld. (2022). 'Effect of carbonated sources on magnesium silicate hydrate (M-S-H)', Materials and Structures, 55,183.

Dung, N. T., & Unluer, C. (2017). Influence of nucleation seeding on the performance of carbonated MgO formulations. Cement and Concrete Composites, 83, 1-9.

Winnefeld, Frank, Eugenia Epifania, Fabio Montagnaro, and Ellis M Gartner. (2019). 'Further studies of the hydration of MgO-hydromagnesite blends', Cement and Concrete Research, 126, 105912.

The 16th International Congress on the Chemistry of Cement 2023 (ICCC2023)
"Further Reduction of CO_2 -Emissions and Circularity in the Cement and Concrete Industry"
September 18–22, 2023, Bangkok, Thailand

The modification of ultra fines on the rheological properties of alkali-activated ternary paste

C.F. Lu[1], Z.H. Zhang[2*], and C.J. Shi[1*]

[1] *Key Laboratory for Green & Advanced Civil Engineering Materials and Application Technology of Hunan Province, College of Civil Engineering, Hunan University, Changsha 410082, P. R. China*
Email: cuifanglu@hnu.edu.cn; cshi@hnu.edu.cn
[2] *Key Laboratory of Advanced Civil Engineering Materials of Ministry of Education, School of Materials Science and Engineering, Tongji University, Shanghai 201804, China*
Email: zhangzuhua@tongji.edu.cn

ABSTRACT

Fast setting and high viscosity are the two main obstacles to obtain better the rheological properties of alkali-activated materials (AAMs). This works aims to remove these obstacles by introducing different ultra fines. In slag-waste ceramic powder-ultra fines systems, the mechanism behind the modification effect of various ultra fines on rheological properties is studied. Results show that the introduction of ultra fine fly ash (UFFA) is beneficial to maintain good rheological properties and control setting, while adding silica fume (SF) harms fresh performance due to the low liquid film thickness and high reactivity. By ^{1}H NMR analysis, no obvious increase in mobile water appears in SF systems in the first 2 h of reaction, as compared to UFFA systems. It indicates that abundant free water is consumed continuously in SF-systems at this stage. Furthermore, the incorporation of 10% UFFA provides superior fresh performance and hardened properties. This study is essential towards better development of excellent formula of high-performance AAMs.

KEYWORDS: *Ultra fines, Alkali-activated ternary paste, Rheology, ^{1}H NMR analysis, Water states*

1. Introduction

Alkali-activated materials (AAMs) are a kind of cementitious material manufactured by alkaline activators and solid aluminosilicate, such as slag, fly ash, metakaolin and other Al-Si containing precursors (Shi, Krivenko and Roy, 2005). In addition to environmental benefits, properly designed AAMs show better mechanical properties, high-temperature stability and durability in aggressive environment compared with Portland cement-based materials (Zhang, Yao and Wang, 2012).

However, the application of AAMs in large-scale projects is still limited, especially the cast-in-situ construction. High viscosity and the regulation of setting time and are the two main obstacles to obtain good rheological properties of AAMs, which is mainly attributed to the complexity of raw materials and activators. AAMs cover a wide variety of aluminosilicates whose different physicochemical properties substantially influence their rheological behavior. Some studies have tried to apply ultra fines to modify the rheological properties of AAMs (Yang *et al.*, 2018; Liu *et al.*, 2020). These studies suggests that the rheological modification of ultra fines is closely related to the water to binder ratio (w/b) and their physicochemical properties (morphology, specific surface area and reactivity).

To better develop high-performance AAMs, this work compared and analyzed the effects of SF and UFFA on the time-dependent rheological behavior and mechanical properties of alkali-activated slag-ceramic powder systems. Furthermore, the mechanism behind the modification effect of various ultra fines on rheological properties is studied by ^{1}H NMR analysis.

2. Experimental methods

Blast furnace slag (SL), waste ceramics powder (CP), SF, and UFFA were used as precursors, which physical properties and XRD patterns are shown in Table 1 and Fig. 1 respectively. A ternary activator consisting of $Na_2O{\cdot}2SiO_2$, NaOH and Na_2CO_3 ($n(SiO_2)/n(Na_2O)$ = 2/3, 2% Na_2O per constituent) was applied to control setting time based on our previous work. To eliminate the potential influence of large amount of dissolution heat from NaOH, alkaline solution was prepared 1 d in advance. The w/b ratio and Na_2O% are constant at 0.4 and 6%, respectively. The SL to CP ratio is 1 in all systems where 0%, 5% and 10% SF/UFFA are introduced.

Table 1 Physical properties of SL, CP, SF and UFFA

Precursors	d_{50} (μm)	Density (kg/cm^3)	Geometric specific surface area (m^2/kg)
Slag	10.59	2843.60	964.17
Ceramic powder	20.95	2566.36	603.34
Silica fume	0.52	2211.67	23139.70
Ultra fine fly ash	2.10	2440.33	3715.17

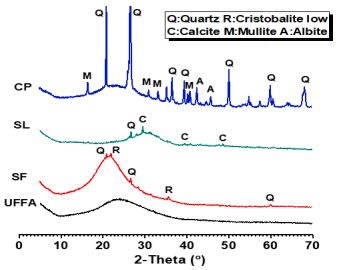


Fig. 1. XRD patterns of SL, CP, SF and UFFA.

The setting time and Mini-slump are measured in compliance with the China standard GB/T 1346-2011 and of GB/T 8077-2012. Liquid film thickness (T_{lf}) is determined based on the published literature (Yang *et al.*, 2018). Anton Paar MCR302 rheometer was applied to measure static yield stress. After 1 min of 100 s^{-1} pre-shearing, the pastes were exposed to a very low shear rate with 0.005 s^{-1} for 1 min to determine the static yield stress, and the test was performed every 10 min during 1 h. Water migration in pastes was monitored by low-field ^{1}H NMR. The transverse relaxation time (T_2) of paste was measured by CPMG pulse sequence in a MAG-MED PM-1030 Analyzer operating at 10 MHz at 20 ℃. The sealed sample was tested in specific time-intervals during 2 h without disturbance.

3. Results and discussions

3.1 Flowability, liquid film thickness and setting

The Mini-slump values and T_{lf} are shown in Fig. 2 and setting times are shown in Fig. 3. Obviously, more mixing water is required for wetting when the SF with high specific surface area is introduced, resulting in a significant reduction of T_{lf} and Mini-slump values. In contrast, the UFFA particles with sufficient stiffness well exhibit the 'ball bearing' effect. Furthermore, UFFA is beneficial to prolong the setting times due to its lower reactivity.

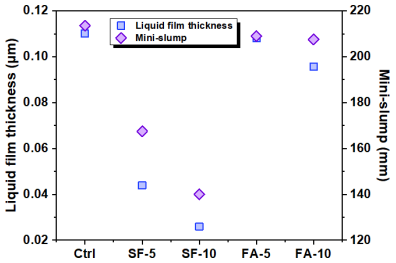


Fig. 2. Liquid film thickness and Mini-slum values of ternary systems.

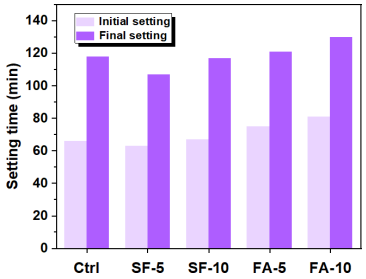


Fig. 3. Initial setting and final setting times of ternary systems.

3.2 Growth of static yield stress

Fig. 4 plots the static yield stress (τ_s) growth of different ternary systems. The 10% SF-system exhibits higher τ_s as compared to the control sample, which is due to the extremely high SSA of SF. Moreover, introducing SF increases the solids fraction and the inter-particle friction, and thereby pastes are more reluctant to flow (Yahia and Khayat, 2001). With time going on, partial dissolution of SF provides additional colloidal HO-Si-OM complexes that enhance the attraction between particles and contribute to form percolate network. During the first 0.5 h of reaction, the UFFA-systems show a comparable or lower τ_s level to that of the control sample, which suggests that UFFA particles play a role as fillers (Yang *et al.*, 2018). After initial mixing, these 'balls' fill the voids and release trapped water, improving the particle packing, and thereby the real liquid-solid ratio in the paste is higher. However, the low reactivity of UFFA is responsible for the low τ_s at later stage.

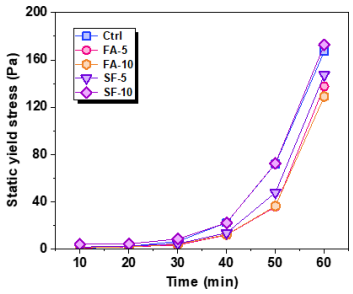


Fig. 4. Static yield stress growth of alkali-activated ternary systems.

3.4 ^{1}H NMR analysis

To well understand the water migration during setting process, the water content in specified T_2 interval can be calculated according to previous literature (Lu *et al.*, 2022). Fig. 5 plots the water content in different states of alkali-activated ternary systems. Immovable water in all samples gradually increases, which indicates a 'more solid' behavior and higher τ_s of pastes. The influence of adding different ultra fines on mobile water is different. An increasing trend of mobile water (a small hump) at the first hour is observed in the UFFA systems and the control sample, which may be attributed to the release of a small amount of free water during the polymerization reaction (Cao *et al.*, 2022). However, no obvious increase of mobile water is found in SF-systems. On the one hand, the introduction of SF severely weakens the dissolution of SL and the subsequent polymerization reaction. On the other hand, partial high reactivity-SF is dissolved with time going on, and accompanied with the release of some $HSiO^{3-}$. However, the dissolution degree of SF needs to be further determined.

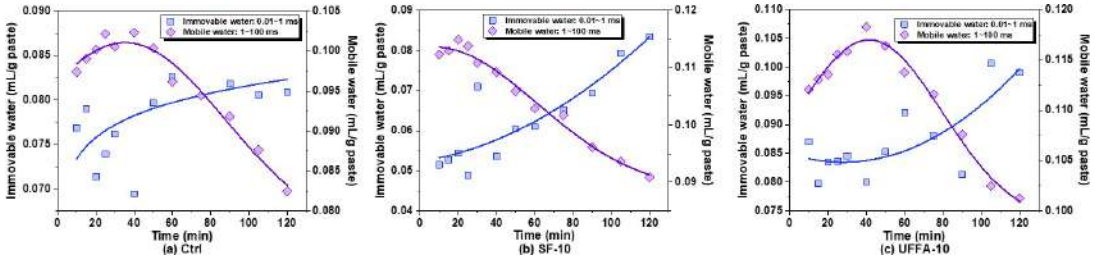


Fig. 5. Evolution of immovable water and mobile water content in different ternary systems.

3.5 Compressive strength

It can be found from Fig. 6 that adding SF seriously damages compressive strength, while UFFA is beneficial to maintain good mechanical properties. On the whole, compared with SF, the introduction of UFFA is more suitable for the preparation of high-performance AAMs, and the optimal replacement content of UFFA is 10%.

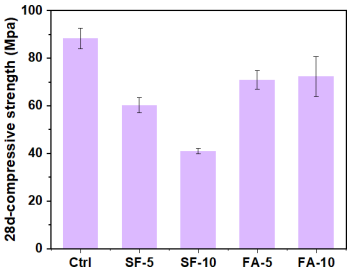


Fig. 6. The 28 d-compressive strength of different ternary systems.

4. Conclusions

The incorporation of SF slightly shortens the setting time and seriously damages rheological and hardened properties, whereas UFFA is beneficial to maintaining good fresh properties. Shorter interparticle spacing in SF-systems means that it is more prone to form a percolate network and to induce higher τ_s. The water migration in pastes are greatly dependent on the characteristics of these ultra fines. By ^{1}H NMR, no obvious increase in mobile water appears in SF-systems in the first 2 h of reaction compared with other systems, which indicates that abundant free water is consumed continuously at this stage. However, the dissolution behavior of ultra fines in the ternary system needs further study to determine their influence on water distribution.

Acknowledgements

The authors are grateful to the financial support by the National Natural Science Foundation of China projects U2001225 and 51878263.

References

Cao, R. *et al.* (2022) 'Relaxation characteristics and state evolution of water during the early-age reaction of alkali-activated slag as monitored by low field nuclear magnetic resonance', *Composites Part B: Engineering*. Elsevier Ltd, p. 118159.

Liu, Y. *et al.* (2020) 'Influence of silica fume on performance of high-strength geopolymer', *Journal of the Chinese Ceramic Society*, 48(11), pp. 1689–1699.

Lu, C. *et al.* (2022) 'Relationship between rheological property and early age-microstructure building up of alkali-activated slag', *Composites Part B*. Elsevier Ltd, 247(June), p. 110271.

Shi, C., Krivenko, P. V. and Roy, D. (2005) *Alkali-activated Cements and Concretes*. Taylor & Francis.

Yahia, A. and Khayat, K. H. (2001) 'Analytical models for estimating yield stress of high-performance pseudoplastic grout', *Cement and Concrete Research*, 31(5), pp. 731–738.

Yang, T. *et al.* (2018) 'Effect of fly ash microsphere on the rheology and microstructure of alkali-activated fly ash/slag pastes', *Cement and Concrete Research*. Elsevier, 109(April), pp. 198–207.

Zhang, Z., Yao, X. and Wang, H. (2012) 'Potential application of geopolymers as protection coatings for marine concrete III. Field experiment', *Applied Clay Science*. Elsevier B.V., 67–68, pp. 57–60.

The 16th International Congress on the Chemistry of Cement 2023 (ICCC2023)
"Further Reduction of CO_2 -Emissions and Circularity in the Cement and Concrete Industry"
September 18–22, 2023, Bangkok, Thailand

Strength development and CO_2 sequestration by carbonation curing of mortar using blast furnace slag fine powder and γ-C_2S

Y. Nishioka[1*], D. Tsuji[2], and M. Kojima[3]

[1] *TAKENAKA Corporation, Chiba, Japan*
Email: nishioka.yukiko@takenaka.co.jp
[2] *TAKENAKA Corporation, Chiba, Japan*
Email: tsuji.daijirou@takenaka.co.jp
[3] *TAKENAKA Corporation, Chiba, Japan*
Email: kojima.masarou@takenaka.co.jp

ABSTRACT

In recent years, there has been a growing interest in carbonation curing with the main purpose of CO_2 sequestration to cementitious materials from the viewpoint of reducing environmental impact. In this study, mortar specimens were prepared by adding fine blast furnace slag powder and γ-C_2S, and carbonation curing was carried out, and examined the strength development, the change of pore structure, and the amount of CO_2 sequestered by carbonation curing. It was confirmed that the strength of water curing specimens decreased as the amount of added γ-C_2S increased, while that of carbonation curing specimens increased. It was also found by mercury intrusion porosimetry that the sample subjected to carbonation curing at an early age had many voids around 100 to1000 nm, and the void distribution was significantly different from that of the water curing sample. Analysis of TG-DTA, XRD, and TC, showed that vaterite was produced in addition to calcite, and that the CO_2 sequestration increased with the addition of γ-C_2S.

KEYWORDS: *γ-C_2S, Carbonation curing, CO_2 sequestration, Mercury intrusion porosimetry, TG-DTA*

1. Introduction

Attempts to improve the performance of concrete by actively carbonizing it have long been considered. Klemm and Berger (1972) reported that the initial strength of concrete is enhanced when it is cured under a high concentration of CO_2 from a young age just after it is demolded, compared with that of concrete without carbonation. In recent years, due to the social trend of decarbonization, studies have been conducted aiming at carbon neutrality of concrete by sequestering CO_2 in concrete. γ-C_2S is known as a mineral with low hydraulic properties and high carbonation reactivity, and its application as a carbonation source in CO_2 sequestration by adding it to concrete has been examined (Higuchi et al (2014) and Wang et al (2022)). In this study, mortar specimens containing blast furnace slag fine powder and carbonation curing mixture (CA) mainly composed of γ-C_2S were prepared in ordinary Portland cement, and carbonation curing was carried out. Strength development, pore structure and amount of CO_2 sequestration by carbonation curing were investigated.

2. Experimental Program

2.1 Mortar Mixture Composition

The cement was used with ordinary Portland cement (C, 3.16g/cm^3), and blast furnace slag fine powder (BFS, 2.91g/cm^3) and carbonation admixture mainly composed of γ-C_2S (CA, 3.04g/cm^3) were added. Silica sand (S, 2.63g/cm^3) was used as fine aggregate. A polycarboxylic acid-based high performance

water reducing agent and antifoaming agent were used to adjust the air volume and the mortar flow.The mortar formulation is shown in Table 1. CA were added at 0, 15, and 30%, and water binder ratios of 40, 50, and 60% were compared.

Table 1: Mixture proportions of mortar

No.	Notation	W/B (%)	S/B (%)	Air (%)	Binder ratio (%)			Unit weight (kg/m^3)				
					C	BFS	CA	W	C	BFS	CA	S
1	W/B50-0	50	2.5	5.0 ±1.0	43	57	0	266	229	303	0	1334
2	W/B50-15	50	2.5		37	48	15	266	197	255	80	1331
3	W/B50-30	50	2.5		30	40	30	266	160	213	160	1326
4	W/B40-30	40	2.0		30	40	30	254	191	254	191	1267
5	W/B60-30	60	2.5		30	40	30	302	151	201	151	1257

2.2 Specimens and Curing Conditions

Specimens with φ50 x 100 mm and 40 x 40 x 160 mm were prepared and sealed at 20℃ for two days, followed by demolding and curing. Carbonation curing was carried out in an accelerated carbonation chamber with a CO_2 concentration of 20%, a temperature of 50℃ and a relative humidity of 40%. As a comparison, air curing at the same temperature and humidity (50℃ and 40%RH) and water curing at 20℃ were also performed.

2.3 Measurement Details

Compressive strength test were performed on φ50 x 100 mm specimens at the time of demolding (2days) and at the ages of 3, 7 and 28 days for each curing. For the carbonated specimens, the depth of carbonation was measured by splitting a 40 x 40 x 160 mm specimen and spraying phenolphthalein solution.
The surface 10 mm of the carbonation exposure surface of the 40 x 40 x 160 mm specimen was split and used for the test. After splitting and collecting the surface layer, the specimen was crushed to 5 mm or less with a hammer, and hydration was stopped by immersion in acetone. After stopping hydration, 2 ~ 5 mm fragments were collected and subjected to vacuum drying for 24 hours as pre-drying, followed by void measurement with a mercury intrusion porosimeter. In addition, the samples after stopping the hydration were pulverized to less than 150μm and subjected to TG-DTA, XRD, and TC. The TC equipment used heats the samples in a radiofrequency furnace and measures the total carbon content of the generated gas with an infrared detector.

3. Experimental Results and Discussion

3.1 Compressive Strength

The results of the compressive strength test are shown in Figure 1 Although the strength (2 days) at the time of demolding decreased as the content of CA increased, carbonation curing enhanced the strength, and the 28days strength was 37N/mm^2 at No.3. On the other hand, the strength decreased as the content of CA increased in air curing and water curing specimens. In air curing specimens, the increase in strength after 3 days of age was small, suggesting that the hydration stagnated due to drying.

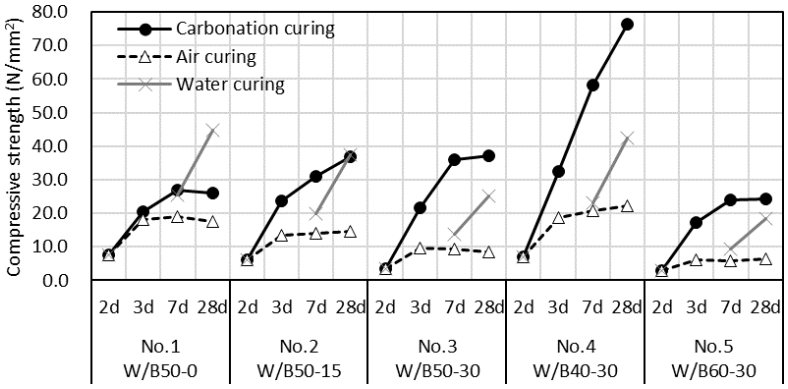


Figure 1: Compressive strength

3.2 Depth of Carbonation and CO_2 Sequestration

Figure 2 shows the depth of carbonation. No.3 and 5 were fully carbonated at 7 days, and at 28 days, all specimens were fully carbonated.

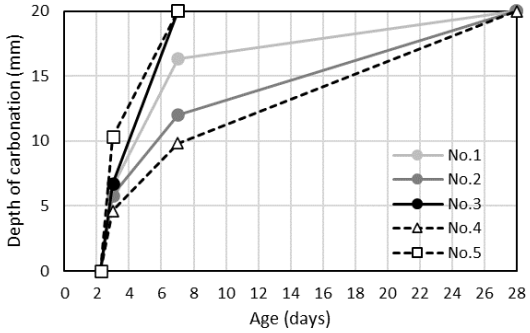


Figure 2: Depth of carbonation

TG curve of No. 3 are shown in the Figure 3. The sample after carbonation curing showed a greater weight loss after 450 ℃, which may be due to the formation of calcium carbonate. It has been reported that vaterite in hardening cement decomposes at lower temperatures than calcite, and in this experiment, it is inferred that the weight loss from the lower temperature is caused by the presence of vaterite. Figure 4 shows the peak of calcium carbonates by XRD. Calcite and vaterite peaks are observed, and the higher the content of CA, the higher the calcium carbonate production.

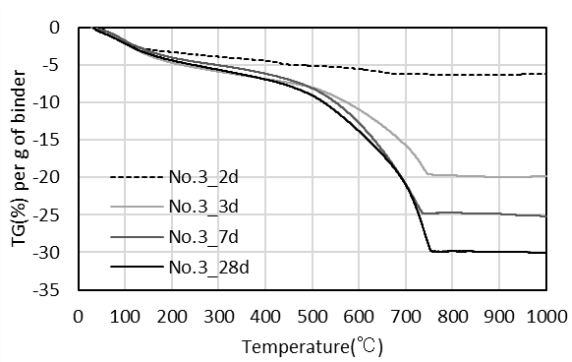


Figure 3: TG curve of carbonated sample (No.3)

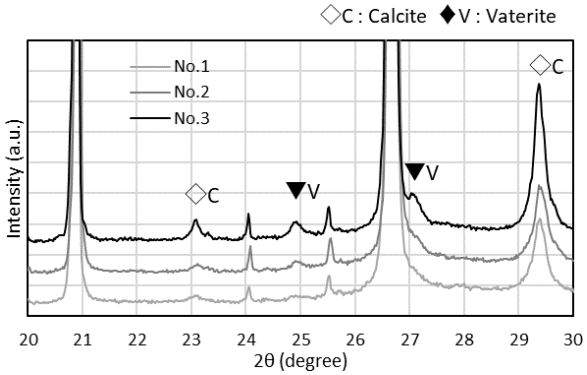


Figure 4: XRD peak of carbonated sample (28d)

CO_2 uptake measured by TC is shown in the Figure 5. All samples were taken from a surface layer 10 mm from the carbonation exposure surface. Compared with the same water-binder ratio, the one with the CA added had higher CO_2 uptake. The decrease in CO_2 uptake at No. 1 and No. 2 is probably due to the higher percentage of BFS and lower amount of CaO compared to No. 3.

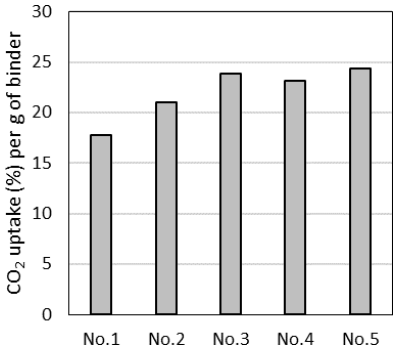


Figure 5: CO_2 uptake of carbonated sample (28d)

3.3 Microstructure Change

Figure 6 and Figure 7 show the results of mercury intrusion porosimetry. Comparing the pore volume around 100 to 1000 nm at 2 and 28 days, it increased slightly for air curing, whereas it decreased for carbonation curing. The carbonation curing specimens had the same total porosity as that of water curing at 28 days, but the porosity distribution was significantly different. The porosity distribution of carbonation cured specimens showed that the maximum peak remained around 500 nm, while in water curing, the 500 nm peak disappeared, and the pore size shifted to a smaller diameter overall.

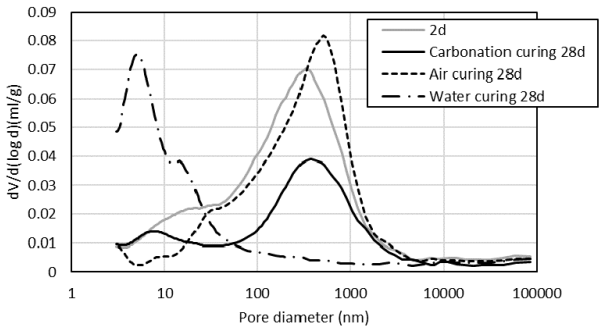


Figure 6: Pore distribution (No.3)

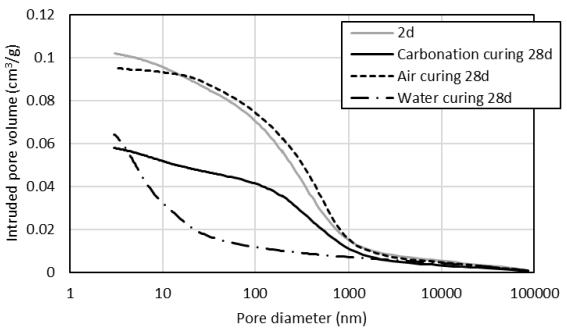


Figure 7: Cumulative intrusion pore volume (No.3)

4. Conclusions

Carbonation curing of mortar with addition of blast furnace slag fine powder and carbonation curing mixture (CA) was carried out, and it was shown that carbonation strength was enhanced by CA and the amount of CO_2 sequestration was increased. It was also found that carbonation curing at an early age resulted in a different pore structure from water curing.

Acknowledgements

This paper is based on results of "Development of Materials, Manufacturing Methods and Quality Control System on Innovative Carbon Negative Concrete", JPNP21014, commissioned by the New Energy and Industrial Technology Development Organization (NEDO).

References

Klemm, W. A., Berger, R. L. (1972) "Accelerated curing of cementitious systems by carbon dioxide: Part I. Portland cement", *Cement and Concrete Research*, 2(5):567-576

Higuchi, T., Morioka, M., Yoshioka, I., Yokozeki, K. (2014) "Development of a new ecological concrete with CO2 emissions below zero", Construction and Building Materials, 67 :338-343

Wang, X., Guo, M., Ling, T. (2022) "Review on CO2 curing of non-hydraulic calcium silicates cements: Mechanism, carbonation and performance", Cement and Concrete Composites, 133 :104641

The 16th International Congress on the Chemistry of Cement 2023 (ICCC2023)
"Further Reduction of CO_2 -Emissions and Circularity in the Cement and Concrete Industry"
September 18–22, 2023, Bangkok, Thailand

Microstructure of MgO-Al_2O_3-SiO_2 binders

M.H.N. Yio[1*], E. Bernard[1,2], H. Chen[1] and R.J. Myers[1]

[1] *UKCRIC Advanced Infrastructure Materials, Department of Civil and Environmental Engineering, Imperial College London, UK*
Emails: marcus.yio@imperial.ac.uk; hongkang.chen20@imperial.ac.uk; r.myers@ic.ac.uk
[2] *Empa, Laboratory for Concrete and Asphalt, 8600 Dübendorf, Switzerland*
Email: ellina.bernard@empa.ch

ABSTRACT

Magnesium (alumino)silicate hydrate (M-(A)-S-H) based binders are low-carbon alternatives to Portland cement, but their microstructure remains poorly understood. This study investigates the compressive strength and microstructure of paste samples with a fixed Mg/Si molar ratio of 1.5 and Al/Si molar ratios of 0 and 1.0 prepared using silica fume (MS) and metakaolin (MK), respectively. The results show that the MK system consistently achieved higher compressive strengths than the MS system. The addition of Na_2CO_3 increased the compressive strength of the MS system but decreased that of the MK system in the presence of excess phosphate. These results are supported by backscattered electron microscopy (BSE) and mercury intrusion porosimetry (MIP) analyses, which revealed increased pore volumes and sizes in the MS system than in the MK system. When Na_2CO_3 was added, the pore volumes and sizes of the MS system decreased, but no consistent changes were observed for the MK system.

KEYWORDS: *M-(A)-S-H, microstructure, pore structure, materials characterisation, low-CO_2 cement*

1. Introduction

Magnesium silicate binders are low-carbon alternatives to Portland cement since the raw material MgO can be derived from Mg-silicate minerals such as olivine without releasing chemically bound CO_2 through, for example, acid digestion combined with electrolysis (Scott et al., 2021). When reactive MgO is mixed with a silicate source (e.g., silica fume) and water, a binding magnesium-silicate-hydrate (M-S-H) phase is formed. M-S-H binders demonstrate high compressive strength (50 to 80 MPa), low pH, excellent fire resistance and potentially high durability (Bernard, 2022).
Due to the limited availability of silica fume, researchers have started investigating the replacement of silica fume with more widely available aluminosilicate sources such as calcined clays. It has been found that the use of metakaolin improves the mechanical properties through the formation of hydrotalcite and M-A-S-H (Shah et al., 2021). The addition of Na_2CO_3 has been found to enhance the mechanical properties further by promoting M-A-S-H formation (Bernard et al., 2023). However, the microstructure of both M-S-H and M-A-S-H binders has not yet been adequately studied, despite their importance to mechanical properties and durability. Therefore, this study investigated the compressive strength and microstructure of M-S-H and M-A-S-H binders, produced with MgO, silica fume (Al/Si = 0) or metakaolin (Al/Si = 1.0), sodium hexametaphosphate as a superplasticizer, and with and without Na_2CO_3, cured from 3 to 91 days. The microstructure was characterised using BSE, MIP and N_2 adsorption.

2. Methodology

Four pastes with a set Mg/Si molar ratio of 1.5 and Al/Si molar ratios of 0 (using MS) and 1.0 (using MK), with and without Na_2CO_3, were prepared according to the mix proportions in Table 1. Reactive MgO (CalMag 92/200, RBH), microsilica (920D, Elkem) and metakaolin (Argical M1200S, Imerys) were used as raw materials. Na_2CO_3 (anhydrous, ≥ 98% purity, VWR) was added at a concentration of 2.5 wt.% binder to all mixes. The water/binder ratio (w/b) was set to 0.68. Sodium hexametaphosphate

(NaHMP) (general purpose grade, Fisher Scientific) was added at varying concentrations to ensure comparable workability across all mixes (Jia et al., 2016). Before wet mixing, the raw materials were homogenised using a powder mixer. NaHMP and Na_2CO_3 were pre-dissolved in the mixing water. Mixing was then performed in a 30 L Hobart mixer for 3 min. All mixes were subsequently compacted in three layers in steel moulds of 50×50×50 mm^3 and then covered with a plastic sheet. After 24 h, the samples were demoulded and cured in a fog room (21 ºC, 98% RH) for 3, 7, 28 and 91 days. For each mix and curing age, four cubes were prepared, three for compressive strength testing and one for BSE, MIP and N_2 adsorption. For BSE observation, a prism of 40×20×8 mm^3 was extracted from the cube while the remaining offcuts were crushed into granules of a few mm for MIP and N_2 adsorption. Hydration was stopped by immersing the samples in isopropanol for 15 min followed by diethyl ether for 5 min. The prism for BSE imaging was epoxy-impregnated and then polished to 0.25 µm. BSE imaging was performed using a Zeiss Sigma 500VP scanning electron microscope at 15 kV accelerating voltage and 8.5 mm working distance. MIP was performed on ~1 g of granules using a Quantachrome Poremaster 60 up to a pressure of 414 MPa to detect pore sizes of down to 3.6 nm. N_2 adsorption was performed on ~1 g of granules, pre-degassed under vacuum at 40 ºC for 24 h, using a Micromeritics 3Flex analyser to determine the BET pore specific surface area (SSA) and mean pore diameter (d). Compressive strength testing was performed using a Controls cube crusher at a loading rate of 0.3 MPa/s.

Table 1: Mix proportions of the binders investigated. MS: silica fume; MK: metakaolin, NaC: sodium carbonate; NaHMP: sodium hexametaphosphate.

Sample ID	Materials (wt.%)						w/b (w/w)	Mg/Si (mol/mol)	Al/Si (mol/mol)
	MgO	MS	MK	Na_2CO_3	Water	NaHMP			
MS_0	29.4	29.4	--	--	41.1	0.1	0.70	1.5	--
MS_NaC	28.6	28.6	--	1.4	40.1	1.2	0.68	1.5	--
MK_0	20.1	--	37.1	--	40.0	2.9	0.70	1.5	1.0
MK_NaC	19.8	--	36.5	1.4	39.4	2.8	0.68	1.5	1.0

3. Results and Discussion

Figure 1 presents the compressive strengths of all the systems investigated as a function of curing time. Irrespective of the binder, the compressive strength increased up to 28 days and then plateaued thereafter. MK_0 consistently had higher compressive strengths than MS_0, attributable to the formation of M-A-S-H and hydrotalcite (Shah and Scott, 2021). The addition of Na_2CO_3 increased the compressive strength in MS_NaC but reduced that in MK_NaC. Na_2CO_3 has been shown to accelerate the formation of M-S-H and M-A-S-H through destabilizing brucite (Bernard et al., 2023). However, in the case of MK_NaC, the formation of M-A-S-H might have been retarded by the presence of excess phosphate, as has been observed with M-S-H (Walling et al., 2015).

Figure 2 shows the BSE images of all systems at 91 days of curing. MS_0 is considerably more porous than MK_0. However, the spaces between MgO and silica fume or metakaolin particles appear to be occupied by M-S-H or M-A-S-H with no definite form. Platelet-like structures, likely to be hydrotalcite, are also observed in MK_0. The incorporation of Na_2CO_3 led to a densification of the microstructure in MS_NaC relative to MS_0, evident by the increased formation of M-S-H (and possibly brucite) in the pore space. This is supported by the presence of MgO particles with a dark rim, indicating an increased reaction of MgO. The effect of Na_2CO_3 in increasing porosity in MK_NaC relative to MK_0 is evident in the BSE images.

Figure 3 shows the cumulative pore size distributions measured by MIP at 7 and 91 days of curing. Overall, the results corroborate the BSE observations (Figure 2). The intruded pore volumes and pore sizes reduced with curing age and were larger in MS_0 than in MK_0. The addition of Na_2CO_3 reduced the pore volumes and pore sizes in MS_NaC, but no consistent effect was observed in MK_NaC, although the pore sizes seemed to increase.

Figure 4 shows the BET pore SSA and mean pore diameters measured by N_2 adsorption. Irrespective of the system, the pore SSA generally increased with curing age up to 28 days, presumably due to the increased formation of M-S-H or M-A-S-H, and their gel pores, similar to C-S-H in Portland cement

systems. However, the pore SSA decreased after 28 days of curing. The reason for this is unclear from the results obtained, but a similar observation has been reported with M-S-H synthesised at a high water/solid ratio of 45 between 1 and 3 years of curing (Bernard et al., 2019). The pore SSA was larger in MS_0 than in MK_0 after 28 days of curing, indicating that a larger amount of M-S-H had formed in MS_0 than M-A-S-H in MK_0. This result also suggests that the higher compressive strengths of MK_0 could be more of a result of physical pore filling by unreacted metakaolin particles. The incorporation of Na_2CO_3 increased the pore SSA in MS_NaC but decreased that in MK_NaC. A general opposite trend was observed with the mean pore diameters, such that the higher the SSA, the smaller the mean pore diameter, confirming the densification of microstructure by M-S-H or M-A-S-H gels.

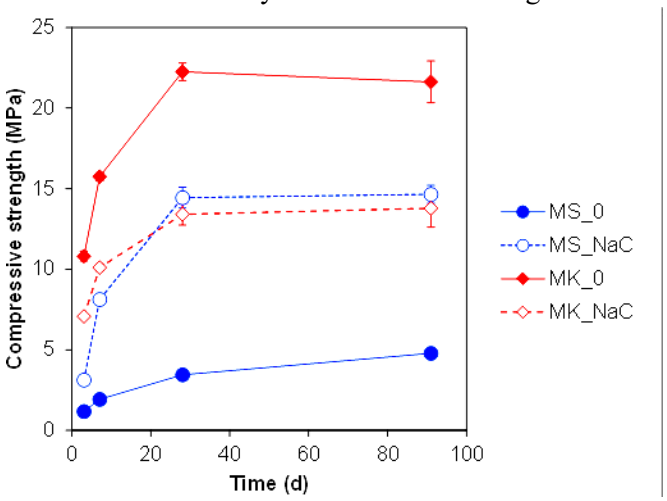


Figure 1: Compressive strength of all systems with curing age. Error bars represent ± standard error.

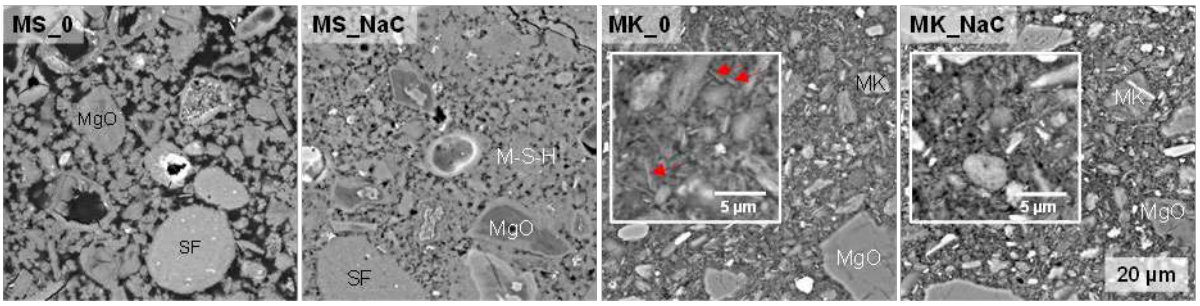


Figure 2: BSE images of all systems at 91 days of curing. Arrows indicate hydrotalcite-like structures.

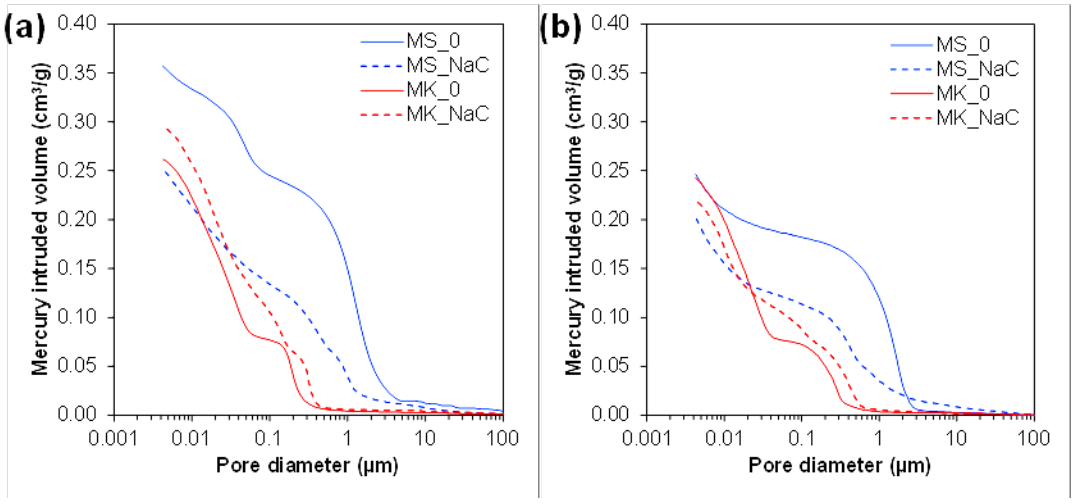


Figure 3: Pore size distribution of all systems at (a) 7 and (b) 91 days of curing measured by MIP.

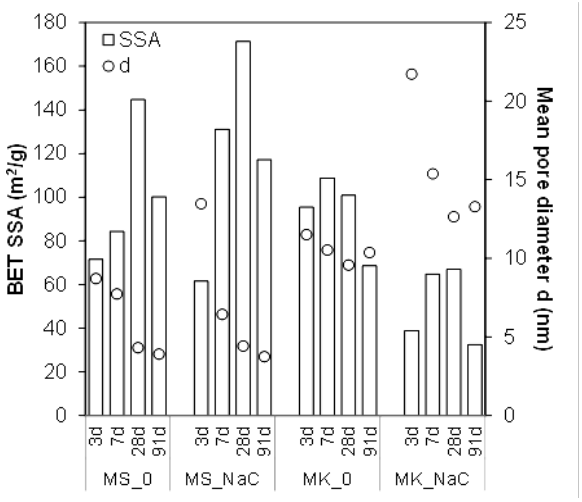


Figure 4: BET SSA and mean pore diameter (d) of all systems with curing age measured by N_2 adsorption.

4. Conclusions

The compressive strength and microstructure of M-S-H and M-A-S-H pastes with an Mg/Si molar ratio of 1.5 and Al/Si molar ratios of 0 (MS) and 1.0 (MK), with and without Na_2CO_3, were investigated. The MK system achieved higher compressive strengths than the MS system at all curing ages. Na_2CO_3 increased the compressive strength of the MS system but reduced that of the MK system, likely due to the presence of excess phosphate. BSE and MIP results showed higher pore volumes and larger pore sizes in the MS system than in the MK system, corroborating the compressive strength results. Na_2CO_3 reduced the pore volume and size distribution of the MS system but no consistent effects were observed for the MK system. However, the pore specific surface areas and mean pore diameters measured by N_2-BET suggest that a larger amount of M-S-H had formed in the MS system than in the MK system, with or without Na_2CO_3, indicating that the higher compressive strength of the MK system could be largely due to pore filling by metakaolin. Work is ongoing to correlate the microstructure and phase assemblages measured by XRD, TGA and NMR, and to understand the effect of phosphate on the formation of M-A-S-H.

Acknowledgements

The research benefitted from EPSRC funding under grant No. EP/R010161/1 and EP/R017727/1. The financial support from the Swiss National Science Foundation (SNSF) for E. Bernard's Postdoc mobility under grant No. P400P2_194345 is also gratefully acknowledged.

References

Bernard, E. 2022. Research progress on magnesium silicate hydrate phases and future opportunities. *RILEM Technical Letters,* 7**,** 47-57.

Bernard, E., Lothenbach, B., Chlique, C., Wyrzykowski, M., Dayzeres, A., Pochard, I. & Cau-dit-coumes, C. 2019. Characterization of magnesium silicate hydrate (M-S-H). *Cement and Concrete Research,* 116**,** 309-330.

Bernard, E., Lothenbach, B., German, A. & Winnfeld, F. 2023. Effect of carbonates on the formation of magnesium silicate hydrates (M-S-H) and magnesium alumino silicate hydrates (M-A-S-H) (Unpublished). *SynerCrete' 23.*

Jia, Y., Wang, B., Wu, Z., Han, J., Zhang, T., Vandeperre, L. J. & Cheeseman, C. R. 2016. Role of sodium hexametaphosphate in MgO/SiO2 cement pastes. *Cement and Concrete Research,* 89**,** 63-71.

Scott, A., Oze, C., Shah, V., Yang, N., Shanks, B., Cheeseman, C., Marshall, A. & Watson, M. 2021. Transformation of abundant magnesium silicate minerals for enhanced CO2 sequestration. *Communications Earth & Environment,* 2**,** 25.

Shah, V., Dhandapani, Y. & Scott, A. 2021. Pore structure characteristics of MgO–SiO2 binder. *Journal of the American Ceramic Society,* 104**,** 6002-6014.

Shah, V. & Scott, A. 2021. Hydration and microstructural characteristics of MgO in the presence of metakaolin and silica fume. *Cement and Concrete Composites,* 121**,** 104068.

Walling, S. A., Kinoshita, H., Bernal, S. A., Collier, N. C. & Provis, J. L. 2015. Structure and properties of binder gels formed in the system Mg(OH)2–SiO2–H2O for immobilisation of Magnox sludge. *Dalton Transactions,* 44**,** 8126-8137.

The 16th International Congress on the Chemistry of Cement 2023 (ICCC2023)
"Further Reduction of CO_2 -Emissions and Circularity in the Cement and Concrete Industry"
September 18–22, 2023, Bangkok, Thailand

Development of Carbonation-cured Low-carbon Precast Concrete Products and Evaluation of Avoided CO_2 Emissions

S. Hoshino[1*], K. Kobayashi[2], Y. Ohgi[2], M. Hashimoto[2], Y. Kirino[2], Y. Hosokawa[2], Kouki Ichitsubo[1] and K. Nomura[1]

[1] *Carbon Neutral Technology Development Project Team, Taiheiyo Cement Corporation, Chiba, Japan*
[2] *Central Research Laboratory, Taiheiyo Cement Corporation, Chiba, Japan*

ABSTRACT

A low-carbon cement characterized by strength development during carbonation curing and reduced CO_2 emissions during manufacturing was developed in this report, with an aim of developing a carbon dioxide capture and utilization (CCU) technology utilizing cementitious materials. Using the low-carbon cement, the authors also developed interlocking (IL) blocks into which CO_2 was fixed through the carbonation curing, as an example of application to precast concrete products. The IL blocks developed were found to satisfy the requirements specified in the Japanese Industrial Standards (JIS). Furthermore, a life cycle assessment (LCA) was performed with a whole series of processes required for the manufacturing of the IL blocks included in the system boundary, which showed that substituting the IL blocks developed in this report for conventional ones could result in avoided CO_2 emissions of 69.1 kg per ton of product. These results indicated that the IL block developed would be an effective CCU technology.

KEYWORDS: *Low-carbon cement, Carbonation curing, Interlocking block, Avoided CO_2 emissions, CCU*

1. Introduction

In the global trend toward carbon neutrality, reducing carbon dioxide (CO_2) emissions is one of the most important issues for the cement industry. The authors had been working on Development of Carbon Circulation Technology for the Cement Industry which was a project funded by the New Energy and Industrial Technology Development Organization (NEDO) of Japan (Taiheiyo Cement Corporation (2022)). In the project, a CO_2 capture facility based on the amine absorption method has been installed at a cement plant to capture CO_2, and development is underway for technologies to utilize the captured CO_2 with the use of cementitious materials and waste including waste concrete and concrete sludge. Among the carbon dioxide capture and utilization (CCU) technologies under development, sequestration of CO_2 in precast concrete products is one of the technologies to utilize CO_2 using cementitious materials. A new cement developed in that study has a lowered CaO content for reduced CO_2 emissions and is characterized by the ability to develop strength during carbonation curing. This cement fixes CO_2 by generating calcium carbonate through the reaction of CO_2 with cement minerals during carbonation curing. Both the reduction of CO_2 emissions from the cement manufacturing process and CO_2 fixation during curing provide a reduction of CO_2 emissions compared to conventional Portland cement. In the aforementioned project, using the low-carbon cement, interlocking (IL) blocks (hereinafter referred to as the carbonation-cured low-carbon IL blocks) were also developed as an example of application to precast concrete products. In this study, manufacturing of the carbonation-cured low-carbon IL blocks was carried out as a CCU technology using cementitious materials, using an actual production line at a precast concrete factory, and the performance of the products was investigated. Furthermore, evaluation was made on avoided CO_2 emissions to be achieved by substituting the carbonation-cured low-carbon IL blocks for conventional ones, thereby verifying the effectiveness as a CCU technology.

2. Carbonation-cured Low-carbon IL Block Manufacturing Test

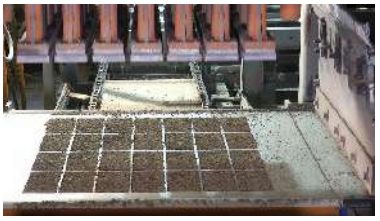
2.1 Test method

The low-carbon cement for the test was manufactured by using a small test kiln with a production

capacity of about 1 ton per hour. Table 1 shows the moduli of the low-carbon cement and also those of a typical ordinary Portland cement (OPC) in Japan for reference. The low-carbon cement for the test has a lower hydraulic modulus (HM) and therefore a lower CaO content as compared to OPC, to reduce the CO_2 emissions related to limestone and thus to raw materials. The low-carbon cement is burned at low temperatures, which also reduces the energy-related CO_2 emissions from the cement manufacturing process. With these two effects combined, CO_2 emissions of cement are reduced. The new design of the low-carbon cement, with the moduli or chemical composition adjusted, enables CO_2 fixation and strength development simultaneously during carbonation curing.

Table 1 Moduli of the low-carbon cement

	HM	SM	IM
Low-carbon cement	1.39	2.99	1.66
OPC (example for reference)	2.24	2.46	1.80



(a) Molding the IL blocks



(b) Carbonation curing chamber



(c) Carbonation-cured low-carbon IL blocks

Fig. 1 Outline of the carbonation-cured low-carbon IL block manufacturing process

The low-carbon cement was used to manufacture the carbonation-cured low-carbon IL blocks. The IL blocks were prepared in two different types, the ordinary type and the water permeable type. Fig. 1 outlines the manufacturing process of the carbonation-cured low-carbon IL blocks. Actual manufacturing equipment at a precast concrete factory was used. Concrete was mixed in a mixer and molded into blocks by using a pressurized vibration molding machine (Fig. 1(a)), and the blocks after the mold removal were cured in a carbonation curing chamber (Fig. 1(b)). The IL blocks had dimensions of 98 mm × 198 mm and a thickness of 80 mm (Fig. 1(c)). Carbonation curing was performed in the curing chamber at an ambient temperature of 30°C in a relative humidity of 80% with a CO_2 concentration of 80% for six consecutive days. The test was performed in two batches for each of the ordinary and water permeable types, producing 336 IL blocks in each batch, or 672 IL blocks of each type.

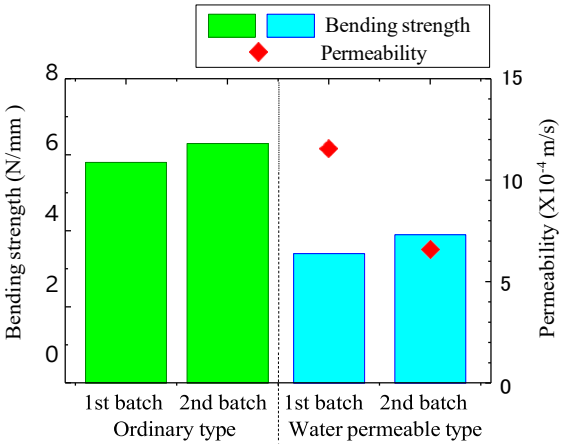


Fig. 2 Bending strength and permeability of the carbonation-cured low-carbon IL blocks
(Averages of three arbitrarily sampled blocks)

Three IL blocks were sampled from each batch after carbonation curing, and the bending strength and permeability were measured in accordance with Japanese Industrial Standards (JIS) A 5371, Precast Unreinforced Concrete Products. The permeability measurement was made only on the water permeable blocks. The amount of fixed CO_2 was determined by measuring the total carbon amount with a carbon/sulfur analyzer, using the IL blocks roughly crushed and then pulverized in a vibratory disk mill.

2.2 Test result

Fig. 2 shows the results of bending strength and permeability of the carbonation-cured low-carbon IL blocks. The ordinary type from the first and second batches had an average bending strength of 5.8 N/mm^2 and 6.3 N/mm^2, respectively, satisfying the specified strength of 5 N/mm^2 or above for roadway IL blocks in JIS A 5371. The average bending strength of the water permeable type was 3.4 N/mm^2 for the first batch and 3.9 N/mm^2 for the second batch, which meets the specified strength of 3 N/mm^2 or above for sidewalk IL blocks. The permeability coefficient of the water permeable blocks was 11.4×10^{-4} m/s for the first batch and 6.6×10^{-4} m/s for the second batch, satisfying the JIS requirement of 1.0×10^{-4} m/s or above. Consequently, it was shown that the carbonation-cured low-carbon IL blocks of the ordinary and water permeable types had satisfactory performance for practical use, meeting the JIS

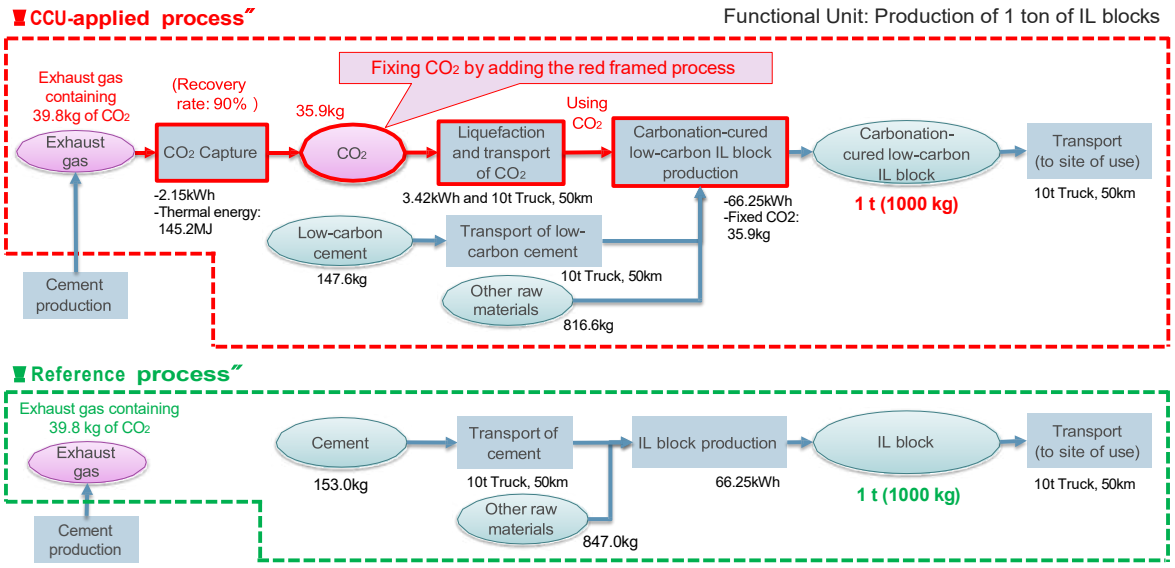


Fig. 3 System boundary of the evaluation

requirements specified for roadway IL blocks and permeable sidewalk IL blocks, respectively. Furthermore, it was found that CO_2 was fixed at a rate of 243 kg/t in the ordinary type and 236 kg/t in the water permeable type, respectively, per unit cement content. Meanwhile, the CO_2 emissions during manufacturing of the low-carbon cement were lower by 265 kg/t compared to OPC. With the amount of reduction in CO_2 emissions by the low-carbon cement added to the amount of CO_2 fixed by the carbonation curing, the CO_2 reduction effect of the carbonation-cured low-carbon IL blocks was calculated to be 508 kg/t-cement for the ordinary type and 501 kg/t-cement for the water permeable type, respectively, as compared to the OPC-based IL blocks.

3 Evaluation of Avoided CO_2 Emissions of Carbonation-cured Low-carbon IL Blocks

3.1 Evaluation method

Fig. 3 shows the system boundary in life cycle assessment (LCA) of CO_2 emissions. The evaluation of the CO_2 emissions described in this section is not limited to the range of materials and products, but also takes into account a series of processes required for practical application, including transport of materials and products, CO_2 capture and manufacturing of precast concrete products. The evaluation was made on the CO_2 emissions per ton of production of the IL blocks. The following steps were included in the scope of evaluation for the process of the carbonation-cured low-carbon IL blocks to which the CCU technologies were applied (hereinafter referred to as the CCU-applied process): 1) CO_2 capture from cement plant exhaust gas / 2) liquefaction of the captured CO_2 / 3) transport of the liquefied CO_2 to a precast concrete factory / 4) transport of the low-carbon cement from a cement plant to the precast concrete factory / 5) manufacturing of the carbonation-cured low-carbon IL blocks / 6) transport of the manufactured IL blocks to a site of use.

A process of general IL blocks was used as the reference in the evaluation, with the following steps included in the scope of evaluation: 1) transport of cement (ordinary Portland cement assumed) from a cement plant to a precast concrete factory / 2) manufacturing of IL blocks / 3) transport of the manufactured IL blocks to a site of use.

Inventory data such as electric power, thermal energy, CO_2 emissions by materials and transport, and CO_2 fixation in each item were set up, and CO_2 emissions of CCU-applied process and reference processes were calculated. In addition, the avoided CO_2 emissions was obtained from the difference between the two processes.

3.2 Evaluation results on avoided CO_2 emissions

Fig. 4 shows the evaluation results on the CO_2 emissions and the avoided CO_2 emissions per ton of carbonation-cured low-carbon IL blocks. For the reference process with general IL blocks, the CO_2 emissions were estimated to be 215.9 kg/t as a sum of cement plant exhaust gas, emissions related to cement and other materials as well as those related to energy in IL block manufacturing, and emissions from transport. The total CO_2 emissions from the CCU-applied process were estimated to be 146.8 kg/t,

which was lower than those from the reference process. This was a result of the decreased emissions related to cement and other materials in IL block manufacturing as well as the reduction effect of CO_2 fixation, despite the increase for CO_2 capture and CO_2 liquefaction and transport. The cause of the decrease in the CO_2 emissions related to cement and other materials in IL blocks manufacturing was the use of the low-carbon cement. The difference in the CO_2 emissions indicated that avoided CO_2 emissions of 69.1 kg/t would be achieved by applying the carbonation-cured low-carbon IL blocks.

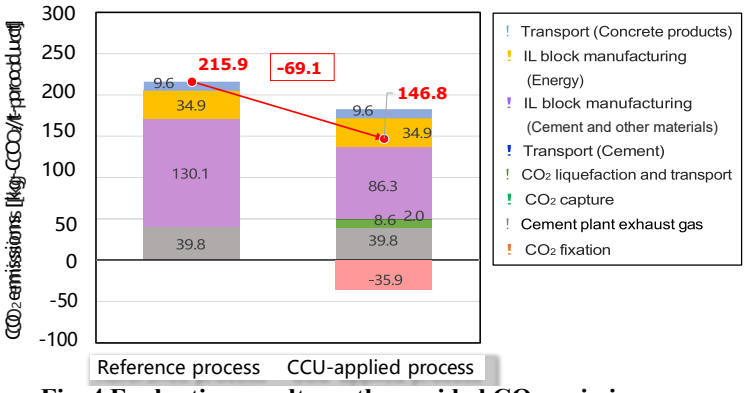


Fig. 4 Evaluation results on the avoided CO_2 emissions per ton of carbonation-cured low-carbon IL blocks

On the assumption of future carbon-free electricity and transport, calculation of CO_2 emissions and avoided emissions were made also for their reduced CO_2 emission factors. The CO_2 emission factors of electricity and transportation shown in Table 2 were given in the calculation. The results of CO_2 emissions and avoided emissions are shown in Fig.5. It was found that the avoided emissions determined as the difference between the two processes would be 69.1 kg/t for the current state, 70.4 kg/t for the target 2030-equivalent state, and 79.6 kg/t for the carbon-free state, showing that the reduction effect would be greater with the progress of carbon-free transition.

Table 2 CO_2 emission factors of electricity and transport used in the calculation

	Present	Target 2030-equivalent state	Carbon-free state
Electricity [kg/kWh]	0.47 (*1)	0.25 (*2)	0
Transport [kg/(t·km)]	0.192	0.192 (*3)	0

(*1) Ministry of the Environment (2021(a))
(*2) Ministry of the Environment (2021(b))
(*3) Current value was substituted because there was no clear and common target value.

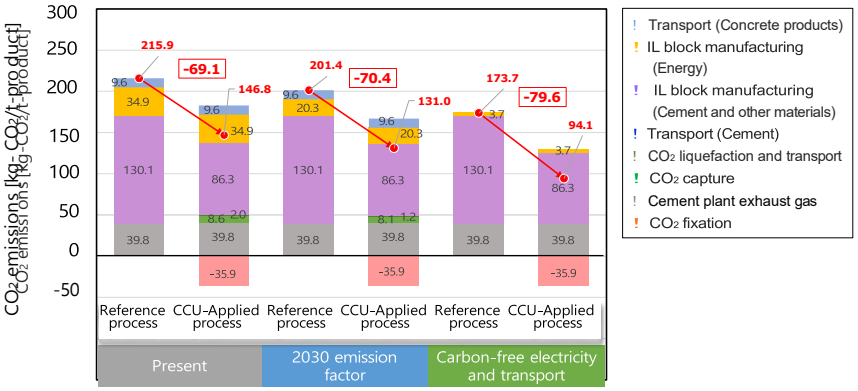


Fig. 5 Evaluation results on the avoided CO_2 emissions assuming future carbon-free electricity and transport

4. Conclusions

Carbonation-cured low-carbon IL blocks were manufactured by carbonation curing in CO_2 gas, and their properties were evaluated as part of development of CCU technologies using cementitious materials. The IL blocks developed were found to satisfy the requirements specified in the Japanese Industrial Standards. A life cycle assessment was performed with a whole series of processes required for the manufacturing of the IL blocks included in the system boundary, which showed that substituting the IL blocks developed in this report for conventional ones could result in avoided CO_2 emissions of 69.1 kg per ton of product. These results indicated that the IL block developed would be an effective CCU technology.

Acknowledgements

This study is the result of Development of Carbon Circulation Technology for the Cement Industry (JPNP20013) which is a project funded by the New Energy and Industrial Technology Development Organization (NEDO) of Japan. The authors appreciate Mizuho Research & Technologies, Ltd. for their great support in the CO_2 reduction effect calculation in Chapter 3.

References

Taiheiyo Cement Corporation (2022) "News Letter: A NEDO-funded project for the Development of Carbon Circulation Technology for the Cement Industry", On: https://www.taiheiyo-cement.co.jp/english/summary/pdf/220204.pdf.

Ministry of the Environment (2021a) "Emission Factors by electricity utility - Performance in FY2021-, On:

https://www.env.go.jp/content/900517763.pdf (in Japanese)
Ministry of the Environment (2021b) “Basis for reductions in measures in the Plan for Global Warming Countermeasures”, On: https://www.env.go.jp/content/000051887.pdf (in Japanese)

The 16th International Congress on the Chemistry of Cement 2023 (ICCC2023)
"Further Reduction of CO_2 -Emissions and Circularity in the Cement and Concrete Industry"
September 18–22, 2023, Bangkok, Thailand

Experimental study on synergy between CO_2 mineralized steel slag and carbonation-cured steel slag-cement paste

L.S. Li[1], T.F. Chen[2*], and X.J. Gao[3*]

[1] *School of Civil Engineering, Harbin Institute of Technology, Harbin 150090, China*

Email: lls970310@163.com

[2] *School of Civil Engineering, Harbin Institute of Technology, Harbin 150090, China*

Email: chentf@hit.edu.cn

[3] *School of Civil Engineering, Harbin Institute of Technology, Harbin 150090, China*

Email: gaoxj@hit.edu.cn

ABSTRACT

A unique synergy between CO_2 mineralized steel slag and carbonation-cured cement paste was proposed. In this study, steel slag was mineralized in a CO_2 chamber for different duration and then added to cement as substitute by the dosage of 20% and 40%. Steel slag-cement paste went through carbonation curing for up to 12 h in the same CO_2 chamber. The barrier layer on CO_2 mineralized steel slag impeded its pozzolanic activity in the early hydration process. As the barrier layer eroded by secondary hydration on the later stage, steel slag was activated and showed better pozzolanic behavior than the unmineralized one. Synergistic carbonation treatment increased the CO_2 sequestration of 20% steel slag-cement paste from 2.4% to 7.1%, nearly doubling that of CO_2 mineralization or carbonation curing. Besides, with synergistic carbonation treatment, the strength of cement mixed with 20% steel slag was increased by 11.6% on 28 d. Several characterization techniques were used to analyze the mechanism of synergistic carbonation treatment. This paper takes a new direction for lowering CO_2 emissions and boosting the carbon sink capacity in ecosystem.

KEYWORDS: *Carbonation curing, steel slag, cement, CO_2 sequestration.*

1. Introduction

As the rising temperature gets more and more attention around the world, countries have announced their goals to be carbon neutral in the future. As an advanced technology for precuring, carbonation curing has attracted many scientists' attention (Zhang et al (2022)). In addition to cement, industrial waste residues are considered as the most promising materials for carbon capture and storage (Chen et al (2022)). Among them, previous experiments proved that steel slag (SS) has unparalleled carbon-capture potential among the wastes (Suescum-Morales et al (2021), Pan et al (2016)). Yet the most common phenomenon is that the dense carbonation layer is confined to the sample surface. How to make CO_2 penetrate into the specimen interior and increase CO_2 sequesration has become a worth discussing topic. A synergistic carbonation treatment was conducted, the pozzolanic activity of CO_2 mineralized SS and the performance of carbonation-cured SS-cement paste were determined.

2. Materials and Methods

Basic oxygen furnace slag was selected as representative of SS for its huge output, provided by Wuhan Weishen technology Co., Ltd (China), and its specific surface is 408 m^2/Kg. SS was prepared with water-to-slag ratio of 0.1, then put into the CO_2 chamber for up to 24 h. After that, CO_2 mineralized SS was ground in to powders with particle size less than 80 μm. SS mineralized for 2 h and 24 h were selected as the objects for subsequent experiments, named PCS (partially CO_2-mineralized SS) and FCS (almost fully CO_2-mineralized SS), respectively. UCS (uncarbonated SS) was selected as the control group. UCS, PCS, and FCS were used as substitute for cement at 20% and 40% dosage. SS-cement paste was prepared with water-to-binder ratio of 0.35, then formed into cubes with 20 mm side and pre-curing in standard condition for 24 h. After demolding, specimens were induced to carbonation curing in CO_2 chamber for up to 12 h. All specimens were cured in standard condition until 28 d. CO_2 concentration was 20% in CO_2 chamber, temperature was 20℃, and relative humidity was kept at 70%. To differentiate, the treatment of SS is

known as CO_2 mineralization, and the treatment of cement paste is known as carbonation curing. Specimens were named by the mixed SS and carbonation curing duration of the paste. Thermal analysis method, acid-alkali dissolution method, and hydration heat evolution method were selected to verify the pozzolanic behavior of UCS, PCS, and FCS. The compressive strength of SS-cement paste was tested on 3 d, 7 d, and 28 d. DTG, Si NMR, and SEM were used to characterize the microstructure and micromorphology of the samples.

3. Results and discussion

3.1 Pozzolanic activity of CO_2 mineralized SS

Fig.1, Fig.2, and Fig.3 correspond to the test results of thermal analysis method, acid-alkali dissolution method, and hydration heat evolution method, respectively. These three methods are widely used to evaluate the pozzolanic activity of materials, and basically with the same principle. The active chemicals (SiO_2 and Al_2O_3) in SS react with $Ca(OH)_2$ in the system, The more active constituent engage in the reaction, the higher the pozzolanic activity of the sample. Fig.1 shows the residual $Ca(OH)_2$ content in samples, it decreases with the increasing CO_2 mineralization time. In Fig.2, the concentration of Si ion and Al ion decreases as the CO_2 mineralization time increases. As shown in Fig.3, CO_2 mineralized SS also affects the heat flow of SS-cement system. Generally, CO_2 mineralization reduces the pozzolanic activity of SS in early stage. But as the hydration proceeds, the activity of CO_2 mineralized SS gradually increases and even exceeds that of UCS.

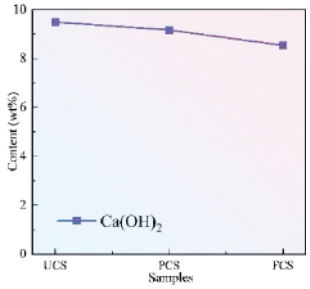


Fig.1 $Ca(OH)_2$ content

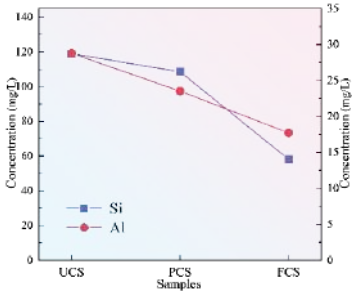


Fig.2 Si ion and Al ion concentration

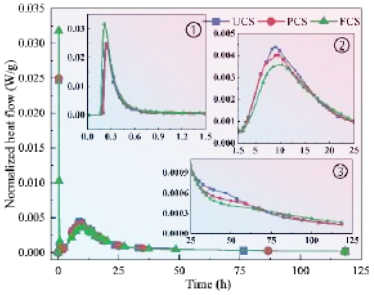


Fig.3 Hydration heat evolution

3.2 CO_2 sequestration

CO_2 sequestration of SS-cement paste was measured by weight loss due to the $CaCO_3$ decomposition, as shown in Fig.4. With synergistic carbonation treatment, CO_2 sequestration has significantly improved. When CO_2 mineralization and carbonation curing act separately, the CO_2 sequestration of cement containing 20% SS increases by 2.5% (20%FCS-0h) and 3.0% (20%UCS-12h), respectively, as compared to 20%UCS-0h. When containing 40% SS, the corresponding values are 5.5% (40%FCS-0h) and 2.1% (40%UCS-12h) as compared to 40%UCS-0h. Surprisingly, under the synergistic action between CO_2 mineralization and carbonation curing, the CO_2 sequestration of SS-cement paste rises by 4.7% (20%SS) and 8.1% (40%SS). Synergistic carbonation treatment has a far better CO_2 sequestration efficiency than traditional single carbonation curing.

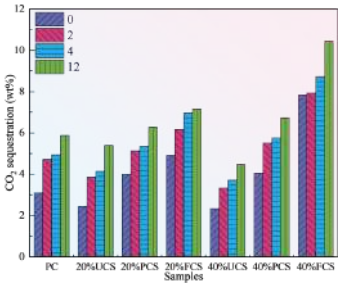


Fig.4 CO_2 sequestration of SS-cement paste

3.3 Compressive strength

Fig.5 and Fig.6 show the compressive strength of SS-cement paste with synergistic carbonation treatment. The addition of SS considerably reduces the early strength, although the strength gap narrows later on. This is because SS promotes secondary hydration. When just the influence of CO_2 mineralization time is considered, it has little effect on cement strength. However, due to the nucleation effect provided by carbonates, appropriate carbonation curing duration can improve strength. On 28 d, synergistic carbonation treatment increased the strength of cement containing 20%SS by 11.6% (20%PCS-2h) compared to the control group (20%UCS-0h). However, at the same age, 40% PCS and 40% FCS were disadvantageous to cement strength. Specimens with higher SS content require a longer period of hydration latency to present the pozzolanic behavior of SS, and the long-term strength (90 d and 180 d) of SS-cement specimens with synergistic carbonation treatment will be proven in the following study.

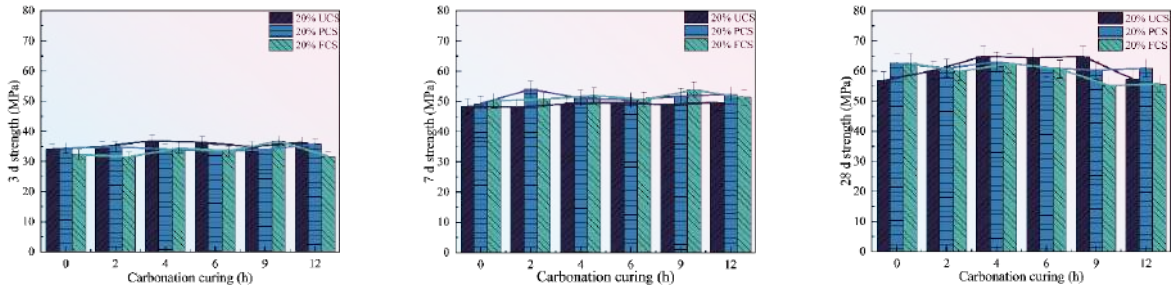


Fig.5 Compressive strength of cement paste with 20% SS

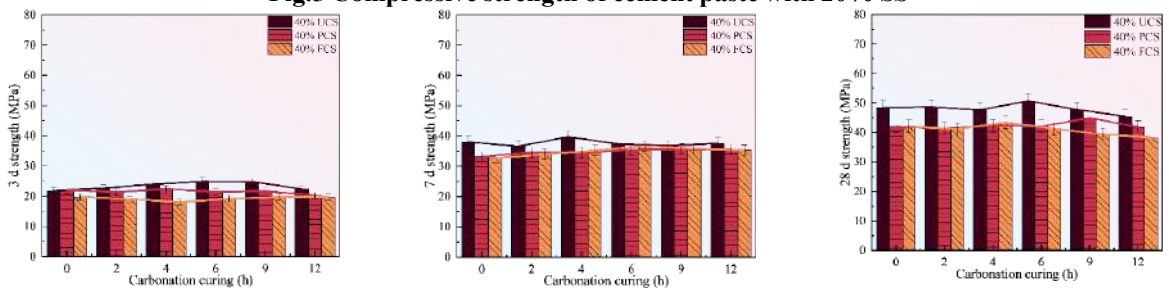


Fig.6 Compressive strength of cement paste with 40% SS

3.4 ^{29}Si MAS NMR

Fig.7 shows the deconvolution results of ^{29}Si NMR spectra on SS-cement pastes with synergistic carbonation treatment. Q denotes C-S-H silicate tetrahedra, while n denotes the number of oxygen atoms bridging to the neighboring silicate tetrahedra, ranging from 0 to 4. The intensity of Q_0, Q_1, and Q_2 fluctuates to varied degrees as a result of the synergy between CO_2 mineralization and carbonation curing. Q_0 becomes narrower and sharper, indicating a decrease in C_2S and C_3S. The chemical environment of silicon atoms in C-S-H gel is reflected in Q_1 and Q_2. Q_1 weakens slightly while Q_2 increases, indicating that C-S-H gel is more likely to be arranged in chain-like conformation. Q_3 and Q_4 represent the hydroxylated surface sites and completely condensed network of the silicate tetrahedrons, respectively, larger peaks imply more amorphous silica in the sample. Synergistic carbonaion results in longer chain and greater degree of polymerization in C-S-H gel.

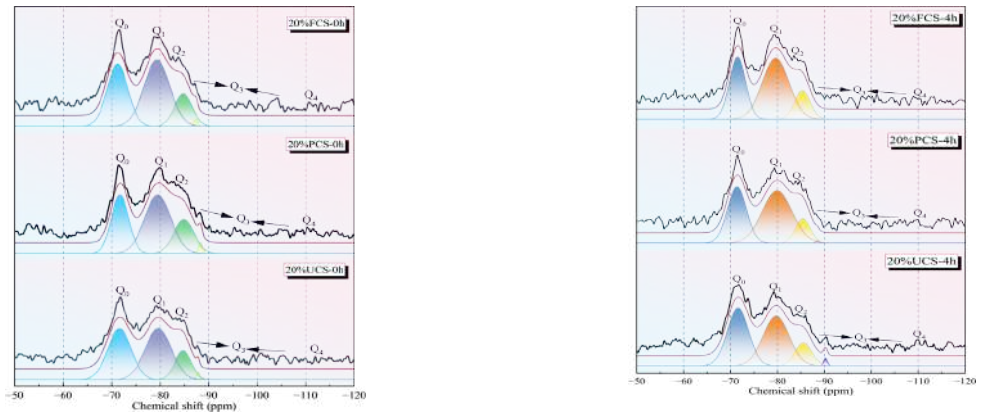
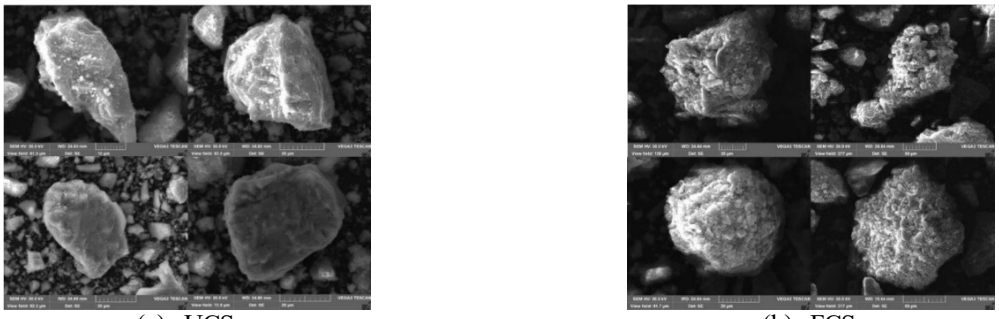


Fig.7 NMR results of SS-cement paste

3.5 SEM

Fig.8 shows the micromorphology of UCS and FCS powders. The UCS surface is visibly smooth with few irregular particles, but the FCS surface is clearly rougher and totally coated with spherical and irregular particles. Apparently CO_2 minaralization forms a barrier layer on the SS surface composed of carbonation and hydration products such as $CaCO_3$, $Ca(OH)_2$, SiO_2, and C_2S. The pozzolanic behavior of the active constituents and the nucleation action of calcium carbonates become more pronounced when the barrier layer dissolves, accelerating cement hydration.



(a) UCS (b) FCS

Fig.8 SEM images of SS before and after CO_2 mineralization

4. Conclusions

This paper discusses the synergy between CO_2 mineralized steel slag and carbonation-cured steel slag-cement paste. The barrier layer limits the pozzolanic activity of steel slag in the early hydration stage. As the barrier layer disintegrates, CO_2 mineralized SS accelerates cement hydration with the released active constituents and nucleation effects. Therefore, the strength of cement mixed with CO_2 mineralized SS performs better in later stage. Synergistic carbonation treatment improves the strength of steel slag-cement paste by up to 11.6% on 28 d. Moreover, CO_2 sequestration has almost doubled. However, other performance of steel slag-cement paste with synergistic carbonation treatment, particularly long-term performance, should be investigated further. In summary, synergistic carbonation treatment provides a new possibility for the development of carbon capture, utilization and storage, as well as contributing to the sustainable development of society.

Acknowledgements

The authors would like to acknowledge the financial support of the National Natural Science Foundation of China (No. U2106220), the Key Project of Natural Science Foundation of Heilongjiang Province (No. ZD2022E008), and the Natural Science Foundation of Heilongjiang Province of China (No. LH2022E071).

References:

Zhang, P. Lewis, J.B. Klein-BenDavid, O. and Garrabrants, A.C. (2022) “The role of environmental conditions on the carbonation of an alkali-activated cementitious waste form”, *Cement and Concrete Research*, 151(2):106645

Chen, L. Zhao, L. Gao, X. and Li, L. (2022) “Modification of carbonation-cured cement mortar using biochar and its environmental evaluation”, *Cement and Concrete Composite*s, 134(2):104764.

Suescum-Morales, D. Kalinowska-Wichrowska, K. and Fernández, J.M. (2021) “Accelerated carbonation of fresh cement-based products containing recycled masonry aggregates for CO_2 sequestration”, *Journal of CO_2 Utilization*, 46(2):101461.

Pan, S.-Y. Adhikari, R. Chen, Y.-H. Li, P. Chiang, P.-C. (2016) “Integrated and innovative steel slag utilization for iron reclamation, green material production and CO2 fixation via accelerated carbonation”, *Journal of Cleaner Production*, 137(2):617-631.

The 16th International Congress on the Chemistry of Cement 2023 (ICCC2023)
"Further Reduction of CO_2 -Emissions and Circularity in the Cement and Concrete Industry"
September 18–22, 2023, Bangkok, Thailand

Hydration of cementitious binders based on magnesium oxide / hydromagnesite blends

F. Winnefeld[1*], A. German[1,2], P. Lura[1,2] , D. Rentsch[3] and B. Lothenbach[1,4]

[1] *Empa, Laboratory for Concrete and Asphalt, Dübendorf, Switzerland*
Email: frank.winnefeld@empa.ch, alexander.german@empa.ch, pietro.lura@empa.ch, barbara.lothenbach@empa.ch
[2] *ETH Zürich, Institute for Building Materials, Zürich, Switzerland*
[3] *Empa, Laboratory for Functional Polymers, Dübendorf, Switzerland*
Email: daniel.rentsch@empa.ch
[4] *NTNU, Department of Structural Engineering, Trondheim, Norway*

ABSTRACT

Cementitious binders based on MgO exhibit a low CO_2 footprint or can even be CO_2-negative, if the MgO is generated from carbonate-free raw materials. One class of such binders are blends of MgO with hydromagnesite. In this study, the hydration products formed in this system were investigated at temperatures between 7 and 60°C. A poorly-crystalline brucite containing some carbonate is the main hydration product. Furthermore, a kind of "gel-water" is observed, which is lost at temperatures above 40-60°C.

KEYWORDS: *Low-CO_2 cement, hydrated magnesium carbonate, magnesium oxide, hydromagnesite, brucite*

1. Introduction

MgO can be used to make a variety of hydraulic binders as well as binders that harden by carbonation (Gartner and Hirao (2018)). Potential raw materials for MgO production are magnesium silicates or Mg-containing brines, which can be carbonated and subsequently partially calcined. The mixture of MgO and basic magnesium carbonates obtained by this process is able to set and harden when mixed with water (Vlasopoulos and Cheseman (2009)). Similar compressive strengths values as for systems based on Portland cement can be reached. If the MgO source originates from carbonate-free raw materials, such cements exhibit a low carbon footprint or could even be carbon-negative.
Recent investigations on the hydration mechanisms of binders based on blends of magnesium oxide and hydromagnesite ($Mg_5(CO_3)_4(OH)_2 \cdot 4H_2O$) revealed the presence of an unknown magnesium carbonate hydrate phase, while artinite ($Mg_2(CO_3)(OH)_2 \cdot 3H_2O$) is predicted by thermodynamic calculations, but not identified in the experiments (Kuenzel et al. (2018), Winnefeld et al. (2019)). The current study, see German et al. (2023) and German (2023) for more details, aims at a detailed investigation of the hydrates formed at temperatures between 7 and 60°C in such binders.

2. Materials and methods

Blends of 70 mass-% MgO (calcined from reagent-grade brucite at 900°C for 6 h) and 30 mass-% reagent-grade hydromagnesite (HY) were used to prepare suspensions with ultrapure water and a water-to-solid ratio of 20. The samples were cured in sealed vessels for 12 months at 7, 20, 40, and 60°C. At the age of testing, the samples were filtered. The further reaction of the solid residue was stopped by solvent exchange (Snellings et al. (2018)). The material was then ground by hand using an agate mortar to a particle size below 63 µm and investigated by X-ray diffraction analyses (XRD), thermogravimetry

coupled with infrared spectroscopy (TGA-IR), Raman spectroscopy and solid state ^{13}C nuclear magnetic resonance spectroscopy (^{13}C CP-MAS NMR). The liquid phase was analysed using a pH meter, ion chromatography and a TOC/TC analyser to determine pH, ion concentrations and inorganic carbon. Further details of the experimental procedures are given in German et al. (2023) and German (2023). Thermodynamic calculations were performed using GEMS (Wagner et al. (2012), Kulik et al. (2013)) coupled with the Nagra/PSI thermodynamic database (Hummel et al. (2002)) and additional data related to magnesium carbonates (Winnefeld et al. (2019), Bernard et al. (2022)).

3. Results

XRD (Fig. 1a) shows that MgO is almost consumed after 12 months, while HY is still present. A low-crystalline brucite forms, which shows broadened and shifted reflections compared to the reagent-grade brucite, which serves as reference. This refers especially to the (001) reflection, which is shifted to higher 2Θ-values. A small hump occurs at 16.1-16.8° 2Θ CuKα for the sample cured at 20°C, which had previously been tentatively assigned to an unknown phase (Kuenzel et al. (2018), Winnefeld et al. (2019)). The hump shifts to higher 2Θ-values for the 40°C sample and vanishes for the 60°C sample. Temperature influences as well the position of the (001) reflection of brucite. At 40°C it is shifted to lower 2Θ values compared to the sample cured at 20°C, and at 60°C the reflection is at the same position as for the brucite reference.
TGA-IR (Fig. 1b) of the sample cured at 20°C shows mass losses, which can be mainly assigned to brucite and HY. Mass balance calculations obtained from TGA-IR and verified by ^{13}C CP-MAS NMR revealed that about 50-75% of the HY has reacted, rather independently from the curing temperature. At the decomposition temperature of brucite, not only H_2O, but also CO_2 is released between 300 and 480°C. This CO_2 release cannot be solely explained by the decomposition of HY, suggesting that either an unknown carbonate phase is decomposed, or that the brucite contains carbonate. In addition, at 30-160°C a mass loss is observed for the 20°C sample, which cannot be assigned to brucite or any known magnesium carbonate and indicates the presence of loosely bound water. For the samples cured at 60°C, this mass loss is not clearly evident.
At least three Raman bands of unknown origin occur in the region of 1025-1080 cm^{-1} regardless of curing temperature (Fig. 2a). The position of the bands is typical for hydrated magnesium carbonates (Edwards et al. (2005)).
^{13}C CP-MAS NMR (Fig. 2b) of the 20°C sample shows two signals for HY (163.4 ppm and 165.6 ppm) and a signal at 167-168 ppm, which was tentatively assigned to sorbed HCO_3^- (Bernard et al. (2022)). Two further resonances at 159.4-160.0 ppm and at 173 ppm could not be assigned to any known magnesium carbonate phase so far. The signals of the 60°C sample are very similar to those at 20°C.
Mg and inorganic carbon concentrations of the liquid phase increase with curing temperature, while the pH decreases (Figure 3a).
Effective saturation indices (SI) for brucite and hydrated magnesium carbonates were calculated by GEMS (Figure 3b). Magnesite is highly oversaturated at all investigated temperatures, but it does not form at the temperatures studied due to kinetic reasons. Artinite, brucite and hydromagnesite are oversaturated as well, and dypingite ($Mg_5(CO_3)_4(OH)_2 \cdot 5H_2O$) is near saturation. Despite being (over)saturated with respect to the pore solution, neither artinite nor dypingite can be identified, in agreement with Kuenzel et al. (2018) and Winnefeld et al. (2019), indicating a kinetic hindrance in formation. Lansfordite ($MgCO_3 \cdot 5H_2O$) and nesquehonite ($MgCO_3 \cdot 3H_2O$) are undersaturated and are not identified as well. Based on the solution chemistry, the ion activity products of various hypothetical hydrated magnesium carbonates, whose compositions were derived from mass balance calculations, were calculated using GEMS. However, the calculations revealed that these hypothetical phases were unstable compared to a mix of brucite and HY of the same bulk composition.

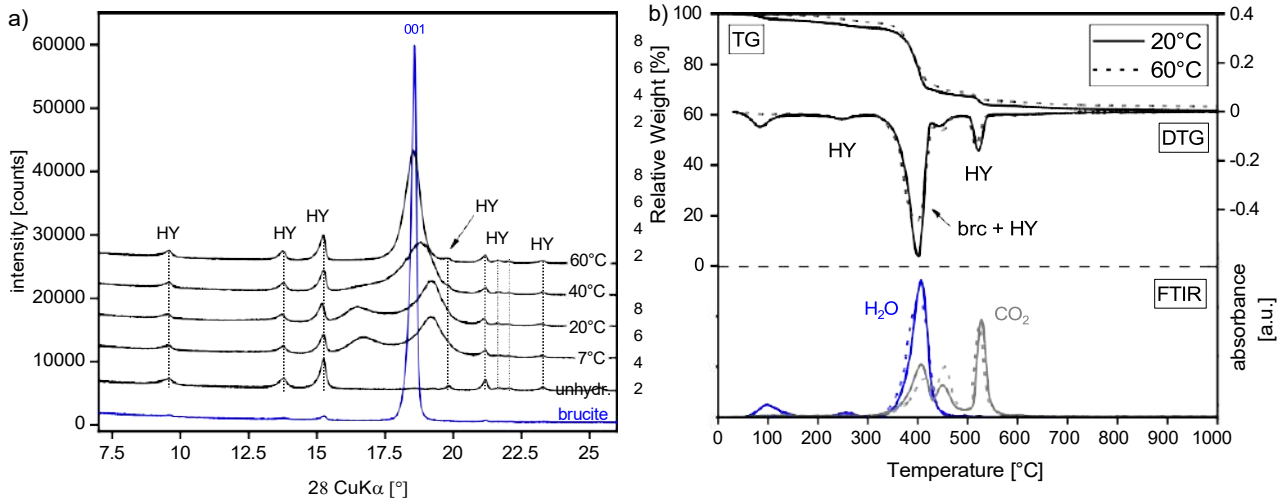


Fig. 1: a) XRD patterns of MgO/hydromagnesite 70/30 blends hydrated at 7, 20, 40 and 60°C for 12 months. The unhydrated sample and the brucite reference are shown for comparison, and b) TGA-IR of MgO/HY 70/30 blends hydrated at 20 and 60°C for 12 months.

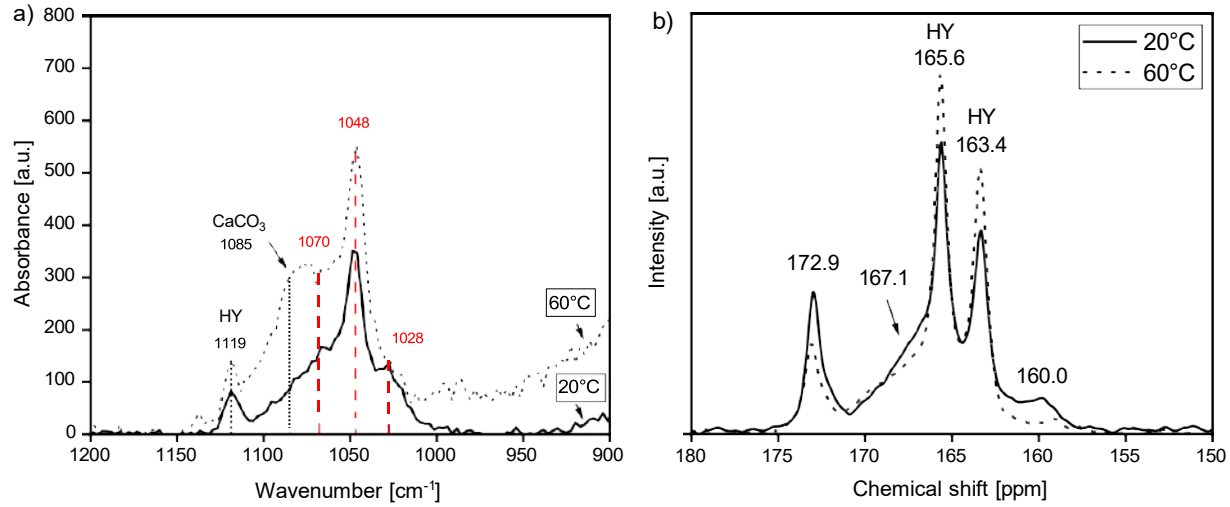


Fig. 2: a) Raman and b) ^{13}C CP-MAS NMR spectra of MgO/hydromagnesite 70/30 blends hydrated at 20 and 60°C for 12 months.

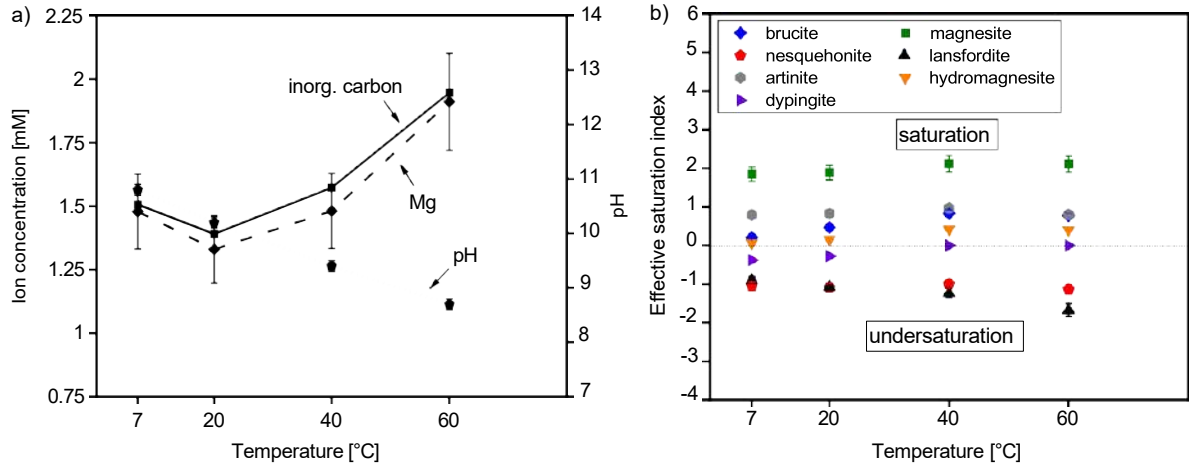


Fig. 3: a) Mg, inorganic carbon and pH of the liquid phase (lines for eye-guide only), and b) effective saturation indices of relevant hydrate phases in MgO/hydromagnesite 70/30 blends after 12 months depending on temperature.

4. Conclusions

The hydration products of blends of MgO and hydromagnesite were investigated at temperatures between 7 and 60°C. The main hydration product is brucite with a low crystallinity. The dissolution of a part of the hydromagnesite during hydration provides carbonate ions; however, no known hydrated magnesium carbonate phase could be identified. Thermodynamic properties of hypothetical hydrated magnesium carbonate phases were estimated, but all phases proved to be thermodynamically unstable. Based on these results, it is therefore suggested that the brucite formed in such systems contains some carbonate. Furthermore, thermogravimetric data shows a significant mass loss in the region of approximately 30-160°C, which is associated with the loss of loosely bound water. Tentatively this water is assigned as a kind of "gel-water" within the low-crystalline brucite. This "gel-water" cannot be identified at 60°C, while the carbonate associated with brucite is still present.

Acknowledgements

Ellina Bernard, Luigi Brunetti, Michele Griffa and Yiru Yan (all Empa) are acknowledged for their support regarding data acquisition, data treatment and discussion of the results.

References

Bernard, E., Lothenbach, B., Rentsch, D., German, A. and Winnefeld, F. (2022) "Effect of carbonates on the formation of magnesium silicate hydrates", *Materials and Structures*, 55(7):183.

Edwards, H.G.M., Villar, S.E.J., Jehlicka, J. and Munshi, T. (2005) "FT-Raman spectroscopic study of calcium-rich and magnesium-rich carbonate minerals", *Spectrochimica Acta A*, 61(10): 2273-2280

Gartner, E. and Sui, T. (2018) "Alternative cement clinkers", *Cement and Concrete Research*, 114: 27-39.

German, A (2023) "Potential use of a low-carbon magnesia (MgO) binder for construction purposes". *PhD Thesis*, ETH Zürich, Switzerland.

German, A., Winnefeld, F., Rentsch, D., Lura, P. and Lothenbach, B. (2023) "Phase analyses of hydrated MgO/hydromagnesite blends for use as potential low-carbon MgO cement", *Cement and Concrete Research*, in preparation.

Hummel, W., Berner, U., Curti, E., Pearson, F.J. and Thoenen, T. (2002) "Nagra/PSI chemical thermodynamic data base 01/01", *Radiochimica Acta*, 90(9-11): 805-813.

Kuenzel, C., Zhang, F., Ferrándiz-Mas, V., Cheeseman, C.R. and Gartner, E.M. (2018) "The mechanism of hydration of MgO-hydromagnesite blends", *Cement and Concrete Research*, 103: 123-129.

Kulik, D.A., Wagner, T., Dmytrieva, S.V., Kosakowski, G., Hingerl, F.F., Chudnenko, K.V. and Berner, U.R. (2013) "GEM-Selektor geochemical modeling package: revised algorithm and GEMS3K numerical kernel for coupled simulation codes", *Computational Geosciences*, 17(1): 1-24.

Snellings, R. et al. (2018), "RILEM TC-238 SCM recommendation on hydration stoppage by solvent exchange for the study of hydrate assemblages", *Material and Structures*, 51(6): 172

Vlasopoulos, N. and Cheeseman, C.R. (2009), "Binder composition", *PCT Patent Application* PCT/GB2009/001610, International Publication Number WO 2009/156740 A1 (12/30/2009).

Wagner, T., Kulik, D.A., Hingerl, F.F. and Dmytrieva, S.V. (2012) "GEM-Selektor geochemical modelling package: TSolMod Library and data interface for multicomponent phase models", *Canadian Mineralogist*, 50(5): 1173-1195.

Winnefeld, F., Epifania, E., Montagnaro, F. and Gartner, E.M. (2019) "Further studies of the hydration of MgO-hydromagnesite blends, *Cement and Concrete Research*, 126: 105912.

Carbonation of iron (Fe)-rich materials for cement/concrete matrices: where are we now?

L.R. Ellwood[1*], R. Snellings[2], and T. Hanein[1*]

[1]*Department of Materials Science and Engineering, University of Sheffield, Sheffield, United Kingdom*
Email: lrellwood1@sheffield.ac.uk and t.hanein@sheffield.ac.uk
[2] *Department of Earth and Environmental Sciences, KU Leuven, Leuven, Belgium*
Email: ruben.snellings@kuleuven.be

ABSTRACT
There is growing interest in the positive use of CO_2 in cementitious systems, with focus generally on the carbonation of materials rich in calcium (Ca)- or magnesium (Mg)-oxides and silicates. However, little research has been dedicated to understanding the carbonation of iron (Fe) containing phases and the carbonation potential of widely available Fe-rich resources.
Establishing the carbonation potential of Fe-rich materials, particularly Fe-rich industrial waste, would help to expand the range of viable materials for CO_2 sequestration and assist efforts to valorise industrial waste. $FeCO_3$ is gaining interest as an alternative cementitious carbonate binder and as Fe-rich resources often have high Ca and Mg content, mixed carbonate binder systems could also be realized. Also of interest is the durability of Fe-rich carbonated cement and its direct or indirect interactions with concrete rebar. In this paper, the state-of-the-art of carbonating Fe-rich materials is outlined, and future research avenues are proposed.

KEYWORDS: *Carbonation, Cement, Fe-rich, Iron, Industrial waste*

1. Introduction

The concept of capturing and sequestering CO_2 was first proposed in 1977 (Figure 1) in response to the growing awareness of the negative impact of CO_2 emissions on the climate (Marchetti (1977)). Since then, interest grew gradually and the mineral carbonation (MC) methods we are now familiar with were introduced properly in the 1990's as a permanent and safe method for disposing of CO_2 (Lackner et al (1995)). Until recently MC has been almost exclusively restricted to alkaline materials containing calcium (Ca) and magnesium (Mg), as they form insoluble carbonates (Huijgen et al (2005)). Alkali elements and other divalent metals also react with CO_2, but alkali bicarbonates are soluble and many divalent metals such as nickel, cobalt and copper are considered too valuable to use as feedstock for carbon sequestration (Pan et al (2012)).

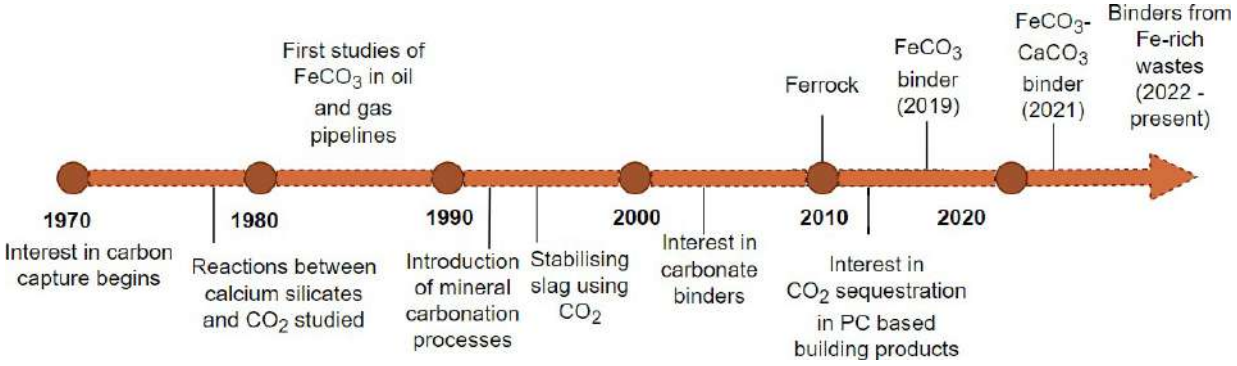


Figure 1: Timeline for the carbonation of Fe-rich resources

Iron (Fe) is sometimes categorised with these valuable metals, however there is an abundance of Fe-rich industrial residues and by-products which are often left untreated, sent to landfill, or used in low-value applications (Srivastava et al (2020)). In the cement industry, iron is almost exclusively used to lower

clinkering temperatures and therefore Fe-rich resources are underexploited. Due to their widespread availability, the utilisation of these resources in combination with CO_2 sequestration would not only widen the pool of resources available for carbon capture, but also presents the opportunity to combine industrial waste management and CO_2 sequestration with the production of useful products for the construction industry.

2. Mineral Carbonation of Fe-rich Materials

Mineral carbonation can be applied in the construction industry in a few key ways: the production of aggregates, supplementary cementitious materials, carbonated binders, and carbonation cured monoliths. Whilst initially studied in the context of geological in situ CO_2 sequestration (Lackner et al (1995)), MC is now performed using various techniques on a wide range of materials.

Fe is commonly present in a range of resources in the form of oxides and/or silicates. Ferrous materials containing Fe(II) are the most desirable for reactions with CO_2 as the iron present is already divalent (allowing formation of $FeCO_3$). However, ferric materials, which contain Fe(III), are more common at the earth's surface. For ferric materials to be of use in CO_2 sequestration an additional reduction step is usually required to reduce Fe(III) to Fe(II) (Palandri et al (2005)).

Blast oxygen furnace (BOF) and electric arc furnace (EAF) slags are often Fe-rich (Luo and He (2021)) but the carbonation of their Fe-containing phases is rarely the focus of research. Non-ferrous metallurgical slags (NFMS) such as those from the copper and lead industry can also be Fe-rich but their lower reactivities mean they have been less well studied in the field of MC (Srivastava et al (2022a)). NFMS have been shown to exhibit dissolution behaviour similar to that of natural materials, so applying knowledge obtained from research into natural Fe-rich minerals may be beneficial (Srivastava et al (2022a)).

Other Fe-rich industrial waste streams such as mine tailings and siltation pond waste have been investigated, as has the treatment of dusts and ashes. A summary of some studies can be seen in Table 1 below.

Table 1: Summary of maximum CO_2 uptake obtained in various Fe-rich waste residues. *mass % element not oxides (determined by ICP-OES).

Material	wt% Fe_2O_3/FeO	Other Major Constituents (oxide wt%)	Maximum CO_2 uptake	Source
EAF Bag House Dust	42.8	CaO 40.2, MgO 4.96, SiO_2 4.49	1 ± 0.04 gCO_2/gBHD	(Ibrahim et al (2019))
EAF Bag House Dust	42.8	CaO 40.2, MgO 4.96 SiO_2 4.49	0.657 gCO_2/gBHD	(El-Naas et al (2015))
Siltation Pond Waste	18.8*	Al 3.21, Ca 1.5, Mg 9.67, Si 19.1*	0.139 gCO_2/gwaste	(Razote et al (2021))
Mineral residue from apatite extraction	22.9	SiO_2 41.9, Al_2O_3 12.3, MgO 9.30, TiO_2 8.17	0.11 gCO_2/gResidue	(Reynes et al (2021))
EAF – Filter Dust	27.66	CaO 36.4, MgO 8.57 SiO_2 6.25, Cr_2O_3 11.91, MnO 5.14 MoO_3, 4.47	0.075 gCO_2/gDust	(Höllen et al (2018))

In most studies the oxidation state of Fe is not specified, so it is difficult to state the direct influence of this on CO_2 uptake. As shown in Table 1 materials with high Ca and Fe content identified through XRF appear to demonstrate the best CO_2 uptake capacity, but it is important to note that CO_2 uptake is heavily influenced by reaction conditions which differ between the studies.

2.3 Influence of Reaction Parameters

As MC studies vary significantly in materials, conditions, and methodologies, direct comparison is challenging and can be misleading. This is not only due to differences in the methods used to calculate CO_2

uptake but also because carbonation reactions of steel slags and other MC materials are dependent on a variety of factors, including temperature, pH, CO_2 pressure, particle size, stirring, liquid/solid ratio and duration. Within these factors there are conflicts in both the temperature and pH requirements that must be optimized. For example, raising the temperature is associated with an increase in reaction rates, but only up to a given limit (Bobicki et al (2012), Luo and He (2021), Pan et al (2012)). This limitation occurs because a higher temperature decreases CO_2 solubility, so at higher temperatures less CO_2 can enter the solution and therefore less CO_2 is able to participate in reactions. The conflict in pH requirements arises as a low pH benefits the dissolution of CO_2 and other reactive ions, however a higher pH benefits the precipitation of carbonates (Luo and He (2021)). Other factors such as increasing CO_2 pressure will assist carbonation, but only if the mass transfer of CO_2 is the rate limiting step (Bobicki et al (2012), Luo and He (2021), Pan et al (2012)). There is also some consensus that smaller particle size in slags is beneficial for carbonation due to an increase in specific surface, shorter diffusion pathways, and because smaller particles tend to have higher Ca and Mg ion content (Luo and He (2021)).

3. Carbonated Fe-Rich Binders

Carbonated binders are an active area of research in the field of low-carbon cement, with research covering carbonation cured PC, magnesium carbonate binders, carbonation of calcium silicates and clinker-free carbonate binders produced from wastes such as metallurgical slags (Shi et al (2019)).

Although carbonate binders have historically relied on the formation of calcium or magnesium carbonate, the chemistry of iron carbonation has recently been utilised to synthesise structural binders. The first example of this is the binder used in "Ferrock", a carbonated structural material produced from waste iron powder (60-69% by weight), fly ash, metakaolin, oxalic acid and limestone powder (Das et al (2014)). Reported reaction products include $FeCO_3$, $CaCO_3$ and carbonate-oxalate cancrinite group materials. However, the binder's strength development is dependent on porosity reduction rather than the formation of specific carbonates. Compressive strength in the range of 30-35 MPa (Figure 2) was achieved after 4 days of carbonation, with a longer carbonation duration seen to increase strength as it is associated with a decrease in average pore size (Das et al (2014)).

Iron carbonate ($FeCO_3$) is known to form an adhesive, passivating layer on the internal surface of carbon steel pipework in the oil and gas industry (Barker et al (2018)) and the principles of this scale formation have been used to investigate the cementing properties of $FeCO_3$ (Srivastava et al (2019), (2020), (2022b)). An $FeCO_3$ binder can be produced by subjecting a fine, compacted iron powder to aqueous carbonation (Srivastava et al (2019)). Siderite forms as a scale on the iron surface and, depending on carbonation conditions, dendritic oxides can form further away from the iron particles (Srivastava et al (2019), (2020)). In contrast to Ferrock and other conventional cementitious binders, the compressive strength of a high purity $FeCO_3$ binder is controlled by the intergrowth of the siderite scales between neighbouring Fe particles, rather than the pore filling of reaction products (Srivastava et al (2019), (2020)).

As many Fe-rich resources contain a range of elements, with Ca often present in large quantities, work is being done to transfer knowledge from a purely $FeCO_3$ binder to mixed binder systems (Srivastava et al (2021)). For example siderite-calcite ($FeCO_3$-$CaCO_3$) binders have been produced through the accelerated carbonation of various $CO_{2(g)}$-H_2O-Fe-$Ca(OH)_2$ systems under different conditions, producing binders with a range of compressive strengths (Figure 2) (Srivastava et al (2021)).

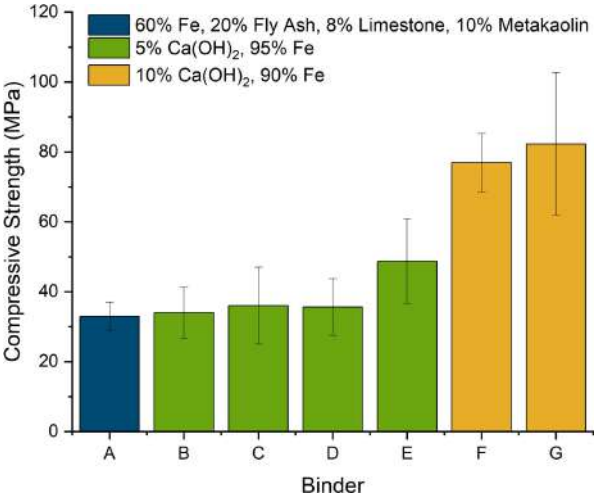


Figure 2: Compressive strengths of Fe-rich binders. A: Ferrock (Das et al (2014)). B to G: $FeCO_3$-$CaCO_3$ binders produced at 60°C under various CO_2 pressures, B:1 bar, C:5 bar, D and F: 10 bar, E and G: 20 bar (Srivastava et al (2021)).

Whilst these studies are limited to using Fe(0) to produce an $FeCO_3$-based binder, they are not only applicable to the valorisation of wastes containing Fe(0), but also present an opportunity to transfer knowledge into other Fe-rich systems (Srivastava et al (2020)) and general concrete durability.
It will be important to establish the durability of Fe-rich carbonated binders prior to their use in practical applications. $FeCO_3$ is stable in low redox conditions and a pH range of roughly 6 to 10 (Langmuir et al. 2005), so the survival of $FeCO_3$-containing binders under various environmental conditions will need to be evaluated. In aqueous conditions dissolved Fe(II) oxidises easily with O_2 which may impact the bound CO_2 in the material and consequently affect the strength and integrity of the binders (Morgan and Lahav 2007).

4. Reinforced Carbonate-based Materials

The relationship between carbonation and concrete rebar is usually discussed in terms of corrosion and property degradation, as carbonation is one of the main degradation processes of reinforced concrete (Fuhaid and Niaz (2022)). The highly alkaline (>pH 12.5) environment surrounding concrete rebar allows a passive oxide layer film to form (Fuhaid and Niaz (2022), Liu et al (2018)) but carbonation of the surrounding area will lower the pH of the pore solution below 9 and consequently destroys the passivating layer (Pu et al (2012)). This destruction of the passivating layer has meant that there has been little research dedicated to investigating the use of rebar in concretes made using carbonate-based or carbonation cured binder systems (Zhang and Shao (2016)). However, here research into the passivating nature of the $FeCO_3$ scale in the oil and gas industry could be of value. If an $FeCO_3$ scale could be produced on rebar, this could act as an alternative passivation method for steel rebar in carbonate-based binder systems. In an $FeCO_3$-based binder system, it is possible that rebar may be naturally passivated and in mixed or other carbonate-based systems it may be of value to investigate if an $FeCO_3$ layer forms naturally, or if rebar can be pre-treated to produce a carbonate layer which survives within the system.

5. Closing Remarks and Recommendations

Research shows that mineral carbonation of Fe-rich materials is viable and could be used to create useful products for the construction industry. The recent development of $FeCO_3$ binders opens an interesting opportunity for research in the field of alternative binder systems and the interactions of $FeCO_3$ containing binders with steel rebar could be a valuable area for new research. A lack of understanding of the dissolution and carbonation mechanisms of iron rich materials/phases limits the development of Fe-rich carbonated binders or other products for use in the construction industry. There has also been little investigation into the formation of $FeCO_3$ binders in more complex systems such as those found in Fe-rich waste streams and systems without Fe(0) present.
Consequently, future work should assess the carbonation potential and mechanisms of Fe-rich materials through dissolution and mineral carbonation experiments to identify which resource streams will be most useful. The formation of $FeCO_3$-containing binders from these resource streams can then be investigated by integrating the knowledge gained from the dissolution and carbonation studies with cementation experiments to understand how $FeCO_3$-containing binders may form in more complex systems (Figure 3). The interactions of rebar with $FeCO_3$ in cementitious systems has not been investigated but could be integrated within the research into $FeCO_3$-containing binders, as little is known about the stability of $FeCO_3$ as a binder or passivating scale. The key aim of this should be to establish whether $FeCO_3$ could form a stable, alternative passivation layer on the rebar towards the production of reinforced carbonate-binder products. Finally, it is important to note that there are further areas of consideration which have not been detailed in this report. For example, there are issues surrounding the treatment of wastewater from MC processes (Chen et al (2021)) as well as the costs of pre-processing materials and using additional chemicals to enhance carbonation reactions. These are areas which must be considered for the successful upscaling of all MC projects.

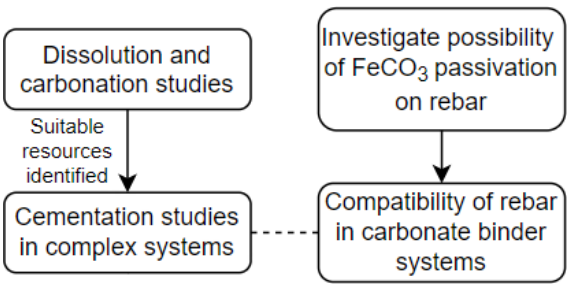


Figure 3: Proposed work program for investigating $FeCO_3$ based cementitious products.

Acknowledgements

This work is funded by UKRI EPSRC grant, "Developing iron-rich cement clinker & understanding ferrite for the valorisation and upcycling of steel slags (FeRICH)" (EP/W018810/1)

References

Al Fuhaid, A. F., and Niaz, A. (2022) "Carbonation and Corrosion Problems in Reinforced Concrete Structures" , *Buildings 2022*, 12(5): 586

Barker, R., Burkle, D., Charpentier, T., Thompson, H., and Neville, A. (2018) "A review of iron carbonate ($FeCO_3$) formation in the oil and gas industry" , *Corrosion Science*, 142: 312–341

Bobicki, E. R., Liu, Q., Xu, Z., and Zeng, H. (2012) "Carbon capture and storage using alkaline industrial wastes" , *Progress in Energy and Combustion Science*, 38(2): 302–320

Chen, Z., Cang, Z., Yang, F., Zhang, J., and Zhang, L. (2021) "Carbonation of steelmaking slag presents an opportunity for carbon neutrality: A review" , *Journal of CO_2 Utilization*, 54: 101738

Das, S., Souliman, B., Stone, D., and Neithalath, N. (2014) "Synthesis and properties of a novel structural binder utilizing the chemistry of iron carbonation" , *ACS Applied Materials and Interfaces*, 6(11): 8295–8304

El-Naas, M. H., el Gamal, M., Hameedi, S., and Mohamed, A.-M. O. (2015) "CO_2 sequestration using accelerated gas-solid carbonation of pre-treated EAF steel-making bag house dust" , *Journal of Environmental Management*, 156: 218–224

Höllen, D., Berneder, I., Capo Tous, F., Stöllner, M., Philipp Sedlazeck, K., Schwarz, T., Aldrian, A., and Lehner, M. (2018) "Stepwise treatment of ashes and slags by dissolution, precipitation of iron phases and carbonate precipitation for production of raw materials for industrial applications" , *Waste Management*, 78: 750–762

Huijgen, W. J. J., Comans, R. N. J., and Huiigen, W. J. J. (2005) "Mineral CO_2 sequestration by carbonation of industrial residues: Literature overview and selection of residue", *Energy Research Centre of the Netherlands*

Ibrahim, M. H., El-Naas, M. H., Zevenhoven, R., and Al-Sobhi, S. A. (2019) "Enhanced CO_2 capture through reaction with steel-making dust in high salinity water" , *International Journal of Greenhouse Gas Control*, 91: 102819

Lackner, K. S., Wendt, C. H., Butts, D. P., Joyce, E. L., and Sharps, D. H. (1995) "Carbon Dioxide Disposal in Carbonate Minerals" , *Energy*, 20: 1153

Langmuir, D., Chrostowski, P., Vigneault, B., and Chaney, R. (2005) "Issue Paper on the environmental chemistry of metals", *U.S. Environmental Protection Agency Risk Assessment Forum*

Liu, X., Niu, D., Li, X., Lv, Y., and Fu, Q. (2018) "Pore Solution pH for the Corrosion Initiation of Rebars Embedded in Concrete under a Long-Term Natural Carbonation Reaction" , *Applied Sciences*, 8: 128

Luo, Y., and He, D. (2021) "Research status and future challenge for CO_2 sequestration by mineral carbonation strategy using iron and steel slag" , *Environmental Science and Pollution Research*, 28(36): 49383–49409

Marchetti, C. (1977) "On geoengineering and the CO_2 problem" , *Climatic Change*, 1: 59–68

Morgan, B., Lahav, O., "The effect of pH on the kinetics of spontaneous Fe(II) oxidation by O2 in aqueous solution – basic principles and a simple heuristic description" , *Chemosphere,* 68: 2080-2084

Palandri, J. L., Rosenbauer, R. J., and Kharaka, Y. K. (2005) "Ferric iron in sediments as a novel CO_2 mineral trap: CO_2–SO_2 reaction with hematite" , *Applied Geochemistry*, 20(11): 2038–2048

Pan, S.-Y., Chang, E. E., and Chiang, P.-C. (2012) "CO_2 Capture by Accelerated Carbonation of Alkaline Wastes: A Review on Its Principles and Applications" , *Aerosol and Air Quality Research*, 12: 770–791

Peys, A., Isteri, V., Yliniemi, J., Yorkshire, A. S., Lemougna, P. N., Utton, C., Provis, J. L., Snellings, R., and Hanein, T. (2022) "Sustainable iron-rich cements: Raw material sources and binder types" , *Cement and Concrete Research*, 157: 106834

Ponomar, V., Yliniemi, J., Adesanya, E., Ohenoja, K., and Illikainen, M. (2022) "An overview of the utilisation of Fe-rich residues in alkali-activated binders: Mechanical properties and state of iron" , *Journal of Cleaner Production*, 330: 129900

Pu, Q., Jiang, L., Xu, J., Chu, H., Xu, Y., and Zhang, Y. (2012) “Evolution of pH and chemical composition of pore solution in carbonated concrete” , *Construction and Building Materials*, 28(1): 519–524

Razote, B. J., dela Cerna, K. M., Patricio, M. J., Eusebio, R. C., Alorro, R., Beltran, A., and Orbecido, A. (2021) “Leaching characteristics of an iron-rich siltation pond waste and its viability in indirect carbon sequestration” , *International Journal of Mining, Reclamation and Environment*, 35(6): 435–450

Reynes, J. F., Mercier, G., Blais, J. F., and Pasquier, L. C. (2021) “Aqueous mineral carbonation of Fe rich olivine by cation complexation using 2,2′-bipidine; concept validation and parameters optimization” , *Applied Geochemistry*, 131: 105029

Shi, C., Qu, B., and Provis, J. L. (2019) “Recent progress in low-carbon binders” , *Cement and Concrete Research,* 122: 227–250

Srivastava, S., Jacklin, R., Snellings, R., Barker, R., Spooren, J., and Cool, P. (2022b) “Experiments and modelling to understand $FeCO_3$ cement formation mechanism: time-evolution of CO2-species, dissolved-Fe, and pH during CO_2-induced dissolution of Fe(0)” , *Construction and Building Materials,* 345: 128281

Srivastava, S., Snellings, R., Meynen, V., and Cool, P. (2019) “($FeCO_3$) cementation by carbonation of iron rich systems” , *15th International Congress on the Chemistry of Cement*, September 2019

Srivastava, S., Snellings, R., Meynen, V., and Cool, P. (2020) “Utilising the principles of $FeCO_3$ scaling for cementation in H_2O-CO_2(g)-Fe system” , *Corrosion Science*, 169: 108613

Srivastava, S., Snellings, R., Meynen, V., and Cool, P. (2021) “Siderite-calcite ($FeCO_3$–$CaCO_3$) series cement formation by accelerated carbonation of CO_2(g)–H_2O–Fe–$Ca(OH)_2$ systems” , *Cement and Concrete Composites,* 122: 104137

Srivastava, S., Snellings, R., Nielsen, P., and Cool, P. (2022a) “Insights into CO_2-mineralization using non-ferrous metallurgy slags: CO_2 (g)-induced dissolution behavior of copper and lead slags” , *Journal of Environmental Chemical Engineering*, 10: 2213–3437

Zhang, D., and Shao, Y. (2016) “Early age carbonation curing for precast reinforced concretes” , *Construction and Building Materials*, 113: 134–143

The 16th International Congress on the Chemistry of Cement 2023 (ICCC2023)
"Further Reduction of CO_2 -Emissions and Circularity in the Cement and Concrete Industry"
September 18–22, 2023, Bangkok, Thailand

Enhancement of the properties of recycled concrete aggregates in different mediums

N. Li[1], C. Unluer[2*]

[1] *Department of Mechanical, Aerospace and Civil Engineering, University of Manchester, M13 9PL Manchester, United Kingdom*
Email: ning.li-3@manchester.ac.uk
[2] *Department of Mechanical, Aerospace and Civil Engineering, University of Manchester, M13 9PL Manchester, United Kingdom*
Email: cise.unluer@manchester.ac.uk

ABSTRACT

This study aimed to improve the mechanical properties of recycled concrete aggregates (RCAs) by enhancing their hydration and carbonation under different mediums involving tap water, river water, and seawater. Samples subjected to these wet carbonation conditions were compared with those cured under conventional dry carbonation conditions. The mechanical performance of RCAs and recycled aggregate concrete (RAC) prepared with the carbonated RCAs was evaluated. Results indicated that the performance of RAC was improved via the involvement of both wet carbonated and dry carbonated RCAs. After being subjected to wet carbonation conditions, the performance of RCAs was enhanced in 1 hour due to the formation of calcium carbonate and ettringite. The associated reduction in total porosity and densification of the microstructure were more efficient when compared to dry carbonation. These improvements were reflected in the compressive strength of RAC samples involving seawater carbonated RCAs, which increased by 88% in comparison to those samples with uncarbonated RCAs. Investigation of the reaction kinetics and microstructural analysis highlighted that the use of seawater as a medium for wet carbonation demonstrated several advantages, including its abundant availability, enhanced CO_2 capture capacity, and rapid improvement on the performance of RCAs' and associated RAC samples. Overall, this study revealed the use of seawater carbonation as a feasible and cost-effective approach to enhance the properties of RCAs and resulting concrete formulations.

KEYWORDS: *Recycled concrete aggregates, wet carbonation, seawater, recycled aggregate concrete, performance*

1. Introduction

Due to an increase in building construction and demolition activities, more than 3 billion tons of recycled concrete aggregates (RCAs) are produced annually (Akhtar and Sarmah, 2018). However, the use of RCAs is relatively low due to their inferior performance in comparison to normal aggregates (NAs) (De Brito and Saikia, 2012). The adhesion of old porous mortar to the surface layer of RCAs results in water absorption and crushing values that are significantly greater than those of NAs. Carbonation not only effectively improves the quality of RCAs, but also permanently sequesters CO_2 (Li et al., 2022). After fully carbonated with 99.9% CO_2, the water absorption of 5-10 mm RCAs could be reduced by 30% and apparent density could be increased by 4.8% (Lu et al., 2019). Pressurized carbonation techniques and flow-through CO_2 curing methods have been developed to improve the carbonation efficiency of RCAs, albeit these processes typically require specialised equipment and a lengthy carbonation time.
Previous studies reported that liquid-solid (wet) carbonation treatment of RCAs presented a higher carbonation efficiency within a few hours than gas-solid (dry) carbonation (Liu et al., 2021; Zajac et al.,

2020). Liu et al. (Liu et al., 2021) reported that the compressive strength of RCAs subjected to wet carbonation (i.e. pure CO_2 was injected into the water at a flow rate of 0.2 L/min/100g RCA) for 6 hours was 7.2% higher than that of concrete samples cured under pressurized dry carbonation (i.e. pure CO_2 pressure of 1 bar and RH of 54±5% at 25°C) for 24 hours. Seawater is rich in Ca^{2+} and Mg^{2+}, which can react directly with CO_2 to form carbonate precipitates and achieve CO_2 fixation. Therefore, using seawater as a medium for the wet carbonation of RCAs could present a feasible and cost-effective method that can make full use of the adsorption potential of seawater. This study focused on enhancing the properties of RCAs by improving their carbonation efficiency and reducing their processing time. Seawater was investigated as a wet carbonation medium and compared with tap water and river water, as well as conventional dry carbonation method. The performance of RCAs and resulting RAC prepared by different carbonation methods was evaluated.

2. Materials and Methodology

2.1 Materials

A Hanson general purpose cement CEM II 42.5N was used to prepare the RCAs. Recycled aggregate concrete (RAC) was prepared with Portland cement (PC) CEM I 52.5R. The chemical compositions of these binders were determined by X-ray fluorescence (XRF) and the results are provided in Table 1. River sand with a maximum size of 2.36 mm and with a specific gravity of 2.63 was used as fine aggregate to prepare the mortar and RAC mixes. Tap, river and sea water were used in wet carbonation and collected locally from Glasgow City, River Kelvin and Port Glasgow, respectively.

Table 1. Chemical compositions (wt.%) of the binders used in this study

	SiO_2	Al_2O_3	Fe_2O_3	CaO	MgO	SO_3	K_2O	Na_2O	LOI
CEM II 42.5N	16.24	4.01	2.08	60.71	1.11	2.75	0.39	0.56	11.5
CEM I 52.5R	19.38	4.94	2.87	62.89	3.4	3.29	0.35	0.35	0.99

2.2 Preparation and carbonation of RCAs

Cement mortars with a water-to-cement (w/c) ratio of 0.5 and a cement-to-sand (c/s) ratio of 1:3 were prepared, and cured at a temperature of 40ºC and a relative humidity (RH) of 95% for at least 3 months. The hardened cement mortar was then crushed and sieved to produce 5-10 mm particles as RCAs. The prepared RCAs were first placed in a wire mesh and submerged into respective liquid mediums (tap, river and seawater) by an elevator. Using the liquid-to-RCA ratio of 10:1 by mass, an industrial-grade CO_2 with a concentration of 99.9% was injected for 60 min, resulting in samples T60, R60 and S60, respectively. The magnetically stirred at a stirring speed of 200 rpm at 25ºC. The CO_2 gas flow rate was kept constant at 0.02 L/min/100g RCAs. Another set of samples (C7d) was subjected to dry carbonation conditions under a CO_2 concentration of 20%, RH of 65±5% and temperature of 25ºC for 7 days.

2.3 Preparation of RAC

The aggregate content of the RAC mixtures consisted of 712 kg/m^3 of sand and 1078 kg/m^3 of RCA, with a w/c of 0.8, which was higher than that of ordinary concrete mixes to avoid a loss in the workability due to the high-water absorption of RCAs. The effective w/c ratio (excluding water absorbed by RCA) was between 0.4 and 0.45. Fresh concrete mixes were cast in 50×50×50 mm steel moulds and compacted by a vibrating table. After curing under ambient conditions for 24 h, all concrete specimens were demoulded and further cured in an environmental chamber set at 20°C and 95% RH for 28 days.

2.4 Experimental Methodology

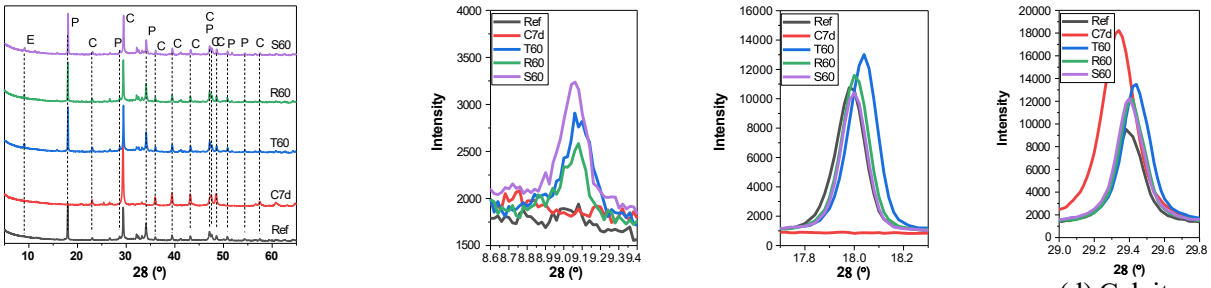
The compressive strength of RAC was measured using a compression machine with a loading rate of 0.5±0.1 MPa/s. Three specimens were tested for each mix and the average values were reported. XRD was performed using an X-ray diffractometer with Cu-Kα radiation. The samples were step-scanned from 5 to 65º (2θ) at a rate of 2º/min at a step of 0.02º. A scanning electron microscope was used to trace the

morphological changes in the microstructure of the RCAs. The dried samples were coated with gold before the SEM observation.

3. Results and Discussion

3.1 XRD analysis of RCAs

Fig. 1 shows the crystalline phases of uncarbonated (Ref.) and carbonated RCAs by different carbonation methods. The main crystalline phases in RCAs were portlandite (P) and calcite (C), along with minor amounts of ettringite (E). Anhydrous phases such as C_2S could also be observed. In samples subjected to dry carbonation, P and E peaks disappeared, while C peaks were enhanced, indicating the complete conversation of hydrate phases into carbonates after 7 days of dry carbonation. In samples subjected to wet carbonation, P, E and C peaks increased compared to the Ref sample. The co-existence of these phases in wet carbonation conditions revealed that hydration reaction accompanied carbonation. Samples carbonated in seawater demonstrated lower P peaks than other samples subjected to wet carbonation, while E peaks were significantly higher. These variations could be an indication of different hydration reactions, in line with the different liquid mediums.



(a) XRD patterns of RCA samples (b) Ettringite (c) Portlandite (d) Calcite

Fig. 1. XRD patterns of RCA samples subjected to different carbonation methods

3.2 Compressive strength

Fig. 2 shows the compressive strength of all hardened RAC samples involving carbonated RCAs at 28 days. The control sample revealed a compressive strength of 21.9 MPa. Compared with the control sample, all the other RAC samples containing wet and dry carbonated RCAs experienced enhancements in their mechanical performance. Accordingly, the compressive strength of the C7d, T60, R60 and S60 samples was improved by 42.2%, 62.8%, 66% and 88%, respectively. Sample S60 achieved the highest compressive strength. Previous studies reported that in addition to the physical properties of RCAs, the chemical reaction between the carbonated paste and the fresh cement paste and the surface morphology of RCAs contribute to the strength enhancement of RAC (Liu et al., 2021).

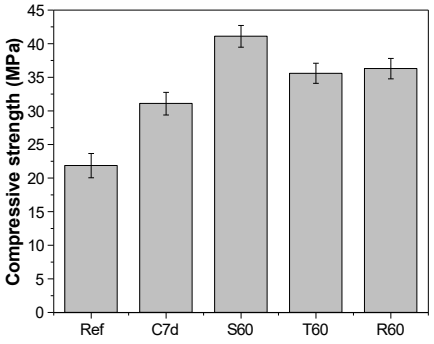
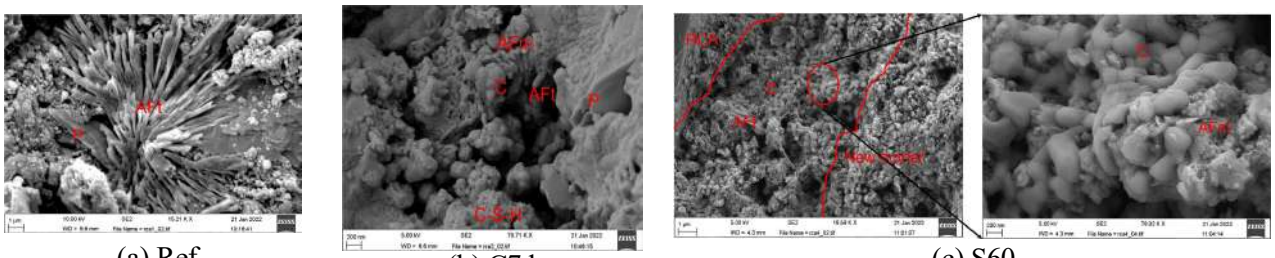


Fig. 2. Compressive strength of RAC samples involving carbonated RCAs at 28 days

3.3 SEM observation

The microstructures of ITZ of RAC samples subjected to different carbonation treatment are presented in Fig. 3. In Ref sample, the ITZ in RAC showed the presence of E and P, which weakened the performance of ITZ, in line with the findings of previous studies (Scrivener et al., 2004). Alternatively, carbonated samples revealed the formation of C with good crystallinity in their ITZ. The precipitation of C contributed to the establishment of a bond with the surrounding paste, thereby improving ITZ performance. In particular, for wet carbonated samples, a large amount of C (i.e. with a particle size of 100-200 nm) accumulated on the surface of RCAs, which agglomerated and was bound tightly to the freshly mixed cement paste, thus increasing the strength of the resulting concrete. In addition, although there are E on the surface of RCA, they are interwoven and covered by C crystals, which significantly reduces the amount of E in ITZ.



(a) Ref (b) C7d (c) S60

Fig. 3. Microstructures of ITZ of RAC samples subjected to different carbonation treatments

4. Conclusions

This study investigated the effects of carbonation under different liquid mediums and dry carbonation on the properties of RCAs and the performance of resulting RAC samples. After being subjected to wet carbonation for only 60 min, the performance of RCAs was enhanced due to the formation of ettringite and calcium carbonate, which increased the solid volume and densified the microstructure. The performance of RAC samples was subsequently improved via the involvement of both wet and dry carbonated RCAs. The use of seawater as a medium for wet carbonation increased compressive strength by 88% and 32.2% compared to those not carbonated and dry carbonation, thereby increasing the efficiency of the carbonation process.

Acknowledgements

The authors acknowledge the financial support from The Royal Society (project ref: ICA\R1\201310).

References

Akhtar, A., Sarmah, A.K. (2018) "Construction and demolition waste generation and properties of recycled aggregate concrete: A global perspective", *Journal of Cleaner Production*, 186: 262-281

De Brito, J., Saikia, N. (2012) "Recycled aggregate in concrete: use of industrial, construction and demolition waste", *Springer Science & Business Media*

Li, N., Mo, L., Unluer, C. (2022) "Emerging CO_2 utilization technologies for construction materials: A review", *Journal of CO_2 Utilization*, 65: 102237

Liu, S., Shen, P., Xuan, D., Li, L., Sojobi, A., Zhan, B., Poon, C.S. (2021) "A comparison of liquid-solid and gas-solid accelerated carbonation for enhancement of recycled concrete aggregate", *Cement and Concrete Composites*, 118: 103988

Lu, B., Shi, C., Cao, Z., Guo, M., Zheng, J. (2019) "Effect of carbonated coarse recycled concrete aggregate on the properties and microstructure of recycled concrete", *Journal of Cleaner Production*, 233: 421-428

Scrivener, K.L., Crumbie, A.K., Laugesen, P. (2004) "The Interfacial Transition Zone (ITZ) Between Cement Paste and Aggregate in Concrete", *Interface Science*, 12(4): 411-421

Zajac, M., Skibsted, J., Durdzinski, P., Bullerjahn, F., Skocek, J., Ben Haha, M. (2020) "Kinetics of enforced carbonation of cement paste", *Cement and Concrete Research*, 131: 106013

The 16th International Congress on the Chemistry of Cement 2023 (ICCC2023)
"Further Reduction of CO_2 -Emissions and Circularity in the Cement and Concrete Industry"
September 18–22, 2023, Bangkok, Thailand

Reaction Kinetics and Mechanical Properties of Alkali-Activated Metakaolin-Limestone Cements

J. Ren[1], N.D. Dowdy[2], D.N. Beatty[3] and W.V. Srubar III[4*]

[1] *University of Colorado Boulder, Boulder, Colorado, USA*
Email: jie.ren@colorado.edu
[2] *University of Colorado Boulder, Boulder, Colorado, USA*
Email: nicolas.dowdy@colorado.edu
[3] *University of Colorado Boulder, Boulder, Colorado, USA*
Email: danielle.beatty@colorado.edu
[4] *University of Colorado Boulder, Boulder, Colorado, USA*
Email: wsrubar@colorado.edu

ABSTRACT

This study investigates the reaction kinetics and mechanical properties of alkali-activated metakaolin-limestone (MKLS) geopolymer cements. The production of metakaolin requires moderate calcination of natural clays. Thus, replacement of metakaolin with limestone could reduce the emissions associated with the production of geopolymer cements. The hypothesis of this work was that limestone, which is predominately calcium carbonate ($CaCO_3$), could serve as a functional filler and a source of small quantities of elemental calcium, improving the mechanical properties of MKLS-based geopolymer cements. This study investigated the effects of limestone content (10% to 50% by mass ratio) on the kinetics of alkali-activation, mineralogy, and compressive strength of MKLS-based geopolymers synthesized using a constant Si/Al ratio = 1.5 and Na/Al ratio = 1.0. The results demonstrate that the limestone content has a significant impact on the aforementioned characteristics. While limestone delayed the acceleration stage of alkali-activation, 10% limestone led to a higher degree of reaction. Geopolymer cements with 50% limestone resulted in a much lower compressive strength compared to other mixes. Samples with 30% limestone exhibited low amorphous content as measured *via* XRD but obtained a similar compressive strength as that of the control (0% limestone), which might be due to the filler effect of limestone, formation of crystalline phases, and calcium participation in the geopolymerization process.

KEYWORDS: *Metakaolin, Limestone, Geopolymers, Reaction Kinetics, Mechanical Properties*

1. Introduction

Recently, there has been a high degree of interest in alkali-activated metakaolin-limestone (MKLS) geopolymer cements, which are considered as a sustainable alternative to portland cement. Kaolinitic clays, from which metakaolin is obtained, and limestone (LS) are more abundant and readily available worldwide compared to other common raw materials for geopolymers (*i.e.*, fly ash and slag) (Perez and Escalante (2020)).

There are multiple benefits of supplementing MK with LS. LS replacement lowers the quantity of alkaline activator that is required for alkali-activation on a per-volume basis. LS replacement also reduces the carbon footprint of resultant cement pastes. In addition, it was reported that the workability and early strength of MK-based geopolymer cements could be improved with addition of LS, due to (1) the larger particle size of LS compared to MK and (2) the filler effect (Qian and Song (2015)). Meanwhile, trace quantities of elemental Ca^{2+} could be released from LS during alkali-activation. Liberated Ca^{2+} could incorporate into sodium aluminosilicate hydrate (N-A-S-H) gel, forming Ca-containing N-A-S-H (N-(C)-A-S-H) gel with a 3D network structure . Despite previous research, limited data exist on the effects of LS on the reaction kinetics and mechanical properties of MKLS-based geopolymers at high replacement levels (>30%).

This study investigates the effect of LS content (0%-50%) on the reaction kinetics, mineralogy, and compressive strength of MKLS-based geopolymer pastes (Si/Al ratio = 1.5, Na/Al ratio = 1.0). First, the reaction kinetics of MKLS geopolymer pastes were measured using isothermal conduction calorimetry (ICC). Next, the mineralogy of the pastes was characterized using X-ray diffraction (XRD). Finally, the compressive strengths of the pastes were measured using mechanical testing.

2. Materials and methods

2.1 Materials

MK was provided by BASF Chemical Corporation (Georgia USA) with a specific density of 2.50. Reagent-grade LS powder (≥99.0%) with a density of 2.93 g/cm^3 was supplied by Sigma Aldrich (CAS No. 471-34-1). The D_{50} of the MK and LS, as measured by laser diffraction, was 4.76 and 19.68 μm, respectively. Anhydrous sodium metasilicate pellets (SiO_2:Na_2O molar ratio = 1:1) purchased from Sigma Aldrich (CAS No. 6834-92-0) were used to prepare the alkaline activator solution. Table 1 shows the chemical composition of the MK and LS. XRD analysis revealed that LS mainly contains calcite and trace quantities of dolomite, whereas MK exhibited a characteristic amorphous hump ranging between 15-30° (2θ) with traces of quartz (SiO_2) and anatase (TiO_2), as expected (data not shown).

Table 1. Chemical compositions of the MK and LS determined by X-ray fluorescence (XRF).

Precursors	Oxide (wt%)										LOI
	SiO_2	Al_2O_3	CaO	Fe_2O_3	Na_2O	K_2O	TiO_2	SO_3	MgO	P_2O_5	(%)
MK	51.9	44.1	0.02	0.37	0.20	0.156	1.54	0.11	0.02	0.078	1.00
LS	<0.07	0.21	54.9	<0.01	<0.04	0.006	0.01	0.07	0.06	0.015	41.6

2.2 Preparation of specimens

To prepare the alkaline activator solution, anhydrous sodium metasilicate pellets were massed, mixed with predetermined amount of tap water, and stirred in a beaker using a magnetic stirrer until all pellets were dissolved. Then, the alkaline activator was allowed to cool for 24 h. Next, dry powders were weighed and mixed together by hand. The alkaline activator was added and the slurry was mixed for 3 min using a high shear-rate mixer. The slurry was cast into 31.75-mm cubic molds and vibrated for 15 s to eliminate entrapped air. The molds were then covered by a plastic film. After one day, samples were demolded and sealed tightly in plastic bags with a controlled curing condition (T = 20 ± 2 °C, RH = 80-90%) and stored until further testing. The water-to-binder, Si/Al, and Na/Al ratios were held constant at 0.9, 1.5, and 1.0, respectively. Detailed mixture proportions are summarized in Table 2.

Table 2. Nomenclature and mixture formulations of the geopolymer-limestone pastes.

Sample name	MK (wt.%)	LS (wt.%)	Sodium metasilicate (wt.%)	w/b ratio	Oxide-molar ratios	
					Si/Al	Na/Al
100MK (Control)	100	0	52.71	0.9	1.5	1.0
90MK_10LS	90	10	47.44	0.9	1.5	1.0
70MK_30LS	70	30	36.90	0.9	1.5	1.0
50MK_50LS	50	50	26.36	0.9	1.5	1.0

2.3 Methods

The reaction kinetics of the geopolymer pastes were measured using ICC at ambient temperature (21 °C). Compressive strength testing was conducted on three samples for each mix after 28 days of curing using an universal testing machine (INSTRON) with a displacement rate at 0.1mm/s. Fragments of samples after the compressive strength test were grinded into powders with particle size less than 75 μm (passing through No.200 sieve) and used for XRD test using Bruker D8 ADVANCE diffractometer (Cu-Kα radiation). The current and acceleration voltage was 40 mA and 40 kV, respectively. The scanning range was 5-70° (2θ) with a scanning rate of 1.2°/min.

3. Results and discussion

The normalized heat flow and cumulative heat released per unit of MK by mass during the first five days of reaction are presented in Fig. 1(a) and Fig. 1(b), respectively. As shown in Fig. 1(a), the acceleration peak (1) exhibited by 100MK shifted from approximately 230 min to approximately 500 min (2) for all samples containing LS, indicating a delay in geopolymerization. As shown in Fig. 1(b), 10% LS replacement yielded a higher cumulative heat release compared to the control 100MK after approximately 1420 min. This finding suggests that 10% LS led to a higher degree of reaction and promoted the formation of additional reaction products. One explanation is that the LS induced a nucleation effect akin to those observed in portland cement pastes and/or led to the formation of C-S-H due to the interaction between trace quantities of calcium (Ca^{2+}) that could have been liberated by the LS during alkali-activation and the silicates provided by the alkaline activator solution (Puligilla et al (2019)). Another possible explanation is that trace quantities of dissolved Ca^{2+} participated in the reaction process with the formation of N-(C)-A-S-H, since more heat would be released when some Ca^{2+} is involved in the geopolymerization process (Ren et al (2022)), or the formation of carboaluminates. In comparison, 30% and 50% replacement levels of LS hindered the overall reaction process, as evidenced by less cumulative heat than that of the other two mixes. Specifically, given the same water-to-binder ratio, a lower amount of sodium metasilicate pellets used for these two mixtures introduced a lower alkalinity (Na_2O content). As a result, the dissolution and reaction kinetics of MK in the interstitial solution of the binding matrix were reduced.

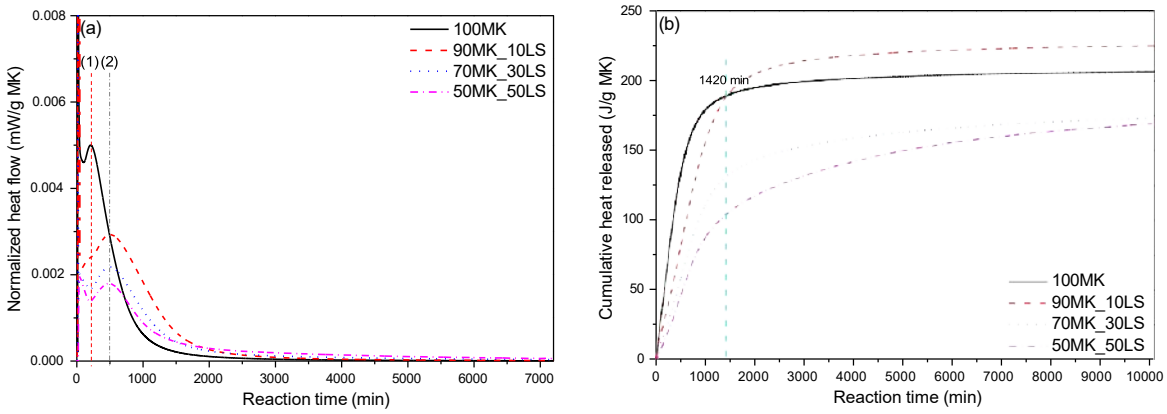


Fig. 1. (a) Normalized heat flow and (b) cumulative heat released during the early reaction process.

The compressive strength of all mixes after 28 days of curing is shown in Fig. 2(a). 100MK, 90MK_10LS and 70MK_30LS samples exhibited similar compressive strengths, while 50MK_50LS exhibited a much lower compressive strength. These data support the heat release data as presented in Fig. 1(b). The reduced strength of 50MK_50LS is likely due to an insufficient paste fraction considering the low alkalinity of the binding system. Nucleation effects were evident in the 90MK_10LS samples and likely occurred also in the 70MK_30LS and 50MK_50LS samples. However, the benefits of nucleation, if any, were outweighed by the high-volume replacements, especially for the 50MK_50LS samples, yielding a reduction in the 28-day compressive strength.

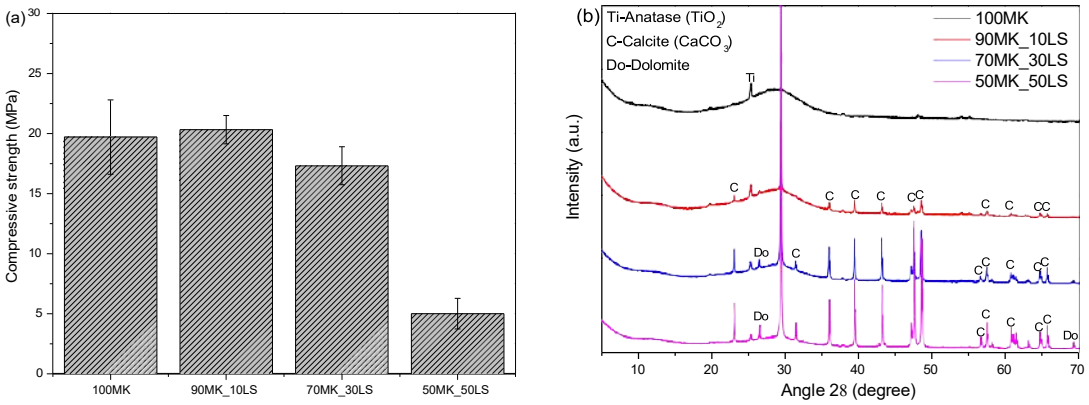


Fig. 2. (a) Compressive strength and (b) mineralogy of all mixes after 28 days of curing.

Based on the XRD patterns in Fig. 2(b), an amorphous hump is evident between 26-29° (2θ) for 100MK and 90MK_10LS, indicating the formation of amorphous reaction products with a different nature compared to that of MK (centered at around 23° 2θ, not shown in the study). According to the literature, the main reaction product is sodium aluminosilicate hydrate gel (N-A-S-H) for 100MK and N-A-S-H containing Ca (N-(C)-A-S-H) (Perez and Escalante (2020)). For 70MK_30LS and 50MK_50LS, this hump is not significant in comparison to the peaks associated with LS (*i.e.*, calcite, dolomite). These results concur well with the lower compressive strength results of the 50MK_50LS specimen. The relatively high compressive strength exhibited by the 90MK_10LS sample can be explained by considering the nucleation effect of LS and possible formation of other calcium carboaluminates phases (Cwirzen et al (2014)), which may have also led to increased strength of the 70MK_30LS samples. Continued XRD quantitative analysis will determine if these phases are present in these samples.

4. Conclusion

MKLS-based geopolymer cements are attracting attention from both academia and industry as a sustainable binder alternative to portland cement. In this study, MKLS-based geopolymer pastes (Si/Al = 1.5, Na/Al = 1.0) using different contents of reagent-grade LS were prepared. The reaction kinetics, compressive strength, and phase assemblages were characterized. The results showed that, in general, LS delayed the alkali-activation process. However, 10% LS promoted the overall degree of reaction, thereby increasing cumulative heat above that of the control formulation. A 30% LS replacement led to similar compressive strengths as the samples with 0% or 10% of LS. Samples with 50% LS decreased the compressive strength considerably, suggesting a significant dilution effect. Further microstructural analyses are required to fully understand the mechanisms behind these results.

References

Cwirzen, A., Provis, J. L., Penttala, V., and Habermehl-Cwirzen, K. (2014) "The effect of limestone on sodium hydroxide-activated metakaolin-based geopolymers", *Construction and Building Materials*, 66, 53-62

Perez-Cortes, P., and Escalante-Garcia, J. I. (2020) "Gel composition and molecular structure of alkali-activated metakaolin-limestone cements", *Cement and Concrete Research*, 137, 106211

Puligilla, S., Chen, X., and Mondal, P. (2019) "Does synthesized C-S-H seed promote nucleation in alkali activated fly ash-slag geopolymer binder? ", *Materials and Structures*, 52(4), 65

Qian, J., and Song, M. (2015) "Study on influence of limestone powder on the fresh and hardened properties of early age metakaolin based geopolymer", Paper presented at the Calcined Clays for Sustainable Concrete: *Proceedings of the 1st International Conference on Calcined Clays for Sustainable Concrete*.

Ren, J., Sun, H., Li, Q., Li, Z., Zhang, X., Wang, Y. and Xing, F. (2022) "A comparison between alkali-activated slag/fly ash binders prepared with natural seawater and deionized water", *Journal of the American Ceramic Society*, 1-15.

The 16th International Congress on the Chemistry of Cement 2023 (ICCC2023)
"Further Reduction of CO_2 -Emissions and Circularity in the Cement and Concrete Industry"
September 18–22, 2023, Bangkok, Thailand

Microstructure of Alkali-activated Slag Paste Modified by Superabsorbent Polymers

Jingbin Yang[1], Didier Snoeck[2], Nele De Belie[3], and Zhenping Sun[4, *]

[1] *Key Laboratory of Advanced Civil Engineering Materials of Ministry of Education, School of Materials Science and Engineering, Tongji University,Shanghai 201804, China*
Email: jingbinyang@tongji.edu.cn
[2] *Department of Building, Architecture and Town Planning, Université Libre de Bruxelles (ULB), Brussels, B-1050, Belgium*
Email: didier.snoeck@ulb.be
[3] *Magnel-Vandepitte Laboratory, Department of Structural Engineering and Building Materials, Ghent University, Gent B-9052, Belgium*
Email:Nele.DeBelie@UGent.be
[4]*Key Laboratory of Advanced Civil Engineering Materials of Ministry of Education, School of Materials Science and Engineering, Tongji University,Shanghai 201804, China*
Email: zhenpingsun@126.com

ABSTRACT

In this study, the impact of superabsorbent polymers (SAPs) on the development of pore structure, internal relative humidity, and moisture migration in alkali-activated slag (AAS) pastes was investigated. The results showed that the addition of SAPs not only created voids in the hardened paste, as indicated by the mercury intrusion porosimetry (MIP) results, but also increased the microscopic pore volume of the paste. The increased differential thermogravimetry (DTG) peak corresponding to the primary hydration product, C(-A)-S-H gel, at 28 days suggests that SAPs resulted in more chemically bound water in the C(-A)-S-H gel structure or enhanced the hydration reaction to generate more C(-A)-S-H gel. The increase in chemically bound water in AAS pastes containing SAPs, along with the changes in the transverse relaxation time (T_2) peak area corresponding to SAPs in the ^{1}H low-field NMR results, is likely due to the gradual release of water during internal curing by SAPs.

KEYWORDS: *superabsorbent polymers, alkali-activated slag, chemically bound water, moisture migration*

1. Introduction

In recent years, superabsorbent polymers (SAPs), a widely-used internal curing material for Portland cement systems (Mechtcherine et al., 2021; Schröfl et al., 2022), have been introduced into AAS systems as well (Li et al., 2020; Oh & Choi, 2018). When the paste hardens, the SAPs release the liquid they absorbed during the mixing process to supplement the water consumption caused by the hydration reaction of AAS and reduce capillary pressure, thus reducing autogenous shrinkage.
The effectiveness of SAPs in reducing autogenous shrinkage in AAS systems has been widely demonstrated, but their impact on the microstructural development of these systems is not yet fully understood. In this paper, the effects of SAPs on the properties, reaction products, pore structure, and internal relative humidity development of water glass-activated slag systems were studied.

2. Materials and methods

2.1 Materials and paste preparation

The chemical composition of the slag is presented in Table 1. A water glass solution was used as an alkali activator, and its modulus was 2.0. The d_{50} of commercially available sodium polyacrylate SAP1 and SAP2 were 422 μm and 246 μm, respectively, and their equilibrium water absorption rates in deionized water, measured using the tea-bag method recommended by RILEM (Snoeck et al., 2018), were approximately 480 g/g and 500 g/g.

The dosage of SAPs was 0.30 (% of the mass of slag), the alkali content ($W_{(Na2O)}/W_{(slag)}$) was 5%, and the water-binder ratio was kept constant at 0.40. The fresh paste was poured into a 40 x 40 x 40 mm^3 cube mould, cured for 1 day at room temperature, demoulded to obtain the AAS paste specimens, and finally stored in a curing room with a temperature of 20 ± 2 °C and relative humidity of ≥95%.

Table 1 Chemical composition of the slag /wt.%

CaO	SiO_2	Al_2O_3	Fe_2O_3	MgO	SO_3	Na_2O	K_2O	TiO_2	MnO	SrO	Others
39.1	31.1	14.3	0.46	8.5	2.06	0.40	0.38	0.69	0.33	0.07	2.61

2.2 Test Methods

The hardened paste was crushed and soaked in ethanol for 24 h, and then dried to a constant weight in a vacuum oven at 40 °C. The dried samples were then powdered and sieved through a 74 μm sieve to obtain a sample for microscopic testing. Thermogravimetric testing of the powdered samples was performed using a SC-TGA Q600 thermal analyzer, with a N_2 protective atmosphere, a temperature range of room temperature to 800 °C, and a heating rate of 10 °C/min. The pore structure of the hardened bulk AAS paste sample was determined using an AutoPore IV 9510 mercury porosimeter. The internal relative humidity in AAS paste was tested using a Collihigh JWSK humidity sensor. Specific test methods on the internal relative humidity can be found in our previous paper (Yang et al., 2021). The continuous collection mode was selected for the first 7 days after mixing, with the data collection system automatically recording a measurement every 5 minutes. At the end of the 7th day, the sensor was placed in the hole for 10 minutes and the humidity value was recorded every day. The sensor was then removed and the upper end of the PVC tube was closed again. A Niumag PQ001 instrument was used for ^{1}H low-field NMR tests. Further information on the ^{1}H low-field NMR tests can be found in our previous paper (Yang et al., 2021).

3. Results and discussion

3.1 Development of pore structure

Fig. 1 shows the pore size distribution of the three hardened AAS pastes obtained by MIP at 3 d and 28 d. The pores of AAS paste are predominantly distributed below 20-30 nm. At 3 d, when compared to the reference sample, the pore distribution of the samples containing SAPs shifted slightly to the right, but the main pore size still remained below 20-30 nm, with a larger pore volume, indicating that the addition of SAPs altered the pore structure of the hardened AAS paste. As the curing time increased to 28 d, the pore volume in the hardened paste further decreased, resulting in a denser structure, but the pore volume of the samples containing SAPs remained larger than that of the reference sample.

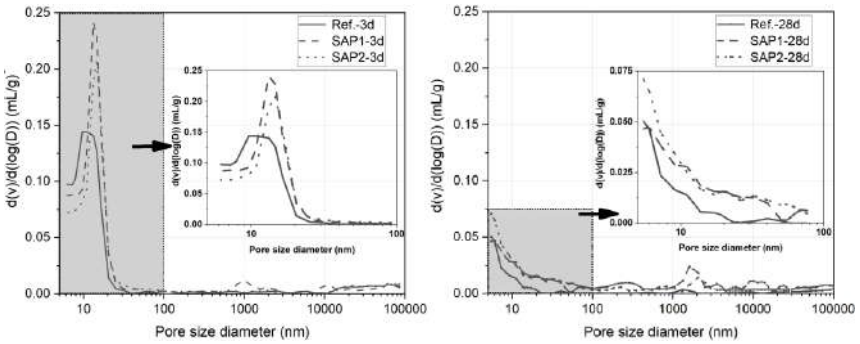


Fig.1 Differential pore size distribution of AAS paste

3.2 Internal relative humidity

Fig.2 shows the change in internal relative humidity of the three AAS pastes within 14 days. From about 1 d after mixing, the internal relative humidity of the AAS paste started to decrease, particularly in the reference sample. Its humidity was approximately 97% at 1 d and then declined rapidly. By 7 d, the humidity had fallen to approximately 85%. After 7 d, the rate of decrease in humidity slowed, reaching approximately 82% by 14 d. When SAPs were added, the decrease in internal relative humidity was significantly reduced, with humidity remaining above 95% at 7 d. The rate of decrease in humidity after 7 d was slightly higher than that seen between 0 and 7 d, which could be due to moisture exchange between

the internal paste and the external environment when the humidity sensor was placed in the PVC tube and some water escaped. Nevertheless, the humidity values for the two samples containing SAPs at 14 d remained above 93%, which was higher than that of the reference sample. Furthermore, the internal relative humidity for the sample containing SAP2 was slightly higher than that for SAP1, which could be due to the fact that SAP2 released more water and had a smaller particle size, leading to a larger surface area in contact with the hardened paste when the dosages were the same.

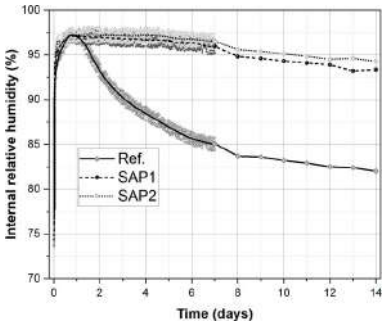


Fig.2 The internal relative humidity of AAS paste

3.3 Moisture migration

Fig. 3 shows the TG and DTG curves of the AAS paste powders at 3 d and 28 d. Due to the low SAP concentration (up to 0.3 wt.%), its impact on the TG and DTG results was neglected, and only the AAS paste matrix was analyzed. All samples exhibit a noticeable DTG peak between 50 °C and 250 °C, which is attributed to the dehydration of the C(-A)-S-H gel during heating (Liu et al., 2020). At 3 days, the DTG peak of the samples with SAPs was smaller than that of the reference sample, which may be because most of the water absorbed by the SAPs had not yet been released. When the total water-binder ratio was kept constant, the remaining free water in the AAS paste matrix for hydration was reduced compared to the reference sample, leading to a decrease in the DTG peak of the C(-A)-S-H gel. However, at 28 days, the DTG peaks of the samples with SAPs were larger than that of the reference sample, with SAP2 showing a larger peak than SAP1. When considering the internal relative humidity results, it can be inferred that despite having the same total water-binder ratio, the water released by the SAPs during curing not only sustained the internal relative humidity of the AAS paste but also converted a portion of it into chemically bound water in the C(-A)-S-H gel.

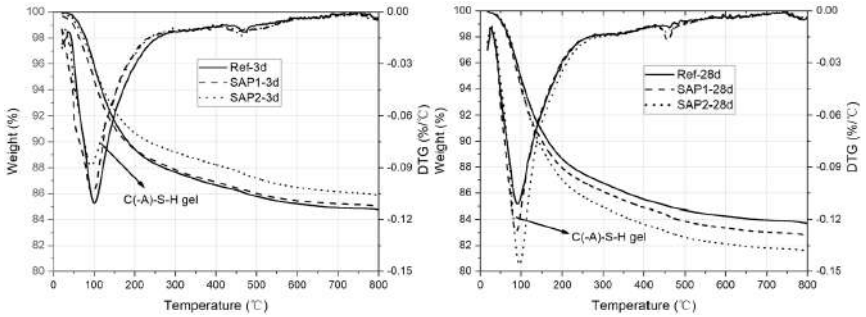


Fig. 3 Thermo-gravimetric analysis (TGA) and derivative thermogravimetric (DTG) curves for AAS paste

Fig.4 illustrates the transverse relaxation time (T_2) distribution of AAS pastes at 3 d and 28 d, as determined through ^{1}H low-field NMR results. In the samples containing SAPs, two T_2 relaxation peaks can be observed. The broad peak is associated with the water in the pores of the AAS paste matrix, which is mainly distributed in T_2 values of less than 1 ms, while the relaxation peak with T_2 values of about 10-100 ms is related to the free water present in the SAPs (Snoeck et al., 2017; Yang et al., 2021). The relaxation peak area reflects the content of free water, with the number below the peak indicating the peak area. The broad peak area and the peak areas corresponding to the SAPs decreased from 3 d to 28 d. The free water in the pores of the hardened paste matrix participated in the hydration of AAS and was consumed and transformed into chemical-bound water in the products, resulting in a decrease in the broad

peak area. The SAPs released the free water absorbed during mixing, resulting in a decrease in their peaks as well.

Compared to the peak area at 3 d, the area of the broad relaxation peaks of the reference sample, SAP1, and SAP2 at 28 d was reduced by 10.8%, 10.3%, and 10.5% respectively, and these results were similar. However, the DTG peaks corresponding to the C(-A)-S-H gel in the samples containing SAPs were larger than those of the reference sample at 28 d, indicating that more chemically bound water was generated from 3 d to 28 d. Hence, it can be inferred that the increase in chemically bound water in the samples containing SAPs compared to the reference samples from 3 d to 28 d may be directly or indirectly converted from the water released by the SAPs.

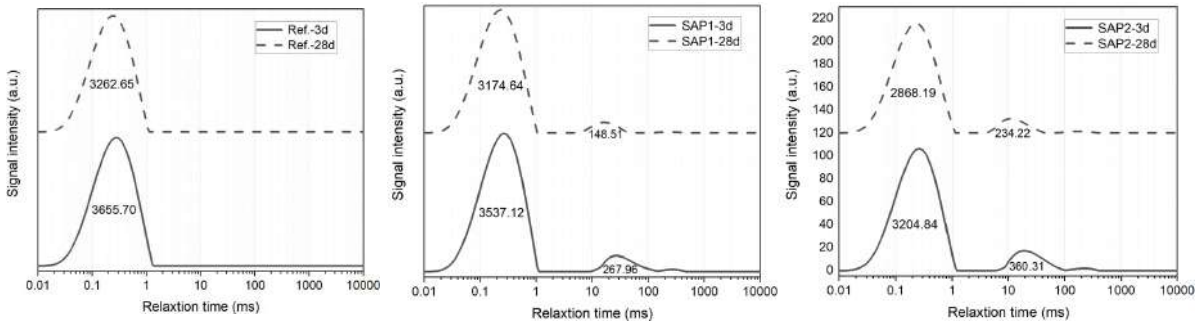


Fig. 4 The transverse relaxation time (T_2) distribution of the AAS paste

3 Conclusions

(1) The addition of SAPs not only created voids in the hardened paste, as indicated by the MIP results, but also increased its pore volume.

(2) The addition of SAPs resulted in an increase in DTG peak of the C(-A)-S-H gel at 28 d, indicating that it led to more chemically bound water in the gel structure or enhanced the hydration reaction to produce a greater amount of C(-A)-S-H gel.

(3) Since the free water in the pores of the AAS paste was consumed during hydration, and the SAPs gradually released water, the broad relaxation peak area and the relaxation peak area corresponding to the SAPs both decreased from 3 d to 28 d. The decrease in the primary relaxation peak area for all three samples was similar during this period. However, at 28 d, the amount of chemical binding water related to the C(-A)-S-H gel was greater in the samples containing SAPs compared to the reference sample. This increase in chemical binding water may be due to the water released by the SAPs.

References

Li, Z., Wyrzykowski, M., Dong, H., Granja, J., Azenha, M., Lura, P., Ye, G. J. C., & Research, C. (2020). Internal curing by superabsorbent polymers in alkali-activated slag. *135*, 106123.

Liu, J., Hu, L., Tang, L., Zhang, E. Q., Ren, J. J. C., & Materials, B. (2020). Shrinkage behaviour, early hydration and hardened properties of sodium silicate activated slag incorporated with gypsum and cement. *248*, 118687.

Mechtcherine, V., Wyrzykowski, M., Schröfl, C., Snoeck, D., Lura, P., De Belie, N., Mignon, A., Van Vlierberghe, S., Klemm, A. J., & Almeida, F. C. (2021). Application of super absorbent polymers (SAP) in concrete construction—update of RILEM state-of-the-art report. *Materials and Structures*, *54*(2), 1-20.

Oh, S., & Choi, Y. C. (2018). Superabsorbent polymers as internal curing agents in alkali activated slag mortars. *Construction and Building Materials*, *159*, 1-8.

Schröfl, C., Erk, K. A., Siriwatwechakul, W., Wyrzykowski, M., & Snoeck, D. (2022). Recent progress in superabsorbent polymers for concrete. *Cement and Concrete Research*, *151*, 106648.

Snoeck, D., Pel, L., & De Belie, N. (2017). The water kinetics of superabsorbent polymers during cement hydration and internal curing visualized and studied by NMR. *Sci Rep*, *7*(1), 9514.

Snoeck, D., Schrofl, C., & Mechtcherine, V. (2018). Recommendation of RILEM TC 260-RSC: testing sorption by superabsorbent polymers (SAP) prior to implementation in cement-based materials. *Materials and Structures*, *51*(5), 116.

Yang, J., Snoeck, D., De Belie, N., & Sun, Z. (2021). Comparison of liquid absorption-release of superabsorbent polymers in alkali-activated slag and Portland cement systems: An NMR study combined with additional methods. *Cement and Concrete Research*, *142*, 106369.

The 16th International Congress on the Chemistry of Cement 2023 (ICCC2023)
"Further Reduction of CO_2 -Emissions and Circularity in the Cement and Concrete Industry"
September 18–22, 2023, Bangkok, Thailand

Utilization of carbonated steel slag powder in cementitious materials

N. Li[1], C. Unluer[2*]

[1] *Department of Mechanical, Aerospace and Civil Engineering, University of Manchester, M13 9PL Manchester, United Kingdom*
Email: ning.li-3@manchester.ac.uk
[2] *Department of Mechanical, Aerospace and Civil Engineering, University of Manchester, M13 9PL Manchester, United Kingdom*
Email: cise.unluer@manchester.ac.uk

ABSTRACT

Steel slag is produced in large quantities as a by-product of primary steel-making, which is mainly landfilled or used as an aggregate. The high reactivity of steel slag with CO_2 makes it an ideal material for CO_2 capture, resulting in the formation of calcite, even at ambient temperatures and pressures. In this study, the direct carbonation of steel slag under 10% CO_2, 25ºC, and ambient pressure was investigated. The carbonated steel slag was then used in the preparation of cement paste samples, where 20% (by mass) of cement was replaced by carbonated steel slag. The prepared samples were cured under ambient conditions for up to 28 days. Results revealed that the carbonation of steel slag mainly occurred in the first 6 hours, enabling an increased CO_2 uptake by 5.2%. Carbonation reaction reduced the content of free calcium oxide in steel slag, resulting in the formation of calcite composed of non-uniform particles. Compared with cement paste samples containing uncarbonated steel slag, those involving steel slag carbonated for 3 hours achieved 22% higher 28-day compressive strengths. However, a decline in strength was observed with an increase in the carbonation duration, which was linked with the carbonation of the silicate phase in steel slag. Overall, this study highlighted the carbon sequestration capacity of steel slag and the potential benefits of this process in enhancing the mechanical and microstructural properties of resulting cement formulations.

KEYWORDS: *Steel slag, carbonation, compressive strength, microstructure, calcite*

1. Introduction

Cement manufacture is responsible for around 8% of global carbon dioxide (CO_2) emissions. A solution to address the reduction of the carbon footprint of construction materials involves the reduction of the cement content by substituting it with a more sustainable alternative (Mahasenan et al., 2003). Over 400 million tonnes of steel slag are produced globally each year from steel and iron production, according to the World Steel Association (Pan et al., 2017). The disposal of industrial wastes to landfill is a waste of resources and can cause significant pollution to farmland and freshwater due to the leaching of heavy metals.
Steel slag is abundant in highly CO_2-reactive minerals, such as α-C_2S, β-C_2S, and free MgO/CaO (Song et al., 2021). The CO_2 uptake capacity of steel slag could range from 200 to 400 g CO_2/kg, depending on carbonation conditions (Humbert and Castro-Gomes, 2019). However, the treatment of steel slag under low CO_2 concentrations and ambient temperature and pressure has not been widely investigated due to the slow carbonation kinetics (Li et al., 2022). The aim of this paper is to develop carbonated steel slag powder (SSP) as a supplementary cementitious material (SCM) in cement pastes. The carbonation kinetics and products of SSP at 10% CO_2 concentrations were investigated via gas-solid carbonation. The carbonated SSP was incorporated into the cement paste at a content of 20% (by mass of binder), followed by an evaluation of the mechanical and microstructural properties of the developed mixes.

2. Materials and Methodology

2.1 Materials

The steel slag was ground in a ball mill grinder to produce a fine powder with particles passing through a sieve size of 125 μm. A high strength Portland cement (PC) CEM I 52.5R with density and specific surface area of 3.15 g/cm^3 and 4200 cm^2/g, respectively, was used to prepare cement paste. The cement and steel slag had the same fineness, thereby the latter could be used as a direct replacement in the prepared mixes. The chemical compositions of the cement and steel slag, determined by X-ray fluorescence (XRF), are provided in Table 1.

Table 1. Chemical composition of cement and steel slag (wt.%)

	SiO_2	Al_2O_3	Fe_2O_3	CaO	MgO	SO_3	K_2O	Na_2O	LOI
Cement	19.38	4.94	2.87	62.89	3.4	3.29	0.35	0.35	0.99
Steel slag	13.88	8.66	22.15	35.95	9.83	0.28	0.06	0.31	3.13

2.2 Carbonation of SSP and sample preparation

The dried SSP was placed in a carbonation incubator under 20°C, 60% RH and 10% CO_2 concentration for 1, 3, 6, 24, 72, 168, 480 and 672 hours (C1h, C3h, C6h, C1d, C3d, C7d, C20d and C28d). Then 20% carbonated SSP by mass of cement was mixed with cement to produce cement paste with a water-to-binder (cement + steel slag) ratio of 0.5. The SSP and cement were added in mixing pot, and then mixed for 90 s until uniform. Then the solution was added, and stirred for the next 3 min. The paste mixes were cast into 20 × 20 × 20 mm^3 cubic moulds and compacted by a vibrating table. After being cured in the laboratory for 24 hours, the specimens were cured under 20°C and 95% RH for 3 and 28 days.

2.3 Experimental methods

The compressive strength of samples was measured using a compression machine, with a loading rate of 0.5 ± 0.1 MPa/s. The tests were carried out on three specimens for each mix and average strengths were taken as results. Thermogravimetric analysis (TGA) was conducted to evaluate the weight loss and corresponding peaks within each sample. 10 mg of each sample in powder form was heated from 30°C to 1000°C under a nitrogen atmosphere at rate of 10 °C/min in a TGA instrument (TGA8000, PerkinElmer). The TGA data was used to estimate the CO_2 uptake during the curing process of each sample, following Eq. (1).

$$CO_2Uptake_{wt.\%} = \text{mass loss between 500 and 950°C/mass at 1000°C} \times 100\% \quad (1)$$

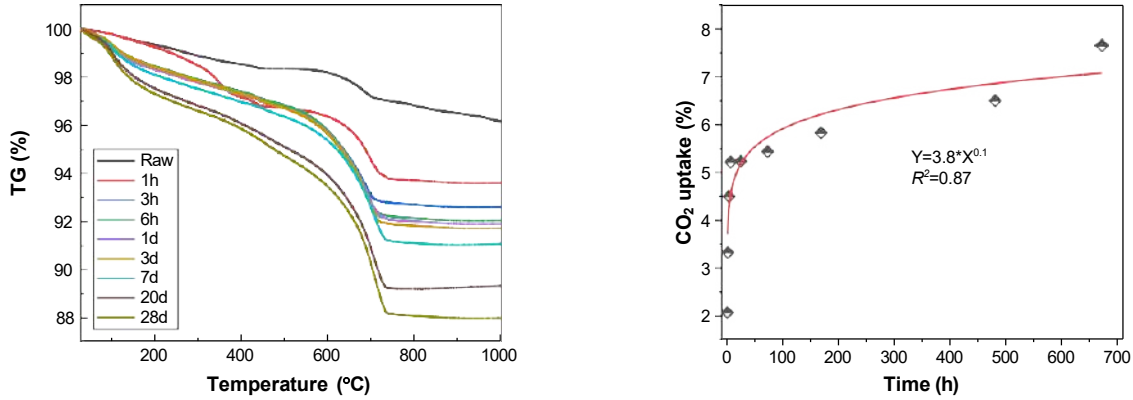
Scanning electron microscopy (SEM) imaging was carried out by a Carl Zeiss Sigma for the microstructural analysis of the hydrate and carbonate phases in each sample. The dried samples were coated with gold before the SEM observation.

3. Results and Discussion

3.1 Carbonation of SSP

Fig. 1 shows the TGA curves and CO_2 uptake development of SSP with different carbonation duration. The mass loss occurred in the range of 30-200°C represent the water loss during the dehydration of reaction products (main C-S-H gel phases), which implies that the SSP presents in the samples experienced some form of hydration reaction. The mass loss occurred in the range of 400-500°C corresponding to dehydration of uncarbonated $Ca(OH)_2$ (Dung and Unluer, 2018), which suggests that uncarbonated calcium and magnesium was still present in the samples following carbonation. The mass loss occurred in the range of 500-800°C represent the decarbonation of magnesium and calcium carbonates (Li et al., 2017). As the carbonation duration increased, the mass loss in this interval gradually increased, indicating that more carbonate was generated. Steel slag has a low hydration reactivity, possessing highly CO_2-reactive minerals such as α-C_2S, β-C_2S, and free MgO/CaO. At a 10% CO_2 concentration, the carbonation of the SSP occurred predominantly within the first 6 hours, when the CO_2 uptake increased from 2.1% to 5.2%. Increasing the carbonation duration to 672 hours resulted in only a 7.7% CO_2 uptake. This is due to the available calcium content of the SSP, and the carbonation was further constrained by the produced calcium carbonate adhering to the surface of the SSP particles. At such a low

CO_2 concentration and atmospheric pressure, it was challenging for CO_2 to penetrate the dense carbonation layer on the particle surface and continue to react with the slag.



(a) TGA curves (b) CO_2 uptake development

Fig. 1. (a) TGA curves and (b) CO_2 uptake development of SSP with different carbonation duration

3.2 Compressive strength

Compressive strength of cement paste samples involving 20% carbonated SSP at 28 days is shown in Fig. 2. The addition of 20% uncarbonated and carbonated SSP significantly reduced the compressive strength of the cement paste. As an example of the 28-day strength, the addition of 20% uncarbonated SSP, C3h, C1d, C7d and C28d SSP reduced the strength of the cement paste by 27.3%, 11.6%, 21.3%, 27.8% and 34.1% respectively. This suggests that shorter carbonation treatment duration (within 3 hours) of the SSP improved the compressive strength of the specimens, whereas longer carbonation treatment durations of the SSP decreased the compressive strength. The prolonged carbonation duration could have, on the one hand, reduced the hydraulic mineral phases in the SSP and, on the other, promoted the transformation of calcium carbonate to the more stable crystalline form of calcite. Shen et al. (Shen et al., 2022) demonstrated that the needle-like whiskers characteristic of aragonite could strengthen cement and significantly improve its mechanical properties. It is worth noting that a longer carbonation duration was more beneficial for early strength. As shown in the Fig. 2, a maximum 3-day compressive strength of 59.2 MPa was achieved with the addition of 20% C7d SSP. The mechanism behind needs to be further explored.

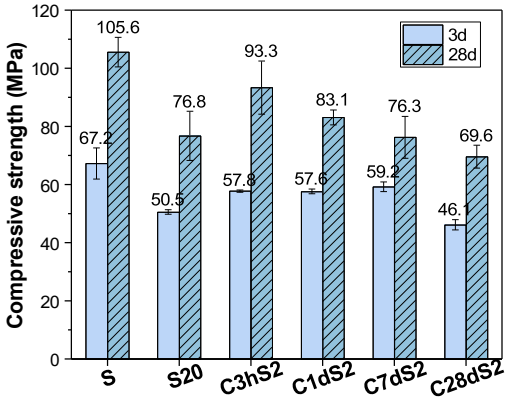
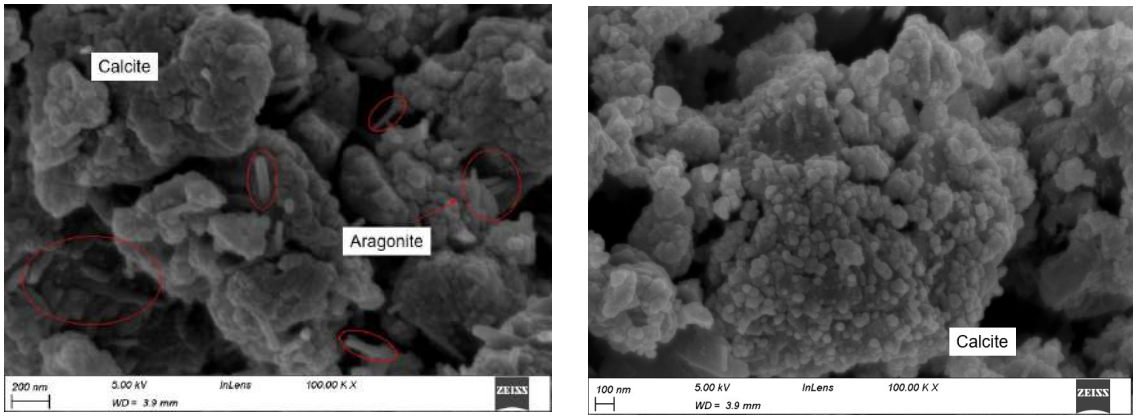


Fig. 2. Compressive strength of cement paste samples involving 20% carbonated SSP at 28 days

3.3 SEM observation

The SEM images of SSP after 3 hours and 28 days of carbonation are presented in Fig. 3. After 3 hours of carbonation, aragonite whisker-rich materials were generated with a length of approximately 200 nm and a diameter of approximately 20 nm. These whiskers acted as microfibres within the cement paste and contributed to the mechanical properties of sample (Shen et al., 2022). After 28 days of carbonation, the SSP consisted primarily of granular calcite crystals with particle sizes between 30 and 50 nm.



(a) C3h (b) C28d

Fig. 3. SEM pictures of SSP with (a) 3 hours and (b) 28 days carbonation

4. Conclusions

This study investigated the carbonation kinetics and microstructure of SSP under 10% CO_2, 25ºC, and ambient pressure. The use of carbonated SSP in cement pastes at 20% by mass of cement was evaluated via the assessment of mechanical and microstructural properties. Carbonation of SSP occurred mainly in the first 6 hours, with a CO_2 uptake of 5.2%. The rate of CO_2 uptake reduced over carbonation duration. The carbonated products were mainly aragonite whisker and granular calcite. The formation of aragonite and calcite contributed to the strength of the cement pastes, resulting in a 22% increase in the strength of the samples when compared to samples with uncarbonated SSP.

Acknowledgements

The authors acknowledge the financial support from The Royal Society (project ref: ICA\R1\201310).

References

Dung, N.T., Unluer, C. (2018) "Development of MgO concrete with enhanced hydration and carbonation mechanisms", *Cement and Concrete Research*, 103: 160-169

Humbert, P.S., Castro-Gomes, J. (2019) "CO2 activated steel slag-based materials: A review", *Journal of Cleaner Production*, 208: 448-457

Li, N., Farzadnia, N., Shi, C. (2017) "Microstructural changes in alkali-activated slag mortars induced by accelerated carbonation", *Cement and Concrete Research*, 100: 214-226

Li, N., Mo, L., Unluer, C. (2022) "Emerging CO2 utilization technologies for construction materials: A review", *Journal of CO2 Utilization*, 65: 102237

Mahasenan, N., Smith, S., Humphreys, K. (2003) "The Cement Industry and Global Climate Change: Current and Potential Future Cement Industry CO2 Emissions", in: Gale, J., Kaya, Y. (Eds.), *Greenhouse Gas Control Technologies - 6th International Conference*, Pergamon, Oxford, pp. 995-1000

Pan, S.-Y., Chung, T.-C., Ho, C.-C., Hou, C.-J., Chen, Y.-H., Chiang, P.-C. (2017) "CO2 Mineralization and Utilization using Steel Slag for Establishing a Waste-to-Resource Supply Chain", *Scientific Reports*, 7(1): 17227

Shen, P., Lu, J., Zhang, Y., Jiang, Y., Zhang, S., Poon, C.S. (2022) "Preparation aragonite whisker-rich materials by wet carbonation of cement: Towards yielding micro-fiber reinforced cement and sequestrating CO2", *Cement and Concrete Research*, 159: 106891

Song, Q., Guo, M.-Z., Wang, L., Ling, T.-C. (2021) "Use of steel slag as sustainable construction materials: A review of accelerated carbonation treatment", *Resources, Conservation and Recycling*, 173: 105740

The 16th International Congress on the Chemistry of Cement 2023 (ICCC2023)
"Further Reduction of CO_2 -Emissions and Circularity in the Cement and Concrete Industry"
September 18–22, 2023, Bangkok, Thailand

Insights into the Role of Carbonation Curing on Calcium Leaching Behavior of Cement Paste

Tiefeng Chen[1*], Xiaojian Gao[2]

[1] *Harbin Institute of Technology, Harbin, China*
Email: chentf@hit.edu.cn
[2] *Key Lab of Smart Prevention and Mitigation of Civil Engineering Disasters of the Ministry of Industry and Information Technology, Harbin, China*
Email: gaoxj@hit.edu.cn

ABSTRACT

Carbonation is generally considered to enhance calcium leaching resistance of cement-based materials. However, many researches demonstrated that carbonation curing may also adversely affect calcium leaching resistance of cement paste. In this paper, calcium leaching behavior of early-carbonated cement paste was investigated in detail. The results show that 8~16-h carbonation curing mitigated the reduction in compressive strength caused by calcium leaching, but further prolongation of carbonation curing caused an increased decline in strength at later leaching stage. The specimens carbonated for less than 16 h possesses improved pore structure by decreasing porosity and volume fraction of larger capillary pores, as well as reduces the negative impact of calcium leaching. Different from calcium leaching results on powdered samples, the decalcification level of C-S-H in cubic specimens was similar or even higher than early-carbonated ones along leaching test. Nonetheless, considering its risk of rapid degradation, excessive carbonation-cured cement-based materials should still be avoided in aqueous environments.

KEYWORDS: *Carbonation curing; Calcium leaching; Cement paste, C-S-H*

1. Introduction

Carbonation curing of cement-based materials is considered as one of promising methods to approach carbon neutral in manufacture of cement and concrete products. In most cases, carbonation curing of cement-based materials is implemented through early accelerated carbonation. It is estimated that precast concrete products can store CO_2 equivalent up to 20 wt% of the binder (El-Hassan, 2013). It is commonly believed that carbonation improves calcium leaching resistance of cement-based materials: the conversion from CH to $CaCO_3$ prevents dissolution of calcium; the denser microstructure hinders the outward diffusion of calcium ions. However, this opinion might be valid for natural carbonation, but things are different for early-carbonated cement paste. Exposing to CO_2 at early age, large amount of C-S-H gel with Ca/Si ratio lower than 1.0 generates in the carbonation reaction, which is more prone to decalcify (Chen, 2019). Besides, it has been experimentally verified that early accelerated carbonation does not necessarily reduce the permeability of cement paste (Schwotzer, 2010). In this research, the strength loss of carbonation-cured cement paste with various accelerated carbonation duration is determined. The change of pore structure, stoichiometric and structural characteristics of C-S-H, and nano-mechanical properties are investigated as well.

2. Experimental methods

2.1 Raw materials and specimen preparation

Portland cement, tap water, and polycarboxylate-based superplasticizer were used to prepare cement paste specimens. After completion of mixing, the fresh mixtures were poured in 50-mm cubic steel molds. These

specimens would be in-mold pre-cured for 6 h and followed by de-mold pre-curing for another 6 h. Then, these specimens were stored in a carbonation chamber for CO_2 exposure at a normal atmospheric pressure with CO_2 concentration of 20%. When CO2 exposure was finished, all the specimens would be stored in a standard curing chamber. Besides, some specimens were placed in the standard curing chamber without carbonation as a standard-cured control group.

2.2 Testing methods

Calcium leaching test was performed on specimens after 3 months of standard curing. 6mol/L NH_4NO_3 solution was used to accelerate calcium leaching test. Carbonation depth was measured on the cross section of specimens using phenolphthalein reagent. The CO_2 uptake percentage was determined by TG-DSC using a simultaneous thermal analyzer. Compressive strength test was performed on three 50-mm cubic specimens with the loading rate of 1.6 kN/s. The information of pore structure was determined applying an AutoPore IV 9510 mercury intrusion porosimetry (MIP) with the pressure range of 0~60000 psi. Energy dispersion X-ray spectra analysis were observed using a scanning electron microscope.

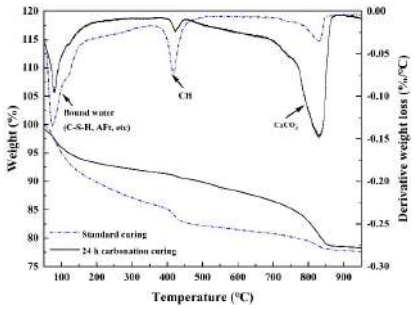
3. Results and discussion

The TG and DTG curves of standard-cured and 24 h carbonation-cured samples were shown in Fig. (a) as an example. The CO_2 uptake percentage is introduced to evaluate carbonation degree of cement mortar as follow (Jang, 2016):

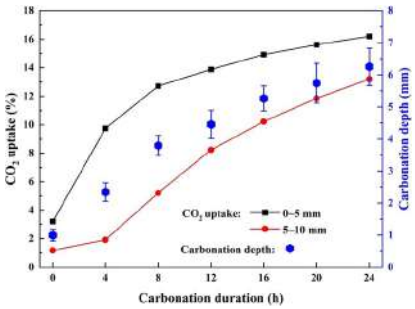
$$CO_2\ uptake = \frac{m550\text{-}m950}{m_0} \times 100\% \quad (1)$$

where m_{550} and m_{950} are the mass of samples at 550°C and 950°C, respectively; m_0 is the initial mass of samples. The carbonation depth measured by phenolphthalein indicator and calculated CO_2 uptake in different depth intervals are presented in Fig. 1 (b). For the samples taken from 0~5 mm, CO_2 uptake increases rapidly in first 4 hours and then gradually slows down. While as for samples from 5~10 mm depth, the increase in CO_2 uptake is minor in first 4 hours, after which the carbonation rate accelerates apparently and then slows down again. This is due to the slow diffusion rate of CO_2 in cement paste specimens, resulting in a lower local CO_2 concentration at 5~10 mm depth in the first 4 hours. The range of fully carbonated zone measured by phenolphthalein is within 7 mm in 24 h carbonation.

Fig. 2 displays the compressive strength of specimens subjected to different calcium leaching duration. Before leaching test, the compressive strength of standard-cured specimen is 61.5 MPa, and the highest is 66.3 MPa, occurring at 8 h carbonation curing. As the carbonation duration exceeds 8 hours, the strength decreases slightly, reducing to 58.4 MPa through 24 h carbonation curing. After 56 d calcium leaching test, the strength of standard-cured specimens reduces to 35.7 MPa. The residual strength of 8 h and 12 h carbonation-cured specimens are highest, corresponding to 44.6 MPa and 45.9 MPa, respectively. Further prolonged carbonation curing reduces the residual strength as well, while it is still higher than standard-curing.



(a) TG and DTG curves



(b) Carbonation depth and CO_2 uptake

Fig. 1 Results of thermal analysis

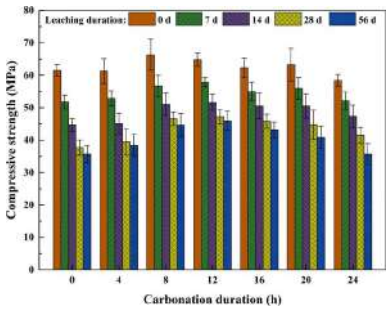


Fig. 2 Compressive strength

The porosity and pore volume fraction of cement paste samples are exhibited in Fig. 3. Early accelerated carbonation within 16 hours modifies the pore structure of cement paste by reducing the porosity and the volume fraction of large capillary pores, which is contributed by $CaCO_3$ precipitation. When carbonation duration exceeds to 16 hours, the porosity begins to increase, resulting from the shrinkage of decalcified C-S-H and lack of moisture. After calcium leaching test, the porosity of all specimens is increased greatly caused by dissolution of CH and C-S-H, as it can be expected. Compared with standard-cured specimens, early accelerated carbonation effectively retards the degradation of pore structure during calcium leaching, especially the samples carbonated for 12 hours.

BSE-EDX analysis is performed to study the change of Ca/Si ratio, and a typical BSE image is presented in Fig. 4, in which the C-S-H loop surrounding the cement clinker can be observed. The detecting spots of EDX were selected within this rim zone of C-S-H.

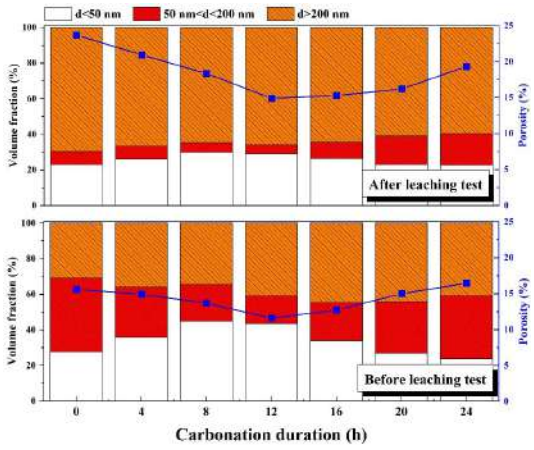


Fig. 3 Information of pore structure

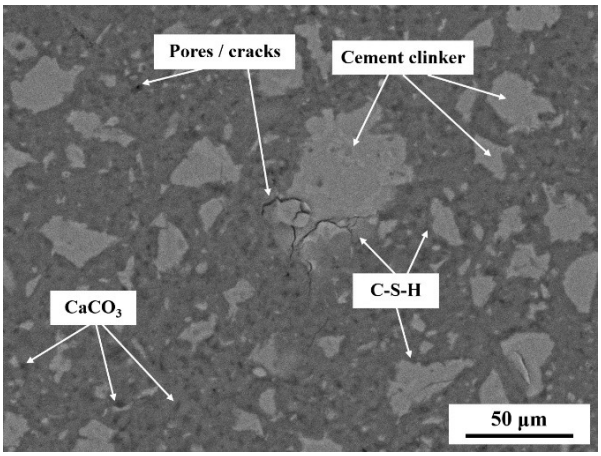
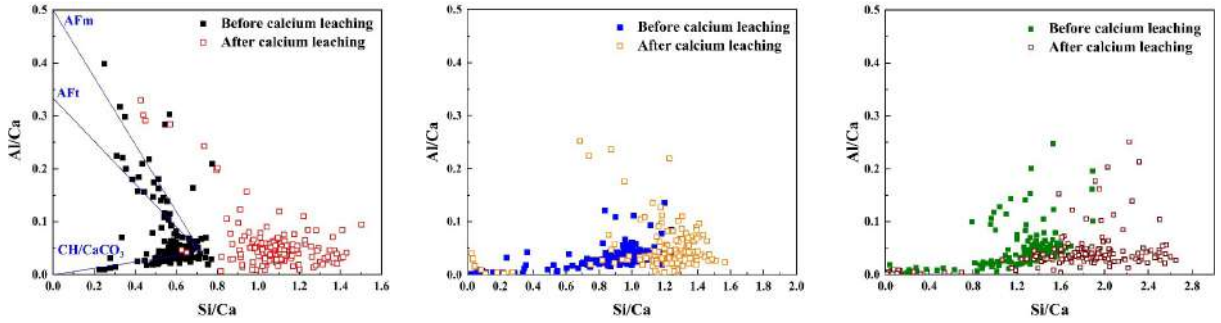


Fig. 4 An example of BSE image

For each sample, more than 100 EDX analysis spots contained atomic percentage of Ca, Si, and Al were collected. Fig. 5 shows the EDX analysis results of the samples obtained by plotting atomic ratio of Si/Ca versus Al/Ca. The coordinates on the y-axis with Al/Ca ratio of 0.5, 0.33, and 0 are corresponding to phases of AFm, Aft, and CH (or $CaCO_3$), respectively (Liu, 2022). Tie lines are drawn in Fig. 5 (a) from the cloud of C-S-H points and different known composition (Shah, 2018). It can be found in Fig. 5 (a)~(c) that carbonation curing and calcium leaching lead to a higher Si/Ca (or lower Ca/Si), implying decalcification of C-S-H.



(a) Standard curing (b) 12 h carbonation curing (c) 24 h carbonation curing

Fig. 5 Results of EDX point analysis by plotting Si/Ca against Al/Ca

The decreasing trend of Ca/Si before and after leaching test is put into Fig. 6. The outliers are mainly distributed outside the upper limit with a very high Ca/Si ratio, corresponding to AFt, AFm, CH/$CaCO_3$, or their mixtures with C-S-H gel. The box bodies are corresponding to the most data-dense areas in the scatter plots in Fig. 5 (a)~(c), which can be approximatively considered as C-S-H. In the leaching process, the mean value of Ca/Si of standard-cured sample decreases apparently, while that of 12 h and 24 h carbonation-cured samples is inconspicuous due to the presence of insoluble $CaCO_3$. Moreover, the Ca/Si ratio of C-S-H for standard-cured sample presents a larger reduction compared with 12 h and 24 h

carbonation-cured samples. The final Ca/Si ratio of C-S-H in standard-cured sample and 12 h carbonation-cured is similar, while that of 24 h carbonation-cured sample is somewhat lower.

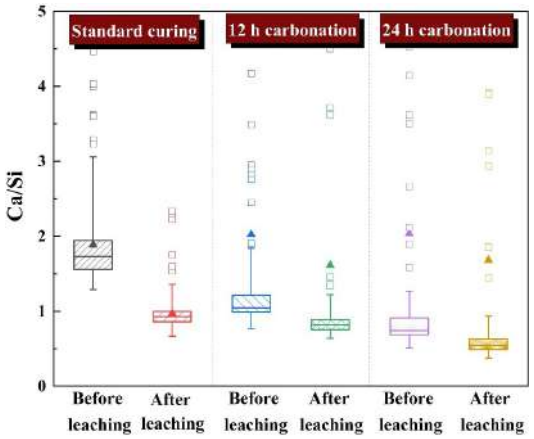


Fig. 6 Decrease in Ca/Si range caused by calcium leaching test

4. Conclusions

In this paper, the impact of carbonation curing on calcium leaching behavior of cement paste was investigated. Based on the results, the following conclusions can be drawn: 1) Appropriate carbonation curing improves calcium leaching resistance of cement paste. The loss in compressive strength of specimens carbonated for 8~16 h is smaller and the residual strength is higher than others. The strength of specimens with longer carbonation duration decreases more slowly in the early stage of calcium leaching and faster in the later stage. 2) The specimens carbonated for less than 16 h possesses improved pore structure by decreasing porosity and volume fraction of larger capillary pores, while longer carbonation duration can adversely affect the pore structure. On the other hand, the increase in porosity induced by calcium leaching is smaller for all the carbonation-cured specimens than standard-cured ones. 3) Both early accelerated carbonation and calcium leaching decrease the Ca/Si ratio of C-S-H, while the latter is more significant. The decalcification of C-S-H for standard-cured samples during calcium leaching is similar to or even more serious than carbonated ones.

Acknowledgements

This work was supported by National Natural Science Foundation of China (No. 52108202), China Postdoctoral Science Foundation (No. 2022M710971) and Natural Science Foundation of Heilongjiang Province of China (No. LH2022E071).

References

El-Hassan, Y.S.H. and Ghouleh, Z. (2013) "Effect of initial curing on carbonation of lightweight concrete masonry units", *ACI Materials Journal,* 110: 441-450.

Chen, T. and Gao, X. (2019) "How carbonation curing influences ca leaching of Portland cement paste: Mechanism and mathematical modeling", *Journal of the American Ceramic Society*, 102: 7755–7767.

Schwotzer, M., Scherer, T. and Gerdes, A. (2010) "Protective or damage promoting effect of calcium carbonate layers on the surface of cement based materials in aqueous environments", *Cement and Concrete Research*, 40: 1410-1418.

Jang, J.G. and Lee, H.K. (2016) "Microstructural densification and CO_2 uptake promoted by the carbonation curing of belite-rich Portland cement", *Cement and Concrete Research,* 82: 50–57.

Liu, M., Zhao, Y., Yu, Z., Cao, Z. (2022) "Binding of Cu(II) and Zn(II) in Portland cement immobilization systems: Effect of C-A-S-H composition", *Cement and Concrete Composites,* 131: 104602.

Shah, V., Scrivener, K., Bhattacharjee, B., Bishnoi, S. (2018) "Changes in microstructure characteristics of cement paste on carbonation", *Cement and Concrete Research,* 109: 184-197.

The 16th International Congress on the Chemistry of Cement 2023 (ICCC2023)
"Further Reduction of CO_2 -Emissions and Circularity in the Cement and Concrete Industry"
September 18–22, 2023, Bangkok, Thailand

Mechanical properties of Hardened Cement Paste Containing Amines

X. Zhuo[1]*, T. Pan[1]*, D. Oh[1]*, R. Kitagaki[1], Y. Elakneswaran[1], H. Senboku[1], R.Saito[2], K.Yano[2], Y. Yoda[2], M. Tsujino[2], A. Nishida[2]

[1] *Faculty of Engineering, Hokkaido University, Kita 13 Nishi 8, Kita-ku, Sapporo, Hokkaido 060-8628, Japan.*
xinjie.zhuo.f4@elms.hokudai.ac.jp
[2] *Shimizu Corporation, Shimizu Institute of Technology, 3 Chome-4-17 Etchujima, Koto Ward, Tokyo 135-8530, Japan.*
ryosuke.saito@shimz.co.jp

ABSTRACT

Carbon dioxide emissions to the atmosphere are the leading cause of climate change and pose a serious risk to the environment. CO_2 can be captured by amines, which are derivatives of ammonia and undergo reversible reactions with CO_2 and form carbamate/bicarbonate. The feasibility for applying amines to concrete have not investigated adequately. Therefore, the purpose of this research is to investigate mechanical properties of hardened cement paste containing amines. To accomplish this, methyl diethanolamine (MDEA) and p-Phenylenediamine (HEPZ) were applied. The weight fraction of each amine mixed with cement paste(water to cement ratio:0.5) was designed to be 5 % respectively. The specimens were sealed and cured at 20 °C. After curing for 7 , 14 , 28 , 56 and 91 days, compression test and splitting tensile test were carried out to acquire the compressive strength, tensile strength, and elastic modulus. The effects of types of amines on mechanical properties to hardened cement paste were systematically investigated. The results indicated that influences on mechanical properties of hardened cement paste were found depending on types of the amines. It was found that MDEA additive effectively improved the early strength of cement paste. On the contrary, PPD additive greatly reduced the early compressive strength of cement paste. After curing for 28 , 56 and 91 days, both MDEA and HEPZ reduced the compressive strength of cement paste. However, tensile strength and elastic modulus were not significantly influenced by MDEA and HEPZ.

KEYWORDS: *CO_2 absorption, MDEA,* HEPZ*, mechanical properties*

1. Introduction

There are several promising technologies for capturing CO_2, but the use of amines for CO_2 capture remains the most mature and commercially available representative chemical process for reducing CO_2 emissions at present according to Mofarahi (2008)
CO_2 is captured by amines through reversible reactions, forming carbamates or bicarbonate ions. Research by Aaron and Tsouris (2005) shows the basic mechanism of the amine-based CO_2 separation and recovery technology is to release CO_2 fixed in a solution containing an amine at a certain temperature by temperature or pressure changes.
The purpose of this study is to evaluate the mechanical properties of hardened cement with two types of added amines, specifically the compressive strength and Young's modulus at each age, as well as the absolute dry density and water absorption rate.

2. Materials

2.1 Preparation of hardened cement paste

The cement paste was prepared with a water-cement ratio of 0.5. A 5% by weight addition of amine was added to the external crack and the mixture was poured into plastic mold of 50 mm × 100 mm dia. Ordinary Portland cement was used for the cement paste.

2.2 Amines to be added

In this study, methyl diethanolamine (MDEA) and 1-(2-hydroxyethyl) piperazine (HEPZ) were selected as the amines to be added. Figure 1 shows the chemical formulas of MDEA and HEPZ.

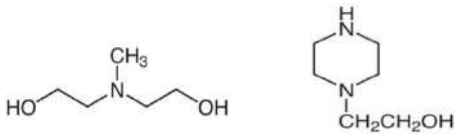


Fig. 1 chemical formulas of MDEA (left) and HEPZ (right)

3. Curing and measurement

3.1 Curing conditions

Two types of curing conditions, A and B, were prepared to conduct the measurements. In curing condition A, cement paste was casted into a plastic mold, and measurement was performed after sealing and curing at 20°C. In curing condition B, after the cement paste was poured into the mold, the specimens were sealed and cured at 20°C for 28 days, and then the specimens were removed from the plastic mold, sealed at the top and bottom ends with aluminium tape with butyl rubber, and placed in an accelerated carbonation chamber at 20°C, 60% RH and 5% CO2 concentration.

3.2 Measurement items

Compressive strength and modulus of elasticity were determined 7, 14, 28, 56 and 91 days after casting for curing condition A and 28, 56 and 91 days for curing condition B. The Archimedes method was used to determine the dry density and water absorption. In each case, three samples were taken for each measurement and the average was calculated.

4. Test results

4.1 Specimens without accelerated carbonation

4.1.1 Compressive strength

The results of compressive strength are shown in Figure 2. In all of the figures in this paper, X represent samples with no diitives, M represent samples with MDEA, H represent samples with HEPZ.

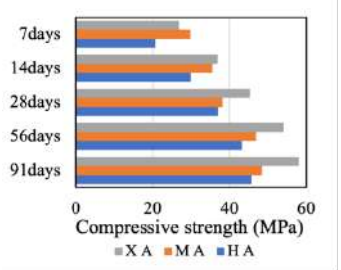


Fig. 2 Compressive strength by age

Compared to cement paste without additives, the compressive strength of cement pastes with 5% MDEA added showed an increase of about 10% at the age of 7 days, but the rate of strength improvement gradually decreased with age, and at the age of 91 days, it remained at 84% of the strength of specimens without additives. Preliminary experiments with MDEA have shown that MDEA accelerates setting. As a result, while the initial strength tends to be relatively high, the hydration reaction at the early age of the material may have some influence on the long-term strength enhancement. On the other hand, the compressive

strength of cement pastes with HEPZ added tended to be smaller than that of the specimen without additives throughout all ages. The specimen with HEPZ added had lower strength than MDEA, and from 7 to 91 days of age, it remained around 79-81% compared to specimens without additives.

4.1.2 Elastic modulus

The results of elastic modulus are shown in Figure 3.

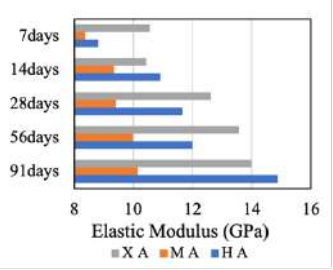


Fig. 3 Elastic Modulus by age

The elastic modulus of cement pastes with 5% MDEA remained around 81%±8% compared to specimens without additives. On the other hand, the elastic modulus of cement pastes with HEPZ tended to be smaller than that of specimens without additives from 7 to 56 days of age and be bigger than that of specimens without additives at 91 days of age.

4.1.3 Dry density and water absorption

Figure 4 shows the dry density of specimens and Figure 5 shows the water absorption of specimens.

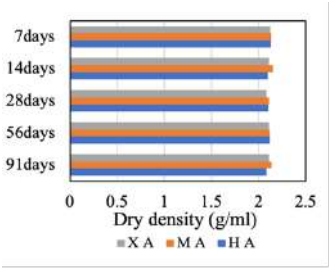


Fig. 4 Dry density by age.

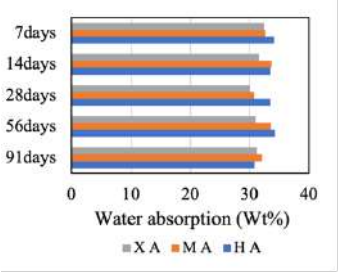


Fig. 5 Water absorption by age

The dry density of cement pastes with a water-cement ratio of 0.5 and the addition of amine solution as an external fraction was generally appropriate according to Burgh and Foster (2017). The dry density of HEPZ was slightly smaller than that of MDEA up to 14 days of age. On the other hand, after 28 days of age, the values were almost the same regardless of the type of amine added. The water absorption tended to decrease with the age of the lumber, regardless of the amine added.

4.2 Specimens with accelerated carbonation

4.2.1 Compressive strength

The results are shown in Figure 6.

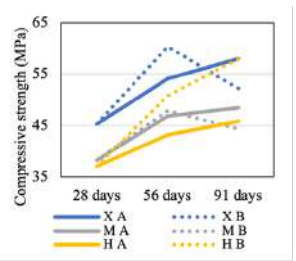


Fig. 6 Compressive strength by age and curing condition

The compressive strength of the specimens with amine added is not expected to decrease significantly when they are subjected to accelerated carbonation for 28 days. Compressive strength of specimens with MDEA under curing condition B was slightly higher than that of specimens under condition A for 56 days of age,

and lower than that of specimens under condition A for 91 days of age. On the other hand, compressive strength of specimens with MDEA under curing condition B was higher than that of specimens under condition A for the whole 91 days of age.

4.2.2 Elastic modulus

The results are shown in Figure 7.

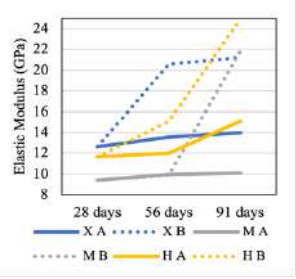


Fig. 7 Elastic Modulus by age and curing condition

Accelerated carbonation significantly increases the elastic modulus of all kinds of the specimens. While the elastic modulus of the specimens with and without accelerated carbonation increased, the behavior of the elastic modulus of the specimens with amine addition varied depending on the type of amine.

4.2.3 Dry density and water absorption

The results of dry density and water absorption are shown in Figures 8 and Figures 9.

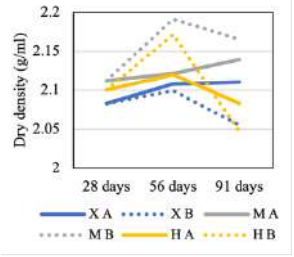


Fig. 8 Dry density by age and curing condition.

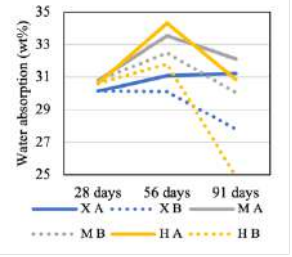


Fig. 9 Water absorption by age and curing condition

No significant changes were observed with or without the addition of amine and with or without accelerated carbonation, but the addition of amine resulted in a slight decrease in the dry density and a slight increase in water absorption. Accelerated carbonation resulted in a slight increase in dry density and a slight decrease in water absorption.

5. Conclusion

In this study, the addition of two types of amines to hardened cement pastes showed the effect of amines on the mechanical properties of cement pastes. In addition to this, it was found that the MDEA additive effectively improved the initial strength of the cement paste, while having the effect of slightly reducing the long-term strength. HEPZ also slightly reduced the compressive strength of the cement paste. No significant changes of compressive strength by accelerated carbonation were observed in cement paste with MDEA, while cement paste with HEPZ had a slight decrease in the compressive strength due to accelerated carbonation.

References

Mofarahi, Khojasteh, Khaledi, and Farahnak. (2008) “Design of CO2 absorption plant for recovery of CO2 from flue gases of gas turbine”

Aaron, Tsouris. (2005) “Separation of CO2 from Flue Gas: A Review”, Separation Science and Technology, 40:1-3, 321-348

Burgh, Foster. (2017) “Influence of temperature on water vapour sorption isotherms and kinetics of hardened cement paste and concrete”, Cement and Concrete Research

The 16th International Congress on the Chemistry of Cement 2023 (ICCC2023)
"Further Reduction of CO_2 -Emissions and Circularity in the Cement and Concrete Industry"
September 18–22, 2023, Bangkok, Thailand

Further Carbon Capture by Semi-Carbonated Concrete Waste Fines through Wet Carbonation Process

Ngoc Kien Bui[1*], Ryo Kurihara[1], Wei Wang[2], Takafumi Noguchi[1], and Ippei Maruyama[1,3]

[1] *Graduate School of Engineering, The University of Tokyo, Tokyo, Japan*
Email: kienbui@g.ecc.u-tokyo.ac.jp
ryo.kurihara@bme.arch.t.u-tokyo.ac.jp
takafuminoguchi@g.ecc.u-tokyo.ac.jp
[2] *School of Materials Science and Engineering, Southeast University, Nanjing, 211189, PR China*
Email: wang-wei@seu.edu.cn
[3] *Department of Environmental Engineering and Architecture, Nagoya University, Nagoya, Japan*
Email: i.maruyama@bme.arch.t.u-tokyo.ac.jp

ABSTRACT

Mineral carbonation from concrete waste is a promising technology to mitigate CO_2 emissions. This study investigated the wet carbonation of concrete waste fines, which have been partly carbonated by another process, such as gas-solid (semi-dry) carbonation under atmospheric air or high-concentration CO_2 gas. The concrete waste fines experienced two stages of carbonation, including semi-dry carbonation and wet carbonation. One of the key advantages of this approach is that excess CO_2 can be efficiently absorbed into the concrete waste fines via wet carbonation, even if the concrete has undergone prior carbonation through another process. X-ray diffraction (XRD) and thermogravimetric analysis (TG-DSC) revealed the decomposition evolution of carbonated concrete waste fines (CWF) by wet carbonation. The results showed that although portlandite was depleted during the gas-solid carbonation process, the carbonation degree of hydrated phases like C-S-H remained low. Wet carbonation accelerated the decalcification process of the hydrated phases and captured more CO_2 into the CWF. The evolution of carbonated phases in concrete fines indicated that metastable polymorphs of calcium carbonate like aragonite still increased through two steps of carbonation (including semi-dry and wet carbonation), while solely the wet carbonation process mainly generates calcite.

KEYWORDS: *concrete waste, wet carbonation, gas-solid carbonation, CO_2 capture, cement paste*

1. Introduction

The 26th Conference of the Parties, the annual global gathering of nations under the United Nations Framework Convention on Climate Change (UNFCCC), is a highly anticipated event in the fight against climate change. With the pressing urgency to address the effects of global warming, many countries have made significant commitments to reducing their carbon dioxide (CO_2) emissions to net zero by 2050. However, estimations indicate that by 2050, CO_2 emissions are expected to increase by 130 % annually. Notably, cement production generates 8 % of anthropogenic CO_2 emissions globally Andrew (2018). Such increasing concentrations of CO_2 in the atmosphere are responsible for climate change Ghacham et al. (2015). To mitigate these issues, several CO_2 storage methodologies have been proposed in previous studies; these include geological, ocean, biological, and mineral sequestration Hepburn et al. (2019). Among the foregoing methodologies, mineral storage is the most reliable method as it offers a high sequestration capacity to mitigate future emissions and ensure permanent CO_2 storage Schneider (2019). Recent efforts to mitigate CO_2 emissions include carbon capture by minerals extracted from concrete Sanjuán et al. (2020). Mineral carbonation from concrete waste (CW) is a CO_2 capture storage methodology. Notably, metal oxides present in various minerals react with CO_2 and form stable carbonate minerals such as calcite, dolomite, and magnesite Sanna et al. (2014). However, the natural CO_2 absorption of concrete structures is still inadequate, and the associated reaction occurs at a slow rate over geological timescales; hence, accelerated carbonation methods have been used to assess carbonation under natural conditions Auroy et al. (2018). One such method is the novel CO_2 sequestration process accomplished by extracting minerals from CW through wet carbonation. Recent studies reported that the wet carbonation

process could aid in the fast carbonation of concrete fines Iizuka et al. (2004), and it has several advantages, such as lower costs and lower chemical consumption rates compared to indirect carbonation Fernández Bertos et al. (2004). Capturing CO_2 from the air using concrete presents a significant challenge due to the protracted process involved. However, there is promising potential to accelerate the CO_2 capture efficiency of concrete that is exposed to the ambient weather environment for a long period through an enforced carbonation process. Most research in the field has focused on the examination of the wet carbonation of fresh concrete fines that have not undergone any carbonation process. There is a growing interest in understanding the effects of wet carbonation on concrete waste fines (CWF) that have undergone long-term natural air carbonation or accelerated CO_2 semi-dry carbonation. Additionally, it is interesting to explore the potential for increased CO_2 capture through the secondary stage of wet carbonation, following a specified level of CO_2 absorption by the CWF subjected to semi-dry carbonation in the first step. Therefore, this research investigates phase assemblages, reaction kinetics, as well as the CO_2 capture ability of CWF under a two-stage carbonation process, beginning with natural air or high CO_2 semi-dry carbonation followed by wet carbonation.

2. Materials and Methods

2.1 Materials

Ordinary Portland cement was used to make hydrated cement paste (HCP) to simulate recycled CWF. The chemical composition of cement is shown in Table 1. The water-to-cement ratio for the HCP was 0.50, and deionized water was used. The HCP specimens were cured for 38 weeks and dried for 7 days at 105 ºC before crushing into <1.18 mm diameter particles to make CWF powder. The powder's particle size distribution, which is determined by the Laser diffraction Microtrac MT3000II, is shown in Fig. 1.

Table 1 Compositions of cement (%)

Composition (%)	SiO_2	Al_2O_3	Fe_2O_3	CaO	MgO	SO_3	Na_2O	K_2O	TiO_2	P_2O_5	MnO
Cement	20.68	4.95	2.73	64.71	1.17	2.56	0.24	0.32	0.27	0.21	0.07

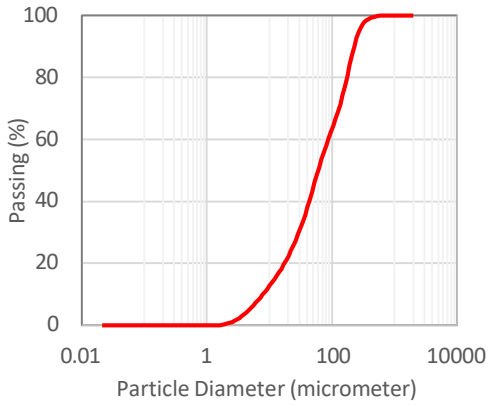


Fig. 1 Particle size distribution of HCP

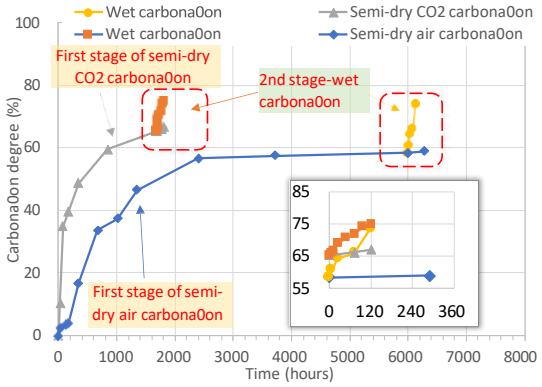


Fig. 2 Carbonation degree of HCP through two-stage carbonation (*Note: subplot enlarged red dashed line area*)

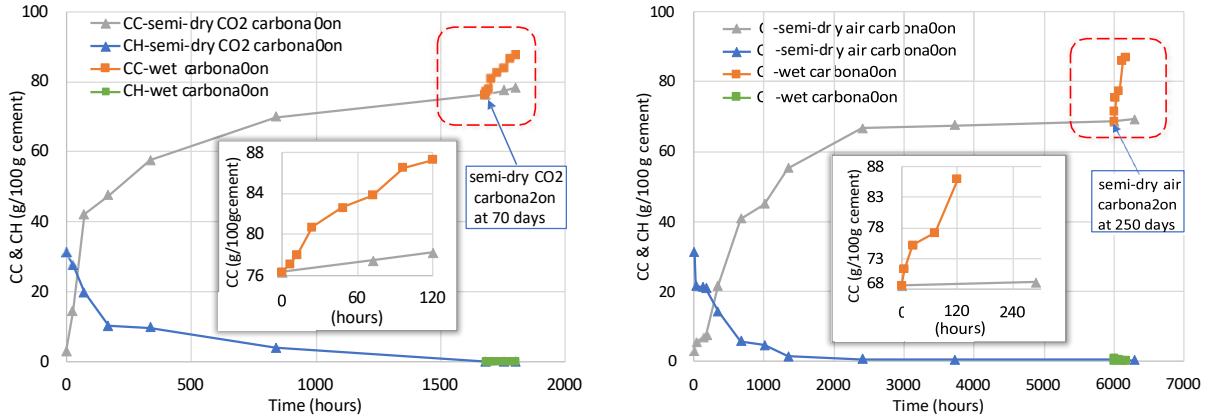
2.2 Methods

The carbonation process of CWF was conducted in a **two-stage approach**. In the first stage, CWF was carbonated under the gas-solid carbonation method, also known as semi-dry carbonation, either under air conditions at 20 ± 1 ºC and the 530 ± 5 ppm CO_2 concentration (semi-dry air carbonation) for a period of 250 days or in an accelerated environment (semi-dry CO_2 carbonation) characterized by a temperature of 20 °C, 60 % RH, and a CO_2 concentration of 5% for 70 days. Upon completion of the semi-dry carbonation process, CWF was subjected to wet carbonation in the second stage for 120 hours. The wet carbonation process of CWF was performed using a mixture of CWF powder and water with a solid-to-liquid ratio of 1:20. The mixture was placed into a tank and agitated with a stirrer operating at 1400 rpm to ensure a homogeneous dispersion of powder in water. Subsequently, CO_2 gas was introduced into the tank under

ambient conditions. The CO_2 gas with a purity >99.5 % was used. The flow rate of the CO_2 gas was fed and controlled by the regulator at 0.1 ml/min. CO_2 bubbling was provided for 120 hours during the test period of wet carbonation. After the carbonation process, periodic samples of HCP were obtained for testing its properties, including Thermogravimetric-Differential Scanning Calorimetry (TG-DSC), X-ray Powder Diffraction (XRD), and Rietveld analyses (by TOPAS (Ver. 6.0, Bruker). XRD was conducted using a Malvern Panalytical–Empyrean S3 diffractometer to quantify the carbonated HCP powder's crystalline phases and amorphous content. Thermogravimetry analysis TG-DSC (STA449F5 Jupiter, NETZSCH) was conducted to quantify the calcium carbonate and portlandite present in the carbonated materials. The characterizations were performed at a heating rate of 10 °C /min and a temperature range of 30–900 °C with nitrogen gas at a 50 mL/min flow rate.

3. Results and discussion

3.1 Reaction kinetics



(a) Semi-dry CO_2 carbonation and wet carbonation (b) Semi-dry air carbonation and wet carbonation

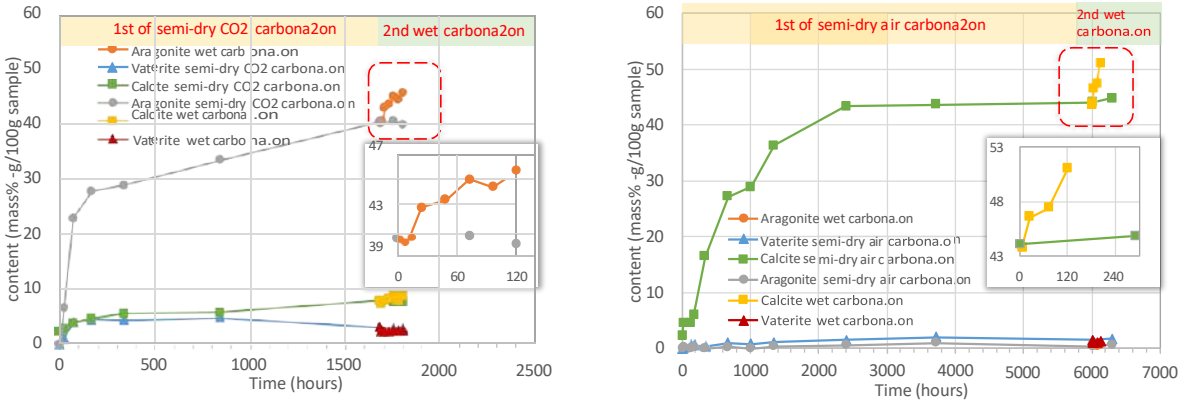
Fig. 3 Reaction kinetics of calcium carbonate (CC) and portlandite (CH) in samples after two-stage of carbonation, including semi-dry and wet carbonation (*Note: subplot enlarged red dashed line area*).

The carbonation degree of HCP and the evolution of CC and CH content in HCP after two-stage carbonation is shown in Fig. 2 and Fig. 3, respectively. The results reveal that at the second-stage carbonation (wet carbonation), the carbonation degree increments 10-20 % over 120 hours, although in the first-stage carbonation (semi-dry carbonation), the carbonation degree reached approximately 60 %. This suggests that the decalcification of C-S-H primarily occurred during the wet carbonation process. Furthermore, the results indicate that conducting carbonation in a two-stage approach increases the carbonation degree of HCP by up to 10-20 %, while conducting it solely in semi-dry carbonation leads to an increase of only 0.2-0.7 % in the same period of carbonation. This is due to the fact that semi-dry carbonation partially decalcifies C-S-H, and initial carbonation in the outer layer of particles hinders CO_2 diffusion into the core, leading to challenges in achieving continuous carbonation. Zajac et al. (2022). The semi-dry carbonation process gradually generated CC and depleted CH, in which the carbonation rate of semi-dry air carbonation is much lower than that of semi-dry CO_2 carbonation; it is due to low CO_2 concentration in the air. It is worth noting that during the first stage of carbonation, the carbonation degree of HCP is 65.2 % after 70 days and 58.4 % after 250 days of semi-dry CO_2 and air carbonation, respectively. However, after only 120 hours of wet carbonation in the second stage, the carbonation degrees are almost equal, reaching around 75 %. This indicates that the carbonation rate in the second stage is regardless of the carbonation degree of the first stage or the environment of carbonation.

3.2 Evolution of calcium carbonate polymorphs in CWF through two-stage carbonation

Calcium carbonate polymorph evolution during the two-stage carbonation of HCP is shown in Fig. 4. Under semi-dry carbonation conditions in the air or high CO_2 concentration, the carbonation of HCP produces three types of calcium carbonate polymorphs: calcite, aragonite, and vaterite. Aragonite is the dominant form during semi-dry CO_2 carbonation, comprising 40.4 % after 70 days, whereas calcite and vaterite

represent only 8.0 % and 3.1 %, respectively. Conversely, semi-dry air carbonation produces primarily calcite (44.1 %), with aragonite and vaterite making up only 0.5 % and 1.6 %, respectively, after 250 days. It is noteworthy that during the first stage, semi-dry CO_2 carbonation, aragonite dominates, and its presence continues to increase in the subsequent wet carbonation stage, a phenomenon rarely observed in wet carbonation where calcite is typically the dominant form of calcium carbonate Zajac et al. (2020). This phenomenon can be attributed to the generation of the aragonite precursor within HCP particles during semi-dry CO_2 carbonation, which subsequently results in the increased formation of aragonite during the wet carbonation process. During wet carbonation, CO_2 diffuses inside the HCP particles, continuously facilitating carbonation and resulting in the formation of aragonite within the particles. However, in the outer parts of the HCP particles, the formation of calcite and the transformation of vaterite to calcite still occur, leading to a slight increase in the amount of calcite during the wet carbonation process. Besides, calcite is the predominant polymorph during semi-dry air carbonation. In the subsequent wet carbonation stage, calcite significantly increases while the amount of aragonite remains relatively low. This phenomenon is likely attributable to the small amount of aragonite precursor generated during the initial stage of semi-dry air carbonation.



(a) Semi-dry CO_2 carbonation and wet carbonation (b) Semi-dry air carbonation and wet carbonation

Fig. 4 Calcium carbonate polymorph formation during semi-dry carbonation and wet carbonation

3.3 CO_2 capture

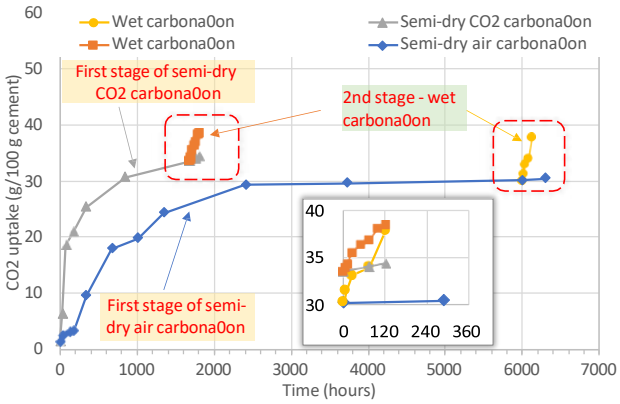


Fig. 5 CO_2 uptake in HCP through two-stage carbonation (*Note: subplot enlarged red dashed line area*).

The amount of CO_2 captured by HCP through two stage carbonation is shown in Fig. 5. In the first stage of carbonation, which involves semi-dry carbonation and exposure to natural air conditions for 250 days, HCP absorbed 30.2 g of CO_2 per 100 g of cement. When this process was extended for 12 more days, this amount increased slightly to 30.4 g per 100 g of cement. During the second stage of carbonation, which involved wet carbonation for only 120 hours, HCP absorbed a significantly higher amount of CO_2, reaching up to 38.2 g per 100 g of cement. Similarly, during semi-dry CO_2 carbonation that lasted for 70 days, HCP captured 34.7 g of CO_2 per 100 g of cement. In the second stage of wet carbonation, the amount of CO_2 absorbed increased to 38.4 g per 100 g of cement. The results demonstrate that wet carbonation significantly accelerated the CO_2 capture process in concrete waste, even if it was previously carbonated to a certain degree. In the wet carbonation stage, the ongoing decalcification and decomposition of C-S-H and other

hydrated phases create favorable conditions for the precipitation of calcium carbonate, allowing for the storage of CO_2 within the CWF particles.

4. Conclusions

Herein, the CWF underwent carbonation through a two-stage approach, comprising a semi-dry (gas-solid) carbonation and a wet carbonation process. Based on the experimental outcomes, the following conclusions can be drawn:

- The carbonation conditions strongly influence the degree of carbonation, and wet carbonation has been found to significantly accelerate the process, even for CWF that have been previously carbonated up to 60 % using semi-dry methods. In comparison, semi-dry air carbonation progresses at a much slower rate than semi-dry CO_2 carbonation under similar humidity conditions.
- During semi-dry CO_2 carbonation, aragonite is the main precipitated polymorph, which acts as a precursor for further increases during the subsequent wet carbonation process. In contrast, semi-dry air carbonation primarily leads to the formation of calcite, which still increases significantly in the wet carbonation stage.
- The rapid decalcification of C-S-H and other hydrated phases during wet carbonation creates favorable conditions for the precipitation of calcium carbonate and the storage of CO_2 inside the CWF particles, leading to an accelerated CO_2 uptake procedure in a relatively short period of time.

In summary, the results indicate that wet carbonation continuously accelerates the absorption of CO_2 into the CWF samples, regardless of whether they were previously exposed to natural air conditions for an extended period or carbonated in an artificial high CO_2 concentration environment in semi-dry carbonation.

Acknowledgments

The authors are grateful for the financial support from the NEDO Moonshot project from Japan Science and Technology Agency, “Research on C^4S, Calcium Carbonate Circulation System for Construction”.

References

Andrew, Robbie M. (2018). “Global CO2 Emissions from Cement Production.” *Earth System Science Data* 10(1):195–217.

Auroy, Martin, Stéphane Poyet, Patrick le Bescop, Jean Michel Torrenti, Thibault Charpentier, Mélanie Moskura, and Xavier Bourbon. (2018). “Comparison between Natural and Accelerated Carbonation (3% CO2): Impact on Mineralogy, Microstructure, Water Retention and Cracking.” *Cement and Concrete Research* 109:64–80.

Fernández Bertos, M., S. J. R. Simons, C. D. Hills, and P. J. Carey. (2004). “A Review of Accelerated Carbonation Technology in the Treatment of Cement-Based Materials and Sequestration of CO2.” *Journal of Hazardous Materials* 112(3):193–205.

ben Ghacham, Alia, Emmanuelle Cecchi, Louis César Pasquier, Jean François Blais, and Guy Mercier. (2015). *CO2 Sequestration Using Waste Concrete and Anorthosite Tailings by Direct Mineral Carbonation in Gas-Solid-Liquid and Gas-Solid Routes*. Vol. 163. Academic Press.

Hepburn, Cameron, Ella Adlen, John Beddington, Emily A. Carter, Sabine Fuss, Niall mac Dowell, Jan C. Minx, Pete Smith, and Charlotte K. Williams. (2019). “The Technological and Economic Prospects for CO2 Utilization and Removal.” *Nature 2019 575:7781* 575(7781):87–97.

Iizuka, Atsushi, Minoru Fujii, Akihiro Yamasaki, and Yukio Yanagisawa. (2004). “Development of a New CO2 Sequestration Process Utilizing the Carbonation of Waste Cement.” *Industrial and Engineering Chemistry Research* 43(24):7880–87.

Sanjuán, Miguel Ángel, Carmen Andrade, Pedro Mora, and Aniceto Zaragoza. (2020). “Carbon Dioxide Uptake by Cement-Based Materials: A Spanish Case Study.” *Applied Sciences 2020, Vol. 10, Page 339* 10(1):339.

Sanna, A., M. Uibu, G. Caramanna, R. Kuusik, and M. M. Maroto-Valer. (2014). “A Review of Mineral Carbonation Technologies to Sequester CO2.” *Chemical Society Reviews* 43(23):8049–80.

Schneider, Martin. (2019). “The Cement Industry on the Way to a Low-Carbon Future.” *Cement and Concrete Research* 124:105792.

Zajac, Maciej, Jørgen Skibsted, Frank Bullerjahn, and Jan Skocek. (2022). “Semi-Dry Carbonation of Recycled Concrete Paste.” *Journal of CO2 Utilization* 63:102111.

Zajac, Maciej, Jørgen Skibsted, Jan Skocek, Pawel Durdzinski, Frank Bullerjahn, and Mohsen ben Haha. (2020). “Phase Assemblage and Microstructure of Cement Paste Subjected to Enforced, Wet Carbonation.” *Cement and Concrete Research* 130(July 2019):105990.

The 16th International Congress on the Chemistry of Cement 2023 (ICCC2023)
"Further Reduction of CO_2 -Emissions and Circularity in the Cement and Concrete Industry"
September 18–22, 2023, Bangkok, Thailand

Fracture properties of in-situ polymerization modified cementitious materials

C.J. Xu[1], Q. Zeng[1]*

[1] *College of Civil Engineering and Architecture, Zhejiang University, Hangzhou, China*

Email: xcj1206@zju.edu.cn; Email: cengq14@zju.edu.cn

ABSTRACT

While it has been reported that the in-situ polymerization of organic polymers during cement hydration can greatly improve the strength of cementitious composites, the fracture processes and properties have not been thoroughly documented in the literature. In this work, cementitious composites with in-situ polymerized sodium acrylate (iPSA) in the dosages of 0%, 4% and 8% were fabricated using a constant water-to-cement ratio of 0.4. Three-point bending (TPB) test was used to record the load-displacement curves of notched iPSA-modified cement paste beams. The characteristics of the stress-strain curves were analyzed to demonstrate the strengthening effect of iPSA on the cement pastes. Digital image correlation (DIC) technique was employed to characterize the fracture process of the specimens, which allowed us to track the cracking traces through image analysis. Classic linear elastic fracture mechanical (LEFM) theory was adopted to quantify the fracture toughness and fracture energy of the iPSA cement pastes. Microscopic tests were conducted to understand the crosslinked organic-inorganic composite structures in the iPSA cement matrix. Mechanisms of toughening enhancement of iPSA on cementitious materials were proposed and discussed. This work would deepen the understanding of fracture behavior of polymer-modified cementitious composites with high potentials of broad engineering applications.

KEYWORDS: *Composites, In-situ polymerization, Fracture, LEFM, Microstructure*

1. Introduction

Ordinary cement-based materials (CBM) are universally used in buildings and infrastructures, owing to the advantages of low cost, ease of fabrication and flexible control on workability. However, low tensile strength and brittleness of the cement matrix restrain its extensive applications and cause cracking and durability problems of existing buildings (Scrivener et al. 2018).

Organic-inorganic hybrids can comprehensively complement the superiority of organic and inorganic phases to improve the properties of composite materials. Organic-inorganic synergistic reinforcement systems in natural and artificial materials are widely used in different industries (Wang et al. 2020). In the field of CBM, macromolecular organic polymers are typically incorporated with CBM as admixtures (Peng et al. 2020). However, this direct addition may lead to an incompatible status between polymer and cement hydrates, resulting in degradation in the strengths and long-term performance of CBM. To overcome this problem, in-situ polymerization has been investigated in CBM. This process could guarantee that the polymerization of organic monomers (e.g. sodium acrylic, acrylamide, etc.) and hydration of cement clinkers proceed synchronously. In this way, the strength, deformability and anti-permeability of CBM can be greatly enhanced without sacrificing other properties (Xu et al. 2022, Liang et al. 2022). The mechanical properties and microscopic characteristics of in-situ polymerization modified cement composites (iPMCCs) have been reported, but the fracture properties have not been systematically studied. Typically, initial flaws such as microcracks and voids inevitably exist in cement matrix due to temperature changes and loadings during or after construction (Zhang et al. 2023). The propagation of these flaws could cause local or total structural failures. Therefore, it is necessary to study the fracture process and parameters of iPMCCs to expand the engineering applications of such composites.

In this work, iPMCCs with sodium acrylic (iPSA) were fabricated. DIC technique was employed to monitor the fracture process of iPSA, and the LEFM theory was applied to calculate and evaluate its fracture toughness and fracture energy. Scaning electron microscopy (SEM) was used to observe the microscopic morphology and the reinforced mechanisms of the polymerized SA in iPMCCs.

2. Materials and methods

2.1 Materials and sample preparation

A Portland cement P·I 42.5 (identical to ASTM type I) was used as the main binder. Main minerals of the cement include: 57.34% C_3S, 18.90% C_2S, 11.25% C_4AF and 6.47% C_3A. Acrylic acid (AA) particles were used as monomers in a sodium hydroxide (NaOH) solution. While ammonium persulfate (APS) and sodium bisulfite (SBS) were used initiators for the in-situ polymerization process. The purity of N, N'-methylene bisacrylamide (MBA) was 99%. Specimens with sodium acrylic (SA) monomer-to-cement ratios of 0%, 4% and 8% were fabricated and labeled as MC0, MC4 and MC8, respectively (Table 1). A constant water-to-cement (w/c) ratio was set to 0.4.

Table 1. Mixing proportions of iPSA

	Cement (g)	Water (g)	AA(g)	NaOH (g)	APS (g)	SBS (g)	MBA (g)
MC0	1000	400	0	0	0	0	0
MC4	1000	400	17.0	30.6	1	1	0.04
MC8	1000	400	34.0	61.3	2	2	0.08

NaOH, AA and initiators were blended in water successively until complete dissolves. A cooling bath environment (around 0 ℃) was used to consume heats generated by the chemical reactions. The in-situ polymerization solution of SA and initiators was prepared, mixed with cement, and stirred to form cement slurries. These fresh iPSA slurries were cast to attain prismatic specimens (180 mm×40 mm×40 mm) with a precast notch of 15 mm in the middle. After curing at room temperature for 24 hours, the specimens were demoulded and further cured under standard conditions until testing ages. Before mechanical testing, white and black paints were used to prepare speckles on the middle part (6 cm × 4 cm) of the surfaces of the iPSA specimens.

2.2 Test methods

Three-point bending (TPB) tests were conducted using Instron hydraulic testing machine. The displacement contol mode with 0.2 mm/min was used for the bending test. To capture surface images of specimens during loading, a high-resolution camera was positioned alongside the Instron device. GOM Correlate computer software was employed to analyze the 2D surface images and extract the information of strain and deformation of the tested specimens.

A FEI QUANTA FEG 650 scaning electron microscopy (SEM) with the accelerating voltage of 20 keV and spot size of 4.0 was applied to perform SEM tests. Small iPSA pieces were collected from the damaged specimens after TPB tests and prepared for SEM observations.

3. Results and discussion

3.1 Fracture process

Fig. 1a demonstrates the loading-displacment curves of all three iPSA groups. From TPB tests, similar linear rises and sudden falls in the load-displacement curves of all iPSA specimens were observed. Slopes of the rising stage of curves decreased as the dosage of SA increased, suggesting that the reduced stiffness of the iPSA specimens was positively correlated with the amount of SA. DIC technology were used to track the position of a series of feature points in a targeted area to analyze the displacement and strain of the target area. The middle area of each specimen was selected as the designated DIC analysis region, with emphasis on a smaller zone located between the pre-notch and the top loading point. Fig. 1b, c, and d show the the change of strain neghogram of all three iPSA groups at different loading times (50%, 80%, 90% and 100% F_{max}). When the applied load increased to about 50% F_{max}, the strains were small and relatively uniform in all groups. However, as the applied load increased to about 80% F_{max} and 90% F_{max}, differences started to occurr among the three groups. No strain concentrations ahead of the prenotch tips were observed in MC0, which may be attributed to the fact that tensile strain of pure cement specimens was too small to be detected by DIC. As for MC4 and MC8, a gradually enlarged area of strain concentrations occured on the tip of the prenotch, especially when the load reached 90% F_{max}. These phenomena suggest that the incorporation of SA can soften the crack tips, and subsquently enhance the deformation capacity and energy consumption of iPSA. This could also explain the raised peak loads and the corresponding displacements

compared with MC0 (Fig. 1a). Finally, penetrating strain concentration regions extending to the loading point appeared, indicating that specimens had fractured.

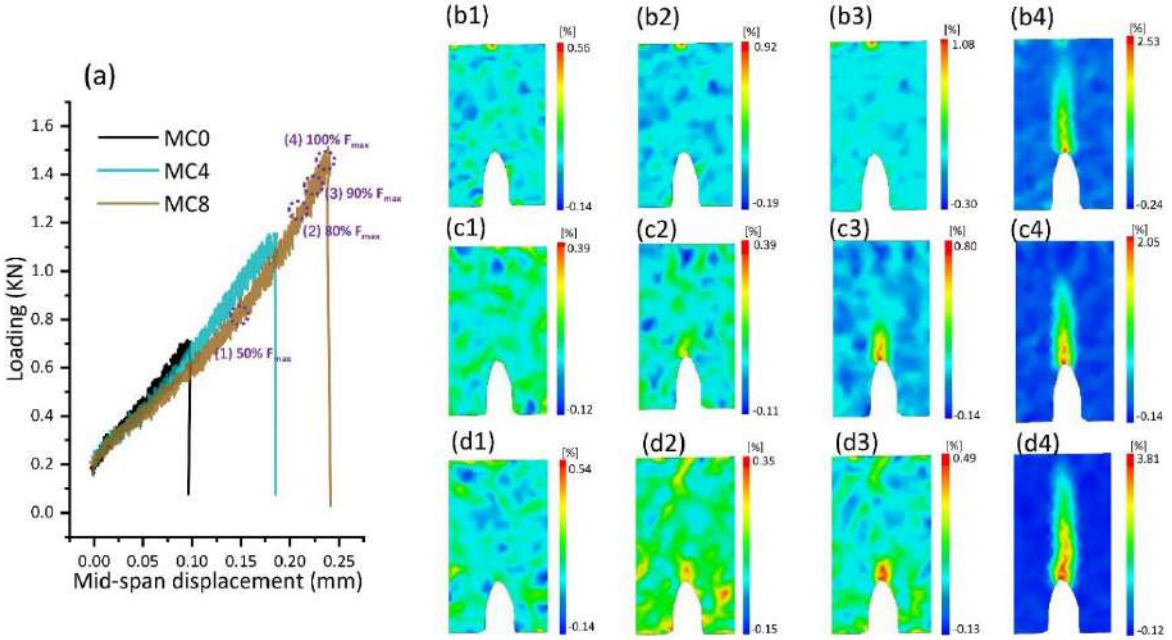


Fig. 1. Load-Displacement curves of TPB tests (a) and strain nephograms of MC0 (b), MC4 (c) and MC8 (d): (1), (2), (3) and (4) represent different loading times, which are 50%, 80%, 90% and 100% of F_{max}, respectively.

3.2 Fracture parameters

The fracture toughness and fracture energy are two important fracture mechanic parameters, which represent the ability to resist crack propagation and the energy required for crack propagation, respectively. According to the LEFM, the fracture toughness (K_{IC}) can be calculated as (Xu and Reinhardt, 1998):

$$K_{"\#} = \frac{\%\text{'}()*+_{,}-..'/0\times\%.^{23}4\times\%.^{25}\times6\times7^{9/3}}{;\times<^{3}} \times f(\alpha) \quad (1)$$

$$f(\alpha) = \frac{\%.\text{AABC}(\%\text{BC})(\text{D.\%'BE.AEC-D.FC}^{3}4}{(\%\text{-DC})(\%\text{BC})^{5/3}} \quad (2)$$

where $F_{/7H}$ is the maximum loading (KN), s, t, h and m are the span (m), thickness (m), height (m) and mass (kg) of the specimen within the span, g is the gravitational acceleration (m/s^{D}) and a_{P} is the effective crack length.

The fracture energy G_R is calculated by:

$$G_R = \frac{S_T\text{-}\%/D\times/0U_T}{V_{WXY}} \quad (3)$$

where $W_{.}$ is the area under load-deflection curve ($N\cdot m^2$), m is the weight of the specimen (kg), $d_{.}$ is the displacement of failure point and $A_{]\^0}$ is the area of ligament (m^2).

The results of fracture toughness and fracture energy are shown in Fig. 2. Substantial increases of both parameters were observed when SA was added to the cement pastes. As SA dosage increased from 0% to 4%, and to 8%, fracture toughness increased from 0.25 $MPa\cdot m^{1/2}$ to 0.42 $MPa\cdot m^{1/2}$ (by 68%, MC4), and further to 0.53 $MPa\cdot m^{1/2}$ (by 112%, MC8). While fracture energy rose from 44 N/m to 118 N/m for MC4 and further to 175 N/m for MC8 (168% and 298%, repsectively, compared with MC0).The remarkable enhancement of K_{IC} and G_f may be ascribed to the enhanced interfacial bonds as demonstrated by MD simulations (Chen et al. 2020). The organic and inorganic phases were interwined and connected sufficiently to generate cement-polymer interpenetrating networks. These networks possess outstanding energy-consumption capacity and inhbit crack propagation.

3.3 Micro morphology

Fig. 3 shows the micro morphology of the fractured iPSA surfaces. Local sites in the pastes were measured to explore the connections of the SA polymer chains with the cement hydrates. For MC8, the SA chains were found to be distributed randomly in the cement matrix. Furthermore, the cross-linked SA polymer chains served as links, connecting adjacent cement hydrates, such as CH-CH (Fig. 3a), CH-CSH

(Fig. 3b) and CSH-CSH (Fig 3c and d). The interpenetrating cement-polymer networks could effectively transfer loads and disspate energy, thereby suppressing crack propagations and enhancing deformations. As a result, the anti-fracture property of the polymer-modified cement pastes was systematically improved (Section 3.2).

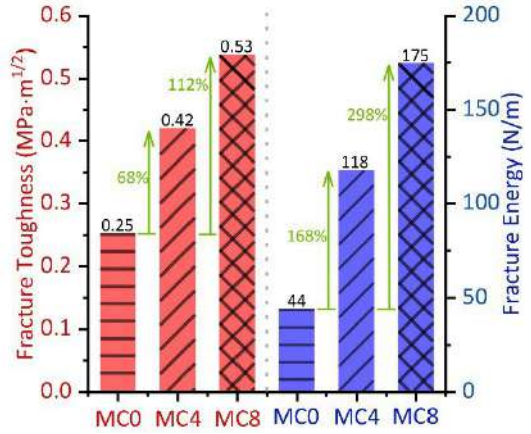


Fig. 2. Calculated Results of fracture toughness (red) and fracture energy (blue)

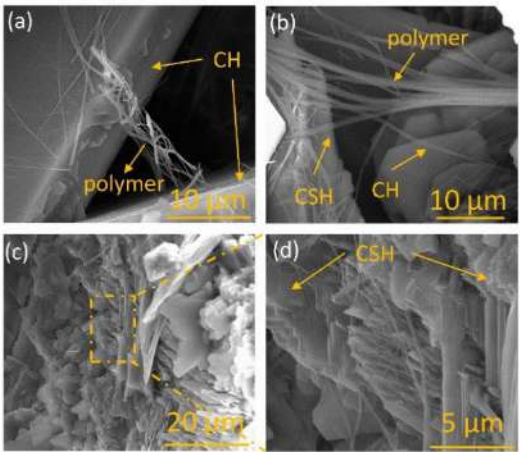


Fig. 3. SEM images of cement matix of MC8

4. Conclusions

In this work, the fracture process and parameters (K_{IC} and G_f) of iPSA were investigated. The major conclusions can be summarized as follows:

1. DIC results revealed that the evolution of surface strain field was recorded at around 80% F_{max} forming a strian concetration region ahead of crack tips for MC4 and MC8. The incorporation of SA can effectively enhance the energy-dissipation capacity and impede crack propagation by blunting crack tips.

2. According to the LEFM theory, the fracture toughness of iPSA increased by 68% and 112% for MC4 and MC8, respectively. While the fracture energy witnessed higher increases of around 168% for MC4 and 298% for MC8. iPSA exhibits a much higher level of crack propagation resistance compared with MC0.

3. At micro scale, SA polymer chains bridge adjacent cement hydrates, constituting a cement-polymer interpenetrating network to withstand external loading and improve mechaincal properties.

Acknowledgements

The research was supported by the National Natural Science Foundation of China (No.52038004).

References

Scrivener K.L., John W.M., and Gartner E.M. (2018) "Eco-efficient cements: potential economically viable solutions for a low-CO_2 cement-based materials industry", Cement and Concrete Research, 114: 2-16

Wang Y.Y., Naleway S.E., and Wang B. (2020) "Biological and bioinspired materials: Structure leading to functional and mechanical performance", Bioactive Materials, 5:745-757

Peng Y., Zhao G.R., Qi Y.X., et al. (2020) " In-situ assessment of the water-penetration resistance of polymer modified cement mortars by μ-XCT, SEM and EDS", Cement and Concrete Composites, 114: 103821

Xu C.J., Dai Y.Q., Peng Y., et al. (2022) "Multi-scale structure of in-situ polymerized cementitious composites with improved flowability, strength, deformability and anti-permeability", Composites Part B: Engineering, 245: 110222

Liang R., Liu Q., Hou D.S., et al. (2022) "Flexural strength enhancement of cement paste through monomer incorporation and in situ bond formation", Cement and Concrete Research, 152: 106675

Zhang W.B., Shi D.D., Shen Z.Z., et al. (2023) "Effect of calcium leaching on the fracture properties of concrete", Construction and Building Materials, 365: 130018

Xu S.L., Reinhardt H.W.(1998) "Crack extension resistance and fracture properties of quasibrittle softening materials like concrete based on the complete process of fracture", International Journal of Fracture, 92 (1): 71–99

Chen B.M. Qiao G., Hou D.S., et al. (2020) "Cement-based material modified by in-situ polymerization: from experiments to molecular dynamics investigation", Composites Part B: Engineering, 194: 108036.

16th International Congress on the Chemistry of Cement
ICCC 2023
BANGKOK, THAILAND

Hydration and Shrinkage Behavior of Copper Slag Activated by Sodium Silicate at Different Na_2O Equivalents

Z.H. Yan [1], Z.P. Sun [2*], H.J. Yang [3], X.J. Shu [4], D.D. Shu [5], W.G. Zhu [6], Q. Luo [7]

[1] *Key Laboratory of Advanced Civil Engineering Materials of Ministry of Education, Tongji University, Shanghai 201804, China*

Email: yanzhuhua@tongji.edu.cn

[2] *Key Laboratory of Advanced Civil Engineering Materials of Ministry of Education, Tongji University, Shanghai 201804, China*

Email: sunzhptongji@163.com

[3] *Key Laboratory of Advanced Civil Engineering Materials of Ministry of Education, Tongji University, Shanghai 201804, China*

Email: yanghaijings@tongji.edu.cn

[4] *Shanghai San Songguo New Materials Co., Ltd., Shanghai 201615, China*

Email: 2391737928@qq.com

[5] *Shanghai San Songguo New Materials Co., Ltd., Shanghai 201615, China*

Email: 453632681@qq.com

[6] *Satellite Chemical Co., Ltd., Zhejiang Jiaxing 85000, China*

Email: zwg@weixing.com.cn

[7] *Satellite Chemical Co., Ltd., Zhejiang Jiaxing 85000, China*

Email: luoqiong@weixing.com.cn

ABSTRACT

Copper slag, an industrial by-product, can exhibit cementitious properties when activated with alkaline activators, and thus can be used to replace part of traditional cement and contribute to the sustainable development of the copper and cement industries. In the present research, sodium silicate was employed as an alkaline activator for copper slag. The effect of Na_2O equivalent on the dissolution of copper slag was assessed by varying the concentration of sodium silicate. Further, the hydration and shrinkage behavior of alkali-activated copper slag was investigated. The results revealed that the hydration process of alkali-activated copper slag was delayed with the increase of Na_2O equivalent. Besides, with the increased Na_2O equivalent, the autogenous shrinkage of alkali-activated copper slag became larger while dry shrinkage decreased, revealing that the autogenous shrinkage dominated the crack generation. Backscattered electron image analysis confirmed that extra sodium silicate also aggravated more coarse pores.

KEYWORDS: *Copper slag, Sodium silicate, Shrinkages*

1. Introduction

Copper slag (CS) is an industrial by-product of copper metal smelting. the manufacturing of one ton of copper metal results in the generation of about 2.2 tons of CS (e.g., Gorai and Jana (2003), Shi and Meyer (2008)). To reduce the storage of CS effectively and minimize the environmental impact caused by

the heavy metal elements in CS, CS can be employed as a new alkali-activated material precursor (e.g., Siakati and Douvalis (2021)). Na_2SiO_3 (SS) solution is superior to NaOH in terms of activating CS (e.g., Yan and Sun (2021)). Previous studies revealed that the dosage of the SS affects the performance of alkali-activated materials (e.g., Melo Neto and Cincotto (2008)). The study aims to explore the hydration and shrinkage behavior of CS activated by sodium silicate at different Na_2O equivalents.

2 Materials and methods

The Blaine-specific surface area of the ground CS was 516 m^2/kg. The alkaline activator is an industrial-grade water glass solution with the modulus (SiO_2/Na_2O) = 2.2. The activator dosages of 6, 8 and 10 wt.% were prepared (calculated as Na_2O equivalent; by weight of CS). For the isothermal calorimetry and porosity test, the specimens were AACS paste with 0.4 water-to-CS ratios. For the drying and autogenous shrinkage test, the mixed composition of the copper slag mortars is shown in Table 1.

Table 1 Mixed composition of the copper slag mortars for compressive strength test

Group	Na_2O equivalent (%)	W/CS	Copper slag (g)	Sand (g)	Additional water (g)	SS (g)
SS6	6	0.5	450.0	1350.0	114.5	196.4
SS8	8	0.5	450.0	1350.0	77.7	261.8
SS10	10	0.5	450.0	1350.0	40.9	327.3

Note: SS: Sodium silicate solution, modulus = 2.2, 29.99 wt.% SiO_2, 13.75 wt.% Na_2O, 56.26 wt.% water; W/CS: Water-to-copper slag ratio, where water includes the water in the activator and additional water

A multi-channel adiabatic calorimeter (TAMAir C08) with a minimum resolution of 0.1 ◦C was used to measure the hydration heat with 70 h of the cementitious material according to GB/T 12959-2008. The autogenous shrinkage was measured according to the corrugated tube method. The specimens for drying shrinkage were cast in a mold with the dimensions of 40 × 40 × 160 mm and cured in a sealed condition (with plastic film) at 20 °C. After curing for 3 days, the specimens were exposed in a room with a constant temperature of 20 ± 3 °C and relative humidity of 50% ± 5%. The length changes of AACS specimens were monitored by using a comparator with a measuring accuracy of 0.001 mm and a balance with an accuracy of 0.01 g, respectively. The coarse porosity of the AACS was determined by backscattered electron image analysis (BSE-IA) by using scanning electron microscopy (SEM, XL30 Philips).

3 Results and discussion

3.1 Hydration heat monitored by isothermal calorimetry

As shown in Fig.1, the duration of the induction period is prolonged with the increase of Na_2O equivalent. The accelerated peak in SS6 appears around 13 h, followed by SS8 and SS10. Besides, the magnitude of the accelerated peak follows the order: SS8>SS6>SS10. Fig.1(b) presents the cumulative heat of AACS during the first 70 h. In the first 20 h of hydration, the cumulative heat decreases with the increase of Na_2O equivalent. But as the reaction continues to 30 h, the cumulative heat of SS10 is the highest.

The higher Na_2O equivalent means more OH^- in the SS solution, which promotes the dissolution of CS and the formation of the reaction products. Thus, the magnitude of the accelerated peak of SS8 is higher than SS6. However, too much OH^- in the solution might hinder further reaction. The faster the product generated, the slower the OH^- penetrated deeply, resulting in the accelerated peak of SS8 appearing later than SS6. When the dosage of SS increased to 10 wt.%, the negative impact of the initial rapid reaction on the later process was more pronounced. Not only the time to the accelerate peak was

delayed, but also the peak magnitude decreased in SS10. However, the duration of the acceleration and deceleration stage of SS10 is the longest, leading to the highest cumulative heat after 30 h.

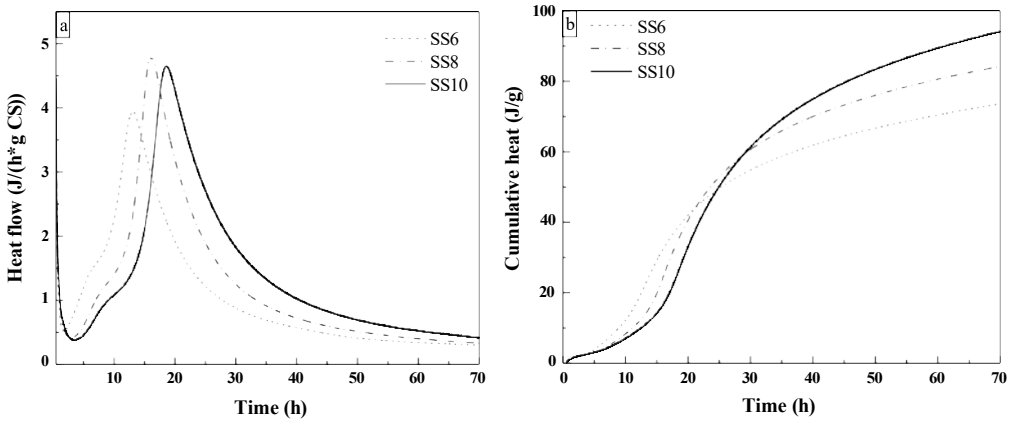


Fig.1 Heat evolution and cumulative heat of AACS pastes.

3.2 Shrinkage

The internal moisture in mortar is continuously evaporated and lost after hardening, leading to drying shrinkage. The drying shrinkage of AACS with 6, 8, and 10 wt.% Na_2O is represented by the depicted curves in Fig.2(a). The drying shrinkage of AACS mortars occurred primarily before 14 d and decreased with the increase of Na_2O. This might be due to the least added water contained in SS10 as shown in Table 1.

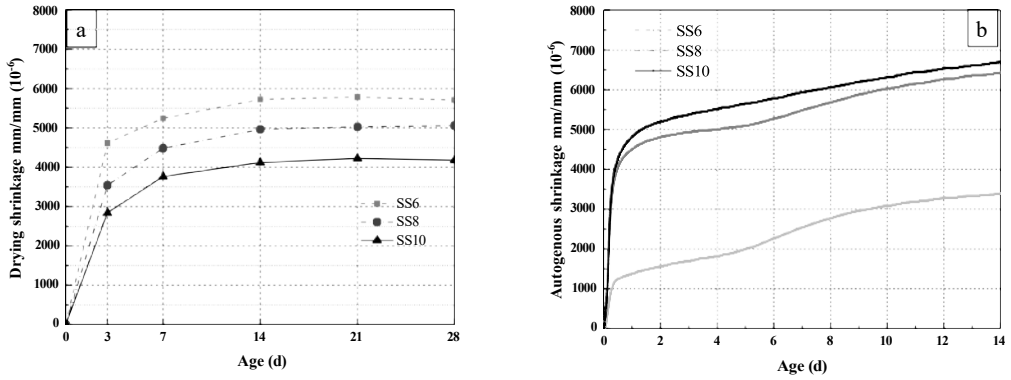


Fig.2 Drying shrinkage (a) and autogenous shrinkage (b) of AACS mortars.

Autogenous shrinkage is the reduction of macroscopic volume occurring without moisture transfer to the exterior surrounding environment. The autogenous shrinkage of AACS mortars as measured by the corrugated tube method is depicted in Fig. 2(b). The specimens with the highest Na_2O content (SS10) exhibited the highest autogenous shrinkage, followed by SS8 and SS6. The hydration process reduces internal relative humidity and capillary negative pressure, which results in autogenous shrinkage. A higher amount of both Na_2O caused a higher reaction degree, leading to larger capillary stress and greater autogenous shrinkage.

3.3 Porosity

Table 2 displays the porosity of AACS measured by BSE-IA. The porosity of SS6, SS8 and SS10 is 4.08%, 7.07% and 7.37%, respectively. The result demonstrates that adding more Na_2O causes a rise in coarse porosity, revealing that autogenous shrinkage predominated in the development of cracks.

Table 2 Porosity of AACS

Group	SS6	SS8	SS10

Porosity	4.08	7.07	7.37

4. Conclusions

(1) The dosage of sodium silicate solution increases as the increase of Na_2O equivalent, delaying the hydration of AACS paste and lengthening the hydration period, which leads to higher cumulative heat at 70 h.

(2) The drying shrinkage of AACS mortars mainly happened before 14 d and decreased with the increase of Na_2O, whereas the autogenous shrinkage increased by adding more Na_2O.

(3) The more Na_2O increases the coarse porosity, revealing that the autogenous shrinkage dominated the crack generation.

Acknowledgments

This work was funded by the National Natural Science Foundation of China (Grant No.51678441), the Science and Technology Commission of Shanghai Municipality (Grant No. 19DZ1202702 and 19DZ1201404), the Housing and Urban-Rural Construction Management Commission of Shanghai Municipality (Grant. No.2021-001-002) as well as the National Natural Science Foundation of China (Project No. 52108240).

References

Gorai, B. and Jana, R.K (2003) “Characteristics and Utilisation of Copper Slag - A Review”, *Resources, Conservation and Recycling*, 39: 299-313

Shi, C., Meyer C. and Behnood, A. (2008) “Utilization of copper slag in cement and concrete”, *Resources, Conservation and Recycling*, 52:1115-1120.

Siakati, C., Douvalis, A. P. and Hallet, V. (2021). Influence of CaO/FeO ratio on the formation mechanism and properties of alkali-activated Fe-rich slags. Cement and Concrete Research, 146:106466

Yan, Z., Sun, Z. and Yang, J. (2021) “Mechanical performance and reaction mechanism of copper slag activated with sodium silicate or sodium hydroxide”, *Construction and Building Materials*, 266:120900

Melo Neto, A., Cincotto, M. and Repettle, W. (2008) “Drying and autogenous shrinkage of pastes and mortars with activated slag cement”, *Cement and Concrete Research*, 38: 565-574

The 16th International Congress on the Chemistry of Cement 2023 (ICCC2023)
"Further Reduction of CO_2 -Emissions and Circularity in the Cement and Concrete Industry"
September 18–22, 2023, Bangkok, Thailand

Low CO_2 footprint and high circular cementitious binders based on mineralized RCF and LF steel slags under synergistic approach.

A. Oleaga. [1*], V. García[1], I. Vegas[1], M. Frías[2]

[1] *TECNALIA, Basque Research and Technology Alliance (BRTA), Astondo Bidea, Edificio 700, Parque Tecnológico de Bizkaia, 48160 Derio, Spain*

Email: asier.oleaga@tecnalia.com ; veronica.garcia@tecnalia.com ; inigo.vegas@tecnalia.com

[2] *Eduardo Torroja Institute for Construction Sciences (IETcc-CSIC), 28033 Madrid, Spain*

Email: mfrias@ietcc.csic.es

ABSTRACT

The CO_2 footprint reduction in conventional Portland cement production constitutes a huge challenge due to the limited availability of low carbon footprint and economic Supplementary Cementitious Materials (SCM) supplies to be employed in clinker substitution. A Carbon Capture and Utilization (CCU) approach based on mineralization by accelerated carbonation of recycled concrete fines (RCF) and ladle furnace (LF) steel slags derived from industrial and urban alkaline waste currents, appears to be a feasible route to reduce sectorial carbon footprint and promote new circular building materials. In this document the CO_2 sequestration on different conditions is calculated, and the mineralogical transformation is monitored by spectral tools (Raman, HSI), for process optimization. Through the applied lab scale carbonation processes, increased reactivity and new pozzolanic phases are generated. Obtained materials are synergistically employed as SCM in novel cementitious binders, resulting in relevant CO_2 savings (-27%) and lower clinker content (<30%) highly circular binders, according to the performed Life Cycle Analysis (LCA).

This research has been developed under NEUCLICEM project, co-funded by IHOBE, the public environmental management company of the Basque Government (Spain), through the program *"Eco-design, demonstration projects on circular economy and strategic eco-innovation"* (2020), (HEIDELBERG MATERIALS), and VOLBAS.

KEYWORDS: *mineralization, alkaline, waste, synergy, SCM*

1. Introduction

Ladle furnace (LF) slag, is a by-product of the steel refining process from electrical arc furnace (EAF), that contains >50% of CaO and MgO oxides, and other major compounds such as Si and Al oxides [1,2]. Rich in ɣ-C_2S, resembles a Portland cement composition, and therefore may have the potential to be used as SCM, despite its high free-lime content, that may cause undersirable volumetric instability. Recycled Concrete fines (RCf), mostly landfilled or underused at present, are the inorganic finest fraction (<5mm) remaining from concrete CDW recycling, which is composed by fine aggregates, hydrated cement paste, un-hydrated componentes of the original cement, and impurities [3], forming an heterogenous and complex alkaline nature waste. Cement Industry, by the other hand, seeks for cost-effective pathways to cut ("net-zero"), their global direct CO_2 emissions (2.2 $GtCO_2$/yr) by 2050 at latest, where 60% of the industry's emissions are 'process emissions' caused by decarbonation of limestone [4]. The massive use of alternative low carbon - high circular SCMs is a priority in the cement industry in their decarbonization roadmap. In this pathway, Carbon Capture & Utilization (CCU) approaches through Accelerated Carbonation Technologies (ACT) applied to such poorly valorised and worlwide major waste currents LF slags and RCf, showed to be an effective way for their upgrade, enabling CO_2 capture and reduce the free CaO and MgO,

while improve their pozzolanic properties and therefore, improving the performance and durability of binders containing such carbonated type SCMs [5,6]. Operating conditions and the technoeconomical feasability of the technology at industrial scale of such processes are still being matter of study throught different approaches. The use of digital tools such as Hyperestpectral (HSI) and Raman may suppose a breakthrough to increase the ACT efficiency [7,8], enabling in-line traceability wastes and CO_2 fixation monitoring, on developing new lower carbon footprint binders with efficiently carbonated RCf and LF slags as SCM, as in NEUCLICEM[1].

2. Experimental program

Material requirements were established targeting the elaboration of normal hardening Hydraulic Road Binders (HRB) UNE EN 13282-2[2] , for which carbonated RCf and LF slags are employed as SCM, substituting partially or totally dosage Pozzolans (P), Limestone (L), and in minor amount of clinker (K). RCf (<4mm) was obtained from a CDW recycler and LF slags from a steel facility located at Basque Country, Spain. Hardened HA25 concrete and a CEMI 52,5R cement pastes were prepared as references. Wastes were dried (105ºC, 24h) and stored removing the air to avoid pre-carbonation. Samples adequation consisted on impurities retirement (metals, bricks, ceramic, glass, plastics, wood, etc.) and sieving (<4mm, <125µm, <90µm, and <63µm). Samples humidity %, main oxides and trace elements (XRF), mineralogy (XRD Rietveld, SEM), free CaO and MgO, sulphates (SO_3), chlorides (Cl^-), reactive CaO and SiO_2, total organic materia (TOC), FTIR-ATR, puzolanicity and activiy index, was measured. CO2 capture was evaluated by measuring the carbonates content (calcimetry Bernard – Eq. 1 to 3), and through the analysis of the CO2 bound in carbonates retrieved from thermal gravimetry (TGA/DSC Mettler Toledo device, 30/900 ºC, 10ºC/min), and comparing with the Steinour's formula [9] for the theoretical CO2 uptake. Characterization by HSI and Raman technologies were also applied, gathering samples spectral signatures.

$$CO_2\ uptake\ (\%) = \frac{co^2\ final\ (\%) - CO_2\ initial\ (\%)}{100 - CO_2\ final\ (\%)} \times 100 \qquad \text{Equation 1}$$

$$\delta CaO\ (\%) = \frac{CO_2\ uptake\ (\%) \times \frac{MWCaO}{MW\ CO_2}}{CaO\ initial\ (\%) - CO_3\ initial\ (\%) \times MWCaO\ /MWCO_3} \times 100 \qquad \text{Equation 2}$$

$$\delta\ (\%) = \frac{CO_2\ uptake\ (\%) \times \frac{1}{MW\ CO_2}}{\sum_k Mk\ initial\ (\%)/MWMk - CO_3\ initial\ (\%)/MWCO_3} \times 100 \qquad \text{Equation 3}$$

Phase 1. Direct gas/solid mineralization through carbonation was developed in 2 phases by a 5L capacity static lab reactor equiped with temperature and pressure controlers. 18 carbonation protocols (<0,5kg/batch) were executed. Variables as solid humidity (5-24%), grain size (<63µm-4mm), pressure (1-5 atm), temperature (20-80ºC), and residence time (1h-4h) were studied. All the protocols used a 100% conc. CO_2 commercial dry flux. Induced mineralogical transformation was followed up by a total of 61 subsamples collection (t=0h, t=0,5h, t=1h, t=1,5h, t=4h) for their cha racterization. Phase 2 developed 2 optimized protocols (3,3kg / batch) to be valorized in the HRB mixtures. The spectral survey employed 2 lineal HSI cameras (Jai V10E, sisuCHEMA) operating at 400-2500nn wavelenght, and a portable Raman device (Figure 1). Both cameras produced a dataset pre-processed for spectral data filtering, enhancing and end-visualization. Well-known reference materials spectra were employed for comparison and set up.

Phase 2 carbonated materials were validated and after a preparation (drying and grinding), up to 8 different HRB blends (a/c ≈ 0,3) were produced (Figure 4): 1 HRB E3 similar to a commercial product (50% K), 1 HRB E2 based on a reference poor in clinker (29% K), and 6 HRB based on the E2 reference, and partial and total susbtitutions of L and P by carbonated RCf and LF slags; additionally, a recycled ceramic waste fine (non carbonated) was employed. Substitutions with carbonated LF slags and RCf achieved up to 10% and 12% respectively of total of the blend, and up to 17% with the ceramic waste. L was substitued by both carbonated LF slag and RCf, an P by the ceramic waste. DOS-6 was (Figure 2) the most synergistic dossage consisting in a combination of carbonated RCf and LF slags, substituting the 100% of L, a 40% of the initial P, with only 26% of K. Mortars fresh characteristics workability and consistence (UNE-EN 1015-3), setting times (UNE-EN 196-3), were measured, and hardened especimens (40x40x16mm) were cured up to 56d ,

[1] NEUCLICEM Eco-innovation towards climatic neutrality in the Cement industry by digitized CO2 capture processes applied to massive alkaline waste currents. https://www.cementosrezola.es/es/neuclicem.

[2] Hydraulic road binders - Part 2: Normal hardening hydraulic road binders - Composition, specifications and conformity criteria.

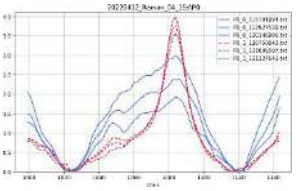
for which mechanical performance (compresion and flexure) and durability was assesed and compared with the reference HRBs. Finally, a Life Cycle Assessment (LCA) (ISO 14040-14044:2006) was elaborated.



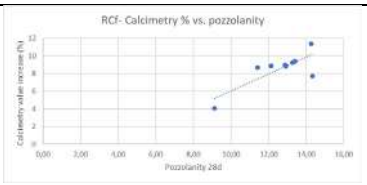
HSI



Raman



Spectral signal by Raman



Calcimetry vs pozzolanity in RCf

Figure 1. Carbonated samples characterization by HSI and Raman and pozzolanity assessment vs. Carbonation degree.



Figure 2. DOSAGE 6 mortar elaboration detail.

HRB	Compounds (%)				Workability (mm)	Initial setting time	w/c
	K	RCf*	LF*	Other			
Ref. HRB E 3	50,4	0,0	0,0	49,6	190,0	3h 47min	0,247
Ref. HRB E 2	29,2	0,0	0,0	70,8	179,5	5h 56min	0,302
DOSAGE 1	29,2	0,0	0,0	70,8	179,7	4h 00min	0,290
DOSAGE 2	29,2	10,0	0,0	60,8	162,5	3h 56min	0,320
DOSAGE 3	29,2	0,0	10,0	60,8	164,0	5h 59min	0,320
DOSAGE 4	29,2	10,0	0,0	60,8	167,1	3h 40min	0,326
DOSAGE 5	29,2	0,0	10,0	60,8	161,0	4h 30min	0,310
DOSAGE 6	26,7	12,0	10,0	51,3	109,5	4h 49min	0,316

Figure 3. Mortar dosages and fresh characteristics.

3. Results and discussion

Calcimetry and TGA/DSC analisies revealed that cement paste CEM I 52,5 R captured most CO_2 (166g CO_2 eq./kg), then the LF slags (117g CO_2 eq./kg), and in minor amounts the RCf (50g eq. CO_2 / kg), and HA25 concrete (29g CO_2 eq./kg). Optimal carbonation conditions for RCf appeared to be in the order of 10% solid humidity, 15% for LF slags, with acceptable efficieny of capture at 1atm and 20ºC. Nearly 100% of the CO_2 capture occurred before 0,5h, by a fast an exothermic reaction, rising 40ºC reactor air temperature. XRD study revealed that free CaO, MgO and Portlandite $Ca(OH)_2$ is fast transformed, and also C_2S phases partially carbonated, yielding new carbonates ($CaCO_3$, $Ca,MgCO_3$). This mineralogical transformation is seen by FTIR-ATR, noticing increased peaks at 1408cm^{-1} $CaCO_3$, and 700cm^{-1} peak displacing to 900cm^{-1} associated with Si-O bonds, product of C_2S decalcification and potential silica polimerization that may benefit the creation of new silica rich gels. Accelerated puzolanity tests demonstrated materials activity increase (x2,5 times) at 28d, as a consequence of the carbonation. Additionally, the HSI camera NIR-SWIR (1000-2500 nm) signal observation permitted to follow the Portlandite $Ca(OH)_2$ transformation on to new $CaCO_3$, through the study of the peaks around 1420nm and 1900-2000nm. RAMAN was useful too in monitoring new calcita peaks around 1083 cm^{-1} wavelength.

HRB specimens test showed that all the mixes with carbonated SCM had increased hardening times than ref., a lower mechanical performance than the commercial HRB E3 reference (50% K), but similar or better mechanical performance than the low-clinker reference HRB E2 (29% K) (Figure 4), used as the base for the new HRB dosages with carbonated SCM. The biggest mechanical gains (+10MPa) over ref. HRB E2 were obtained for specimens containing up to 10% of carbonated LF slags (DOS-3, DOS-5), where limited gains (+1MPa) were obtained with the carbonated RCf. The mechanical gain increases continuously through time, streching the performance gap for LF bearing HRB, achieving up to +10Mpa in compressive rand +2Mpa in flexure resistances at 28d. DOS-6 achieved identical performance than HRB E2 reference. Life Cycle Analyisis (LCA) determined that although DOS-3 and DOS-5 showed outstanding mechanical performances in comparisson to HRB E2, the major CO_2 footprint reduction was obtained by DOS-6 (350g eq. CO_2 / kg), for which CO_2 footprint reduction was 9,3% lower than HRB E2 (386g eq. CO_2 / kg), and -27,0% than commercial HRB E3 (477g eq. CO_2 /kg). In addition, the reduction on the virgin raw material consumption was lowered by -270kg/t. DOS-6 was considered thus, the most balanced HRB dosage considering both overall environmental footprint reduction, and optimal mechanical performance.

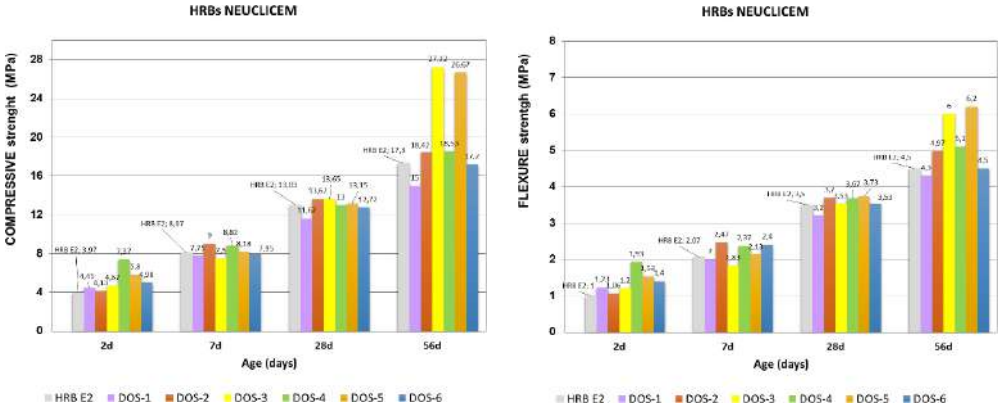


Figure 4. Compressive and Flexural strengths of the NEUCLICEM HRB specimens.

4. Conclusions

ACT applied of concrete fines (RCF) and ladle furnace (LF) steel was proven to be successful in the target of capturing and fixing CO_2 (up to 166g eq.CO_2/kg) by gas/solid fast lab reactions (<0,5h). It was demonstrated that pozzolan activity increases (x2.5) as carbonation degree increases. HSI and Raman study showed that novel mineral phases can be monitored and that can constitute valuable tools to optimize future industrial scale processes, reducing residence times and mineral driven transformation. Additionally, carbonated RCF and LF wastes used as SMC in HRB binders showed to be beneficial to obtain mechanical performance gains resulting in lower environmental footprint (-27% CO_2, -270kg/t of VRM) than a commercial HRB.

Acknowledgements

Special thanks to Raúl Crespo (HEIDELBERG MATERIALS), Alberto Juarrero (VOLBAS). Special thanks to the research project CIDECAR ref. PID2021-122390OB-C21, funded by AEI, eRDF funds, and Spain's Ministry of Science, Innovation.

References

[1] Manso JM, Losáñez M, and Polanco JA, González JJ (2005). "Ladle furnace slag in construction" *J Mater Civil Eng*; 17:513–8.

[2] Setién J, Hernández D, and González JJ (2009). "Characteristics of ladle furnace basic slag for use as a construction material". *Constr Build Mater*; 23:1788–94

[3] Frías, M., Vigil de la Villa, R., Martínez-Ramírez, S., Fernández-Carrasco, L., Villar-Cociña, E., & García-Giménez, R. (2020). "Multi-Technique characterization of a fine fraction of CDW and assessment of reactivity in a CDW/Lime system". *Minerals,* 10(7), 590.

[4] International Energy Agency IEA, Cement Sustainability Initiative (2018) "*Technology Roadmap Low-Carbon Transition in the Cement Industry"*.

[5] Pan, S. Y., Chang, E. E., & Chiang, P. C. (2012). *"CO2 capture by accelerated carbonation of alkaline wastes: a review on its principles and applications"*. Aerosol and Air Quality Research, 12(5), 770-791.

[6] Skocek, J., Zajac, M., & Ben Haha, M. (2020). *"Carbon Capture and Utilization by mineralization of cement pastes derived from recycled concrete"*. Scientific Reports, 10(1), 1-12.

[7] Krupnik, D., & Khan, S. (2019). *"Close-range, ground-based hyperspectral imaging for mining applications at various scales: Review and case studies"*. Earth-science reviews, 198, 102952.

[8] Xian, X., Mahoutian, M., Zhang, S., Shao, Y., Zhang, D., & Liu, J. (2023). *"Converting industrial waste into a value-added cement material through ambient pressure carbonation"*. Journal of Environmental Management, 325, 116603.

[9] H. H. Steinour, *"The Ultimate Products of the Carbonation of Portland Cement".* Res. Dept Portland Cem. Assn Unpubl., (1956).

The 16th International Congress on the Chemistry of Cement 2023 (ICCC2023)
"Further Reduction of CO_2 -Emissions and Circularity in the Cement and Concrete Industry"
September 18–22, 2023, Bangkok, Thailand

Understanding the role of carbon nanotubes in low-caron concrete: from experiment to molecular dynamics

Kai Cui[1,2], Jun Chang[1*]

[1] *Dalian University of Technology, Dalian, China*
Email: jiancaick@dlut.edu.cn
[2] *City University of Hong Kong, Hong Kong, China*
[1*] *Dalian University of Technology, Dalian, China*
Email: mlchang@dlut.edu.cn

ABSTRACT

Improving concrete's macro performance and durability is conducive to energy saving and emission reduction and is in line with the green and sustainable development concept. We innovatively proposed an effective method using dispersed CNTs to pre-saturated sand resulting in the dispersed CNTs distributed in the ITZ. We compared the methods of adding dispersed CNTs and dispersed CNTs pre-saturated sand. We also explored the macro performance, hydration process, and microstructure of low-carbon sulfoaluminate cement-based concrete through experiments and MD (molecular dynamics) simulations. The 28d compressive strength of CS2 (adding dispersed CNTs pre-saturated sand) compared with C0 (without adding CNTs) and C2 (adding dispersed CNTs) improved by 27.8% and 10.1%, respectively, while the 28d flexural strength enhanced by 16.7% and 6.3%, respectively. The primary mechanism is attributed to the adsorption and nucleation effect of CNTs; the CNTs promoted the generation of more AFt (ettringite) and AH_3 (gibbsite), which improved the hydration degree. MD simulation also verified this mechanism, which modeled the change of Ca^{2+} mobility under the influence of CNTs addition. Ca^{2+} has a greater density distribution closer to the substrate under the effect of CNTs addition, indicating that substrate with CNTs addition has a stronger force on Ca^{2+}. The stronger binding force between Ca^{2+} and substrate with the CNTs addition leads to a decrease in the density of Ca^{2+} in solution, which promotes further hydrolysis of the cement to release more Ca^{2+} for charge balance. The CNTs dispersed at the ITZ have a seeding effect; AFt and AH_3 are generated around the CNTs, which reduces the width of the ITZ, dramatically promotes the combination of CNTs and the ITZ, and effectively improves the microscopic structure of the ITZ.

KEYWORDS: *Carbon nanotubes, Sulfoaluminate cement, Low-carbon, Hydration, MD simulation*

1. Introduction

As we all know, the ITZ (interfacial transition zone) is the concrete matrix's weakest area. The thickness of ITZ is usually 5 μm to 100 μm, accounting for about 25% of the total volume of the matrix, as presented in Lu et al (2022). ITZ enhancement is significant for concrete performance. Chang et al. ground the cement and then mixed it with sand and water. Chang et al (2020) found the ground cement would pre-encapsulate the sand and be mixed with the unground cement, which could effectively improve ITZ. This research inspired our work to propose a new idea of nano-engineering to improve cement-based composites. We first used surfactant, superplasticizer, and ultrasonic to disperse CNTs and formed a CNTs dispersion; then, we poured sand into the carbon nanotube dispersion leading to the sand pre-saturate by the CNTs dispersion, and we mixed the sand with silica fume. The CNTs wrapped on the sand surface can directly improve the ITZ and enhance macro performance. The unique material ratio of RPC can further disperse CNTs, and silica fume can disperse CNTs through mechanical and chemical methods to form dense interfaces. Sand has a shearing effect on carbon nanotubes.We prepared low-carbon reactive powder concrete through two aspects of improvements. One is to use SAC (sulfoaluminate cement), a low-carbon cement with good durability. On the other hand, a new method for CNTs dispersion is proposed to maximize the advantageous properties of CNTs. We qualitatively and quantitatively characterized the changes of hydration products

before and after CNT modification and the evolution of the microstructure of ITZ through experiments. We simulated the interaction of CNTs on sulfoaluminate cement hydration at the nano-level and revealed the mechanism of CNTs addition on SAC hydration. This study achieved effective dispersion of CNTs through nano-engineering, which effectively improved macro performance and durability of reactive powder concrete and provided a new idea for nanomaterials to enhance cement-based composites.

2. Experiment and molecular dynamics sumulation

2.1 Materials and experiment process

SAC is provided by Tangshan Polar Bear Co., Ltd. SF (Silica fume) is from Elkem Materials Co., Ltd. A polycarboxylate superplasticizer with a reduction rate of about 30% is prepared. The particle size of the sand is 0.12mm-0.83mm and Shenzhen Nano port Co., Ltd produced the CNTs. The experiment process is shown in Fig.1. We named samples without adding CNTs as the C0 group. The samples without pre-saturated sand but with 0.05 wt% and 0.08 wt% CNTs addition were named C1 and C2 groups. The samples with pre-saturated sand and the addition of 0.05 wt%, 0.08 wt%, and 0.12 wt% CNTs were named CS1, CS2, and CS3 groups. Gum arabic powder (GA) as a dispersant of CNTs.

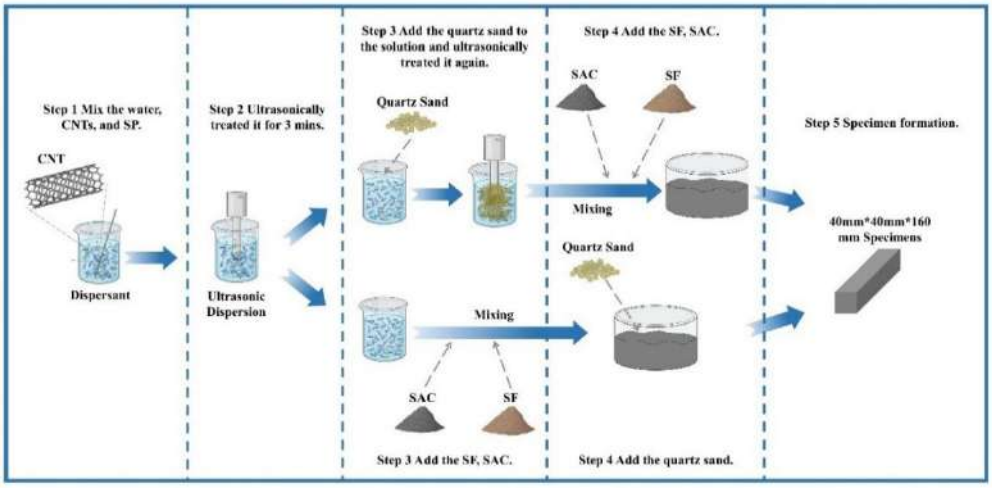


Fig.1. The preparation process of RPC samples.

2.2 Test methods

The Tam air, XRD, and TG were used to analyse the hydraion products. The appropriate vacuum layer was added, as shown in Fig.2.

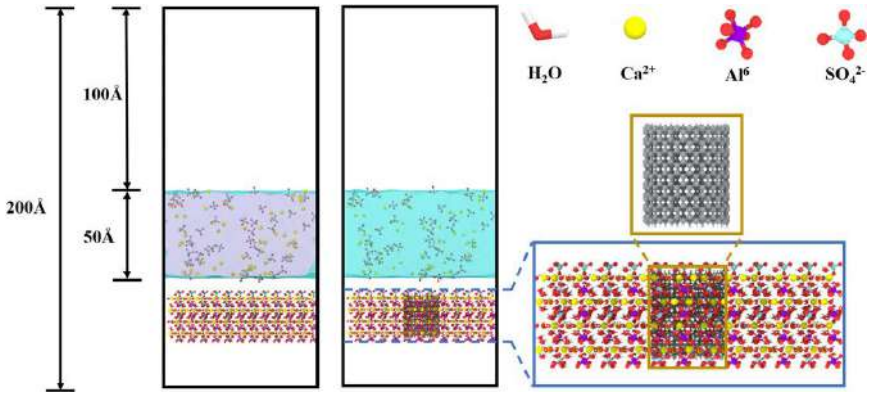


Fig.2. Atomic models of $CaSO_4$ solution transport in the AFt with/without CNTs addition.

3. Results and discussion

The 1d and 28d flexural strengths of the C0 group are 6.4MPa and 10.2MPa, respectively. For groups C1 and C2, the flexural strengths at 1d and 28d were 15.6%, 6.9%, 17.2%, and 9.8% higher than those of C0.

Adding CNTs can enhance the concrete's compressive strength, which is the same as the conclusions of other research, including Jung et al (2020). For the CS1 group, the 1d and 28d flexural strength increased by 21.8% and 11.8% than that of C0, respectively, and the flexural strength at 1d and 28d of CS2 and CS3 groups were 28.1%, 16.7%, and 20.3%, 12.7% higher than C0, respectively. Similarly, the 28d compressive strengths of C1, C2, CS1, CS2, and CS3 increased by 7.2%, 16.1%,20.3%, 27.8%, and 23.9%, respectively than C0 group. Interestingly, the strategy of dispersed CNTs pre-saturated sand can significantly improve the matrix's flexural strength, proving the feasibility of enhancing the matrix through nano-engineering. The improvement of the macro performance is attributed to the nucleation and adsorption effect of CNTs, which promoted the dissolution of ions, accelerated hydration, provided reaction sites for the formation of AFt and AH_3.

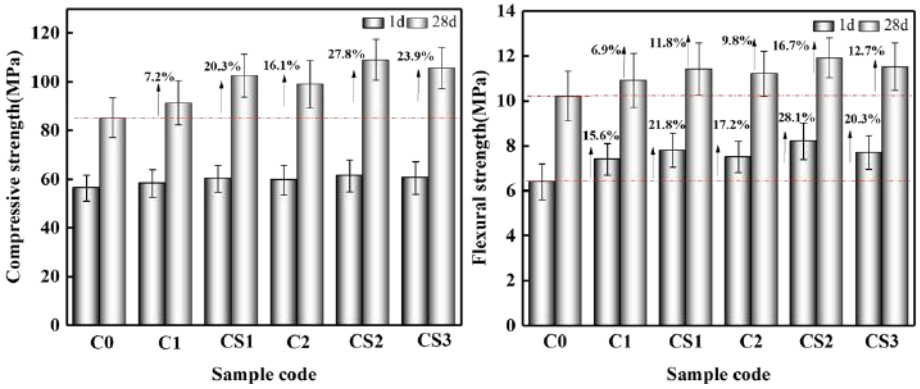


Fig.3. Mechanical properties of RPC.

As shown in Fig.4 and Fig.5, the primary mechanism is attributed to the adsorption and nucleation effect of CNTs; the CNTs promoted the generation of more AFt (ettringite) and AH_3 (gibbsite), which improved the hydration degree. MD simulation also verified this mechanism, which modeled the change of Ca^{2+} mobility under the influence of CNTs addition. Ca^{2+} has a greater density distribution closer to the substrate under the effect of CNTs addition, indicating that substrate with CNTs addition has a stronger force on Ca^{2+}, The stronger binding force between Ca^{2+} and substrate with the CNTs addition leads to a decrease in the density of Ca^{2+} in solution, which promotes further hydrolysis of the cement to release more Ca^{2+} for charge balance.

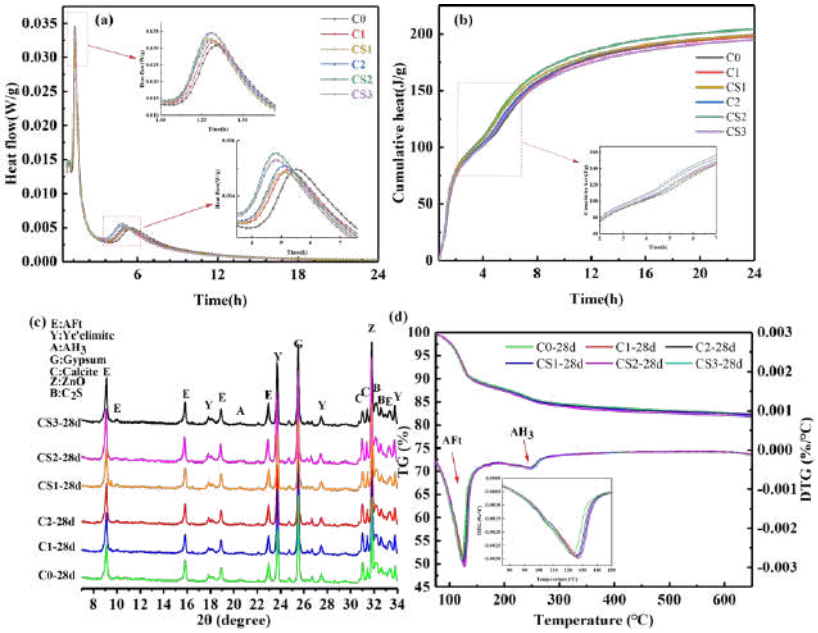


Fig.4. Hydration of RPC.

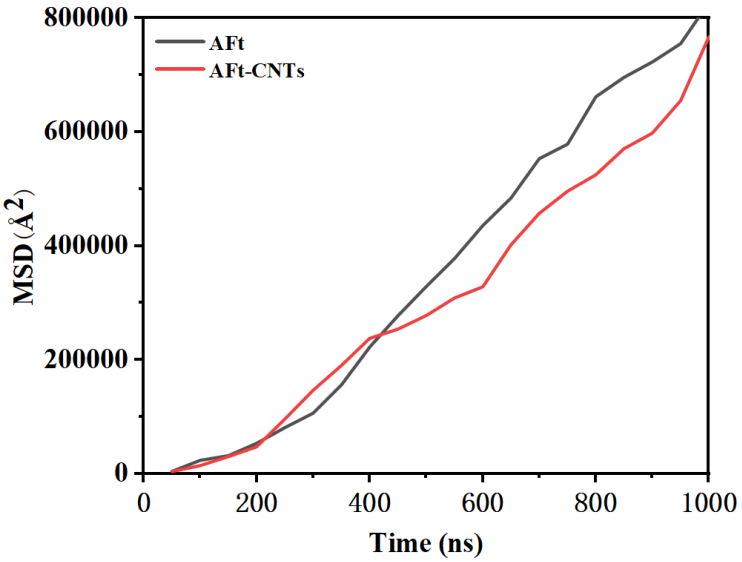


Fig.5. The MSD curves of Ca^{2+} ion on AFt with/without CNTs.

3. Conclusions

1. The 28d compressive strength of CS2 (dispersed CNTs pre-saturated sand) compared with C0 (the control group without adding CNTs) and C2 (dispersed CNTs) increased by 27.8% and 10.1%, respectively, and the flexural strength increased by 16.7 % and 6.3%, respectively. The method of dispersed CNTs pre-saturated sand by nano-engineering has a better enhancement efficiency on the mechanical property than previous studies.
2. The absorption of Ca^{2+} by CNTs leads to further hydrolysis of cement and promotes further hydration of the matrix. Ca^{2+} has a greater density distribution closer to the substrate under the effect of CNTs addition, indicating that substrate with CNTs addition has a stronger force on Ca^{2+}. The stronger binding force between Ca^{2+} and substrate with the CNTs addition results in a decrease in the density of Ca^{2+} in solution, which promotes further hydrolysis of the cement to release more Ca^{2+} for charge balance.

Acknowledgements

This work was funded by the National Natural Science Foundation of China (52172015) and the Fundamental Research Funds for the Central Universities in China (DUT21ZD201).

References

Lu D, Shi X, and Zhong J.(2022) “Nano-engineering the interfacial transition zone in cement composites with graphene oxide”, Construction and Building Materials,356:129284.

Ansari WS and Chang J.(2020) “Influence of fine cement sand paste in preparation of cementitious materials”, Construction and Building Materials,230:116928.

Jung M, Lee Y, Hong S and Moon J.(2020) “Carbon nanotubes (CNTs) in ultra-high performance concrete (UHPC): Dispersion, mechanical properties, and electromagnetic interference (EMI) shielding effectiveness (SE)”, Cement and Concrete Research, 131:106017.

The 16th International Congress on the Chemistry of Cement 2023 (ICCC2023)
"Further Reduction of CO_2 -Emissions and Circularity in the Cement and Concrete Industry"
September 18–22, 2023, Bangkok, Thailand

Accelerated Carbonation of Brucite Recovered from Desalination Reject Brine for Construction Applications

I. Singh[1], R. Hay[2], and K. Celik[3,*]

Division of Engineering, New York University Abu Dhabi, Abu Dhabi, P.O. Box 129188, United Arab Emirates
[1]Email: is81@nyu.edu
[2]Email: rh137@nyu.edu
[3,]Email: kemal.celik@nyu.edu*

ABSTRACT

The present study investigated the recovery of brucite from reject brine using different precipitating agents (ethanolamine, ammonium hydroxide, calcium oxide, and sodium hydroxide) and differences in their mechanical properties due to direct carbonation. The strength development was studied using compacted pellets of brucite powders synthesized using different precipitating agents and subjected to carbonation under 20% CO_2 and 80% RH at 30 °C conditions. Brucite powders synthesized using different precipitating agents showed differences in their micro-structural properties, affecting the type and amount of binding hydrated magnesium carbonate (HMC) phases and compressive strength. The compressive strength of the carbonated pellets was found to be in the range of 19-33 MPa for different brucite powders suitable for non-structural applications. Data from thermogravimetry (TG) and X-ray diffraction (XRD) measurements revealed that different types and amounts of HMC phases could be formed in brucite powders synthesized using different precipitating agents, which could lead to the observed difference in their compressive strength. The results from this study are significant to better optimize the compressive strength of brucite recovered from reject brine.

KEYWORDS: *Reject brine, precipitating agent, accelerated carbonation, compressive strength, sustainable construction materials*

1. Introduction

Widespread consumption of ordinary Portland cement as a primary ingredient of concrete accounts for ~7.4% of global anthropogenic CO_2 emissions leading to aggravation of global warming and climate change (Hay and Celik, (2020), Sanjuán et al. (2020a)). Adoption of CO_2 capture, utilization, and storage technologies (CCUS) is essential for the construction sector to mitigate these adverse impacts (Sanjuán et al. (2020b)). Therefore, research efforts are directed toward the development of alternative construction materials with CO_2 uptake/sequestration capabilities. Reactive magnesium oxide (MgO) cement (RMC) has attracted significant attention as a low-carbon material due to its ability to gain strength through permanent CO_2 sequestration (Dung et al. (2019)). It has been recently demonstrated that CO_2 emissions of Mg-based cements could be further reduced by direct utilization of brucite ($Mg(OH)_2$) as a construction material (Shahbaz et al. (2022)). A recent study demonstrated that brucite could be recovered from the reject brine of the desalination process using a cost and energy-efficient precipitation process (Singh et al. (2022)). Direct carbonation of compacted brucite pellets could result in the formation of carbonate phases leading to rapid strength gain appropriate for non-structural applications. The factors leading to a rapid strength development of brucite under carbonation could include nanosized particles and high surface area. Different precipitating agents could lead to a difference in the overall particle size and surface area of synthesized brucite powders due to a difference in their solubility in the water (Dong et al. (2018)). Moreover, a change in the precipitating agent is also expected to affect the formation of secondary phases and the overall purity of the synthesized brucite. The change in physical and chemical properties of brucite will inevitably influence the formed carbonation phases and strength development; however, the mechanism is yet to be understood. In the present study, brucite powders were synthesized using four different precipitating agents (i) ethanolamine (C_2H_7NO), (ii) ammonium hydroxide (NH_4OH), (iii) calcium oxide (CaO), and sodium hydroxide (NaOH) and their microstructural properties were investigated. Compacted pellets prepared using the brucite powders synthesized by different precipitating agents were carbonated under 20% CO_2 80% RH at 30 °C carbonation curing to compare their compressive strength.

Physio-chemical characterizations were carried out on the carbonated powders to explain the observed compressive strength. Important results have been presented in the paper.

2. Methodology

Brucite powders in this study were synthesized using a previously reported procedure (Singh et al. (2022)). Reject brine from a multi-effect distillation (MED) process was acquired from Total Tractebel Emirates O&M, Al Taweelah A1 Power & Desalination Plant, Abu Dhabi, UAE, and used after filtration with Whatman filter papers (grade 2). In summary, different amounts of precipitating agents (8185 mg C_2H_7NO, 4258 mg NH_3 containing NH_4OH solution, 1180 mg CaO, and 2000 mg NaOH) were added to the 250 ml brine with 2000 rpm stirring at room temperature (Singh et al. (2022), Shahbaz et al. (2022)). Solid phase precipitating agents (CaO, NaOH) were first dissolved in 50 ml reject brine. This solution was then promptly added to the rest of the 200 ml brine. Liquid phase precipitating agents (C_2H_7NO, NH_4OH) were added directly to the reject brine. The reaction was kept on stirring for 4 hrs. The powders were separated and washed with 330 ml of deionized water using centrifugation to remove reaction by-products. White precipitates after the washing were dried in an oven for 12 h at 100 °C. Oven-dried precipitates were manually ground to obtain the brucite powders.
Compacted cylindrical pellets (10 mm diameter) of brucite powders were prepared using a compression die for carbonation and investigation of compression strength. To prepare the pellets, water and brucite were mixed in 0.6 w/b (water to binder ratio), and 1200 mg of wet powders were used in each pellet. The average length of the compacted pellets was 9.97 mm, 11.65 mm, 10.90 mm, and 10.15 mm for brucite powders synthesized using C_2H_7NO, NH_4OH, CaO, and NaOH, respectively. The powders were compressed under 2.5 MPa pressure with a 0.5 mm/min loading rate using a 5 kN Universal Testing Machine (UTM). Then, the brucite pellets were cured under 20% CO_2 and 80% RH at 30 °C conditions for 7 days. The X-ray diffraction (XRD) patterns were collected using a PANalytical Empyrean diffractometer. The scanning electron microscopy (SEM) images were obtained using a field−emission microscope Quanta FEG 450. Thermogravimetry and differential thermogravimetry (TG-DTG) measurements were performed using NETZSCH TG 209F1 Libra Thermal Analyzer. The BET-specific surface area (SSA) of the brucite powders was measured using a 3Flex surface characterization analyzer (Micromeritics).

3. Results and discussion

The XRD patterns and SEM images of the synthesized brucite powders are given in Fig. 1. XRD patterns in Fig. 1(i) confirmed that brucite could be successfully synthesized from the reject brine via all the precipitating agents used in the study, i.e., C_2H_7NO, NH_4OH, CaO, and NaOH. Molar contents of the precipitating agents used in the reactions were chosen accordingly to maximize the recovery of the brucite powders. The formation of $CaCO_3$ phases could also be seen in the XRD patterns. Aragonite was the dominating $CaCO_3$ phase in brucite synthesized using C_2H_7NO and NH_4OH, whereas calcite formation was favored in the brucite powders synthesized using NaOH and CaO. The formation of aragonite could be favored with the utilization of C_2H_7NO and NH_4OH as the lower pH and the presence of Mg^{2+} ions in brine inhibits calcite precipitation (Dong et al. (2018)).

SEM images of the brucite powders in Fig. 1(ii) indicated a flake-like morphology of the brucite powders synthesized from different precipitating agents with dimensions in the range of 40-150 nm. Brucite powders synthesized using NaOH were hexagonal in shape, whereas powders from other precipitating agents showed an irregularly shaped morphology. SEM images also exhibited a difference in the aggregation of the individual flakes and their thickness for brucite precipitated from different precipitating agents. Brucite precipitated using NaOH showed the lowest aggregation and highest thickness of the flakes. The morphological differences also led to a difference in the SSA of the brucite powders. The BET SSA of the brucite powders measured from N_2 adsorption-desorption was ~67 m^2/g, ~58 m^2/g, ~56 m^2/g, and ~40 m^2/g synthesized using C_2H_7NO, NH_4OH, CaO, and NaOH, respectively.

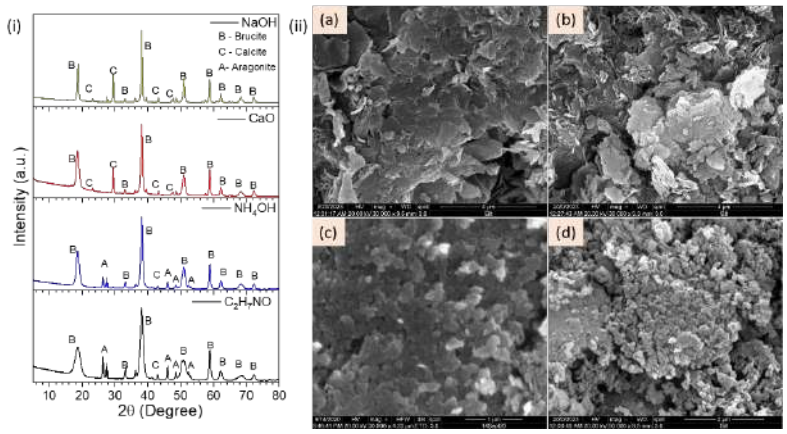


Fig. 1: (i) XRD patterns of the synthesized brucite powders using different precipitating agents, and (ii) SEM images of the synthesized brucite powders using (a) C_2H_7NO, (b) NH_4OH, (c) CaO, and (d) NaOH.

Fig. 2 shows the compressive strength of the brucite pellets subjected to carbonation curing under 20% CO_2 80% RH at 30 °C for 7 days. Carbonated brucite pellets exhibited compressive strength in the ~19-33 MPa range after 7 days of carbonation curing, where brucite synthesized using ethanolamine gained maximum strength (~33 MPa) followed by NaOH (~31 MPa), and CaO (~ 29 MPa) (Singh et al. (2022)). However, the compressive strength of brucite pellets from NH_4OH powders was lower at ~19 MPa. It is observed that the overall compaction (final length) of the brucite pellets could also impact the strength of the pellets, which could be caused by a difference in their surface area and the wettability of the synthesized powders. Therefore, compacted pellets of brucite from NH_4OH (with maximum length) showed a lower strength, possibly caused by an increased distance between the brucite particles/grains compared to other pellets. In addition, factors such as particle size and overall purity would also contribute to the observed variation in the strength of brucite pellets.

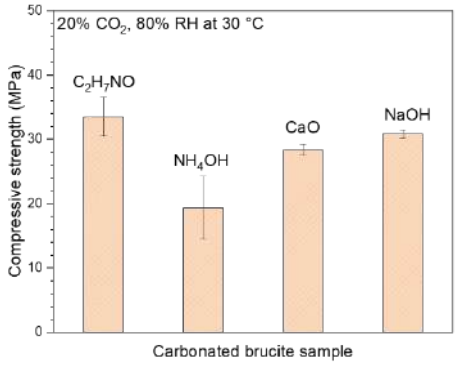


Fig. 2: Compressive strength of the compacted brucite pellets carbonated for 7 days under 20% CO_2 80% RH at 30 °C carbonation curing

The XRD patterns and SEM images of the carbonated brucite powders synthesized using different precipitating agents are given in Fig. 3 (i, ii). The XRD patterns confirmed the formation of nesquehonite as a primary carbonation phase in the carbonated brucite powders synthesized using C_2H_7NO, NH_4OH, and NaOH. The formation of nesquehonite is not observed, as seen in the XRD patterns of the carbonated brucite powders synthesized using CaO. The formation of nesquehonite as a high-density carbonation phase could be responsible for the increase in the strength of the compacted pellets of brucite synthesized using NaOH and C_2H_7NO. However, as discussed earlier, the lower compaction in brucite synthesized from NH_4OH led to a lower density and associated strength, even in the presence of the nesquehonite phase. The XRD data also indicated the difference in the type (crystalline and amorphous) and amount of formed HMC phases could affect the compressive strength of the compacted brucite synthesized using different precipitating agents.

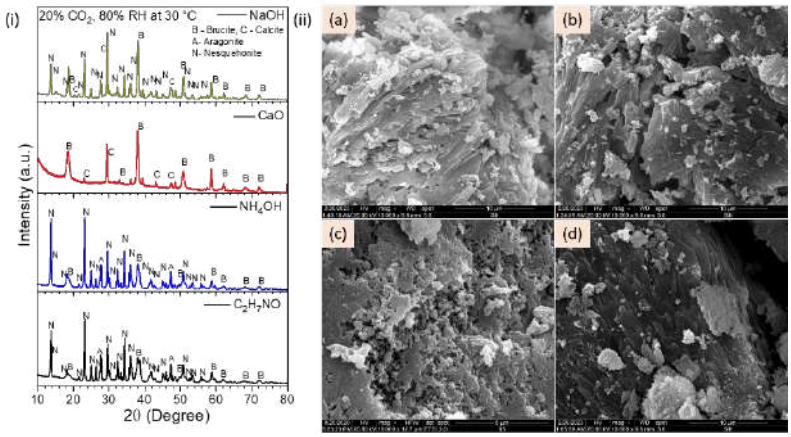


Fig. 3: (i) XRD patterns of the brucite pellets synthesized using different precipitating agents and carbonated for 7 days under 20% CO_2 80% RH at 30 °C carbonation curing, and (ii) SEM images of the carbonated brucite powders synthesized using (a) C_2H_7NO, (b) NH_4OH, (c) CaO, (d) NaOH

SEM images in Fig. 3(ii) showed the formation of rod-shaped morphologies in carbonated brucite powders synthesized using C_2H_7NO, NH_4OH, and NaOH, which could be attributed to the nesquehonite HMC phase. However, SEM micrographs of carbonated brucite powders from CaO depict the formation of interconnected networks of brucite particles which could be attributed to the formation of amorphous HMC phases (Singh et al. (2022)). TG-DTD data of the synthesized and carbonated powders obtained from grounded pellets is given in Fig. 4(a,b). DTG plots in Fig. 4(b) exhibited a clear increase in the dehydration contribution from the carbonated powders compared to synthesized powders in Fig. 4(a), indicating the formation of HMC phases. A difference in the temperature of dehydration contribution from carbonated brucite from CaO (~100 °C) with other powders (~150 °C) confirmed the presence of different HMC phases. A reduction in the dehydroxylation contributions from brucite and the appearance of new contributions above 410 °C also confirmed the formation of new HMC phases within brucite pellets (Singh et al. (2022)). In addition, the formation of nesquehonite in carbonated brucite synthesized from C_2H_7NO, NH_4OH, and NaOH was reflected in higher differential weight loss above 410 °C and lower weight loss at ~400 °C indicating higher conversion of brucite to HMC phase compared to brucite synthesized from CaO.

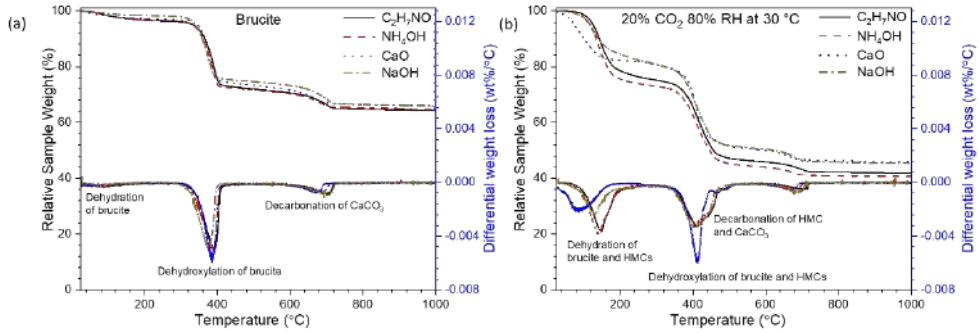


Fig. 4: TG-DTG plots of the carbonated brucite powders (a) synthesized and (b) and carbonated for 7 days under 20% CO_2 80% RH at 30 °C carbonation curing

4. Conclusions

This paper investigated the strength development in compacted pellets of brucite powders synthesized from reject brine using different precipitating agents and carbonated under 20% CO_2 80% RH at 30 °C conditions. Brucite powders synthesized using different precipitating agents showed differences in composition, morphology, and surface area. It was revealed that compacted pellets of brucite synthesized using different precipitating agents achieved compressive strength in the range of 19-33 MPa. The variation in their strength could arise due to a combination of factors such as differences in the surface area, particle size, purity of brucite powders, and type and amount of formed HMC phases.

Acknowledgments

The support received from the Abu Dhabi Department of Education and Knowledge (ADEK) for the grant ADHPG−RA686 is acknowledged. This work was supported by the NYUAD Center for Interacting Urban Networks (CITIES), funded by Tamkeen under the NYUAD Research Institute Award CG001. The authors also thank Tamkeen for funding the NYUAD Water Research Center under the NYUAD Research Institute Award (project CG007).

References

Dong, H., Yang, E., Unluer, C., Jin, F., Al-Tabbaa, A. (2018) "Investigation of the properties of MgO recovered from reject brine obtained from desalination plants," *Journal of Cleaner Production*, 196: 100-108

Dung, N.T., Lesimple, A., Hay, R., Celik, K., Unluer, C. (2019) "Formation of carbonate phases and their effect on the performance of reactive MgO cement formulations," *Cement and Concrete Research*, 125: 105894

Hay, R. and Celik, K. (2020) "Hydration, carbonation, strength development and corrosion resistance of reactive MgO cement-based composites," *Cement and Concrete Research*, 128: 105941

Sanjuán, M.Á.; Andrade, C.; Mora, P.; Zaragoza, A. (2020a) Carbon Dioxide Uptake by Cement-Based Materials: A Spanish Case Study," *Applied Sciences*, 10: 339.

Sanjuán, M.A.; Argiz, C.; Mora, P.; Zaragoza, A. (2020b) "Carbon Dioxide Uptake in the Roadmap 2050 of the Spanish Cement Industry," *Energies*, 13: 3452.

Shahbaz, F., Singh, I., Krishnan, P. and Celik, K. (2022) "Life cycle assessment of brucite and synthetic MgO produced from reject brine using different alkalis," *Journal of Cleaner Production*, 380(2): 135071

Singh, I., Hay, R. and Celik, K. (2022) "Recovery and direct carbonation of brucite from desalination reject brine for use as a construction material," *Cement and Concrete Research*, 152: 106673

The 16th International Congress on the Chemistry of Cement 2023 (ICCC2023)
"Further Reduction of CO_2 -Emissions and Circularity in the Cement and Concrete Industry"
September 18–22, 2023, Bangkok, Thailand

Enhancing Carbonation of Reactive Magnesium Oxide Cement (RMC)-Based Composites with Cenospheres

X. Wang[1], K. Celik[2*]

[1] *Engineering, New York University Abu Dhabi, Abu Dhabi, UAE*
Email: xw1742@nyu.edu
[2*] *Engineering, New York University Abu Dhabi, Abu Dhabi, UAE*
Email: kemal.celik@nyu.edu

ABSTRACT

As a potentially sustainable alternative to ordinary Portland cement (OPC), reactive magnesium oxide cement (RMC) is capable of sequestering carbon dioxide (CO_2) permanently through carbonation. However, the limited hydration and carbonation in RMC-only formulations have greatly compromised the CO_2 absorption, hence, the mechanical performance of RMC-based composites. In this study, RMC is replaced with cenospheres at 30%, and the carbonation, thermal properties, and composition weight are investigated and compared with the reference matrix with no cenosphere replacement. The study reveals that a significant enhancement of carbonation is achieved by replacing 30% of RMC with cenospheres in the formulation, accompanied by improved thermal insulation and lightweight property at 7 days. With the incorporation of cenospheres in RMC-based composites, the CO_2 sequestration potential of RMC can be greatly increased.

KEYWORDS: *reactive magnesium oxide cement; cenosphere; carbonation enhancement; CO_2 sequestration, multifunctional construction material*

1. Introduction

Reactive magnesium oxide cement (RMC) is considered a sustainable alternative to ordinary Portland cement (OPC) due to its lower calcination temperature during its production (700-1000 ºC vs. 1450 ºC) (Walling and Provis (2016)) and its capability to develop strength by sequestrating CO_2 (Unluer and Al-Tabbaa (2013), Dung et al. (2019), Hay et al. (2023)). It can also be synthesized from seawater or waster brine obtained from desalination plants (Shahbaz et al. (2022)). After mixing with water, RMC will be converted to brucite ($Mg(OH)_2$), which then reacts with dissolute CO_2 to form hydrated magnesium carbonates (HMCs). The carbonation phases provide binding ability by establishing an interconnected network (Vandeperre and Al-Tabbaa (2007), Dung and Unluer (2017)) and lead to the reduction in porosity (Dung et al. (2019)). However, the initial hydration and carbonation reactions will form brucite and HMCs layers, which inhibit the further diffusion of CO_2 in the RMC matrix (Dung et al. (2019),). It significantly limits the conversion of MgO to HMCs, which has a negative impact on the microstructural development and mechanical performance of RMC samples. Additives such as hydrated magnesium carbonates (Unluer and Al-Tabbaa (2013)), calcined limestone (Hay and Celik (2022)) and $CaCO_3$ polymorphs (Hay et al. 2023) were demonstrated to enhance the carbonation of RMC-based composites at different levels.

Cenospheres, derived from fly ash which is the residue of the burning process at coal-fired power plants, are hollow spherical particles with stiff shells comprised mostly of silica and alumina (Rheinheimer et al. (2017)). Cenospheres have particle sizes of up to several hundred microns (Hanif et al. (2017)). Due to their hollow interior, cenospheres are ideal for producing ultra-lightweight cement with low thermal conductivity (Blanco et al. (2000)). Previous studies have incorporated fly ash into RMC-based composites as a filler (Vandeperre and Al-Tabbaa (2007), Unluer and Al-Tabbaa (2013)). However, limited investigation has been done on the influence of cenospheres on the hydration, carbonation, thermal properties, and composition weight of RMC-based composites. In this study, the influence of

cenospheres on density, compressive strength, thermal conductivity, and hydration and carbonation products of RMC-based composites was systematically investigated. This study provides useful information for developing lightweight thermal insulation RMC-based composites for their use in construction.

2. Materials and methods

2.1 Materials and mixture design

The RMC supplied by Richard Baker Harrison (UK) and LS300 cenosphere purchased from Cenostar (USA) were used in this study. Their oxide compositions analyzed by X-ray fluorescence (XRF), along with the physical properties, are given in Table 1. Magnesium acetate solution at a concentration of 0.1 M was used as the hydration agent (HA) to enhance the hydration of RMC. Two RMC-based composites with 0 and 30 wt.% of RMC replaced by cenospheres were investigated. The mixes were designated as M100C0 and M70C30, respectively. The magnesium acetate solution to solid weight ratio was maintained at 0.6.

Table 1 Oxide compositions and physical properties of RMC and cenosphere

	Oxide compositions										Physical properties
	SiO_2	Al_2O_3	Fe_2O_3	CaO	MgO	SO_3	Na_2O	K_2O	TiO_2	P_2O_5	Specific gravity (g/cm^3)
RMC	1.42	0.55	0.98	2.71	93.80	0.16	-	0.05	0.01	0.14	3.02
Cenosphere	56.22	33.24	2.99	1.57	-	0.36	2.90	1.13	1.19	0.13	0.85~0.95

2.3 Methods

Compression tests were conducted to examine the mechanical behavior of composites with or without cenosphere replacement. The cast samples for all composites were produced using cylindrical molds of Ø25 mm x 25 mm. The cast samples were stored in a sealed box at room temperature (22 ± 2°C) and with a relative humidity of 99% for 3 days to ensure adequate hydration. Then, all samples were transferred into a chamber with an environment of 20% CO_2 and 80% RH at 30 °C to accelerate the carbonation. The compressive strengths of all samples were evaluated after 7 days of exposure to the accelerated carbonation. The density of samples was measured using a helium-based pycnometer (AccuPy II, Micromeritics, USA). The thermal conductivities of the cylindrical samples were measured using a Hot Disk TPS 500 S thermal analyzer (Thermtest, Sweden). Identification of hydration and carbonation phases within samples was performed by X-ray diffraction (XRD) and thermal gravimetric analysis (TGA). XRD patterns were recorded on a PANalytical Empyrean spectrometer using Cu Kα radiation source (40 kV, 40 mA) with a scanning rate of 0.02 ° 2θ/step from 5 to 55 ° 2θ. A data collection time of 200s per step was adopted. TGA was conducted on a Netzsch TG 209 F1 thermogravimetric analyzer from 25 °C to 1000 °C with a heating rate of 10 °C/min under nitrogen flow at a flow rate of 100 ml/min.

3. Results and discussion

3.1 Compressive strength, density, and thermal conductivity

The measured properties for M100C0 and M70C30 samples are presented in **Table 2**. The M100C0 samples achieved an average compressive strength of 29.8 MPa after 7-day accelerated carbonation. For M70C30 samples, the compressive strength decreased to 22.7 MPa, which was 24% less than the ones with M100C0. The average density of the M100C0 and M70C30 samples was 2.18 g/cm^3 and 1.76 g/cm^3, respectively. The density was reduced by 19% for M70C30 samples mainly because of the hollow and lightweight nature of the cenospheres. The specific compressive strength of RMC-based samples only reduced by 6% from 13.7 kN·m/kg to 12.9 kN·m/kg with the addition of cenospheres. Besides, the thermal conductivity reduced significantly from 1.536 W/mK to 0.602 W/mK, which was 61%, with the incorporation of only 30 wt.% cenospheres due to their hollow nature creating an insulating effect. The

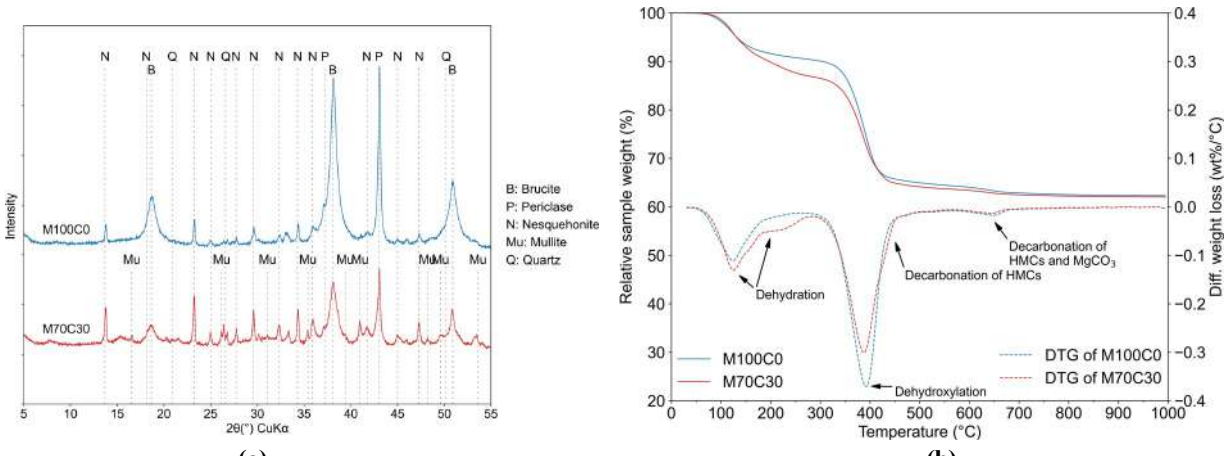
results demonstrated that incorporating cenospheres in the RMC paste provided reduced structural weight and thermal conductivity without compromising the mechanical properties significantly.

Table 2 Properties of M100C0 and M70C30 samples carbonated for 7 days

Property	M100C0	M70C30
Density (g/cm3)	2.18 ± 0.03	1.76 ± 0.04
Compressive strength (MPa)	29.8 ± 1.0	22.7 ± 0.2
Specific compressive strength (kN·m/kg)	13.7	12.9
Thermal conductivity (W/mK)	1.536 ± 0.053	0.602 ± 0.056

3.2 Hydration and carbonation phases

Fig.1 (a) presents the XRD results of M100C0 and M70C30 samples with a 7-day carbonation period. The main phases observed in the M100C0 sample were unhydrated periclase, brucite, nesquehonite, and a small amount of quartz from raw materials. While after the incorporation of 30% cenospheres in the RMC, intenser peaks of nesquehonite can be observed compared with the M100C0 sample. The main phases present in cenospheres used in this study are mullite and quartz. The introduction of cenospheres also led to a reduction of peak intensities for uncarbonated brucite. As the hydration product of MgO, brucite will be consumed by reacting with CO_2 and H_2O and beings transformed into hydrated magnesium carbonates, mainly nesquehonite, in this study. The combination of less RMC content available in M70C30 and increased carbonation capability both contributed to the reduction in the amount of brucite with the incorporation of 30% cenospheres. Since the unhydrated periclase peaks were still presented in M70C30, which contained less MgO, it indicates that the transformation from MgO to $Mg(OH)_2$ had reached its upper limit without depleting the MgO content for both composites. As a result, it is postulated that enhanced carbonation was the main reason for the reduction of brucite content in composites incorporated with cenospheres. The quantification results based on XRD-Rietveld analysis are provided in **Table 3**. The results reveal a significant reduction in the brucite content following the inclusion of cenospheres during carbonation, confirming its conversion to nesquehonite. This finding suggests that the addition of cenospheres has effectively facilitated the formation of nesquehonite in the M70C30 samples, thereby enhancing the carbonation process within the system.



(a) **(b)**

Fig.1 (a) XRD and (b) TGA results for M100C0 and M70C30 samples carbonated for 7 days

Table 3 Phase contents based on XRD-Rietveld analysis and weight loss based on the RMC content in each mix for M100C0 and M70C30 samples at 7 days

		M100C0	M70C30
Phase contents based on XRD-Rietveld analysis	Periclase	20.1	15.3
	Brucite	73.8	45.1
	Nesquehonite	6.0	27.8
	Mullite	0.0	11.9
	Goodness of fit	5.1	3.5
Weight loss per RMC content at different temperature stages	40 – 300 °C	9.90	19.23
	300 – 460 °C	24.53	31.13
	460 – 900 °C	3.20	3.79

The weight loss and differential weight loss results for both composites after 7 days of carbonation are presented in **Fig.1 (b) and Table 3**. The endothermic peaks of dehydration, dehydroxylation, and decarbonation were annotated in the figures. As shown in **Fig.1 (b)**, early weight loss in samples up to around 300 °C was attributed to the dehydration of water bonded to HMCs. It can be observed that the hump in the range of 125 °C to 300 °C broadened with the incorporation of cenospheres. The increase in weight loss in this temperature region suggested an increase of hydrated carbonation products in M70C30 samples which is consistent with the XRD results. The strong endothermic peaks with centers at 390 °C were due to the dehydroxylation of brucite. The significant reduction in the content of brucite in M70C30 was attributed to its transformation into hydrated carbonation products. A shoulder peak at approximately 440 °C accompanied by the brucite peak corresponds to the decarbonation of HMCs. An increase in the shoulder's intensity and width confirms the higher content of HMCs in the M70C30 sample. Decarbonation peaks at 530 °C and 650 °C were attributed to the decomposition of HMCs and $MgCO_3$, which is postulated that these phases were inherent in the raw RMC. The quantitative analysis reveals that a substantial proportion of weight loss takes place within the temperature range of 300-460 °C. This weight loss can be primarily attributed to the dehydroxylation of uncarbonated brucite or certain hydrated magnesium carbonates, as well as the decarbonation of nesquehonite (Dung and Unluer, 2016). It is worth noting that pastes with higher cenosphere content demonstrate a more pronounced weight loss, indicating a more extensive decomposition of hydration and carbonation products.

4. Conclusion

The current study systematically investigated the influence of cenospheres on the density, compressive strength, thermal conductivity, and hydration and carbonation products of RMC-based paste. The RMC-based samples incorporating 30 wt. % of cenospheres show excellent performance with a significant reduction (61%) in thermal conductivity compared to the pure RMC samples. Although the compressive strengths of the RMC-based paste have been reduced by incorporating cenospheres, only a small decrease (6%) in specific compressive strength was observed.

In addition, XRD and TGA results show that cenospheres in the RMC matrix promoted the formation of hydrated carbonation phases, specifically nesquehonite. The XRD quantification results prove that the incorporation of cenospheres in RMC-based composites has greatly increased the CO_2 sequestration potential of RMC. The conclusions point towards an effective way of enhancing the carbonation of RMC samples and provide useful information for the further development of lightweight thermal insulation RMC-based composites.

Acknowledgments

This work was supported by the NYUAD Center for Interacting Urban Networks (CITIES), funded by Tamkeen under the NYUAD Research Institute Award CG001. The authors also thank Tamkeen for funding the NYUAD Water Research Center under the NYUAD Research Institute Award (project CG007).

References

Blanco, F. *et al.* (2000) "Characteristics and properties of lightweight concrete manufactured with cenospheres", *Cement and Concrete Research*, 30(11), pp. 1715–1722.

Dung, N.T. *et al.* (2019) "Formation of carbonate phases and their effect on the performance of reactive MgO cement formulations", *Cement and Concrete Research*, 125, p. 105894.

Dung, N.T. and Unluer, C. (2016) "Improving the performance of reactive MgO cement-based concrete mixes", *Construction and Building Materials*, 126, pp. 747–758.

Dung, N.T. and Unluer, C. (2017) "Carbonated MgO concrete with improved performance: The influence of temperature and hydration agent on hydration, carbonation and strength gain", *Cement and Concrete Composites*, 82, pp. 152–164.

Hanif, A., Lu, Z. and Li, Z. (2017) "Utilization of fly ash cenosphere as lightweight filler in cement-based composites – A review", *Construction and Building Materials*, 144, pp. 373–384.

Hay, R. and Celik, K. (2022) 'Enhancing carbonation of magnesium oxide (MgO) cement (RMC)-based composites with calcined limestone," *Cement*, 9, p. 100037.

Hay, R., Peng, B. and Celik, K. (2023) "Filler effects of CaCO3 polymorphs derived from limestone and seashell on hydration and carbonation of reactive magnesium oxide (MgO) cement (RMC) ", *Cement and Concrete Research*, 164, p. 107040.

Hay, R. et al. (2023) "Proportioning, carbonation, performance assessment, and application of reactive magnesium oxide cement–based composites with superplasticizers", *Journal of Materials in Civil Engineering*, 35(2), p. 04022405.

Rheinheimer, V. et al. (2017) "Multi-scale study of high-strength low-thermal-conductivity cement composites containing cenospheres", *Cement and Concrete Composites*, 80, pp. 91–103.

Shahbaz, F. et al. (2022) "Life cycle assessment of brucite and synthetic MgO produced from reject brine using different alkalis", *Journal of Cleaner Production*, 380, p. 135071.

Unluer, C. and Al-Tabbaa, A. (2013) "Impact of hydrated magnesium carbonate additives on the carbonation of reactive MgO cements", *Cement and Concrete Research*, 54, pp. 87–97.

Vandeperre, L.J. and Al-Tabbaa, A. (2007) "Accelerated carbonation of reactive MgO cements", *Advances in Cement Research*, 19(2), pp. 67–79.

Walling, S.A. and Provis, J.L. (2016) "Magnesia-Based Cements: A Journey of 150 Years, and Cements for the Future?", *Chem. Rev.*, p. 35.

The 16th International Congress on the Chemistry of Cement 2023 (ICCC2023)
"Further Reduction of CO_2 -Emissions and Circularity in the Cement and Concrete Industry"
September 18–22, 2023, Bangkok, Thailand

Shrinkage in carbonatable binders: Are the cementitious standards applicable for non-hydraulic lime-cement systems?

G.S. Munhoz[1*] and G. Ye[2]

[1] *Delft University of Technology, Delft, The Netherlands*
Email: g.dasilvamunhoz-1@tudelft.nl
[2] *Delft University of Technology, Delft, The Netherlands*
Email: g.ye@tudelft.nl

ABSTRACT

Recently approved regulations that aim to mitigate the release of greenhouse gases have been pushing the construction industry into reducing its carbon dioxide (CO_2) footprint. Therefore, promoting new low-carbon cements and carbonatable binders have been some of the strategies adopted. Lime has been trending as a green binder because it consumes less energy during production and due to the CO_2 capture during its hardening process. However, a new generation of binders demands a new generation of characterization standards. Given the absence of guidelines to measure the shrinkage of air lime-cement systems, the suitability of cementitious standards – ASTM C191:2021 (Vicat setting), ASTM C1698:2019 (autogenous shrinkage), and EN 12390-16:2019 (total shrinkage) – was addressed. Four mixtures were studied (C0L100, C33L67, C50L50, and C100L0). The first digit corresponds to the cement (CEM II/A-L 32.5R), and the second corresponds to the air lime (CL90S) content, both in the percentage of binder volume. Regarding the Vicat setting, the samples could be measured satisfactorily. On the autogenous shrinkage, the lack of interaction with CO_2 prevented lime carbonation, meaning limited hardening for those samples. Therefore, ASTM C1698:2019 was not suitable for lime-based materials. For the total shrinkage, EN 12390-16:2019 was suitable but complementary tests are needed to distinguish individual contributions (chemical, autogenous, and carbonation) to the total shrinkage. The results showed expansion for the groups with lime (especially for lime-cement, where lime acted as a catalyst). The expansion was associated with the carbonation of the unbounded portlandite. Finally, future studies should investigate chemical and carbonation shrinkage at early ages since the autogenous method was not capable of monitoring the volume instability of lime-based mortars.

KEYWORDS: *Air lime; carbon capture; cementitious standards; shrinkage.*

1. Introduction

Looking back to the past, it is impossible not to mention the construction works based on different processes using lime as a binder. Alvarez et al (1995) wrote about how Egyptians, Chinese, Mayans, Greek, Romans, and other civilizations relied on air and hydraulic lime for more than 7,000 years to promote infrastructure development in their societies. Every civilization empirically mastered the work with lime (as much as they could), and this expertise was spread and improved through the generations.
Lanas et al (2004) and Carran et al (2012) argue that the constant search for advances led Joseph Aspdin, in 1824, to come up with a ground-breaking alternative to lime binders: the Portland cement. The material that could set and develop strength faster, with more consistent behavior and better water-tightness capacity, quickly overtook the construction market. The overtake by the Portland cement has been solid enough to persist until today (Mehta and Monteiro (2006)). That said, lime – which was once widely employed as a building solution – has now been mostly limited to the conservation of the built heritage and masonry applications, as shown by Oliveira et al (2017) and Olaniyan (2020).
Despite the decaying trend for lime-based applications, the growing environmental concerns related to Portland cement have questioned its status quo. Hence, new sustainable alternatives have been studied, such

as supersulfated cement (Pinto et al (2020)), alkali-activated materials (Li et al (2021)), and lime itself (Olaniyan (2020)) – given its CO_2 absorption capacity and lower temperatures during production.
One might wonder about the relevance of studying lime since it dates several thousand years. Well, as briefly addressed before, all the expertise around lime was either empirical and got lost with time or has become obsolete with the industrialization of the lime production process. The Pyramids, Greek temples, and Roman monuments were most likely lime-based built (Alvarez et al (1995)), but we still do not know how. Therefore, to overcome this scenario, the chemical, physical, and mechanical characterization of lime has been the scope of several researchers in the past decades (Cizer et al (2012); Pavía and Brennan (2018); Vasović et al (2021)). However, one of the biggest problems that remain is the absence of standardized test protocols and replicable literature studies.
Thus, the objective of this paper is to raise awareness for the lack of standards in the characterization of lime-based materials. To do so, we assess the applicability of the standards available for cementitious binders focusing on the volume instability, more precisely, the shrinkage behavior of air lime-based materials. Understanding the shrinkage in lime-based materials is of fundamental relevance because this way, we can ensure that the durability and the structural integrity of new and historic buildings are not jeopardized in the short or long term due to volumetric changes.

2. Materials and Methods

The shrinkage behavior of four mixtures was monitored (C100L0, C50L50, C33L67, C0L100). The first (after C) and second (after L) digits correspond to the cement and lime volume contents (%), respectively.

2.1 Materials

The mortar mixtures were produced with hydrated air lime (type CL90S) and Portland cement with added limestone (CEM II/A-L 32.5R). Siliceous sand (granulometry 0 – 2 mm) and potable tap water was used in the mixtures. The chemical characterization of the binders is described in Table 1.

Table 1 - Chemical composition (%) of the binders determined by XRF

	CaO	SiO_2	Al_2O_3	Fe_2O_3	SO_3	MgO	K_2O	TiO_2	Na_2O	Others[1]
Air lime	98.72	0.12	0.06	0.06	0.07	0.80	0.03	-	0.03	0.10
Cement	73.16	15.44	3.67	3.13	2.54	0.92	0.37	0.28	0.19	0.30

[1]It may include negligible contents of P_2O_5, SrO, Cl, ZnO, MnO, BaO, ZrO_2, PbO, Rb_2O, and Y_2O_3.

Regarding the sand, the loose bulk density was 1.76 g/cm^3, the specific gravity was 2.62 g/cm^3, and the water absorption was 0.07 %. The mineralogical composition was determined by XRD (scan 5° - 75°, counting time per step 1.25 s, step size 0.020° 2θ), showing SiO_2 as the major compound. The mortars were designed following the 165 mm consistency recommended by EN 459-2:2021. The mixing procedure followed EN 196-1:2016. The mixture composition of the mortars is shown in Table 2.

Table 2 - Mixture details at the mortar level

Group	Cement (kg/m^3)	Lime (kg/m^3)	Sand (kg/m^3)	Water (kg/m^3)
C100L0	340	-	1677	252
C50L50	176	65	1741	248
C33L67	118	86	1742	256
C0L100	-	131	1760	265

2.2 Methods

This study addresses some of the available standards (i.e., ASTM C191:2021, ASTM C1698:2019, and EN 12390-16:2019) applicable to cementitious materials to characterize the shrinkage behavior in air lime-based systems cured according to EN 1015-11:2019. A brief description is stated in sequence.

- ASTM C191:2021 – Vicat setting: the "Method B" was chosen to determine the setting time (and as a requirement for the autogenous shrinkage test) because it is a relatively simple procedure. It uses equipment that is generally available in laboratories (favoring replicability), and it allows moisture and CO_2 exchange with the environment (thus, carbonation). Results are an average between two replicates. The setting was measured under (53 ± 1) % RH and (19 ± 1) ºC. Results were treated statistically.

- ASTM C1698:2019 – Autogenous shrinkage: This approach allows measuring the shrinkage under isothermal conditions and no-moisture exchange even before demolding, which is relevant for lime-cement systems, since demolding takes place between 1-3 days (lime content < 50%, in mass) or 5 days (cement content < 50% in mass), according to EN 1015-11:2019. Results are an average between two replicates. Autogenous shrinkage was measured in sealed specimens at the mortar level up to 28 days after casting and under (53 ± 1) % RH and (19 ± 1) ºC. Results were treated statistically.

- EN 12390-16:2019 – Total shrinkage: The total length change was measured considering the moisture, temperature, and CO_2 interaction. Results are an average between two replicates, measured up to 56 days after casting. After curing, specimens were stored under (53 ± 3) % RH and (19 ± 3) ºC.

3. Results and Discussion

The setting times according to the ASTM C191:2021 and the results on the autogenous shrinkage measurements according to ASTM C1698:2019 are summarized in Table 3.

Table 3 - Final setting and autogenous shrinkage results

	Final setting (hours:minutes:seconds)	Autogenous shrinkage (µm/m)					
		0 days	1 day	3 days	5 days	7 days	28 days
C100L0	04:38:00	0.000	1.955	-3.713	-4.946	-7.754	-13.500
C50L50	08:37:43	0.000	1.698	-0.856	-0.778	-0.626	-2.875
C33L67	12:30:00	0.000	6.180	4.226	3.990	2.983	2.359
C0L100	35:22:50	0.000	299.540	383.097	409.847	420.115	461.910

As seen in Table 3, the final set took longer for the mixtures with greater lime content, as expected. The slow setting in lime-based materials is associated with the limited availability of alumina and silicate phases (see Table 1). According to Cizer et al (2012), the setting of air lime relies on the drying of excess water (which might lead to shrinkage) and the carbonation (from the surface inwards). Thus, considering the results obtained and the data available in the literature, the ASTM C191:2021 proved to be a reasonable approach to measure the setting time of lime-based systems.
Regarding the autogenous shrinkage, given the sealed environment, no carbonation (hence, limited hardening) was expected within the lime-based groups. This behavior was confirmed, as seen in Table 3. The greater the lime content, the greater the expansion. This expansion does not necessarily represent a length increase but (most likely) the dissolution of $Ca(OH)_2$. This hypothesis agrees with Fourmentin et al (2015). In contact with water, the hydrated lime releases the Ca^{+2} and hydroxyl ions. In contact with cement, it alters the precipitation and growth rate of C-S-H (leading to reassociation and shrinkage). A future investigation into the chemical shrinkage is needed to detail this behavior.
The total shrinkage is shown in Figure 1. While cement shrunk and lime-cement specimens expanded, pure lime specimens remained practically stable, proving that the lime-cement interaction caused the specimens to behave differently than the pure lime/cement ones.

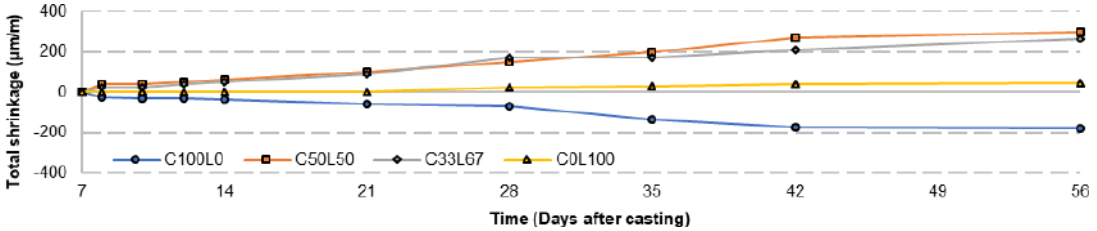


Figure 1 - Progress of the total shrinkage

It is known that while the carbonation of calcium-based phases in cement leads to reassociation (and, thus, shrinkage), the calcium-based elements in lime are not as strongly bonded, and its carbonation promotes expansion (Li et al (2020)). This explains the behavior observed in Figure 1. In addition, Fourmentin et al (2015) showed that, in contact with cement, lime act as a catalyst, which explains the different behavior of the lime-cement groups. According to Fourmentin et al (2015), in lime-cement systems, lime-based precipitations usually happen in the cement pores (from the surface inwards). Thus, chemical and physical investigations on the pore structure are needed to confirm this theory.

4. Conclusions

Lime has been trending as a greener solution to Portland cement due to its lower calcination temperature and CO_2 binding capacity. However, its characterization remains a challenge due to the absence of standards and replicable studies. This paper addressed cementitious standards to characterize the shrinkage behavior of lime-based systems. ASTM C191:2021 was adequate to measure the setting time. The autogenous shrinkage proposed by ASTM C1698:2019 was not suitable due to the lack of hardening. The EN 12390-16:2019 procedures for total shrinkage were adequate, but the curing conditions established by EN 1015-11:2019 must be taken into consideration. Complementary tests are needed to understand the individual influence of drying and carbonation on the shrinkage behavior and the pore structure.

Acknowledgements

This research has been carried out within the framework of the EU SUBLime network. This Project has received funding from the European Union's Horizon 2020 research and innovation programme under Marie Sklodowska-Curie project SUBLime [Grant Agreement n◦955986].

References

Álvarez, J.I., Martín, A. and García Casado, P.J. (1995) "Historia de los morteiros", *Revista PH*, 13: 52-73

Carran, D., Hughes, J., Leslie, A. and Kennedy, C. (2012) "A Short History of the Use of Lime as a Building Material Beyond Europe and North America", *International Journal of Architectural Heritage*, 6: 117-146

Cizer, O., Rodriguez-Navarro, C., Ruiz-Agudo, E., Elsen, J., Van Gemert, D. and Van Balen, K. (2012) "Phase and Morphology Evolution of Calcium Carbonate Precipitated by Carbonation of Hydrated Lime", *Journal of Materials Science*, 47: 6151-6165

Fourmentin, M., Faure, P., Gauffinet, S., Peter, U., Lesueur, D., Daviller, D., Ovarlez, G. and Coussot, P. (2015) "Porous structure and mechanical strength of cement-lime pastes during setting", *Cement and Concrete Research,* 77: 1-8

Lanas, J., Bernal, J.L.P., Bello, M.A. and Galindo, J.I.A. (2004) "Mechanical Properties of Natural Hydraulic Lime-Based Mortars", *Cement and Concrete Research*, 34: 2191-2201

Li, B., Sun, Z., Hu, K. and Yang, J. (2020) "Influence of carbonation on the volume change of hardened cement pastes", *Construction and Building Materials*, 260: e119709

Li, Z., Delsaute, B., Lu, T., Kostiuchenko, A., Staquet, S. and Ye, G. (2021) "A Comparative Study on the Mechanical Properties, Autogenous Shrinkage and Cracking Proneness of Alkali-Activated Concrete and Ordinary Portland Cement Concrete", *Construction and Building Materials*, 292: e123418

Mehta, P.K. and Monteiro, P.J.M. (2006) *Concrete: Microstructure, Properties and Materials*, McGraw Hill, NYC

Olaniyan, S.A. (2020) "Impact of Changing Microstructural Compositions of Lime Based Mortar on Flexibility: Case Study of Sustainable Lime-Cement Composites", *Advances in Science, Technology and Engineering Systems Journal*, 5: 1488-1498

Oliveira, M.A., Azenha, M., Lourenço, P.B., Meneghini, A., Guimarães, E.T., Castro, F., and Soares, D. (2017) "Experimental Analysis of the Carbonation and Humidity Diffusion Processes in Aerial Lime Mortar", *Construction and Building Materials*, 148: 38-48

Pavia, S. and Brennan, O. (2018) "Portland Cement-Lime Mortars for Conservation", *Historic Mortars*, 129–142.

Pinto, S.R., Angulski da Luz, C., Munhoz, G.S. and Medeiros-Junior, R.A. (2020) "Durability of Phosphogypsum-Based Supersulfated Cement Mortar against External Attack by Sodium and Magnesium Sulfate", *Cement and Concrete Research*, 136: e106172

Vasović, D., Terzovic, J., Kontic, A., Okrajnov-Bajic, R. and Sekularac, N. (2021) "The Influence of Water/Binder Ratio on the Mechanical Properties of Lime-Based Mortars with White Portland Cement", *Crystals*, 11: e958

The 16th International Congress on the Chemistry of Cement 2023 (ICCC2023)
"Further Reduction of CO_2 -Emissions and Circularity in the Cement and Concrete Industry"
September 18–22, 2023, Bangkok, Thailand

Compressive strength, pore structure and hydration of alkali-activated slag-waste ceramic powder-silica fume ternary system

Y. Deng[1,2,3], Z. Zhang[4*], and C. Shi[1,2,3]

[1] *Key Laboratory for Green & Advanced Civil Engineering Materials and Application Technology of Hunan Province , College of Civil Engineering, Hunan University, Changsha, 410082, P. R. China*
[2] *International Science Innovation Collaboration Base for Green & Advanced Civil Engineering Materials of Hunan Province, Hunan University, Changsha, 410082, P. R. China*
[3] *Key Laboratory of Building Safety and Energy Efficiency of the Ministry of Education, Hunan University, Changsha, 410082, P. R. China*
Email: dengyulin@hnu.edu.cn (Y. Deng) cshi@hnu.edu.cn (C. Shi)
[4] *Key Laboratory of Advanced Civil Engineering Materials of Ministry of Education, School of Materials Science and Engineering, Tongji University, Shanghai, 201804, P. R. China*
** Corresponding author E-mail: zhangzuhua@tongji.edu.cn*

ABSTRACT

The preparation of alkali-activated materials can eliminate a large number of industrial by-products, and has the advantages of low resource and energy consumption and low CO_2 emission. However, green construction is now difficult to achieve only through the application of mature industrial by-products such as ground granulated blast furnace slag (GGBS) or silica fume (SF). Therefore, it is necessary to consider using more types of industrial waste, e.g. ceramic waste, in construction. The effects of slag-ceramic ratio, silica fume content on compressive strength, pore structure and hydration degree of alkali-activated slag-waste ceramic powder (WCP)-silica fume mortars have been investigated. With the increase of waste ceramic powder content, the compressive strength of mortar increased first and then decreased. This is related to the combined effects of smaller porosity and reduced reaction degree. Therefore, the correlation between the compressive strength, pore structure and hydration of alkali-activated slag-waste ceramic powder-silica fume ternary mortar was investigated. The results of this paper are conducive to a better understanding of the utilization of waste ceramic powder on alkali-activated material.

KEYWORDS: *Waste ceramic powder, Alkali-activated material, Compressive strength, Hydration, Microstructure*

1. Introduction

Alkali-activated materials (AAMs) are a new type of water-hard cementitious material obtained by the reaction of precursor with a certain amount of alkaline substances, such as sodium hydroxide solution and water glass solution, at room temperature or under high temperature. In recent decades, there has been considerable interest in the use of industrial by-products, such as granulated blast furnace slag (GGBS), silica fume (SF), fly ash, kaolin, burnt coal gangue, steel slag, and so on, as precursors of AAMs in order to reduce the environmental impact associated with the production of cement.

China has long been the world's top producer and consumer of ceramics. More than 20 million tons of ceramic waste are produced per year during the manufacture and utilization of ceramics (Sun et al. 2022). The use of ceramic waste to developing low-carbon AAMs can reduce the waste of land resources needed to landfill ceramic waste, as well as air and water pollution; additionally, it can decrease the expense of cement preparation and contribute to the growth of economic benefits.

WCP is typically not utilized as the only precursor but instead is blended with slag, fly ash, and metakaolin for the preparation of AAMs because it generally exhibits low alkaline activity. Some researchers have investigated the potential of waste ceramic powder (WCP) as an alkali-activated precursor of high-

performance AAMs. They found that the waste ceramic powder can improve the workability, mechanical strength, and durability of alkali-activated mortars. Huseien et al. (2019) reported that the workability of the alkali-activated slag-ceramic mixture or alkali-activated ceramic-slag-fly ash system can be enhanced by incorporating WCP. However, AAMs can show better or worse compressive strength with increasing ceramic content in different research. This implies that the underlying mechanism of ceramics affecting the compressive strength of AAMs is still not understood. Thus, this paper aims to clarify the effect of WCP on compressive strength of AAMs, and to achieve a better understanding of the relationship between microstructure, hydration degree, and mechanical strength.

2. Experimental

2.1 Materials

The chemical composition of GGBS, WCP and SF can be determined by X-ray fluorescence analysis, as shown in Table 1. The particle size ranges from 1.4 μm to 148 μm, and d_{50} is 16.11 μm. Industrial-grade NaOH powder (AR) with a purity of more than 99%. An industrial-grade $Na_2O{\cdot}3.3SiO_2$ with a concentration of 38.5% is used.

Table 1. Chemical composition of slag

	SiO_2	Al_2O_3	CaO	Fe_2O_3	MgO	Na_2O	K_2O	SO_3	LOI
GGBS	26.61	15.67	42.73	1.64	4.35	0.39	0.47	2.14	3.60
Waste ceramic powder	70.37	19.9	0.85	1.55	1.41	2.3	3.01	0.06	
Silica fume	95.38	-	1.84	0.61	0.26	0.16	-	-	2.48

2.2 Mixture design, sample preparation and test methods

By mixing NaOH powder and 38.5% $Na_2O{\cdot}3.3SiO_2$ solution, the alkali activator with a modulus of 1.0 was obtained. The activator was set at a fixed Na_2O dosage of 4%. The water/binder (w/b) ratio was 0.4 and the binder/sand ratio was 1:3. The composition of the binders is given in Table 2.

Table 2. Binder composition and compressive strengths of corresponding mortars

	C70S30	C50S50	C80S20	C0S100	SF5	SF10
GGBS	30	50	80	100	47.5	45
Waste ceramic powder	70	50	20	0	47.5	45
Silica fume	0	0	0	0	5	10
Compressive strength at 7 d (MPa)	41.1	59.9	73.5	77.5	59.4	54.0
Compressive strength at 28 d (MPa)	50.9	78.9	96.2	85.7	67.5	66.4

Pour the prepared activator solution into the mixing pot first, then add slag powder, and stir at low speed for 120s. Then stop for 15s, scrape the slurry from the blade and wall into the pot, and finally stir at high speed for 120s. All samples are prepared at room temperature (about 20°C).

The heat release of the reaction of the binders was conducted at 20 ± 0.02 °C using TAM Air Calorimeter. Binder components of about 4 g were placed into an ampoule bottle and then placed into the calorimeter. The required water or alkaline solution was injected and mixed for about 3 min. When the solution was injected into the bottle, the data acquisition system commenced at the same time. Each measurement lasted for 3 days.

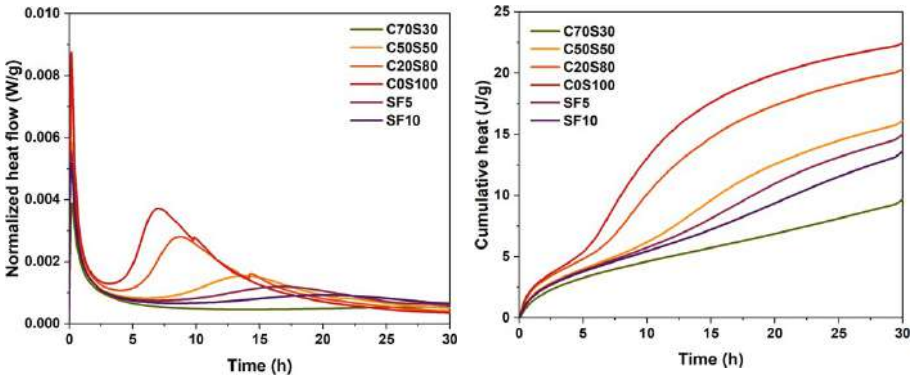
The paste is soaked in absolute ethanol for 2 days to stop the reaction, then taken out and placed in a vacuum oven at 40°C to dry for 30 hours. Samples are ground into powder and passed through a 300-mesh sieve. The powder is analyzed by Netzsch STA 409PC thermal analyzer with a measured temperature range of 50°C -850°C, and the heating rate is 10 °C /min.

Using a MAG-MED proton nuclear magnetic resonance spectroscopy (NMR) PM-1030, operating at 10 MHz, the total porosity and pore distribution of the cylindrical samples were assessed at 28d. The intrinsic spectrometer's dead time was 15 s, and the 90° pulse's length was 100 ns. A sample was placed in an NMR glass tube provided by the NMR manufacturer and then in the NMR machine after being initially saturated with clean water under vacuum for 48 hours using an automated water saturation system. The T_2 relaxation time was measured using Carr-Purcell-Meiboom-Gill (CPMG) measurements with a 30 mm probe to create the recorded NMR signals. The decay of the CPMG echo intensity was subjected to the inverse Laplace

transform technique. 64 scans were performed, with a recycle delay of 5 s and a sampling interval of 0.08 s. Before then, a standard was measured using a known amount of water.
According to GB/T 50081, the compressive strength of the cubic samples was measured after 7 and 28 days at room temperature. Using a TYA-300B machine, the tests were conducted at a 2.4 kN/s loading rate. Three samples of each mixture were examined, and this publication reports the mean value.

3. Results and discussion

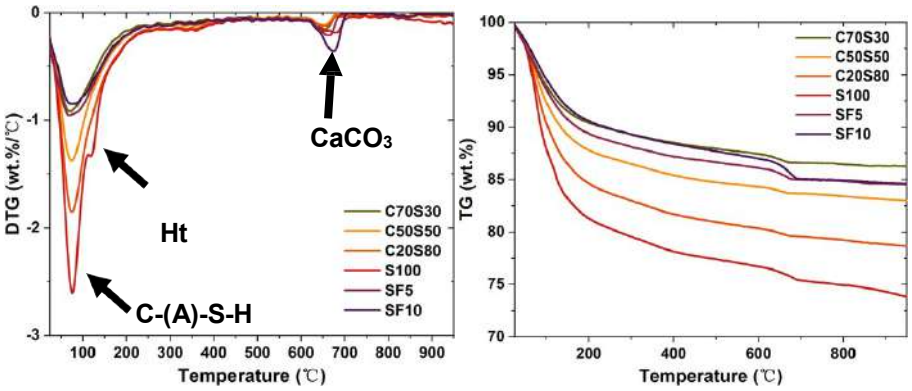
The compressive strength results of mortars at 7 d and 28 d are shown in Table 1. The 7-day compressive strength decreases with the increasing content of the waste ceramic powder. And the 28-day compressive strength increases first and then decreases with the content of ceramic powder, reaching 96.2 MPa when the content of WCP is 20%. For silica fume, it decreases slightly both 7- and 28-day compressive strength of alkali-activated ceramic-slag mortars.
The exothermic reaction during alkali activation can be measured by isothermal calorimetry. Figure 1 shows the hydration heat curves for different WCP contents. An exothermic peak occurred immediately within a few minutes after the slurry was added to the isothermal calorimeter, mainly related to the wetting of the solid powder material, indicating that the solid powder began to dissolve. With the increase of ceramic powder content and silica fume content, the initial heat release peak decreases, indicating that the initial dissolved heat release of ceramic powder and silica fume is less than that of slag.
After about 3–7 hours, a brief period of dormancy started. The thermal evolution curve of the pastes showed a clear second exothermic peak after the induction period, which is primarily connected to the exothermic process of alkali-activated material depolymerization-polycondensation and is associated with the creation of gel phase hydration products. The second exothermic peak demonstrates that the exothermic peak declined with rising WCP concentration. The total heat release is greatest when the WCP content was 0%, followed by C20S80, C50S50, SF5, SF10 and C70S30, as shown in Fig. 1(b). Overall, the inclusion of WCP and SF decreases the exotherm during the induction phase, the total hydration heat and the exotherm during the polymerization reaction.



(a) Heat release rate **(b) Heat of reaction**

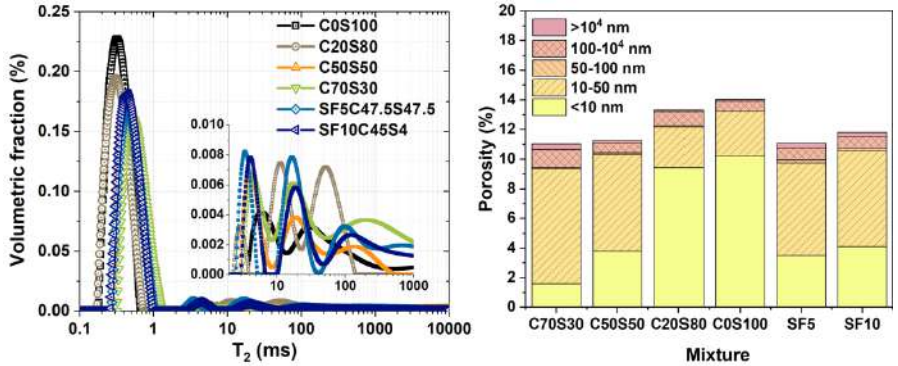
Figure 1. Heat evolution for different binders

Fig 2 shows the TGA and DTG curves of samples cured for 28 d. At 28 d, all samples with ceramic powder included similar hydration products: C-(A)-S-H gel and calcium carbonate ($CaCO_3$). In addition, S100 sample also reacted to produce hydrotalcite (Ht). With the increasing content of WCP and SF, C-(A)-S-H gel content gradually decreases. This might contribute to the low activity of waste ceramic powder.
Fig 3 shows the T_2 distribution and corresponding pore distribution statistics. WCP reduces the porosity of mortars, especially for pores below 50 nm (roughly corresponding to T_2 being 1 mm). While the pore below 10 nm decreases and the pore between 10-50 nm increases because C-S-H gel (gel pore less than 10 nm) is converted to C-(A)-S-H gel (gel pore mainly tens of nanometers) when WCP included. SF slightly increases the porosity and large pore content without changing the diameters of micro- and macro-pores. This could be a result of the worse workability caused by the silica fume's high specific surface area. In short, WCP reduces the porosity and makes the pores less than 50 nm rougher; SF slightly increases the porosity and leads to more macro-pores.



(a) DTG (b) TGA

Figure 2. DTG and TGA curves of sample cured for 28 d



(a) T_2 (b) Pore distribution

Figure 3. T_2 curves and pore distribution of sample cured for 28 d

In general, the porosity and gel content of a material influence its strength. Although ceramic powder's low activity means that it decreases gel content at 28 d, it can fill capillary pores and lessen porosity, which benefits strength. The 28 d-compressive strength can be maximized after the ceramic powder reaches the proper dosage (20% in this study), while the 7 d-compressive strength keeps decreasing with the increase of ceramic content, because the negative effect of the degree of early reaction on the strength of WCP outweighs the positive effect of the decrease in porosity. More research is required since gel and pore are related to the particle size and reactivity of WCP.

4. Conclusions

20% WCP increased the 28-day compressive strength of alkali-activated slag mortar by 12.3%, and SF caused a decrease in strength and reduced gel. WCP reduces the porosity while SF increases the porosity. The negative effect of ceramics on reactivity degree and the positive effect on porosity co-affect the compressive strength.

Acknowledgments

The authors are grateful for the financial support from the National Natural Science Foundation of China project U2001225.

References

Sun, X.W., Shao, J.H., Wang, Q.S. and Wu, L.H. (2022) “Talking about the Research on the Recycling of Waste Ceramics”, *Foshan Ceramic*, 32(11): 45-47

Huseien, G.F., Sam, A.R.M., Shah, K.W., Asaad, M.A., T., M.Md. and Mirza, J. (2019) “Properties of ceramic tile waste based alkali-activated mortars incorporating GBFS and fly ash”, *Construction and Building Materials*, 214: 355-368

The 16th International Congress on the Chemistry of Cement 2023 (ICCC2023)
"Further Reduction of CO_2 -Emissions and Circularity in the Cement and Concrete Industry"
September 18–22, 2023, Bangkok, Thailand

Hydration, microstructure and macro-properties of high belite MgO expansive cement

C. Lyu[1*], C. Yu[2], and J. Liu[3]

[1] *School of Materials Science and Engineering, Southeast University, Nanjing 211189, P.R. China*
Email: chen_lyu@seu.edu.cn
[2] *State Key Laboratory of High Performance Civil Engineering Materials, Sobute New Materials Co., Ltd, Nanjing 211103, P.R. China*
Email: yucheng@cnjsjk.cn
[3] *School of Materials Science and Engineering, Southeast University, Nanjing 211189, P.R. China*
Email: liujiaping@cnjsjk.cn

ABSTRACT

High belite MgO expansive cement is widely used in hydraulic engineering in China to solve the thermal cracking of super large mass concrete. Additionally, the research and application of high belite cement (HBC) is of great significance to effectively reduce the CO_2 emission and energy consumption in full lifecycle of concrete.
In this study, hydration kinetics, hydration products, microstructure, mechanical property and volume deformation of high belite cement-based materials with/without MgO expansive additive (MEA) were investigated. Due to significant differences in mineral compositions, the hydration rate and hydration heat of high belite cement were much lower than ordinary Portland cement (OPC). It leads to slower microstructural formation and development of HBC, which was confirmed by the results of XRD, MIP, SEM and mechanical strength. However, high belite cement-based materials had denser microstructure and higher mechanical strength at later ages because of more C-S-H gels from hydration of C_2S phases. The addition of MEA slightly delayed early hydration of cements but had almost no effect on later hydration and microstructure. Nevertheless, the strength development of mortars especially flexural strength was altered to varying degrees because of expansive stress from MEA hydration. Moreover, hydration of MEA can effectively reduce shrinkage of no matter OPC or HBC over a long period. Interestingly, HBC containing much dead-burnt MgO also showed equally remarkable reduction of volume shrinkage although the hydration degree of dead-burnt MgO proved to be very low. It suggests that dead-burnt MgO in cement itself has stronger potential for long-term compensation of shrinkage.
This work indicates the direct and potential values of high belite MgO expansive cement in improving the service performance of concrete and reducing CO_2 emission from the perspective of hydration and microstructure.

KEYWORDS: *high belite cement, hydration, microstructure, MgO, properties.*

1. Introduction

The thermal shrinkage of mass concrete caused by hydration heat is the important reason for shrinkage cracking of hydraulic engineering. HBC is an environmental-friendly building-materials with low energy consumption and CO_2 emission due to lower limestone, energy demand and calcination temperature in cement production (Cuesta et al (2021)). Because of quite low hydration heat of HBC, it can significantly reduce the internal temperature rise of mass concrete (Wang et al (2018a)). Thus, it is usually used for mass concrete structures in China, i.e. dams. Compensation of shrinkage with delayed expansion of MgO hydration is also an effective method to reduce cracking risk of mass concrete (Mo et al (2014)). MgO expansive cement and MEA are important ways to compensate shrinkage with MgO. Despite high belite MgO expansive cement with low heat release and compensating shrinkage is gradually applied to dams in

recent years, there is a lack of evaluation of its long-term application from the perspective of microstructure and macro-property.
In this study, hydration kinetics, hydration products, microstructural development, mechanical property and volume deformation of high belite MgO cement with/without MEA were investigated.

2. Raw materials and Methodology

OPC (C0), three kinds of high belite MgO expansive cement (C1, C2, C3) and MEA were adopted in this study. The chemical and phase compositions of raw materials are listed in Table 1. The activity value of MEA was 183s by citric acid method (Mo et al (2010)). Quartz sand was used to prepare mortars.

Table 1 Compositions and specific surface areas of raw materials.

	Phase compositions (w.t%)				Chemical compositions (w.t%)							BET
	C_3S	C_2S	C_3A	C_4AF	SiO_2	Al_2O_3	Fe_2O_3	CaO	MgO	SO_3	LOI	m^2/g
C0	52.5	17.5	5.0	8.9	21.50	5.26	2.74	58.78	1.88	3.02	2.33	1.11
C1	36.2	38.8	0.6	13.6	22.69	3.54	4.22	60.24	2.18	2.61	1.82	1.31
C2	31.4	43.4	0.5	12.3	22.13	3.81	4.27	59.10	3.51	2.24	1.27	1.51
C3	20.6	48.3	0.4	12.8	21.24	3.88	4.39	57.04	5.21	1.88	2.27	1.03
MEA	-	-	-	-	3.40	0.57	0.58	1.39	89.20	-	4.87	23.51

For reducing bleeding, the w/c ratio of all pastes was 0.35. In addition to four groups of pure cement paste, another two groups of OPC paste were combined with MEA to maintain the same total MgO content as C1 (2.2%) and C3 (5.2%). The fresh pastes were used for hydration heat. The rest pasted were sealed and cured at 20℃ to specified age for XRD, MIP, SEM and autogenous shrinkage. The samples were soaked with isopropanol for 72 h to stop hydration before testing. The mortars (40mm×40mm× 160mm) were prepared with the w/c ratio of 0.4 and cured in 20℃ to specified ages for mechanical properties.

3. Results and discussion

3.1 Hydration kinetics

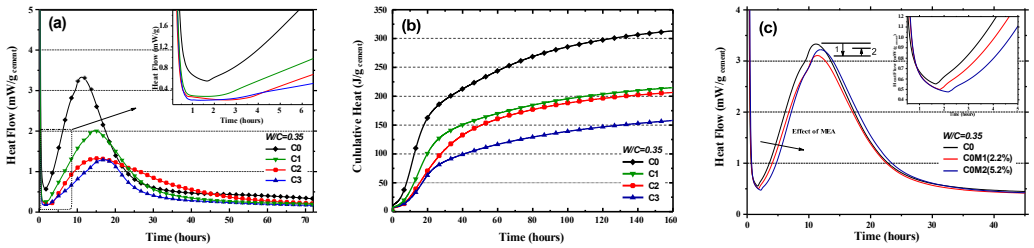


Fig. 1 The hydration heat rate (a) and cumulative heat release (b) of pure cement pastes, and the hydration heat rate of pastes combined with MEA (c).

The hydration heat results of pastes are shown in Fig. 1. The induction period of HBCs is longer than that of OPC. The silicate reaction peak of HBC is much lower than OPC's, which indicates the weak hydration reaction of HBC at early ages. The significant difference of kinetics is due to differences in mineral compositions of cements (Wang et al (2018b)). The heat release of HBC is also far lower than that of OPC. The 7-day hydration heat of C0 is 310 J/g, but 7-day hydration heat of HBC containing the least C_3S (C3) was only 155 J/g (50% C0). It suggests that HBC with slow and less hydration exotherm is very helpful to improve thermal cracking of mass concrete. In addition, MEA proportionately prolonged the induction period and start point of acceleration period, which resulting in a delay in cement hydration.

3.2 Hydration products

As shown in Fig. 2, the hydration degree of HBC was lower than that of OPC, and the amorphous C-S-H and portlandite from hydration were also less than that of OPC in early periods. However, with the continuous hydration reaction, the quantity of C-S-H from HBC is more than OPC's. The gel/crystal ratio of different cement had significant difference in later period of hydration (Wang et al (2018a)). The dead-burnt periclase in cement was not significantly reacted from the XRD results. Fig. 3(a) shows reduction of portlandite peak and increase of clinker minerals peak with the addition of MEA. It also indicates that

MEA inhibited the early hydration of cement. This is consistent with the results of hydration kinetics. However, MEA had almost no significant effect on later hydration reaction, as shown in Fig. 3(b).

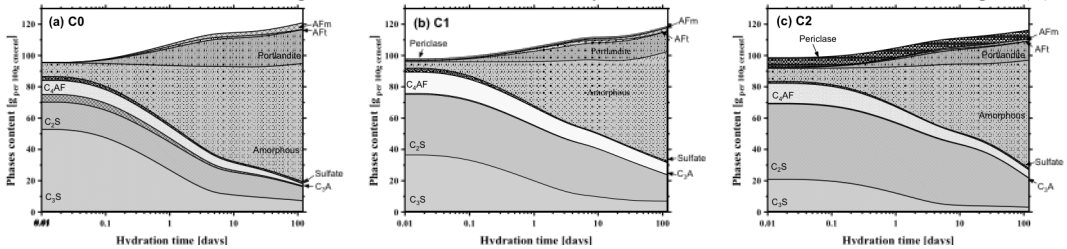


Fig. 2 The hydration products evolution of cement pastes over time. It was calculated by XRD.

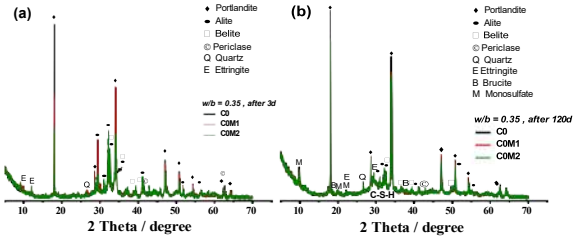


Fig. 3 The XRD patterns of composite pastes at early ages (a) and late ages (b).

3.3 Microstructure

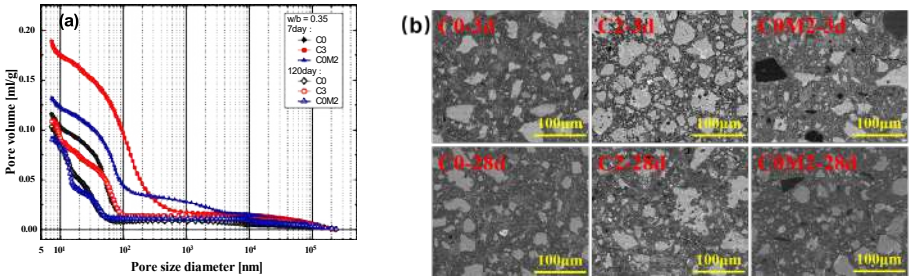


Fig. 4 The pore structure (a) and microstructure (b) of different hardened pastes at different ages.

As can be seen from Fig. 4(a), the porosity of HBC paste is much higher than that of OPC paste because of lower hydration degree in early periods. However, the porosity of HBC decreased rapidly with hydration reaction, and reached a similarly low value as that of OPC in later period. The differences in microstructure evolution between OPC and HBC can be observed by SEM in Fig. 4(b), the microstructure of HBC paste was also quite dense in very later periods. The internal porosity of MEA particle is very high (Mo et al (2010)). Therefore, more pores with sizes of 10^2-10^4 nm were introduced in early periods, increasing in the total porosity and formation a 'platform' on pore volume curve. As the MEA reacted, formed brucite quickly filled in these pores, thus not affecting the later microstructure of hardened paste.

3.4 Deformation

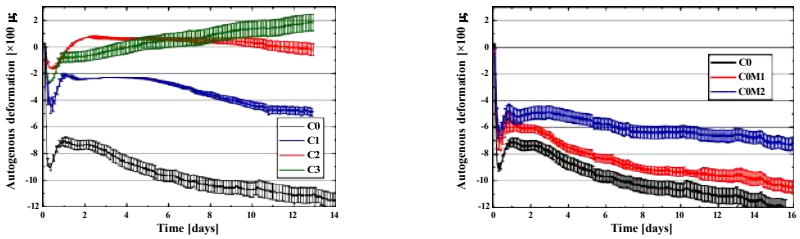


Fig. 5 Autogenous shrinkage of pure cement pastes (left) and pastes combined with MEA (right).

Autogenous shrinkage of pastes from the initial setting is shown in Fig. 5. Autogenous shrinkage of HBC paste was much smaller than that of OPC paste. The HBC paste containing the most MgO (C3) showed a continuous micro-expansion behavior. Due to expansion stress caused by hydration, MEA also reduced autogenous shrinkage of cement paste. With the increase of MEA, the autogenous shrinkage trend of paste was further weakened. It was also found that dead-burnt MgO in clinker can compensate long-term shrinkage of paste more effectively than additional MgO (MEA), even if their contents were the same.

3.5 Strength

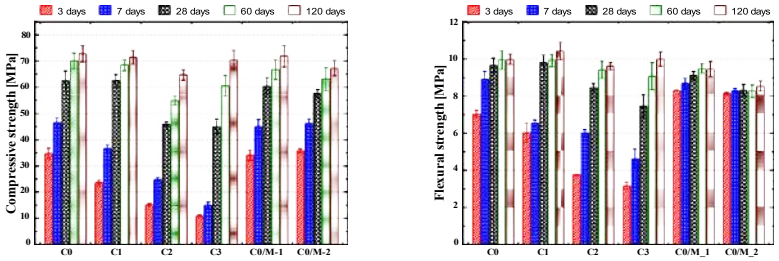


Fig. 6 Compressive strength (left) and flexural strength (right) of mortars.

Fig. 6 shows the results of compressive and flexural strength of different mortars. Compared with OPC, HBC mortars showed lower early compressive and flexural strength due to low hydration degree and the microstructure with high porosity (Wang et al (2018b)). With the decline of C_3S/C_2S, the compressive and flexural strength at 3d, 7d and 28d showed obvious decreasing tendencies. However, the mechanical properties of HBC mortars increased obviously with continuous hydration of cement. The strength of HBC mortars gradually approached that of OPC mortars after 28 days, due to optimized hydration products compositions and densification of microstructure in later periods. MEA had no obvious effect on compressive strength, but reduced flexural strength. The flexural strength of mortars mixed with MEA further decreased with ages.

4. Conclusions

As well as significate improving thermal cracking of mass concrete, HBC can effectively reduce CO_2 emissions in service life of concrete. Thus, it is a very potential material for future engineering structures. This study investigated that the hydration kinetics, microstructure, mechanical properties and volume deformation of high belite MgO expansive cement, as well as impacts of MEA.

Because of difference in mineral compositions, the reaction rate and released heat of HBC hydration were much lower than that of OPC hydration. Thus, the processes of hydration degree increasing and microstructural evolution were slower, which caused the high porosity and relatively low mechanical strength for HBC composites in early periods. However, benefited from continuous hydration of C_2S, microstructural compactness and mechanical property of HBC were even better than OPC's in very late periods. MEA slightly delayed early hydration, but had no significant impact on long-term microstructure and compressive strength. Nevertheless, flexural strength development was significant altered because of expansive stress from MEA hydration. Moreover, addition of MEA can effectively reduce shrinkage over a long period. However, dead-burnt MgO in high-belite expansive cement showed more remarkable reduction of volume shrinkage although its hydration degree was very low. It declares that dead-burnt MgO has stronger potential for long-term shrinkage compensation.

The results also suggest that high belite expansive cement can improve properties and durability of concrete from hydration and microstructure. Therefore, the application of high belite MgO cement could effectively reduce CO_2 emissions in the whole service process of cementitious composites.

References

Cuesta, A., Ayuela, A. and Aranda, Q. (2021) "Belite cements and their activation", *Cement and Concrete Research*, 140: 106319

Wang, L., Dong, Y., Zhou, S.H., et al (2018) "Energy saving benefit, mechanical performance, volume stabilities, hydration properties and products of low heat cement-based materials", *Energy & Building*, 170: 157-169

Mo, L.W., Deng, M., Tang, M.S., et al (2014) "MgO expansive cement and concrete in China: Past, present and future", *Cement and Concrete Research*, 57: 1-12

Mo, L.W., Deng, M. and Tang, M.S. (2010) "Effects of calcination condition on expansion property of MgO-type expansive agent used in cement-based materials", *Cement and Concrete Research*, 40(3): 437-446

Wang, L., Yang, H.Q., Zhou, S.H., et al (2018) "Hydration, mechanical property and C-S-H structure of early-strength low-heat cement-based materials", *Materials Letters*, 217: 151-154

The 16th International Congress on the Chemistry of Cement 2023 (ICCC2023)
"Further Reduction of CO_2 -Emissions and Circularity in the Cement and Concrete Industry"
September 18–22, 2023, Bangkok, Thailand

Development of Magnesium Silicate Hydrates from Brucite and Silica Fume

Padmaja Krishnan[1], Inderjeet Singh[2], and Kemal Celik[3*]

[1] *Division of Engineering, New York University Abu Dhabi, Abu Dhabi, P.O. Box 129188, United Arab Emirates*
Email: pk2464@nyu.edu
[2] *Division of Engineering, New York University Abu Dhabi, Abu Dhabi, P.O. Box 129188, United Arab Emirates*
Email: is81@nyu.edu
[3*] *Division of Engineering, New York University Abu Dhabi, Abu Dhabi, P.O. Box 129188, United Arab Emirates*
Email: kemal.celik@nyu.edu

ABSTRACT

Desalination is commonly adopted in arid regions to combat water scarcity issues. The desalination process results in a concentrated waste stream, brine, disposal of which can be technically and economically challenging. The desalination brine is a valuable source of many minerals, including magnesium hydroxide or brucite ($Mg(OH)_2$). Brucite, extracted from desalination brine, when directly used as a binder, may reduce the carbon dioxide (CO_2) emissions from the concrete industry. However, several difficulties exist in using brucite due to its high-water requirement and subsequent high porosity resulting in lower compressive strengths. To enhance the compressive strength of brucite for practical applications, this study explored the development of magnesium silicate hydrates (M-S-H) from brucite and silica fume (SiO_2) using different molar ratios of Mg/Si and investigated the compressive strengths, and the physio-chemical properties of the M-S-H formed. The results indicate that the compressive strengths of brucite-silica composites depended on the Mg/Si ratio and were similar or higher compared to mortars containing only brucite under accelerated carbonation conditions (20% CO_2 and 80% relative humidity). This also demonstrated the CO_2 sequestration potential of M-S-H. Results indicate that the utilization of brucite-silica composites as construction materials may have the potential to further reduce CO_2 emissions from the concrete industry.

KEYWORDS: *Magnesium oxide, silica fume, carbonation, magnesium silicate, CO_2 sequestration*

1. Introduction

As the search for binders with low carbon dioxide (CO_2) emissions continues to intensify, magnesium-based cements such as reactive magnesium oxide cement (RMC) are becoming increasingly popular. This is due to their lower production temperatures (700 – 1000 °C) compared to ordinary Portland cement as well as their ability to sequester CO_2 as part of their strength gain mechanism. However, reactive magnesium oxide (MgO) cement is predominantly produced from magnesite ($MgCO_3$) calcination, contributing to direct CO_2 emissions. In a bid to reduce direct CO_2 emissions, few studies have explored MgO or brucite (magnesium hydroxide, $Mg(OH)_2$) production from desalination brine (Dong et al. 2017, Dong et al. 2018, Singh et al. 2022). The desalination process, commonly used in arid regions to combat water scarcity issues, results in a concentrated waste stream, brine, disposal of which can be technically and economically challenging. Brucite extracted from desalination brine, if utilized directly as a binder, may reduce the CO_2 emissions from the construction industry.

Few studies have explored the utilization of brucite as a binder (Badjatya et al. 2022, Singh et al. 2022). However, direct utilization of brucite as a binder is challenging due to its high-water requirement and subsequent high porosity resulting in lower compressive strengths (Zhang et al. 2014). To enhance the workability and strength of the brucite pastes, pre-compaction of the pastes have been carried out before curing (Badjatya et al. 2022, Singh et al. 2022). While it may be possible to compact small specimens in the laboratory, this may not be viable for larger specimens produced in construction sites. Therefore, an

alternate solution is needed that does not rely on external compaction and ensures sufficient compressive strength for the brucite composites. One such solution could be utilizing co-binders such as silica fume with the brucite. Brucite and silica fume can react with water and form magnesium silicate hydrate (M-S-H) as the "binding phase" (Zhao et al. 2019), resulting in significant strength gain (Singh et al. 2020, Taj et al. 2023). Studies have also revealed that a magnesium-containing silicate layer can form relatively quickly at room temperature when MgO or brucite is in contact with amorphous silica and water (Jin et al., 2013). The composition and properties of the M-S-H formed depend on several factors, such as the ratio of Mg/Si, reagents, temperature, alkalinity of the blend, etc. (Wei et al. 2011). While the above studies suggest the potential of M-S-H, few studies have explored the development of M-S-H under carbonation curing conditions. Given the growing emphasis on the CO_2 sequestration potential of cementitious binders, the evaluation of the strength gain in brucite-silica fume composites cured under accelerated carbonation conditions is necessary. The main objective of this study is to evaluate the effect of varied Mg/Si ratios on the compressive strength of brucite-silica composites and understand the physio-chemical properties of the M-S-H formed using thermogravimetry (TG) and X-ray diffraction (XRD) analysis.

2. Materials and Methods

2.1 Materials, mixture design, and sample preparation

Commercially available brucite (Sigma Aldrich) and silica fume were used for the sample preparation. Standard sand conforming to ASTM C778 (American Society for Testing and Materials (ASTM) 2017) was used as a fine aggregate for producing mortar samples. Triplicates of cylinder mortar specimens of diameter 25 mm and height 25 mm were produced for the compressive strength measurements. The specimen sizes were kept small since it is difficult to accommodate larger specimens in the carbonation chamber. A water-to-binder ratio (W/B) of 0.70 was adopted since both brucite and silica fume have high water consumption. Superplasticizer was avoided since this study is a basic characterization to evaluate the influence of silica fume on brucite composites. The sand-to-binder ratio was maintained at 2.75 for the mortar specimens as stipulated in ASTM C109 (American Society for Testing and Materials (ASTM) 2021). The cementitious materials (brucite and silica fume) were mixed in a 4.8 L Hobart mixer for 2 min, then mixed with sand before deionized water was added. The mixing was continued for another 3 min. To understand the influence of silica fume on the properties of brucite, three ratios of Mg/Si (0.5, 1.0, and 1.5) were used. The samples were designated as Mg/Si 0.5, Mg/Si 1.0, and Mg/Si 1.5, respectively, and the mix proportions are summarized in Table 1. Corresponding paste samples were prepared for physio-chemical characterization.

After mixing and casting, the samples were cured in the laboratory air at 22 ± 2 ºC for 1 day. After 24 hours, the samples were demolded and placed in a carbonation chamber where they were exposed to concentrated CO_2 (20% CO_2 and 80% RH at 30 ºC) to accelerate the carbonation.

Table 1. Mortar mix composition (normalized by mass of the cementitious materials, brucite, and silica fume)

	Brucite	Mg/Si 0.5	Mg/Si 1.0	Mg/Si 1.5
Deionized water	0.7	0.7	0.7	0.7
Brucite	1	0.33	0.49	0.59
Silica fume	-	0.67	0.51	0.41
Sand	2.75	2.75	2.75	2.75

2.2 Experimental Methods

Compression testing of the brucite-silica mortar specimens was performed at a loading rate of 0.75 MPa/s, as recommended by ASTM C109 (American Society for Testing and Materials (ASTM) 2021), using a 100 kN compression machine. The specimens were tested for compressive strength at 7 and 28 days.

At the age of 28 days, the corresponding carbonated paste samples were crushed into powders and were used for XRD and TG analysis. Around 30 mg of the paste samples were used for the TG, which was

performed under a temperature regime ramped from 25 ºC to 1000 ºC at 10 ºC/min using a TG 209 F1 Libra. The XRD was carried out with a PANalytical Empyrean, Cu Kα radiation source. A fixed divergence slit of 1/2° was used to minimize stray X-ray and noise signals. The scanning was done at 40 mA, 40 kV under a programmable gonio mode with a 2θ angle between the source and the detector (PIXel3D) varied from 5 to 70º. A step of 0.013 º with an acquisition time of 350 s was adopted.

3. Results and discussion

3.1 Compressive strength

The average compressive strengths of mortars containing only brucite and brucite-silica composites are shown in Fig. 1. The compressive strengths of control specimens containing only brucite reached 5.4 MPa after 7 days of carbonation curing. For the brucite-silica composites, the compressive strengths increased with an increase in the brucite amount. Specimens with Mg/Si 0.5 showed similar compressive strength as the control specimens, while Mg/Si 1.0 and 1.5 showed around 123% and 235% higher compressive strengths compared to the brucite specimens at 7 days. The increase in strength can be due to the formation of M-S-H in addition to the hydrated magnesium carbonates, which are formed by the carbonation of brucite. With further carbonation curing, the compressive strength increased by around 44% for the brucite mortars from 7 to 28 days. However, the compressive strengths for the Mg/Si 1.5 samples were similar for 7 and 28 days of curing. It is possible that the incorporation of silica fume densified the structure due to the filling effect of the particles, and the formation of M-S-H might have hindered the further diffusion of CO_2 into the specimens. Nevertheless, the compressive strengths for the Mg/Si 1.0 and 1.5 specimens were around 90% and 115% higher than those containing only brucite at 28 days, indicating the better performance of the brucite-silica composites.

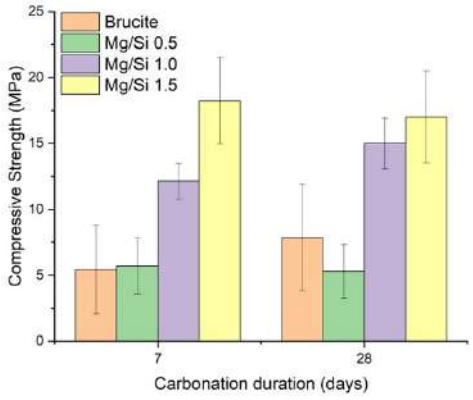


Fig. 1. Compressive strength development of brucite and brucite-silica fume composites under accelerated carbonation (20% CO_2, 80% RH at 30 ºC).

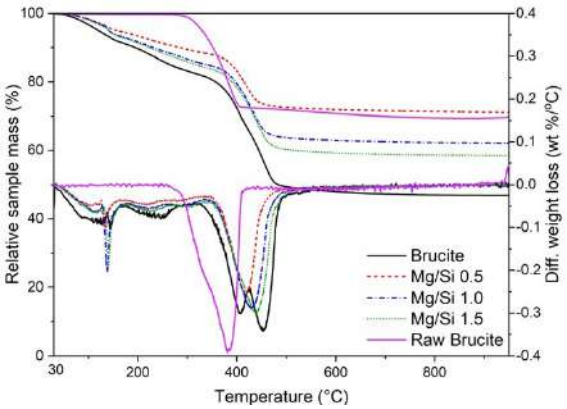


Fig. 2. Thermogravimetric analysis for brucite, Mg/Si 0.5, Mg/Si 1.0, and Mg/Si 1.5 paste samples subjected to accelerated carbonation (20% CO_2, 80% RH at 30 ºC) for 28 days in comparison to raw brucite without carbonation.

3.2 Hydration and carbonation reactions using thermogravimetric analysis

The weight loss and differential weight loss of the pastes obtained using TG measurements are shown in Fig. 2. Uncarbonated or raw brucite reveals weight loss initiated at around 300 °C with an endothermic peak center at 385 °C. In comparison, the carbonated brucite reveals a decomposition peak centered at around 120 °C, which can be attributed to the dehydration of hydrated magnesium carbonates (HMCs) (Hay et al., 2023). There is also significant rightward shifting of the main endothermic peak to around 405 °C for the carbonated brucite compared to the non-carbonated raw brucite sample. The carbonated brucite also reveals another peak centered at 455 °C, possibly due to the decomposition of crystalline and amorphous carbonation phases, according to literature (Hay et al., 2023).

The brucite-silica pastes reveal a sharp peak at around 140 °C, possibly due to the weight loss due to the pore water and water locked in the M-S-H gel (Zhang et al., 2014). The two peaks present for carbonated brucite are also replaced by a broader peak in the brucite-silica pastes. Studies have suggested that when the temperature exceeds 430 °C, dehydroxylation of the Mg-OH and Si-OH groups in M-S-H may occur (Zhang et al. 2018); hence the presence of this peak suggests the formation of M-S-H. As the ratio of Mg/Si increases, the peak shifts further to the right. According to the literature, carbonate phases tend to decompose at higher temperatures (Taj et al., 2023). Therefore, it is possible that as the Mg/Si ratio increased, higher amounts of HMCs were formed compared to M-S-H. However, further investigation is necessary to understand the evolution of HMCs and M-S-H and their respective contribution to the strength gain of the composites.

3.3 Phase identification with X-ray diffraction

The XRD results of the carbonated pastes at 28 days are presented in Fig. 3. Carbonated brucite shows characteristic peaks at 18.6, 38.0, 50.8, 58.6, and 68.2° 2θ (Hay et al., 2023). These peaks become less prominent for the brucite-silica pastes with Mg/Si ratios of 0.5 and 1.0 and increase for the Mg/Si 1.5 sample. This indicates a partial carbonation of brucite, and further studies are necessary to evaluate the extent of brucite carbonation. Furthermore, M-S-H is known to be not well crystallized, with broad peaks occurring at 19.7, 26.7, 35.0, and 59.9° 2θ (Roosz et al. 2015) and the broad peaks present in the brucite-silica samples suggests the formation of M-S-H. Further studies using Fourier-transform infrared spectroscopy (FT-IR) and nuclear magnetic resonance (NMR) spectroscopy will help to better understand the M-S-H phases formed.

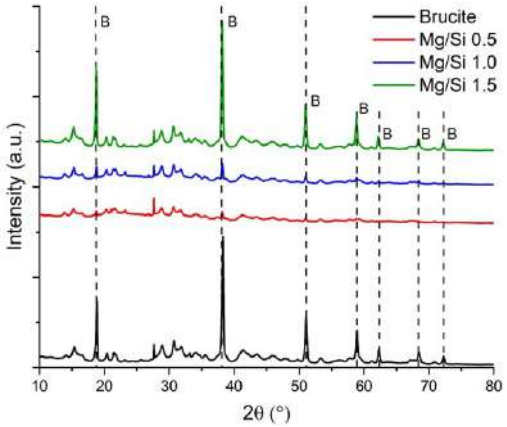


Fig. 3. X-ray diffraction for brucite, Mg/Si 0.5, Mg/Si 1.0, and Mg/Si 1.5 pastes subjected to accelerated carbonation (20% CO_2, 80% RH at 30 ^{o}C) for 28 days.

4. Conclusions

To enhance the castability and compressive strength of brucite and promote its utilization as a construction material, this study explores the incorporation of silica fume with brucite. The results show that the compressive strength of the brucite-silica fume mortars under accelerated carbonation curing depended on the Mg/Si ratio, and the strengths were similar or higher compared to mortars containing only brucite. The physio-chemical characterization (thermogravimetric and x-ray diffraction) revealed the likely formation of magnesium silicate hydrates (M-S-H) due to the reaction of brucite and silica fume in the presence of water. While further investigation is necessary to understand the characteristics of the Mg/Si produced and optimize the Mg/Si ratios, the results reveal the promising potential of CO_2 sequestering brucite-silica composites.

Acknowledgments

The support received from the Abu Dhabi Department of Education and Knowledge (ADEK) for the grant ADHPG−RA686 is acknowledged. This work was supported by the NYUAD Center for Interacting Urban Networks (CITIES), funded by Tamkeen under the NYUAD Research Institute Award CG001.

The authors also thank Tamkeen for funding the NYUAD Water Research Center under the NYUAD Research Institute Award (project CG007).

References

American Society for Testing and Materials (ASTM) (2017). ASTM C778-17: Standard Specification for standard sand. 100 Barr Harbor Dr., PO box C-700, West Conshohocken, Pennsylvania, ASTM International.

American Society for Testing and Materials (ASTM) (2021). ASTM C109/C109M-21: Standard Test Method for Compressive Strength of Hydraulic Cement Mortar. ASTM Standards. 100 Barr Harbor Dr., PO box C-700, West Conshohocken, Pennsylvania, ASTM International.

Badjatya, P., A. H. Akca, D. V. Fraga Alvarez, B. Chang, S. Ma, X. Pang, S. Kawashima (2022). "Carbon-negative cement manufacturing from seawater-derived magnesium feedstocks." *Proceedings of the National Academy of Sciences* 119(34): e2114680119.

Dong, H., C. Unluer, E.-H. Yang and A. Al-Tabbaa (2017). "Synthesis of reactive MgO from reject brine via the addition of NH4OH." *Hydrometallurgy* 169: 165-172.

Dong, H., C. Unluer, E.-H. Yang and A. Al-Tabbaa (2018). "Recovery of reactive MgO from reject brine via the addition of NaOH." *Desalination* 429: 88-95.

Hay, R., B. Peng and K. Celik (2023). "Filler effects of CaCO3 polymorphs derived from limestone and seashell on hydration and carbonation of reactive magnesium oxide (MgO) cement (RMC)." *Cement and Concrete Research* 164: 107040.

Jin, F. and A. Al-Tabbaa (2013). "Thermogravimetric study on the hydration of reactive magnesia and silica mixture at room temperature." *Thermochimica acta* 566: 162-168.

Roosz, C., S. Grangeon, P. Blanc, V. Montouillout, B. Lothenbach, P. Henocq, . . . S. Gaboreau (2015). "Crystal structure of magnesium silicate hydrates (MSH): The relation with 2: 1 Mg–Si phyllosilicates." *Cement and Concrete Research* 73: 228-237.

Singh, G. B., C. Sonat, E. Yang and C. Unluer (2020). "Performance of MgO and MgO–SiO2 systems containing seeds under different curing conditions." *Cement and Concrete Composites* 108: 103543.

Singh, I., R. Hay and K. Celik (2022). "Recovery and direct carbonation of brucite from desalination reject brine for use as a construction material." *Cement and Concrete Research* 152: 106673.

Taj, K., B. Akturk and S. Ulukaya (2023). "Influence of carbonation curing and nano-silica incorporation on compressive strength and micro-structural development of binary RMC-based systems." *Journal of Building Engineering*: 105856.

Wei, J., Q. Yu, W. Zhang and H. Zhang (2011). "Reaction products of MgO and microsilica cementitious materials at different temperatures." *Journal of Wuhan University of Technology. Materials Science Edition* 26(4): 745.

Zhang, T., L. J. Vandeperre and C. R. Cheeseman (2014). "Formation of magnesium silicate hydrate (MSH) cement pastes using sodium hexametaphosphate." *Cement and Concrete Research* 65: 8-14.

Zhang, T., J. Zou, B. Wang, Z. Wu, Y. Jia and C. R. Cheeseman (2018). "Characterization of magnesium silicate hydrate (MSH) gel formed by reacting MgO and silica fume." *Materials* 11(6): 909.

Zhao, H., T. Hanein, N. Li, A. Alotaibi, A. Li, S. Walling and H. Kinoshita (2019). *Acceleration of MSH gel formation through the addition of alkali carbonates*. Proceedings of the 15th International Congress on the Chemistry of Cement (ICCC 2019), Sheffield.

The 16th International Congress on the Chemistry of Cement 2023 (ICCC2023)
"Further Reduction of CO_2 -Emissions and Circularity in the Cement and Concrete Industry"
September 18–22, 2023, Bangkok, Thailand

Spatial and Temporal Analysis of Carbonation Depth via Raman Spectroscopy and Imaging

S. R. Kumar, S. Srivastava, and N. Garg*

Department of Civil and Environmental Engineering, University of Illinois Urbana-Champaign, Urbana, United States

Email: sr58@illinois.edu, sonalis@vt.edu, nishantg@illinois.edu

ABSTRACT

Several techniques have been used to quantify the extent of carbonation in cement. But underlying challenges become imminent in using these techniques. XRD and TGA are bulk analysis techniques, which cannot track carbonation progress over time, on the same sample surface. Raman spectroscopy and imaging, being non-destructive, can be a useful technique to overcome some of these challenges. This study investigates the carbonation of OPC pastes of at a water/cement ratio of 0.4 through the conventional pH test, confocal Raman imaging, and Raman spectroscopy. At 3, 5, and 7 days, the amount of carbonation of the specimen is about 75 %, 85 %, and 90 % respectively, depicted by the phase maps of calcite and portlandite. It is observed that the depth of carbonation obtained using Raman imaging and spectroscopy is higher than the pH test, due to its ability to map partially carbonating zones. Thus, Raman imaging and spectroscopy provide insight into the evolution of carbonation over time and can be a complementary non-destructive tool to quantify the extent of carbonation of cement-based materials.

KEYWORDS: *Carbonation, Raman Imaging, Confocal Raman Spectroscopy.*

1. Introduction

To understand and quantify the progress of the carbonation of cementitious material over time, several past analytical techniques have been used by researchers. Some of them include - the use of pH indicators, Lo and Lee (2002), X-ray diffraction (XRD), scanning electron microscopy (SEM), Shah et al. (2018), and solid-state nuclear magnetic resonance (NMR), Liu et al. (2019). Among all the techniques mentioned above, using pH indicators such as phenolphthalein is quick, easy, and convenient. These tests indicate a boundary, on either side of which lies a carbonated and a non-carbonated zone. However, a major drawback of this simple test is that it only differentiates a fully carbonated zone from an uncarbonated one without illustrating the dynamic progress of the carbonation front over time. Furthermore, these bulk tests require many hours of sample preparation, which might not represent the actual sample conditions. Hence, there is a prodigious amount of potential in developing a non – destructive technique to track the carbonation of cement-based systems over time.

One technique that stands out in this regard is Raman imaging, which can provide in-situ (no sample preparation involved) and operando (representing actual sample condition). Raman imaging has been used for various applications, including the phase quantization of anhydrous cements, Polavaram and Garg (2021), phase mapping of granites, Polavaram and Garg (2021b), and in-situ monitoring of the early age of hydration kinetics of cements, Loh et al. (2021). Raman imaging has been used for other applications, including the phase quantization of anhydrous cements, Polavaram and Garg (2021), phase mapping of granites, Polavaram and Garg (2021b). Furthermore, Raman imaging has been used to understand the evolution of carbonation of cement paste, Srivastava and Garg (2022) and to monitor the early surface carbonation of hardened cement pastes subjected to both natural and accelerated carbonation, Zhang et al. (2022). Carbonate ions show a strong Raman scattering signal, even at low concentrations, attributed to the ν_1 CO_2 frequency at a wavenumber of 1090 cm^{-1}.

In this study, the evolution of the carbonation front over time for a water/cement (w/c) ratio of 0.4 cured for 1 day is mapped using large-area Raman imaging. High-quality spatial and temporal maps were obtained, which clearly showcase dynamic changes in the nucleation, growth, and precipitation of portlandite at 3600 cm^{-1} and calcite at 1086 cm^{-1}. The positive growth of the calcite front and the negative growth of the portlandite front indicate the progression of the dynamic carbonation front over time. Raman scans aided by image analysis assisted in quantifying the extent of carbonation of cement pastes. It is observed that the carbonation depth obtained using Raman imaging is higher than the depth obtained using the conventional pH test, which can be attributed to the ability of Raman imaging to identify and distinguish between a partially carbonated and a fully carbonated zone. This study shows that large-area Raman imaging can be worthwhile in unraveling questions posed by exceedingly heterogeneous systems such as cementitious binders.

2. Materials and Methods

2.1 Sample Preparation

Type 1 OPC was used to cast paste samples in prismatic plastic molds of 10 mm × 10 mm × 30 mm with a water/cement (w/c) of 0.4. After 24 hours of sealed curing in the plastic mold, the prisms were demolded and cured for 1 day by submerging them in a saturated lime solution under a controlled temperature of 22 °C for uniform hydration. After the completion of the curing regime, the specimens were conditioned in a vacuum chamber for 1 day to maintain a uniform moisture level in specimens. Post that, the prisms were coated with epoxy on five sides to facilitate the unidirectional ingress of CO_2 at a concentration maintained at 20 %, relative humidity at 65 %, and temperature at 50 °C. Upon completing the carbonation regime, the prisms were cut into two halves longitudinally using a low-speed saw-cutting machine. Raman scans were performed on one half, while pH measurements were taken on the other.

2.2 pH Test

The phenolphthalein indicator solution was made by mixing 1% by wt. of indicator in a 70–30% blend of ethanol and distilled water sprayed on freshly cut prisms at the end of its carbonation regime. The pH test took within a few minutes (< 5 minutes) in total to reveal a pink color change if the area is non-carbonated while a colorless region indicating a carbonated region.

2.2 Raman Imaging – Confocal Raman

Raman spectra were collected using a Raman confocal microscope (WITec Alpha 300 series SNOM microscope) on the cement paste specimens post-carbonation. Polarized Raman spectra were obtained using a 532 nm excitation laser with an excitation power of 10 mW and a 600 gr/mm grating coupled with a charged coupled device (CCD) with a spectral resolution of 40 μm/pixel. The entire scan lasted for about an hour.

2.3 Raman Spectroscopy – Touch Raman Ball Probe

External Raman probe is used with Horiba Raman spectroscopy at a 785 nm wavelength and a holographic grating with a grating groove density of 685 gr/mm spectrometer. A laser power of 90 mW with an acquisition time of 6 seconds was used. A movable sample stage was used, and spectra were collected using a ball probe. At the tip of the ball lens, light focused on the specimen, which was moved after every 0.5 mm to obtain a carbonation profile across the cross-section. The Raman spectra are collected from 89 – 3507 cm^{-1} and the entire scan over the carbonated surface lasted for less than 45 minutes.

3. Results and Discussion

3.1 Chemical imaging

Large-area Raman imaging was performed on a carbonated cement paste specimen post its carbonation regime. The corresponding phase maps of calcite (1086 cm^{-1}) and portlandite (3618 cm^{-1}) are mapped as shown in Figure 1. The calcite phase map initially, pre – carbonation, can be attributed to limestone in the cement and initial carbonation of the specimen, which was attempted to be minimized. It can be observed that the positive movement of the calcite front inwards and the negative movement of the portlandite front indicate the movement of the carbonation front. This front is clearly visible at the end of 1 day, which further proceeds inwards at the end of 3, 5, and 7 days. At the end of 1 day, over 50% of the specimen is carbonated, which is depicted by this distinct front of carbonation, and the intensity of calcite and portlandite phases. At the end of 3 and 5 days, there is an increase in the amount of carbonation of the specimen to about 75 % and 85 % respectively, with a visible increase in the intensity of calcite in the carbonated front. At the end of 7 days, about 90 % of the specimen is carbonated with a small portlandite front. Furthermore, it can be inferred that at the end of 7 days, almost all phases in the system are carbonated, which is clear since > 95 % area of the Raman image is calcite.

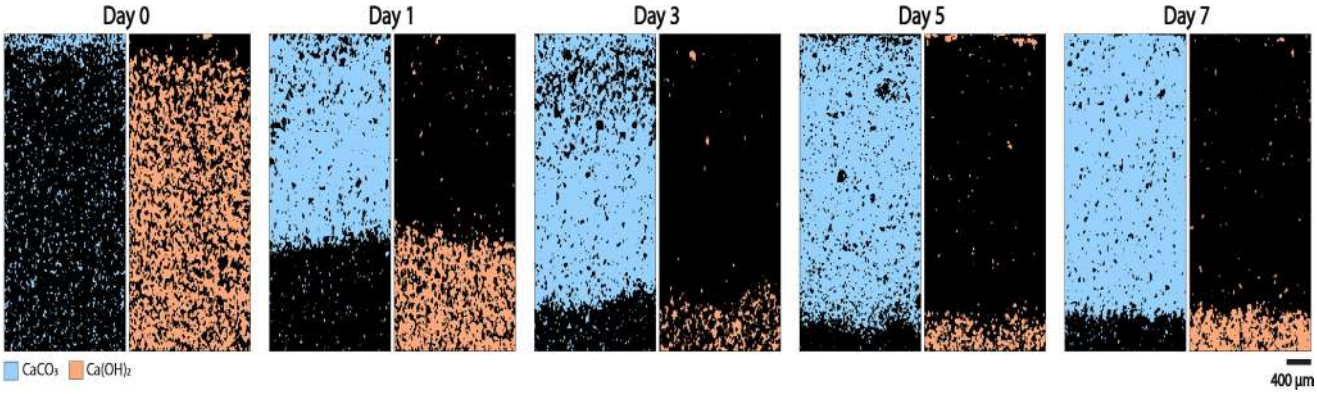


Figure 1. Raman images of calcite and portlandite on a hydrated cement paste specimen subjected to carbonation with a spectral resolution of 10 µm/pixel.

3.2 Carbonation rate comparison

A comparison between the carbonation rate for specimens cast with a 0.4 w/c obtained using confocal Raman, pH test, and Raman ball probe test can be visualized in Fig. 2. The pH test was performed on the sample to measure the carbonation depth after each carbonation regime, on one half of the prism while the second prism was used for confocal Raman imaging and spectroscopy. Interestingly, confocal Raman imaging and Raman ball probe show a non – zero depth, unlike the pH test. Also, it can be observed that by using Raman imaging, the depth of carbonation is higher than that obtained from the pH test which agrees with Lo and Lee (2002). This can be attributed to the fact that Raman imaging is more sensitive to locating a partial carbonation front, unlike using a pH indicator. Moreover, the carbonation depth obtained from the Raman ball probe closely matched the depth obtained using confocal Raman imaging, which further encourages the use of the Raman probe as a cost-effective non-destructive analysis technique.

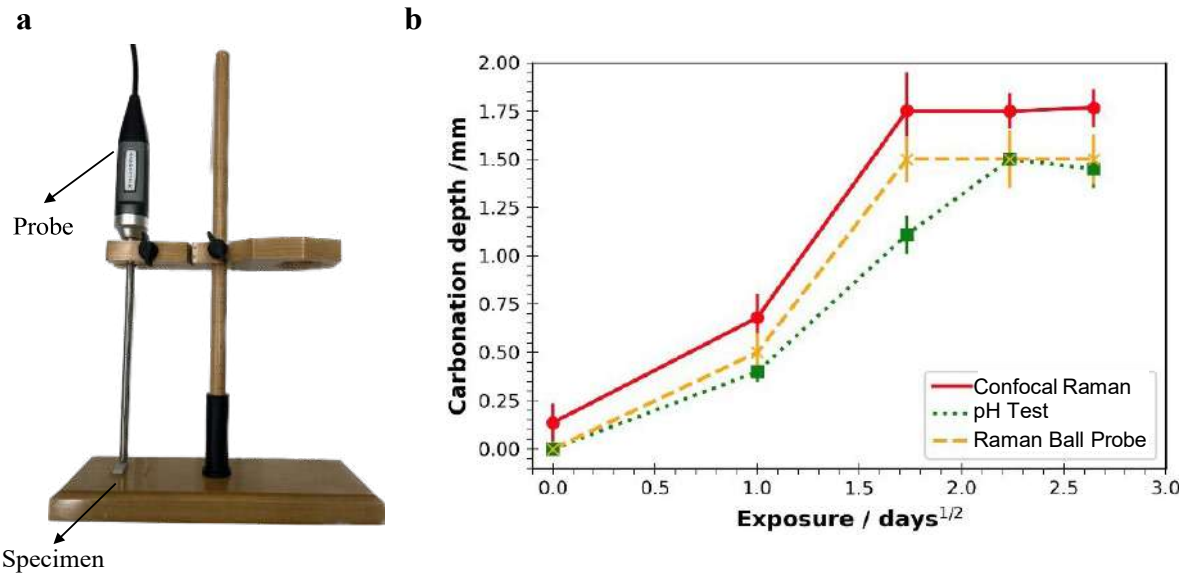


Figure 2. a) Raman ball probe used to calculate carbonation depth and b) Comparison between the carbonation depth measured using confocal Raman instrument, pH test, and Raman ball probe for carbonated cement paste with time for w/c= 0.4.

4. Conclusions and Further Research

This study observes the carbonation phenomenon in cement paste specimens using Raman spectroscopy. The positive growth of the calcite front and the negative growth of the portlandite front indicate the progress of carbonation over time. The results obtained from Raman imaging correlate well with the pH indicator test and provide information on the dynamic front of carbonation. It is observed that the carbonation depth obtained using Raman imaging is higher than the depth obtained using the conventional pH test, which can be due to the ability of Raman imaging to identify and distinguish between a partially carbonated and a fully carbonated zone. In the future, other deterioration mechanisms of concrete can be studied using Raman imaging which can be used as a complementary tool to other conventional characterizing techniques.

Acknowledgments
This research was carried out in part in the Materials Research Laboratory Central Research Facilities, and Core Facilities at the Carl R. Woese Institute of Genomic Biology at the University of Illinois.

References

Lo, Y., & Lee, H. M. (2002). Curing effects on carbonation of concrete using a phenolphthalein indicator and Fourier-transform infrared spectroscopy. *Building and Environment*, *37*(5), 507–514.

Shah, V., Scrivener, K., Bhattacharjee, B., & Bishnoi, S. (2018). Changes in microstructure characteristics of cement paste on carbonation. *Cement and Concrete Research*, *109*, 184–197.

Liu, W., Li, Y. Q., Tang, L. P., & Dong, Z. J. (2019). XRD and 29Si MAS NMR study on carbonated cement paste under accelerated carbonation using different concentration of CO2. *Materials Today Communications*, *19*, 464–470.

Srivastava, Sonali, and Nishant Garg. "Tracking Spatiotemporal Evolution of Cementitious Carbonation via Raman Imaging." *Journal of Raman Spectroscopy*, 2022,

Polavaram, K. C., & Garg, N. (2021). Enabling phase quantification of anhydrous cements via Raman imaging. *Cement and Concrete Research*, *150*.

Polavaram, K. C., & Garg, N. (2021b). High-fidelity and high-resolution phase mapping of granites via confocal Raman imaging. *Scientific Reports*, *11*(1), 8022.

Loh, H. C., Kim, H. J., Ulm, F. J., & Masic, A. (2021). Time-Space-Resolved Chemical Deconvolution of Cementitious Colloidal Systems Using Raman Spectroscopy. *Langmuir*, *37*(23), 7019–7031.

Zhang, K., Yio, M., Wong, H., & Buenfeld, N. (2022). Real-time monitoring of carbonation of hardened cement pastes using Raman microscopy. *Journal of Microscopy*, *286*(2), 126–133.

Lo, Y., & Lee, H. M. (2002). Curing effects on carbonation of concrete using a phenolphthalein indicator and Fourier-transform infrared spectroscopy. *Building and Environment*, *37*(5), 507–514.

The 16th International Congress on the Chemistry of Cement 2023 (ICCC2023)
"Further Reduction of CO_2 -Emissions and Circularity in the Cement and Concrete Industry"
September 18–22, 2023, Bangkok, Thailand

Carbon Dioxide Absorption by Amine Mediated Calcium-Silicate-Hydrate (C-S-H)

K. Kopitha1*, Y. Elakneswaran[1], R. Kitagaki[1], H. Senboku[1], Y. Yoda[2], R. Saito[2], M. Tsujino[2], and A. Nishida[2]

[1] *Faculty of Engineering, Hokkaido University, 8 Chome Kita 13 Jonishi, Kita Ward, Sapporo, Hokkaido 060-8628, Japan.*
[2] *Shimizu Corporation, Shimizu Institute of Technology, 3 Chome-4-17 Etchujima, Koto Ward, Tokyo 135-8530, Japan.*

Email: kopitha.kirushnapillai.n2@elms.hokudai.ac.jp

ABSTRACT

Carbon dioxide (CO_2) emissions are a major contributor to climate change, and while cement-based materials possess the potential to capture CO_2 through mineralisation, the reaction rate remains relatively slow. Therefore, there is a pressing need to develop an appropriate solvent to enhance the mineralisation process. While amines, a derivative of ammonia, are currently the most advanced CO_2 capture technique, their potential in cement-based materials has not been fully explored. As calcium-silicate-hydrate (C-S-H) is the major Ca-bearing phase in hydrated cement-based materials which reacts with CO_2 during carbonation, it is necessary to study the absorption of CO_2 using amine with C-S-H. Therefore, this study is centred on investigating a more efficient solvent for CO_2 absorption by assessing the CO_2 absorption potential of diverse types of amines. The amines under consideration have the capacity to form bicarbonates during CO_2 absorption, such as tertiary and sterically hindered amines. C-S-H with varying Ca/Si ratios of 1 and 1.5 was utilised, and the effectiveness of methyl diethanolamine (MDEA) and 2-(methylamino)ethanol (MAE) was evaluated after mixing with water and C-S-H and subjected to accelerating carbonation. After undergoing the carbonation process, the sample was filtered, and the resulting precipitate was analysed using thermogravimetric analysis (TGA) to determine the amount of precipitated $CaCO_3$ and subjected to a phenolphthalein test as well. Additionally, the liquid phase was analysed for pH, providing insight into the carbonation of C-S-H. Furthermore, the study systematically investigated the impact of the Ca/Si ratio and amine type on CO_2 absorption. The study's outcomes unveiled that MAE exhibited the highest efficacy in CO_2 absorption compared to other amines. These findings could potentially provide new insights into CO_2 capture and suggest promising industrial applications.

KEYWORDS: *mineralisation, CO_2 capture, cement-based materials, calcium-silicate-hydrate (C-S-H), sterically hindered amines*

1. Introduction

The increasing levels of carbon dioxide (CO_2) emissions have become a major concern for the global community as it exacerbates the effects of climate change and threatens the planet's delicate ecosystem. The cement and building industry is one of the largest CO_2 emissions contributors. In order to mitigate these emissions, carbon capture technologies have been proposed as a promising solution. Mineral carbonation, also known as CO_2 mineralisation, has emerged as a promising solution for carbon capture and utilisation or storage (CCU/S) to mitigate carbon dioxide emissions. Consequently, it has garnered significant attention from researchers and industry experts, as evidenced by numerous studies and reports [1]. Even though cement production is a significant contributor to CO_2 emissions, cement-based materials

have the capacity to capture CO_2 and form thermodynamically stable calcium carbonate through CO_2 mineralisation.
Calcium silicate hydrate (C-S-H) is a crucial constituent in cement systems, as it possesses the ability to capture CO_2 and undergo carbonation. The susceptibility of C-S-H to carbonation is due to its high surface area and its amorphous structure, which provide numerous reactive sites for CO_2 to react. Moreover, the presence of calcium ions in the C-S-H structure facilitates the carbonation process by providing a source of carbonate ions, which are essential for the formation of $CaCO_3$. The carbonation of C-S-H not only results in the fixation of CO_2 but also improves the durability of cement-based materials by reducing their porosity and enhancing their mechanical properties. Notwithstanding the potential benefits of CO_2 mineralisation, the slow kinetics of the carbonation process poses a significant obstacle to its widespread application. As such, there is a pressing need to identify and implement an effective technology for the expeditious capture of CO_2. One such technology that is increasingly adopting is using solvents, such as amines, which are derivatives of ammonia and undergo reversible reactions with CO_2 and form carbamate/bicarbonate to augment CO_2 capture in alkaline wastes like fly ash and slag.
However, the use of amines with cement-based materials is limited. Before considering their use, it is necessary to study the reaction mechanism of the main hydrated phases in cement-based materials, such as C-S-H and $Ca(OH)_2$, with amines and identify suitable amines that do not alter their chemistry. Therefore, this study focuses on finding an appropriate amine for CO_2 capture while studying its reaction mechanism with C-S-H. To achieve this, 2-(methylamino)ethanol (MAE) for hindered amines and methyl diethanolamine (MDEA) for tertiary amines were selected and mixed with C-S-H (with a Ca/Si ratio of 1 and 1.5) and water to evaluate the CO_2 capture ability of each amine. Indicators of carbonation of C-S-H, such as carbonated products and pH, were measured after carbonation. Additionally, the study systematically investigated the effect of the Ca/Si ratio and amine type on CO_2 absorption.
The novelties of this study include exploring amines in conjunction with C-S-H for CO_2 capture, assessing the ability of each type of amine for CO_2 capture and selecting a compatible amine for CO_2 capture in cement-based materials. These findings will help harness the ability of C-S-H to capture and fix CO_2 through carbonation, enabling the construction industry to play a significant role in reducing greenhouse gas concentrations in the atmosphere.

2. Reaction Mechanism

Amines, organic compounds containing a nitrogen atom, are commonly categorised into primary, secondary, and tertiary amines based on the number of hydrogen atoms substituted at the amino nitrogen. However, the reactivity of amines can also vary depending on their structure and functional groups. Specifically, when reacting with CO_2, amines can be categorised into two distinct groups based on the resulting product.
The first group of amines, carbamate-forming amines, comprises primary and secondary amines. These amines react with CO_2 to form carbamates, compounds containing a central carbon atom bonded to a nitrogen atom and an oxygen atom. The second group, bicarbonate-forming amines, primarily consist of tertiary amines. These amines react with CO_2 to form bicarbonates, compounds containing two oxygen atoms and a central carbon atom.
Interestingly, for amines with steric hindrance, also known as sterically hindered amines, the presence of a large substituent adjacent to the amino group can lower carbamate stability and weaken the N-H bond. As a result, these amines tend to undergo greater hydrolysis, leading to bicarbonates forming instead of carbamates. Thus, tertiary and sterically hindered amines are more likely to form bicarbonates during their reaction with CO_2.
Amines that fall into the bicarbonate-forming amines are particularly useful in cement-based materials, as they can bind with Ca ions present in hydrated phases like $Ca(OH)_2$ and C-S-H and form more calcite, which subsequently reduces the porosity in the material.
These Ca ions, which can vary depending on Ca/Si ratio, can react with CO_2, forming calcite and decalcified silica gel (or silica gel). Numerous researchers have extensively studied calcium-silicate-hydrate carbonation (Liu et al., 2022), involving a complex interplay of decalcification and polymerisation of the C-S-H. In the presence of amine, bicarbonate formation increases; hence more calcite forms by getting Ca ions from C-S-H. The chemical structures of MAE and MDEA are presented in Fig. 1. In the presence of Ca ions, MAE and MDEA can undergo carbonation reactions to form $CaCO_3$

and regenerate the amine solvent. These reactions are depicted by equations (1) through (6).



MAE ($CH_3NHCH_2CH_2OH$) MDEA ($CH_3N(C_2H_4OH)_2$)

Fig. 1. Chemical structure of MAE and MDEA

Physical solubility of CO_2

$$CO_{2(g)} \rightleftharpoons CO_{2(l)} \quad (1)$$

CO_2 absorption

For MAE,

$$CO_{2(l)} + 2MAE \rightleftharpoons MAEH^+ + MAECOO^- \quad (2)$$

$$MAECOO^- + H_2O \rightleftharpoons MAE + HCO_3^- \quad (3)$$

For MDEA,

$$MDEA + CO_{2(l)} + H_2O \rightleftharpoons MDEAH^+ + HCO_3^- \quad (4)$$

Mineralisation

$$Ca^{2+} + CO_3^{2-} \rightleftharpoons CaCO_3 \downarrow \quad (5)$$

Amine regeneration

$$MAEH^+/MDEAH^+ \rightleftharpoons MAE/MDEA + H^+ \quad (6)$$

3. Materials and Methods

The synthesis of C-S-H was performed at a temperature of 50˚C, employing $Ca(OH)_2$ and SiO_2 with molar ratios of 1:1 and 1.5:1, respectively, in pure water at a water-to-powder ratio of 20 mL/g. The resulting mixture was sealed after N_2 purging and cured for 10 days. Upon completion of the curing process, the resulting slurry was subjected to filtration using a suction filter, followed by washing solid particles using deionised water in triplicate to eliminate the ions adsorbed on the C-S-H surface. The washed solid particles were freeze-dried for 48 hours and stored in a desiccator to prevent carbonation prior to analysis. The synthesised C-S-H was then characterised using multiple analyses before use.

Two types of solutions were prepared to investigate the effect of amines on aqueous solutions, one with amines (MAE or MDEA) and the other without, at a water + amine to powder (C-S-H) ratio of 10 mL/g. These solutions were then exposed to carbonation under controlled conditions, including a CO_2 concentration of 5 vol%, a flow rate of 2 L/min, a relative humidity of 60 ± 10%, and a temperature of 20 ± 2ºC for 5 hours. Upon completion of the carbonation process, the resulting samples were filtered, and the solid particles were subjected to Thermogravimetric Analysis (TGA) and phenolphthalein test after drying at 40ºC for 24 hours, and the liquid phase underwent pH analysis. In addition, the remaining analysis, such as Fourier transform infrared (FTIR), X-ray diffraction (XRD) and Scanning electron microscope (SEM), is to be carried out in future.

4. Results and Discussion

The high purity of C-S-H was confirmed as no other phases were found in the XRD and TGA pattern. Fig. 2. illustrates the impact of various amines on calcite formation during the carbonation process in C-S-H with Ca/Si ratios of 1.0 and 1.5. The content of calcium carbonate, which is an indication of the carbonation rate, can be calculated by the weight loss from around 500ºC to 800ºC in TGA curves. It can be seen that MAE show a higher formation of calcite compared to MDEA and control samples in both C-S-H with Ca/Si ratio of 1.0 and 1.5. It is mainly due to its higher reaction rate as its stoichiometry supports converting carbamate to bicarbonate, contributing to an improved CO_2 absorption rate in MAE. MDEA shows less carbonation than MAE as it only acts as a sink for protons produced by slow CO_2

hydrolysis; however, it shows a higher calcite formation than the control sample. Additionally, C-S-H with a higher Ca/Si ratio exhibits an increased propensity for calcite formation owing to the greater availability of Ca ions. This phenomenon remains unaltered in the presence of amine as well. However, there were two different opposite opinions in past studies on the effect of the Ca/Si ratio on the carbonation of C-S-H (Liu et al., 2022).

The decrease in pH is a recognised indicator for the carbonation of C-S-H and can be detected using the phenolphthalein spray test, which induces colour changes as demonstrated in Fig. 3. The appearance of pink colour after spraying the phenolphthalein solution confirms the alkalinity of the samples under consideration. Fig. 3. reveals a strong correlation between the intensity of the pink shade and the Ca/Si ratio of C-S-H, where a higher Ca/Si ratio corresponds to a darker pink colour. This suggests that C-S-H with higher Ca/Si ratios exhibit greater basicity during a specific carbonation period. Furthermore, all samples demonstrate a significant shift in colour from dark to light when the amine is involved.

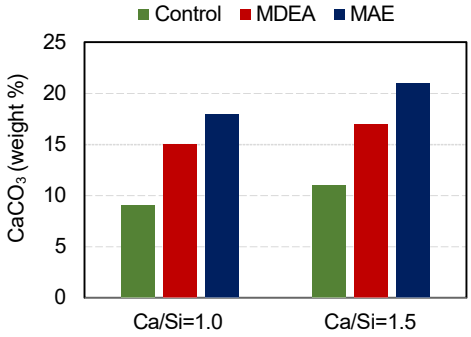


Fig. 2. Effect of different amines and Ca/Si ratio on the formation of calcite during carbonation in C-S-H

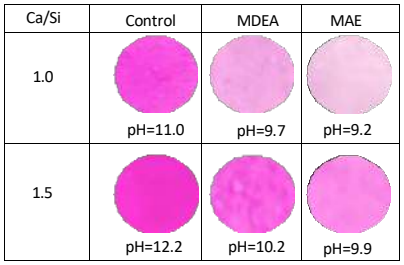


Fig. 3. Changes of colour indicated by phenolphthalein spray test for samples with different Ca/Si ratios and amines

Only calcite formation and pH change are not enough to consider carbonation, so further studies should be considered in future work of this study to understand the mechanism of C-S-H carbonation in the presence of amines.

5. Conclusions

After careful analysis and consideration of the available data, the following conclusions can be drawn:

1) MAE is a more effective solvent for CO_2 absorption than MDEA and the control sample, as demonstrated by its superior performance across all Ca/Si ratios tested.

2) C-S-H with a higher Ca/Si ratio tends to carbonate more rapidly due to the increased availability of Ca ions for calcite formation. Notably, this phenomenon persists even in the presence of amines.

These findings have important implications for optimising carbon capture technologies, with amine promising as a potential candidate for use in large-scale CO_2 capture systems.

References

Liu. X, Feng. P, Cai. Y, Yu. X, Yu. C and Ran. Q (2022) "Carbonation behaviour of calcium silicate hydrate (C-S-H): Its potential for CO_2 capture", *Chem. Eng. J.* 431-134243

The 16th International Congress on the Chemistry of Cement 2023 (ICCC2023)
"Further Reduction of CO_2 -Emissions and Circularity in the Cement and Concrete Industry"
September 18–22, 2023, Bangkok, Thailand

Enzymatic Carbon Sequestration in Cementitious Materials

X. Chen[1*], Z. Zhang[2], and U. Angst[3]

[1] *ETH Zürich, Zürich, Switzerland*
Email: xiulin.chen@ifb.baug.ethz.ch
[2] *ETH Zürich, Zürich, Switzerland*
Email: zhidongz@ifb.baug.ethz.ch
[3] *ETH Zürich, Zürich, Switzerland*
Email: ueli.angst@ifb.baug.ethz.ch

ABSTRACT

Concrete can act as a carbon sink since CO_2 penetrates and reacts with $Ca(OH)_2$ in concrete resulting in the carbonation of concrete, which is a natural process. However, this process is slow due to different factors. Carbonic anhydrase (CA) is a group of enzymes that could be a promising candidate to accelerate CO_2 sequestration. CA acts as a catalyzer for CO_2 hydration to H^+ and HCO_3^- and has been reported to increase the reaction rate by about 10^7 times compared to the process in the absence of CA. Larger amounts of CO_2 may thus be sequestered via carbonation in a shorter period. We aim to achieve efficient atmospheric CO_2 sequestration in cementitious materials with the help of CA. Preliminary results show that CA maintains enzyme activity and accelerates CO_2 hydration in alkaline solutions representative for concrete. Cement pastes with trace amounts of CA exhibited higher carbonation rate at the early stage compared to CA-free cement pastes. While these results are encouraging, more research is needed for further understanding the mechanisms of CA carbonation acceleration in concrete.

KEYWORDS: *CO_2 Sequestration, Carbonic Anhydrase, Cementitious Materials*

1. Introduction

The emission of CO_2 has increased rapidly in the last decades which has pushed the global environment out of safe boundaries. Research has focused on different technologies for reducing atmospheric CO_2, such as geological sequestration, chemical absorption, physical separation, membrane separation and biological fixation (Stewart & Hessami 2005). Nowadays, the biological sequestration technique has attracted many types of research to mitigate the influence of excessive CO_2 because of its low cost and eco-friendliness compared to widely used geological and chemical techniques (Arora 2018).

Bio-sequestration is usually achieved by living organisms, such as bacteria and fungi, via Microbially Induced Calcite Precipitation (MICP) process. MICP is a widespread biochemical process with the formation of $CaCO_3$ crystals in nature all around the world. MICP is the result of interactions between metabolic activities with organic and inorganic compounds present in the surrounding environment. The major metabolic processes involved in MICP include urea hydrolysis, photosynthesis, denitrification, dissimilatory sulphate reduction, nitrate reduction (Song, et al. 2022). However, the chemical environment around the living organisms may negatively affect MICP, such as high pH, low water content, and limited energy source. All living organisms require appropriate living conditions to maintain the metabolic activities for MICP. In addition, the heterotrophic living organisms are not able to use the atmospheric CO_2 directly, instead they produce CO_2 during the respiration.

A very important enzyme produced by living organisms is involved in MICP, namely carbonic anhydrase (CA), which can accelerate CO_2 hydration dramatically compared to that of process in the absence of CA. CA is an enzyme containing Zn^{2+} in its active site, and it catalyzes the reversible reaction of CO_2 and H_2O (Eq. 1) (Shekh, et al. 2012).

$$CO_2 + H_2O \leftrightharpoons HCO_3^- + H^+ \quad (1)$$

The charges on Zn^{2+} attract the oxygen of H_2O and the binding of H_2O to Zn^{2+} lowers the pKa of H_2O, promoting the removal of H^+ and leaving OH^- bound to Zn^{2+}. The CO_2 hydration is initiated by the nucleophilic attack of zinc-bound OH^-, generating zinc-bound HCO_3^-. The active sites are regenerated by replacing HCO_3^- with H_2O and the catalysis cycle continues (Shekh, et al. 2012). The unique catalytic properties of CA lead to the acceleration of CO_2 sequestration by accelerating hydration of CO_2 and release HCO_3^- up to 10^7 time faster than the CO_2 hydration process in the absence of CA (Bond, et al. 2001).
Concrete can act as a carbon sink since CO_2 penetrates concrete and reacts with cement hydration products to produce $CaCO_3$ in the presence of water. Nevertheless, the rate of natural carbonation process in concrete is limited due to different factors, such as CO_2 concentration in the atmosphere, water content in the concrete, and concrete porosity. Our hypothesis is that CA may be applied for accelerating the carbonation process in concrete due to the excellent catalysis efficiency. In this study, the performance of CA enzyme for CO_2 sequestration in cementitious materials was investigated.

2. Materials and Methods

2.1 Solution pH Measurements

To study the CA activity in the high pH environment, the pH of NaOH solution with different CA concentrations was monitored upon exposure to air. A higher pH decrease rate suggests a higher CA activity. 10 mL of 6 mM NaOH solutions contained 0, 1.2, 2.4 μM CA (from Sigma-Aldrich), respectively, were prepared for pH measurements. The pH sensor was placed in solution at given intervals to monitor the pH changes.

2.2 Cement Pastes Preparation

A CA solution with a concentration of 20 μM was prepared by dissolving the CA enzyme powder into deionized water. CEM I 42.5 N cement from Holcim was used to prepare cement paste with a water-to-cement ratio of 0.4. 200 g of cement was mixed in a mixer at a low speed (approximately 140 RPM) for 30 s, and then 80 g of water containing 1 ml of the 20 μM CA solution was slowly added while the mixer continued at the low speed for 60 s. After checking that no dry materials settled at the bottom, the mixing continued for 60 s at the speed of about 580 RPM. The thoroughly mixed materials were cast in plastic bottles with diameter of 31 mm and sealed for curing. The control samples without CA were prepared in the same way but without adding CA powder into water. The plastic bottles were removed after curing for 17 days and the cement pastes were cut into slices with 2 mm thickness. The slices were divided into three groups and exposed to different environments, namely, 20% CO_2, natural carbonation (ambient environment), and sealed in plastic containers, respectively. The slices were crushed and sieved to select particle sizes in range of 0.6 - 1.2 mm for further analyses after 3, 7, and 14 days, respectively.

2.3 Thermogravimetric Analysis (TGA)

TGA tests were performed with Q50 TGA (TA instruments) under the purge flow of nitrogen gas with a rate of 20 mL/min. About 50 mg cement paste were collected for each measurement, and the measurement was performed following the program of (1) heating from room temperature to 105 °C with the rate of 10 °C/min, (2) holding for 30 min, and (3) heating from 105 °C to 1000 °C with the rate of 10 °C/min (Zhang & Scherer 2020).

3. Results

3.1 Solution pH

CA catalyzes the hydration of CO_2, and consequently, H^+ ions from the reactions are released to the surrounding solution resulting in a pH decrease. Therefore, measuring pH is a viable method to monitor the progress of this enzymatic reaction (Mirjafari, et al. 2007). The results are shown in Figure 1. Faster pH

decrease was achieved with higher CA concentration. The results show that the CA enzyme is active at high pH environment and can effectively accelerate CO_2 hydration.

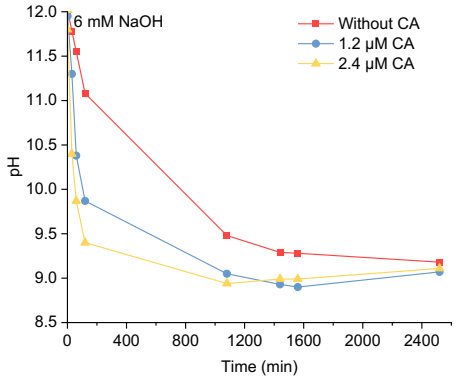


Figure 1. pH of 6 mM NaOH solution with 0, 1.2, 2.4 μM CA, respectively.

3.2 Thermogravimetric Analysis (TGA)

The weight losses curves can be obtained from TGA tests. Figure 2a) shows that samples exposed to 20% CO_2 exhibited the highest weight losses, which is due to the most thermal decomposition of the carbonate phases. The natural carbonation groups showed slightly higher weight losses than that of sealed groups. Several peaks can be identified due to decomposition of different phases from the derivative weight losses curves in Figure 2b). First peak between 105 and 200 °C is due to the release of water from C-S-H and/or the decomposition of small amounts of ettringite (Hall, et al. 1996). The peaks at around 450 °C referring to the decomposition of CH, which is one of the main hydration products of cement. The sealed and natural carbonation groups display higher CH peaks than that of samples exposed to 20% CO_2 since more CH was carbonated to $CaCO_3$ for higher CO_2 concentration. The following larger peaks in higher temperature range can be assigned to the decomposition of $CaCO_3$. The samples exposed to 20% CO_2 exhibit multi-peaks at the range of 550 to 750 °C. The peaks at lower temperature are believed to be metastable $CaCO_3$, such as vaterite and aragonite, and peaks at higher temperature are due to calcite, which has the highest thermodynamic stability among the polymorphs (Radha, et al. 2010).
The temperature range of different peaks were identified individually for each derivative curve. The amount of $CaCO_3$ shown in Figure 2c) was calculated from the derivative curves. For the samples exposed to 20% CO_2, CA enzyme acts as a booster for carbonation and more $CaCO_3$ was obtained during the first week, while after one week the samples without CA exhibited the same amounts of $CaCO_3$, indicating the CA effect might be supressed. The explanation for this "catch-up" could be that samples with CA enhanced carbonation process and reached the maximum carbonation faster than these without CA. Another hypothesis is that further carbonation became difficult after 1 week at 20% CO_2, possibly due to microstructural changes. For instance, the precipitation of $CaCO_3$ may form shells on CH crystals so that HCO_3^- (and CO_3^{2-}) ions cannot easily reach the interior of CH crystals for further reaction. Another reason could be that the pores in the surface layer of cement paste were blocked with $CaCO_3$, hindering CO_2 ingress into deeper layer. The samples exposed to natural carbonation conditions exhibited much lower $CaCO_3$ formation, which can be explained by the CO_2 concentration that was 500 times lower than for the series exposed to 20% CO_2.

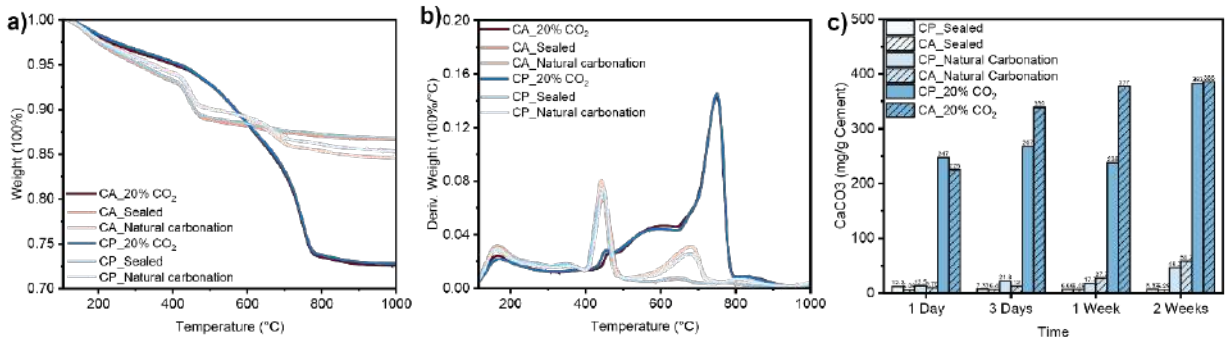


Figure 2. a) TGA weight loss curves for cement paste with and without CA, and b) derivative weight loss curves with and without CA (Only curves of samples in different environment after 14 days are shown). c) the calculated $CaCO_3$ amount in cement pastes. CP refers to cement paste without CA enzyme and CA refers to cement paste with CA enzyme.

4. Conclusions

The catalytic ability of CA suggests a promising potential for CO_2 sequestration applications in cementitious materials. In this study, we evaluated the CA enzyme activity under high pH conditions and quantified the CO_2 sequestration capacity of the enzymatically modified cement pastes. The pH measurements results indicated that CA could maintain the enzyme activity in high alkaline conditions and CA can effectively accelerate the CO_2 hydration. Higher CO_2 hydration process could be achieved with a higher CA concentration. In cement pastes, CA could accelerate carbonation process at the early stage, then the carbonation was retarded probably due to the microstructural changes. Further experiments will be conducted to investigate porosity, pore structures, and other microstructure properties in order to further understanding the interactions between CA and the cement paste. Although the CA enzyme does not affect the ultimate CO_2 sequestration capacity of materials, it can significantly accelerate the process of CO_2 sequestration in cementitious materials. As a result, a substantially greater amount of CO_2 can be sequestered within the same time period when CA is present compared to when it is absent.

Acknowledgements

The authors would like to mention that the work reported here is part of a large initiative at ETH Zurich, entitled “Advanced Engineering with Living Materials” (https://map.ethz.ch/research/alive.html).

References

Arora, N. K. (2018). Bioremediation: a green approach for restoration of polluted ecosystems. *Environmental Sustainability, 1*(4), 305-307.

Bond, G. M., Stringer, J., Brandvold, D. K., Simsek, F. A., Medina, M.-G., & Egeland, G. (2001). Development of integrated system for biomimetic CO2 sequestration using the enzyme carbonic anhydrase. *Energy & Fuels, 15*(2), 309-316.

Hall, C., Barnes, P., Billimore, A. D., Jupe, A. C., & Turrillas, X. (1996). Thermal decomposition of ettringite Ca-6[Al(OH)(6)](2)(SO4)(3).26H(2)O. *Journal of the Chemical Society-Faraday Transactions, 92*(12), 2125-2129.

Mirjafari, P., Asghari, K., & Mahinpey, N. (2007). Investigating the application of enzyme carbonic anhydrase for CO2 sequestration purposes. *Industrial & Engineering Chemistry Research, 46*(3), 921-926.

Radha, A. V., Forbes, T. Z., Killian, C. E., Gilbert, P. U. P. A., & Navrotsky, A. (2010). Transformation and crystallization energetics of synthetic and biogenic amorphous calcium carbonate. *Proceedings of the National Academy of Sciences of the United States of America, 107*(38), 16438-16443.

Shekh, A. Y., Krishnamurthi, K., Mudliar, S. N., Yadav, R. R., Fulke, A. B., Devi, S. S., & Chakrabarti, T. (2012). Recent Advancements in Carbonic Anhydrase-Driven Processes for CO2 Sequestration: Minireview. *Critical Reviews in Environmental Science and Technology, 42*(14), 1419-1440.

Song, M. Z., Ju, T. Y., Meng, Y., Han, S. Y., Lin, L., & Jiang, J. G. (2022). A review on the applications of microbially induced calcium carbonate precipitation in solid waste treatment and soil remediation. *Chemosphere, 290*, 133229.

Stewart, C., & Hessami, M. A. (2005). A study of methods of carbon dioxide capture and sequestration - the sustainability of a photosynthetic bioreactor approach. *Energy Conversion and Management, 46*(3), 403-420.

Zhang, Z. D., & Scherer, G. W. (2020). Measuring chemical shrinkage of ordinary Portland cement pastes with high water-to-cement ratios by adding cellulose nanofibrils. *Cement & Concrete Composites, 111*.

The 16th International Congress on the Chemistry of Cement 2023 (ICCC2023)
"Further Reduction of CO_2 -Emissions and Circularity in the Cement and Concrete Industry"
September 18–22, 2023, Bangkok, Thailand

Role of Mixing Temperature on CO_2 Mineralization of Cement-based Materials

Won Kyung Kim[1], Junboum Park[2], and Juhyuk Moon[3*]

[1] *Department of Civil and Environmental Engineering, Seoul National University, Seoul, 08826, Republic of Korea*
Email: semgua@snu.ac.kr
[2] *Department of Civil and Environmental Engineering, Seoul National University, Seoul, 08826, Republic of Korea*
Email: junbpark@snu.ac.kr
[3] *Department of Civil and Environmental Engineering, Seoul National University, Seoul, 08826, Republic of Korea*
Email: juhyukmoon@snu.ac.kr

ABSTRACT

In-situ CO_2 mixing technology is a representative carbon capture and utilization (CCU) that could permanently store carbon dioxide (CO_2) in a certain mineral phase. Due to the relatively easy implementation, it is being evaluated in many countries and several real case applications have been already achieved. In this study, the absorbed CO_2 concentration as a function of water temperature was examined. The results demonstrate that the temperature of water plays a crucial role in mineral carbonation, as higher temperatures lead to a considerable rise in CO_2 uptake. It was confirmed that the early precipitation of calcium carbonate ($CaCO_3$) affects the development of mechanical strength. Thermogravimetric analysis (TGA) and X-ray diffraction analysis (XRD) confirmed the precipitated $CaCO_3$ in early age and revealed its impact on later stage of hydration with regard to the stability of hydration products. Furthermore, quantitative analysis of $CaCO_3$ was conducted at different curing period by comparing experimental results and thermodynamic modeling based on the CO_2 content.

KEYWORDS: *In-situ CO_2 mixing, Carbon dioxide, Mineral carbonation, Temperature*

1. Introduction

The emission of significant amount of greenhouse gases has led to abnormal climate patterns that have attracted global attention. The need to utilize carbon dioxide (CO_2) produced in various industry is becoming apparent. As a means of utilizing CO_2, this study employed in-situ CO_2 mixing technology to uptake gaseous CO_2 in cement paste. By introducing CO_2 during the mixing of cement-based materials, this mineral carbonation leads to the formation of calcium carbonate ($CaCO_3$). In this study, the temperature of the mixing water was set as a variable to maximize CO_2 uptake. Moreover, the existence of $CaCO_3$ that had precipitated was investigated using microstructural analysis, and the impact on the mechanical strength was confirmed.

2. In-situ CO_2 mixing

The in-situ CO_2 mixing is a mineral carbonation technology that precipitates $CaCO_3$ during the mixing process of cementitious materials by injecting CO_2 (Hepburn et al (2019)). The clinker minerals that make up cement induce dissolution of abundant calcium ions (Ca^{2+}) through a hydration reaction. The injected gaseous CO_2 dissolves and dissociates in the cementitious mixture to form carbonate (CO_3^{2-}) and then precipitates $CaCO_3$ through the combination of Ca^{2+} and CO_3^{2-} as shown in the following chemical equation (1-3).

$$C_3S + 3H_2O \leftrightarrow 3Ca^{2+} + SiO_2 + 6OH^- \quad (1)$$

$$C_2S + 2H_2O \leftrightarrow 2Ca^{2+} + SiO_2 + 4OH^- \quad (2)$$
$$Ca^{2+} + CO_3^{2-} \leftrightarrow CaCO_3 \quad (3)$$

The solubility of CO_2 in a solution depends on various factors, including the temperature, pressure, and the chemical properties of the solution. However, in general, the solubility of CO_2 is relatively low compared to other gases like oxygen and nitrogen. This is because CO_2 is a nonpolar molecule, which means it is less likely to interact with polar solvent molecules like water.
Additionally, the solubility of CO_2 is affected by the pH of the solution. When CO_2 dissolves in water, it can react with H_2O to form carbonic acid (H_2CO_3) and it can exist stably as CO_3^{2-} as the pH of the solution increases (Dodds et al (1956), Zeebe et al (2001)). To absorb CO_2 in cementitious materials, a chemically dissociative process is required, where it is advantageous to form highly alkaline conditions that facilitate ionization. In here, dissociation is defined as the process of CO_2 gradually releasing hydrogen ions (H^+) and ionizing into CO_3^{2-}. Equation (4-6) describes the process of dissolution of CO_2 and dissociation of H_2CO_3.
The high alkalinity of the pore solution in cementitious mixtures, with a pH value over 13, creates a highly favorable environment for H_2CO_3 dissociation to occur (König et al (2019)). This process allows H_2CO_3 to release H+ and form bicarbonate (HCO_3^-) and CO_3^{2-} ions, contributing to the overall buffering capacity of the solution and preventing the accumulation of excessive gaseous CO_2. If the CO_2 is not fully dissociated and can remain as bubbles that rise to the surface and escape into the air.

$$CO_2 + H_2O \leftrightarrow H_2CO_3 \quad (4)$$
$$H_2CO_3 \leftrightarrow HCO_3^- + H^+ \quad (5)$$
$$HCO_3^- + H^+ \leftrightarrow CO_3^{2-} + 2H^+ \quad (6)$$

3. Methodology and results

3.1. Sample preparation

To perform in-situ CO_2 mixing at laboratory scale, a mixer and CO_2 concentration sensor were placed in the chamber shown in Figure 1. In particular, the chamber is designed to be hermetically sealed to precisely measure the CO_2 concentration. Monitoring the remaining amount of CO_2 is crucial to accurately calculate the amount of absorbed CO_2 through in-situ CO_2 mixing. The operational procedure of the equipped chamber for in-situ CO_2 mixing involves placing all the necessary materials (cement, water, CO_2 gas concentration sensor, etc.) inside the sealed chamber that blocks the inflow of outside air, and injecting CO_2 gas up to a concentration of 10 vol%. Once the CO_2 concentration inside the chamber has stabilized, the mixing process can begin while continuously monitoring the concentration. The main objective of this study is to improve the uptake of CO_2 and $CaCO_3$ precipitation by enhancing the solutiliby of cement. Therefore, we varied the temperature of the mixing water and analyzed its effect on CO_2 uptake during in-situ CO_2 mixing. The experiment involved mixing water at three different temperatures: 5℃, 25℃, and 50℃, with Ordinary Portland cement (OPC) and a water-to-cement ratio (w/c) of 0.5. As a result of in-situ CO_2 mixing, as the water temperature increased, the CO_2 uptake also increased from about 1.5 vol% to 1.8 vol%.

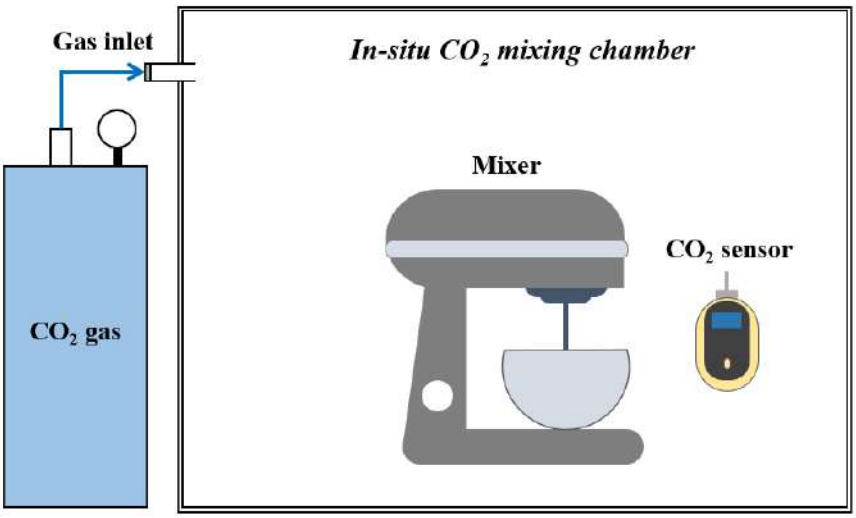


Figure 1. Schematic view of in-situ CO_2 mixing chamber

3.2. Mechanical properties testing

The temperature and flow diameter of the paste were measured right after mixing to investigate how in-situ CO_2 mixing affected its workability. As the CO_2 uptake increased, the mixing of CO_2 in fresh cement paste led to an increase in temperature of the mixture and a significant reduction in flow diameter from approximately 95 mm to 80 mm. In addition, a cubic sample with a side length of 5mm was prepared and demolded after 24 hours. The paste's compressive strength was then measured on each of the following curing days: 1, 3, 7, 14, 28 days. This study also analyzed how water temperature affected the mechanical properties of the paste mixed under CO_2 condition, in relation to the hydration reaction. Consequently, specimens with higher CO_2 uptake showed a significant increase in early strength of about 16 MPa on the first day of curing, which was about 6 MPa higher than that of 5℃ samples.

3.3. Microstructural analysis effect

For the microstructural analysis, the specimens were pre-treated through hydration suspension at each curing day. Afterwards, the specimens were subjected to thermogravimetric analysis (TGA) and X-ray diffraction analysis (XRD) to verify the presence of precipitated $CaCO_3$. In the TGA results for all samples immediately after mixing, about 1.5 % or more of $CaCO_3$was newly precipitated through in-situ CO_2 mixing. Additionally, in-situ CO_2 mixing was implemented by thermodynamic modelling, and the development of hydrates was compared to the TGA results. The measured CO_2 uptake (vol %) during the in-situ CO_2 mixing process was converted to weight (g) and applied to the simulation. The experimentally validated CO_2 uptake was assumed to be fully decomposed in the thermodynamic modelling. Overall microstructural analysis indicated that an increase in CO_2 uptake, resulted in a higher precipitation of $CaCO_3$ at the early stage. The simulations effectively illustrated this early precipitation of $CaCO_3$ and compared its impact on other cement compounds and hydration products.

4. Conclusions

The objective of our research is to improve CO_2 uptake and $CaCO_3$ precipitation in cement-based mixtures by using water at different temperatures for in-situ CO_2 mixing. We found that increasing the water temperature led to higher solubility of the cement clinker, resulting in greater CO_2 uptake. Furthermore, the early precipitation of $CaCO_3$ accelerated the hydration reaction and significantly increased the early compressive strength. Our findings demonstrate that the efficiency of mineral carbonation can be improved through in-situ CO_2 mixing by solely adjusting the mixing water temperature, without the need for any additional admixture.

Acknowledgements

This work was supported by Korea Institute of Energy Technology Evaluation and Planning(KETEP) grant funded by the Korea government(MOTIE)(20212010200080, Development of In-situ carbonation technology using CO2 released from cement industry).

References

Hepburn, C., Adlen, E., Beddingtong, J., Carter, E.A., Fuss, S., Mac Dowell, N., Minx, J.C., Smith, P. and Williams, C.K. (2019) "The technological and economic prospects for CO2 utilization and removal", *Nature*, 575(7781): 87-97

Dodds, W.S., Stutzman, L.F. and Sollami, B.J. (1956) "Carbon dioxide solubility in water", *Industrial & Engineering Chemistry Chemical & Engineering Data Series*, 1(1): 92-95

Zeebe, R.E. and Wolf-Gladrow, D. (2001) "CO2 in seawater: equilibrium, kinetics, isotopes", *Gulf Professional Publishing*, 65

König, M., Vaes, J., Klemm, E. and Pant, D. (2019) "Solvents and supporting electrolytes in the electrocatalytic reduction of CO2", *Iscience*, *19*: 135-160

The 16th International Congress on the Chemistry of Cement 2023 (ICCC2023)
"Further Reduction of CO_2 -Emissions and Circularity in the Cement and Concrete Industry"
September 18–22, 2023, Bangkok, Thailand

Experience of a real precast and site-cast application of alkali-activated GGBS based binder concrete

A. Kiiashko[1*]; F. Cussigh[2]; L. Frouin[1]; R. Alfani[1]; D. Achard[3]; M. Chaouche[4]

[1] *Ecocem Materials LTD, 4 Place Louis Armand, 75012 Paris, France*
*akiiashko@ecocem.ie**
[2] *Vinci Construction, 5 Cours Ferdinand de Lesseps, 92500 Rueil-Malmaison, France*
francois.cussigh@vinci-construction.fr
[3] *Ecocem France, Horizon Sainte Victoire, 970 Rue René Descartes, 13100 Aix-en-Provence, France*
dachard@ecocem.fr
[4] *ENS Paris-Saclay, CNRS Laboratoire de Mécanique Paris-Saclay, 91160, Gif-sur-Yvette, France*
mohend.chaouche@gmail.com

ABSTRACT

The construction industry, like many other sectors, is facing a serious challenge that requires an immediate and drastic reduction in carbon emissions. To achieve this, a reduction in the use of Portland cement clinker is mandatory. The use of alternative cements based on industrial by-products can significantly accelerate the process of emissions reduction. One example of such cements is a ground granulated blast-furnace slag (GGBS) activated by sodium carbonate (Na_2CO_3). This type of cement, widely used in the former Soviet Union, has received a new lease on life in recent years. Over fifteen thousand cubic meters of concrete, destined for use in both ready-mix (structural reinforced concrete) and heavy precast concrete (tunnel segments), have been poured in recent years demonstrating its potential and versatility. The use of this binder as an alternative to a conventional CEM I results in a drastic reduction of embodied carbon per cubic meter of concrete. This paper presents a study on the use and performance, from the standpoints of rheology, mechanical performance and durability, of such concretes in industrial settings to encourage the use of such alternative binders.

KEYWORDS: *Alkali-activated concrete, sodium carbonate activation, sustainability, eco-friendly concrete, industrial applications*

1. Introduction

The effects of climate change are becoming more visible around the world. Deregulation of the seasons leads to snowfalls in Europe in April and then to unprecedented heat that destroys the entire harvest in the summer, renders habitation infeasible in many parts of the African continent, leads to the destruction of ancient tropical forests in Latin America, etc. By acting immediately, there is still an opportunity to avoid critical changes. For this, a drastic reduction in CO_2 emissions is required (Wyns, 2023). Many industrial sectors have already begun the active introduction of technologies that, although they do not cancel out the negative impact, they at least prevent even greater greenhouse gas emissions with a constant increase in the needs of the growing population of the planet.
The construction industry is one of the largest CO_2 emitters worldwide (Syngros et al., 2017). Over the past few decades, efforts have been made to reduce energy losses and thus reduce gas emissions during the operation of buildings. However, this has not yet led to a significant reduction, as the overall consumption has increased every year. At the same time, the use of materials with a low impact on the environment is only in the initial stages for industrial scale applications. Sustainable construction should be sought, including smart buildings, low environmental impact materials, large-scale recycling and the valorisation of different wastes (Labaran et al., 2022). There is no universal solution that can solve all problems. Individually, each method has its own advantages and disadvantages.

In the building materials sector, concrete is the most used material. Due to the significant volumes, the production leads to significant CO_2 emissions, 90-95% of which is associated with the binder used. It is not worth repeating how the production of Portland cement clinker, as the most common type of binder, leads to significant greenhouse gas emissions. Carbon capture and storage technology might help in reduction of these emissions. This requires not only significant financial resources but is often very complicated due to the significant demand for decarbonized energy or the impossibility of transportation/storage of the resulting liquefied gas (Plaza et al., 2020). Therefore, more significant efforts should be directed towards reducing the consumption of clinker by the increased use of various SCMs and the development of new types of binders based on these materials (large range of industrial wastes, as well as natural sources like limestone, pozzolans, and clays).

2. Description of the binder preparation technology

In the present article, the experience of the use of an alkali-activated GGBS based-binder activated by Na_2CO_3 at industrial scale is presented. This type of the binder was already used in the Ukrainian SSR (Krivenko, 2017; Palomo et al., 2014; Provis, 2018). Several studies have demonstrated that it can provide excellent long-term mechanical and durability properties (Bernal et al., 2013; Shi. et al., 2006). One of the most positive qualities of this type of activation is its higher safety (pH of around 12.9 when the concrete is in the fresh state) compared to activation with highly alkaline solutions (sodium silicate or hydroxide for ex.) which require a high degree of protection of the workers and can even be hazardous to conventional equipment. However, poor rheological properties and low early age strength have been reported (Conte & Plank, 2019; Kovtun et al., 2015), which were the main obstacles in recent years for market adoption. This issue was solved by using an appropriate retarding additive, which also has a fluidifying effect (Kiiashko et al., 2021). In addition, to achieve high fluidity for ready-mix concrete applications, the compositions were optimised. For the moment, superplasticizers available on the market cannot provide the same degree of workability and rheological control as they can with binders composed largely of Portland cement. For this reason, the retarding additive described previously is used. Further, the coarse and fine aggregates are proportioned to promote workability. To achieve the desired fresh state properties, a limestone filler (d50=7µm) is added to increase the paste volume, increasing the distance between the aggregates and therefore reducing the shear rate experienced by the paste fraction. The limestone filler is pre-blended into the binder meaning that the ratio between powdered components is fixed and not decided at the batching plant.
The decision to pre-blend the binder was taken to simplify the use of this binder at the batching plant. All ingredients (including GGBS, limestone, and Na_2CO_3) are carefully mixed in the binder factory (Ecocem France, Dunkerque). The end user is therefore required to occupy only one silo with this binder. In cases where extended open time was required (>90 minutes with a slump >180mm), a supplementary retarder in liquid form is used and added to the concrete using existing equipment used for superplasticiser addition. In total, slightly more than 6000 tons of this “all-in-one binder” was manufactured and used in 2021-2022, mainly in France, and commercialised under the name of “Ecocem Ultra” by Ecocem France to produce “Exegy ultra-low carbon concrete” by Vinci Construction Group.

3. Ready mix concrete

The concrete using this Na_2CO_3 activated GGBS was prepared and delivered in the same way as conventional ready-mix concrete based on Portland cement. In the cases presented here, the concrete was prepared with a Water/Binder ratio between 0.38 and 0.40 and consistency class of S4 and higher (slump >180mm using an Abrams’ cone, EN 12350-2) and higher. The concrete was placed using the concrete bucket, even if the pumping of this type of concrete is also possible and was carried out on other sites. Table 1 presents essential information on the concrete used on three construction sites in France.
In contrast to all the advantages of this type of binder (low carbon impact, safety), one of its disadvantages is sensitivity to low temperatures, specifically the impact on early strength development. In the case of the Olympic village (concrete slabs), concrete was poured mostly in winter when average daily temperatures are typically less than 10°C. To increase the rate of strength development at early age, after placing, the concrete was covered with heat-insulating mats equipped with warm air supply to maintain the average concrete temperature at between 15-20°C during the first 48h.

Table 1 Main information about the concrete used for the ready-mix application

	Total binder including limestone filler, kg/m^3	**Sand**	**Coarse aggregates**	**Concrete class as designed**	**Average compressive strength values measured via cylinder (MPa)**		**Consistency as in EN 12350-2**	**Average CO_2 equivalent emissions of 1m^3 of fresh concrete**
					7 days	28 days		
Olympic village (floor slabs)	400…450	Natural sands 0-1 and 0-4 mm.	Mix of crushed and alluvial gravels 4-12 and 10-20 mm	C 25/30 XF1	18	30	S4 and SF1 for 90 minutes	65 kg.$CO_{2.éq}$/m^3
Administrative 2 storey building (full building, except the foundations)	450	Natural sands 0-4 mm	Alluvial gravels 4-11 and 11-22 mm	C 25/30 XF1	30	50	S4 for 90 minutes	85 kg.$CO_{2.éq}$/m^3
I3F, Two residential 7 storey houses (full building, except the foundation slab)	450…490	Natural sands 0-1 and 0-4 mm.	Mix of crushed and alluvial gravels 4-12 and 10-20 mm	C 30/37 XF1	25	45	S4 and SF1 for 120 minutes	85 kg.$CO_{2.éq}$/m^3

In the case of the two other projects (Fig. 1), metal formwork with heating elements was used during the manufacture of vertical elements. The curing temperature was about 50°C during the first 16h to ensure that demoulding could take place the next day to respect the worksite productivity targets that have historically been dictated by the early age strength development of concrete containing very high clinker content. Typically, demoulding in France on the construction site occurs between 16h and 24h. The amount of CO_2 emitted during the heat curing process can vary depending on various factors (source of energy, duration, outdoor temperature, etc.) and falls between 5 and 20 kg/m^3. Even taking this into account, the overall CO_2 emissions is still much lower compared to concrete with high clinker content. When early strength is not required and demoulding can take place after 2 or 3 days, then these emissions do not occur at all. The concrete characteristics was systematically controlled on all construction sites.



Fig. 1, Construction site I3F (France, 2022). All concrete on the photo is based on GGBS activated by Na_2CO_3

4. Pre-cast concrete elements

Subway tube tunnel segments were prepared in a precast plant, using a stiff concrete with steel and polypropylene fibres to ensure fire and flexural resistance (no steel reinforcement was used). Three types of aggregates (0-1 mm and 0-4 mm sand, and crushed limestone gravel with size 4-20mm) and 475 kg/m^3 of the binder were used. The consistency class S1 was required so that the element maintains its shape without the need for formwork. The production cycle includes steam curing of the fresh concrete during 5-6 hours at 55-60°C to ensure that handling of the element is possible after very short period. The eq. CO_2 of fresh concrete was 100 kg/m^3. The average compressive strength evolution is presented in Fig. 2. The values were measured on 150x150 mm cubes cured under the same conditions as the tunnel segments. After only 5h of heat curing, more then 20MPa was achieved. Significant strength development is observed between 28 and 90 days. These results were further confirmed by assessing the compressive strength of core samples from the tunnel segments after being stored outside. A full-scale compressive strength test and a 3-point flexural strength were also performed (Fig. 3). The elements were also tested

for fire-resistance (temperature rising to 1200°C for 2 hours). No significant destruction or degradation of the element was observed. The results confirmed that the elements fulfilled all the required specifications.

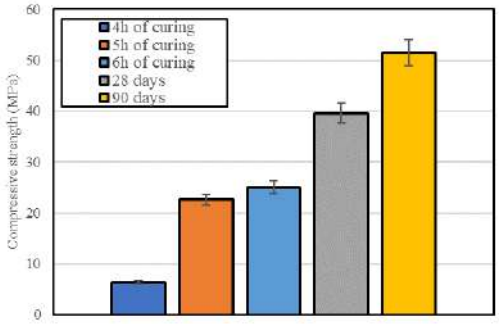


Fig. 2, Compressive strength of the concrete after heat curing for 6h (≈60°C) and during further storage at 20°C



Fig. 3, Full scale 3-point flexural strength test of the tunnel segment

5. Conclusions

Several years' experience of full-scale production and use of sodium carbonated GGBS activated binder confirmed the possibility of its use to produce ready-mix and pre-cast type concrete for different construction projects. The use of such a binder has many benefits (low CO_2 emissions, durability, safety), but it is important to carefully evaluate the specific project requirements and conditions to evaluate suitability. No additional investment in equipment or any significant change in construction methods is required (conventional equipment is suitable for this binder). The open time can be easily controlled by the addition of the setting retarder in case of long transportation (over 1h) or elevated outdoor temperatures in summer (>30°C). However, it is important to note that the use of this alkali-activated GGBS binder requires careful consideration of the mix design and curing conditions to ensure optimal performance. The early age strength (<24h) can be significantly improved by heat curing with the temperature of 40-60°C when this is required by the project. This type of alternative binder can significantly contribute to a reduction of the carbon emissions of the cement and concrete industries. However, only carefully considered decisions and joint efforts of all players can achieve the goals set to reduce greenhouse gas emissions.

References

Wyns, A. (2023). COP27 establishes loss and damage fund to respond to human cost of climate change. *The Lancet. Planetary Health*, *7*(1), e21–e22.

Syngros, G., Balaras, C. A., & Koubogiannis, D. G. (2017). Embodied CO 2 Emissions in Building Construction Materials of Hellenic Dwellings. *Procedia Environmental Sciences*, *38*, 500–508.

Labaran, Y. H., Mathur, V. S., Muhammad, S. U., & Musa, A. A. (2022). Carbon footprint management: A review of construction industry. In *Cleaner Engineering and Technology* (Vol. 9). Elsevier Ltd.

Plaza, M. G., Martínez, S., & Rubiera, F. (2020). CO_2 capture, use, and storage in the cement industry: State of the art and expectations. In *Energies* (Vol. 13, Issue 21). MDPI AG.

Krivenko, P. (2017). Why alkaline activation - 60 years of the theory and practice of alkali-activated materials. In *Journal of Ceramic Science and Technology* (Vol. 8, Issue 3, pp. 323–333). Goller Verlag.

Palomo, A., Krivenko, P., Garcia-Lodeiro, I., Kavalerova, E., Maltseva, O., & Fernández-Jiménez, A. (2014). A review on alkaline activation: New analytical perspectives. *Materiales de Construccion*, *64*(315).

Provis, J. L. (2018). Alkali-activated materials. *Cement and Concrete Research* (Vol. 114, pp. 40–48). Elsevier Ltd

Bernal, S. A., San, R., & Deventer, J. S. J. Van. (2013). Natural carbonation of aged alkali-activated slag concretes. *Materials and Structures*, *4*, 693–707.

Shi., C., Krivenko, P. V., & Roy, D. (2006). *Alkali-Activated Cements and Concretes*. Taylor & F.

Conte, T., & Plank, J. (2019). Impact of molecular structure and composition of polycarboxylate comb polymers on the flow properties of alkali-activated slag. *Cement and Concrete Research*, *116*(July 2018), 95–101.

Kovtun, M., Kearsley, E. P., & Shekhovtsova, J. (2015). Chemical acceleration of a neutral granulated blast-furnace slag activated by sodium carbonate. *Cement and Concrete Research*, *72*, 1–9.

Kiiashko, A., Chaouche, M., & Frouin, L. (2021). Effect of phosphonate addition on sodium carbonate activated slag properties. *Cement and Concrete Composites*, *119*.

The 16th International Congress on the Chemistry of Cement 2023 (ICCC2023)
"Further Reduction of CO_2 -Emissions and Circularity in the Cement and Concrete Industry"
September 18–22, 2023, Bangkok, Thailand

Promoting Carbonization of Hardened Cement Paste by Wet-Dry Cycle

D. Oh [1*], Z. Zhao[1], Y. Wang[1], R. Kitagaki[1], T. Masuo[2], and T. Noguchi[3]

[1] *Faculty of Engineering, Hokkaido University, Kita 13 Nishi 8, Kita-ku, Sapporo, Hokkaido 060-8628, Japan.*
[2] *Masuo Recycle Co.,Ltd, 18-1, Nishinippori 2-chome, Arakawa-ku, Tokyo, 116-0013, Japan*
[3] *Graduate School of Engineering, the Univ. of Tokyo, 7-3-1, Hongo, Bunkyo-ku, Tokyo, 113-8656, Japan*

Email: ekdud333@eng.hokudai.ac.jp

ABSTRACT

The global population growth and rapid industrial development of the past century have resulted in exponential emissions of CO_2, which are held responsible for global warming. Cement production causes CO_2 emissions, but waste concrete after demolition has the potential to compensate for a part of this emission by using as recycled material. Portlandite ($Ca(OH)_2$) and calcium-silicate-hydrate (C-S-H) in waste concrete can afford to absorb CO_2 but are recycled without being sufficiently carbonated because there is not enough space for long-term storage. In other words, if it can promote the carbonization of waste concrete, the concentration of CO_2 in the atmosphere can be reduced more efficiently. In this study, to examine methods for promoting carbonation of waste concrete under atmospheric conditions, the degree of carbonation according to environmental conditions, especially humidity, was measured using hardened cement paste fine (HCPF) with a particle size of 0.6 to 1.18mm. The amount of CO_2 absorption of HCPF is evaluated by thermogravimetric analysis (TGA). The result of TGA of 7 days shows that the consumption of $Ca(OH)_2$ and calcite production were the largest in HCPF under the condition of RH 80%. However, the presence of vaterite and aragonite due to the CO_2 absorption of C-S-H was almost absent. On the other hand, in HCPF under the condition of RH 60-80 (wet-dry cycle), the presence of amorphous calcium carbonate (ACC), vaterite, and aragonite, as well as calcite, was found. Therefore, the total amount of CO_2 absorption was greatest in an environment with wet-dry cycle. These results indicate that the decomposition of C-S-H and $Ca(OH)_2$ are promoted in the wet-dry cycle environment, and thus CO_2 can be absorbed more effectively. Based on these results, this study proposes an optimal condition for promoting the carbonization of waste concrete.

KEYWORDS: *CO_2 absorption, carbonation, waste concrete, hardened cement paste fine, wet-dry cycle*

1. Introduction

CO_2 emissions due to cement production have increased significantly for decades, and to solve this problem, CO_2 emissions countermeasures using waste concrete containing calcium silicate hydrate (C-S-H) and portlandite ($Ca(OH)_2$) has been in the spotlight recently. Waste concrete absorbs CO_2 in the atmosphere while being piled up for about a month before being recycled as roadbed materials or recycled aggregates. During this limited period, it is important to increase the carbonation speed to improve the CO_2 absorption efficiency of waste concrete before recycling it. Factors affecting the degree of concrete carbonation can divide into internal factors such as particle size, water-cement ratio, and type of cement, and external factors such as relative humidity, temperature, and CO_2 concentration. In particular, during the concrete carbonation process, water acts as a solvent in which solids and CO_2 can dissolve and as a reaction medium in which dissolved ions combine to precipitate carbonates (Pan et al

(2018)). Therefore, this study analyzed the effect of relative humidity on the degree of carbonation of hardened cement paste, which mimicked the binder part of waste concrete. In addition, the degree of decomposition of C-S-H according to the periodic humidity change was analyzed to know the effect of the wet-dry cycle on the promotion of carbonation of hardened cement paste.

2. Materials and Methods

2.1 Materials

This study used laboratory-made cement paste to mimic the binder part of waste concrete and to dissolve the disproportion by the difference in the amount of aggregate in waste concrete. The ordinary portland cement provided by Taiheiyo Cement Corporation was used for cement pastes with water-to-cement ratios of 0.6. The cement paste was sealed curing for more than 28 days at 20℃. After curing, hardened cement paste was crushed by a ball mill and sieved. The target particle size of hardened cement paste is between 0.6 and 1.18 mm, assuming fine-crushed hardened cement paste detached from concrete waste in actual demolition site in Japan. The degree of hydration of cement paste before carbonation was 69.94%, obtained from the result of TGA and calculated according to the methods proposed by Bhatty (1986).

2.2 Methods

2.2.1 Experiment conditions

The hardened cement paste fines (HCPFs) with a particle size between 0.6 and 1.18mm were put in desiccators under the constant humidity condition of RH60, RH80, and the cycle RH60-80 of 30 minutes, 1 hour, 2 hours, and 4 hours. The temperature and the CO_2 concentration in desiccators were 20℃ and 0.03%, respectively. The experiment conditions are shown in Table 1.

Table 1. Experiment conditions

Relative humidity	RH 60	RH 80	RH 60-80
Cycles	-	-	0.5 h, 1 h, 2 h, 4 h
Temperature and CO_2 concentration	20℃, 0.03% (concentration in the atmosphere)		
Particle size of HCPF	0.6 ~ 1.18 mm		
Periods	3 days, 7 days, 14 days		

2.2.2 Thermogravimetric analysis (TGA)

The amount of CO_2 absorption of hardened cement paste can be analyzed by thermogravimetric analysis (TGA). After carbonation was carried out for 3 days, 7 days, and 14 days under each relative humidity condition, TGA was measured. In this experiment, before measuring TGA, carbonated HCPFs were dried for more than 24 hours in a vacuum desiccator, which has a condition of 30℃. The measurement was performed from 20℃ to 950℃ at a heating rate of 10℃/min and maintained at 950℃ for 1 hour under an N_2 atmosphere.

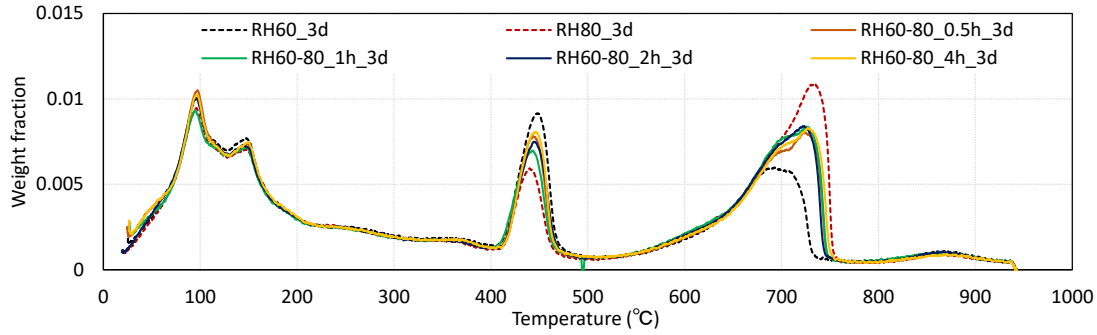
3. Result and Discussion

The TGA results are shown in Figure 1(a)-(c). Referring to Zajac et al (2022) and Wang et al(2019) researchs, the thermal decomposition temperature of calcium carbonate ($CaCO_3$) crystals was determined as follows; amorphous calcium carbonate (ACC) or poorly crystalline $CaCO_3$ (500~650℃), aragonite and vaterite (650~720℃) and, calcite (720~770℃). During the early stage, RH80 produces the most calcite. On the 7 days, in all samples except for RH60, almost the same amount of calcite was produced. In

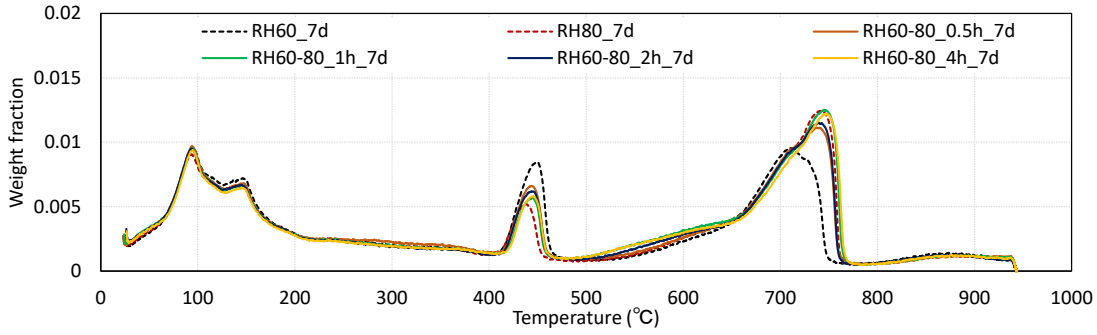
addition, it can be seen that ACC or poorly crystalline $CaCO_3$, aragonite, and vaterite were produced in the RH60-80 regardless of their cycles. On the 14 days, it was found that ACC or poorly crystalline $CaCO_3$, absent in RH80, was also produced in RH60. According to Drouet et al (2019), the polymorphic transformation from the metastable state to the thermodynamically stable state is suppressed at low RH due to the lack of water in the pores.

Figure 2(a)-(b) shows the ratio of $Ca(OH)_2$ and CO_2 absorption by period from the result of the TGA. During the early stage, the consumption of $Ca(OH)_2$ was higher in the order of RH60, RH60-80, and RH80, and the cycle of RH60-80 did not have a significant effect. On the 7 days, the amount of $Ca(OH)_2$ consumption was almost the same for RH80 and RH60-80 (cycle: 1h, 4h), but the amount of CO_2 absorption was higher for RH60-80 than for RH80. It can be seen that the amount of CO_2 absorbed by C-S-H was larger than that of RH80. RH60 had the lowest $Ca(OH)_2$ consumption and CO_2 absorption during the early stage, but the CO_2 absorption became almost the same as RH80 on the 14 days.

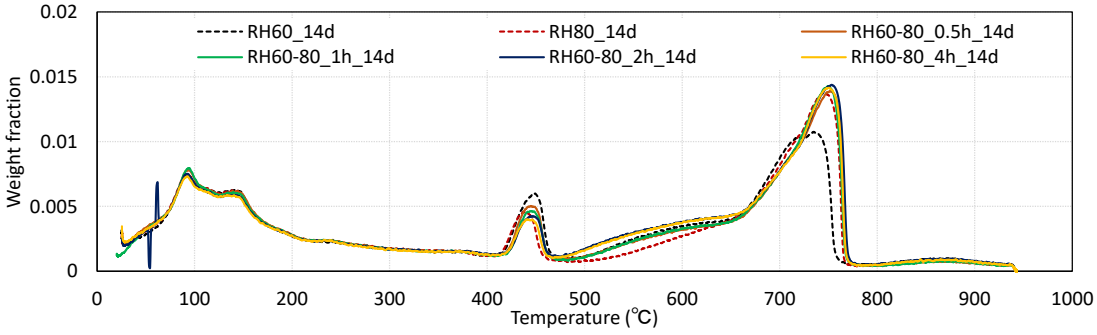
Next, the $CaCO_3$ production rate by each source of calcium was calculated from the TGA results to determine the crystal structures of $CaCO_3$ depending on the calcium sources for each humidity condition. The result is shown in Figure 3. In the early stage, $CaCO_3$ generated from $Ca(OH)_2$ was dominant at RH80, and the amount of $CaCO_3$ was the highest in RH80 among all samples. Figure 1(a) shows that most of these $CaCO_3$ were calcite. At RH60-80, C-S-H was decomposed by repeated drying and wetting over time, and the amount of $CaCO_3$ generated from C-S-H on 7 and 14 days was larger than that of RH80. From the results of TGA(Fig.1(b)-(c)), it was found that the production rate of ACC or poorly crystalline $CaCO_3$, aragonite and vaterite in RH60-80 was higher than that of RH80. And this result is consistent with the other researcher's results which are that aragonite and vaterite are generally obtained from the carbonation of C-S-H and sulfoaluminate phases (Drouet et al (2019)).



(a) 3 days



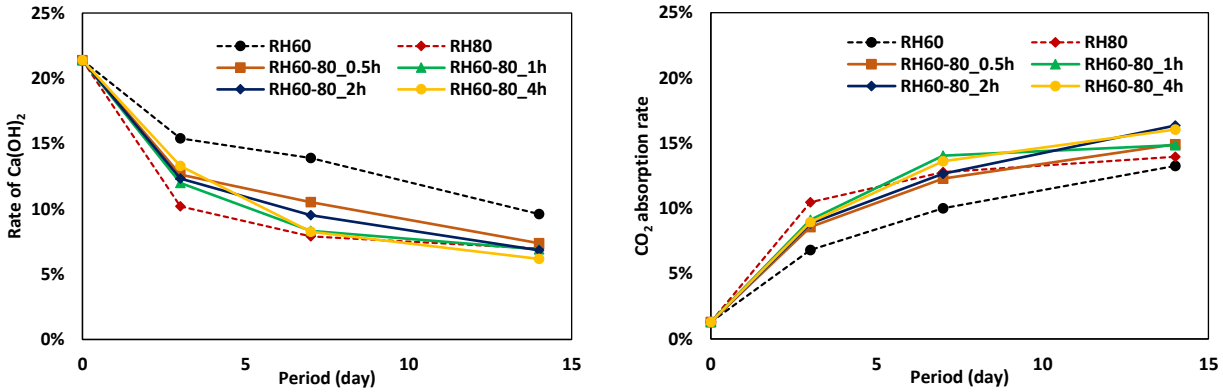
(b) 7 days



(c) 14 days
Fig. 1 The results of TGA

4. Conclusions

In this study, TGA was conducted to investigate the CO_2 absorption rate depending on RH, which influences the degree of concrete carbonation, and the degree of carbonation promotion by the dry-wet cycle. This study found that the most $CaCO_3$ was initially produced at RH80, which is the high relative humidity, due to the decomposition of $Ca(OH)_2$. However, as time passed, the decomposition of C-S-H at RH60 was promoted and generated ACC or poorly crystalline $CaCO_3$, aragonite and vaterite on 14 days. Moreover, it was found that the wet-dry cycle promoted CO_2 absorption more effectively by decomposing more $Ca(OH)_2$ than RH80 and more C-S-H than RH60.



(a) Rate of $Ca(OH)_2$ (b) CO_2 absorption rate

Fig 2. The rate of $Ca(OH)_2$ and CO_2 absorption rate of each samples

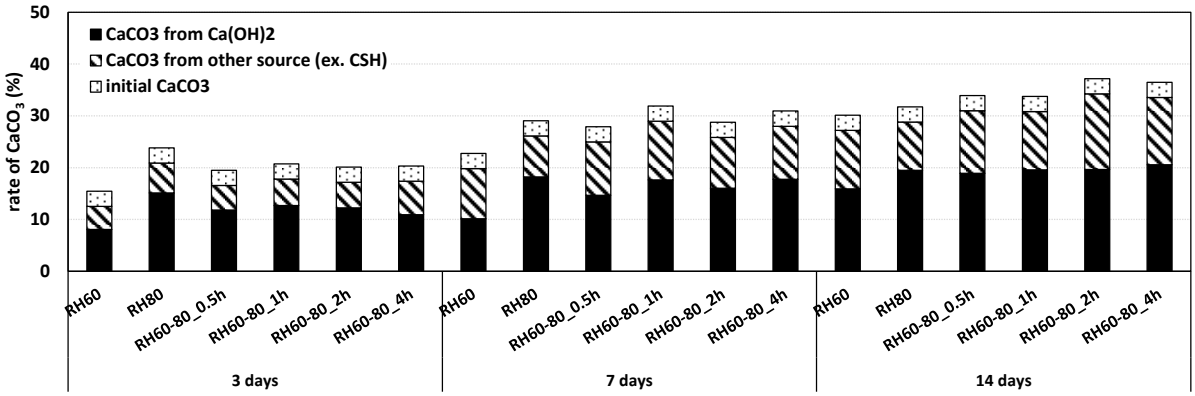


Fig. 3. Calcium carbonate production rate by each source of calcium

Acknowledgements

This research was funded by the NEDO Moonshot Research and Development Program, "C4S Research and Development Project, Calcium Carbonate Circulation System for Construction" (Project manager: Prof. Takafumi Noguchi, The University of Tokyo).

References

Pan, S.Y., Ling, T.C., Park, A. A and Chiang, P.C. (2018) "An overview: reaction mechanisms and modelling of CO_2 utilization via mineralization", *Aerosol Air Qual. Res* 18:829–848

Bhatty, J. (1986) "Hydration versus strength in a portland cement developed from domestic mineral wastes - a comparative study", *Thermochim. Acta* 106:93–103

Zajac, M., Skibsted, J., Bullerjahn, F. and Skocek, J. (2022) "Semi-dry carbonation of recycled concrete paste", *Journal of CO_2 Utilization* 63: 102111

Wang, D., Fang, Y., Zhang, Y. and Chang, J. (2019) "Changes in mineral composition, growth of calcite crystal, and promotion of physico-chemical properties induced by carbonation of β-C_2S", *Journal of CO_2 Utilization*, 34: 149–162

Drouet, E., Poyet, S., Bescop, P., Torrenti, J.M. and Bourbon X. (2019) "Carbonation of hardened cement pastes: Influence of temperature", *Cement and Concrete Research*, 115: 445–459

The 16th International Congress on the Chemistry of Cement 2023 (ICCC2023)
"Further Reduction of CO_2 -Emissions and Circularity in the Cement and Concrete Industry"
September 18–22, 2023, Bangkok, Thailand

Global Warming and its Consequences for the Construction Industry

Prof. Dr. Johann Plank [1*], X. Wang[2]

[1] Department of Chemistry, Technical University of Munich, Munich, GERMANY

E-mail: johann.plank@tum.de

[2] Department of Chemistry, Technical University of Munich, Munich, GERMANY

E-mail: xinyue.wang@tum.de

ABSTRACT:

Construction and urban infrastructure including heating & cooling of buildings amount for ~ 40 % of total CO_2 emission and present by far the largest source of CO_2 release. In the following, current steps by the global construction industry to reduce its CO_2 footprint are presented. Those include:

1) Migration to low or zero carbon binders by replacing Portland cement clinker with calcined clay, slag or other pozzolanic materials. Note that cement accounts for ~ 8 % of total global CO_2 release. 2) Capture of CO_2 released in cement plants and its utilization e.g. for concrete hardening or disposal on carbon capture & storage (CCS) wells. 3) Application of highly effective thermal insulation materials on buildings to save energy. 4) Replacing fossil fuels by "green" energy including solar, geothermal and wind energy for heating and air conditioning. 5) Concepts for mega cities to avoid unnecessary heat-up by placing plants on facades, roofs, walls, etc. which absorb CO_2 and shelter against solar radiation. 6) Timber is no alternative to concrete with respect to CO_2 emission.

These measures require a complete rethinking in construction to achieve a "green" transformation.

KEYWORDS: *Climate Change; CO_2 emission; Low Carbon Binders; Thermal Insulation; Green Cities*

1. Introduction

The construction industry has been identified as the largest single sector responsible for CO_2 release. As much as 40% of total anthropogenic CO_2 results from construction materials and the built environment including heating, cooling and operation (Gholipour (2022)). For example, cement production contributes to ~ 8 % of global CO_2 liberation and ranges only slightly behind that from fossil fuels (coal, oil and gas). In the clinkerization process, about 65 % of total CO_2 emission assigned to Portland cement production is released from the decomposition of limestone ($CaCO_3$), and much less from burning fuel. To improve its environmental balance, new concepts such as clinker substitution by less CO_2-intensive reactive binders and materials, or by capturing the CO_2 liberated and injecting it into subterraneous reservoirs (carbon capture & geological storage, CCS) have been proposed.

Even more significant than from cement production is the release of CO_2 from heating and/or cooling of buildings. From the ~ 40 % of total anthropogenic CO_2 associated with construction, no less than 30 % result from this source, thus presenting by far the largest single source contribution to global warming. Evidently, a drastic decrease of energy consumption in this sector is mandatory to achieve climate goals.

Moreover, modern mega cities present "hot spots" on the planet, because of a lack of green environment such as from trees and fields. There, the surface temperature rises particularly high as a result of solar radiation reflection by glass facades, and by the storage of solar energy in concrete walls, roads, etc. In

consequence, concepts are sought which can reduce the excessive temperature increase in cities and reduce energy demand there. Finally, using timber to replace at least a portion of the concrete is considered in the construction industry. The feasibility of this alternative will be assessed.

2. Approaches to reduce the CO_2 footprint of cement

It is estimated that the global cement industry releases about 3.2 billion tons of CO_2 annually, which corresponds to about 8 % of the current greenhouse gas (GHG) emission of ~ 41 billion tons in 2021.

2.1 Shifting to Low Carbon Composite Cements

The construction industry already has started to shift from ordinary Portland cement (OPC) holding 95 % clinker (which results in ~ 820 kg CO_2 released per ton of cement) to composite cements with substantially reduced clinker contents (see **Table 1**) (Möller (2020)). These figures demonstrate that low carbon "green" cements are indeed possible.

Table 1 CO_2 emission from common types of cements used in Germany.

Type of cement*	Clinker content	CO_2 emission [kg/ton]
CEM I	95 %	817
CEM II / A	90 %	635
CEM II / B	65 %	516
CEM II / C -M	50 %	397
CEM III / A	35 %	178
CEM III / B	20 %	159

* Composition of these cements according to DIN EN 1045 (2013 edition).

To facilitate those low clinker contents, supplementary cementitious materials (SCMs) including fly ash, slag, burnt oil shale (a speciality in Germany) and – perhaps in the future - calcined clays along with higher limestone contents are utilized. According to **Table 1**, a reduction of the clinker content to 50 % and below is required to slash the CO_2 emission of cement by half which is necessary to achieve climate neutrality (= net zero CO_2 emission). Thus, a "green cement" exhibiting neutral effect on climate must target such substantial reduction in its clinker content.

Fly ash and slag (which are by-products from coal power plants and the iron and steel industry), the most commonly used SCMs, may disappear within the next decades. Consequently, other substitute materials will be required which will be described in section 2.3.

2.2 Carbon Capture and Storage (CCS) and Carbonation Curing

Another avenue probed by the cement industry is to capture CO_2 from the exhaust gas stream, compress it to supercritical CO_2 and inject it into underground storage sites such as depleted oilfield (Marchetti (1977)). The principle of CCS is illustrated in **Figure 1**. CCS is seen as an inevitable key technology to reduce the atmospheric CO_2 at a faster pace. For example, HeidelbergCement plans to inject 400,000 tons of CO_2 annually at its Brevik plant in Norway, thus reducing its CO_2 output there by 50 % and becoming a climate neutral cement manufacturer. Other companies including Lehigh Cement (Canada), Dalmia Cement (India), Anhui Conch (China) and Taiwan Cement have announced similar approaches.

Another concept to reduce CO_2 emission from a cement plant involves using the CO_2 gas stream to cure e.g. precast concrete elements or recycled concrete (esp. fines). Exposure of fresh concrete to CO_2 results in a gain in strength. Investigations suggest that ~ 5 % of its weight can be taken up by concrete as CO_2 (Yang

(2014)).

Although, CCS may become extremely critical for other industries, it has to be seen whether it will play a major role in the global cement industry, simply because of its high cost. In particular, as clinker substitution by supplementary materials (SCMs) offers a viable alternative to reduce CO_2 emission from cement considerably.

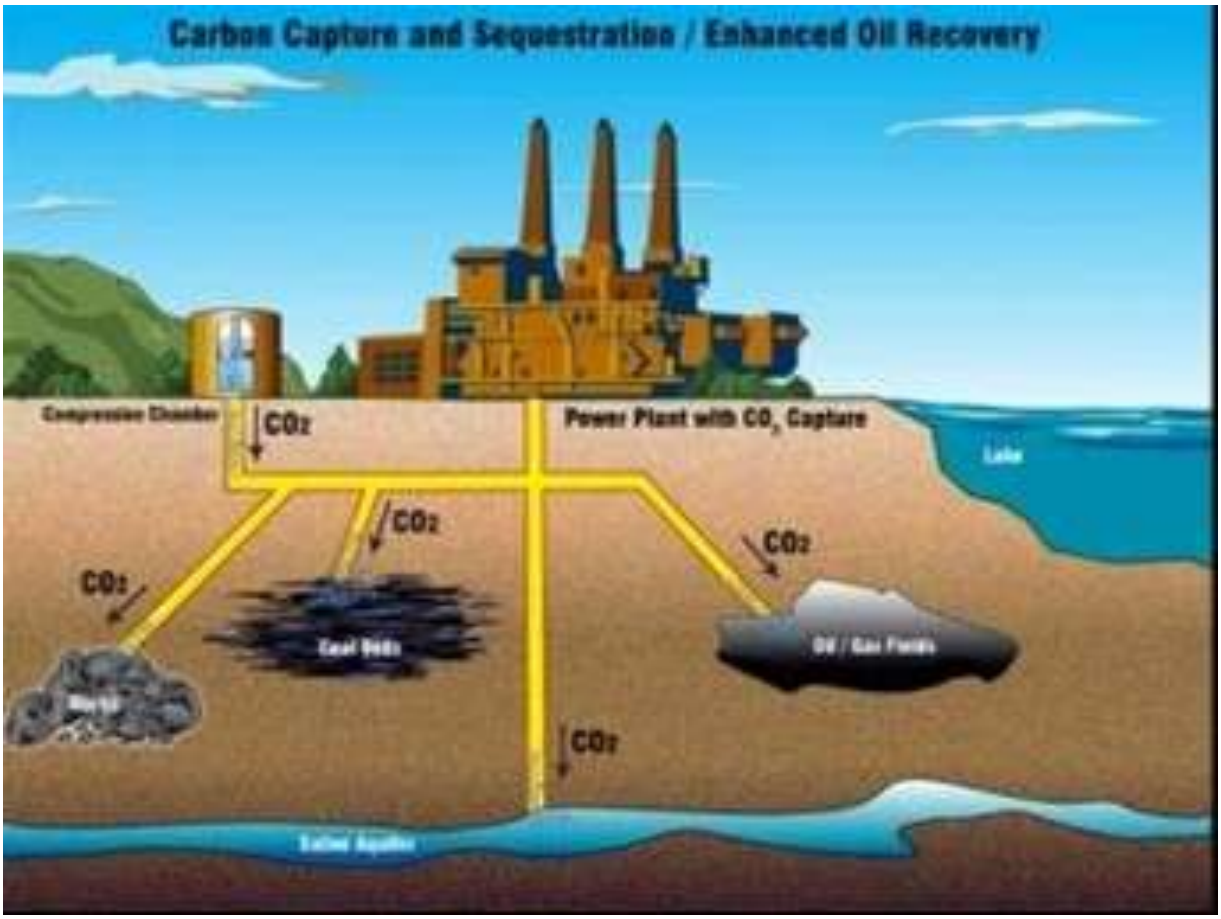


Figure 1 Illustration of the principle of CO_2 Capture and underground Storage (CCS) in depleted oil or gas fields, coal beds or saline aquifers.

2.3 Calcined Clay and Slag Composite Cements

From today's perspective there is no doubt that clinker substitution will prevail as the quickest and most feasible pathway for the cement industry.

Thermally activated (calcined) clays and slag present the main realistic options for large-scale clinker replacement. Clays (aluminosilicates) are ubiquitous and hence globally available in unlimited quantities. In a rotary kiln or flash calciner they first dehydrate and then partly or completely dehydroxylate. The degree of dehydroxylation depends on the calcination temperature and the type of clay. When blended with cement clinker, calcined clays react with $Ca(OH)_2$ to form C-A-S-H, a crystalline product similar to C-S-H from OPC.

Recently, a calcined clay - limestone blended cement designated as LC^3 has been introduced (Scrivener et al (2018)) which contains only 50 % clinker, 30 % calcined clay, 15 % limestone and 5 % gypsum. This cement exhibits a CO_2 footprint of approx. 580 kg CO_2/ton and can develop early (1 day) strength comparable to that of OPC, if a raw clay with ≥ 45% kaolin is used in the calcination.

An issue in highly calcined clay blended cements is to achieve slump retention in concrete. Common slump-retaining polycarboxylates (PCEs) fail in those systems (Li et al (2021)). The admixture industry is challenged to identify more suitable polymers for those systems.

Slag from the iron industry (GGBFS) presents another potential clinker substitute. At higher clinker substitution rates, activation of the slag with an alkaline compound (NaOH, Na_2SiO_3, Na_2CO_3 or Na_2SO_4) becomes necessary to promote hydration kinetics and early strength development. The future availability of slag appears to be uncertain, as the iron producing industry is probing hydrogen technology to abandon the use of coal and concomitant CO_2 emission.

At last, it should be mentioned that limestone can also be used to replace clinker in modest quantities, with no loss in performance. This substitution presents as alternative option, because of almost zero CO_2 emission in limestone recovery, very low cost and the abundant availability of limestone.

3. Improved Thermal Insulation of Buildings

As presented in the introduction, the main contribution to CO_2 emission from construction is released during the service life of buildings, either from heating or cooling. To prevent this, effective thermal insulation systems need to be installed on all exterior walls during construction or rehabilitation.

In order to achieve this goal, the concrete needs to exhibit superior insulation properties, or an insulation system is applied to the concrete. In the first case, a gradient concrete such as shown in **Figure 2** can be applied, or the wall is constructed in a sandwich mode consisting of one adhesive inner layer and two external layers, while the space between them is filled with an insulating material such as extruded polystyrene (EPS) or glass wool. Currently, such external insulation and finish system (EIFS) is very common.

EIFS allows a substantial decrease of the energy used to heat or cool, and reductions of up to 75 % are possible, thus transforming the building into a "zero energy" house.

Recently, even much more effective insulation materials based on silica aerogels have been introduced, which exhibit an extremely low heat conduction factor λ (0.013 - 0.025 W/m*K). They can provide the same insulating effect as EIFS at about one tenth of layer thickness. A sample of a commercial aerogel granulate is displayed in **Figure 2**.

Aerogel and hybrid composite materials have clearly made thermal insulation of buildings much more versatile. They can contribute more than any other measure to reduce anthropogenic CO_2 emission from buildings.

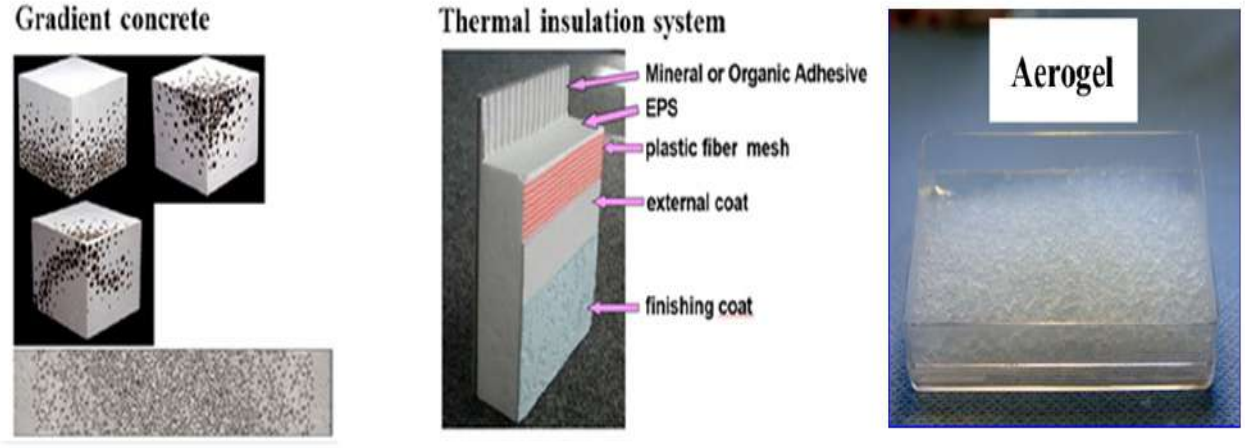


Figure 2 Gradient concrete (left), build-up of an external insulation and finish system (EIFS; middle), sample of a commercial silica aerogel granulate (right)

4. "Zero Emission" and "Zero Energy" Buildings

Even when perfectly insulated, buildings still require energy for minor heating and/or cooling. Modern technology allows to bring down CO_2 emission substantially by installing photovoltaic panels and utilizing wind energy. Even more intriguing is the use of geothermal energy which is completely independent of

sunshine and wind. The concept involves injecting cold water into a subterraneous formation with a temperature of > 50 °C, ideally > 100 °C (see **Figure 3** (left)), as producing steam which is used to feed electricity generators. Countries which are prominent in the utilization of geothermal energy include Iceland, USA, Japan, Indonesia, Italy, Kenia, Turkey, Philippines and New Zealand.

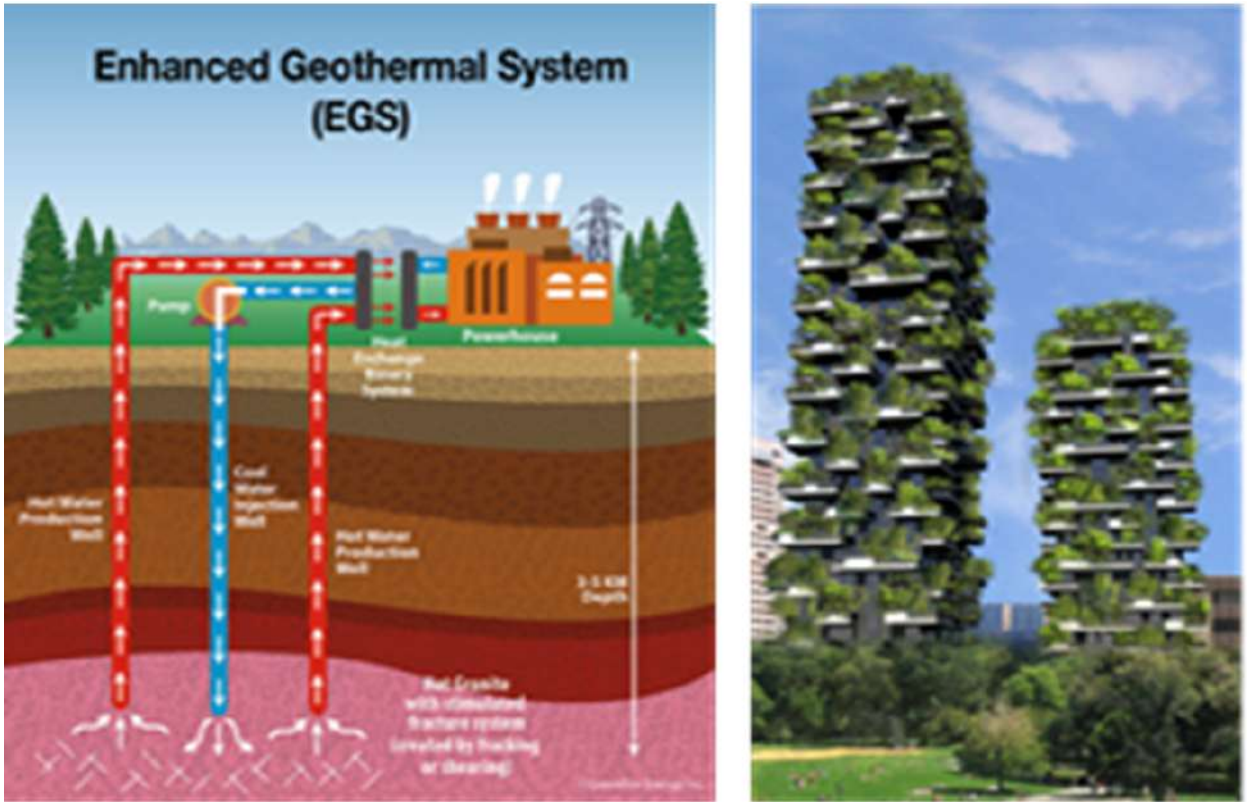


Figure 3 Schematic illustration of an enhanced geothermal system (left); Examples of modern architectural design for "green" buildings (right).

5. Re-Designing Our Mega Cities

Apart from the measures above, a complete re-thinking of the principle design of our cities will be necessary to achieve the turning point with respect to CO_2 emission. This involves fundamental architectural changes as well as a completely different city plan. Generally, our cities need to incorporate more nature into the habitat. For example, apartment buildings can be furnished with plants and trees on the balcony, or facades can be covered with dangling plants (see **Figure 3** (right)). This way, not only CO_2 is taken up from the atmosphere, but also the building is sheltered against direct solar radiation and the consequential heating up effect. Hence, the design and architecture of our cities will need to change fundamentally to reduce atmospheric CO_2 and to cope with the challenges from global warming.

6. Timber – an Alternative for Concrete?

A discussion has begun whether concrete should be replaced by timber. First, the CO_2 footprint of concrete only is ~ 300 kg CO_2/m^3 because its main components are sand and gravel, not cement. In comparison, the CO_2 footprint of timber cut in the Amazonas rain forest of Brazil was found at 23,800 kg CO_2/ton (Campos (2021)) which is immensely higher than that for concrete. Hence, from an environmental point of view using Amazonas timber should be discouraged, even more so because rain forests absorb large amounts of CO_2 and moderate our global rain patterns. Note that an average tree takes up ~ 10 tons of CO_2 over its lifetime. Other studies on timber recovered from forests which are near cities present values for the CO_2 footprint of 400 - 800 kg CO_2/ton (Burnett (2006)). These data signify that even in a best case scenario timber cannot match the environmental balance of concrete and therefore does not present a realistic

alternative to concrete.

7. Summary and Conclusion

Construction will play a most prominent role in combating climate change, and so far the significance of its contribution has been rather underestimated. In order to reduce CO_2 emission by at least 50 % (which is required to become "climate neutral"; note that only 50% of CO_2 released stay permanently in the atmosphere because the other 50% are taken up by the ocean and the biosphere; hence, governments have set a 50% target for CO_2 reduction), multiple steps need to be taken including:

- Reduce the CO_2 footprint of cement by lowering its clinker content to less than 50 %, while achieving similar performance properties as OPC. (Bistline (2022))
- Carbon capture and geological storage (CCS)
- Carbon capture and utilization (CCU), e.g. carbonation curing
- Effective thermal insulation of buildings, as it can provide the highest reduction in CO_2 emission across all sources.
- Heating and cooling of buildings should be powered by green energy from solar, wind and/or geothermal energy rather than from fossil fuels.
- Timber is not an environmentally friendlier alternative to concrete.
- Establishing "green" cities by rethinking the urban design

It is obvious that the goals relating to CO_2 reduction can be achieved only through international cooperation and a concerted global effort.

References

Gholipour, H.F., A. Arjomandi, and S. Yam. (2022). Green property finance and CO_2 emissions in the building industry. Global Finance Journal, 51, 100696.

Möller, H. (2020). Möglichkeiten und Grenzen CO_2-armer Zementproduktion, BETON, 10, 392–398.

Yang, K.-H., E.-A. Seo, and S.-H. Tae. (2014). Carbonation and CO2 uptake of concrete. Environmental Impact Assessment Review, 46, 43-52.

Marchetti, C. (1977). On geoengineering and the CO2 problem. Climatic change, 1(1), 59-68.

Scrivener, K., Martirena, F., Bishnoi, S., & Maity, S. (2018). Calcined clay limestone cements (LC3). Cement and Concrete Research, 114, 49-56.

Li, R., Lei, L., Sui, T., & Plank, J. (2021). Approaches to achieve fluidity retention in low-carbon calcined clay blended cements. Journal of Cleaner Production, 311, 127770.

Campos, É.F.D.E., K.R.G. Punhagui, and V.M. John.(2021). CO2 footprint of Amazon lumber: A meta-analysis. Resources, Conservation and Recycling,. 167,105380.

Burnett, J. (2006). Forestry Commission Scotland greenhouse gas emissions comparison carbon benefits of timber in construction. A report by the Edinburgh Centre for Carbon Management Ltd.

Bistline, J., et al. (2022). Actions for reducing US emissions at least 50% by 2030. Science,. 376(6596), 922-924.

The 16th International Congress on the Chemistry of Cement 2023 (ICCC2023)
"Further Reduction of CO_2 -Emissions and Circularity in the Cement and Concrete Industry"
September 18–22, 2023, Bangkok, Thailand

Investigating the influence of addition of γ-C_2S and Carbon Dioxide on concrete performance and CO_2 absorption

K. Avadh[1*], Y. Yoshida[2], K. Seki[3], T. Mukai[4] and T. Torichigai[5]

[1] *Kajima Technical Research Institute,Concrete and Construction Materials Group, Tokyo, Japan*

Email: avadh@kajima.com
[2] *Kajima Corporation, Kyushu Branch, Fukuoka, Japan*

Email: yoshyuma@kajima.com
[3] *Kajima Technical Research Institute, Concrete and Construction Materials Group, Tokyo, Japan*

Email: sekike@kajima.com
[4] *Kajima Technical Research Institute, Concrete and Construction Materials Group, Tokyo, Japan*

Email: mukaitos@kajima.com
[5] *Kajima Technical Research Institute, Concrete and Construction Materials Group, Tokyo, Japan*

Email: torichig@kajima.com

ABSTRACT

To reduce the adverse environmental impact of construction, innovative methods, and materials to enhance the storage of CO_2 in concrete are required. One way is to replace cement in concrete with binders that emit less CO_2 in manufacturing and have a higher potential to absorb CO_2. One such innovative material is γ-$2CaO.SiO_2$ (γ-C_2S), which is the γ phase of di-calcium silicate. By replacing cement with blast furnace slag and γ-C_2S in concrete, authors have developed CO_2-SUICOM, environment friendly concrete that can absorb CO_2 as it hardens thus making the entire concreting process carbon negative.

In the current study, the potential of γ-C_2S as a CO_2 capture material to enhance the CO_2 absorbing capacity of concrete during kneading is explored. The experimental results illustrate that using the proposed pre-mixing mixing method, workability as per construction standards can be achieved along with improvement in compressive strength compared to specimens with the same cement content. Also, thermo-gravimetric analysis (TG-DTA) reveals that the amount of CO_2 stored inside concrete has increased.

KEYWORDS: *Carbon negative, Carbon utilization and sequestration, Concrete, Dry Ice, Workability*

1. Introduction

Cement, which is essential to build economic and durable infrastructure, is also responsible for a huge amount of CO_2 emissions into the environment. To mitigate the harmful effects, the focus of researchers is shifting towards developing alternative binder compositions which can reduce the clinker content in concrete thus reducing the overall CO_2 emissions. It has become imperative to develop materials that have the potential to absorb a greater amount of CO_2 than they emit during production. γ-C_2S is one such special admixture that causes an emission of only 124.5 Kg of CO_2 per ton produced but has the capacity to absorb around 500 Kg of CO_2 per ton. It is the γ phase of C_2S, which unlike β-C_2S does not hydrate but only reacts with CO_2 in the presence of water to form calcium carbonate and silica (Shoji et al. (2013)). Previously, γ-C_2S has been used in combination with blast furnace slag and cement clinker by researchers

develop a concrete mix design which can achieve carbon negativity on carbonation curing (Yoshioka et al. (2013)).

Apart from storing CO_2 in concrete using carbonation chambers, it is also beneficial to determine ways to store CO_2 in concrete while mixing. Researchers have developed innovative methods to facilitate the addition of CO_2 gas in concrete during mixing and enhance the strength properties of concrete (Monkman et al. (2017)). However, some research has also shown that the direct addition of CO_2 in the form of gas or dry ice directly into concrete causes loss in slump. Hence, after comparing various mixing methods, it was concluded that pre-mixing γ-C_2S along with sand, gravel and dry ice as shown in Figure 1, helps in retaining the workability of concrete. Further, using the pre-mixing method, the compressive strength of concrete could be improved such that cement content in the concrete could be reduced by 5%. Hence, the proposed method facilitated CO_2 reduction (Avadh et al. (*Under Review*)). However, the dry ice amount added in this study was only 0.6% of the total powder content which is quite less. Therefore, it is important to investigate the effect of increasing the amount of dry ice while mixing concrete.

In this study, the previously proposed pre-mixing method is used to store CO_2 in concrete during mixing. The study investigated the effect of increasing the amount of dry ice mixed in concrete on slump, concrete temperature and compressive strength. Also, the amount of CO_2 stored is confirmed using thermogravimetric analysis (TG-DTA).

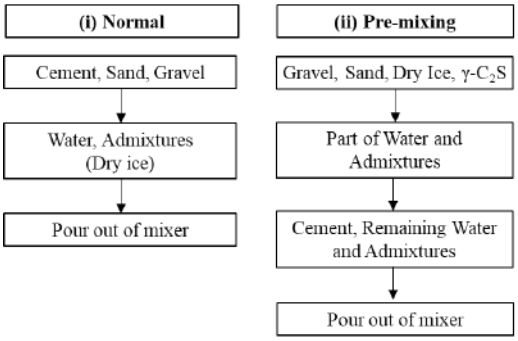


Figure 1 : Mixing procedures used in this study

2. Experimental scheme

2.1 Materials

For the experimental investigation, ordinary Portland cement (OPC) was used as the binder while γ-C_2S was used as the CO_2 capture material with chemical and physical properties as shown in Table 1. Crushed sand and gravel with density of 2.61 g/cm^3 and 2.65 g/cm^3 respectively were used to make concrete.

Table 1 : Chemical and physical properties of cement and γ-C_2S

	CaO	SiO_2	Al_2O_3	Fe_2O_3	MgO	SO_3	Na_2O	K_2O	LOI	Density (g/cc)	SSA (cm^2/g)
OPC	63.8	20.5	5.1	3.1	1.2	2.0	0.3	0.4	2.6	3.16	3310
γ-C_2S	63.9	33.9	1.0	0.4	0.1	0.4	0.1	0.1	0.1	2.85	1500

2.2 Mixing method

In this study, two different mixing methods have been employed as shown in Figure 1. The normal mixing method is the standard method normally followed in experimental laboratories. In the proposed pre-mixing method, sand, gravel, γ-C_2S and some amount of water are initially mixed following which the remaining amount of cement and water is added. This gives ample time for γ-C_2S to react with dry ice and form in-situ calcium carbonate thus preventing any reaction between CO_2 and cement which leads to prevention of loss in slump.

2.3 Mix design and experimental cases

To understand the effect of increasing the amount of dry ice on concrete properties, four different cases as shown in Table 2 were investigated. The W/C for each case was fixed at 52.5% to clearly understand the effect of carbonation of γ-C_2S using dry ice on cement hydration and strength evolution. Cases containing γ-C_2S had increased powder content with a W/P of 50%.

Table 2: Concrete mix design corresponding to experimental cases

No.	Name	W/P* (%)	W/C (%)	Dry ice (%×P)	Unit Weight (kg/m^3)					Mixing method	Remarks
					W	C	γ-C_2S	S	G		
1	C	52.5	52.5	0.0	175	332	0	800	986	Normal	Base case
2	DG-0.0	50.0	52.5	0.6	175	332	18	800	986	Pre-mixing	5% γ-C_2S added
3	DG-1.0	50.0	52.5	1.0	175	332	18	800	986		
4	DG-5.0	50.0	52.5	5.0	175	332	18	800	986		

*P = Weight of Cement + Weight of γ-C_2S

2.4 Slump and compressive strength tests

The temperature and slump of the concrete mix were measured as per JIS A 1156 and JIS A 1101 respectively. Further, the compressive strength was obtained using cylindrical specimens of diameter 100 mm and height 200 mm after 1,7, and 28 days of sealed curing at 20˚C and 60% RH.

2.5 Thermo-gravimetric analysis (TG-DTA)

TG-DTA was conducted to determine the amount of CO_2 stored in concrete using the pre-mixing method. Assuming that the aggregate does not absorb CO_2, samples were prepared using only powders i.e. γ-C_2S and cement following the pre-mixing method. The paste was poured into cylindrical molds of 50 mm diameter and 100 mm height and samples for analysis were collected after allowing the paste to cure for one day at 20˚C and 60% RH. Hydration was stopped in the collected samples using acetone. TG-DTA was conducted under nitrogen gas flow till 1000˚C at a rate of 20˚C /min. The amount of CO_2 stored was measured by measuring the loss in weight between 600˚C to 850˚C.

3 Results and discussion

3.1 Slump and temperature

The results of the slump flow and temperature for each mix design have been shown in Figure 2(a). Comparing the results of case C and DG-0.0, slump increases as the amount of powder increases from 332 kg/m^3 to 350 kg/m^3. For the cases mixed with the pre-mixing method, as the amount of dry ice increases from 0% to 1% the slump does not change but a further increase in dry ice amount to 5% causes a slight reduction in slump. However, no significant effect of the addition of dry ice has been observed on temperature.

3.2 Compressive strength

The section discusses the impact of increasing the amount of dry ice content on the compressive strength of concrete mixed using the proposed pre-mixing method. The compressive strength results in Figure 2(b), are shown as a percentage of the base case i.e. “C” with the actual strength shown as numbers on top of corresponding bar plots. It can be observed that as the amount of dry ice added in the first step of mixing increases, the 1 day compressive strength reduces. This could be attributed to the fact that calcium carbonate and silica formed due to carbonation of γ-C_2S hinders the initial hydration process hence

causing a delay in acquiring 1 day compressive strength. The reason for the delay in strength evolution needs further investigation. However, the 7 day and 28 day strengths increase as the amount of dry ice increases from 1.0 % to 5% showing the beneficial effects of adding dry ice to concrete. Also, the later age compressive strengths show significant improvement of up to 20% compared to case "C" which has the same cement content.

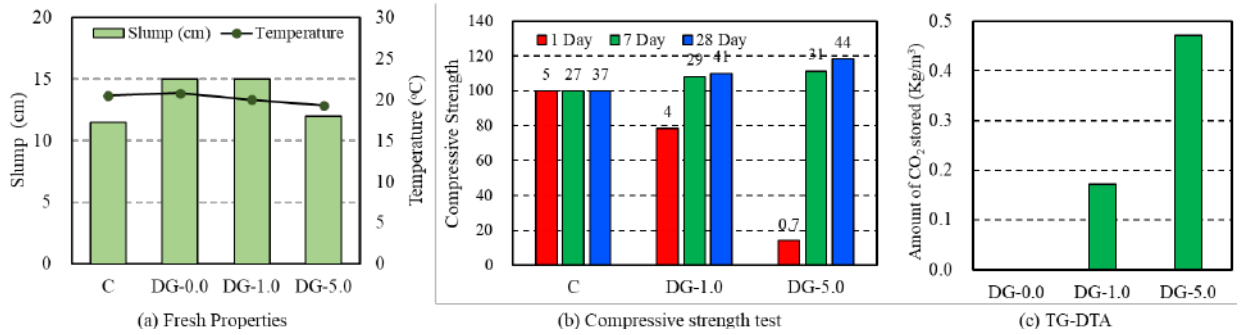


Figure 2 : Effect of increasing the amount of dry ice in the pre-mixing method

3.3 Amount of CO_2 stored

The amount of CO_2 stored while pre-mixing γ-C_2S and dry ice was measured using TG-DTA and the results are shown in Figure 2(c). Considering, the amount of CO_2 present in the case DG-0.0 as base, the amount of CO_2 stored in DG-1.0 and DG-5.0 is calculated by subtracting the measured CO_2 amount of DG-0.0 from other cases. It can be observed that the amount of CO_2 stored in concrete increases as the amount of dry ice added increases from 1% to 5%.

4 Conclusions

In the current study, γ-C_2S and dry ice are pre-mixed with sand, gravel and some part of the water which is followed by the addition of cement and remaining water. The results show that slump decreases on increase in the amount of dry ice but it can be adjusted using an appropriate amount of admixture. Further increasing the amount of dry ice delays the gain in initial strength but later age strength improves. Also, the amount of CO_2 stored in concrete increases with in the dry ice amount.

Acknowledgements

This paper is based on results of "Development of Materials, Manufacturing Methods and Quality Control System on Innovative Carbon Negative Concrete", JPNP21014, commissioned by the New Energy and Industrial Technology Development Organization (NEDO).

References

Avadh, K., Yoshida, Y., Torichigai, T. and Watanabe, K., (2023) "Experimental investigation on the effect of mixing dry ice and γ-C_2S in concrete", *Proceedings of the Japan Concrete Institute*, (45), (Under Review)

Monkman, S., MacDonald, M., "On Carbon dioxide utilization as a means to improve the sustainability of ready-mixed concrete", (2017), *Journal of cleaner production*, 167

Shoji, M., Higuchi T., Yamamoto, K. and Morioka, M., (2013), "Manufacturing of γ-C_2S used by calcium hydroxide and its CO_2 emission", *Cement science and concrete technology*, 67

Yoshioka, I., Obata, D., Nanjo, H., Yokozeki, K., Torichigai, T., Morioka, M. and Higuchi, T. (2013) "New ecological concrete that reduces CO_2emissions below zero level: New method for CO_2 capture and storage", *Energy Procedia*, 37: 6017-6025

The 16th International Congress on the Chemistry of Cement 2023 (ICCC2023)
"Further Reduction of CO_2 -Emissions and Circularity in the Cement and Concrete Industry"
September 18–22, 2023, Bangkok, Thailand

Investigating Carbonation and Hydration of Reactive Magnesia Cement using Advanced Characterization Methods

N.Z. Elmesalami[1] and K. Celik[2*]

[1] *New York University, New York, United States*
Email: nze2002@nyu.edu
[2] *New York University, New York, United States*
Email: kemal.celik@nyu.edu

ABSTRACT

Reactive MgO cement (RMC) is an alternative, low-carbon binder to ordinary Portland cement (OPC). RMC reacts with water and absorbs environmental CO_2 to precipitate hydrated magnesium carbonates (HMCs). Depending on CO_2 curing conditions and RMC composition, various polymorphs of HMCs precipitate, which affects the strength of the final RMC-based composite. In this study, polymorphism in HMCs is studied by visualizing the hydration and carbonation reactions of RMC using a specialized in-situ gas cell with transmission electron microscopy (TEM). The first step of the experiments is the sample preparation which involves ball milling, centrifugation, and sonication to obtain the right particle size and distribution for the analyses. The in-situ experiments are then conducted by flowing gases into and out of the gas cells at the required concentrations and temperatures. Various mixtures of water vapor and CO_2 gas are used to investigate their effects on the nucleation pathways during the precipitation of HMCs. The reactions are also conducted at different temperatures, from 25˚C to 300˚C, to investigate the effect of temperature on the formation of the different HMC phases. In addition, changes in the sample morphology and phases can be captured with videos and images taken using in-situ TEM. Diffraction patterns and lattice images collected from TEM can also provide information about the different phases of HMCs formed during the experiments. These results help provide valuable information on polymorphism in magnesium carbonates, which will, in turn, aid in evaluating and enhancing the properties of RMC.

KEYWORDS: *Reactive magnesia cement, carbonation, in-situ transmission electron microscopy*

1. Introduction

Concrete is the second most consumed material on Earth after water (Sakai and Noguchi (2012), Mehta and Monteiro (2014)). Despite the advantageous properties of concrete, its high carbon footprint has pushed the need for alternative low-carbon materials. The high carbon footprint of concrete is mainly attributed to the production of ordinary Portland cement (OPC), accounting for 7% of global carbon emissions (Fransen et al (2021)). Reactive MgO cement is one potential low-carbon alternative to ordinary Portland cement. RMC reacts with water to form magnesium hydroxide, and in the presence of CO_2, it carbonates to form various polymorphs of hydrated magnesium carbonates (HMCs). The HMCs form a binding material akin to that of cement paste. Different HMC polymorphs form depending on factors such as CO_2 partial pressure, water content, temperature, and pH. The main HMCs that form include nesquehonite, dypingite, hydromagnesite, artinite, and magnesite (Al-Tabbaa (2013), Soares and Castro-Gomes (2021)). The resulting HMCs have different densities and strengths, and since they co-precipitate during the hydration and carbonation processes, the ultimate strengths of the final RMCs can be highly variable. This high variability in the ultimate strengths of RMCs hinders their acceptance in the construction industry. Therefore, this study aims at understanding the hydration and carbonation reactions of reactive magnesia binders by experimentally evaluating the nucleation and growth of HMCs during the reactions. This would eventually allow maneuvering the formation of the denser HMC phases over the less dense ones improving the strength and properties of RMC.

2. Methodology

Samples of reactive magnesia were obtained from two different suppliers. Both samples are light-burned, high-reactivity magnesia, and their compositions and properties are shown in Table 1.

Table 1. Composition and properties of magnesia samples

Parameters	Magnesia Sample 1	Magnesia Sample 2
MgO	92.4%	98.2%
CaO	1.72%	0.8%
SiO_2	2.52%	0.35%
Fe_2O_3	0.82%	0.15%
Median particle size (before grinding)	-	3 – 8 μm
Surface area (before grinding)	-	60 m^2/g
Activity index	48 seconds	8 seconds

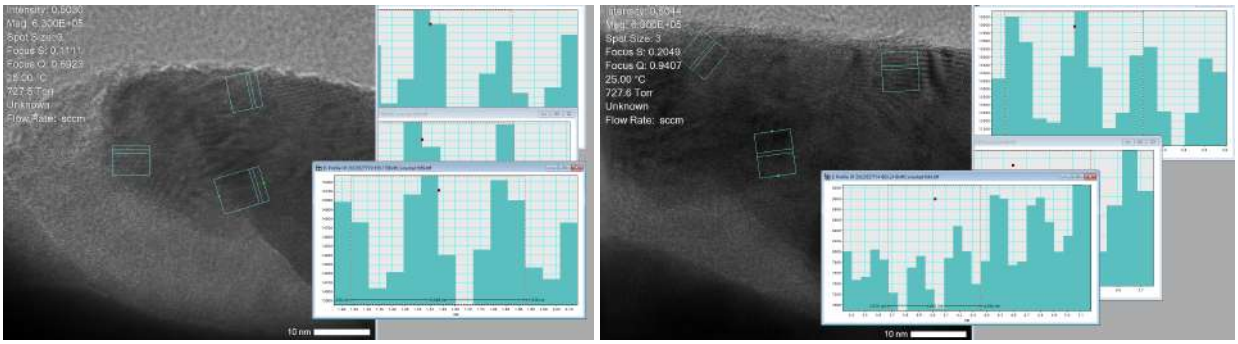
A transmission electron microscope is used to image the material at the micro and atomic scales. The TEM system used for the experiments is a ThermoFischer Talos F200X model with an accelerating voltage of 200 kV. A specialized in-situ gas cell TEM holder is utilized, which allows the flow of gases at specified concentrations and flow rates onto the sample. The gas cell used is the Atmosphere System by Protochips® which has a holder tip volume of a maximum of 1 μL and can operate at temperatures of 25˚C to 1000˚C, at pressures of 1 to 760 Torr, and for gas flow rates of 0.005 to 1 mL/min.

The first step of the experiment is the sample preparation process. The samples are first ground in a ball mill for at least 8 hours using zirconia jars and balls at 500 rpm, following the recommended grinding method for optimizing the reactivity of light-burned magnesia in the study by Khalil and Celik (2019). Then, the ground powder is collected and prepared in isopropanol solvent in glass vials. The sample solution is then sonicated for at least 30 minutes. The sample particles need to be as small as possible since the gas cell can only accommodate particle sizes of less than 5 μm in thickness, and better images can be taken using TEM when the particle thickness is small. Therefore, to collect the smallest-sized particles from the solution, the solution is kept to settle overnight. Then the supernatant is collected from the solution for drop casting onto the TEM chips.

The gas cell with the sample on the chip is then assembled at the tip of the holder, and the holder is inserted into the TEM for imaging. Before running the experiments, the samples are first imaged for long durations under the direct beam of the microscope to determine the beam effect on the samples. Then, the gas connections are set up, and the required parameters are set prior to run the experiment. For the experiments, the gas mixture used is 80% CO_2 gas and 20% water vapor at a pressure of 70 Torr. The experiments are conducted at three temperatures of 25˚C, 50˚C, and 250˚C.

3. Results and Discussion

Initially, lattice images are obtained for the MgO samples in dry mode before running the gases. The high intensity of the TEM electron beam can sometimes cause damage to samples in the form of distorted lattice structures or morphology. Therefore, the samples are first exposed to a direct electron beam for a long period of time to determine any beam effect on the samples. This is conducted at room temperature and atmospheric pressure before flowing gases to determine the sole effect of the electron beam. Figure 1 shows lattice images of the MgO sample before and after exposure to the electron beam for 1 hour.

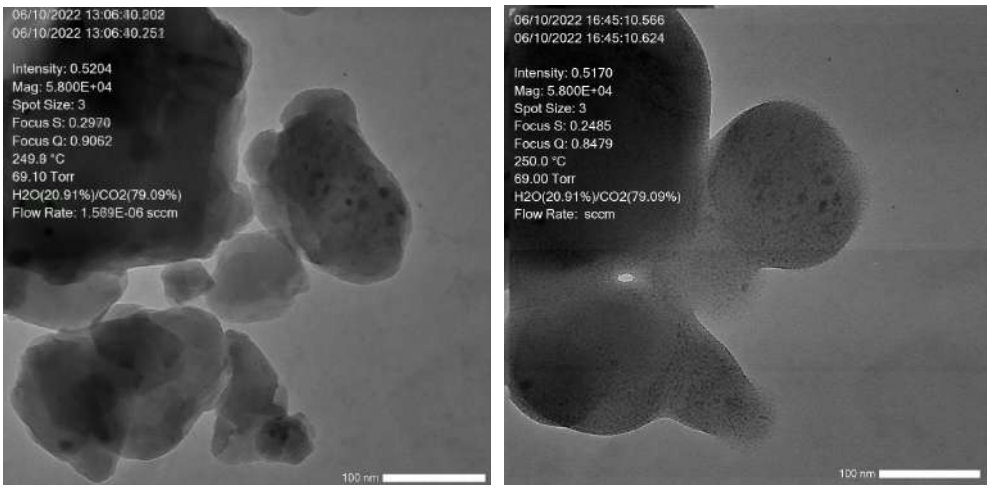


(a) (b)

Figure 1. TEM images of MgO sample before flowing gases (a) before electron beam exposure and (b) after direct electron beam exposure for 1 hour. Lattice parameter remains unchanged at a value of about 0.069 nm

The results show that the MgO lattice remained stable under the direct electron beam for one hour of exposure with a measured lattice parameter of about 0.069 nm. This ensured the MgO sample would remain stable under the high intensity of the electron beam and that any observed changes should result from the reactions taking place after flowing the gases.

Next, the first experiment is conducted by flowing the gas mixture at 25˚C. However, significant carbon contamination occurred at this temperature, and the images were blurry. Carbon contamination is one of the common problems that can occur during TEM imaging, and it is more pronounced in the experiments conducted in this study due to the use of CO_2 gas. One solution to avoid carbon contamination is to conduct the experiment at high temperatures to avoid carbon build-up in the gas cell. Therefore, the experiment was repeated at a higher temperature of 50˚C. However, carbon contamination was still observed at 50˚C, so a much higher temperature of 250˚C was used for the next experiments. Figure 2 shows the experiment results at 250˚C for the first sample, Magnesia Sample 1, after running the experiment for about 3 hours and 40 minutes.

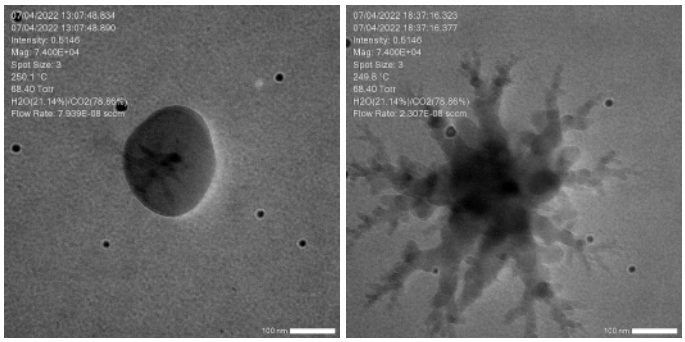


(a) (b)

Figure 2. TEM images of Magnesia Sample 1 (a) at the start of the experiment and (b) after flowing the gas mixture for about 3 hours and 40 minutes

The recorded images show changes in the morphology of the MgO particles from close to angular to more rounded shapes after about 20 minutes of flowing the gas mixture. About 55 minutes later, the particle edges start breaking out, and small particulates are noticed to form at the broken edges, as can be seen in Figure 2(b). This pattern continues, and more particulates form at other MgO particle edges in the sample. Diffraction patterns collected at the locations of the newly formed particulates only show halos or blurred rings, indicating the formation of amorphous materials. This is suspected to be amorphous magnesium carbonate; however, further studies are needed to confirm this finding.

The same experiment is repeated on the second sample, Magnesia Sample 2, and the TEM results are shown in Figure 3. Similar to Magnesia Sample 1, new particle formations were also noticed.



(a) (b)

Figure 3. TEM images of Magnesia Sample 2 (a) at the start of the experiment and (b) after flowing the gas mixture for about 5 hours and 30 minutes

However, the particle formation, in this case, exhibited a peculiar fractal growth that was observed to occur at a much faster rate under direct beam exposure. After about 5 hours and 30 minutes of flowing gases, almost all of the initially round MgO particles changed into tree-like structures following the fractal formations. Diffraction patterns collected from the newly formed structures also showed halos indicating that these structures are amorphous. As with Magnesia Sample 1, this is also suspected to be amorphous magnesium carbonate. Similar findings were reported by Jeon et al (2020), in which fractal growth of magnesium carbonate was observed under TEM to occur on the surface of Al_2O_3-supported eutectic mixture-promoted MgO sorbents.

4. Conclusions

Despite the potential of reactive magnesia cement to reduce carbon emissions from the concrete industry, some limitations still need to be addressed. One of its limitations is the variability in the ultimate strengths of the final composite owing to the co-precipitation of various HMC polymorphs during the hydration and carbonation reactions. It is anticipated that the precipitation of these polymorphs can be maneuvered to form the high-density HMCs over the low-density ones, thus improving the ultimate strength of RMC. In this study, the nucleation and growth phenomenon of HMC from MgO is imaged using a specialized in-situ gas cell in a TEM to observe the reactions in real time. The results showed the formation of an amorphous form of HMC in the form of small particulates that break out and nucleate at the edges of the MgO particles. In an MgO sample from a different source, the growth of the HMC particles from MgO was observed to occur in a fractal growth pattern, similar to results reported in another study in the literature (Jeon et al (2020)). The precipitated HMC is suspected of amorphous magnesium carbonate following the halos obtained from TEM diffraction patterns. Further studies will be conducted using other characterization methods to confirm this finding.

Acknowledgments

This work was supported by National Science Foundation (NSF) under award number 2103056. The authors express their gratitude and sincere appreciation to Core Technology Platforms (CTPs) experts, specifically Dr. Renu Pasricha, for their guidance and assistance with some experiments.

References

Sakai, K. and Noguchi, T. (2012) “The Sustainable use of Concrete.”

Mehta, P.K. and Monteiro, P. J. (2014) “Concrete: Microstructure, Properties, and Materials.”

Fransen, T. et al. (2021) "Toward a Tradable Low-Carbon Cement Standard: Policy Design Considerations for the United States."

Al-Tabbaa, A. (2013) “Reactive magnesia cement,” *University of Cambridge Press*.

Soares, E.G. and Castro-Gomes, J. (2021) “Carbonation curing influencing factors of Carbonated Reactive Magnesia Cements (CRMC) - A review,” *Journal of Cleaner Production*, 305, 127210.

Khalil, A. and Celik, K. (2019) “Optimizing reactivity of light-burned magnesia through mechanical milling,” *Ceramics International*, 45(17), 22821-22828.

Jeon, H., Trivino, M.L.T., Hwang, S., Moon, J.H., Yoo, J., and Seo, J.G. (2020) “Unveiling the carbonation mechanism in molten salt-promoted MgO-Al_2O_3 sorbents”, *Journal of CO_2 Utilization*, 39, 101153

The 16th International Congress on the Chemistry of Cement 2023 (ICCC2023)
"Further Reduction of CO_2 -Emissions and Circularity in the Cement and Concrete Industry"
September 18–22, 2023, Bangkok, Thailand

Quantitative analysis of carbon dioxide bound by carbonation of belite

Y. Ohgi [1*], Y. Kirino [1], Y. Hosokawa [1]

[1] *Taiheiyo Cement Corporation, Central Research Laboratory, Chiba, Japan*
Email: yoshifumi_ohgi@taiheiyo-cement.co.jp

ABSTRACT

A quantitative study was carried out on carbon dioxide (CO_2) bound by carbonation of belite by means of thermogravimetry-differential thermal analysis (TG-DTA) and total carbon analysis (TC). According to X-ray diffraction (XRD) and scanning electron microscopy with energy dispersive spectrometry (SEM-EDS) analyses, the carbonated belite analyzed in this study had constituent phases consisting of calcite, aragonite and silica gel containing a small amount of calcium oxide. Quantitative analysis by TG-DTA showed that the amount of CO_2 derived from decarbonation of calcium carbonate occurring at above 600°C was about 80% in mass of the CO_2 found by the TC. It was revealed by thermogravimetry-mass spectroscopy (TG-MS) analysis that the remaining 20% came from decarbonation at low temperatures around 300 to 600°C. Since decarbonation of calcium carbonate was usually considered not to occur at temperatures lower than 600°C, the authors investigated the origin of the decarbonation by means of Fourier transform infrared spectroscopy (FTIR) and selective dissolution using salicylic acid-methanol. The analysis results pointed out that decarbonation of calcium carbonate could also occur at low temperatures in the presence of both calcium carbonate and silica gel. The CO_2 bound by carbonation of belite is present in the form of calcium carbonate, which coexists with silica gel. This was thought to be the reason why the thermal analysis showed the decarbonation at low temperatures.

KEYWORDS: *Calcium silicate, β-C_2S, Carbonation, CO_2 uptake, Calcium carbonate*

1. Introduction

It has been reported that in the thermal analysis of carbonated calcium silicate phases, decarbonation occurred from around 400°C, which is lower than the decarbonation temperature range of typical calcium carbonate (e.g., Bukowski and Berger (1979)). Previous studies suggest that this low-temperature decarbonation may be due to vaterite, aragonite or amorphous calcium carbonate (ACC) (e.g., Ashraf and Olek (2018)). However, the single phases of vaterite, aragonite and ACC all transform thermally to calcite, the stable phase, followed by decarbonation, and therefore decarbonation does not occur from the low-temperature region of around 400°C. Goto et al. (1995) showed the decarbonation after thermally transition of the metastable phases, and indicate that the low-temperature decarbonation in the carbonated calcium silicate was not caused by transformation or existence of the metastable phases. The question remains as to what the low-temperature decarbonation is derived from. In this study, various analyses were conducted on the carbonated β-C_2S (belite) to quantitatively examine the bound CO_2, including attribution of the decarbonation at the low-temperature in the thermal analysis.

2. Experimental

2.1 Material

(1) Preparation of carbonated belite

Belite was synthesized according to the previous study (Nijima et al. (2014)). The synthesized belite was ground to a Blaine specific surface area of 4070cm^2/g. Water was added to 10% of the mass of belite, and the mixture of them were pressed into cylindrical shaped pellets of approx. φ30mm×20mm. The pellets

were cured for 7 days at temperature of 30°C, relative humidity (RH) of 80%, and CO_2 concentration of 80%. After curing, they were ground. Then, 10% of water was added to the mass of the ground sample, and the mixture of them were pressed into the pellets with the shape already descrived and cured for 7 days under the environment described above. This cycle was repeated once more for further carbonation. In total, the curing period was 21 days at a temperature of 30°C, RH of 80%, and CO_2 concentration of 80%. After curing was completed, the sample was vacuum-dried for 7 days.

(2) Hydrochloric acid treatment of carbonated belite

Hydrochloric acid (2mol/L) was added at a ratio of 30mL to 1g of the carbonated belite. The residue not dissolved in hydrochloric acid was collected by centrifugation. The collected residue was washed well with ion exchange water and vacuum-dried for 7 days. The residue obtained by this process is hereafter denoted as HCl residue.

(3) Mixture preparation of calcite and HCl residue

Calcite and HCl residue were weighed to a mass ratio of 1:1 and mixed in a mortar. Two types of calcite were used in this study. One was a reagent with a purity of >99.5% (Kanto Chemical Co.). The other was created by heating vaterite. Vaterite was synthesized based on the previous study (Hargis et al. (2021)). In short, 500 mL of an aqueous solution containing 0.7mol of $(NH_4)_2CO_3$ was added to 1L of an aqueous solution containing 0.7mol of $CaCl_2$ and 1.4mol of NH_3. After the solution was stirred for 1 minute, vaterite was collected by filtration. This vaterite was heated at 420°C to obtain calcite.

2.2 Analysis

Thermogravimetry-differential thermal analysis/mass spectroscopy (TG-DTA/MS) was measured with the temperature range from room temperature to 950°C. The rate of temperature increase was 20°C/min, and the furnace atmosphere was He. *m/z*=18 for H_2O and *m/z*=44 for CO_2 were measured.

Fourier transform infrared spectroscopy (FTIR) was measured by the KBr tablet method.

Powder X-ray diffraction (XRD) data were recorded with Cu *k*α radiation (40 kV and 40mA).

Tortal carbon (TC) was determined by measuring the CO_2 released by combustion of the sample at 1250°C with a non-dispersive mtehod.

The pellet after 21 days of carbonation curing was embedded in epoxy resin and polished. The specimen was analyzed by scanning electron microscopy with energy dispersive spectrometry (SEM-EDS).

Selective dissolution method using salicylic acid was performed. A solution of 7.5g salicylic acid dissolved in 60ml of methanol was added to 2g of sample and stirred. The insoluble residue was then filtered off using a membrane filter with pore size of 0.1μm, washed with methanol, and dried. The mass of the insoluble residue was measured to caluculate the parcentage of the residue to the initial 2g sample.

3. Results and discussion

(1) Constituent phases of carbonated belite

Calcite, aragonite, belite and silica gel were recognized in the XRD pattern and FTIR spectrum of the carbonated belite (see Figs. 3 and 4). Moreover, the observation by SEM-EDS shows the presence of the silica gel around the unreacted belite particles and the calcium carbonate around the silica gel, as well as the absence of the unreacted belite and the presence of the calcium carbonate around the silica gel. All the silica gel analyzed by SEM-EDS contained a small amount of CaO. In summary, the results of the analyses show that the silica gel with a small amount of CaO and the calcium carbonate (calcite and aragonite) were formed by the carbonation of belite. In the previous studies on the carbonation of belite (e.g., Ashraf and Olek(2018)), it was reported that silica gel containing CaO and calcium carbonate were formed, which was consistent with the results explained above.

(2) Evaluation of bound CO_2

Fig. 1 shows the TG and DTG of the carbonated belite. The decarbonation temperature of the calcium carbonate was determined from the DTG curve accourding to Umetsu et al. (2021). In the present study, start and finish of the decarbonation temperature were 633°C and 770°C, respectively, and the mass loss rate, in this temperature range, which means CO_2 content, was 19.9%. On the other hand, the CO_2 content determined by the TC was 26.0%. The CO_2 content determined by the DTG was equivalent to about 80% of that determined by the TC. From the MS spectra of the carbonated belite shown in Fig. 2, it was found that a very small amount of CO_2 was released from room temperature to about 300°C, and that after this temperature, the amount of released CO_2 tended to increase significantly. A very small amount of CO_2 was also observed after 770°C, which was regarded as the completion of the decarbonation based on the

DTG curve. The area fractions corresponding to the temperature range from room temperature to 300°C, 300 to 633°C, 633 to 770°C, and 770 to 950°C in the MS spectra corresponding to CO_2 were 0.86%, 18.10%, 80.48%, and 0.56%, respectively. The area fraction is proportional to the amount of CO_2. The released CO_2 for the temperature range of 633 to 770°C are consistent with the finding that the amount of CO_2 determined by the DTG was equivalent to 80% of the amount of CO_2 determined by the TC. The remaining 20% corresponded to CO_2 released at temperatures between 300 and 633°C. In this study, 300, 633, and 770°C were selected, which may differ to some extent due to differences in the materials, carbonation conditions, analytical conditions, etc (e.g., Ashraf and Olek(2018), Morandeau A. et al. (2014)). Fig. 2 also shows H_2O was released up to about 700°C. The released H_2O was thought to be derived from physically-bound water and dehydration of silica gel (Morandeau A. et al. (2014)). It should be added that although the previous study associated the release of H_2O after 400°C with ACC (Zajac M. et al. (2022)), its presence was not clearly confirmed from the above analytical results in the present study.

(3) Examination of CO_2 released in low-temperature region

The various analyses were conducted on the sample obtained by heatingt the carbonated belite at 550°C to investigate the reaction in the temperature range of 300 to 633°C.

According to the XRD patterns (Fig. 3), the diffraction intensity corresponding to aragonite decreased and that corresponding to calcite increased after heating, showing the heat-induced phase transition from aragonite to calcite. The diffraction intensities corresponding to belite were almost the same before and after heating, suggesting that there was almost no change in its amount. No mineral phases other than aragonite, calcite, and belite were observed in the XRD pattern of the heated carbonated belite. The FTIR spectra (Fig.4) show that the absorption peak corresponding to silica gel was lowered by heating, and it was considered that the amount of silica gel decreased.

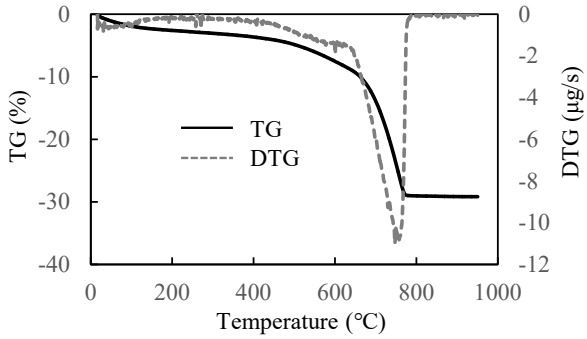


Fig.1 TG and DTG of carbonated belite

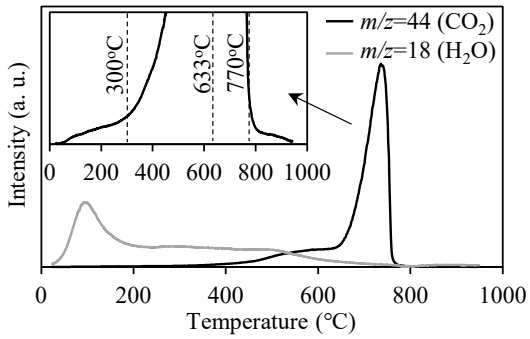


Fig.2 MS spectra of carbonated belite and magnified view corresponding to *m/z*=44

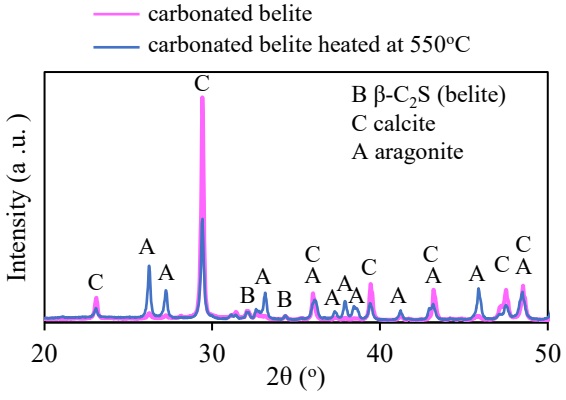


Fig.3 XRD pattern

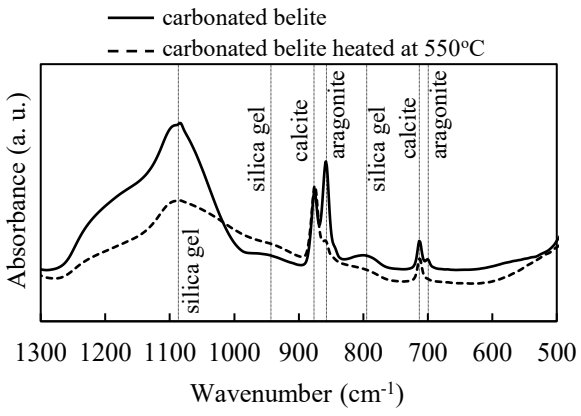


Fig.4 FTIR spectra

The parcentage of the insoluble residue by the selective dissolution process of the carbonated belite before and after heating at 550°C was 92.9% and 81.9%, respectively. Even considering that a mass loss of the carbonated belite heated at 550°C was 8.3%, the parcentage of the insoluble residue of the heated belite was lower. Calcium carbonate is almost insoluble in salicylic acid-methanol solution, and the main soluble components are calcium silicate phases such as C_3S, C_2S and C-S-H (Kondo and Ohsawa(1969)). The lower parcentage of the insoluble residue of the heated carbonated belite implies the formation of a

calcium silicate phase. This calcium silicate phase is assumed to exist as an amorphous phase because the XRD patterns show that the amount of belite did not change before and after heating, and further, no mineral phases other than aragonite, calcite, and belite was identified. Aragonite, calcite, and belite are chemically abundant in CaO components. It my be possible that belite reacted with silica gel to form calcium silicate phase. However, it is considered that aragonite or calcite reacted with the silica gel after decarbonation because CO_2 was released in the low-temperature region,

Next, the possibility of decarbonation at the low-temperature region when calcium carbonate and silica gel coexist was verified.

(4) Decarbonation behavior of calcite and HCl residue

The TG-MS of the mixtures of calcite and HCl residue, identified as silica gel, are shown in Fig. 5. In the case of reagent calcite or calcite via vaterite alone, mass loss was observed after about 600°C in both cases, whereas in the mixtures with HCl residue, CO_2 was released from about 400°C. The decomposition of calcite may have beeen catalyzed by the presence of silica gel.

Calcite and aragonite were present as calcium carbonate in the carbonated belite. It is not clear which of these phases decomposed at low temperatures. However, when calcite via vaterite was used, the degree of the decarbonation at low temparatures was higher, implying that the contribution of aragonite, which is also a metastable phase, may be more significant. The chemical composition of silica gel is considered to be strictly different between HCl residue and the silica gel in the carbonated belite. The composition of silica gel that promotes the decarbonation of calcium carbonate at low temperatures will be a reserch topic for future study.

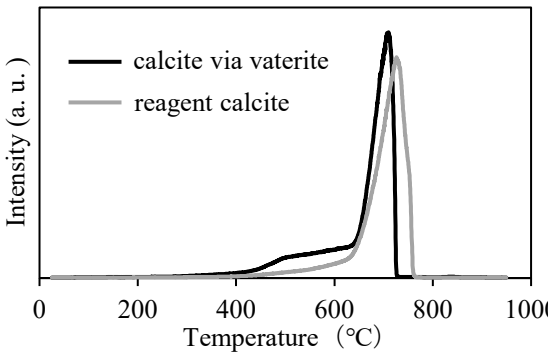


Fig. 5 MS spectra of mixtures of calcite and HCl residue

4. Conclusions

A quantitative study was carried out on CO_2 bound by carbonation of belite. Constituent phases of the carbonated belite were calcite, aragonite and silica gel containing a small amount of CaO. Quantitative analysis by TG-DTA showed that the amount of CO_2 derived from decarbonation of calcium carbonate occurring at above 600°C was about 80% in mass of the CO_2 found by the TC. It was revealed by TG-MS analysis that the remaining 20% came from decarbonation at low temperatures around 300 to 600°C. Though decarbonation of calcium carbonate was usually considered not to occur at temperatures lower than 600°C, the analysis results pointed out that decarbonation of calcium carbonate could occur at low temperatures in the presence of both calcium carbonate and silica gel.

References

Ashraf, W. and Olek, J. (2018) "Elucidating the accelerated carbonation products of calcium silicates using multi-technique approach", *Journal of CO_2 Utilization*, 23: 61-74

Bukowski, J. M. and Berger, R. L. (1979) "Reactivity and strength development of CO_2 activated non-hydraulic calcium silicates", *Cement and Concrete Research*, 9(1): 57-68

Goto, S. et al. (1995) "Calcium Silicate Carbonation Products", *Journal of the American Ceramic Society*, 78(11): 2867-2872

Hargis, C. W. et al. (2021) "Calcium Carbonate Cement: A Carbon Capture, Utilization, and Storage (CCUS) Technique", *Materials*, 14(11): 2709

Kondo, R. and Ohsawa, S. (1969) "Studies on a method to determine the amount of granulated blastfurnace slag and the rate of hydration of slag in cements", *Yogyo-Kyokai-Shi*, 77(2): 39-46

Morandeau A. et al. (2014) "Investigation of the carbonation mechanism of CH and C-S-H in terms of kinetics, microstructure changes and moisture properties", *Cement and Concrete Research* 56: 153-170

Nijima, S. et al. (2014) "Effects of manufacturing conditions on hydration reactivity of synthesized C_2S solid solution", *Cement Science and Concrete Technology*, 68(1): 96-102

Umetsu, M. et al. (2021) "CO_2 absorption and products in carbonated Portland cements", *Cement Science and Concrete Technology*, 75(1): 34-41

Zajac M. et al. (2022) “Mechanisms of carbonation hydration hardening in Portland cements”, *Cement and Concrete Research* 152: 106687

The 16th International Congress on the Chemistry of Cement 2023 (ICCC2023)
"Further Reduction of CO_2 -Emissions and Circularity in the Cement and Concrete Industry"
September 18–22, 2023, Bangkok, Thailand

Early hydration of low-energy cements from clinkers doped with combination of dopants

M. Boháč[1*], D. Kubátová[1], and T. Staněk[1]

[1] *Research Institute for Building Materials, Brno, Czech Republic*
Email: bohac@vush.cz, kubatova@vush.cz, stanek@vush.cz

ABSTRACT

The early hydration and rheological properties of fresh cement pastes prepared from low-energy clinkers activated with SO_3 and co-doped with Li_2O, CuO, and MgO were studied. SO_3 and selected foreign elements act as mineralizers and fluxes, partly incorporated in clinker phases and change their phase composition and texture. Reactive cements can be prepared from this clinker with low LSF and alite/belite ratio opposite to OPC. Heat flow development of cement pastes during early hydration was determined by isothermal calorimetry. Technological parameters were correlated with the rheological properties of cement pastes determined by rotational rheometer in flow regime. The role of dopants in the early hydration of cement pastes and its structuration is discussed in the paper. Co-doping with Li accelerates early hydration but compromises long-term strengths while Cu slows down early hydration reactions showing good later ages performance. Cement pastes' flow properties can be divided into 4 periods with respect to reaching the steady state.

KEYWORDS: *Belite-rich cement, SO_3 activation, mineralizers, early hydration, rheology*

1. Introduction

One of the alternative cement clinkers with lower GHG emissions compared to ordinary Portland cement (OPC) are reactive belite-rich clinkers. They contain the same clinker minerals as OPC clinker but the alite/belite ratio is the opposite. The ideal clinkering temperature is usually close to 1350 °C, which is about 100 °C lower than the average for OPC, which can lead to somewhat lower kiln heat consumption and permit more use of low-grade kiln fuels (Gartner & Sui, 2018).
The paper builds on the previous study of low-energy clinkers (Boháč et al., 2022) and aims at cements' early hydration properties. Since the rheology of this type of low-energy cement, not to mention the influence of co-dopants on sulfate balance, has been studied only to a small extent, its determination is an essential step before its consideration and possible future application.

2. Materials and Methods

Clinkers doped with the combination of SO_3 anions (Staněk & Sulovský, 2015) and cation (2% MgO, 1% CuO and 0.5% Li_2O) were synthesized in laboratory furnaces at 1350°C. $LiCO_3$, $MgCO_3$, and CuO were used as the source of Li, Mg, and Cu respectively. Sulfate was in the form of chemical grade gypsum. The raw meal was prepared from common cementitious materials. Detailed information on clinkers' preparation and properties are given in (Boháč et al., 2022). Cements (BS reference, with co-dopants: BS Li, BS Cu and BS Mg) were prepared by grinding clinker in the laboratory ball mill to the same fineness ~ 400 $cm^2.g^{-1}$. Chemical grade gypsum – $CaSO_4.2H_2O$ (G) was added to cement in an amount optimized according to early strengths and heat flow development. Based on the test results, gypsum content was selected for each doped clinker for further study: BS – 4 wt.% G, BS Li –3 wt.% G, BS Cu – 1 wt.% G, BS Mg – 3.5 wt.% G.

The fineness of cements was determined by Blaine method. Soundness, standard consistency and setting times were monitored for cement pastes and strength development after 2, 7, 28 and 90 days on mortars according to EN 196.
Calorimetry tests were performed on cement pastes at 25 °C using TAM Air 8 channel isothermal calorimeter. To prevent the overheating error due to high values of heat flow, only four grams of cement were weighed in a 20 ml plastic ampoule, and water was added outside the calorimeter (w/c=0.4). The paste was then stirred for 2 min at a speed of 2 revs/s ex-situ and then placed in a calorimeter with the reference sample. Reference was deionized water in an amount corresponding to the heat capacity of the paste.
Rheological testing was performed on a rotational rheometer DHR (TA Instruments). The geometry of coaxial cylinders was used with a vane rotor. Stainless steel four-blade vane rotor ø 28 mm, length 42 mm, and outer cylinder (cup) with grooved walls ø 30.2 mm. The operating gap was 4000 μm. The w/c was 0.4 for all samples, and all tests were tested at 25 °C. The course of the setting was followed in flow peak hold regime at constant shear rate steps 1, 2, 3… 10 s-1 with 60 s step time and 5-s sampling intervals. The cement pastes with w/c=0.3 and 1% of PCE superplasticizer were mixed in a laboratory mixer with scraper for 90 s than the paste was scraped with spatula and mixed for another 90 s. 170 g of the paste was placed in the outer cup and tempered at 25 °C in the jacket, then the sample was pre-sheared for 60 s at 20 s-1 and left resting for 30 s. The sample conditioning time was 125 s. The whole procedure takes 12 min. The material was then left at rest for 2 minutes before the next measurement. The pastes were tested each 15 min until the start of the setting.

3 Results and Discussion

3.1. Technological properties of cements

Cements of a similar density were ground to same fineness (**Table 1**). Good volume stability of cements is evidenced by low values of soundness. The soundness for BS Cu was not possible to determine due to very slow strength development.

Table 1 Fineness, soundness, standard consistency and setting times of cements

	Specific density	Specific surface	Soundness	Standard consistency	Start of setting	End of setting
	($g.cm^{-3}$)	($m^2. kg^{-1}$)	(mm)	(%)	(hh:mm)	(hh:mm)
BS	3.24	398.7	1	29.3	2:30	4:10
BS Li	3.26	400.3	1	29.7	2:10	3:00
BS Cu	3.29	398.7	-*	28.3	9:10	11:10
BS Mg	3.31	399.4	0.7	31.3	2:30	4:00

*Not able to determine

Strength development was monitored on standard mortars after 2, 7, 28 and 90 days (**Table 2**). BS, BS Li and BS Mg cements has decent early and long-term strengths. BS Cu shows prolonged strength development, which is gradually comparable to reference BS. Acceleration of hydration is evidenced by slightly higher 2d strength for BS Li, but this trend is not supported at later ages. Compared to ordinary Portland cement CEM I, the water demand is average for BS Cu, a little larger for BS, BS Li and significantly larger for BS Mg (**Table 1**).

Table 2 Compressive strength development of mortars

Compressive strength (MPa)			
2d	7d	28d	90d

	f_c	er	f_c	er	f_c	er	f_c	er
BS	22.0	0.8	41.3	0.8	58.5	2.2	62.8	2.2
BS Li	23.7	0.4	37.0	0.6	48.4	0.8	53.6	2.6
BS Cu	10.7	0.5	26.9	4.5	57.2	4.1	59.1	4.1
BS Mg	18.0	0.4	41.0	0.4	58.0	2.9	61.4	5.4

3.2. Isothermal calorimetry vs setting of cement pastes

Setting times of BS and BS Mg are similar. Li accelerates the start of the setting by 20 min and the end of setting by more than 1 hour. BS Cu is characterized by an extremely long induction period with the start of the setting after 9 hours and 10 min. Since the early hydration and the start of the setting are mainly affected by alite content and its crystal size, it is assumed that the effect of Li and Cu are analogous to clinker burned at typical temperatures. Several authors have previously reported the effect of Li salts on PC hydration (Wang, Qian, Qu, & Guo, 2018). Due to the doping of CuO, the setting time is significantly extended.

The course of setting determined by the Vicat needle test was compared to heat flow development for cements with selected gypsum content. Setting times are affected by dopants accordingly to heat flow development. The start of the setting relates to the onset of the main calorimetric peak and the end of setting to its offset.

The alite content and size are important parameters affecting the main peak's position, intensity and width (Boháč et al., 2022). The accelerated effect of lithium is a combination of the nucleation effect on nano Li (Wang et al., 2018) and increased alite content compared to reference compensated by relatively larger alite crystals, which slows the early stages of hydration. Similarly to previous findings (Tao, Zhang, Li, Wang, & Hu, 2019), the CuO slows the hydration due to increased alite size. The course of the initial hydration of the MgO-doped sample is very similar to the reference. A well-defined second aluminate peak related to the depletion of gypsum (Bullard et al., 2011) can be seen as the shoulder of the main peak in the deceleration period. Concerning cement composition and fineness, the mutual position of these two peaks shows proper sulfation of cement and is closely related to strength in a hardened state. Li accelerate the C_3S and C_3A reaction, evidenced by the exotherms' position. The second hump occurring approximately 13-15 hours is attributed to the C_3A. Due to the accelerated dissolution of C_3A, this hump occurs earlier (12h).

3.3. Rheology of pastes

The time of 60 seconds was taken to reach the steady state of the suspension (Roussel, 2005, 2006; Roussel, Lemaître, Flatt, & Coussot, 2010). There are 4 periods concerning reaching the steady state of the cement paste on flow curve/time plot: 1. Continuous deflocculation during initial reactions; a continuous decrease of stress at a constant rate, 2.Deflocculation to steady-state behaviour (Jarny et al., 2005); stress decrease at a constant rate reaching the plateau, 3.Deflocculation during the period of slow reactions; a continuous slow increase of stress at a constant rate, 4. The setting, a fast increase of stress at a constant rate.

The length of the initial period characterized by a sharp decrease in stress differs depending on the composition of cement and gypsum content. The second period of slow reactions allows for determining the steady-state behaviour. The time of reaching this short hydration period, where the rate of structural build-up is slow, mainly depends on the composition of cement and hydration reactions kinetics. Dynamic yield stress can be approximated according to the procedure proposed by Russel (Roussel, 2006). The time of reaching the steady state was 45 - 60min for BS ref, 75-90 min for BS Li, 30-45 min for BS Cu and 30-45 min for BS Mg. There is a good correlation between C_3A and gypsum content and the length of the initial period determined by rheometry. C_3S also takes part in initial reactions, but it is well known that its dissolution rates decelerate very quickly. The characteristic time of deflocculation is around 60 s for reference, Cu and Mg-doped sample. A larger value is seen for Li doped sample, where the time of initial reactions is longer compared to other samples.

Reaching the third period after a short window of very slow structural-build up, slow but continuous development of the structure is characterized by a slow increase of stress measured at constant stress. Structuration becomes dominant, and the stress increases at constant shear rate despite the deflocculation. Similarities can be found between the course of the heat flow curve and the rate of structural build-up not only at this stage of hydration. Stress increases linearly over this period. While BS Li has a rapid rather exponential increase in stress, BS Cu is gradual. Although BS Cu has a structural build-up, the bonds are weaker and easier to break by shearing, and as a consequence, the stress increase is not as exponential as with the other doped samples. The fourth period, limited by the adhesion of the material to the measuring geometry, is characterized by fast increase of the shear stress that relates to the start of the setting.

4. Conclusions

Early hydration properties SO_3 doped clinkers considerably vary depending on the co-dopant. Li, as a co-dopant, accelerates early hydration but compromises long-term strengths. Cu slows down early heat and strength development but shows good later-age performance. Mg doping increases the water demand, but the properties are similar to reference cement. The start of the settings correlates to the onset of the main calorimetric peak and the end of setting to its offset. Describing rheological properties, there are 4 periods with respect to reaching the steady state of the cement paste.

Acknowledgements

Thanks are due to project No. 23-05122S, financed by the Czech Science Foundation.

References

Boháč, M., Kubátová, D., Krejčí Kotlánová, M., Khongová, I., Zezulová, A., Novotný, R., … Všianský, D. (2022). The role of Li2O, MgO and CuO on SO3 activated clinkers. *Cement and Concrete Research*, *152*(November 2021). https://doi.org/10.1016/j.cemconres.2021.106672

Bullard, J. W., Jennings, H. M., Livingston, R. A., Nonat, A., Scherer, G. W., Schweitzer, J. S., … Thomas, J. J. (2011). Mechanisms of cement hydration. *Cement and Concrete Research*, *41*(12), 1208–1223. https://doi.org/10.1016/j.cemconres.2010.09.011

Deng, Q., Zhao, M., Rao, M., & Wang, F. (2020). Effect of CuO-doping on the hydration mechanism and the chloride-binding capacity of C4AF and high ferrite Portland clinker. *Construction and Building Materials*, *252*, 119119. https://doi.org/10.1016/j.conbuildmat.2020.119119

Gartner, E., & Sui, T. (2018). Alternative cement clinkers. *Cement and Concrete Research*, *114*, 27–39. https://doi.org/10.1016/j.cemconres.2017.02.002

Jarny, S., Roussel, N., Rodts, S., Bertrand, F., Le Roy, R., & Coussot, P. (2005). Rheological behavior of cement pastes from MRI velocimetry. *Cement and Concrete Research*, *35*(10), 1873–1881. https://doi.org/10.1016/j.cemconres.2005.03.009

Papo, A. (1988). The thixotropic behavior of white Portland cement pastes. *Cement and Concrete Research*, *18*(4), 595–603. https://doi.org/10.1016/0008-8846(88)90052-X

Roussel, N. (2005). Steady and transient flow behaviour of fresh cement pastes. *Cement and Concrete Research*, *35*(9), 1656–1664. https://doi.org/10.1016/j.cemconres.2004.08.001

Roussel, N. (2006). A thixotropy model for fresh fluid concretes: Theory, validation and applications. *Cement and Concrete Research*, *36*(10), 1797–1806. https://doi.org/10.1016/j.cemconres.2006.05.025

Roussel, N., Lemaître, A., Flatt, R. J., & Coussot, P. (2010). Steady state flow of cement suspensions: A micromechanical state of the art. *Cement and Concrete Research*, *40*(1), 77–84. https://doi.org/10.1016/j.cemconres.2009.08.026

Staněk, T., & Sulovský, P. (2015). Active low-energy belite cement. *Cement and Concrete Research*, *68*, 203–210. https://doi.org/10.1016/j.cemconres.2014.11.004

Tao, Y., Zhang, W., Li, N., Wang, F., & Hu, S. (2019). Predicting Hydration Reactivity of Cu-Doped Clinker Crystals by Capturing Electronic Structure Modification. *ACS Sustainable Chemistry and Engineering*, *7*(6), 6412–6421. https://doi.org/10.1021/acssuschemeng.9b00327

Tattersall, G. H. (1955). The rheology of Portland cement pastes. *British Journal of Applied Physics*, *6*(5), 165–167. https://doi.org/10.1088/0508-3443/6/5/304

Wang, J., Qian, C., Qu, J., & Guo, J. (2018). Effect of lithium salt and nano nucleating agent on early hydration of cement based materials. *Construction and Building Materials*, *174*, 24–29. https://doi.org/10.1016/j.conbuildmat.2018.04.073

The 16th International Congress on the Chemistry of Cement 2023 (ICCC2023)
"Further Reduction of CO_2 -Emissions and Circularity in the Cement and Concrete Industry"
September 18–22, 2023, Bangkok, Thailand

Alkali activated cements based on natural and designed blends of clay and calcium carbonate sources

N.R. Rakhimova[1*], R.Z. Rakhimov[1]

[1] *Kazan state university of architecture and engineering, Kazan, Russian Federation*
Email: nailia683@gmail.com

ABSTRACT

In this study, natural and designed mixtures of calcined clay and calcium carbonate minerals were examined as binary precursors for alkali-activated cements (AACs). The effects of the formulation-processing factors on the reaction phases composition and properties of fresh and hardened pastes of blended AACs were investigated. It was stated that hydraulic AACs can be derived from calcined marl incorporated with limestone powder containing 5.8–7.0% of calcined clay minerals and 54.6–60.5% of calcite, or non-hydraulic AACs from a mixture consisting of 20-30% metakaolin and 70-80% limestone powder. A high content of limestone in AACs accompanied by a low content of calcined clay minerals and improvements in the performance of the fresh and hardened AAC pastes are provided by filler, dilution, nucleation, and chemical effects. The reaction products and microstructures of alkali-activated metakaolin-limestone and calcined marl-limestone cement-based hardened pastes were investigated using thermal and XRD analyses.

KEYWORDS: ***clay, limestone, cement, alkali***

1. Introduction

The range of supplementary cementitious materials applied in increasing volumes for Portland clinker replacement in blended cements has been revised in recent decades to establish more available and widespread sources than traditional ones, such as blast furnace slag, fly ash, etc. As a result, clay and calcium(magnesium) carbonate sources have been identified as the promising materials for producing low- and non-clinker cements including alkali-activated cements (AACs). This research work focused on studying the effects of influencing factors on the performance of fresh and hardened pastes, and reaction products of AACs derived from natural and designed clay mineral-calcium carbonate blends.

2. Materials and methods

The marl, metakaolin (MK), limestone (LS), and sodium metasilicate (Na_2SiO_3) were applied to prepare the AAC paste samples. The dry mixes were kneaded for approximately 10 min with an alkali reactant solution. The fresh pastes were manually cast into 25 × 25 × 25-mm cubic moulds and vibrated for 1 min to remove entrapped air. Two sets of samples were then prepared. The CS of the first set of samples was tested after 2, 7, and 28 days age of curing at ambient temperature (25 °C) and 98% relative humidity. The second set of hardened AAC pastes was tested after steam curing, following a thermal curing program of 24 h of presetting, 4 h to reach the desired temperature, 12 h of dwell time at 80 °C, and 3 h of cooling.
The workability of the fresh pastes was evaluated using flow-table tests according to EN 1015-3. The water/binder ratio was regulated to maintain constant flowability ranging from 29.5 to 30.0 cm. The setting times were measured using the Vicat needle method according to EN 196-3. The intenerate coefficient was calculated using the ratio of the CS of the waterish samples for 48 h to that of the dry samples. X-ray diffraction (XRD) and thermal analyses (TG/DSC) were conducted on ground clays and AAC hardened pastes. The XRD results were obtained using a D2 Phaser X-ray diffractometer in a Bragg-Brentano θ–2θ configuration with Cu Kα radiation operating at 40 kV and 30 mA. Data analysis was performed using the DIFFRAC plus Evaluation Package EVA Search/Match and PDF-2 ICDD database. The mineralogical composition of the clays was determined by analyzing the X-ray diffractograms of the software product Diffrac.eva V3.2. An STA 443 F3 Jupiter simultaneous thermal analysis apparatus was used for the

TG/DSC. The clays and hardened AAC pastes were heated from 30 °C to 1000 °C at a heating rate of 10 °C/min. The data were analyzed using Netzsch Proteus Thermal Analysis software. Scanning electron microscopy (FEI XL-30ESEM) was performed at an accelerating voltage of 20 keV.

3. Results

3.1. Properties of fresh and hardened AAC pastes

3.1.1. Properties of fresh and hardened AAC pastes based on calcined marl as natural mix of clay and calcium carbonate minerals

The influence of the quantity of LS, SS, and curing conditions on the properties of hardened and fresh AAC pastes is shown in Figs. 1,2.

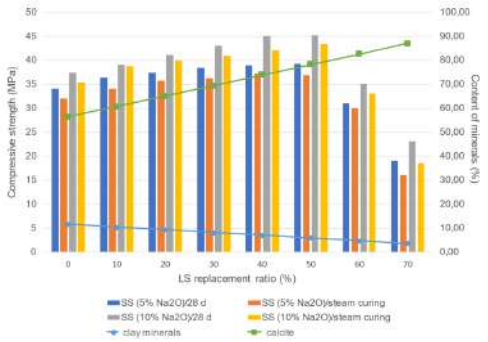


Fig. 1. The influence of the quantity of LS, SS, and curing conditions on the CS of the hardened AAC pastes

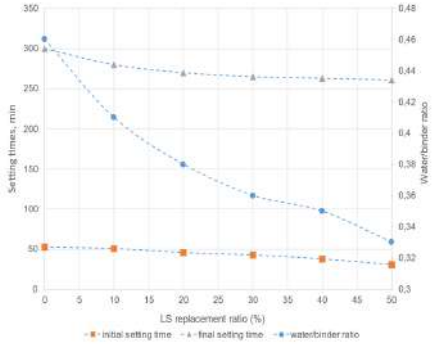


Fig. 2. The properties of the fresh AAC pastes

It can be observed from the presented data that the dosage of SS - 5–10% was optimal. The compressive strength (CS) of the hardened pastes cured at ambient temperature was up to 39.3 MPa, whereas for those thermally cured was up to 45.2 MPa. The incorporation of up to 40–50% of LS leads to an increase in CS, and further replacement of CM by LS considerably deteriorates the CS of the hardened blended AAC pastes. The highest mechanical performance corresponded to a low content of calcined clay minerals (5.8–7.0%) and high content of calcite (54.6–60.5%). By increasing the amount of LS in the range of 0–50%, a decrease can be observed in the setting times and water/binder ratio from 0.46 to 0.32.

3.2.2. Properties of fresh and hardened AAC pastes based on MK and C/M carbonate minerals

Fig. 3 presents the CS results of the samples based on the MK-LS. According to the obtained results, CS is highest when the LS content is in the range of 70–80%. After curing at ambient temperature, the CS of the steam-cured MK-LS samples was 21.7–32.2 MPa, and 7.1–10.6 MPa. The molar ratios Si/Al and Na/Al for pastes activated by SS at Na_2O of 5% were 2.69–3 and 0.62–0.93, and at Na_2O of 10% were 3.31–3.93 and 1.24–1.86, respectively. The replacement of MK by LS decreased the water/binder ratio from 0.7 to 0.58. Setting of the fresh paste shortened setting times - initial from 42 to 13 min, and the final from 67 to 30 min.

Fig. 4 shows the CS development over time of AAC based on CM and optimal formulations listed in Table 3 also showing the densities and intenerate coefficients of the samples.

The filler effect of LS results in an increase in packing density of mixed precursor particles, and consequently an increase in the density of hardened AAC pastes. Furthermore, the intenerate coefficient shows that CM-based formulations are related to hydraulic cements, whereas those based on MK are non-hydraulic binder systems. The hardened pastes based on CM and MK demonstrate dissimilar CS development characteristics. Hardened paste based on MK develops an average of 75% of the 28 day strength in 2 days, followed by a further insignificant increase in CS. The strength development of CM-based hardened pastes is different and has a logarithmic character that is specific to binder systems based on C-S-H.

3.3. Reaction products and microstructure of hardened pastes

The results of the X-ray diffraction and thermal analyses are shown in Figs. 5-8, performed for the formulations listed in Table 3.

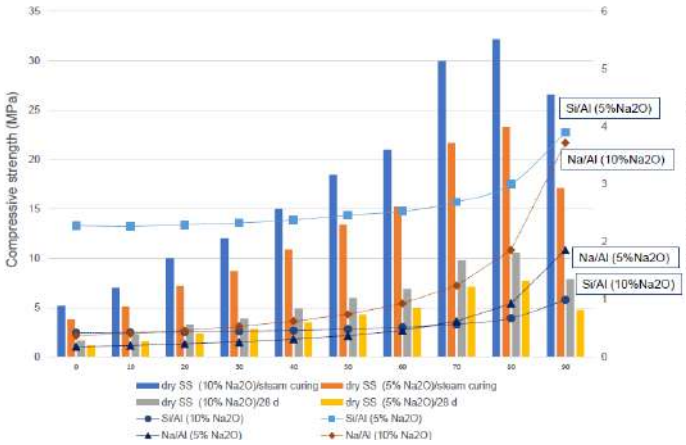


Fig. 3. The CS results of hardened MK-LS pastes

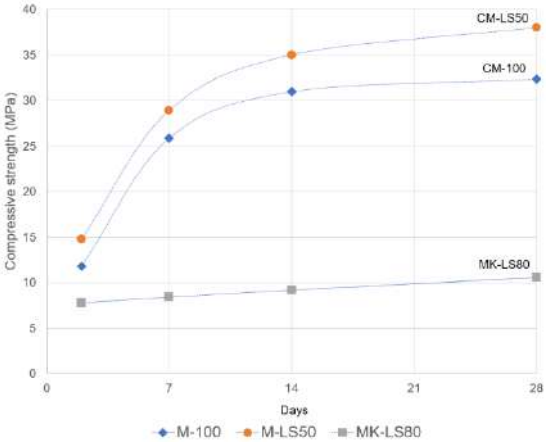


Fig. 4. The CS development of optimal formulations

Table 3. Alkali-activated blended cements formulations, the intenerate coefficients, and density of the hardened pastes

Abbreviation	MK (%)	CM (%)	LS (%)	The intenerate coefficient	Density, g/sm^3
CM-100	-	100	-	1	1.75
CM-LS40	-	60	40	1	1.88
CM-LS50	-	50	50	1	1.91
MK-LS80	20	-	80	0.3	1.67

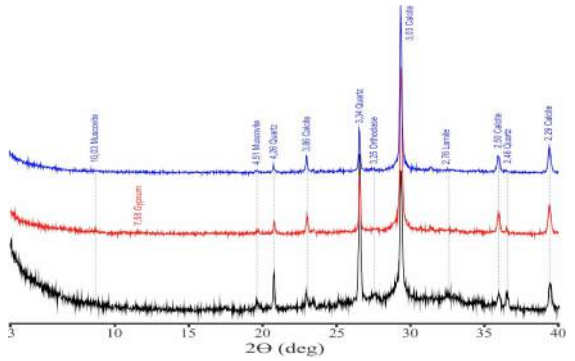


Fig. 5. X-ray diffractograms of CM-based hardened pastes

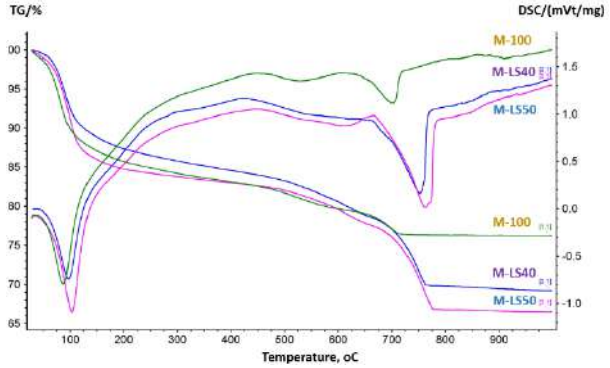


Fig. 6. Thermal analyses (TG/DSC) of CM-based hardened pastes

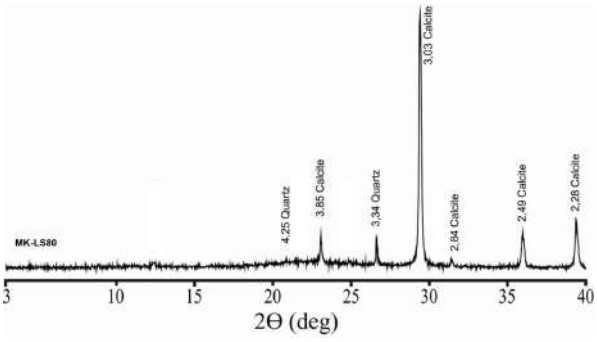


Fig.7. X-ray diffractograms of MK-LS80-based hardened pastes

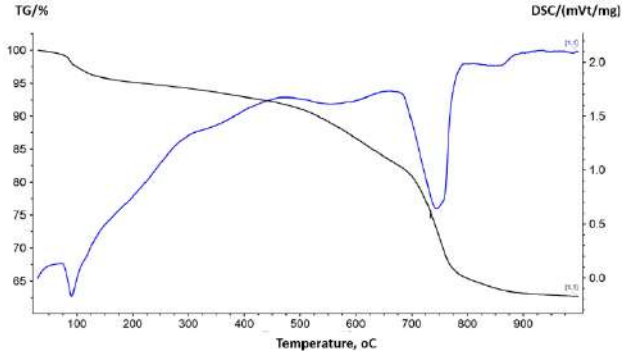


Fig. 8. Thermal analyses (TG/DSC) of MK-LS80-based hardened pastes

quartz, calcite, anhydrite, and dicalcium silicate. Given the constituents of precursors, namely reactive Si, Al, and Ca, as well as dicalcium silicate, and based on previous results in the field of high-Ca AACs, the gel composition in accordance with D'Elia et al. 2018, is apparently a mixed sodium (calcium) aluminosilicate hydrate N-(C)-A-S-H, aluminium-enriched C-S-H gel (C-A-S-H), and C-S-H gels. The

hardened MK-LS80 paste (Fig.7) is different in the area of amorphous hump, which is centralized between 26 and 29°2Θ, indicating the formation of N-A-S-H and N-(C)-A-S-H mixed gels SS-activated MK-LS systems. Obtained data are in agreement with results reported by Perez-Cortes and Escalante-Garcia, J. (2020a,b). Unreacted calcite and quartz were also identified. The shift in the hump may be indicative of the difference in the chemical composition of the binder gels formed in the CM and MK-based blended systems. The thermal analysis reported in Figs.6,8 allows the identification of the differences in the reaction mechanisms in the CM-LS- and MK-LS-based systems. The mass loss values in the area of 50–175 °C, which reflect water evaporation and dehydration from the gel reaction product, can be considered as an indicator of the amount of binder gel formed. The mass losses in the range of 650–820 °C refers to residual calcite. Alkali activation of CM resulted in an increase in mass loss from 0.95 to 12.91% in the temperature diapason of 50–175 °C, accompanied by a decrease in mass loss from 9.53% to 6% in the range of 650–820 °C, confirming the formation of a noticeable amount of aluminosilicate gel with the participation of calcite in the reaction process. Meanwhile, considering the mass loss in the same temperature areas, the binder gel formation process was less intensive in the MK–LS system.

3. Conclusions

The results of comparative studies on natural and designed clay-calcium carbonate minerals as binary precursors for AACs production are presented in this study. The reaction product assemblage and properties of fresh and hardened pastes based on AA binary precursors consisting of natural or designed blends of calcium carbonate and clay minerals are conditioned on (i) partial (only calcination of clay minerals) or full calcination of blend clay+calcium carbonate (co-calcination); (ii) ratio of clay/calcium carbonate minerals; (iii) dosage of alkali reactant; and (iv) curing parameters.

The incorporation of LS into AACs based on CM or MK decreased water demand, shortened setting times, and improved mechanical performance. The effect of LS on the properties of fresh AAC pastes was based on the dilution effect. The strengthening effect of LS was based on filler, nucleation, and chemical effects. The chemical effect increased after thermal treatment of the marl.

In the designed AAC based on the binary precursor MK-LS, MK is the main reactive precursor that forms a mineral matrix in the form of sodium aluminosilicate hydrate gel N-A-S-H, whereas calcium carbonate is a much less reactive secondary precursor that modifies the main binder gel by forming sodium (calcium) aluminosilicate hydrate gel N-(C)-A-S-H. An intermixed mineral matrix consisting of N-A-S-H and N–(C)-A-S-H gels binds the LS particles by forming a consolidated material. However, binder gel amount and composition cannot compensate for the low water resistance of raw calcium carbonate.

Calcination of the natural blend of clay and calcium carbonates leads to the dehydroxylation of clay minerals and partial decomposition of calcium carbonate, accompanied by the formation of dicalcium silicate. Compared to MK-LS, alkali activation of CM-LS results in the formation of a higher amount of binder gel with a greater extent of Ca incorporation into the structure of Na aluminosilicate gel and the formation of Ca aluminosilicate and Ca silicate hydrogels. This provides an alkali-activated CM-LS system with better mechanical properties and continuous strength development, including under wet conditions. Moreover, water-resistant consolidated materials based on CM-LS blends can be obtained when the calcined clay mineral content is only 5.8–7.0%.

Given that the optimal contents of MK and CM in the binder system are 20% and 50%, respectively, it is evident that the energy consumption for the production of AACs based on CM-LS will be 2.5 times higher compared to those based on MK-LS. However, AACs based on CM-LS are water resistant and have a CS 1.3 times higher than that of MK-LS.

References

D'Elia, A., Pinto, D., Eramo, G., Giannossa, L.C., Ventruti, G., Laviano, R. (2018) "Effects of processing on the mineralogy and solubility of carbonate-rich clays for alkaline activation purpose: mechanical, thermal activation in red/ox atmosphere and their combination", *Applied Clay Science*, 152: 9–21

Perez-Cortes, P., Ivan Escalante-Garcia, J. (2020a) "Design and optimization of alkaline binders of limestone-metakaolin – A comparison of strength, microstructure and sustainability with portland cement and geopolymers", *Journal of Cleaner Production*, 273: 123118

Perez-Cortes, P., Escalante-Garcia, J.I. (2020b) "Alkali activated metakaolin with high limestone contents - statistical modeling of strength and environmental and cost analyses", *Cement and Concrete Composites*, 106: 103450

The 16th International Congress on the Chemistry of Cement 2023 (ICCC2023)
"Further Reduction of CO_2 -Emissions and Circularity in the Cement and Concrete Industry"
September 18–22, 2023, Bangkok, Thailand

Evaluation of iron ore tailing in alkali-activated cement

T.V. Melo[1*], F.S. Faria [2], N. Tokudome[3], M.A. Longhi[4]

[1]Federal University of Ouro Preto, Belo Horizonte, Brazil
Email: taina.varelamelo@gmail.com
[2] Federal University of Rio de Janeiro, Rio de Janeiro, Brazil
Email: filipe.soares.faria@gmail.com
[3] Circlua, São Paulo, Brazil
Email: naguisa.tokudome@gmail.com
[4] Circlua, Belo Horizonte, Brazil
Email: marlonlonghi@gmail.com

ABSTRACT

The development of alternatives to Portland cement with low or no clinker content has been constantly studied around the world. However, the scarcity of raw materials it is an issue to make the product on a scalable level, being the major challenge for this technology. In this way, the mining industry appears as a potential supplier of materials for these solutions due to the large amount of material generated. The iron ore production process basically generates two solid tailings, one during the extractive process and the other during processing and mineral recovery. These tailings are accommodated in piles and dams, compromising the environment, community safety and production effectiveness. However, such residues may have specific characteristics that enable their use in construction, and when added in different proportions to an alkali-activated cement, they can potentially increase mechanical performance. Thus, the present work aims to characterize physically, chemically, and mineralogically an ultrafine iron ore tailing (UIOT), and analyze the substitution of 5%, 10%, 15%, 20% and 25% of alkali-activated cement (AAC) by tailings. The results indicated that with up to 10% of ultrafine in the composition it is possible to maintain the mechanical performance in compression similar to AAC, and with up to 25% substitution, all specimens achieved compressive strengths above 40 MPa. The binder intensity index of the matrices with cement incorporating UIOT in place of AAC were higher than the reference mixture. The simple replacement of cement by ultrafine tailings reduces the associated CO_2 emissions as well as adds value to the waste material. A thermal process in the tailing and an adjustment in the dosage of activated alkali cement can improve the performance of this material.

KEYWORDS: *Clinker Free cement*, *alkali-activated cement, iron ore tailings, circular economy.*

1. Introduction

The production process of Portland cement involves several factors such as high energy costs, carbon emissions and extraction and consumption of raw materials. (Lehne and Preston, 2018). This industry is traditional for having a well-established process, which consists of calcination by combustion of raw material at high temperature.
The development of a low environmental impact cement requires sustainability initiatives like low energy consumption, and the development of local raw materials. As a result of global social and technological development, mining, steel, and other industries have been growing, and with this growth comes an increase in residues generated and the environmental liabilities of these industries (Tayebi-Khorami et al., 2019; Kalisz et al., 2022). The possibility of using these residues as an alternative raw material for alkali-activated cement reduces the environmental impact associated with generating industries and enhances the technology of this potential material. In the processing of iron ore tailing, the sandy material is removed from general waste and used in the construction industry as iron ore sand. The remaining portion is also rich in quartz and includes quantities of iron and clay, has reduced fineness but limited applications in

industries. This study aims to evaluate chemical, physical, and mineralogical characteristics and the use of ultrafine iron ore tailing (UIOT) as a substitute for up to 25% of activated alkali cement (AAC).

2. Materials and methods

The cement tested was an alkali-activated cement (AAC) using sodium hydroxide as activator, with compressive strength class ≥ 40 MPa after 28 days of curing, produced in a demonstrative scale factory in Brazil. This factory uses a fully electrified process, and benefits all the raw material, including the alkaline activator itself, with a quantity of residual material or co-products in its production of more than 90%.
The iron ore tailing used in this study is from the state of Minas Gerais in Brazil, and it is a fine material (<30 μm) generated in the concentration stages of iron ore processing called flotation and/or magnetic separation. The only processing performed for this test was grinding, to obtain a fineness and surface area similar to AAC, therefore this material was used as a filler in this study.
The methodology is divided in two parts and the first is the characterization of the UIOT, aiming at its use as a filler in the AAC. The second part consist of evaluating the compressive strength of cement and the workability of mortars with different proportions of UIOT on ACC.
Physical characterization and chemical composition were performed on AAC and UIOT. The granulometric distribution of the particles was performed on CILAS equipment, using laser granulometry technique with isopropyl alcohol. Real density was performed on QuantaChrome helium (He) Stereopycnometer equipment (pycnometer). Bulk density was determined according to Brazilian standard (ABNT NBR 1972, 2021). Specific surface area was determined on QuantaChrome Nova 1000e equipment according to BET method with nitrogen as the analysis gas. Chemical composition was evaluated by the X-ray fluorescence technique using the Panalytical Axios Fast equipment.
Complementary analyzes of mineralogy and loss of mass were determined on UIOT to correlate its influence on compressive strength and its potential use as a precursor. X-ray diffraction analysis (XRD) focused on identifying and determining the levels of crystalline mineral phases using Shimadzu/LabX6000 equipment from ISIPM, and the phases quantification was determined by Rietveld method. The mass loss analysis over the temperature increases from 100°C to 1000°C was performed using the thermogravimetry technique using the NETZSCH 449 F3 Jupiter equipment.
For compressive strength, different contents of UIOT were used in substitution of AAC (5, 10, 15, 20 and 25%), the test were performed at ages of 1, 3, 7 and 28 days of curing and workability of the mortar on fresh state was measured with constant w/b ratio. Both tests were determined by ABNT NBR7215 (2019).

3. Results

The particle size of UIOT is slightly smaller than AAC, and due to the low levels of substitution, this variation is barely noticeable in the distribution curve (**Error! Reference source not found.**) and complementary physical characteristics in Table 1. The physical characteristics, such as surface area and characteristic diameter, were consistent with the granulometric curves, that is, it showed similarity in relation to the size of the AAC and UIOT grains. The real density of the UIOT was higher than that of the AAC, corroborating the chemical composition that exhibits a high content of iron oxides in the UIOT. Thus, increasing the UIOT content increases the density of the cement.

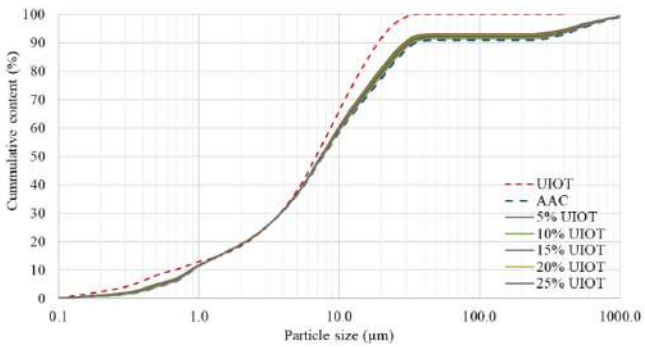


Figure 1 Particle size distribution of: AAC, UIOT and AAC + UIOT as additive in different percentages.

Table 1 Physical characteristics of AAC and UIOT

ID	D10 (µm)	D50 (µm)	D90 (µm)	Real density (g/ cm³)	Bulk density (g/ cm³)	Specific surface area (m²/g)
AAC	0.9	7.6	22.3	2.83	1.29	0.84
UIOT	0.7	6.9	19.0	3.46	1.29	0.83

The chemical composition of the UIOT (Table 2) is consistent with the X-ray diffraction and thermogravimetry tests presented in Figure 2. Using Rietveld quantification technique, the content of 38.3% of Quartz, 21.4% of Kaolin, 17% of Hematite, 16.7% Goethite, 5.7% Muscovite and 0.9% Gibbsite, were observed (Figure 2 (a)). The mineralogy results are consistent with the thermogravimetric results, since the amount of mass loss of 3,54% in the range of 200°C - 400°C associated with Gibsite and Goethite dehydroxylation, and 2.9% in the range of 400°C - 600°C associated with Kaolinite dihydroxylation. Using the method of kaolinite calculation proposed by Avet and Scrivener (2020), a kaolinite amount of 21.5 % is calculated, while Rietveld's quantification method indicated 21.4%.

Table 2 Chemical characteristic of AAC and UIOT (%)

ID	SiO_2	Al_2O_3	Fe_2O_3	CaO	MgO	TiO_2	Na_2O	K_2O	MnO	LOI
AAC	34.30	9.49	0.94	39.20	4.47	0.41	4.00	0.50	0.34	5.70
UIOT	35.29	7.58	48.91	0.05	0.14	0.28	-	0.23	1.60	5.87

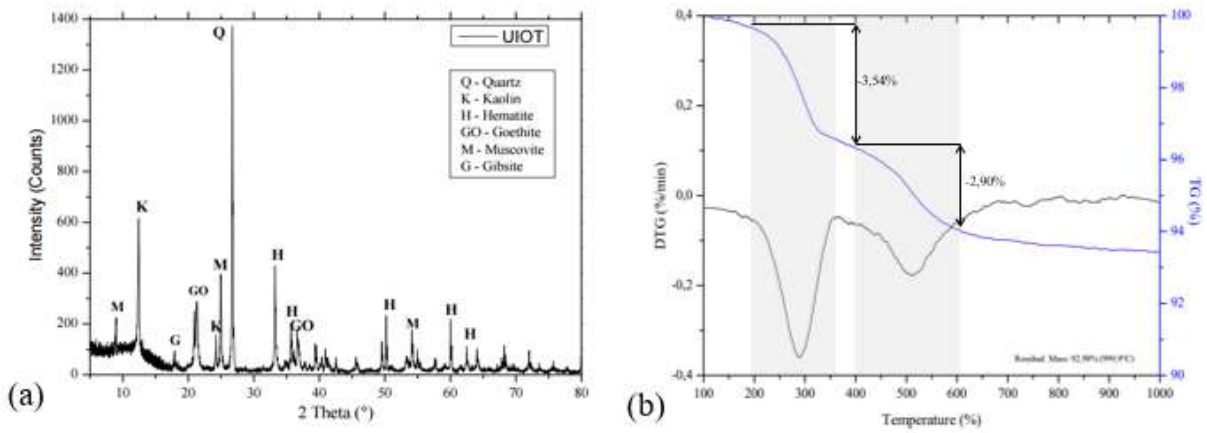


Figure 2 (a) X-ray diffraction of UIOT and (b) Thermogravimetric analysis of UIOT

Thus, the UIOT is a material of reduced granulometry, with a high content of quartz and iron phases, and with a considerable content of kaolinite. As it is, it does not show pozzolanic reactivity, but due to the kaolinite content, this property can be obtained from thermal process.

In the current condition, the UIOT was used as a filler, replacing the cement portion. Regardless of mechanical performance, this replacement reduces the CO_2 footprint associated with the material produced, as well as adds value to a waste that is currently an environmental liability.

Related to the effect of UIOT in ACC, as show in the **Error! Reference source not found.**, it is possible to observe the outcome of UIOT contents ranging from 5% to 25%. The impact is more pronounced at early ages, where there is an expressive reduction in performance, which becomes less significant over the course of the hardening period. The use of UIOT did not affect the workability conditions. Even with reduction of compressive strength, all mortars reached strengths above 40 MPa at 28 days (AAC strength class).

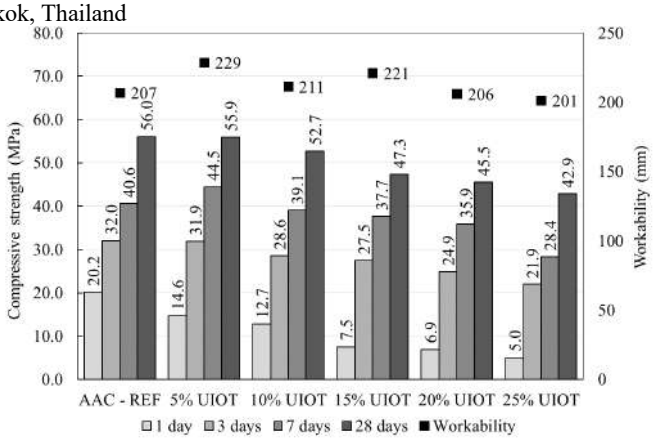


Figure 3 Alkali-activated cement compressive strength and mortar workability on flow table.

As shown in Table 3, the binder intensity (BI) index – measure the amount of binder necessary ($kg.m^{-3}$) to deliver 1 MPa considering the results of 28 days, the contents of 5 and 10% are the most effective. Although binder intensity index increases as UIOT replacing ACC rises, it is worth mentioning that the incorporation of UIOT implies a reduction of carbon footprint and cost, associated with maintenance of the strength class (40 MPa) of the reference mixture. Another benefit related is the proper disposal of the tailings, which is currently deposited in dams. In a future study or considering industrial scale, is possible to increase the addition, from the thermal treatment of UIOT and from the optimization of the cement design conditions.

Table 3 Binder intensity index of evaluated mortars

Mixture	AAC - REF	5% UIOT	10% UIOT	15% UIOT	20% UIOT	25% UIOT
Binder intensity ($Kg.m^{-3}$/MPa)	8,98	9,02	9,58	10,70	11,14	11,84

4. Conclusions

Based on the results presented in this work, it is possible to conclude that:

- The UIOT is mainly composed of SiO_2, Al_2O_3 and Fe_2O_3 in minerals of quartz, kaolin, hematite, goethite, muscovite, and gibbsite. Due to physical and mineralogical characteristics, it is possible to use UIOT as a filler and, if calcined, also as a precursor.
- Despite being an inert material and with granulometry similar to AAC, UIOT maintained the resistance of the evaluated matrices above 40 MPa (class of the studied cement).
- As it is a mining waste, the incorporation of UIOT up to 25% as a substitute of AAC, is an alternative to reduce the carbon footprint of alkali-activated cement and add value to a waste material.

References

ABNT NBR 1972 (2021) 'Agregados - Determinação da massa unitária e do índice de vazios', NBR16972. Rio de Janeiro: Associação Brasileira de Normas Técnicas.

ABNT NBR7215 (2019) 'Cimento Portland - Determinação da resistência à compressão'. Rio de Janeiro: Associação Brasileira de Normas Técnicas.

Avet, F. and Scrivener, K. (2020) 'Simple and Reliable Quantification of Kaolinite in Clay Using an Oven and a Balance', in, pp. 147–156. Available at: https://doi.org/10.1007/978-981-15-2806-4_17.

Basson, E. (2015) Steel in the circular economy - A life cycle perspective, Worldsteel Asscociation.

Kalisz, S. et al. (2022) 'Waste management in the mining industry of metals ores, coal, oil and natural gas - A review', Journal of Environmental Management, 304(November 2021). Available at: https://doi.org/10.1016/j.jenvman.2021.114239.

Lehne, J. and Preston, F. (2018) Making Concrete Change; Innovation in Low-carbon Cement and Concrete. Chatham House.

Tayebi-Khorami, M. et al. (2019) 'Re-thinking mining waste through an integrative', Minerals, 9(5)(2019), p. 286. Available at: https://doi.org/10.3390/min9050286.

The 16th International Congress on the Chemistry of Cement 2023 (ICCC2023)
"Further Reduction of CO_2 -Emissions and Circularity in the Cement and Concrete Industry"
September 18–22, 2023, Bangkok, Thailand

An alkali-activated cement factory in Brazil: quantification of CO_2 emissions for a class of cements

T. F. Oliveira [1*], N. B. Justen [2], T. V. Melo [3], and M. A. Longhi [4].

[1] *Federal University of Ouro Preto, Belo Horizonte, Brazil*
Email: thainafariaoliv@gmail.com
[2] *Circlua, Belo Horizonte, Brazil*
Email: nicolejusten@gmail.com
[3] *Federal University of Ouro Preto, Belo Horizonte, Brazil*
Email: taina.varelamelo@gmail.com
[4] *Circlua, Belo Horizonte, Brazil*
Email: marlonlonghi@gmail.com

ABSTRACT

The need to control and reduce CO_2 emissions has intensified the development of clean technologies. The synergy between the mining, steel, and cement industries, driven by the necessity for decarbonization, and the circular economy of these industries, allowed the creation of the first alkali-activated cement factory in Brazil. This Brazilian cleantech is governed by the decarbonization of the industry, circular economy, and scalability. To attend these premises, it uses a fully electrified production process, using different wastes from the steel and mining industry, both in the development of precursors and in the production of activators. The massive use of these materials assists in reducing tailings piles as well as eliminating tailings dams. Thus, the objective of this work is to present the main decision-making factors related to CO_2 emissions, and the total CO_2 emissions for different cements produced. Production inputs, as well as the process associated with the activator, represent the largest contribution to CO_2 emissions. Considering that a new sodium silicate production process is used, which uses iron ore sand in an electrified process, this value is consistently lower than the silicates available on the market. The use of renewable energy sources also presents a great improvement associated with the process. The adjustment of the formulation, combining different potential materials, provided the best formulation design and allowed different compressive strength classes of cement with a factor of 0,6 MPa/kg of CO_2.

KEYWORDS: *Alkali-activated cement, CO_2 emissions, factory, circular economy, decarbonization.*

1. Introduction

The production of Portland cement is related to several environmental issues, such as carbon emissions, consumption of natural raw materials, and high energy costs (Lehne & Preston, 2018). To reduce these negative impacts, great attention has been given to alkali-activated cement as an alternative to Portland cement. This type of material generally exhibits low carbon emission associated with high mechanical performance and allows the use of local raw materials and industrial residues (Provis, 2018).

The development of a low environmental impact cement requires circularity, low energy consumption, and the development of local raw materials. With the increase in mining, steel, and other industries, the volume of waste material generated increases the environmental liability of these industries (Basson, 2015; Kalisz et al., 2022; Tayebi-Khorami et al., 2019). The possibility of using these materials as raw materials for alkali-activated cement boosts the technology and reduces the impact associated with previous activities. Targeting a production on an industrial scale, the availability of these materials guarantees the supply of raw materials, but it's important to take into account various other factors such as proximity to the raw material source, processing requirements, energy needs, and product design. Aiming at sustainable development, the analysis of CO_2 emissions, associated with product performance, must be a decision-making factor.

The greatest contribution to CO_2 emissions in alkali-activated cements is associated with the activator portion (Habert & Ouellet-Plamondon, 2016). The possibility of reducing emissions from this factor is associated with the development of new routes and technologies (Passuello et al., 2017). Both in the development of activators and precursors, the use of industrial waste is beneficial because it does not require a mining process, as well as for reducing environmental liabilities. However, even though it is a residual material, without CO_2 allocation, the majority of the raw material, which is the precursor, needs to be transported and often needs a complementary drying, calcination, and grinding process, which requires energy. The influence of these factors must be understood for each material in the implementation of an industrial factory. Thereby, this study used the analysis of CO_2 emissions as an industrial decision-making tool, in multifactorial impact analysis, to obtain the design of different classes of cement with low CO_2 emissions for a real alkali-activated factory.

2. Methodology

The methodology of the Intergovernmental Panel on Climate Change (IPCC, 2014) was adopted and the Ecoinvent database (2023) was used to obtain the emission factors to evaluate CO_2 emissions. The delimitation adopted was cradle-to-gate (A1-A3).

The work is divided into two parts, the first, simulating different boundary conditions for the evaluation of CO_2 emission. This part presents CO_2 quantification as a decision-making tool. Initially, eight potential raw materials (Figure 1) destined for the production of activated alkali cement were chosen to evaluate the CO_2 emissions. Different combinations, with different materials, were evaluated, as well as different supply distances for the materials (average distance of 100 km to 500 km) and different electrical energy sources (solar, hydraulic, wind, or Brazil energy mix). In the first part of the analysis, different conditions were evaluated in order to identify the main influencing factors.

The second part quantifies the CO_2 emission for the different cements produced on a factory scale, based on the conditions observed in the previous stage. The factory starts operating with some important premises:

- the entire process must be fully electrified, including all thermal transformations;
- the activator used must be produced on-site, using mining waste as a source of silica;
- more than 90% of the raw material must be of waste origin.

An adjustment of the formulation was carried out by combining some of these materials and the compressive strength was obtained through the Brazilian standard methodology NBR 7215 (ABNT, 2019). Based on the mechanical performance results, three classes of alkali-activated cement with a compressive strength at 28 days above 32, 40, and 60 MPa were identified as C1, C2, and C3, respectively. These three cements range from general-purpose applications to applications with high initial performance. The electricity used in the factory comes from the free energy market, from a hydroelectric source. The average transportation (road transportation) of materials is less than 100km and the packaging is in big bags. The efficiency of the alkali-activated cements C1, C2, and C3 was evaluated through the ratio of compressive strength (MPa) at 28 days and the total kg·CO_2.

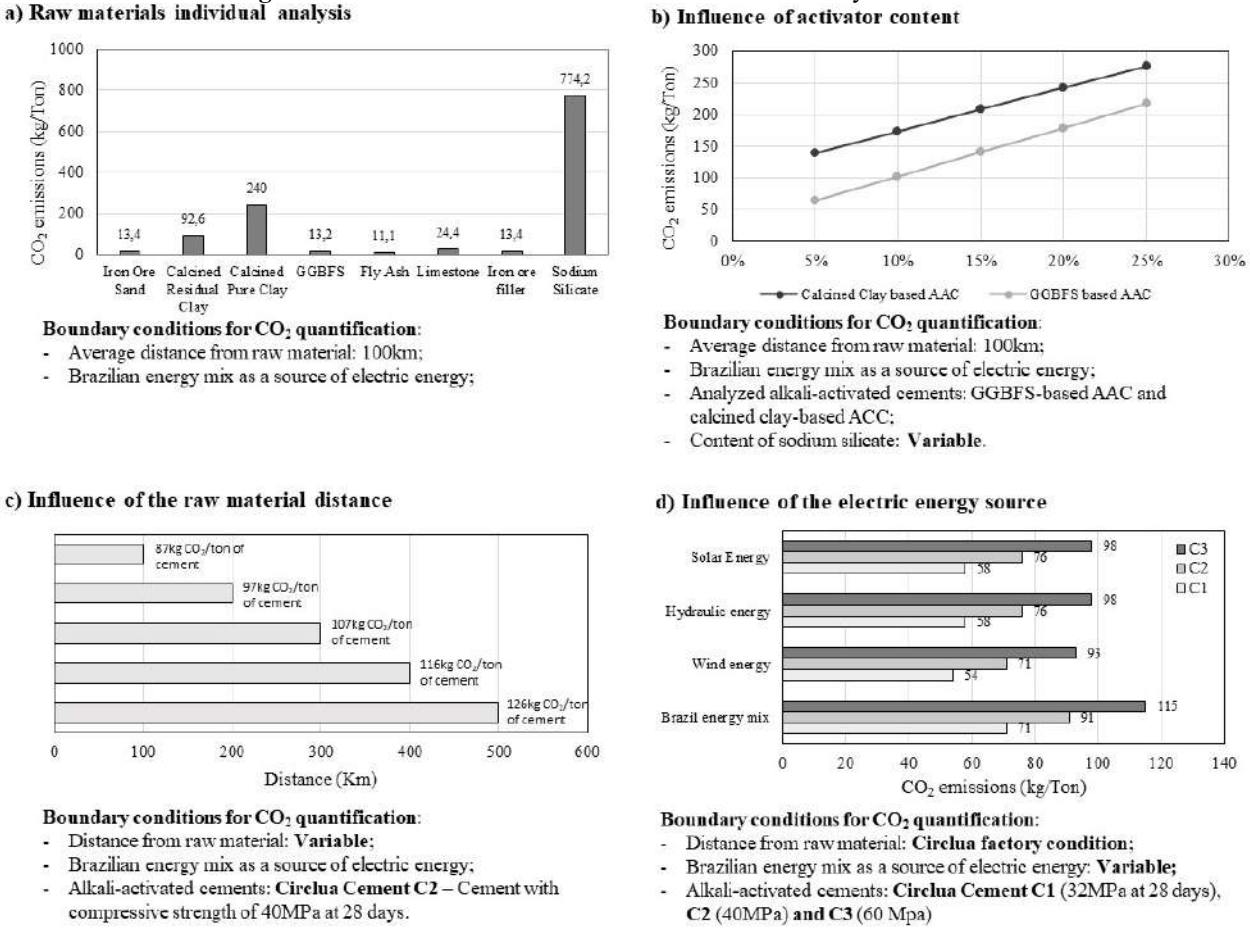
3. Results

The results and discussions related to CO_2 emissions considering different boundary conditions are shown in Figure 1. In relation to raw materials, calcined clays have a considerable content of CO_2 emissions compared to GGBFS and Fly ash, due to the need of processing and/or mining. However, the raw material with the biggest CO_2 emissions is the activator, in this case, sodium silicate. Usual sodium silicates present values of CO_2 emissions between 1,76 to 2,24 tons·CO_2 / ton (Ouellet-Plamondon & Habert, 2020). The activator used in this study was produced using an alkaline fusion process, using iron ore sand as a source of silica, in a total electrified process, and presents emissions of 0,736 tons·CO_2 / ton, showing a significant reduction in total emissions in relation to usual sodium silicates. Following this direction, Figure 1b shows the influence of the sodium silicate produced when is combined with aluminosilicate materials like calcined clay and GGBS. The activator proportions evaluated do not necessarily represent what should be adopted,

each precursor has an ideal activator content, not necessarily those shown in the second graph. The increase in the sodium silicate proportions contributes linearly to the total CO_2 emissions of cements.

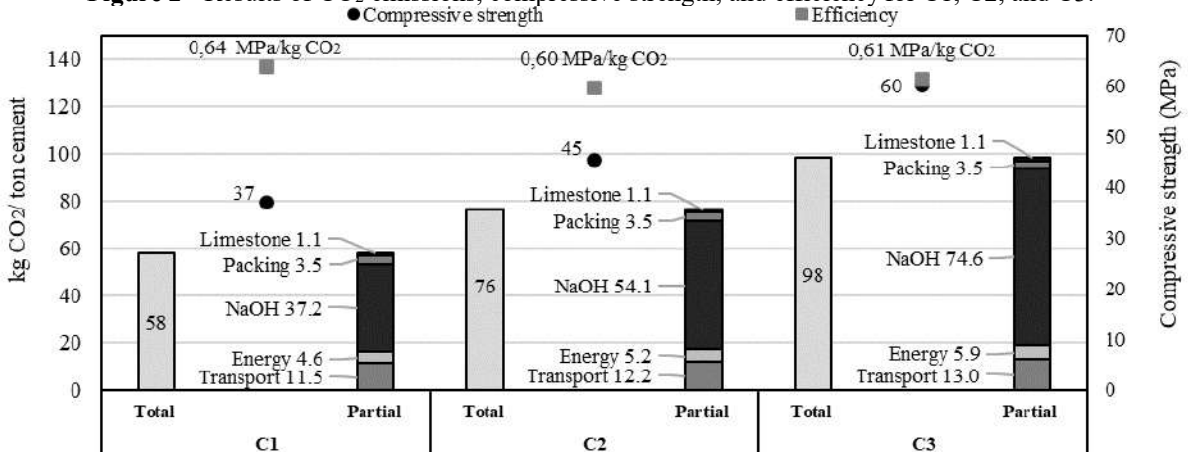
The analysis of raw material distance (Figure 1c) demonstrates that for every 100 km added, there is a 10% increase in CO_2 emissions related only to transport. Therefore, the location of the factory close to the source of raw materials is a determining factor to reduce emissions. Finally, the influence of the electric energy source (Figure 1d) demonstrates that the supply of electricity in Brazil already has reduced CO_2 emissions due to renewable energy sources. The possibility of using a free energy market further reduces the emission factor, especially wind energy.

Figure 1 - Results of CO_2 emissions for different boundary conditions.



With the identification of the main CO_2 emission factors, three types of cement were designed with a view to resistance to 28 days and lower levels of emissions within the capabilities of the factory. Figure 2 presents the results of these three cement formulations. The three types of cement emit only 10% to 17% of the CO_2 emitted by Portland cement, considering a world average of 590 kg CO_2/ton (IEA, 2022). The efficiency factor among all formulations appears to be closely matched, which can be explained by the linear correlation with the activator used (represented by NaOH), with a corresponding increase in both compressive strength and CO_2 emissions. The impact of NaOH on the total emissions is noticeable, followed by the emissions of transport, energy, packing, and limestone. The main way to enhance the efficiency factor is through the reduction of NaOH content, and maintenance or increases of compressive strength. Even if not shown directly in the figure, precursor processing is the main contributor to transport steps and energy consumption. Although the emissions related to energy consumption during the production process and transportation of residues are relatively low compared to the individual emissions of NaOH, they can still have an impact and be improved by selecting raw materials that require minimal processing and are located closer to the factory.

Figure 2 - Results of CO_2 emissions, compressive strength, and efficiency for C1, C2, and C3.



4. Conclusions

In conclusion, the study evaluated the CO_2 emissions in the production of alkali-activated cements. The quantification of CO_2 was used as a decision-making tool for choosing raw materials, production conditions and mixture design, and then the first class of cements was analysed in terms of emissions and mechanical performance. The results showed that sodium silicate, used as an activator, was the major contributor to CO_2 emissions, followed by calcined clays. The analysis of different boundary conditions showed that the use of wind energy as a source of electricity and the proximity of the raw materials to the factory also contributes significantly to the reduction of CO_2 emissions. The efficiency factor (MPa/Kg CO_2) among the three cement formulations (C1, C2, and C3) was found to be closely matched, with a linear correlation between the rise in sodium silicate content, the increase in CO_2 emissions, and compressive strength. We concluded that the reduction or optimization of sodium silicate content, added to the use of local residual raw materials, and renewable energy sources make it possible to obtain low-emission alkali-activated cement, contributing to the transition to a more sustainable and environmentally friendly construction industry.

References

Basson, E. (2015). Steel in the circular economy - A life cycle perspective. In *Worldsteel Asscociation*. https://www.worldsteel.org/en/dam/jcr:00892d89-551e-42d9-ae68-abdbd3b507a1/Steel+in+the+circular+economy+-+A+life+cycle+perspective.pdf

Habert, G., & Ouellet-Plamondon, C. (2016). *Recent update on the environmental impact of geopolymers* (pp. 17–23). RILEM technical letters. https://doi.org/https://doi.org/10.21809/rilemtechlett.2016.6

IEA. (2022). *Cement*. https://www.iea.org/reports/cement

IPCC. (2014). *Supplement to the 2006 IPCC Guidelines for National Greenhouse Gas Inventories : Wetlands Task Force on National Greenhouse Gas Inventories* (M. F. and T. T. Takahiko Hiraishi, Thelma Krug, Kiyoto Tanabe, Nalin Srivastava, Baasansuren Jamsranjav (ed.)).

Kalisz, S., Kibort, K., Mioduska, J., Lieder, M., & Małachowska, A. (2022). Waste management in the mining industry of metals ores, coal, oil and natural gas - A review. *Journal of Environmental Management*, *304*(November 2021). https://doi.org/10.1016/j.jenvman.2021.114239

Lehne, J., & Preston, F. (2018). *Making Concrete Change; Innovation in Low-carbon Cement and Concrete*. Chatham House. https://www.chathamhouse.org/2018/06/making-concrete-change-innovation-low-carbon-cement-and-concrete

Ouellet-Plamondon, C., & Habert, G. (2020). Life cycle assessment (LCA) of alkali-activated cements and concretes. In *Handbook of Alkaliactivated Cements, Mortars and Concretes*. Woodhead Publishing Limited. https://doi.org/10.1533/9781782422884.5.663

Passuello, A., Rodríguez, E. D., Hirt, E., Longhi, M., Bernal, S. A., Provis, J. L., & Kirchheim, A. P. (2017). Evaluation of the potential improvement in the environmental footprint of geopolymers using waste-derived activators. *Journal of Cleaner Production*, *166*, 680–689. https://doi.org/10.1016/j.jclepro.2017.08.007

Provis, J. L. (2018). Alkali-activated materials. *Cement and Concrete Research*, *114*, 40–48. https://doi.org/10.1016/j.cemconres.2017.02.009

Tayebi-Khorami, M., Edraki, M., Corder, G., & Golev, A. (2019). Re-thinking mining waste through an integrative. *Minerals*, *9(5)*(2019), 286. https://doi.org/10.3390/min9050286

The 16th International Congress on the Chemistry of Cement 2023 (ICCC2023)
"Further Reduction of CO_2 -Emissions and Circularity in the Cement and Concrete Industry"
September 18–22, 2023, Bangkok, Thailand

Effect of CO_2 concentration on amount of carbonation in Mortar

K. Seki[1*], K. Avadh[2], M. Sakai[3], T. Mukai[4] and T. Torichigai[5]

[1] *Kajima Technical Research Institute, Concrete and Construction Materials Group, Tokyo, Japan*

Email: sekike@kajima.com
[2] *Kajima Technical Research Institute, Concrete and Construction Materials Group, Tokyo, Japan*

Email: avadh@kajima.com
[3] *Kajima Technical Research Institute, Concrete and Construction Materials Group, Tokyo, Japan*

Email: sakaimi@kajima.com
[4] *Kajima Technical Research Institute, Concrete and Construction Materials Group, Tokyo, Japan*

Email: mukaitos@kajima.com
[5] *Kajima Technical Research Institute, Concrete and Construction Materials Group, Tokyo, Japan*

Email: torichig@kajima.com

ABSTRACT

To reduce the adverse effects of global warming, new ground-breaking and energy-efficient methods are required to enhance CO_2 utilization and sequestration in concrete. The authors at Kajima Technical Research Institute have developed Carbon-Capture concrete (CCC). CCC is made using cement, blast furnace slag (BFS), γ di-calcium silicate (γ-C_2S), and is carbonation cured after 1 day of sealed curing. Hence carbonation progresses simultaneously with the hydration of cement and BFS. Previous research has shown that the rate and amount of carbonation in CCC primarily depends upon the carbonation curing condition i.e. temperature, relative humidity and CO_2 concentration. Further, the results indicate the performance of CCC with respect to carbonation even at lower CO_2 concentrations is impressive. In this study, the effect of the concentration of CO_2 on the carbonation of CCC mortar paste was investigated.

Hence, to understand the effect of CO_2 concentration, the specimens made using cement, BFS and γ-C_2S are carbonation cured at 50°C and 40% R.H. with varying concentrations of CO_2 (10%, 20%, 30%, 50%, 100%). Thermo-gravimetric analysis (TG-DTA) clearly shows that the amount of calcium carbonate produced due to carbonation increases with an increase in the concentration of CO_2 gas.

KEYWORDS: *CO_2 concentration, Calcium carbonate, Carbon utilization and sequestration, TG-DTA*

1. Introduction

Various policies are being implemented in Japan to achieve a carbon-neutral society by 2050. In the field of construction, storing CO_2 gas through the mineralization of CO_2 into concrete by carbonation curing is expected to significantly contribute to achieving carbon neutrality. To maximize the mineralization of CO_2 gas into concrete, the authors have been actively developing and investigating carbonation curing under varying temperatures and relative humidity. In order to produce large amounts of carbonation-cured concrete, it is imperative to utilize CO_2 from a wide variety of emission sources, such as exhaust gases emitted from factories and chemical plants. Since exhaust emissions include a mixture of various gases, CO_2 gas needs to be separated and captured from them to obtain high concentration. If various carbon dioxide gases can be utilized in carbonation curing of concrete, the effective use of CO_2 will be further promoted, and the manufacturing sites of precast concrete will expand.

On the other hand, since CO_2 concentration varies depending on the emission source, it is important to understand its effect on the speed and amount of carbonation by concrete. In this study, the low carbon emitting carbon capture concrete (CCC) developed in Kajima Technical Research Institute by replacing 70% of cement with a mixture of industrial by-products such as blast furnace slag (BFS) and γ-dicalcium silicate (γ-C_2S) was seal cured for 1 day followed by carbonation curing. Hence, simultaneous hydration and carbonation reactions occurred in the mortar mix. Keeping the temperature and relative humidity parameters constant, the influence of the concentration of CO_2 on the speed and amount of calcium carbonate produced in mortar specimens was evaluated. Thermo-gravimetric analysis (TG-DTA) was used to measure the amount of $CaCO_3$ formed due to carbonation.

2. Carbonation Test With Various CO_2 Gas

2.1 Experimental Outline

In the future, concentration of carbon dioxide gas used for carbonation curing is expected to vary depending upon the CO_2 capture and recovery technology from factory exhaust and its feasibility. Therefore experimental cases considered in this study are shown in Table 1. In the cases of concentration of CO_2 up to 50%, pre-mixed gas of carbon dioxide and nitrogen in the desired ratio was used, whereas to investigate the effect of 100% concentration, only CO_2 gas was used. The gas was supplied at a rate of 2L/min and the temperature and relative humidity were fixed at 50°C and 40% respectively.

Table 1 Experimental cases

Case	CO_2 Concentration (vol%)	Curing Condition
1	Sealed curing (0%)	Temperature: 50°C Humidity: 40%R.H.
2	10	
3	20	
4	30	
5	50	
6	100	

2.2 Materials and Mortar Mix Property

The materials used in this study and their properties are listed in Table 2. Ordinary Portland Cement was used as the binder, and the mixture consisting of blast furnace slag and γ-dicalcium silicate (γ-C_2S) i.e. γ-phase of Belite was used as the cement substitutes. γ-C_2S is a special admixture that does not hydrate but directly reacts with CO_2 to carbonate. The mix-proportion of mortar is shown in Table 3. The water to powder ratio was set at 50%, and the proportion of OPC, BFS, and γ was set referring to previous studies (Torichigai et al. (2000)).

Table 2 Materials used for mortar

symbol	summary
W	Water, density 1.00 g/cm^3
OPC	Ordinary Portland cement, density 3.16 g/cm^3, CaO content 63.78%, $CaCO_3$ content 3.4%
BFS	Blast furnace slag fine powder, density 2.92 g/cm^3, CaO content 43.76%, $CaCO_3$ content 1.0%
γ	Dicalcium silicate γ phase, density 2.95 g/cm^3, CaO content 63.89%, $CaCO_3$ content 0.0%
S	Crushed sand, density 2.64 g/cm^3, CaO content 1.62%, $CaCO_3$ content 0.0%
WRA	Water reducing agent, lignin sulfonic acid compounds and Polyol composite

Table 3 Mix proportion of mortar

W/P (%)	Unit Weight (kg/m^3)				
	W	OPC	BFS	γ	S
50.0	243	146	194	146	1446

P=OPC+BFS+γ

2.3 Specimen Preparation and Test Conducted

Cylinders of diameter 50 mm and height 100 mm were made using mortar mix as shown in Table 3, and initially, seal cured at 20°C for 1 day. After initial curing the specimens were left at 20°C and 60% RH for 3 hours, and then transferred into a carbonation chamber for curing under the conditions shown in Table 1. After carbonation for 6 days, the specimens were first broken into two halves along the vertical axis and sprayed with a 1% phenolphthalein solution on the surface to confirm the carbonated area. Samples for TG-DTA were taken from the carbonated area, the collected samples were then soaked in acetone to stop hydration followed by crushing using a pestle and mortar. The samples were then dried at 20°C for one week under nitrogen flow. TG-DTA was performed by increasing the temperature upto 1000°C at 20°C/min under Nitrogen gas flow using a Thermogravimetry and differential thermal analyzer (Thermoplus EVO2, Rigaku). In this study, the mass loss between 0°C - 200°C is considered to be due to the decomposition of chemically bound water, CSH gel, ettringite etc., 405°C - 515°C was assumed to be due to the decomposition of calcium hydroxide and between 600°C and 800°C was assumed to be due to pyrolysis of calcium carbonate.

3. Experimental Results and Discussion

3.1 Amount of Calcium Carbonate

The effect of the concentration of CO_2 on the degree of carbonation was measured through mass loss observed in TG-DTA as shown in Figure 1 and the derivative of mass loss (DTG) as shown in Figure 2. Considering the uncarbonated seal cured specimen, it can be observed that after 6 days, the hydration progressed normally as shown by mass loss and peaks at 0°C - 200°C and 405°C - 515°C in DTG Curve. The small peak at 600°C and 800°C shows the presence of calcium carbonate in the raw material which is around 1.42%. In the case of samples carbonated under the varying concentrations of CO_2 gas, it can be observed that all samples show a similar mass loss trend till 600°C in Figure 1 and the absence of peaks in the DTG curve in Figure 2. This shows that the hydrated products such as CSH gel, Calcium hydroxide were absent after carbonation curing of 6 days. Further, as the concentration of CO_2 gas increased, the mass loss between 600 to 800 increased and also the height of the peak in the DTG curve increased, indicating that for the same duration of carbonation, the degree of carbonation increases with the concentration of CO_2 gas. Hence, from the absence of peaks in the DTG curve until 600°C, it can be assumed that the products formed due to the hydration of cement and the pozzolanic reaction of BFS such as CSH gel, CASH, calcium hydroxide, and γ-C_2S etc. were directly carbonated to form calcium carbonate.

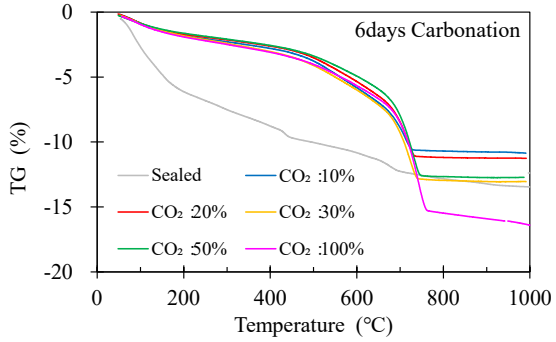


Figure 1 : Mass loss measurement

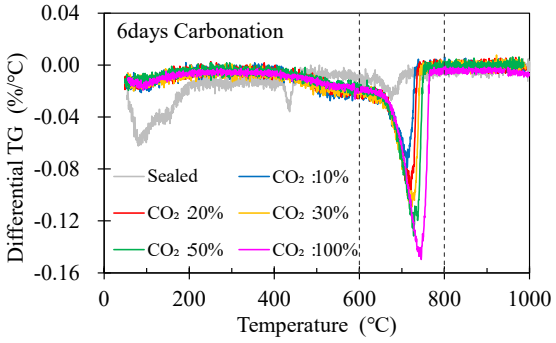


Figure 2 : DTG curves

Figure 3 illustrates the relationship between the concentration of CO_2 gas and the amount of calcium carbonate in mortar. It can be observed that the amount of calcium carbonate formed after 6 days of curing increases with the concentration of CO_2. Interestingly, as shown in Figure 4, the plot of the amount of $CaCO_3$ formed and the square root of the concentration of CO_2 gas shows a linear trend that intersects the y-axis at 1.42% which is the amount of $CaCO_3$ present in the uncarbonated sample. It has been previously reported that carbonation of mortar specimens involves the entry of CO_2 gas into the pores and its dissolution into the pore water. Following this, the dissolved CO_2 gas reacts with dissociated ions of Calcium Hydroxide and also reacts with CSH gel formed as a result of the hydration of C_2S and C_3S present

in cement. Hence, the formation of calcium carbonate depends upon the diffusion of CO_2 gas into pores and the amount of hydrated products (Papadakis et al. (1989). Also, the carbonation products have been shown to precipitate over calcium hydroxide crystal and hydration products, consequently forming a protective coat of calcium carbonate over them which continues to grow thicker as carbonation continues. This hinders with the progress of carbonation of the inner core (Wang et al. (2021)). As per the authors the observed increase in the formation of calcium carbonate with an increase in the concentration of CO_2 gas could be attributed to the fact that as the concentration of CO_2 gas in the carbonation chamber increases, the partial pressure of CO_2 gas increases, thus enhancing the dissolution of CO_2 gas in the water present in the pores. Since the dissolution of CO_2 gas improves, a greater amount is available to react with the hydration products and the γ-C_2S present in mortar thus increasing the amount of carbonation. Further, with the increase in the concentration of CO_2 gas, it is also possible that CO_2 gas penetrates through the dense layer of calcium carbonate formed over calcium hydroxide and other hydration products and hence is able to react with the protected inner core, of calcium hydroxide, other hydration products and γ-C_2S thus increasing their contribution and the amount of calcium carbonate formed after 6 days of carbonation curing.

This study shows that the degree of carbonation increases with an increase in the concentration of CO_2 gas however, to gain a deeper understanding of the kinetics and mechanism involved further investigation is needed. It is important to separate the effect of diffusion and dissolution of CO_2 gas in the pore solution from the effect of CO_2 concentration on the hydration and carbonation reaction kinetics. Further, it is also important to investigate the effect of the concentration of CO_2 gas on the progress of carbonation with time.

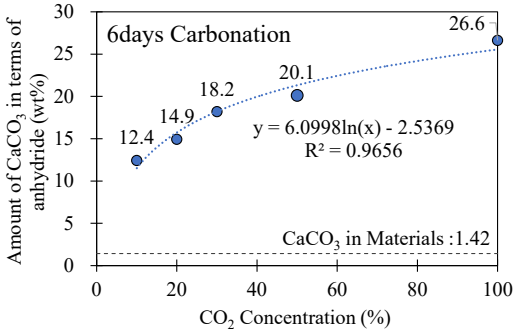


Figure 3 : Relationship between CO_2 concentration and amount of $CaCO_3$ formed

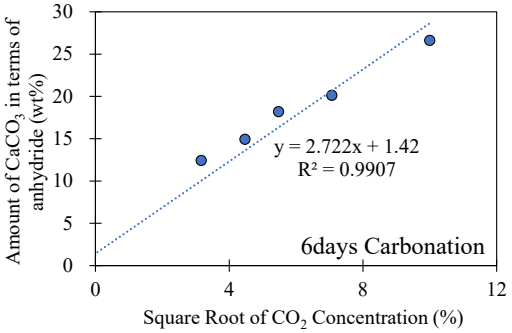


Figure 4 : Effect of CO_2 concentration on $CaCO_3$ content

4. Conclusions

In this study, the effect of the concentration of CO_2 gas on the amount of carbonation of mortar specimens was investigated using TG-DTA. The amount of calcium carbonate tended to increase as the concentration of CO_2 increased. Also, the amount of $CaCO_3$ in the carbonated samples was found to have a linear relationship with the square root of CO_2 concentration.

Acknowledgments

This paper is based on results obtained from a project, JPNP16002, commissioned by the New Energy and Industrial Technology Development Organization (NEDO).

References

Papadakis, V. G., Vayenas, C. G., Fardis, M. N. (1989) "A reaction engineering approach to the problem of concrete carbonation", *AiChE Journal*, 1639-1650 October 1989

Torichigai, T., Yokozeki, K., Yoshioka, I., Mori, T. (2019) "Physical Properties and Manufacturing Method of the Concrete Extremely Reducing CO_2 Emissions by Using C_2S and Carbonation Curing", *International Workshop. CO_2 Storage in Concrete*, 24-25 June 2019, lfsttar, Marne La Vallee, France

Wang, D., Noguchi, T., Nozaki, T., Higo, Y. (2021) "Investigation of the carbonation performance of cement-based materials under high temperatures", *Construction and Building Materials*, 272

Fundamental understanding of carbonation mechanism of aluminosilicate based material: A state-of-the art review

F.Z. Xie, C. Li, Q. Ren, W.B. Gao, Z.W. Jiang*

Key Laboratory of Advanced Civil Engineering Materials of Ministry of Education, School of Materials Science and Engineering, Tongji University, shanghai, China

Email: jzhw@tongji.edu.cn

ABSTRACT

Carbonation and utilization of aluminosilicate based solid waste are foundational to decarbonize cement production by creating a waste-to-value or carbon-to-value economy. Many studies have focused on the influence of different parameters on the CO_2-uptake and strength development during mineral carbonation, whereas the results are difficult to directly comparative analysis and even contradictory from each other. Meanwhile, limited literature review can be found regarding contrastive analysis of different research results according to separate rate controlling step. The objective of this study is to enable a thorough understanding of the acting mechanism for influence factors with respect to different study systems and the interaction of complex parameters from the commonality and individuality viewpoint. The influence of performance controlling factors on carbonation reaction mechanism of silicate material are systematically analyzed and summarized based on rate controlling steps during carbonation reaction process, which are consist of phase boundary controlled stage, product layer CO_2 diffusion controlled stage and CO_2 diffusion and calcium ion dissolution controlled stage. In regard to individual rate controlling step, the mechanism of action for dominant factors are highlighted and expounded. The combination of optimal carbonization stages concentrating on carbonation reaction mechanism is proposed, which is beneficial to flexibly adjustment depending on the target requirement.

KEYWORDS: *carbonation reaction, aluminosilicate based solid waste, controlling factors, carbonation kinetics, carbonation mechanism*

1. Introduction

Nowadays, lots of aluminosilicate based solid waste as industrial by-product not only present low value-added utilization and utilization efficiency, but also result in serious environment pollution via stacking outdoor. The carbonation aluminosilicate based solid waste as a potential way is able to consume a mass of solid waste and immobilize lots of CO_2, which is beneficial to realize a waste-to-value or carbon-to-value economy. The carbonation reaction condition is dynamically changed with the carbonation reaction proceed. Although the influence of different parameters on the carbonation reaction mechanism are mostly studied, the carbonation reaction mechanism for different carbonation processes are not still clearly identified. The research focus on the thorough understanding for carbonation reaction kinetics of aluminosilicate based solid waste in order to optimize the individual rate controlling step.

2. Carbonation kinetics

Aluminosilicate based solid waste are mainly made up of different calcium silicate phases, which consist of tricalcium silicate, β-dicalcium silicate, γ-dicalcium silicate, tricalcium disilicate and monocalcium silicate and so on. The carbonation reaction of different calcium silicate phases with respect to the dispersed particles are divided into two different stages: phase-boundary-controlled stage and product layer CO_2 diffusion-controlled stage (e.g., Ashraf and Olek (2018a)). It is worth noting that based on the dense structure of compact calcium silicates, the third carbonation reaction stage, which is named CO_2 diffusion and calcium ion dissolution-controlled stage, is found, as shown in Fig.1 (e.g., Zhao and Liu (2021)). With respect to three different carbonation stages, the extent of the influence for different factors on the carbonation rate are dynamically variational as the development of carbonation reaction, due to the reaction mechanism of every carbonation stage are apparently distinguish. The controlling factors in regard to different carbonation stages need to be further highlighted in order to the combination of optimal carbonization stages concentrating on the properties of raw material and reaction conditions.

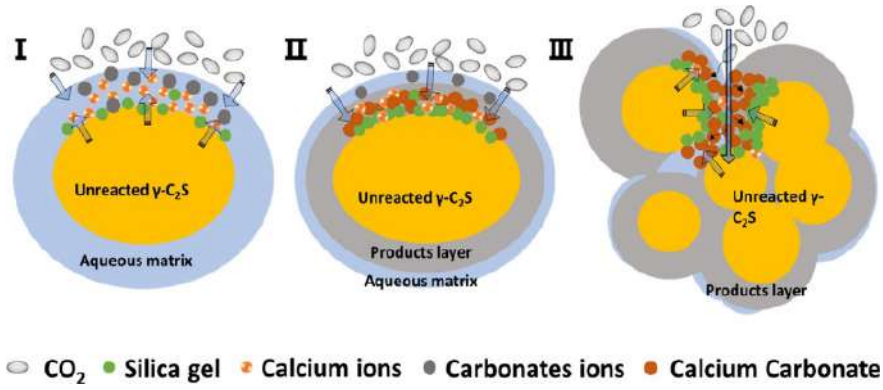


Fig.1 Schematic diagram of the carbonation reaction mechanism

2.1 Phase-boundary-controlled stage

Based on the phase-boundary-controlled stage, the carbonation reaction rate not only depend on the reaction interface of raw material and the nucleation rate, but also principally on the property of the starting calcium silicate phases. The rapid nucleation and precipitation of calcium carbonates are generated, the product layer is gradually formed and tend to more and more densification. On account of significant difference for the chemical composition of calcium silicate phases, the crystallographic structures of different calcium silicate phases are significantly disparate. C_3S and C_2S phases are mainly made up of isolated silicate tetrahedrons, which is assigned to orthosilicate group of minerals. In addition to this, the rankinite phase is mainly composed of sorosilicate groups including isolated double silicate tetrahedra, and wollastonite phase possess lots of inosilicate groups involving silicate tetrahedra of chain structure (e.g., Hansen and Jakobsen (2003), Ashraf and Olek (2018b)). Depending on the form of the different calcium silicate phases, β-C_2S phase possess the maximum carbonation reaction rate constant, followed by C_3S, γ-C_2S, C_3S_2 and CS phases. The carbonation activation energies for different calcium silicate phases are observed to be in the range of 5~35 kJ/mol, which are consistent with the properties of calcium silicate phases (e.g., Ashraf and Olek (2018a)). The carbonation activation energies of hydraulic calcium silicates (i.e., β-C_2S and C_3S) are found to be 7.5 and 5.5 kJ/mol, respectively. However, carbonation activation energies of non-hydraulic calcium silicates (γ-C_2S, C_3S_2, and CS) are in the range of 25–35 kJ/mol. Meanwhile, the nucleation rate of calcium carbonates is largely determined via the property of raw material. Therefore, as for the phase-boundary-controlled stage, the carbonation reaction rate is mainly determined by the properties of the aluminosilicate based solid waste, which are primarily made up of different type and proportion of calcium silicate phases.

2.2 Product layer CO_2 diffusion-controlled stage

With respect to the product layer CO_2 diffusion-controlled stage, the carbonation reaction rate is determined by the type of carbonation product and the CO_2 diffusion. As the phase-boundary-controlled stage over, the diffusion of CO_2 through the product layer become the rate-limiting factor due to the residual space of particles is relatively beneficial to the transmission of CO_2 compared to the product layer. The evolution trend for Ca/O and Ca/Si ratio of the carbonation product were observed based on BSE-EDS analysis with the carbonation reaction proceed. As for γ-C_2S phase, the variation trend for Ca/O ratio of the carbonation product increase from 0.33 to maximum value of 0.5, indicating that the resistance of CO_2 transmission and a large number of dissolution of calcium ions from calcium silicate phases. Meanwhile, the decrease trend for Ca/Si ratio of silica-rich product is also present, which further demonstrate lots of calcium ions dissolution from raw material (e.g., Zhao and Liu (2021)). During the carbonation reaction for different calcium silicate phases based on the same reaction condition, the maximum levels of carbonization products generated are approximate. However, lots of calcium carbonation with various metastable polymorphs including aragonite, vaterite and amorphous calcium carbonate, and the different polymerization degree of Ca-modified silica gel phase are generated, which consist mostly of Q_3 of crosslinked silicate tetrahedrons or hydroxylated surface sites and Q_4 of fully polymerized silicate sites (e.g., Shtepenko and Hills (2006), Chang and Fang (2016)). Therefore, the formation rate of carbonation product, which influence the type of calcium carbonate and density of structure for product layer at the early age, depend on the carbonation reaction rate deciding to the degree of CO_2 diffusion. Carbonation reaction condition with the combination of different influence factors such as temperature, partial pressure, relative humidity and CO_2 concentrations and so on, work together to the formation rate of carbonation product. The carbonation rate increases gradually as the relative humidity (RH) rise from 0 to 60%, however, decreases again with increasing the RH from 60% to 100%, which is attributed to that excessive water block the pores on the surface of solid and limit the penetration of CO_2 to a higher depth (e.g., Mistry and Mehra (2019), Pan and Chen (2015)). Based on the same carbonation reaction conditions, carbonation reaction rate constants of pure calcium silicate phases generally increase with the temperature rise from 35℃ to 60℃, which is found to increase from 0.07 to 0.2 for C_3S phase. CO_2 diffusion coefficient represents the capacity of mass transfer, which directly affects CO_2 dissolution and transport and so on (e.g., Shukla and Ranjith (2010)). The effect of carbonated reaction on CO_2 mass transfer is different with the situations for the CO_2-brine/pure water systems, in which CO_2 diffusion and transport occur faster than reaction. Based on the chemical reactions, the diffusive boundary layer is stabilized and convective mixing is further inhibited (e.g., Ghoshal and Kim (2016)). CO_2 diffusion coefficient of compacted recycled aggregate for carbonated curing 30 days with 53% and 95% RH are about 6.2×10^{-7} m^2/s and 4.5×10^{-7} m^2/s, respectively. When the carbonated curing 90 days, CO_2 diffusion coefficient are respectively 5.7×10^{-7} m^2/s and 7.5×10^{-7} m^2/s (e.g., Hou and Lux (2023), Hou and Mahieux (2021)). CO_2 diffusion coefficients of carbonated discs of hydrated cement paste increase more than ten times when the water/cement ratio is increased from 0.4 to 0.8 (e.g., Houst and Wittmann (1994)). Due to double effects and dynamic change of impact factors as the development of carbonation reaction, based on the regulation and control mechanism of specific products and structure for product layer, carbonation reaction condition is optimization designed during the product layer CO_2 diffusion-controlled stage, which will be beneficial to the CO_2 diffusion and the best development of performance.

2.3 CO_2 diffusion and calcium ion dissolution-controlled stage

The CO_2 diffusion and calcium ion dissolution-controlled stage is determined via both the CO_2 diffusion

and the dissolution of calcium ions. With respect to γ-C_2S phase in the late carbonation stage, the Ca/O ratio of the carbonation product gradually decrease from the maximum value of 0.5 to the steady value of 0.4, and the Ca/Si ratio of silica-rich product also obviously decrease. The results indicate the resistance of between the dissolution and migration of calcium ions from calcium silicate phases and CO_2 diffusion. Meanwhile, the rapid shrinkage of micro-pores leads to the dense structure and decrease the permeation of CO_2, which limit the development of further carbonation reaction. During the CO_2 diffusion and calcium ion dissolution-controlled stage, the variation of calcium ions concentration is observed due to the resistance of the CO_2 diffusion and the dissolution of calcium ions, resulting in that the aragonite replacing to calcite gradually become the dominant crystalline form of calcium carbonation. Therefore, the further carbonation reaction for the third stage should focus on the accelerate dissolution of calcium ions via the combination of influence factors. For example, the addition of organics with polar groups is beneficial to facilitate the dissolution of calcium ions, the higher concentration of calcium ions is in favor of the formation of calcite (e.g., Ashraf and Olek (2018a)). The variation of dominant crystalline forms of calcium carbonate highlight that the dissolution and migration of calcium ions act as an important role in the third stage of carbonation. The effect of CO_2 pressure on the carbonation reaction rate is complex. High CO_2 pressure is beneficial to the dissolution and diffusion of CO_2, however, harmful to the stability of carbonate precipitation and accelerate the plugging of pores on the surface and so on (e.g., Back and Kuehn (2008), Santos and Bouwel (2013)). Therefore, during the CO_2 diffusion and calcium ion dissolution-controlled stage, the carbonation reaction rate depends mainly on the CO_2 diffusion by increasing partial pressure for the third stage and adjusting the evolution of microstructure, and the dissolution and migration of calcium ions by the introduction of polar groups, which will be able to mitigate the transmission obstruction. It is interesting to noted that the compressive strength of carbonated γ-C_2S compacts increase from 85MPa in constant gas pressure of 4 bar to 110MPa based on the stepwise pressurization (rise from 1bar of the early age to 3MPa of 24-72h.

3. Conclusions

The study focuses on the fundamental understanding of carbonation mechanism of aluminosilicate based solid waste including different calcium silicate phases. Based on the carbonation reaction mechanism analysis, the carbonation reaction of different calcium silicate phases are divided into three stages: phase-boundary-controlled stage, product layer CO_2 diffusion-controlled stage, CO_2 diffusion and calcium ion dissolution-controlled stage. The carbonation reaction rate for the first stage depends mostly on the reaction interface and properties of raw material, which should focus on the different type and proportion of calcium silicate phases. With respect to the product layer CO_2 diffusion-controlled stage, the carbonation reaction rate is determined by the type of carbonation product and the CO_2 diffusion, concentrating on that the regulation and control mechanism of specific products and structure for product layer based on the optimal combination of the impact factors. The CO_2 diffusion and calcium ion dissolution-controlled stage is controlled via both the CO_2 diffusion and the dissolution of calcium ions working on the increasing partial pressure and the introduction of polar groups, respectively. The combination of optimal carbonization stages concentrating on the controlling factors in regard to different carbonation stage is proposed.

Acknowledgements

The authors gratefully acknowledge the financial supports provided by National Natural Science Foundation of China (U22B2076, 51878480, 52078369), National Key Research and Development Projects, and the Fundamental Research Funds for the Central Universities.

References

Ashraf, W. and Olek, J. (2018a) "Carbonation activated binders from pure calcium silicates: Reaction kinetics and performance controlling factors", *Cement and Concrete Composites,* 93: 85–98

Ashraf, W. and Olek, J. (2018b) "Elucidating the accelerated carbonation products of calcium silicates using multi-technique approach", *J. CO2 Util.,* 23: 61-74

Back, M. and Kuehn, M. et al. (2008) "Reactivity of alkaline lignite fly ashes towards CO_2 in water", Environ. Sci. Technol. 42 (12): 4520-4526

Chang, J., Fang, Y. and Shang, X. (2016) "The role of β-C_2S and γ-C_2S in carbon capture and strength development", *Mater. Struct.,* 49: 4417–4424

Ghoshal, P. and Kim, M.C. et al. (2016) "Reactive-convective dissolution in a porous medium: The storage of carbon dioxide in saline aquifers", Phys Chem Chem Phys, 19 (1): 644-655

Hansen, M.R., Jakobsen, H.J. and Skibsted, J. (2003) "29Si chemical shift anisotropies in calcium silicates from high-field 29Si MAS NMR spectroscopy", *Inorg. Chem.* 42(7): 2368–2377

Hou, Y. and Lux, J. et al. (2023) "Evolution of microstructure and CO2 diffusion coefficient of compacted recycled aggregates during carbonation investigated by X-ray tomography", Construction and Building Materials, 372 (3): 130715

Hou, Y. and Mahieux, P.Y. et al. (2021) "Carbonation rate of compacted recycled aggregates for sub-base layers of pavement", Constr. Build. Mater., 312: 125420

Houst, Y.F. and Wittmann, F.H. et al. (1994) "Influence of porosity and water content on the diffusivity of CO_2 and O_2 through hydrated cement paste", Cement and Concrete Research, 24 (6): 1165–1176

Mistry, N.B. and Mehra, R.S. et al. (2019) "Towards efficient calcium extraction from steel slag and carbon dioxide utilisation via pressure-swing mineral carbonation", React. Chem. Eng. 4: 52–66

Pan, S.Y. and Chen, Y.H. et al. (2015) "High-gravity carbonation process for enhancing CO_2 fixation and utilization exemplified by the steelmaking industry", Environ. Sci. Technol. 49 (20): 12380–12387

Shtepenko, O., Hills, C., Brough, A. and Thomas, M. (2006) "The effect of carbon dioxide on β-dicalcium silicate and Portland cement", *Chem. Eng. J.* 118(1-2): 107–118

Santos, R.M. and Bouwel, J.V et al. (2013) "Accelerated mineral carbonation of stainless steel slags for CO_2 storage and waste valorization: effect of process parameters on geochemical properties", Int. J. Greenh. Gas Control. 17: 32–45

Shukla, R. and Ranjith, P. et al. (2010) "A review of studies on CO2 sequestration and caprock integrity", Fuel, 89 (10): 2651-2664

Zhao, S.X. and Liu, Z.C. et al. (2021) "Effect of Extended Carbonation Curing on the Properties of γ-C_2S Compacts and Its Implications on the Multi-Step Reaction Mechanism", *ACS Sustainable Chem. Eng.,* 9(19): 6673−6684

The 16th International Congress on the Chemistry of Cement 2023 (ICCC2023)
"Further Reduction of CO_2 -Emissions and Circularity in the Cement and Concrete Industry"
September 18–22, 2023, Bangkok, Thailand

Preservation of α' Dicalcium Silicate (C_2S) under SO_2-Containing Atmosphere

O. Abdalla[1*], C. Rößler[2], M.N. Campbell-Bannerman [3], R. Chaliulina[1], A. Elhoweris [1]

[1] Gulf Organization for Research and Development, Qatar Science and Technology Park, Doha, Qatar

Email: o.abdalla@gord.qa

[2] Finger Institute for Building Materials Science, Bauhaus-University Weimar, Coudraystr. 11, 99421 Weimar, Germany

Email: Christiane.Roessler@uni-weimar.de

[3] School of Engineering, University of Aberdeen, AB24 3UE, United Kingdom

Email: m.campbellbannerman@abdn.ac.uk

ABSTRACT

Mitigating greenhouse gas emissions is one of the main approaches to tackle the current environmental crisis. The decarbonation of the cement industry could significantly lower anthropogenic carbon emissions by limiting the average temperature rise to 2°C. Alternative cement formulations such as calcium sulfoaluminate (C$A) have great potential in partly replacing the current families of cement due to their lower carbon footprint, rapid strength gain, fast curing time, and lower shrinkage. The eco-friendly characteristics of C$A cement are attributed to reduced amounts of limestone used for production and lower synthesis temperatures. The challenge facing the production of C$A cement is mainly its requirement of high amounts of alumina which hinders the economic viability at the commercial scale. Alumina is essential for the formation of the ye'elimite phase which heavily contributes to early-age strength development. A promising technique to improve the process' economics is to reduce the alumina content requirement while preserving the early-age strength. This can be achieved by stabilizing the high temperature α' polymorphs of dicalcium silicate to ambient conditions. A technique was previously developed wherein elemental sulfur is utilized as a source of fuel and mineralogical control factor that provides the sulfur oxide needed to both preserve α' dicalcium silicate and form ye'elimite in the clinker. Synthesis of α'C_2S was carried out here with a focus on Na, K, B, and P as additives under a sulfur-containing atmosphere. The results display the successful stabilization of about 80% α'C_2S upon quantification. Hydration experiments showed that the isothermal heat release of α'C_2S deviates significantly from beta-C_2S. Highest degree of hydration was achieved with the boron stabilized α'C_2S. Interestingly after 6 days of hydration both investigated α'C_2S showed no portlandite formation but only calcium silicate hydrates (C-S-H).

KEYWORDS: *calcium sulfoaluminate (C$A), ye'elimite, alpha prime belite, low carbon cement, SEM-EDX-EBSD*

1. Introduction

Approximately 8% of global carbon dioxide emissions are emitted during the production of cement (Pearce, 2021). Various techniques, such as the utilization of alternative fuels and alternative cement formulations, have been explored to decrease these emissions. Calcium sulfoaluminate (C$A) cements are ye'elimite rich formulations that are produced at low temperatures and provide a reduction of raw material derived carbon emissions up to 35%-40% (Tao et al. 2023). However, the economic viability of these formulations suffers due to the increased Al_2O_3 content required in its raw mix designs. Replacing a portion of the raw mix Al_2O_3 with SiO_2 (at conventional C$A production temperatures) leads to a product with increased belite (C_2S) content and a consequently reduced early age strength. The stabilization of high temperature polymorphs of dicalcium silicate could serve as a strategy to compensate for the aforementioned loss in mechanical performance. The alpha prime (α') group of polymorphs are highly reactive when hydrated and are the most effective hydraulic forms of C_2S when preserved under normal conditions (Ghosh et al. 1979). Cuesta et al. reported the stabilization of α'C_2S through doping mechanism of B and Na/B. When boron was added, a tetrahedral borate anion replaced silicon, while a triangular planar anion replaced silicon in the case of sodium/boron doping, resulting in a new stabilized α'-C_2S structure with ratios of α'-$Ca_{1.85}Na_{0.15}(SiO_4)_{0.85}(BO3)_{0.15}$ (Cuesta et al. 2012). In a recently developed clinker production technique, a C$A cement was produced via the combustion of sulfurous fuels (Galan et al. 2017; Al Horr, 2017) to provide both the sulfate precursor (via gas-solid sequestration) and a contribution towards heat needed for the C$A cement production process. Elhoweris et al. investigated the effect of this technique on the preservation of α' dicalcium silicate in C$A clinker at laboratory scale. The study demonstrated that, when using an SO_2 containing atmosphere and alkali dopants, α' C_2S containing C$A clinkers could be effectively preserved to ambient conditions by air cooled quenching (Elhoweris, 2020).

2. Methodology

2.1 C_2S Synthesis

Various batches of C_2S were synthesised using stoichiometric amounts of calcium carbonate ($CaCO_3$) and silicon dioxide (SiO_2) by incorporating potassium carbonate (K_2CO_3) and sodium carbonate (Na_2CO_3) i.e., K and Na as alkali additives and sodium tetraborate decahydrate ($Na_2[B_4O_5(OH)_4] \cdot 8H_2O$) and calcium phosphate ($Ca_3(PO_4)_2$) i.e. B and P with concentration ranging from (1 wt.% to 4 wt.%). Results shown here for samples PNa44 and BK11 (numbers indicate weight percentage of doping agent, i.e., PNa 44 is a C_2S synthesised with 4 wt.-% P and 4 wt.-% Na respectively). The C_2S were fired at 1300°C for 5 hrs under SO_2 containing conditions in a bottom loading furnace with gas mixture %vol of 0.62, 77.44, and 21.94 for SO_2, nitrogen and air respectively followed by a rapid cooling step. Hydration experiments are compared with standard beta-C_2S (obtained from Vush, Czech Republic). All samples were ground to a similar specific surface area of ~ 500 m^2/kg ± 20 m^2/kg.

2.2 Characterization of Synthesized C_2S and Hydration Experiments

Isothermal heat release of C_2S was measured over a period of 142 h at w/c of 0.5. Hydration was stopped by immersing samples in isopropanol for 2h. For SEM analysis, samples were embedded in epoxy resins and polished according to standard protocols. SEM and back scattered electron (BSE) imaging combined with energy dispersive X-Ray spectroscopy (EDX) investigations were carried out in high vacuum. For XRD, the samples were ground, and measurements were performed using Cu radiation. Some of the XRD samples were also heated from room temperature to 1000°C and measured for heat flow and weight loss.

3. Results and Discussions

3.1 Characterization of Synthesized Clinkers

Amongst all the synthesised samples of different binary additive combinations, the BK11 and PNa44 showed the highest percentages of α' C_2S preservation within the clinker sample, e.g., about 80% and 75%

respectively as determined by XRD-Rietveld analysis. Other silicates phases that were present included beta C_2S, NCS and C_3S_2.

3.2 Hydration of the Synthesized Clinkers

Results in Figure 1 show the heat flow of the selected C_2S hydrated using w/c of 0.5 during the first 142 hrs. The beta-C_2S shows the typical heat release curve, characterised by an induction, acceleration, and deceleration period. BK11 and PNa44 samples show two main hydration peaks, whereby for the BK11, first hydration maximum occurs at the earliest stage and the second maximum is most pronounced. The highest total heat observed, after 140 h of hydration, was that of sample BK11 at 64.38 J/g.

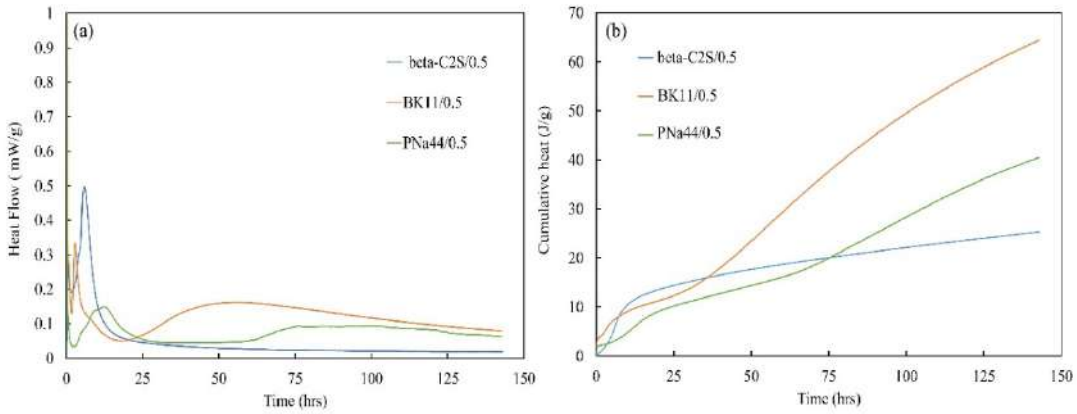


Figure 1: a) Isothermal heat release rate and b) cumulative heat release of C_2S pastes (w/c 0.50)

The microstructure of 6-days hydrated samples were evaluated by BSE imaging and EDX mapping analysis as shown in Figure 2. Results show that, after six days of hydration, the anhydrous material were predominately present, with only a minor amount of hydration products observed. Surprisingly, hardly any portlandite was identified, by BSE images and EDX mapping data, in BK11 and PNa44. Only the beta C_2S could be observed to have the common phase assemblage of hydrated belite, which is portlandite and C-S-H. The amount and thickness of C-S-H phases is largest in BK11 compared to PNa44 and beta-C_2S. The fewest amount of hydrates was seen in PNa44, which, after 6 days, was in a weakly solidified state. To confirm findings from the SEM-EDX analyses, DTA/TG analysis of 6 days hydrated clinkers were performed, with the corresponding mass loss data presented in Figure 3. The results confirmed that in PNa44 and BK11 no portlandite had formed, due to modifications in the reaction kinetics upon the addition of dopants. The total mass loss after 6 days of hydration is highest for BK11 (11.99 %) and lowest for beta C_2S (4.47 %), i.e., confirming SEM results.

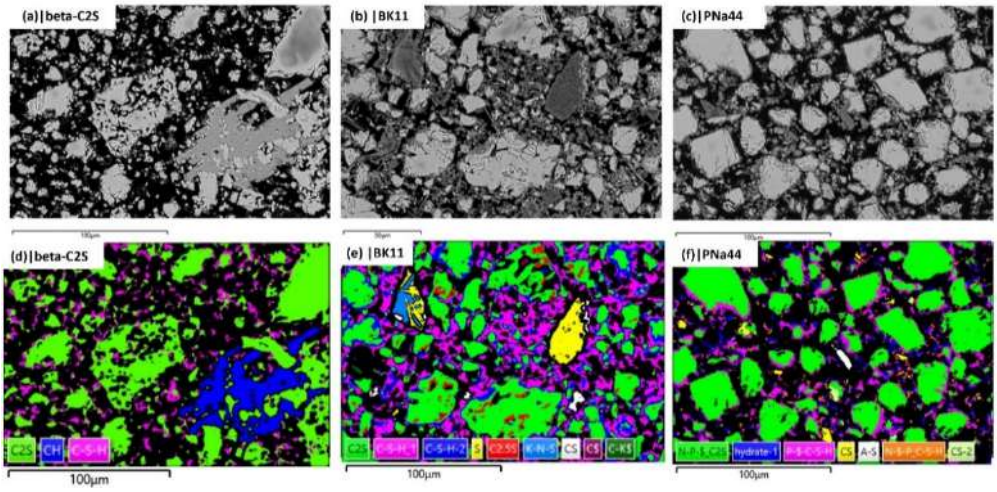


Figure 2: SEM-BSE images (a, b, c) and phase maps (d, e, f) derived from EDX analysis of 6 days hydrated C_2S, a/d) beta-C_2S, b/e) BK11 and c/f) PNa44, black color= epoxy/pores

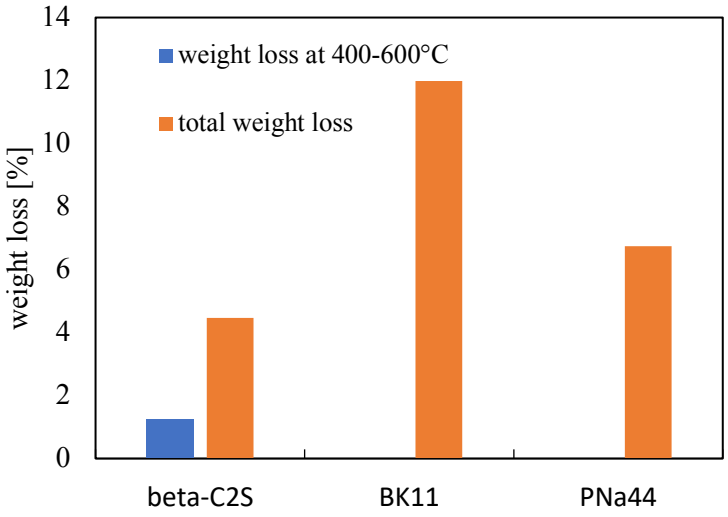


Figure 3: Weight loss (TG) after of 6 days hydration.

4. Conclusions

In conclusion, alpha prime C_2S was successfully synthesized at low temperature with the aid of alkali, boron and phosphorous based additives, rapid cooling and SO_2 containing atmosphere. The hydration studies also revealed that, the heat release of alpha prime C_2S differs significantly from regular beta-C_2S in that the main hydration is split into two peaks. This might have been caused by the fact that the samples contain alpha C_2S but also beta C_2S and some rankinite, more investigations are needed. After 6 days hydration, the boron - potassium stabilised C_2S showed the highest degree of reaction compared to beta-C_2S and the PNa44 sample. In both alpha prime C_2S containing samples, no portlandite formed after 6 days of hydration. First insights by SEM-EDX analysis (results not shown here) indicate that the C/S ratio of the C-S-H phases in BK11 is around 2, which could explain the absence of portlandite. If the reason for this is the stabilisation under SO_2 atmosphere will be revealed during further studies with samples synthesis at ambient conditions.

References

Cuesta, Ana, Enrique R. Losilla, Miguel A.G. Aranda, Jesús Sanz, and Ángeles G. De La Torre. 2012. "Reactive Belite Stabilization Mechanisms by Boron-Bearing Dopants." *Cement and Concrete Research* 42 (4). Elsevier Ltd: 598–606.

Elhoweris, Ammar, Isabel Galan, and Fredrik P. Glasser. 2020. "Stabilisation of α ′ Dicalcium Silicate in Calcium Sulfoaluminate Clinker." *Advances in Cement Research* 32 (3): 112–24.

Fred Pearce. 2021. "Can the World's Most Polluting Heavy Industries Decarbonize?" *Yale School of Environment*.https://e360.yale.edu/features/can-the-worlds-most-polluting-heavy-industries-decarbonize.

Galan, Isabel, Ammar Elhoweris, Theodore Hanein, Marcus N Bannerman, and Fredrik P Glasser. 2017. "Advances in Clinkering Technology of Calcium Sulfoaluminate Cement." *Advances in Cement Research* 29 (10): 405–17.

Ghosh, Surendra N., P. Bhaskara Rao, A. K. Paul, and K. Raina. 1979. "The Chemistry of Dicalcium Silicate Mineral." *Journal of Materials Science* 14 (7): 1554–66.

Horr, Yousef Al, Ammar Elhoweris, and Esam Elsarrag. 2017. "The Development of a Novel Process for the Production of Calcium Sulfoaluminate." *International Journal of Sustainable Built Environment* 6 (2). The Gulf Organisation for Research and Development: 734–41.

Tao, Yaxin, A V Rahul, Manu K Mohan, Geert De Schutter, and Kim Van Tittelboom. 2023. "Recent Progress and Technical Challenges in Using Calcium Sulfoaluminate (CSA) Cement." *Cement and Concrete Composites* 137: 104908.

The 16th International Congress on the Chemistry of Cement 2023 (ICCC2023)
"Further Reduction of CO_2 -Emissions and Circularity in the Cement and Concrete Industry"
September 18–22, 2023, Bangkok, Thailand

Chloride Diffusion and Migration into Concrete Made with Ternary Cements (Clinker, Blast-furnace Slag and Coal Fly Ash)

M.A. Sanjuán[1*], R.A. Rivera[2], D. A. Martín [3], and E. Estévez[2]

[1] *The Spanish Institute of Cement and its Applications (IECA) and Department of Science and Technology of Building Materials, Civil Engineering School, Technical University of Madrid, 28040 Madrid, Spain*
Email: masanjuan@ieca.es
[2] *Department of Cement Chemical Testing, LOEMCO, Technical University of Madrid (UPM), 28906 Madrid, Spain*
Email: rosa.rcornelio@alumnos.upm.es, eestevez@loemco.com
[3] *Mine and Energy Engineering School, Technical University of Madrid (UPM), 28003 Madrid, Spain*
Email: domingoalfonso.martin@upm.es

ABSTRACT

Cement manufacturing processes are associated with emissions of large amounts of carbon dioxide formed mainly by the clinker burning process. This is a serious global climate change issue since the increase in carbon dioxide concentrations in the atmosphere has direct impacts on global warming. Consequently, utilization of blended Portland cements with high amount of additions can be the main lever to reduce the impact of its activity on the environment. Ternary Portland cements with a high content of cement constituents different from clinker can provide some climate change advantages. In this paper, ternary Portland cements incorporate different contents of coal fly ash (VA), ground granulated blast-furnace slag (S), and clinker (K). Cements made with S or VA have good pozzolanic characteristics improving both the mechanical strength and durability at later ages. Accordingly, it is worth to conduct research of chloride ions diffusion into concrete made with ternary Portland cements incorporating VA and S, which is an important consideration in the concrete mix design. Chloride ion ingress into concrete and the resulting damage, i.e., cracking and spalling due to the steel reinforcement corrosion is a major concern to the durability and service-life of reinforced concrete structures. Therefore, this paper carried out rapid chloride migration test according to NT BUILD 492 to determine the chloride migration coefficient from non-steady-state migration experiments. Unfortunately, this method is unable to provide information about the time, after which the critical chloride ions concentration is reached at the steel reinforcement surface. Consequently, the chloride ions diffusion coefficient was also assessed and compared to the migration coefficient. It was calculated following the NT BUILD 443 standard, whose main drawback is the testing duration. Ternary cements made with S and VA exhibited lower chloride diffusion coefficients than concrete made without additions.

KEYWORDS: *Ternary cements, chloride diffusion, coal fly ash, granulated blast-furnace slag*

1. Introduction

With the rapid growth of population and cities, the demand for Portland cement has increased considerably. This phenomenon is especially damaging as it can increase the risk of more severe climate change impacts. Currently, Portland cement production accounts for approximately 7.4% of global anthropogenic carbon dioxide emissions (2.9 Gtons in 2016) (Sanjuán et al. 2020a). Therefore, it is the second largest emitting production sector after the iron and steel sector. However, considering only carbon dioxide emissions from Portland cement manufacturing is insufficient to establish a complete carbon footprint since concrete uptake carbon dioxide through the process of mortar and concrete carbonation. Accordingly, this process could be a carbon sink in the life cycle inventory of concrete.

One way to lower carbon dioxide emissions in the cement manufacturing sector is to reduce the amount of clinker in the Portland cement by using additions, which are natural or industrially produced materials (Sanjuán et al. 2020b). Industrial wastes such as coal fly ash (VA) and ground granulated blast-furnace slag (S) have recently gained relevance as durable, as well as sustainable cement constituents for their environmental and social benefits (Rivera et al. 2020). There is, therefore, reason to conclude that the final properties of ternary systems are achieved as result of the individual characteristics combination of their constituents and synergy (Rivera et al. 2021).

2. Experimental

2.1. Materials

Laboratory ternary cements were manufactured by blending a CEM I 42.5 R Portland cement according to EN 197-1 (Sanjuán and Argiz, 2012) supplied by Holcim, Spain, with coal siliceous fly ash (VA) and ground granulated blast-furnace slag (S) provided by Cementos Tudela Veguín, S. A., Spain. Table 1 shows the chemical properties determined following the EN 196-2 (2014). The granulated blast-furnace slag was ground at two fineness of 3489 cm^2/g (SA) and 4630 cm^2/g (SB) for concrete A and B, respectively. Therefore, SA and SB have the same chemical composition.

Table 1. Chemical composition of CEM I 42.5 R, SA, SB, and VA (%).

Constituent	SiO_2	Al_2O_3	Fe_2O_3	CaO	MgO	SO_3	Na_2O	K_2O	LOI	IR [1]	Cl^-
CEM I 42.5 R	20.51	4.30	3.01	60.38	3.61	3.14	0.16	0.81	2.78	1.44	0.05
SA & SB	35.96	10.61	0.40	42.89	7.10	2.02	0.30	0.46	0.00	–	–
VA	53.79	19.54	10.20	4.44	1.83	0.84	2.03	1.83	1.73	17.41	–

[1] Insoluble residue measured by the Na_2CO_3 method (EN 196-2).

2.2. Cement and Concrete Mix Design

Four ternary cements were made for this study by uniting all the cement constituents: CEM I 42.5 R, coal fly ash (VA) and ground granulated blast-furnace slag (SA and SB), and two concrete qualities were manufactured (Table 2) to evaluate the chloride resistance performance of the four ternary cements.

Table 2. Cement and concrete mix design.

Code	Cement (%)	SA/SB (%)	VA (%)	Slag—Fineness (cm^2/g)
CEM I	100	0	0	–
SA25VA25	50	25	25	3489
SA40VA25	35	40	25	3489
SB25VA25	50	25	25	4630
SB40VA25	35	40	25	4630

Concrete mix design	Cement	sand	gravel	water	additive
A (kg/m^3)	250	880	1100	172	5.0
B (kg/m^3)	350	840	1100	172	5.0

2.4. Methods

Concrete cylindrical specimens (Ø15 × 30 cm) made according to EN 12390-2 (2019) were cured under water and tested for compressive strength at 28 and 90 days according to EN 12390-3 (2019).
Chloride diffusion coefficient was determined following the procedure defined in NT BUILD 443 standard (1995). Four concrete cylindrical specimens of Ø100 mm × 200 mm were made for each type of cement and concrete. Two concrete slices of 100±1 mm thick were cut from each Ø100 mm × 200 mm sample. The non-steady-state chloride migration coefficient was determined by using the rapid chloride migration (RCM) test defined in NT BUILD 492 (1999).

3. Results and discussion

3.1. Compressive strength

Compressive strength results at 28- and 90-days of concretes A and B are shown in Figure 1. The minimum compressive strength (f_{ck}) for C30/37 concrete at 28-days is 30 MPa and 45 MPa for C45/55 concrete (EN 206, 2016). The fineness effect is more evident in concrete B than in concrete A.

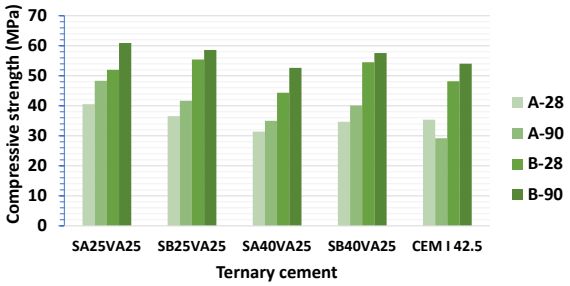


Figure 1. Compressive strength of concretes A and B, at 28-days and 90-days.

SA25VA25 and SB25VA25 cements, used in A and B concretes, increased the compressive strength at 28 and 90 days in comparison with CEM I concrete. This elemental fact suggests that a substantial synergic effect of both the ground granulated blast-furnace slag and coal fly ash has been developed in the system (Rivera et al. 2020). Furthermore, the finer the blast-furnace slag (concrete A), the higher enhancement of compressive strength is.

3.2. Chloride Diffusion Coefficient

Figure 2 shows the effective chloride diffusion coefficient, D_{eff}, after 90 days of testing. The mechanical strength studies suggested that concrete B could present a lower chloride ingress resistance than concretes A. This was confirmed by the natural chloride diffusion coefficients obtained for concrete A and B made with CEM I (17.3×10^{-12} m^2/s and 8.99×10^{-12} m^2/s, respectively). Ternary cements in concrete B presented quite similar coefficients (2.89×10^{-12} m^2/s – 3.36×10^{-12} m^2/s), whereas a broader range of coefficients was found in concrete A made with coal fly ash and ground granulated blast-furnace slag (4.98×10^{-12} m^2/s – 7.64×10^{-12} m^2/s). In view of these findings, this increase in chloride ingress resistance would be due to the concrete mix design more than to the type of cement. The effective chloride diffusion coefficient, D_{eff}, in concrete A made with SA25VA25, is by far the greatest. An atypical factor could have affected this result. Using incorrect quantities of water and cement (very high water/cement ratio = 0.69), often results in sub-par performance. By contrast, the same cement in concrete B (water/cement ratio = 0.49) leads to similar values than the rest of the ternary cements.

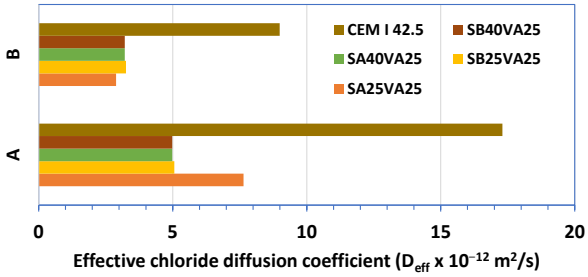


Figure 2. Effective chloride diffusion coefficient ($D_{eff} \times 10^{-12}$ m^2/s).

3.3. Non-steady-state Chloride Migration Coefficient of Concrete

Concrete B made with SA40VA25 ternary cement presented the lowest chloride migration coefficient ($0.53 \cdot 10^{-12}$ m^2/s) and concrete A made with CEM I exhibited the highest chloride migration coefficient ($2.97 \cdot 10^{-12}$ m^2/s) (Figure 3). Type A concrete mixes (40% of slag and 25% of fly ash) showed a resistance to chloride ingress enhancement (chloride diffusion and migration coefficients are $2.89 \cdot 10^{-12}$ m^2/s and

$0.53 \cdot 10^{-12}$ m^2/s, respectively). Summing up, this very good chloride diffusion resistance may be attributed to the combined effect of ground granulated blast-furnace slag and coal fly ash. Similar conclusions have been reported with cements containing 10% of silica fume and 20% of coal fly ash (Hassan et al. 2022). D_{nssm} in concrete A, made with SA25VA25, is lower than is the case for the SB25VA25, but in concrete B the reverse obtains. This again confirms the peculiar performance of concrete A made with SA25VA25.

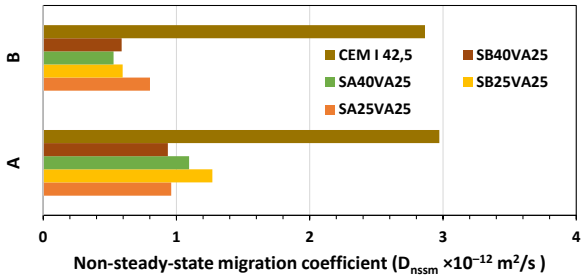


Figure 3. Non-steady-state migration coefficient (D_{nssm} $\times 10^{-12}$ m^2/s).

Chloride migration coefficients were lower than the chloride diffusion ones. However, the opposite outcome has been reported in the literature (Frederiksen et al. 1997). Argiz et al. (2018) and Pontes et al. (2021) found good correlations between the effective chloride diffusion and chloride migration tests.

4. Conclusions

There was a significant difference between the values of the diffusion (NT BUILD 443) and migration (NT BUILD 492) coefficient, which was between 3 and 8 times lower the migration coefficient than the diffusion one. Overall, the rapid chloride migration (RCM) test is a reasonable indicator of the chloride ingress resistance of concretes, having been able to distinguish concrete produced with different types of cements. Nevertheless, we can only compare protective properties, related to the chloride penetration resistance of concrete. Thus, it cannot be used to estimate the service life of reinforced concretes. In view of these findings, this increase in chloride ingress resistance would be due to the concrete mix design more than to the type of cement. Nevertheless, it can be considered that ternary-cement-concretes are very suitable to produce concretes exposed to the corrosion induced by chlorides exposure classes.

References

Argiz, C., Moragues, A. and Menéndez, E. (2018) "Use of ground coal bottom ash as cement constituent in concretes exposed to chloride environments", *J. Clean. Prod.*, 170: 25–33. https://doi.org/10.1016/j.jclepro.2017.09.117

Hassan, M., Elahi, A., Asad, M. (2022) "Performance of Fibre Reinforced Self Compacting Concrete against Chloride Attack", *Eng. Proc.,* 22: 5. https://doi.org/10.3390/engproc2022022005

NT BUILD 443 (1995). Concrete, hardened: Accelerated chloride penetration. Nordtest: DK-2630 Taastrup, Denmark, 1995.

NT BUILD 492 (1999). Concrete, mortar and cement-based repair materials, chloride migration coefficient from non-steady-state migration experiments. Nordtest: DK-2630 Taastrup, Denmark, 1999.

Pontes, J., Bogas, J.A., Real, S. and Silva, A. (2021) "The Rapid Chloride Migration Test in Assessing the Chloride Penetration Resistance of Normal and Lightweight Concrete", *Appl. Sci.*, 11: 7251. https://doi.org/10.3390/app11167251

Rivera, R.A., Sanjuán, M.Á. and Martín, D.A. (2020) "Granulated Blast-Furnace Slag and Coal Fly Ash Ternary Portland Cements Optimization", *Sustainability*, 12: 5783. https://doi.org/10.3390/su12145783

Rivera, R.A., Sanjuán, M.Á., Martín, D.A. and Costafreda, J.L. (2021) "Performance of Ground Granulated Blast-Furnace Slag and Coal Fly Ash Ternary Portland Cements Exposed to Natural Carbonation", *Materials*, 14: 3239. https://doi.org/10.3390/ma14123239

Sanjuán, M.A. and Argiz, C. (2012) "The new European standard on common cements specifications EN 197-1:2011", *Mater. Constr.*, 62: 425–430. https://doi.org/10.3989/mc.2012.07711

Sanjuán, M.Á., Andrade, C., Mora, P. and Zaragoza, A. (2020a) "Carbon Dioxide Uptake by Cement-Based Materials: A Spanish Case Study", *Appl. Sci.,* 10: 339. https://doi.org/10.3390/app10010339

Sanjuán, M.A., Argiz, C., Mora, P. and Zaragoza, A. (2020b) "Carbon Dioxide Uptake in the Roadmap 2050 of the Spanish Cement Industry", *Energies,* 13: 3452. https://doi.org/10.3390/en13133452

The 16th International Congress on the Chemistry of Cement 2023 (ICCC2023)
"Further Reduction of CO_2 -Emissions and Circularity in the Cement and Concrete Industry"
September 18–22, 2023, Bangkok, Thailand

The study of relationship between capability of CO_2 absorption and strength and pore structure using blast furnace slag cement

E. Ishikawa[1*], Y. Nishioka[2], and T. Iyoda[3]

[1] *Shibaura Institute of Technology, Tokyo, Japan*
Email: ishikawa.erika.t3@sic.shibaura-it.ac.jp
[2] *Takenaka Corporation, Chiba, Japan*
Email: nishioka.yukiko@takenaka.co.jp
[3] *Shibaura Institute of Technology, Tokyo, Japan*
Email: iyoda@shibaura-it.ac.jp

ABSTRACT

Cement that is main component of concrete is one of the highest CO_2 emission materials, on the other hands, it can react with CO_2 and absorb it after hydration. Therefore, it is one of the carbon neutral methods for concrete to reduce amount of cement, and adsorb more CO_2 than emission from manufacturing process. This study aims at setting CO_2 emission from concrete life cycle as net zero by carbonation and putting into practical application. And thus, we evaluated the relationship between CO_2 balance, compressive strength and pore structure using different blast furnace slag's replacement ratio and fineness powder. The result showed that the compressive strength of mortar which is high content of blast furnace slag was down by carbonation. In addition, maximum capability of CO_2 absorption correlate with CaO content form using material, on the other hand, to use higher content of Portland cement made carbonation depth less. We also examined admixture combination to keep out compressive strength down by carbonation and get CO_2 balance using not only blast furnace slag but also particular admixture based γ-C2S which can react with CO_2 and then it made compressive strength increased. The result showed that using γ-C2S with carbonation didn't occur compressive strength down, whereas carbonation depth is less than without γ-C2S.

KEYWORDS: *blast furnace slag, compressive strength, pore structure, CO_2 balance*

1. Introduction

In recent years, it is pressing need to reduce emission of CO_2 that is a factor in global warming, and all industries are required to make the transition to decarbonized society. In the Japanese construction industry, concrete using highly substituted cement admixtures such as ECM cement is being developed to reduce the use of clinker, which emits a large amount of CO_2 during production. On the other hand, since the main component of concrete is hydrates with calcium like $Ca(OH)_2$, it is possible to absorb a large amount of CO_2 by carbonation. Therefore, combining those methods is expected to lead to CO_2 balance. However, depending on the mix proportion of admixture, it is difficult to organize the CO_2 balance simply by the substitution ratio because the amount of calcium that absorb CO_2 decreases, and the carbonation rate is different. In addition, there is little knowledge about effects of carbonation on strength and porosity using admixtures.
In this study, we focused on blast furnace slag fine powder (GGBS), which can be replaced with a large amount of cement. we evaluated the relationship between CO_2 absorption, compressive strength and pore structure using different GGBS replacement ratio and fineness powder. We also examined admixture combination to keep out compressive strength down by carbonation and get CO_2 balance using not only GGBS but also particular admixture based γ-C2S which can react with CO_2 and then it made compressive strength increased.

2. Materials and Methods

2.1 Materials and Mix Proportion of Mortar

Table1 shows the mix proportion of mortar. In this study, 3 types of powder were mixed in accordance with each mix proportion. Ordinary Portland cement with 2% SO_3 is replaced by GGBS which is added anhydrous gypsum as 4 % SO_3 contained in GGBS. In addition, mix proportion using γ-C2S were added it 20% as powder substitution. We use LEAF (Denka Co., Japan) as γ-C2S. The mix proportion was set at a constant water-cement ratio of 50% and powder: fine aggregate ratio was set at 1:3. We mixed using mortar mixer, and cast it into specimens of 40×40×160mm.

Table1 Mix Proportion of Mortar

Symbol	W/P [%]	P:S	GGBS		Binder ratio [weight %]			CO_2 emission of binder [g/kg]
			Replacement [%]	fineness [cm^2/g]	OPC	GGBS	γ-C2S	
N	50	1:3	0	-	100	0	0	764
BA			30	4000	70	30	0	543
BB			50		50	50	0	395
BC			70	3000, 4000, 8000	30	70	0	247
N･γ			0	-	80	-	20	643
BA･γ			30	4000	56	24	20	466
BB･γ			50		40	40	20	348
BC･γ			70	3000, 4000, 8000	24	56	20	230

2.2 Curing condition

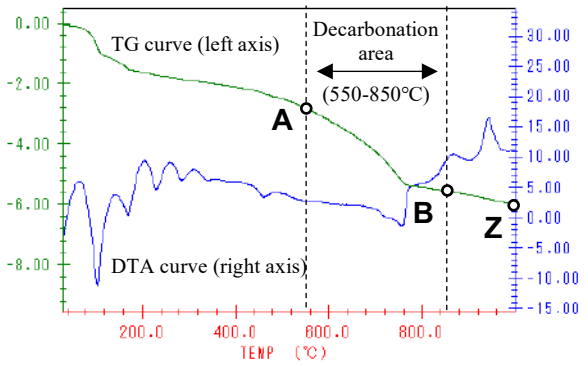
After casting the mortar, the specimens were demolded at the age of 2 days and were cured in 3 types of environment; carbonation (20℃, 60% RH, CO_2 concentration was 5%), water curing (20℃, 60% RH), air curing (20℃, 60% RH, CO_2 concentration was 0.05%) for 7, 28, and 56 days.

2.3 Testing methods

After curing, flexural strength and compressive strength test was carried out according to JIS R 5201. Also, carbonation depth was measured by spraying with a 1% solution of phenolphthalein at the broken cross-section between flexural strength test and compressive strength test. In addition, we measured pore amount on BA, BB, and BC which age was 56 days, because they weren't coloured all area by phenolphthalein sprayed. As a sample, we used one of the pieces after measuring carbonation depth, which were cut parallel to the cross section by wet cutter. CO_2 absorption was also measured in some sample.

2.3.1 Measuring amount of CO_2 absorption

The CO_2 absorption was measured by differential thermos-gravimetric analysis (TG-DTA) date using carbonation area that didn't colored by phenolphthalein. The age of all sample were 56 days. All of samples were granulated by hammer and preserved in acetone for 4 hours and after that dry by a vacuum desiccator to stop hydration. TG-DTA was performed from room temperature to 1000℃ at a heating rate of 20℃/min. under nitrogen. Figure1 shows how to calculate the amount of CO_2 absorption. The decarbonation ratio was determined from the weight loss at 550 to 850℃ because the inflection point of the DTA curve wasn't clear. And all so, the amount of CO_2 absorption was calculated from the difference in the decarbonation ratio between before and after of carbonation.



Sample weight (befor TG-DTA) : X (mg)
Sample weight (after TG-DTA) : X-Z (mg)
Binder percent in them : 1/4
Decarbonation ratio : C=(B-A)/(X-Z)*4 (binder %)
CO_2 absorption(% in binder)
= after carbonation «C» - before carbonation «C»

Figure 1 method of calculated amount of CO_2 absorption

2.3.2 Porosity test

The samples were saturated with water by a vacuum desiccator. After measuring the saturated weight and the weight in water, the samples were left to dry at 40℃ until their weights became constant, and the weight in an absolutely dry state was then measured. Porosity was calculated by Archimedes method.

3. Results and discussion

3.1 Carbonation depth and amount of CO_2 absorption

Figure 2 shows the carbonation depth. Regardless of using γ-C2S or not, BB and BC weren't colored all area by phenolphthalein sprayed at 28days. Also, BA weren't colored all area at 56 days. Focusing on the effect of using γ-C2S when the all area were not carbonated, low GGBS replacement rates show that carbonation depth of using γ-C2S resulted deeper than without γ-C2S. On the other hand, high GGBS replacement rates show that carbonation depth of using γ-C2S resulted smaller than without γ-C2S.
Figure 3 shows the relationship between the percentage of CaO in the binder and the amount of CO_2 absorption in carbonation area. The red dotted line is maximum capability of CO_2 absorption that caluculated from the amount of CaO. The case of using GGBS show correlation, and the lower GGBS replacement rates is closer to the maximum. But N was out of line regardless of using γ-C2S or not. Therefor, the using well combination of admixtures not only reduce CO_2 emissions, but also be able to made the high potential of CO_2 absorption. Eventually, it will be expected to lead the CO_2 balance.

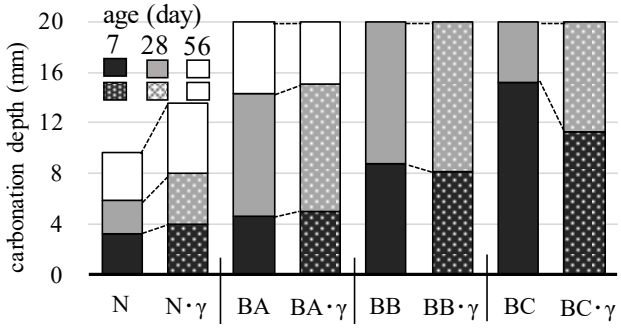


Figure 2 carbonation depth

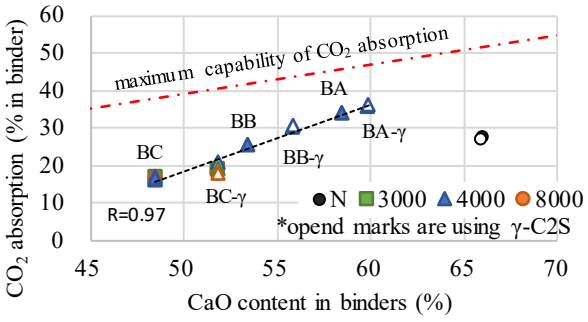


Figure 3 relationship between CaO and CO_2

3.2 Carbonation and compressive strength

Figure 4 shows the relationship between GGBS replacement ratio and compressive strength of GGBS with Blaine's fineness of 4000 cm^2/g at 56 days of age. The result without γ-C2S, the strength of N, BA, and BB increased in the order of water curing, carbonation, and air curing. But for BC with high GGBS replacement

ratio, carbonation resulted in lower strength development than the other curing conditions. On the other hand, the results of using γ-C2S, N, BA, and BB showed the highest strength development in carbonation, and the strength of BC was comparable to that in water curing. Figure 5 shows the results of BC using different fineness of GGBS. Using higher fineness GGBS resulted higher strength, but similar trends were observed in the difference of curing methods.

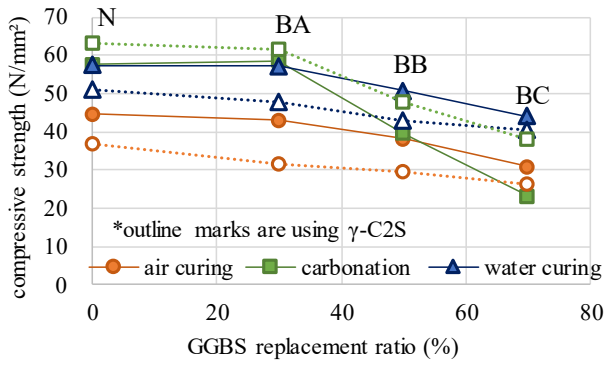


Figure 4 strength and GGBS replacement ratio

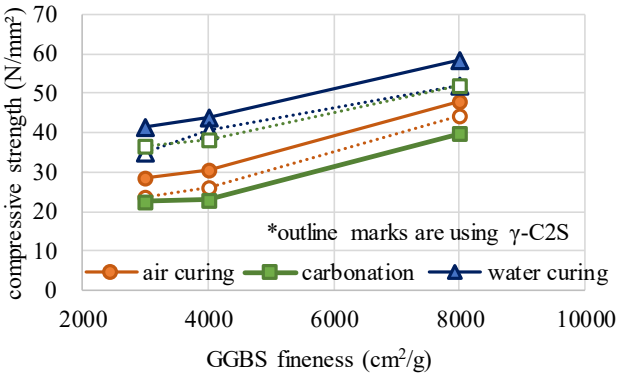


Figure 5 strength and GGBS fineness

3.3 Carbonation and pore structure

Figure 6 shows the porosity of BC at 56 days. The case of without γ-C2S, the total porosity with carbonation was larger than with water curing. But using γ-C2S, it was had the opposite result.
Figure 7 shows the moisture deviation rate in pore from water discharge condition to absolutely dry at 40°C. Regardless of using γ-C2S or not, the samples with carbonation showed faster rate of water deviation than water curing in the early time of drying. Mizuno et al. reported that concrete with GGBS has a complex pore structure, but carbonation of C-S-H caused pore coarsening and changing to continuous pore structure. We assume that BC with carbonation increased the speed of water deviation by changing to continuous pore structure. However, $CaCO_3$ which produced by carbonation of γ-C2S filled in some of pore and also increased strength.

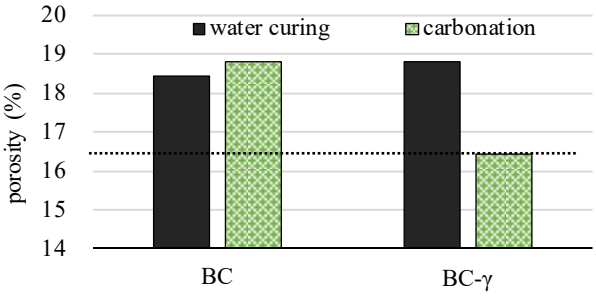


Figure 6 total porosity of B70

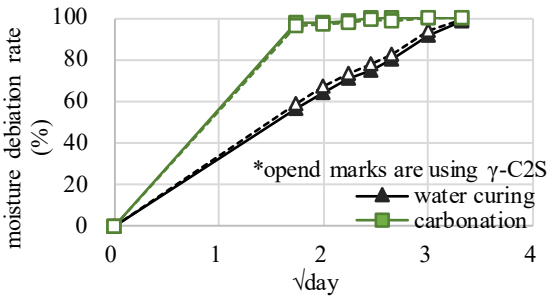


Figure 7 moisture deviation rate in pore

4. Conclusions

Mortars with high GGBS replacement with carbonation showed an increase in total porosity and also tendency for compressive strength to be less pronounced than water curing. However, the combination of the addition of γ-C2S and carbonation showed a trend toward improvement in both of them.

Acknowledgements

This paper is based on results of "Development of Materials, Manufacturing Methods and Quality Control System on Innovative Carbon Negative Concrete", JPNP21014, commissioned by the New Energy and Industrial Technology Development Organization (NEDO).

References

Kenzo, W., Kosuke, Y., Noboru S., and Etsuo, S. (2011) “The mechanism of pore reduction due to carbonation reaction of γ-2CaO·SiO2 and pozzolanic admixtures with low-heat-Portland-cement”, Japanese Journal of JSCE E2, Vol.68, No.1, 83-92

Minoru, M., Kenji, Y., Tsuyoshi, T., Kousuke, Y. (2010) “Manufacturing of γ-C2S used by industrial raw material and its evaluation of CO2 emission”, Cement Science and Concrete Technology, No.64, 29-33

16th International Congress on the Chemistry of Cement
ICCC 2023
BANGKOK, THAILAND

Effect of Low Temperature Calcination on Pozzolanic Activity of Volcanic Powder

Fanyuan Mu[1,2], Zhengping Sun[1,2,3*], Chunsheng Wang[4] and Xing Yang[4]

[1] *Key Laboratory of Advanced Civil Engineering Materials of Ministry of Education, Tongji University, 201804 Shanghai, China*

Email: grtszhp@163.com
[2] *School of Materials Science and Engineering, Tongji University, 201804 Shanghai, China*

Email: grtszhp@163.com
[3] *Research Center of Intelligent Evaluation and Restoration Engineering Technology of Urban Pipe Network of Shanghai Water Bureau, Shanghai 201900, China*

Email: grtszhp@163.com
[4] *Xizang Wuyang Industry Co. Ltd., Lasa 85000, China*

Email: fymu@foxmail.com

ABSTRACT

The volcanic powder found in Tibet has a high crystal content, which results in low pozzolanic activity. In this paper, TG-DSC and XRD were used to explore the excitation effect of low temperature calcination (lower than 1000 ℃) on the pozzolanic activity of volcanic powder. The results showed that the appropriate calcination temperature and time can promote the transformation of crystals in the volcanic powder to amorphous form, and effectively improve its pozzolanic activity. The optimum calcination time is 1 hour. When the calcination time is less than 1 hour, the activity of the volcanic powder increases with the prolongation of the calcination time, and the activity of the volcanic powder does not change significantly after more than 1 hour. The activity of volcanic powder is highest when the calcination temperature is 800 ℃, and even decreases when the calcination temperature exceeds 800 ℃.

KEYWORDS: *volcanic powder, low temperature calcination, pozzolanic activity, amorphous*

1. Introduction

China is rich in volcanic rock resources, and a large amount of natural volcanic ash material is distributed in the southeast and southwest borders(Yuan et al, 2020). Due to the different formation history and conditions, the types of volcanic rocks and their volcanic ash activity are quite different(Fares et al, 2016). Among them, the volcanic powder in Tibet has a high crystal content with low pozzolanic activity, making it difficult to be used as an auxiliary gelling material in cement and concrete(Chen et al, 2001). Therefore, improving the pozzolanic activity of volcanic powder in Tibet is the focus of effectively utilizing volcanic powder in Tibet. In this study, volcanic powder was pretreated by low-temperature calcination to explore the effect of low-temperature calcination method on the physical and chemical properties of volcanic powder and its pozzolanic activity.

2. materials and test methods

The specific surface area of the raw materials used in the experiment is 450 cm^2/g. Its particle size distribution is shown in Fig. 1, Its chemical composition is shown in Table 1, and the XRD pattern is shown in Fig. 2.

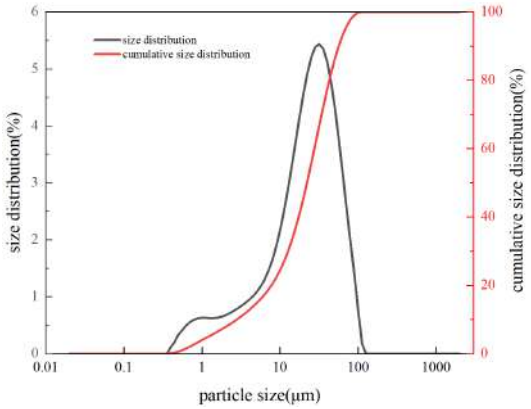


Fig. 1 Particle size distribution of volcanic powder

Table 1 Chemical composition of volcanic powder

mineral admixture	chemical components/%							
	SiO_2	Al_2O_3	Fe_2O_3	CaO	K_2O	Na_2O	MgO	SO_3
volcanic powder	55.87	17.51	9.12	6.99	3.98	2.53	2.01	/

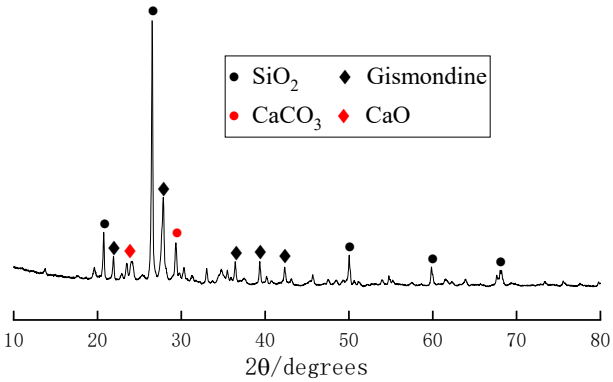


Fig. 2 XRD pattern of volcanic powder

The selected volcanic powder was calcined at different selected calcination temperatures for a certain time. The calcination was carried out in a muffle furnace with a heating rate of 20 °C/min and a cooling rate of 35 °C/min.
The content of volcanic powder in cement is 30%.

3. Results and discussion

The effect of volcanic powder at different calcination temperatures on the strength of the cement is shown in Fig. 3. When the calcination temperature does not exceed 600°C, the low-temperature calcination has no obvious effect on the activity of the volcanic powder. When the calcination temperature exceeds 600°C, the early strength of the cement will decrease with the increase of the calcination temperature, but 28-day strength will be significantly improved.

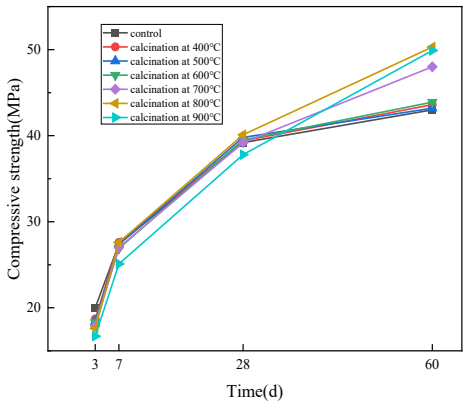


Fig. 3 Effect of volcanic powder at different calcination temperatures on the strength of cement

Two calcination temperatures of 500°C and 800°C were selected to explore the effect of calcination time of volcanic powder on the strength of the cementitious material system, and the results are shown in Fig. 4. The results show that when the calcination temperature is lower than 600°C, different calcination times have no significant effect on the activity of volcanic powder. When the calcination temperature exceeds 600°C, a shorter calcination time will lead to insufficient activation of the volcanic powder and lower strength in the later stage. A longer calcination time will reduce the early strength of cement, and the impact on the later strength is the same as that of calcination for 1 hour. Therefore, the best calcination time is one hour.

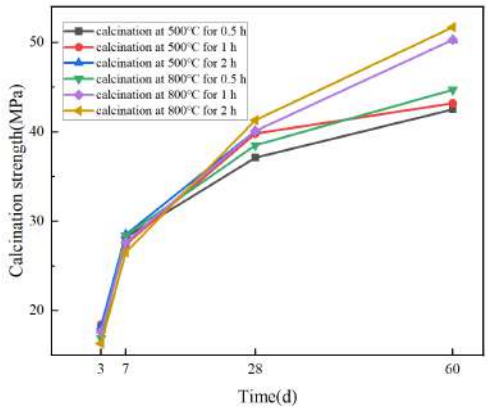


Fig. 4 Effect of volcanic powder at different calcination time on the strength of cement

Furthermore, from the TG-DSC curve of volcanic powder (Fig. 5), when the calcination temperature does not exceed 600 °C, the volcanic powder does not produce heat absorption or exotherm, and its crystal structure does not change. When the calcination temperature exceeds 600 °C, the volcanic powder begins to transform from crystal to glass, and the microstructure of the particles also changes. The lamellar structure of the volcanic powder particles disappears (Fig. 6), so the filling effect in the early stage of hydration is reduced, resulting in a certain degree of decline in the early strength of the gelled system. Due to the increase of the vitreous body, more volcanic powder participates in the hydration of the cement in the later stage of hydration, resulting in a significant increase in the strength of the later stage of the cement.

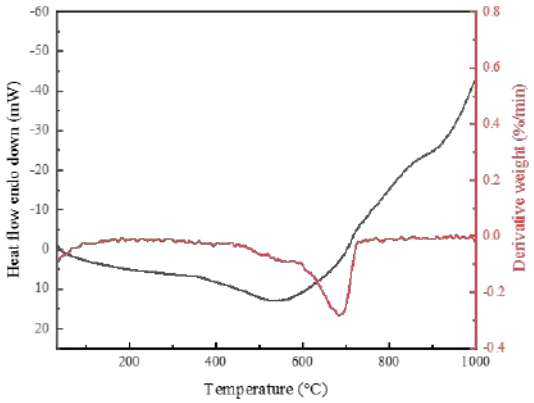
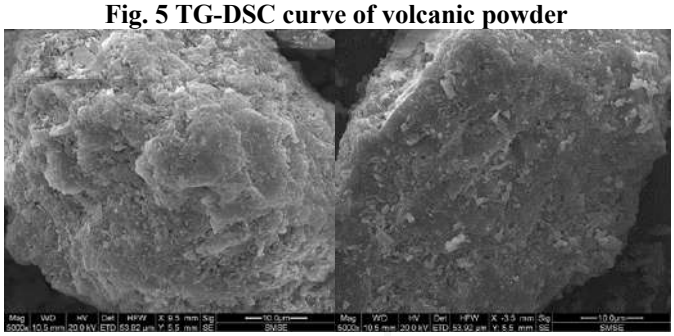


Fig. 5 TG-DSC curve of volcanic powder



(a) Uncalcined volcanic powder; (b) 800°C calcined volcanic powder

Fig. 6 Effect of calcination on microstructure of volcanic powder particles

4. Conclusion

Based on the analysis of experimental data developed in the present study, following conclusions can be drawn:

1. Low-temperature calcination at an appropriate temperature can help improve the pozzolanic activity of volcanic powder. The optimal calcination temperature for volcanic powder is 800°C. When the calcination temperature is lower than 600°C, low-temperature calcination has no significant effect on the activity of volcanic powder. When the calcination temperature exceeds 800°C, the activity of volcanic powder has no significant change compared with 800°C, which is not conducive to the low-carbon and green development of cement.
2. The optimal calcination time is one hour. Short-term calcination cannot effectively improve the activity of volcanic powder, while long-term calcination reduces the early strength of cement but does not significantly increase the later strength.
3. Calcining at low temperature causes the crystals in the volcanic powder to transform into vitreous, which significantly increases the reactivity of the volcanic powder.

References

Yuan Q., Yang Z. & Shi C. et al. (2020). Fundamentals on Application of Natural Pozzolans in Cement-based Materials: a Review. *Bulletin of Chinese Ceramic Society*, *39*(8): 2379-2392.

Fares, G., Alhozaimy, A., Alawad, O. A., & Al-Negheimish, A. (2016). Evaluation of powdered scoria rocks from various volcanic lava fields as cementitious material. *Journal of Materials in Civil Engineering*, *28*(3), 04015139.

Chen Q. & Qian G. (2001). Feasibility of Using Tibet's Pozzolan as Mineral Admixture of Concrete. *Hydro-Science and Engineering*, (4), 22-26.

The 16th International Congress on the Chemistry of Cement 2023 (ICCC2023)
"Further Reduction of CO_2 -Emissions and Circularity in the Cement and Concrete Industry"
September 18–22, 2023, Bangkok, Thailand

Development of plaster-like materials from magnesium carbonates

Kanwal Shahid[1*], Hoang Nguyen[1,2], Cise Unluer[3] and Paivo Kinnunen[1]

[1] *Fibre and Particle Engineering Research Unit, University of Oulu, Pentti Kaiteran katu 1, 90014 Oulu, Finland*
Email: Kanwal.Shahid@oulu.fi
Email: Paivo.Kinnunen@oulu.fi

[2] *Swiss Federal Laboratories for Materials Science and Technology (Empa), Laboratory for Concrete & Asphalt, Dübendorf, 8600, Switzerland*
Email: Hoang.Nguyen@oulu.fi

[3] *Department of Mechanical, Aerospace and Civil Engineering, University of Manchester, Manchester M13 9PL, United Kingdom,*

Email: cise.unluer@manchester.ac.uk

ABSTRACT
The use of (NQ, $MgCO_3 \cdot 3H_2O$) as a precursor to produce construction materials, particularly non-structural components, is a promising route due to synergies in waste utilization with the carbon capture and utilization (CCU) industry. This study investigates the use of NQ as a construction material in the development of plasterboard-like applications. NQ is synthesized using two different routes: (1) wet carbonation and (2) chemical synthesis. NQ can be activated via thermal treatment at around 150–175°C, after which the dehydrated NQ can hydrate to form a plaster-like product, similar to gypsum plaster. The reaction kinetics, mechanical properties, microstructure, phase assemblage, and evolution of the developed plasters using NQ synthesized from two different routes were studied. The influence of trace elements (i.e. sulfate and ammonium) on the performance of plasters was also considered. In terms of reaction kinetics, the nucleation and growth rates of the two polymorphs synthesized via wet carbonation and chemical route differed, especially after thermal activation and rehydration. Rehydrated NQ via carbonation was associated with other hydrated magnesium carbonates such as hydromagnesite after 28 days of curing. Rehydrated NQ via the chemical synthesis route was accompanied with magnesium carbonate hydrate and hexahydrate. Products cast using these NQ revealed 28-day strengths between 6 and 8 MPa.

KEYWORDS: *Carbon dioxide; carbon capture, and utilization; dehydrated nesquehonite; hemihydrate; plasterboard*

1. INTORDUCTION

Decarbonization of the industrial and power sectors is one of the primary focuses of current research efforts in the context of mitigating climate change (Pietzcker et al. 2021). Industrial roadmaps frequently recommend carbon capture pathways and technology as the safe route to achieving medium and long-term decarbonization objectives. Given the abundance of suitable minerals and wastes, the mineralisation of carbon dioxide as carbonates is one of the key carbon capture and utilization (CCU), pathways that have been suggested (Zevenhoven R et al. 2017). Though, the carbonation process of minerals tends to be costly with other side effects such as the vast amount of side waste products and its ecological footprint. This is the situation of $MgCO_3 \cdot 3H_2O$, nesquehonite (NQ). Despite being naturally occurring, it primarily results from the thermal processing of Mg-containing rocks like serpentine and CO_2 mineralisation. In this framework, we describe the promising results of our experiments on the reaction of NQ

produced using two different routes and its incorporation with calcium sulfate hemihydrate at different ratios in producing plasters. We present data on the experimental synthesis routes of nesquehonite, as well as the characterization of the solid product.

2. Methodology

This section elaborates on nesquehonite (NQ) synthesized by the wet carbonation route and the chemicals mix route.

2.1 Nesquehonite (NQ) synthesis methods

In this study, NQ was prepared using two different methods. The first method involved wet carbonation of an aqueous solution of magnesium hydroxide, where CO_2 was introduced into the solution from a gas cylinder via a mass flow controller at an 80-100 cc/min flow rate while stirring at high speed in a glass beaker. The pH of the solution was continuously monitored using a pH probe since it significantly affects carbonate precipitation. The obtained solid product was then vacuum filtered and rinsed with water, isopropanol, and diethyl ether, respectively, followed by air drying at room temperature and atmospheric pressure. The second method of preparing NQ was the chemical mix route, where 1 molar solution of magnesium chloride and ammonium carbonate was prepared separately and allowed to saturate before mixing in a parallel mixing mode while stirring at 750 rpm at ambient temperature for an hour. The resulting white suspension was collected. The solid product was separated from the liquid via vacuum filtration, then rinsed with water to remove excess sulfate, isopropanol to remove excess water, and diethyl ether before being air dried at room temperature for several hours. Overall, both methods produced white powder NQ, and the samples were placed at 40°C before further characterization.

2.2 Mix development

NQ was synthesized using both wet carbonation and chemical methods, subjected to thermal activation via heating for 24 hours at 160°C, while ensuring that no carbon dioxide was lost during this activation process, as presented by Jauffret et al 2015. Gypsum was also thermally activated to obtain hemihydrate (Cs·0.5 H) by heating at 148°C for 24 hours. After heating, both De-hydrated NQ (De-NQ) and hemihydrate were kept in the oven to cool down and then stored in a dessicator to prevent any exposure to moisture. To create admixtures of De-NQ with hemihydrate, the mix ratios were controlled by volume fraction based on the density of raw materials. The mixing process involved adding a calculated amount of dried De-NQ and hemihydrate powder to a clean container, as specified in Table 1. Prior to preparing the paste, powder samples were homogenized using a lab-scale homogenizer for two hours until a homogenized sample of two dry powders was achieved. The resulting admixture was then mixed in a solid/to liquid ratio of 1:1 to provide sufficient water for rehydrating it before being cast in a casting mold with specifications of $1\times1\times4$ cm^3. The molds were placed in a tight plaster bag for the next 24 hours to allow the reaction in a closed environment. Afterward, the molds were placed in an oven at 40°C for two hours. The molds were removed from the oven and allowed to cool at room temperature for another two hours before the casted samples were de-molded for further analysis.

Table 1. The mix recipe of hemihydrate with De-NQ was synthesized using carbonation and chemical route.

Samples (Mixes)	Short form-ID	NQ (g)	Hemihydrate (g)
100 % Rehydrated-NQ via Carbonation	100% Re-NQ (Carbo)	10	-
100 % Rehydrated-NQ via	100% Re-NQ (Chem)	10	-

Chemical route			
100% Hemihydrate	100% Cs.0.5H	-	10
75% Rehydrated-NQ via Carbonation/ 25% Hemihydrate	75% Re-NQ (Carbo)	7,0171	2,9829
75% Rehydrated-NQ via Chemical route/ 25% Hemihydrate	75% Re-NQ (Chem)	7,1210	2,879
50% Rehydrated-NQ via Carbonation/ 50% Hemihydrate	50% Re-NQ (Carbo)	4,3950	5,6049
50% Rehydrated-NQ via Chemical route/ 50% Hemihydrate	50% Re-NQ (Chem)	4,4857	5,5143

2.3 Material Characterization

The different mixes samples of Re-NQ and hemihydrate were characterized at different time periods of 7, 14, and 28 days of hydration reaction. Before characterization, the samples were immersed in isopropanol for 24 hours to stop the hydration process. After hydration stoppage, the excess isopropanol was drained, and the samples were left for air drying followed by 2-hour oven drying at 40°C. To understand the phases in mixed samples collected at different times, quantitative XRD analysis was used with silicon (Si) as an external standard. Isothermal conduction calorimetry was used to monitor the evolution of heat during the re-hydration of De-NQ and the mixes of De-NQ with hemihydrate (TAM Air, TA Instruments, the U.S.).

3. Results and Discussion

Fig. 1 (a) presents the heat flow of 100% Re-NQ via wet carbo and mixes and (b) chemical route and mixes in comparison to the (c) hemihydrate. The narrowing of mixed samples of Re-NQ via carbo with hemihydrate loading demonstrated that the reaction started a bit late but stabilized fast as compared to the wider peak of 100% Re-NQ via carbo where the hydration started at an early stage perhaps taking a long time to attain the stability. In the case of 100% Re-NQ via chemical synthesis (b), the higher and narrow peak presents rapid hydration. The influence of hemihydrate addition to the NQ was most obvious in this case as the peaks become shorter and broader. Plus, the hydration reaction of these blends is delayed as compared to the 100% Re-NQ via chemical samples. These findings are new insights into the effect of different synthesis routes and their mixes with hemihydrate behaviour towards the hydration reaction.

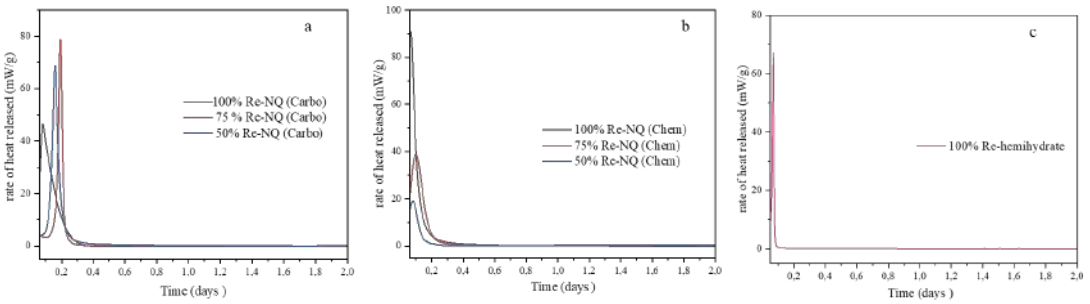


Fig. 1 Heat flow of all samples under ambient conditions (a) NQ samples via carbonation and homogenized with hemihydrate (replacement up to 25% and 50%), (b) NQ via chemical route and mixed with hemihydrate (replacement up to 25% and 50%), and (c) heat flow of rehydrated hemihydrate (as a reference).

Fig. 2 (a) shows the XRD spectra of Re-NQ via (carbo), (chem), and the mixes with hemihydrate after 28 days of curing. In the case of 100% Re-NQ via carbo after 28 days of hydration, the formation of amorphous hydromagnesite (b), and conversation to dypingite can be observed.

Moreover, in comparison with 75% Re-NQ via carbo mix sample, a trace of aragonite (calcium carbonate) is found as per the reaction of calcium from hemihydrate with carbonate of NQ during this curing time. For the 100% Re-NQ (chem), there are strong reflexes that are associated with the NQ and the presence of hexahydrate. In comparison with 75% Re-NQ (chem) and hemihydrate mix the peak intensity of NQ was reduced due to the reaction during hydration and transformation to calcium sulfate hydrate.

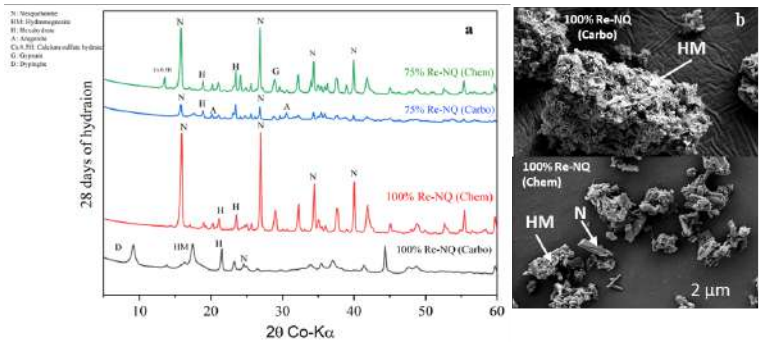


Fig 2. (a) XRD patterns of all samples after 28 days of hydration and (b) SEM images of identified phases.

4. Conclusions

This paper presented findings of the CCU process for nesquehonite (NQ). NQ can be obtained via different synthesis routes, while after activation, the crystal can be used as a plaster or plasterboard substitute. Results have shown that the kinetics of NQ synthesis differ between the two routes and the resulting blends with hemihydrate exhibit varying properties. XRD analysis confirmed that NQ synthesized via the carbonation route converted to dypingite and hydromagnesite, whereas NQ synthesized chemically remained stable even after rehydration. In blends of NQ and hemihydrate, the calcium from hemihydrate reacted with carbonate in 75% Re-NQ via the chemical synthesis route, leading to the formation of calcite. For 75% Re-NQ via the carbonation resulted in the formation of aragonite.

While the product requires further development, current projections indicate that NQ synthesized by different routes has the potential to be used in certain building applications. Future studies will focus on the identification of potential additives such as activators, accelerators, and retarders that can enable optimal setting time, while presenting minor effects on the durability and volumetric stability of the final product. Moreover, manufacturing process optimization can be performed to achieve comparable or improved performance to the conventional gypsum plaster process. This optimization can include improvements in the calcination process, setting time, demolding, and drying, thereby reducing production time and energy consumption, while producing a high-quality plaster.

Acknowledgments:

This work was funded by Business Finland project, PILCCU (7296/31/2021). P.K. acknowledges financial support from Kvantum institute (University of Oulu) and Academy of Finland (grants 322085, 329477 and 326291). Part of the work was carried out with the support of the Centre for Material Analysis, University of Oulu, Finland.

References

Jauffret, G. Morrison, J. Glasser, F. (2015) "On the thermal decomposition of nesquehonite", *Journal of Thermal Analysis and Calorimetry*, 122(2): 601-609.

Zevenhoven, R. Slotte, M. Koivisto, E. (2017) "Serpentinite Carbonation Process Routes using Ammonium Sulfate and Integration in Industry", *Energy Technology*, 5(6): 945-954.

Pietzcker, R.C. Osorio, S. Rodrigues, R. (2021) "Tightening EU ETS targets in line with the European Green Deal: Impacts on the decarbonization of the EU power sector", *Applied Energy*, 293: 116914.

The 16th International Congress on the Chemistry of Cement 2023 (ICCC2023)
"Further Reduction of CO_2 -Emissions and Circularity in the Cement and Concrete Industry"
September 18–22, 2023, Bangkok, Thailand

Suitability of Low purity Limestone for Limestone Calcined Clay Cement (LC^3) Production

Lupesh Dudi[1*], and Shashank Bishnoi[2]

[1] *Indian Institute of Technology Delhi, New Delhi, India*
Email: lupeshdudi@gmail.com
[2] *Indian Institute of Technology Delhi, New Delhi, India*
Email: bishnoi@iitd.ac.in

ABSTRACT

Speedy and continuous development in the infrastructure industry is driving up cement production and carbon dioxide emissions. Currently, 8% of total carbon dioxide emission is from the cement industry. Additionally, increasing cement demand is distressing natural resources required for conventional cement production. In such a state, using a combination of SCMs to further lower the clinker factor is a reasonable approach. Limestone calcined clay cement (LC^3) is one such cement which composes of clinker, calcined clay, limestone, and gypsum. Calcined clay used in LC^3 is widely available across the globe. However, good-quality limestone reserves are already used for clinker production, and using them for addition in LC^3 may not be an efficient choice. It is known that aluminates present in clay or cement require only a limited amount of calcium carbonate to form carbo-aluminate phases, remaining limestone acts only as an inert filler. Based on this observation from the literature, the suitability of using low-purity limestone to produce LC^3 has been explored. In this study two limestones i.e high purity and low purity along with three grades of calcined clay (kaolinitic content of 40-80%, have been used to assess the suitability of using low-purity limestone in LC^3 production. A comparison between blends based on compressive strength development, iso-thermal calorimetry, and setting time has been made in the present study. It has been observed that the addition of low-purity limestone doesn't change the hydration kinetics of LC^3 in the initial days as observed from iso-thermal calorimetry curves. Additionally, no evident effect on compressive strength development has been observed, strength results were within error for all blends. Hence, it will be more efficient, cost-effective, and eco-friendly to use low-purity limestone for LC^3 production.

KEYWORDS: *Low-carbon cement, low-purity limestone, calcined clay, hydration, and strength development.*

1. Introduction

The rapid expansion of the construction industry in recent decades has placed significant pressure on the global environment and natural resources, which are being depleted to meet the growing demand. A high volume of cement is being consumed leading to substantial carbon dioxide emissions, i.e cement industry accounts for 8% of global carbon dioxide emissions and contributes to the depletion of natural reserves of limestone, clays, and gypsum. Limestone is a crucial raw material in cement production, serving as the primary source of calcium in the clinker. Currently, the cement industry faces two major challenges: carbon dioxide emissions associated with cement production and dwindling reserves of high-quality limestone suitable for cement production. The recently developed limestone calcined clay cement (LC^3) provides an effective solution to these issues. appearance.

LC^3 is a three-component mixture consisting of ordinary Portland cement (clinker + gypsum), calcined clay, and limestone, with a common clinker factor of 0.5. LC^3's reduced carbon footprint is primarily due to a lower clinker factor, the calcination of clays at temperatures between 800-900℃, which is much lower than the clinker formation temperature, and the addition of limestone by simple grinding. Gettu et al. (2019) reported that compared to ordinary Portland cement, LC^3 emits up to 30% less carbon dioxide.

Chemical reactions in the LC^3 system indicate that only a small portion of calcite is required to react with aluminate phases, Krishnan and Bishnoi (2020). Therefore, the use of cement-grade limestone is unnecessary for LC^3 production. Furthermore, carbonate sources are easier to replace than clinker or clay, as long as the addition or replacement does not have any negative effects. Thus, the use of low-purity limestone would be more cost-effective and environmentally friendly. The availability of a diverse range of limestone throughout India also increases the possibility of LC^3 production. In this study, the effects of using different grades of limestone on strength development and hydration characteristics were investigated for varying kaolinitic content in the blend. The subsequent sections provide further details on the study's findings and the suitability of using low-purity limestone in LC^3 production.

2. Materials and Methods

A 43-grade ordinary Portland cement (OPC) procured from the market was used directly. Calcined clay (approximately 80% kaolinitic content in clay) was procured from a clay company in Gujarat was used. Two grades of limestone were procured from a cement plant, i.e high-purity (approximately 80% calcite content) and low-purity (approximately 55% calcite content). Limestone was grounded in a laboratory ball mill at a charge-to-ball ratio of 1:5 for 9000 revolutions. Low-purity limestone had quartz as an impurity. Quartz being less grindable remains coarser or higher energy is invested for the grinding process, although finer limestone is obtained due to energy transfer mechanism (Gupta (2020)). The LC^3 blends were prepared by blending the powdered raw materials. Gypsum used had a purity of approximately 88%. To vary the kaolinitic content from 80% to 40%, crushed quartz was used as an inert material for replacing high-grade calcined clay i.e 100% - calcined clay, 75% - calcined clay + 25% - quartz, and 50% - calcined clay + 50% - quartz. The composition of all the blends is given in table 1.

Table 1. Composition of the blends studied.

Blend Name	*OPC (%)*	*Calcined Clay (C) (%)*	*High-purity Limestone (H) (%)*	*Low-purity Limestone (L) (%)*	*Quartz (Q) (%)*	*Gypsum (G) (%)*
Specific gravity	3.19	2.63	2.73	2.68	2.65	2.64
C-H	53.35	29.10	14.55	-	-	3
C-L	53.35	29.10	-	14.55	-	3
3C-H-Q	53.35	21.82	14.55	-	07.28	3
3C-L-Q	53.35	21.82	-	14.55	07.28	3
2C-H-2Q	53.35	14.55	14.55	-	14.55	3
2C-L-2Q	53.35	14.55	-	14.55	14.55	3

Iso-thermal calorimetry was performed to access the effect of limestone purity on the heat of hydration and cumulative heat realized up on hydration at 27°C for 72 hrs at a fixed water-to-binder ratio of 0.40 using Calmetrix I-cal 8000. IS-4031 was followed to determine the setting time for all blends. Additionally, compressive strength was determined by casting standard 70.6*70.6*70.6 mm mortar cubes. The cement to sand ratio was kept constant at 1:3, and the water to binder ratio was fixed at 0.40. Flow for all the blends was targeted between 130 to 150 mm, to achieve the required flow adequate superplasticizer dosage was added.

3. Results

3.1 Iso-thermal Calorimetry

Calcite content in the limestone does not appear to have a significant effect on the rate of heat evolution, since comparable peak power levels and acceleration slopes were observed during an initial 48 hours of hydration (Fig. 1-a). Likewise, an identical cumulative heat released was observed on replacing high-purity limestone with low-purity limestone for all the grades of calcined clay (Fig. 1-b). In LC^3, the secondary hydration peak corresponding to aluminates was observed to be influenced by the amorphous metakaolin present in the system. With increasing aluminate content in the system, the secondary

hydration peak was observed to shift towards the main hydration peak and become shaper, this has also been observed by Zunino and Scrivener (2022) for blends prepared with synthesized tricalcium silicate and tricalcium aluminate.

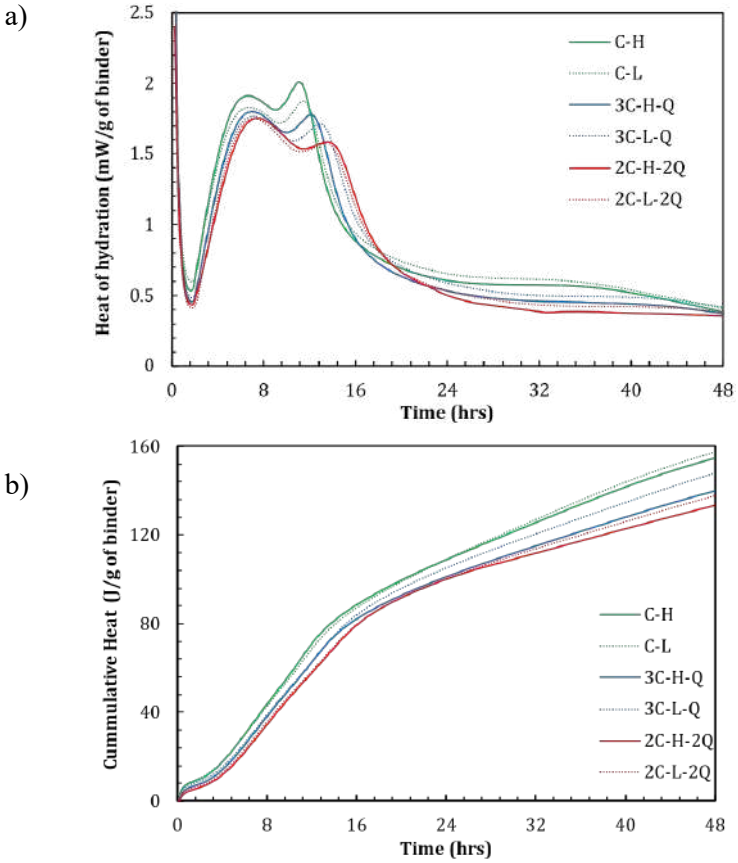


Figure 1. Calorimetry results for all the blends a) rate of heat evolution, and b) Cumulative heat released from hydration.

3.2 Setting Time

At the same kaolinitic content on replacement of high-purity limestone with low-purity limestone, identical setting behavior was observed. Interestingly as the kaolinitic content in the blend increases, initially, there is an increase in the initial setting time which again falls on further increasing the content indicating there exists a maximum in-between, also observed by Brooks and Johari (2001). However, the effect on the final setting time was not pronounced.

Table 2. Setting time for all the blends.

Blend Name	Initial Setting time (hr:min)	Final Setting time (hr:min)
C-H	02:40	04:23
C-L	02:31	04:19
3C-H-Q	03:13	04:34
3C-L-Q	03:08	04:28
2C-H-2Q	02:36	04:14
2C-L-2Q	02:26	04:18

3.3 Compressive Strength

Fig. 2 illustrates the compressive strength results for all blends studied in the present work. Strength at 3 days was similar, even though different calcite content was present in the system, as initial strength

development comes from clinker hydration and fast-reacting calcined clay. However, a comparable 28-day strength indicates that even 55% calcite content was enough to react with aluminates present in the system to form hemi- and mono- carbo-aluminate phases. As expected, the 3-day strength of the blends decreased with the decreasing kaolinitic content present in the system (Avet and Scrivener (2018)). However, as the hydration continues the 28-day compressive strength was identical for all the blends, higher than 43MPa.

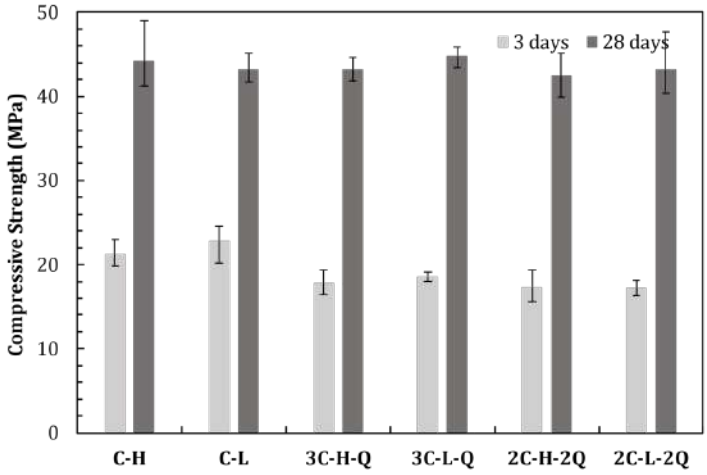


Figure 2. Compressive strength of all the blends.

4. Conclusions

This study demonstrated that calcite content as low as approximately 55% was enough to obtain comparable initial hydration characteristics, setting time, and compressive strength. The results indicated that only a limited amount of calcite reacts with the aluminates present in the system to form carbo-aluminates, while the remainder serves only as a filler. As a result, rejected limestone available in the vicinity of cement plants can be utilized to reduce the burden on cement-grade limestone reserves.

Acknowledgments

Aalborg cement is acknowledged for making the Future-cem technology available to us. For the Low Carbon Cement Project, the authors are grateful for the support of Swiss Agency for Development and Cooperation (SDC).

References

Avet, F., & Scrivener, K. (2018). Investigation of the calcined kaolinite content on the hydration of Limestone Calcined Clay Cement (LC3). *Cement and Concrete Research*, *107*, 124–135. https://doi.org/10.1016/j.cemconres.2018.02.016

Brooks, J. J., & Johari, M. A. M. (2001). Effect of metakaolin on creep and shrinkage of concrete.

Gettu, R., Patel, A., Rathi, V., Prakasan, S., Basavaraj, A. S., Palaniappan, S., & Maity, S. (2019). Influence of supplementary cementitious materials on the sustainability parameters of cements and concretes in the Indian context. *Materials and Structures*, *52*(1), 10. https://doi.org/10.1617/s11527-019-1321-5

Gupta, V. K. (2020). Effect of particulate environment on the grinding kinetics of mixtures of minerals in ball mills. *Powder Technology*, *375*, 549–558. https://doi.org/10.1016/j.powtec.2020.07.072

Krishnan, S., & Bishnoi, S. (2020). A numerical approach for designing composite cements with calcined clay and limestone. *Cement and Concrete Research*, *138*, 106232. https://doi.org/10.1016/j.cemconres.2020.106232

Zunino, F., & Scrivener, K. (2022). The influence of sulfate addition on hydration kinetics and C-S-H morphology of C3S and C3S/C3A systems. *Cement and Concrete Research*, *160*, 106930. https://doi.org/10.1016/j.cemconres.2022.106930

The 16th International Congress on the Chemistry of Cement 2023 (ICCC2023)
"Further Reduction of CO_2 -Emissions and Circularity in the Cement and Concrete Industry"
September 18–22, 2023, Bangkok, Thailand

Influence of acetate on the carbonation of brucite ($Mg(OH)_2$)

N. Kamala Ilango[1*], H. Nguyen[1,2], F. Winnefeld[2] and P. Kinnunen[1]

[1] *Fibre and Particle Engineering Research Unit, University of Oulu, Oulu, Finland*

Email: nirrupama.kamalailango@oulu.fi; hoang.nguyen@oulu.fi; paivo.kinnunen@oulu.fi
[2] *Empa, Swiss Federal Laboratories for Material Science and Technology, Laboratory for Concrete and Asphalt, Dübendorf, Switzerland*

Email: frank.winnefeld@empa.ch

ABSTRACT

Magnesium-rich minerals can capture and store CO_2 as stable magnesium carbonate minerals and can be utilized to produce construction materials with low or even negative carbon footprints. Organic ligands influence the growth and morphology of the magnesium carbonates. Among these ligands, acetate is known to enhance the formation of carbonates. However, there is no clear link between the influence of this ligand and the hydration of MgO, which potentially leads to a different pathway of mineralization. To address this gap, we investigated the influence of Mg-acetate on the properties of brucite precipitated by hydrating MgO in aqueous solution (w/s = 20). Subsequently, carbonation of precipitated brucite under different temperature (80 and 202 °C), steam pressure (0 and 15 bar) and CO_2 pressure of 20 bar was also studied. The phase assemblage and the morphology of the carbonated mineral was measured. Data reveals that the addition of Mg-acetate results in a poorly crystalline brucite, and alters the morphology and the composition of the precipitate as evident from scanning electron microscopy, X-ray diffraction and thermogravimetry analyses. The characteristics of the (hydrated) magnesium carbonates formed seem to depend on the properties of the brucite seed as precursor and the reaction conditions. This work gives insights on role of organic ligands in modifying the properties of brucite and tailoring the properties of minerals to maximize the carbon capture efficiency.

KEYWORDS: *Brucite, Hydrothermal, Low carbon cements, (hydrated) magnesium carbonates, Mineral carbonation.*

1. Introduction

With more than 10 000 Gt of Mg/Ca-rich minerals (Sanna et al. (2014)) available, it offers immense potential for carbon mineralization and to the development of low-carbon or negative carbon binders. Carbon storage and utilization (CSU) has been recognized as a key step towards achieving climate goals put forward by Intergovernmental Panel on Climate Change (IPCC). The need to reduce the carbon footprint of cement industry which presently accounts for ~8% of global CO_2 emissions along with the increasing demand for construction materials due to increase in population, infrastructure development projects around the globe offers high-volume application for the carbonated minerals. The key challenges in using Mg-based minerals for carbon mineralization are low reactivity of Mg-silicates. However, recent development in technologies for extraction of MgO or brucite from Mg-silicates has opened new opportunities (Nduagu et al. (2012) and Scott et al. (2021)).

Many studies have focused on the development of hydrated magnesium carbonate (HMCs) binders (Dung et al. (2017), Kuenzel et al. (2018), Winnefeld et al. (2019) and Nguyen et al. (2021)). Primary challenge in using MgO or brucite as precursor is the formation of the reaction products as a passivation layer over the surface of the mineral, hindering further reaction. Organic ligands have proved to be effective chelating agents that can steer the reaction pathways and kinetics of MgO-based binders. Several works from Dung et al. (2017) have shown increased carbonation potential and mechanical performance for

reactive magnesium cements when Mg-acetate was used as hydration agent. The increase in the formation of carbonate phases in the presence of Mg-acetate was attributed to increased formation of magnesium hydroxide, which in turn carbonates to form HMCs. However, there is no clear understanding on the role of acetate on the hydration of MgO to form brucite with varying mineral properties, which could in turn lead to a different pathway of mineralization and is the focus of this study. To this end, the hydration of MgO in an aqueous environment with 0.1 M Mg-acetate solution as the hydrating agent has been done. Further, the hydrated precipitates (brucite) were carbonated in a high-pressure reactor at two different temperatures (80 and 202 °C), and at constant CO_2 pressure of 20 bar. The findings of this work will contribute to a better understanding of role of ligands and mineral properties on different mineralization pathways and in turn can maximize carbon sequestration potential.

2. Materials and Methods

2.1 Materials

MgO was prepared in the laboratory by calcining magnesium hydroxide ($Mg(OH)_2$) purchased from VWR chemicals (assay ~99.7%) at 900 °C for 6 hours to produce reactive magnesia. The median particle size was about 8 μm as measured from laser diffraction spectroscopy. Magnesium acetate tetrahydrate ($Mg(CH_3COO)_2.4H_2O$) was obtained from Sigma-Aldrich (assay ≥ 99%) and used without further treatment to prepare 0.1M solution in deionized water.

2.2 Sample preparation

Synthetic brucite was be prepared by reaction calcined MgO with 0.1 M Mg-acetate at water to solid ratio of 20. MgO was hydrated in a closed beaker and the solution was continuously stirred with a magnetic rotor at 250 rpm for 6 hours and further allowed to react at static condition till 24 hours. The precipitates were then collected through vacuum filtration (2μm filter paper, 90 cm diameter) followed by washing with isopropanol and diethyl ether and drying at 40 °C for 15 minutes. In this study, laboratory-grade brucite was used as reference.
The carbonation of the brucites was done using a 2.5 L high pressure reactor (RVD-2-250, with maximum pressure of 250 bar, and 250 °C temperature). The precursor was homogenously mixed with 20% (by wt.) of water and was subjected to carbonation at constant CO_2 pressure (P_{CO2}) of 20 bar and at two different temperatures (80 and 202 °C). The samples were placed inside the autoclave and was heated to the desired temperature. A water source (100 ml) was placed at the bottom of the reactor. This enabled 100% relative humidity in the case of 80 °C and at 202 °C the presence of water built a steam pressure (P_{steam}) of 15 bar. CO_2 was flushed with pressurized-CO_2 for about 2 min after the desired temperature was reached. The reaction conditions were maintained for 15 minutes, and the pressure was immediately released, and the system was cooled down with a heat exchanger with the cooling rate of about 3 °C/min. The solid precipitates were then collected and dried at 40 °C for 2.5 hours.

2.3 Methods

Thermal analysis of the precipitates was measured using TG, Precisa (prepASH 129, TEOPAL). The temperature was increased from 30 °C to 1000 °C with a ramp of 10 K/min. About 0.45 to 0.5 g of sample were loaded in an alumina crucible, and N_2 atmosphere was used. The morphologies of the hydrated and carbonated samples were studied using JEOL field emission scanning electron microscopy (FESEM). An accelerating voltage of 5 kV and a working distance of about 10-15 mm were used. The images were taken using secondary electron mode. Platinum coating at 40 mA for 40 s was done to reduce charging.

3. Results and Discussion

The influence of acetate on the properties of brucite precipitated from 0.1 M Mg-acetate solution and the subsequent carbonation of the precipitates at different temperature and steam pressure is discussed in this section.

3.1 Hydration

The morphology of the reference brucite and brucite formed in 0.1 M Mg-acetate solution (synthesized brucite) is shown in Fig. 1. It can be noted that the presence of acetate leads to the formation of thin sheet-like layers with larger diameter than the regular hexagonal morphology of brucite. The thermal decomposition of the reference and synthesized brucite is presented in Fig. 1c. It could be noted that MgO has completely reacted with 0.1 M Mg-acetate solution to form brucite. The dehydroxylation of synthesized brucite is at about 300 °C. The shift in the thermal decomposition of brucite to lower temperature compared to reference indicates lower particle size and/or lower crystallinity of brucite that is formed in the presence of Mg-acetate.

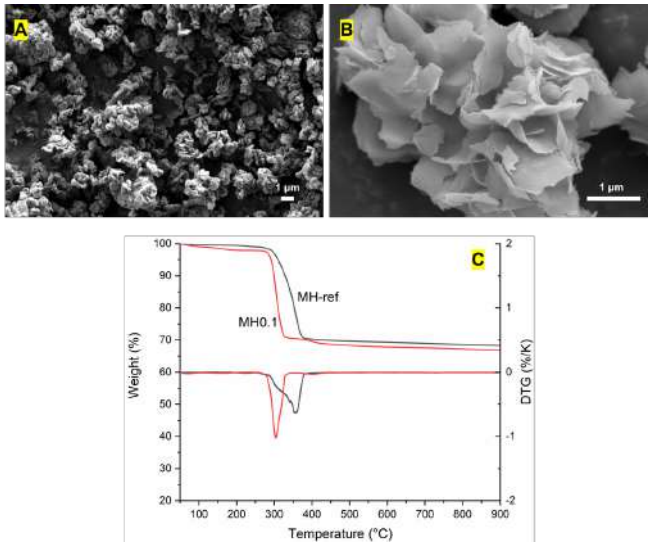


Fig. 1. Morphology of reference brucite (A), brucite synthesized in 0.1 M Mg-acetate (B) and the thermogravimetric analysis of the both the brucite samples (C).

3.2 Carbonation

The morphology and the thermal decomposition of reference and synthesized brucite carbonated in the high-pressure reactor at 80 °C and CO_2 pressure of 20 bar for 15 mins is shown in Fig. 2. It is evident that the reference brucite reacts with CO_2 at 80 °C to form hydromagnesite. However, no clear HMCs could be identified for synthesized brucite. The dehydroxylation/ dehydration around 180 °C, however, indicate the presence of unknown reaction product.

Fig. 2. Morphology and thermogravimetric analysis of brucite after carbonation at 80 °C and CO_2 pressure of 20 bar. (A) reference brucite, (B) brucite synthesized in 0.1 M Mg-acetate and (C) TG-DTG showing the formation of hydromagnesite and unreacted brucite in the case of reference brucite and possible hydrated magnesium carbonate phases in synthesized brucite.

Fig. 3 shows the morphology and the thermal behaviour of samples reacted at 202 °C. The increase in temperature to 202 °C builds a steam pressure of 15 bar in the reactor in addition to the CO_2 pressure (20 bar). The effect of the steam pressure on the carbonate products formed is evident. In this condition, brucite both reference and synthesized, react to form anhydrous magnesium carbonate ($MgCO_3$).

However, it could be noted that the rate of reaction of synthesized brucite is higher. The amount of $MgCO_3$ formed as calculated from the mass loss between 480 °C to 650 °C is about 10% for reference and 26% for acetate modified brucite.

Fig. 3. Morphology and thermogravimetric analysis of brucite after carbonation at 202 °C with steam pressure of 15 bar along with CO_2 pressure of 20 bar. (A) reference brucite, (B) brucite synthesized in 0.1 M Mg-acetate and (C) TG-DTG showing the formation of magnesite along with unreacted brucite for both cases.

4. Conclusions

In this study, the influence of acetate on the properties of precipitated brucite in aqueous solution and the subsequent carbonation of the dried precipitates at different temperatures and steam pressure (constant P_{CO2}) was elucidated. It was observed that the acetate alters the morphology and the crystallinity of the precipitated brucite. The synthesized brucite when subjected to carbonation showed to have a profound influence on the carbon mineralization pathway. At 80 °C, unknown carbonate phases formed compared to the formation of hydromagnesite in the case of reference brucite. With increased temperature and steam pressure, though magnesite was the main carbonate mineral to form in both precursors, the rate of reaction of synthesized brucite was higher that the reference. Further, the effect of steam pressure on the phases formed is also evident. The result from this study is a step towards enhanced CO_2 sequestration by tailoring mineral properties. Further, it paves way for the utilization of the resulting carbonated mineral with controlled morphologies and properties (Carbon capture and utilization, CCU) to produce low carbon construction material.

Acknowledgements

The authors would like to acknowledge the financial support from the University of Oulu & The Academy of Finland Profi5 326291, as well as the Academy of Finland project 329477. A part of the material characterization was carried out with the support from the Centre for Material Analysis, University of Oulu, Finland.

References

Dung, N.T. and Unluer, C. (2017) "Sequestration of CO_2 in reactive MgO cement-based mixes with enhanced hydration mechanisms", Construction and Building Materials, 143: 71–82.

Kuenzel, C., Zhang, F., Ferrándiz-Mas, V., Cheeseman, C.R. and Gartner, E.M. (2018) "The mechanism of hydration of MgO-hydromagnesite blends", Cement and Concrete Research, 103: 123–129.

Nduagu, E., Björklöf, T., Fagerlund, J., Wärnå, J., Geerlings, H. and Zevenhoven, R. (2012) "Production of Magnesium Hydroxide from Magnesium Silicate for the Purpose of CO_2 Mineralisation- Part 1: Application to Finnish Serpentinite", Minerals Engineering, 30: 75-86.

Nguyen, H., Santos, H., Sreenivasan, H., Kunther, W., Carvelli, V., Illikainen, M. and Kinnunen, P. (2022) "On the carbonation of brucite: Effects of Mg-acetate on the precipitation of hydrated magnesium carbonates in aqueous environment", Cement and Concrete Research, 153: 106696.

Sanna, A., Uibu, M., Caramanna, G., Kuusik, R. and Maroto-Valer, M. M. (2014) "A Review of Mineral Carbonation Technologies to Sequester CO_2", Chem. Soc. Rev., 43 (23): 8049–8080.

Scott, A., Oze, C., Shah, V., Yang, N., Shanks, B., Cheeseman, C., Marshall, A. and Watson, M. (2021) "Transformation of Abundant Magnesium Silicate Minerals for Enhanced CO_2 Sequestration", Communications Earth and Environment, 2 (1): 1–6.

Winnefeld, F., Epifania, E., Montagnaro, F. and Gartner, E.M. (2019) "Further studies of the hydration of MgO-hydromagnesite blends", Cement and Concrete Research, 126: 105912.

The 16th International Congress on the Chemistry of Cement 2023 (ICCC2023)
"Further Reduction of CO_2 -Emissions and Circularity in the Cement and Concrete Industry"
September 18–22, 2023, Bangkok, Thailand

Synthesis of Calcium Sulfoaluminate-Belite Cement from Lignite Bottom Ash Using Clinkerization and Hydrothermal-Calcination

M. Thala[1], P. Wattanachai[3,4], S. Wansom[5], N. Setthaya[6], F. Winnefeld[7], P. Chindaprasirt[8], K. Pimraksa[1,2*]

[1] *Department of Industrial Chemistry, Faculty of Science, Chiang Mai university, Thailand*
[2] *Center of Excellence in Materials Science and Technology, Faculty of Science, Chiang Mai University, Thailand*
[3] *Department of Civil Engineering, Faculty of Engineering, Chiang Mai university, Thailand*
[4] *Science and Technology Park, Chiang Mai University (STeP), Thailand*
[5] *National Energy Technology Center (ENTEC), National Science and Technology Development Agency (NSTDA), Thailand*
[6] *Division of Chemistry, School of Science, University of Phayao, Thailand,*
[7] *Empa, Swiss Federal Laboratories for Materials Science and Technology, Switzerland*
[8] *Sustainable Infrastructure Research and Development Center, Faculty of Engineering, Khon Kaen University, Thailand*

*Email: kedsarin.p@cmu.ac.th**

ABSTRACT

This research aimed to compare the characteristics and properties of calcium sulfoaluminate-belite cement using lignite bottom ash as a main source of alumina, silica, and calcium oxide by different synthesis methods, namely conventional clinker and hydrothermal-calcination, respectively. A clinker composition with ye'elimite and belite in a ratio of 50:50 by mass was targeted at. The firing temperature was chosen between 1,050-1,250°C. NaF and CaF_2 were used as dopants to investigate their effect on ye'elimite and belite formation. The phase compositions of the obtained clinkers were characterized by X-ray diffrcation, and their hydration was followed by isothermal calorimetry and X-ray diffraction. The results show that contents of ye'elimite and belite increase with an increase in firing temperature, but deviated from the targeted composition because of formation of minor phases. Gehlenite is the main minor phase, which increases when the temperature is above 1,150°C. Apart from gehlenite, minor phases such as CA, C_4AF, C_2A and anhydrite are also found in products obtained from clinkering, while C_4AF, ternesite and anhydrite are formed as minor phases using hydrothermal calcination. Clinkering yielded higher ye'elimite contents than hydrothermal calcination, while belite content was comparable. The addition of NaF and CaF_2 reduce the quantity of ye'elimite and belite and promotes gehlenite formation in the clinkering process. In hydrothermal-calcination, the dopants significantly improve the formation of ye'elimite on the expenses of minor calcium aluminate phases.

KEYWORDS: *Bottom ash, Calcium sulfoaluminate-belite cement, Clinkering, Hydrothermal calcination, Ettringite*

1. Introduction

Calcium sulfoaluminate-belite ($C\hat{S}AB$) cement has been proposed as an environmentally friendly cement because of its lower energy consumption and lower CO_2-emissions when compared to Portland cement (PC) (De la Torre et al. (2011), Winnefeld and Lothenbach (2010)). $C\hat{S}AB$ cement contains ye'elimite ($C_4A_3\hat{S}$) and belite (C_2S) as major phases. Its benefits include rapid hardening, high resistance to sulfate attack, self-stressing and volume stability (Chen and Juenger (2012), Pimraksa and Chindaprasirt (2018)). The production temperature is about 1,250°C using conventional clinkering (Ben Haha et al. (2019), El Khessaimi et al. (2018)), and can be reduced to 1,050-1,150°C using hydrothermal-calcination (Rungchet et al. (2016), Bouha et al. (2022)). Compared to PC, a lower lime saturation factor (LSF) and the

incorporation of wastes in the raw meal are possible (Rungchet et al. (2017), Kramar et al. (2019)). In this work, CŜAB clinkers were synthesized using conventional clinkering and hydrothermal-calcination, respectively. Lignite bottom ash (BA) was used as a source of SiO_2 and Al_2O_3. $Al(OH)_3$ and flue gas desulfurization gypsum (FGDG) were used as a corrective material and sulfate source, respectively. The effect of mineralizers (NaF and CaF_2) on the phase contents (Kacimi et al. (2006)) was also investigated. Mineralogical compositions and heat of hydration of the synthesized clinkers (in blends with FGDG) were characterized to confirm their quality.

2. Experimental

BA and FGDG from Mae Moh Power Plant, Thailand, were used as starting materials. $Al(OH)_3$ (97.0% purity) was used as a corrective material. $CaCO_3$ (96.7% purity) and $Ca(OH)_2$ (96.0% purity) were used for a correction of CaO content in conventional clinkering and hydrothermal-calcination, respectively. Chemical and mineralogical compositions of BA and FGDG are presented in Table 1. Raw meal proportions were stoichiometrically calculated targeted at a ratio of ye'elimite to belite of 50:50 by mass. NaF and CaF_2 at 1 and 2 mass-% were added to study an effect of mineralizers on cement phase formation.

Table 1 Chemical compositions of starting materials in mass-%

	SiO_2	Al_2O_3	Fe_2O_3	CaO	K_2O	MgO	P_2O_5	TiO_2	SO_3
BA	31.4	15.3	13.9	26.3	1.9	2.8	-	0.4	7.8
FGDG	3.0	1.2	0.3	44.4	0.0	0.9	0.1	-	50.1

For clinkering, starting materials were homogenized by grinding using a ball mill. For hydrothermal calcination, starting materials were mixed in deionized water using a magnetic stirrer. Afterwards the suspension was hydrothermally treated at 124°C, 1.3 bar for 3 h. The hydrothermal reaction products were filtered and dried. Both clinkering and hydrothermal products were placed in an alumina crucible for firing by an electric furnace at 1,050 – 1,250°C (5°C/min and dwelling time for 1 h) with air quenching. The obtained CŜAB cement clinkers were characterized by XRD (Bruker D4 Endeavor diffractometer) using CuKα radiation (λ=1.54Å) and a step size 0.02°/ 0.1 s. Phase identification and quantification was performed using DIFFRAC.EVA software. Hydration of the synthesized clinkers was investigated by isothermal calorimetry. The ground clinkers were blended with FGDG in a way that all ye'elimite and all calcium aluminate phases can be converted to ettringite. Isothermal calorimetry was performed on pastes at 25°C up to 24 h using a w/c of 0.50.

3 Results and discussion

3.1 Mineralogical compositions of CŜAB clinkers

Table 2 shows the quantitative phase contents of CŜAB clinkers obtained from clinkering and hydrothermal-calcination, respectively, at different firing temperatures. For clinkering at 1,050°C, measurable contents of calcium aluminate phases and minerals from the starting materials are still found. When the temperature increases, ye'elimite ($C_4A_3\hat{S}$) is formed, and gehlenite (C_2AS) transforms into $C_4A_3\hat{S}$ and C_2S. At 1,150°C, $C_4A_3\hat{S}$ and C_2S contents are strongly increased, but still below the target. Over 1,150°C, the quantity of ye'elimite is slightly increased with a reduction of belite content. Calcium aluminate phases (CA and CA_2) are changed into gehlenite instead of ye'elimite at 1,200°C presumably due to insufficient CaO content, although a sufficient supply of CaO content is provided in the raw meal based on the theoretical requirement of ye'elimite.

Table 2 Synthesized products after clinkering and hydrothermal-calcination at different firing temperatures.

	$C_4A_3\hat{S}$	C_2S	C_2AS	C_3S	C_3A	$C_{12}A_7$	CA	CA_2	C_4AF	$C_5S_2\hat{S}$	$C\hat{S}$	CH	CaO	SiO_2	MgO
Clinkering															
1,050°C	4.2	12.1	19.6	1.0	1.7	7.4	7.0	12.7	4.7	-	10.8	12.2	4.2	1.7	0.7
1,100°C	18.1	19.8	13.9	1.6	1.1	5.5	8.1	6.9	7.5	-	6.6	9.3	-	0.9	0.6
1,150°C	38.4	28.3	13.4	1.0	-	0.9	10.5	1.7	1.4	-	2.7	-	-	0.2	1.7
1,200°C	39.3	26.6	30.5	0.1	0.1	0.9	-	-	0.0	-	2.4	-	-	-	0.1
1,250°C	39.4	22.5	34.6	0.1	0.4	0.1	-	-	0.8	-	1.8	0.2	-	-	0.2
Hydrothermal calcination															
1,050°C	10.7	14.2	20.4	0.8	0.7	4.6	8.5	5.9	8.9	9.8	6.9	1.2	6.7	0.7	-
1,150°C	25.4	30.1	12.7	1.5	0.7	2.0	-	-	12.0	11.7	3.8	-	0.1	-	-

For hydrothermal-calcination, main hydrothermal products are monosulfate ($C_4A\hat{S}H_{12}$) and siliceous hydrogarnet (C_3ASH_4). After calcination at 1,050°C, the hydrothermal products are decomposed to form $C_4A_3\hat{S}$ and C_2S. Gehlenite and ternesite ($C_5S_2\hat{S}$) are also found at this temperature. When the temperature increases to 1,150°C, $C_4A_3\hat{S}$ and C_2S increase, while the contents of calcium aluminate phases decrease. At the same firing temperature, clinkers obtained from clinkering yield higher $C_4A_3\hat{S}$ contents than those from hydrothermal-calcination, while C_2S contents are comparable. C_4AF is the preferred calcium aluminate phase in hydrothermal calcination, while clinkering leads to the formation of CA and CA_2.

Table 3 shows the quantitative XRD of CŜAB clinkers with 1.0-2.0 mass-% of NaF and CaF_2 obtained at 1,150°C. For the samples done by clinkering, $C_4A_3\hat{S}$ and C_2S decrease, and gehlenite increases with higher additions of NaF and CaF_2. On the contrary, the dopants significantly improve the formation of $C_4A_3\hat{S}$ using hydrothermal-calcination. Additions of 1 mass-% of NaF and CaF_2 gave higher $C_4A_3\hat{S}$ and C_2S than 2 mass-%. Ye'elimite and belite contents obtained from hydrothermal-calcination are comparable to those using clinkering when 1 mass-% dopants were applied. NaF and CaF_2 play a great role on a decrease in activation energy for cement phase formation. Ternesite disappears and hence more calcium sulfate is available for ye'elimite formation. It is worth noting here that the XRD reflections of β-C_2S are slightly shifted with addition of dopants.

Table 3 Quantitative XRD of clinkers with dopants obtained from clinkering and hydrothermal calcination at 1,150°C

Dopants	$C_4A_3\hat{S}$	C_2S	C_2AS	C_3S	C_3A	$C_{12}A_7$	CA	CA_2	C_4AF	$C_5S_2\hat{S}$	$C\hat{S}$	CaO	SiO_2	MgO	Fe_2O_3	Fe_3O_4	$C_{10}S_3\hat{S}_3(OH,F,Cl)_2$
Clinkering																	
No dopant	38.4	28.3	13.4	1.0	-	0.9	10.5	1.7	1.4	-	2.7	-	0.2	1.7	-	-	-
1 mass-% NaF	17.4	20.0	48.5	1.2	1.1	3.5	-	-	0.4	-	1.0	-	-	-	-	3.3	3.6
2 mass-% NaF	12.8	22.3	46.8	1.2	1.0	6.6	-	-	1.6	-	-	-	-	-	0.3	3.7	3.8
1 mass-% CaF_2	29.1	16.4	41.3	1.2	0.5	0.4	-	-	2.7	-	2.1	-	-	-	-	3.4	2.9
2 mass-% CaF_2	31.4	18.8	33.0	0.0	0.8	3.1	-	-	1.7	-	1.1	-	-	-	-	4.0	6.2
Hydrothermal-calcination																	
No dopant	25.4	30.1	12.7	1.5	0.7	2.0	-	-	12.0	11.7	3.8	0.1	-	-	-	-	-
1 mass-% NaF	37.2	27.8	25.5	1.6	1.2	-	-	-	1.5	-	1.7	-	-	-	0.2	3.3	-
2 mass-% NaF	34.9	26.1	27.6	1.5	0.9	-	-	-	4.2	-	1.7	-	-	-	0.1	3.0	-
1 mass-% CaF_2	37.9	32.4	20.1	1.0	1.3	-	-	-	1.4	-	2.2	-	-	-	0.3	3.4	-
2 mass-% CaF_2	30.7	23.8	33.0	0.3	1.0	-	-	-	2.0	-	2.1	-	-	-	0.0	3.5	3.54

3.2 Hydration

The synthesized CŜAB clinkers were mixed with FGDG allowing the full reaction of ye'elimite and calcium aluminate phase to ettringite according to equations (1) and (2) using w/c = 0.5. Heat of hydration and hydration products as determined by XRD are shown in Fig. 1. The heat flow of the samples obtained by clinkering shown in Fig. 1 (a), with 1.0 mass-% of CaF_2 that contained lower ye'elimite content than the non-doped sample, shows a faster early kinetics (both 1st & 2nd peaks). The doped sample shows an additional 3rd peak. Moreover, the cumulative heat of the sample doped with 1.0 wt% CaF_2 is higher than for the reference. For the hydrothermally calcined clinkers doped with 1 wt% of NaF and CaF_2, as shown in Fig. 1 (b), a significant difference in dissolution peak intensity is revealed than for the samples obtained by calcination despite the same ye'elimite content. However, the non-doped sample, which contains a lower ye'elimite content, shows the highest intensity of the first peak, probably due to the presence of C_4AF and ternesite. The clinkers generated by hydrothermal-calcination show a higher heat flow than those made by clinkering, particularly for the first peak. Related to the second peak, the undoped sample is faster than the doped samples. The hydration of these clinkers has to be explored in more details in order to understand their behaviors correctly. Main hydration product of all samples is ettringite ($C_6A\hat{S}_3H_{32}$).

$C_4A_3\hat{S} + 2C\hat{S}H_2 + 34H \rightarrow C_6A\hat{S}_3H_{32} + 2AH_3$ (1) and $3CA + 3C\hat{S}H_2 + 32H \rightarrow C_6A\hat{S}_3H_{32} + 2AH_3$ (2)

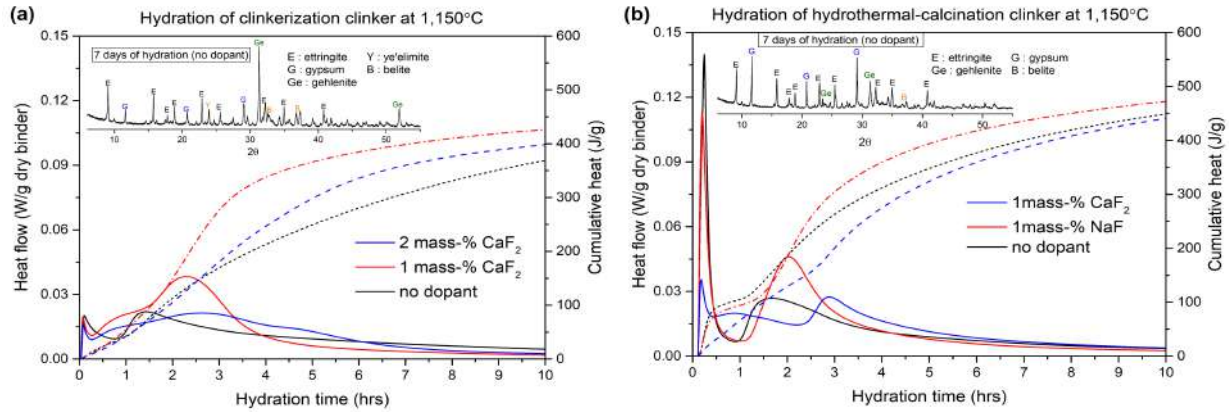


Figure 1 Heat flow curves (0-10 hrs) and hydration products (7 days) of clinkers obtained from clinkerization (a) and hydrothermal-calcination (b)

3. Conclusions

Ye'elimite and β-C_2S are the main phases obtained from both conventional clinkering and hydrothermal-calcination at 1,150°C using BA and FGDG as main starting materials. NaF and CaF_2 doping tends to increase ye'elimite content in hydrothermal calcination, but increase gehlenite content in conventional clinkering. The doped clinkers also tend to undergo faster hydration than the non-doped clinkers.

Acknowledgements

This research was financially supported by the Thailand Graduate Institute of Science and Technology (TGIST) and the Center of Excellence in Materials Science and Technology, Faculty of Science, Chiang Mai University.

References

Ben Haha, Mohsen, Frank Winnefeld, and Alexander Pisch. (2019). "Advances in Understanding Ye'elimite-Rich Cements." *Cement and Concrete Research* 123 (September): 105778.

Chen, Irvin A., and Maria C.G. Juenger. 2012. "Incorporation of Coal Combustion Residuals into Calcium Sulfoaluminate-Belite Cement Clinkers." *Cement and Concrete Composites* 34 (8): 893–902.

De la Torre, Ángeles G., Antonio J. M. Cuberos, Gema Álvarez-Pinazo, Ana Cuesta, and Miguel A. G. Aranda. (2011). "In Situ Powder Diffraction Study of Belite Sulfoaluminate Clinkering." *Journal of Synchrotron Radiation* 18 (3): 506–14.

El Khessaimi, Y., Y. El Hafiane, A. Smith, R. Trauchessec, C. Diliberto, and A. Lecomte. (2018). "Solid-State Synthesis of Pure Ye'elimite." *Journal of the European Ceramic Society* 38 (9): 3401–11.

Kacimi, Larbi, Angélique Simon-Masseron, Abdelhamid Ghomari, and Zoubir Derriche. (2006). "Influence of NaF, KF and CaF_2 Addition on the Clinker Burning Temperature and Its Properties." *Comptes Rendus Chimie* 9 (1): 154–63.

Kramar, S., L. Žibret, E. Fidanchevska, V. Jovanov, B. Angjusheva, and V. Ducman. (2019). "Use of Fly Ash and Phosphogypsum for the Synthesis of Belite-Sulfoaluminate Clinker." *Materiales de Construcción* 69 (333): 176.

Nabila Bouha, Faiza, Larbi Kacimi, and Angeles G. De la Torre. (2022). "Manufacture of Rich-Sulfoaluminate Belite Cement at Low Temperature from Waste Mixture by Dry and Hydrothermal Processes." *Construction and Building Materials* 314 (January): 125641.

Pimraksa, Kedsarin, and Prinya Chindaprasirt. 2018. "Sulfoaluminate Cement-Based Concrete." In *Eco-Efficient Repair and Rehabilitation of Concrete Infrastructures*, 355–85. Elsevier.

Rungchet, A., P. Chindaprasirt, S. Wansom, and K. Pimraksa. (2016). "Hydrothermal Synthesis of Calcium Sulfoaluminate–Belite Cement from Industrial Waste Materials." *Journal of Cleaner Production* 115 (March): 273–83.

Rungchet, A., C.S. Poon, P. Chindaprasirt, and K. Pimraksa. (2017). "Synthesis of Low-Temperature Calcium Sulfoaluminate-Belite Cements from Industrial Wastes and Their Hydration: Comparative Studies between Lignite Fly Ash and Bottom Ash." *Cement and Concrete Composites* 83 (October): 10–19.

Winnefeld, Frank, and Barbara Lothenbach. (2010). "Hydration of Calcium Sulfoaluminate Cements - Experimental Findings and Thermodynamic Modelling." *Cement and Concrete Research* 40 (8): 1239–47.

The 16th International Congress on the Chemistry of Cement 2023 (ICCC2023)
"Further Reduction of CO_2 -Emissions and Circularity in the Cement and Concrete Industry"
September 18–22, 2023, Bangkok, Thailand

CO_2 mineralization of silicate minerals and the potential inhibiting effect of amorphous silica-rich surface layers

K. Coopamootoo[1*] and C.E. White[1]

[1] *Department of Civil and Environmental Engineering, and Andlinger Center for Energy and the Environment, Princeton University, Princeton, United States*

Email: kumaran.coop@princeton.edu, whitece@princeton.edu

ABSTRACT
The production of Portland cement clinker occurs by the decomposition of calcite ($CaCO_3$) in limestone, and this leads to 5-8% of anthropogenic CO_2 emissions. CO_2 mineralization of cement-based silicate constituents, including non-Portland cement clinker phases such as wollastonite ($CaSiO_3$), can be thought of as the reverse of this reaction and a technique that, if well-understood and tailored, could achieve significant CO_2 uptake to help counterbalance emissions from limestone decomposition. Mineralization occurs through the extraction of calcium cations from silicates dissolving in an aqueous environment and subsequent $CaCO_3$ precipitation. However, as cations are extracted, a structural rearrangement occurs at the surface of partially reacted silicate grains forming amorphous silica-rich surface layers (ASSLs). The ASSLs can inhibit further cation extraction and ultimately, the efficiency of mineralization. Very little is known about the conditions necessary to form ASSLs, their characteristics, or properties. In this work, we investigate the formation, resultant structure and properties of ASSLs when synthesized crystalline γ-belite (γ-C_2S or γ-$CaSiO_4$) dissolves in an acidic environment. γ-C_2S is hydraulically inactive and is therefore a candidate for CO_2 mineralization, which is similar to that of $CaSiO_3$ and naturally abundant $(Mg,Fe)_2SiO_4$ (olivine). Here, we map out the relationship between solution composition during the dissolution of γ-C_2S, and the composition and some structural characteristics of the residual solids left post-dissolution. Such findings aid in determining which dissolution conditions form ASSLs and which ones can best mitigate their formation during CO_2 mineralization of γ-C_2S and other important silicate minerals.

KEYWORDS: *CO_2 mineralization, γ-belite, dissolution, surface layers*

1. Introduction

Anthropogenic CO_2 emissions, such as from Portland cement manufacture, contribute significantly to global warming. One solution to reduce and maintain atmospheric CO_2 at a lower level is the sequestration of CO_2, and one such technique, known as mineralization, involves its reaction with silicate minerals to form stable carbonates (Krevor and Lackner (2011)). Silicate minerals are abundantly present within the Earth's crust, e.g., as olivine, and constitute some of the main hydraulic phases of Portland cement. The non-hydraulic silicate γ-C_2S, whose reaction with CO_2 is akin to the CO_2 mineralization of olivine, forms the basis of this study. γ-C_2S has a strong affinity for CO_2 adsorption (Goto et al. (1998), Fang et al. (2016)) and this has been exploited in the design of some new sustainable cements such as the one reported by Higuchi et al. (2014) composed of fly ash and γ-C_2S, and the ordinary Portland cement (OPC), α-quartz and γ-C_2S system reported by Saito et al. (2007). However, past studies have mostly focused on the application of γ-C_2S, without delving deeply into the CO_2 mineralization mechanism itself. The first step in the mineralization process of γ-C_2S is the dissolution of the silicate mineral, typically in acidic to neutral environments, during which its orthorhombic crystalline structure is broken down. The metal cation Ca^{2+} and a portion of the silica leach into solution; the remaining silica undergoes polymerization, thereby forming a barrier between the mineral surface and the solution (Wild et al., 2019). This barrier, known as amorphous silica-rich surface layers (ASSLs), hinders further dissolution of the primary silicate mineral (Oelkers et al., 2018). It has been suggested that this hindrance occurs by a decrease in the transport of aqueous species through ASSLs, with soluble reactants (e.g., H^+ ions) being

unable to reach the mineral surface while product species accumulate near the surface leading to local solution saturation (Wild et al., 2019). To mitigate the effect of ASSLs on dissolution, an understanding of their formation and properties is necessary, and specifically how these relate to the species present in the reaction mixture and the reaction conditions.

The aim of this study is to correlate the chemistry of the solution during the dissolution of γ-C_2S with the properties of the ASSLs. We start by synthesizing γ-C_2S, which is subsequently characterized by X-ray diffraction (XRD). Then, a portion of this γ-C_2S is dissolved in an acidic environment. The solid residue (if present) is analyzed using Fourier-transform infrared spectroscopy (FTIR), small-angle X-ray scattering (SAXS) and scanning electron microscopy (SEM). Overall, this study offers some insight into which solutions can potentially lead to the formation of ASSLs when γ-C_2S dissolves, as well as some first results on their properties. The next steps in our research will involve investigating the effects of temperature and pressure on the properties of the ASSLs formed on γ-C_2S.

2. Methodology

2.1 Synthesis of γ-C_2S

96% pure $Ca(OH)_2$ and 99.8% pure amorphous SiO_2 (both in powder form) were sourced from Sigma-Aldrich. The two materials were mixed at a ratio of 2:1 M in a Retsch Planetary Ball Mill PM 100 for 3 h using a zirconia-based container and beads. The resulting mixture was heated in a crucible inside a box furnace at a rate of 10 ºC/min to 1400 ºC, after which it was held at this temperature for 3 h and then allowed to cool down at a rate of 5 ºC/min. XRD patterns of the sample before and after calcination were obtained using a Bruker D8 Advance diffractometer and Cu-radiation; this data is shown in Figure 1. The internal standard CaF_2 was also added to a portion of the sample before carrying out XRD to determine sample purity (i.e., degree of crystallinity). The crystallinity was found to be dependent on the cooling rate applied in the furnace, with 5 ºC/min producing the highest percentage of crystalline γ-C_2S at ~97%.

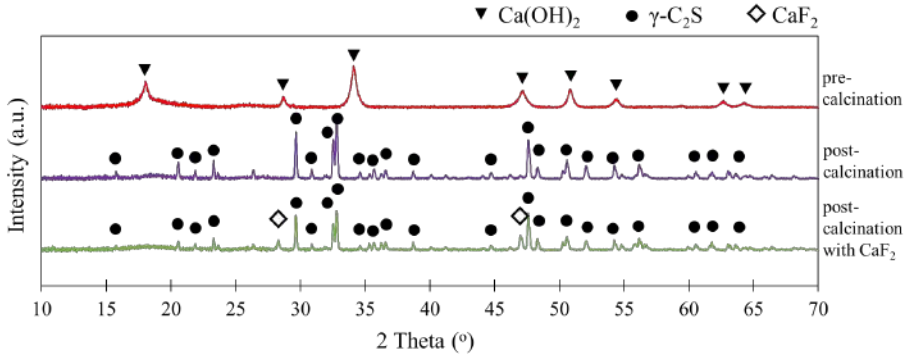


Figure 1: XRD patterns of γ-C_2S (γ-Ca_2SiO_4) after ball-milling, post-calcination and post-calcination with CaF_2

The Brunauer–Emmett–Teller (BET) technique was used to determine the surface area of the γ-C_2S sample (using a Micromeritics 3Flex instrument and N_2 as the analysis gas), resulting in a value of 0.40 m^2/g.

2.2 Dissolution of γ-C_2S and Characterization of ASSLs

1 g of γ-C_2S was dispersed in an acidic medium. This consisted of 500 ml of Milli-Q water, whose pH was adjusted with HCl (37% assay, sourced from Sigma-Aldrich), held at 80 ºC in polytetrafluroethylene (PTFE) reactors. For this study, the effects of solution pH 1 and 2 were investigated due to these conditions being likely to lead to extensive formation of ASSLs (Wild et al., 2019). The dissolution experiment ran for a duration of 1 h. During this time, the solution was continually stirred. After dissolution, the solid residue was separated from the supernatant via filtration. Then, the filter paper was washed with Milli-Q water to detach the residue from it. Finally, the residue-water solution was centrifuged, and the excess liquid decanted. This process (filter, wash, centrifuge) was deemed necessary since initial trials failed to obtain sufficient residue directly from the filter paper. The resulting slurry was mildly dried in the oven at 30ºC for 2 h. The slurries from the pH 1 and 2 solutions were named S1 and S2 respectively for ease of comparison. Their composition was analysed using ATR-FTIR on a PerkinElmer Frontier Spectrometer, while some structural details were uncovered using SAXS on a

Xeuss 3.0 instrument. The filtrate was also preserved, but for characterization purposes beyond the scope of this paper.

3. Results and Discussion

3.1 Silicate connectivity of γ-C_2S and slurries S1 and S2

Figure 2 presents the FTIR spectra of γ-C_2S, S1 and S2. Altogether, the spectra present multiple intense bands between 810 cm^{-1} and 1200 cm^{-1}. These can be ascribed to the different modes of [SiO_4]-tetrahedra, which can accommodate between 0 to 4 non-bridging oxygen atoms, i.e., have only Si-O-Si groups, Si-O^- groups or a combination of both (Van Herk et al. (1989), Park et al. (2002)). The spectrum of γ-C_2S closely matches the one of olivine (Van Herk et al., 1989) in terms of the shapes and positions of the bands between 810 cm^{-1} and 930 cm^{-1}. The latter are associated to the stretching vibrations of Si-O^- groups, which is a key feature of the orthorhombic crystalline structure. The sharpness of these bands typically correlates to the presence of calcium in the structure (Park et al. (2002)). The spectrum of S2 is almost identical to that of γ-C_2S; this could mean that following dissolution at pH 2 for 1 h, S2 still contained a high proportion of unreacted γ-C_2S. On the other hand, the features linked to the Si-O^- group are absent in the spectrum of S1, and this suggests that no γ-C_2S was left following its dissolution. According to Ellerbrock et al. (2022), the band between 1050 cm^{-1} and 1200 cm^{-1} correlates to the asymmetric stretching vibration of Si-O-Si. Park et al. (2002) associated the wavenumbers in this region to [SiO_4]-tetrahedra with 0 non-bridging oxygen atoms for completely polymerized silica structures, and Van Herk (1989) obtained a similar spectrum for amorphous silica. During dissolution, once Ca^{2+} ions are extracted from γ-C_2S, Si-O-Si groups typically form as the remaining SiO_4^{4-} anions polymerize, thereby resulting in silica in solution and ASSLs at the surface of the γ-C_2S grains. Here, it is unclear if the band associated with polymerized silica in S1 is attributed to ASSLs, silica that had precipitated in solution during the dissolution reaction, or both.

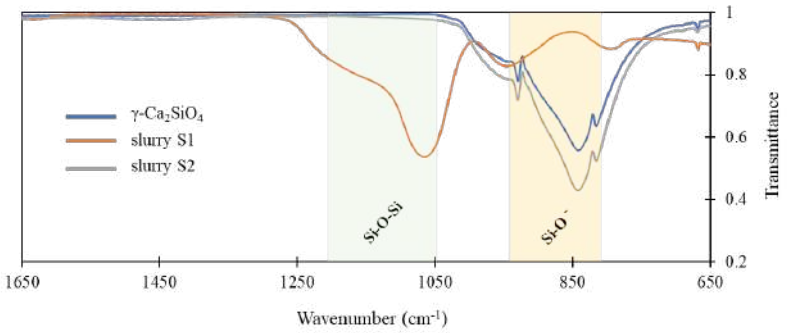


Figure 2: FTIR spectra of γ-C_2S (γ-Ca_2SiO_4) and the dried slurries

3.2 Nanostructural characteristics of γ-C_2S and slurries S1 and S2

Figure 3a illustrates the SAXS distributions of γ-C_2S, S1 and S2, measured across four configuration modes (extra-small, small, medium and wide angles) and combined, to cover an extensive q-range. This typically allows the interpretation and modelling of some key structural features. All the curves in Figure 3a exhibit a change in gradient between q = 0.003 A^{-1} and 0.005 A^{-1}, where they shift from an apparent Guinier regime (at lower q) to the Porod regime. Using the Unified scattering function, which combines Guinier's law reflecting the size of the grain features and Porod's law based on the structure of the same features (Beaucage, 1995), we modeled this region using the 'Unified fit' module of the XSACT software. The modeled curves are shown in the inset in Figure 3a. Assuming that these features are smooth and spherical, we derived their radii of gyration (R_g) as 88.4 nm, 73.4 nm and 82.9 nm for γ-C_2S, S1 and S2 respectively. However, Guinier's law is only valid when $q_{min}R_g < 1.3$, and this is not satisfied for the derived R_g values (e.g., 0.003 $Å^{-1}$ × 734 Å = 2.2). Insight on features within this length scale (~50-100 nm and larger) requires the use of ultra-small angle scattering or electron microscopy techniques. As seen in Figure 3b-d, electron microscopy images reveal γ-C_2S grains of at least 5 µm in size, where the grains present multiple irregular facets, defects and cracks at a scale of ~10-100 nm (Figure 3c). An additional Guinier region is present in S1 at q ~ 0.02 A^{-1}, shown by the shaded green region in Figure 3a. Using the same model and assumptions as before, the radius of gyration of the corresponding feature in S1 was derived as ~10.9 nm. According to Figure 3d, we believe that this feature could be due to a porous

silica structure. However, additional investigation is required to determine if the characteristic size (~10.9 nm) is associated with nanosized pores or the silica morphology (i.e., size of fundamental silica particle).

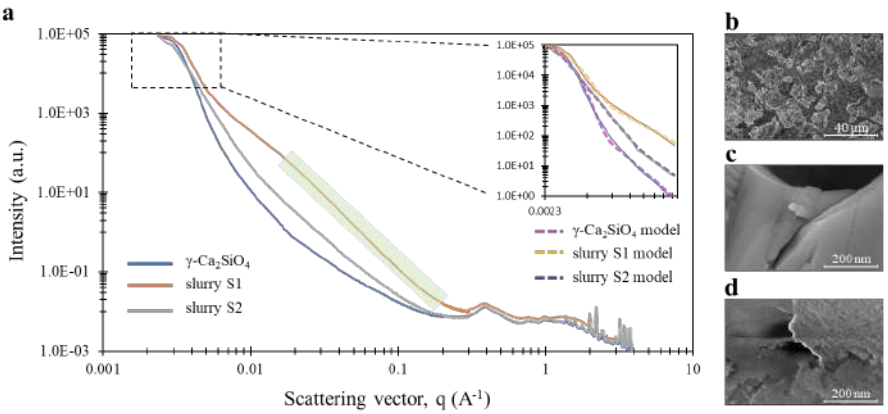


Figure 3: a. SAXS curves of γ-C_2S (γ-Ca_2SiO_4) and the dried slurries. Inset shows the Unified-fit model of the lower q-range. The green shaded region outlines the higher q-Porod regime of S1; SEM images showing b. γ-C_2S grains; c. the features on the γ-C_2S grains; d. the porous structure in S1

4. Conclusions

The aim of this investigation was to determine the effect of solution composition on the dissolution of γ-C_2S using acid solutions at pH 1 and 2, and the formation of amorphous silica-rich surface layers (ASSLs). We tested the residual solids with FTIR and SAXS, showing that pH 1 led to maximum dissolution of γ-C_2S and the formation of polymerized silica, where any ASSLs that could have formed were indistinguishable from silica. On the other hand, minimal dissolution of γ-C_2S occurred at pH 2. From SAXS it was discovered that polymerized silica identified in the pH 1 system contained features of size ~10.9 nm (radius of gyration) which could be indicative of pore size or other morphological features. As a next step, small-angle neutron scattering (SANS) will be used to determine if pores or solid morphological features are responsible for the characteristic size seen using SAXS. Efforts to separate ASSLs from precipitated silica in solution will also be undertaken.

References

Beaucage, G. (1995) "Approximations Leading to a Unified Exponential/Power-Law Approach to Small-Angle Scattering", *Journal of Applied Crystallography*, 28(6): 717-728

Ellerbrock, R., Stein, M. and Schaller, J. (2022) "Comparing Amorphous Silica, Short-Range-Ordered Silicates and Silicic Acid Species by FTIR", *Scientific Reports*, 12(11708)

Fang., Y., Chang, J. and Shang, X. (2016) "The Role of β-C_2S and γ-C_2S on Carbon Capture and Strength Development", *Materials and Structures*, 49(10): 4417-4424

Goto, S., Nakamura, A and Ioku, K. (1998) "Hardening of Calcium Silicate Compounds by Carbonation", *Muki Materiaru*, 5(272): 22-27

Higuchi, T., Morioka, M., Yoshioka, I. and Yokozeki, K. (2014) "Development of a New Ecological Concrete with CO_2 Emissions Below Zero", *Construction Building Materials*, 67: 338-343

Krevor, S.C.M. and Lackner, K.S. (2011) "Enhancing Serpentine Dissolution Kinetics for Mineral Carbon Dioxide Sequestration", *International Journal of Greenhouse Gas Control*, 5(4): 1073-1080

Oelkers, E.H., Declercq, J., Saldi, G.,D., Gislason, S.R. and Schott, J. (2018) "Olivine Dissolution Rates: A Critical Review", *Chemical Geology*, 500: 1-19

Park, J.H., Min D.J. and Song, H.S. (2002) "FT-IR Spectroscopic Study on Structure of $CaO-SiO_2$ and $CaO-SiO_2-CaF_2$ Slags", *ISIJ International*, 42(4): 344-351

Saito, T., Sakai, E., Morioka, M. and Daimon, M. (2007) "Carbonation Reaction of Calcium Silicate Hydrates by Hydrothermal Synthesis at 150°C in OPC-γ-C_2S-α-quartz Systems", *Journal of Advanced Concrete Technology*, 5(3): 333-341

Van Herk, J., Pietersen, H.S. and Schuiling, R.D. (1989) "Neutralization of Industrial Waste Acids with Olivine – The Dissolution of Forsteritic Olivine at 40-70°C", *Chemical Geology*, 76: 341-352

Wild, B., Daval, D., Micha, J., Bourg, I.C., White, C.E. and Fernandez-Martinez, A. (2019) "Physical Properties of Interfacial Layers Developed on Weathered Silicates: A Case Study Based on Labradorite Feldspar", *The Journal of Physical Chemistry C*, 123(40): 24520-24532

The 16th International Congress on the Chemistry of Cement 2023 (ICCC2023)
"Further Reduction of CO_2 -Emissions and Circularity in the Cement and Concrete Industry"
September 18–22, 2023, Bangkok, Thailand

Two-Step Synthesis of Low-Lime Cement and its Hydration

R. Siauciunas[1]*, A. Eisinas[1], D. Rubinaite[1], and I. Gedeike[1]

[1] *Department of Silicate Technology, Faculty of Chemical Technology,*
Kaunas University of Technology, Radvilenu pl. 19, Kaunas LT-50254, Lithuania
*Email: *raimundas.siauciunas@ktu.lt; anatolijus.eisinas@ktu.lt; dovile.rubinaite@ktu.lt; inga.knabikaite@ktu.lt*

ABSTRACT

Ordinary Portland cement (OPC) industry is responsible for 5–7% of global annual greenhouse gas emissions. The search for alternative cementitious materials with a lower CO_2 footprint is one of the major challenges that the cement industry and the scientific community have been facing in the past decades. Thus, this work examines the possibility of creating environmentally friendly (low lime) binders by combining hydrothermal synthesis and mechanochemical/thermal activation at low temperatures. The work aimed to obtain a complex effect: to increase the reactivity of Ca/Si/Al composite compounds and the stability of their active modifications.

In the course of activities, calcium silicate hydrate (α-C_2SH, $Ca_2(HSiO_4)(OH)$) and calcium aluminate (katoite; $Ca_3Al_2[(OH)_4]_3$) were synthesised under hydrothermal conditions. For the initial mixtures, the prepared precursors were blended (90-100% of α-C_2SH and 0–10% of katoite) and quartz sand (1:1 by mass) was added. The mixtures were activated: 1) mechanically (5 min, 950 rpm) or 2) mechanochemically/thermally (30 min, 450 °C), and used for further research. The mineral composition of the formed complex binders, its physical and chemical properties, as well as the values of the heat flow and cumulative heat during hydration, were determined. The results demonstrate that this technology allows for the loosening of additional molecular bonds and increases the reactivity of the compounds.

KEYWORDS: *low-lime cement, hydrothermal synthesis, α-C_2SH and katoite activation, heat flow*

1. Introduction

Today, global manufacturing of widely used OPCs accounts for 5–7% of global greenhouse gas emissions (Andrew (2019)) and tools used as clinker additives (Panesar and Zhang (2020)), alternative fuels (Chatterjee and Sui (2019)), energy cost optimization (Nidheesh and Kumar (2019)), and engineering solutions (Haber *et al*. (2010)) have already reached a level, which shows that further investments are not economically viable. For this reason, the strategic direction of research worldwide is to create an alternative to OPC binders with analogous mechanical and durability properties.

In recent years, Limestone Calcined Clay Cements (LC_3) have been developed. LC_3 is an innovative blended PC that includes the additives of metakaolin and limestone (Scrivener *et al.* (2018)). The problem is that kaolinite clays are widespread only in some regions of the world. Therefore, it is necessary to look for other ways to reduce CO_2 emissions. One of them is the production of binding materials with a lower molar ratio of CaO/SiO_2 (Gartner and Siu (2018)), in which the main mineral would be not alite $3CaO\cdot SiO_2$, but belite $2CaO\cdot SiO_2$. This would allow 15 to 20% of energy savings during the production and require ~ 25% less raw materials that contain carbonate (Mohamed *et al.* (2018)). Accordingly, a lower amount of CO_2 would be emitted into the environment. Unfortunately, this approach faces two issues: 1) the energy consumption and CO_2 emissions are not reduced enough to meet the IEA's target, i.e., for the cement industry to reduce its emissions from 2.0 Gt to 1.55 Gt by 2050 (IEA (2018)); 2) in the initial stages of hydraulic hardening, the mechanical strength of belite is low (Ludwig and Zhang (2015)).

To tackle the first problem, it is important to investigate the feasibility of producing concrete in which the binder is calcium silicate hydrates instead of anhydrous calcium silicate. In this case, high temperature synthesis is no longer needed (Link *et al.* (2015)). The most promising compound at this point is α-C_2SH. This mineral can be obtained during the hydrothermal synthesis at 130–220 °C from raw materials rich in limestone and silica (Richarson (2008)). Unfortunately, α-C_2SH has no hydraulic binding properties.

Garbev et al. (2014) proposed one of the ways to activate this mineral: the principle covers intense milling of α-C_2SH with a silica-rich compound, which plays the role of micro-milling bodies (mechanochemical activation). This method allows the disruption of the hydrogen bonds. Link *et al.* (2015) suggested another activation method – a hydraulic binder production by calcinating the synthesized α-C_2SH. The results indicated that given the calcination temperature of 420 °C, α-C_2SH converts into γ-C_2S, amorphous phase, and x-C_2S, of 600 °C – into β-C_2S. Nevertheless, the second problem remains. Belite is characterized by substantially lower hydraulic activity and contributes to concrete strength only in later ages. In the case of OPC, the aluminate phase provides the initial strength, which is not present in the mentioned belite cements. Therefore, this work attempts to solve this problem by blending α-C_2SH with katoite and applying activation methods.

2. Research Outcomes

The task of the work: to develop a fast-curing and environmentally friendly hydraulic low-lime cement by combining hydrothermal synthesis of calcium silicates and aluminates hydrates and their mechanochemical/thermal activation at low temperatures.

2.1 Materials and Methods

Opoka and chalk marl samples were taken from Stoniskiai and Juodziai (Lithuania) quarries and milled in ball mill until specific surface area by Blaine S_a = 970 and 890 $m^2 \cdot kg^{-1}$, respectively. Chemical composition of the rocks is shown in Table 1. These raw materials were burnt at 825 °C for 2 h (until the $CaCO_3$ present in both these rocks decomposes) and a mixture with a molar ratio of CaO/SiO_2 = 2.0 was prepared from them. A product, in which the predominant compound is α-C_2SH (Fig. 1), was synthesized under hydrothermal conditions in autoclave (*Parr Instruments*, USA) (200 °C, 16 h, water/solid (W/S) = 10, stirred at 100 rpm). The conditions for the preparation of mixtures, their calcination, hydrothermal synthesis, and so on, are described in detail in our previous work (Siauciunas *et al.* (2014)).

Table 1. Oxide composition of Stoniskiai quarry opoka and Juodziai guarry chalk marl, wt%

Material	CaO	SiO_2	Al_2O_3	K_2O	MgO	Fe_2O_3	SO_3	Other	LOI
Opoka	30.69	38.70	2.38	0.56	0.93	1.03	0.65	0.42	24.64
Chalk marl	51.87	3.72	0.87	0.22	0.29	0.42	0.10	0.52	41.99

CaO and Al_2O_3 were obtained by burning reagents $Ca(OH)_2$ and $Al(OH)_3$ (*Sigma-Aldrich*, Germany) at 550 °C for 1 h or at 475 °C for 4 h, respectively. Katoite from the mixture with molar ratio of CaO/Al_2O_3 = 2.8 was synthesized under hydrothermal conditions too (130 °C, 4 h, W/S = 10 in unstirred suspension). These conditions were chosen according to previously published data (Eisinas *et al.* (2020)). The chemical composition of the raw materials was determined by X-ray fluorescence spectrometry (*Bruker X-ray S8 Tiger WD*, Germany; Rh tube with energy of up to 60 keV). Their mineral composition, as well as the composition of the synthesized samples, was investigated by X-ray diffraction analysis (*Bruker X-ray D8 Advance*, Germany; the range 2θ = 3–70° at a scanning speed of 6 $°\cdot min^{-1}$ was set). To determine the mineral quantitative composition, the research was supplemented with the Rietveld refinement method (10% ZnO additive was mixed into the samples, and *Diffrac.Topas 4.2* software was used). The thermal transformations taking place in the samples were investigated by the method of simultaneous thermal analysis STA (DSC–DTG; *Linseis PT1000*, Germany; N_2 atmosphere, 40–1000 °C, heating rate – 10 $°C\cdot min^{-1}$). The granulometric composition was determined with a *Cilas 1090 LD* analyser (France; sensitivity: 0.04–500 μm). Heat evolution rate of the samples during hydration was investigated using an eight-channel isothermal calorimeter TAM Air III (*TA Instruments*, USA).

2.2 Results and discussion

According to XRD data, calcite was the main mineral of opoka (Fig. 1, curve 1.) As well, four different modifications of SiO_2 were identified: quartz, cristobalite, tridymite and amorphous (from Rietveld refinement). After calcination at 825 °C for 2 h (Fig. 1, curve 2): $CaCO_3$ decomposition was almost complete, and a dominant amount of CaO was obtained. Also, during the process amorphous SiO_2, tridymite and cristobalite reacted (which led the formation of calcium silicates: wollastonite and calcium olivine), and only traces of quartz could be identified.

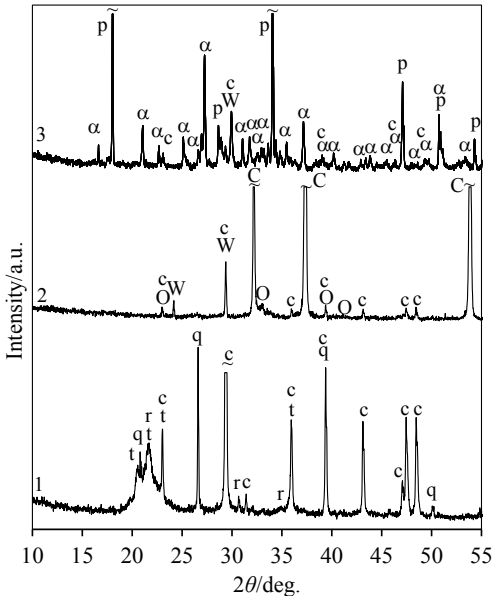


Fig. 1. XRD patterns of raw (*1*), burnt at 825 °C for 2 h (*2*) opoka and hydrothermal synthesis product (*3*). Indexes: C – CaO, c – calcite, q – quartz, t – trydimite, r – cristobalite, W – wollastonite, α – α-C_2SH, P – portlandite, O – calcium olivine

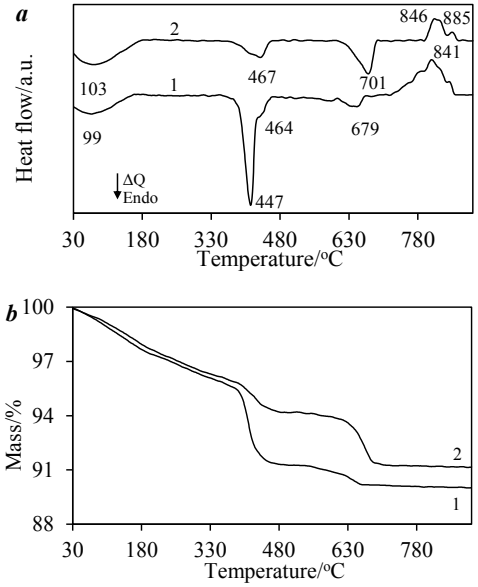


Fig. 2. DSC (*a*) and TG (*b*) curves of product synthesized from opoka and chalk marl mixture with CaO/SiO_2 = 2.0 at 200 °C for 16 h. 1 – product, 2 – the same after dissolving $Ca(OH)_2$ in distilled water

While analyzing the product of hydrothermal synthesis, which was obtained from the chalk marl–opoka mixture, somewhat unexpected XRD results were obtained. In addition to the main peak of α-C_2SH (d = 0.327 nm), very intense peaks were observed at d = 0.532 and d = 0.266 nm (Fig. 1, curve 3). They correspond to the crystallographic planes (002) and (004) (intensity growth occurs in the same crystallographic direction as the peak of portlandite d = 0.490 nm, which corresponds to the (001) plane). In order to avoid this phenomenon, the samples for XRD analysis were not pressed, but just spread freely in the sample's holder. The solution almost solved the data problem, as the obtained by STA showed.

The content of portlandite was determined by dissolving it in distilled water (W/S = 500). X-ray diffraction analysis confirmed that after 5 min, all $Ca(OH)_2$ had dissolved, because the peaks of portlandite were no longer identified in the curve. Additionally, it can be stated that a-C_2SH did not dissolve during the process, since the intensity of its characteristic peaks decreased by only 0.5%. The intensity of the endothermic effect in the temperature range of 420-460 °C significantly decreases (Fig. 2, a, curves 1 and 2). The mass loss was 4.61%, while that of the washed product was 1.84% (Fig. 2, b, curves 1 and 2). Mass balance calculations showed that the synthesis product contained 11.39% $Ca(OH)_2$. This correlates well enough with the data from the Rietveld analysis, which established that the product contained 13.44% portlandite.

Subsequently, to determine the influence of the mechanochemical and thermal activation processes on the hydraulic activity of the designed binding material, the following samples were prepared from synthesized calcium silicates and aluminates:

1. α-C_2SH mixture with sand (1:1 by mass), mechanochemical treatment at 950 rpm for 5 min;
2. the same as No. 1, additional thermal treatment at 450 °C for 0.5 h;
3. (90% α-C_2SH + 10% C_3AH_6) mixture with sand (1:1)
4. (90% α-C_2SH + 10% C_3AH_6) mixture with sand (1:1), mechanochemical treatment (950 rpm, 5 min);
5. the same as No. 4, additional thermal treatment at 450 °C for 0.5 h);

Their quantitative mineral composition is presented in Table 2, and the microcalorimetric data – in Fig. 3.

Table 2. Rietveld refinement data of samples after mechanochemical and thermal treatment

Phase composition*	Quartz	α-C_2SH	$CaCO_3$	$Ca(OH)_2$	Katoite	Wollastonite	Mayenite	Amorphous
Sample No. 3	51.12	13.91	2.10	6.72	4.59	6.96	-	14.12
Sample No. 4	46.19	12.66	1.93	5.35	4.68	7.33	-	21.42
Sample No. 5	52.12	7.47	2.52	3.74	-	10.16	8.53	15.00

*In all samples, the amount of 1.13 nm tobermorite ranged from 0.44 to 0.49% (not shown in the table)

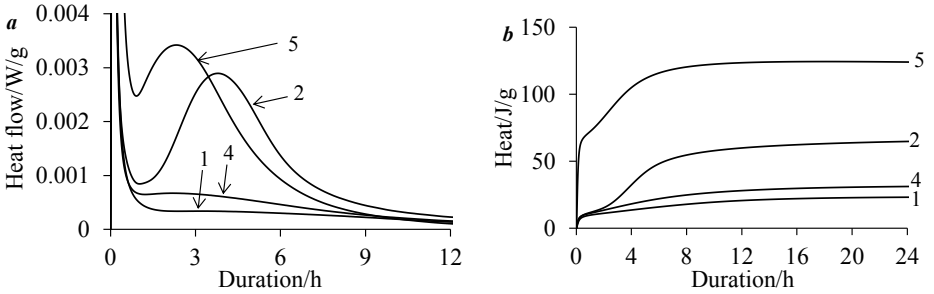


Fig. 3. Heat evolution rate (*a*) and cumulative heat (*b*) of the samples No. 1, 2, 4, and 5

It was investigated that the addition of katoite had a positive effect on the early stage of samples hydration, as it not only compensated for the altered amount of α-C_2SH, but also increased the heat flow (Fig. 3, *a*, curves 4 and 5) and amount of cumulative heat released (Fig. 3, *b*, curves 4 and 5). There is a possibility that fast curing binders can be obtained from such mixtures, but this remains to be verified in practice.

3. Conclusions

1. The work examines the possibility of increasing the hydraulic activity of composites obtained from calcium silicate and aluminate hydrates by means of mechanochemical or mechanochemical/thermal activation and preliminarily investigates their suitability for the production of a fast-hardening low-lime binder.
2. Katoite was found to significantly increase the amount of heat released during the hydration of the samples. Adding 10% of this compound to α-C_2SH increases cumulative heat from 22 to 31 J/g after intensive grinding with sand, and after additional burning at 450 °C – even up to 124 J/g.

Acknowledgements
This research was funded by a grant (No. S-MIP-21-4) from the Research Council of Lithuania.

References

Andrew, R.M. (2019) "Global CO_2 emissions from cement production, 1928–2018". *Earth System Science Data*
Chatterjee, A. and T. Sui T. (2019) "Alternative fuels – effects on clinker process and properties". *Cement and Concrete Research,* 123, No. 105777
Eisinas, A., *et al.* (2020) "Cu^{2+} ion adsorption by synthetic mayenite and its thermal stability". *Ceramics International,* 46(18): 29429-29435
Garbev, K., *et al.* (2014) "Preparation of a novel cementitious material from hydrothermally synthesized C–S–H phases. *Journal of the American Ceramic Society,* 97(7): 2298-2307
Gartner E. and Siu T. (2018) "Alternative cement clinkers". *Cement and Concrete Research,* 114: 27-39
Habert, G., *et, al.* (2010) "Cement production technology improvement compared to factor 4 objectives". *Cement and Concrete Research*, 40(5): 820-826
IEA (2018) "Technology Roadmap – Low-Carbon Transition in the Cement Industry", *IEA, Paris*
Link, T., *et al.* (2015) "Reactivity and phase composition of Ca_2SiO_4 binders made by annealing of alpha-dicalcium silicate hydrate". *Cement and Concrete Research*, 67: 131-137
Ludwig, H.M. and Zhang W. (2015) "Research review of cement clinker chemistry". *Cement and Concrete Research*, 78(A): 24-37
Mohamed, Y.A., *et al.* (2018) "Calculation of the formation process of clinker inside the rotary cement kiln", *Proceedings of the Voronezh State University of Engineering Technologies,* 80(1): 233-239
Nidheesh, P.V. and Kumar M.S. (2019). "An overview of environmental sustainability in cement and steel production", *Journal of Cleaner Production*, 231: 856-871
Panesar, D.K. and Zhang, R. (2020) "Performance comparison of cement replacing materials in concrete: Limestone fillers and supplementary cementing materials – A review". *Construction and Building Materials,* 251, No. 118866
Richardson, I.G. (2008) "The calcium silicate hydrates". *Cement and Concrete Research,* 38(2): 137-158
Scrivener, K., *et al.* (2018) "Calcined clay limestone cements (LC3)". *Cement and Concrete Research,* 114: 49-56
Siauciunas R., *et al.* (2014) "Tribochemical and thermal activation of α-C_2S hydrate as precursor for cementitious binders". *Journal of Thermal Analysis and Calorimetry*, 118: 817–823

The 16th International Congress on the Chemistry of Cement 2023 (ICCC2023)
"Further Reduction of CO_2 -Emissions and Circularity in the Cement and Concrete Industry"
September 18–22, 2023, Bangkok, Thailand

The optimal water conditions for the accelerated carbonation curing of cement-based materials incorporating dicalcium silicate

M. Ushiro[1, a*], T. Mori[1, b], M. Takase[2], K. Namiki[3], and S. Noda[2,3]

[1] *Omi Plant, Denka Co., Ltd., Itoigawa, Niigata, 949-0393, Japan*

[2] *Department of Applied Chemistry, Waseda University, 3-4-1 Okubo, Shinjuku-ku, Tokyo 169-8555, Japan*

[3] *Waseda Research Institute for Science and Engineering, Waseda University, 3-4-1 Okubo, Shinjuku-ku, Tokyo 169-8555, Japan*

[a] *masataka-ushiro@denka.co.jp,* [b] *taiichiro-mori@denka.co.jp*

ABSTRACT

To date, various technologies have been developed to reduce CO_2 emissions during cement production. CO_2 fixation in hardened concrete is one such technology, and γ-dicalcium silicate (γ-C_2S) has attracted attention as a key component of this process. γ-C_2S is a non-hydraulic mineral that readily undergoes carbonation and so can replace a portion of the cement, acting as a filler while generating porous concrete during the hydration process. As a result, carbonation readily progresses in the interior of the concrete and the extent of carbonation is increased. γ-C_2S can also react with CO_2 to improve the strength of concrete, analogous to cement hydration acting as a binder. Here, we examined the means of improving the practical applicability of this technique. The optimal conditions to accelerate the carbonation curing of γ-C_2S in the presence of water were determined and the effects of these conditions on the efficiency of carbonation and on end properties were evaluated. The data indicate that the carbonation depth, CO_2 concentration, and compressive strength can all be increased by adjusting the water content of the mortar/γ-C_2S mixture.

KEYWORDS: *γ-C_2S, CO_2 emissions, carbonation curing, CO_2 fixed concrete*

1. Introduction

The cement industry, which emits large amounts of CO_2 during processes such as clinkering, must develop innovative technologies to achieve carbon neutrality. One such technology involves converting CO_2 into solid minerals that might have applications as construction materials. Various processes have been reported but the commercial use of these techniques has been limited because of technical and market challenges (Li et al., 2022). Accelerated carbonation-cured concrete incorporating γ-dicalcium silicate (γ-C_2S), a non-hydraulic mineral that readily undergoes carbonation, is one example of this technology (Higuchi et al., 2014). However, achieving carbonation deep within concrete can be costly and time consuming; hence, improvements in the efficiency of carbonation are required. It has been suggested that water is important for the carbonation of γ-C_2S (Ushiro et al., 2014). The efficiency of water in carbonation curing has been evaluated indirectly by using humidity, which is relatively easy to control, as a parameter because the water content of concrete is usually determined by the mix design, curing conditions, and start time of carbonation. On this basis, we investigated the effect of water content on the carbonation reactivity of γ-C_2S under constant environmental conditions using dedicated batch-type equipment, and the effect of water content on the efficiency of mortar carbonation.

2. Materials and Methods

2.1 Materials

Table 1 summarizes the mineral compositions and physical properties of the ordinary Portland cement (OPC) and two different γ-C_2S compounds used herein. The pure γ-C_2S was manufactured from reagent

$CaCO_3$ and SiO_2 in an electric furnace. The other γ-C_2S, termed impure γ-C_2S herein, was manufactured from a by-product primarily containing $Ca(OH)_2$ and SiO_2 powder in a rotary kiln.

Table 1. Compositions and physical properties of the ordinary Portland cement (OPC) and γ-C_2S

Materials	Mineral composition (mass%)						Density (kg/m^3)	Specific surface (m^2/kg)
	C_3S	β-C_2S	C_3A	C_4AF	γ-C_2S	C_3S_2		
OPC	56.6	22.6	11.0	7.4			3160	339
Pure γ-C_2S	-	-	-	-	100	-	3000	306
Impure γ-C_2S	-	9.1	-	-	63.8	24.3	3040	226

2.2 Accelerated carbonation curing of pure γ-C_2S

The effect of water in terms of accelerating the carbonation curing of pure γ-C_2S was evaluated using the apparatus shown in Figure 1. During these trials, a sample cell and CO_2 reservoir were positioned in a temperature-controlled chamber. Pure γ-C_2S was then mixed with a specific amount of water in the sample cell, with air pumped out to produce a vacuum, after which, the CO_2 reservoir was used to fill the sample cell with pure CO_2 gas. The chamber was subsequently heated to 30 °C, and valve A was opened to initiate carbonation curing of the pure γ-C_2S. The degree of carbonation of each sample was determined by first calculating the initial quantity of CO_2 in the CO_2 reservoir based on pressure using the ideal gas law ($PV = nRT$). The initial partial pressure and mass of CO_2 in the chamber (P and M) and the same quantities at a later time (P′ and M′) were related as follows: $P/M = P'/M'$. Pressure change related to water evaporation was measured by supplying Ar instead of CO_2, and the result was used to derive P and P' of CO_2 from the total pressure in the carbonation experiment. The amount of CO_2 reacted with the pure γ-C_2S was calculated based on the difference between the residual quantity of CO_2 obtained above and the initial amount. This value was divided by the initial pure γ-C_2S mass to give the amount of fixed CO_2 per unit mass of specimen.

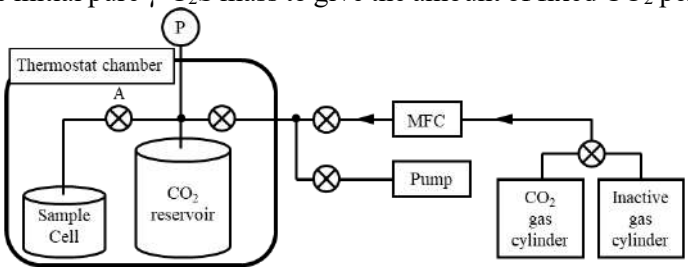


Figure 1. Diagram of the batch-type accelerated carbonation curing apparatus.

2.3 Accelerated carbonation curing of hardened cement paste with impure γ-C_2S

The cement paste employed in this study was formulated with powder consisting of 50% cement and 50% impure γ-C_2S, and a water to powder ratio of 0.5. In each trial, a quantity of paste was transferred into a mold (4 × 4 × 0.5 cm) that was then sealed and cured at 20 °C for 24 h. After demolding, the specimen was immersed in acetone under reduced pressure to prevent hydration and remove unreacted water, then dried for 24 h in an oven at 40 °C. The dried samples were divided into small pieces and a specific quantity of water was then added to each piece to adjust the water content artificially; each piece was transferred in turn into the equipment shown in Figure 1, and finally, the carbonation of each piece was evaluated following exposure to a specific amount of CO_2 at 30 °C using the same procedure outlined in Section 2.2.

2.4 Accelerated carbonation curing of mortar with impure γ-C_2S

The mortar used in this work was formulated with powder consisting of 50% cement and 50% impure γ-C_2S, a water to powder ratio of 0.5, and a powder to sand ratio of 3. In these trials, a quantity of mortar was transferred into a mold (4 × 4 × 16 cm) that was then sealed and cured at 20 °C for 24 h. After demolding, the specimen was dried using the same procedure outlined in Section 2.3. A specific amount of water was then added to each dried specimen to adjust the water content artificially. Accelerated carbonation curing was carried out in the curing tank at 40 °C in an atmosphere containing 20% CO_2 at 90% relative humidity. After 3 and 7 days of accelerated carbonation curing, the carbonation depth, CO_2 content, and compressive strength were evaluated. Carbonation depths were determined using a phenolphthalein solution; this was

sprayed on a cross-section of each sample and the portion that did not change color was considered to represent the carbonated area. The CO_2 content was obtained using an inorganic carbon analyzer in conjunction with a colorimetric procedure, whereby the CO_2 generated by dropping hydrochloric acid onto the sample was trapped in a liquid and quantified using titration. The compressive strength of each mortar specimen was ascertained based on the JIS R 5201 procedure.

3. Results and Discussion

3.1 Effect of adding water on the amount of CO_2 fixed by pure γ-C_2S

Figure 2 shows the relationship between accelerated carbonation curing of pure γ-C_2S and the amount of CO_2 fixed per unit mass of pure γ-C_2S. The proportion range of added water to powder (added w/p) was 0 to 0.5. The quantity of CO_2 fixed reached a maximum at an added w/p of 0.25 and decreased at higher or lower proportions. It has been reported that the presence of water is essential for this carbonation reaction to occur. It is also known that some water is necessary for the carbonation reaction to occur in cement paste, although an excess of water inhibits the diffusion of CO_2 (Dung et al., 2014). These data suggest that an added w/p of 0.25 provided sufficient water to allow for the dissolution of CO_2 and promotion of the carbonation reaction of pure γ-C_2S without inhibiting the diffusion of CO_2.

3.2 Effect of water content on the fixing of CO_2 in hardened cement paste with impure γ-C_2S

The effects of water content on CO_2 fixation in hardened cement paste were evaluated, employing added water to dried specimen (added w/s) proportions of 0 to 0.3. Figure 3 summarizes the results and shows that the relationship between the added w/s proportion and quantity of fixed CO_2 exhibited a similar trend to that seen in Figure 2. An added w/s proportion of 0.2 gave the highest amount of fixed CO_2. In the case of cement paste with impure γ-C_2S, the accelerated carbonation reaction was evidently greatly affected by the water concentration, in the same manner as the pure γ-C_2S reaction was affected.

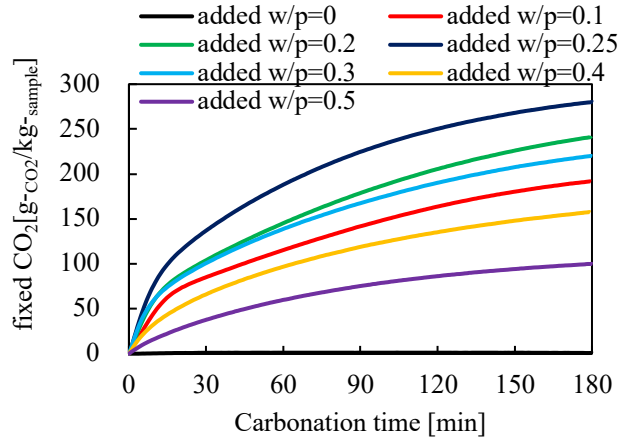


Figure 2. Amount of fixed CO_2 as a function of time for various added w/p per unit mass of pure γ-C_2S.

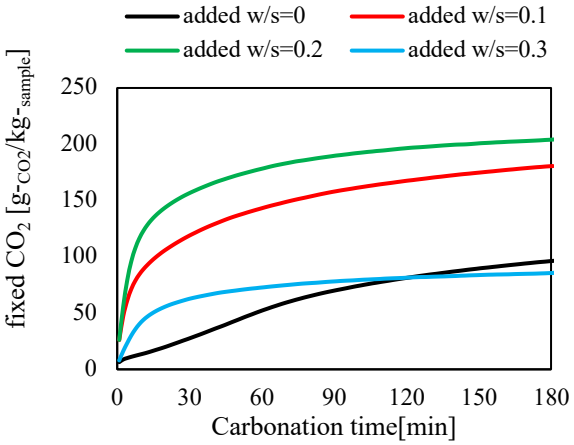


Figure 3. Relationship between the amount of water added and quantity of CO_2 fixed in cement paste.

3.3 Effect of water content on carbonation rate and properties of mortar with impure γ-C_2S

The effect of water content on the accelerated carbonation curing of mortar with impure γ-C_2S was investigated by artificially adjusting the water content. The added water proportions relative to the amounts of OPC and γ-C_2S (powder content) in the mortar specimens (added w/p) were 0 to 0.3. As a reference, a demolded mortar specimen without additional processing was also evaluated. Photographs showing the carbonation depths of the mortar samples (Figure 4) indicate that the greatest carbonation depth was obtained at an added w/p of 0. This cross-section was completely carbonated after 3 days, while the added w/p = 0.1 specimen was completely carbonated after 7 days. Carbonation of the reference sample and those having added w/p proportions of 0.2 and 0.3 occurred more slowly and there were no significant differences between these specimens. Figures 5 and 6 summarize the CO_2 content and compressive strength of each specimen, respectively. In contrast to the data in Figure 4, an added w/p proportion of 0.1 gave the highest CO_2 content and compressive strength, followed by a ratio of 0. The CO_2 content and compressive strength

of the other samples were all lower and similar to one another. Here, we address the above-mentioned discrepancy. Reducing the amount of added water provided little to no water within the microstructure of the mortar, such that the suppression of CO_2 diffusion by water was minimal. As such, the cement hydrates inside the mortar underwent rapid carbonation. The presence of an optimal amount of water was necessary for the carbonation reaction of γ-C_2S. Reducing the water content inside the microstructure resulted in more efficient CO_2 diffusion, but the carbonation reaction of γ-C_2S was inhibited. A w/p proportion of 0.1 likely balanced the carbonation reaction of γ-C_2S with the diffusion of CO_2. At a w/p proportion of 0, the water content was insufficient for the carbonation reaction of γ-C_2S, such that the CO_2 content and compressive strength were low despite a greater carbonation depth. The reference sample and specimens having w/p proportions of 0.2 and 0.3 had too much water to allow diffusion of CO_2 inside the mortar.

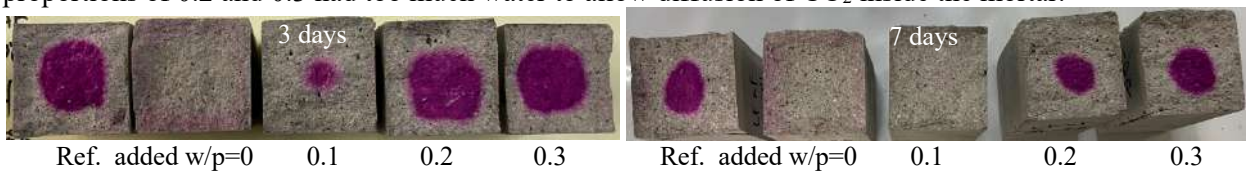


Figure 4. Cross-sections of mortar specimens sprayed with a phenolphthalein solution.

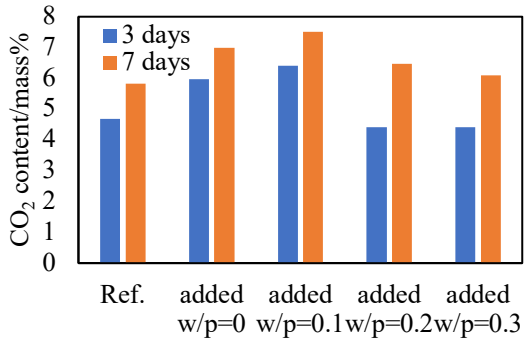


Figure 5. CO_2 content in mortar specimens.

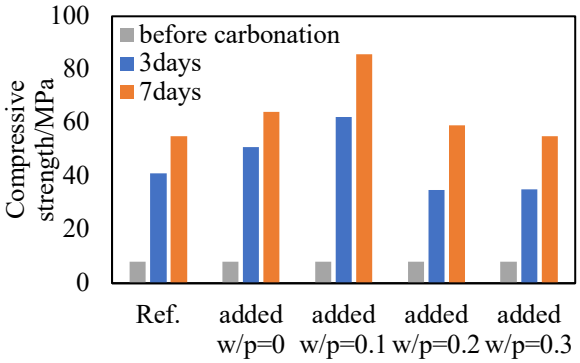


Figure 6. Compressive strength of mortar specimens.

4. Conclusions

The effects of water conditions on the accelerated carbonation curing of γ-C_2S and cement with γ-C_2S were evaluated, and the optimal conditions were ascertained. The following conclusions can be drawn.
(1) The amount of fixed CO_2 in pure γ-C_2S was maximized at an added w/p proportion of 0.25 at 30 °C.
(2) The maximum amount of fixed CO_2 in cement paste containing impure γ-C_2S was obtained at an added w/s proportion of 0.2 at 30 °C.
(3) The highest CO_2 content and compressive strength were obtained at an added w/p proportion of 0.1 at 40 °C in the case of mortar incorporating impure γ-C_2S.

Acknowledgements

This paper is based on results of "Development of Materials, Manufacturing Methods and Quality Control System on Innovative Carbon Negative Concrete", JPNP21014, commissioned by the New Energy and Industrial Technology Development Organization (NEDO). We thank David Wacey, PhD, from Edanz (https://jp.edanz.com/ac) for editing a draft of this manuscript.

References

Li, Mo, and Unluer. (2022) "Emerging CO_2 utilization technologies for construction materials: A review", *Journal of CO_2 Utilization*, 65(102237)

Higuchi, Morioka, Yoshioka, and Yokozeki. (2014) "Development of a new ecological concrete with CO_2 emissions below zero", *Construction and Building Materials*, 67(C): 338-343

Ushiro, Shoji, Morioka and Maruyama (2014) "Influence of water on carbonation of γ-C_2S and carbonation behavior of hardened paste containing γ-C_2S", *Cement Science and Concrete Technology*, 68: 186-191

Dung, Unluer (2019) "Performance of reactive MgO concrete under increased CO_2 dissolution", *Cement and Concrete Research*, 118: 92-101

The 16th International Congress on the Chemistry of Cement 2023 (ICCC2023)
"Further Reduction of CO_2 -Emissions and Circularity in the Cement and Concrete Industry"
September 18–22, 2023, Bangkok, Thailand

Leaching-Induced Mass Loss Characterisation of Calcium Sulfoaluminate Binders Using Acid Titrimetry

Tom Damion[1*] and Piyush Chaunsali[2]

[1] *Ph.D. Candidate, Department of Civil Engineering, IIT Madras, Chennai, India*

Email: tomdamion@gmail.com

[2] *Assistant Professor, Department of Civil Engineering, IIT Madras, Chennai, India*

Email: pchaunsali@civil.iitm.ac.in

[*] *Corresponding author*

ABSTRACT

Acid resistance of binders is crucial in structures that are subjected to acidic environment, such as sewer structures. Calcium sulfoaluminate (CSA) based binders are potential candidates for their utilization in structures exposed to acidic environment. Mass loss has been extensively used as a criterion to evaluate acid resistance. However, mass loss by itself is not sufficient as there could be mass gain due to gypsum deposition, which may create difficulty in assessing the relative performance as reported in previous acid attack studies. Acid consumption provides an alternative and effective criterion to evaluate acid resistance complementing the mass loss results. Titration technique was used to characterize the deterioration and leaching was evaluated with ICP-OES. Leaching is important in organic acid attack, such as citric acid, as it results in complex formation which is attributed as a major cause for heavy deterioration. Hence, a new method is proposed to evaluate the leaching-induced mass loss.

KEYWORDS: *ICP -OES, calcium sulfoaluminate cement, acid attack, titration, mass loss*

1. Introduction

Calcium sulfoaluminate (CSA) cement manufacturing contributes to lower CO_2 emission as compared to Portland cement (Sharma et al. 2021). Hydrated CSA cement, similar to the acid resistant calcium aluminate cement (CAC), contains aluminium hydroxide and can be a potential candidate for sewer structures. Sewers are large infrastructure, and the usage of sustainable and durable binder leads to reduction in their carbon footprint. Hence, durability of hydrated CSA cement with respect to acid resistance needs to be evaluated.

CSA-based binders have good acid neutralisation capacity (ANC) (Albino et al. 1996; Berardi et al. 1997). CSA cement (CaO: 42.25%, SO_3: 8.82%, Al_2O_3: 36.46%) and PC-CSA blends were found to have lower penetration depths than that of PC (Cao et al. 2022). In an in-situ sewer exposure experiment reported by (Bakera and Alexander 2022), it was found that CSA cement outperformed sulfate resisting Portland cement. In a previous study by the authors, CSA cement (CaO: 39.8 %, SO_3: 14.5 %, Al_2O_3: 20.9 %, SiO_2: 14 %) was outperformed by PC in 1% sulfuric acid solution. However, in case of citric acid attack, CSA cement outperformed PC because of the higher amount of tri-calcium di-citrate hexahydrate (expansive in nature) formation from calcium hydroxide in PC (Damion et al. 2022). At a higher concentration of acid, CSA (CaO – 44.4%, SiO_2 – 10.7%, SO_3 – 8.7%, and Al_2O_3 – 31.75%) cement reported higher mass loss (Dyer 2017). However, when the unattacked core area was compared, CSA cement had a higher percentage of the unattacked area than Portland-based binders.

In conventional acid immersion tests, specimens are often immersed in dilute acid solution. The pH of this acid solution increases with time depending on the neutralisation capacity of the binders (Onuaguluchi and Banthia 2022). The pH increment needs to be arrested to simulate a sustained constant pH acid attack in sewers. This can be done by titrating with concentrated acid along with proper stirring. The titration time and amount of acid titrated are measured to calculate the average acid consumption rate (Min and Song 2018). This type of constant pH method can be automated with the help of an autotitrator

as reported by (Irico et al. 2020), where replacement of exposure solution was also adopted. In the previous work (Damion and Chaunsali 2022), autotitrator was used to conduct acid attack tests and novel methods were developed to evaluate the acid resistance. The effect of acid-induced leaching of elements on acid resistance of binders is discussed in this paper. The analytical procedure to evaluate leaching-induced mass loss will be discussed in detail.

2. Materials and Methods

Portland Cement (PC) of grade 53 as per IS 12269: 2013 and commercially available high ye'elimite CSA cement CSA(HY), and CAC were used. The oxide compositions of the three binders are shown in the Table 1.

Table 1 Oxide composition of binders

Binders	SiO_2	CaO	Al_2O_3	SO_3	Fe_2O_3	MgO	K_2O	TiO_2	SrO	Na_2O	LOI*
PC	21.2	58.1	6.9	2.8	5.1	1.0	0.8	0.5	0.0	0.1	3.1
CSA (HY)	14.0	39.8	20.9	14.5	3.6	2.8	0.5	1.1	0.1	0.2	1.8
CAC	8.3	32.5	43.6	4.3	2.4	0.7	0.0	3.8	0.1	0.3	3.4

LOI*: Loss on ignition

Prismatic specimens (dimension: 10 ×10 × 60 mm) of cement pastes were cast at water-to-cement (w/c) ratio of 0.4 (by wt.) and cured for 28 days at 25°C and 65% relative humidity environment. The acid exposure was conducted using an automatic titrator (Metrohm 916 Ti Touch). Cured monolithic specimens were taken for constant pH experiment (STAT). Constant pH of 1 and 3 were maintained by titrating with diluted sulfuric acid (5%) and citric acid (1M), respectively. Three specimens were transferred to a 500 ml beaker containing 250 ml acid solution of pH 1 or 3 (sulfuric or citric as per the test). The autotitrator maintains constant pH along with continuous stirring at 450 – 500 rpm. Since the dosing of acid increased the acid volume, fresh acid solution was used after 24 hours or after the constant pH attainment, whichever occurred earlier. Inductively Coupled Plasma Optical Emission Spectroscopy (ICP-OES) was performed on the solution collected. The solution was diluted 10 – 100 times before the ICP-OES analysis.

3. Results

3.1 Sulfuric Acid

Acid attack led to mass loss of cement paste through its transformation into weak acid attack product. Leaching might also have contributed to the mass loss. In fact, leaching of these elements weakens the neutralised region in specimens, ultimately leading to deterioration. The concentration of leached elements in case of sulfuric acid attacked CSA(HY) is tabulated in Table 2.

Sulfur content in the exposed sulfuric acid solution was mainly from the residual sulfate in the solution and from the leached sulfur. The sulfur content in CSA(HY) exposure solution was the highest. This could be mainly attributed to the sulfate leaching. Absence of sulfate consumption points to the anion independent acid attack mechanism of CSA as mentioned in (Damion and Chaunsali 2022).

Table 2 illustrates the procedure for calculation of mass loss contributed by these elements. Further in

Table 2, the proportion of individual leached elements (A) to that of the initial amount (B) is shown.
The oxide composition can be considered as the amount of oxide (g) in 100g of raw binder. This can be converted to mole number by dividing with oxide molecular weight. Then number of moles of element in

1g raw binder has been determined. As the water to cement ratio is 0.4, amount of element oxides in 1g hydrated paste is 71%. The number of moles of element in hydrated binder was determined, followed by the amount of element (mg) in 1g of hydrated binder (B). Similar calculations were performed for PC and CAC.

Table 2 Mass loss estimation procedure for sulfuric acid attack induced leaching in CSA(HY)

Element symbol and Wavelength (nm)	Concentration (mg/l) from total sample weight (37.75g)	Concentration contributed from per g of sample (mg/l)/g	Amount of ions (mg/g) in total solution volume 364 ml (A)	Weight of total leached ion (mg) from 1 g sample	mass loss % due to leaching from 1g	Initial element(mg) in 1g hydrated (B)	% of individual ions leached (A/B)
Al 308.215	989.3	26.2	9.5			80.6	11.8
Ca 317.933	789.8	20.9	7.6			206.3	3.7
Fe 238.204	180.4	4.8	1.7			18.5	9.4
K 766.490	11.24	0.3	0.1			3.0	3.7
Mg 285.213	217.9	5.8	2.1			12.3	17.0
S 181.975	13250	351.0	127.8			42.3	
Si 251.611	106.8	2.8	1.0	22.1	2.21%	47.6	2.2

The mass contributed by major elements except sulfur and the total leaching induced mass loss is shown in Figure 1. The higher leaching of Al in CSA(HY) and CAC binders was attributed to the relative higher proportion of alumina bearing phases in these binders and the neutralisation of aluminum hydroxide.

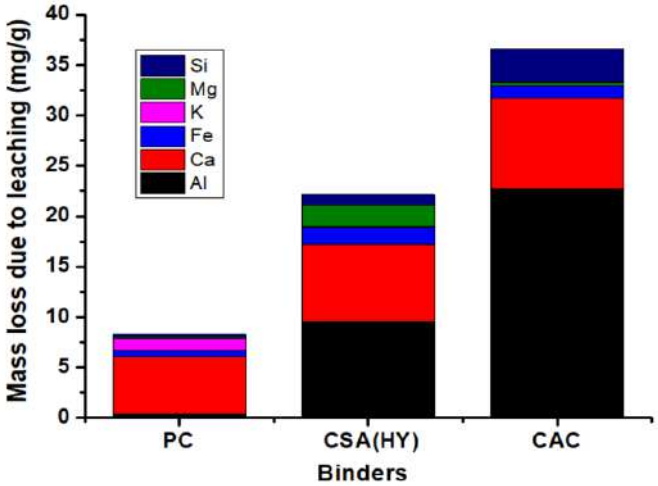


Figure 1 Mass loss due to leaching of Al, Ca, Fe, K, Mg, and Si in sulfuric acid STAT pH 1

3.2 Citric Acid

The leached calcium ions mainly form expansive citrate salt in case of citric acid attack with PC and other ions form complexes in solution. The complexolysis mechanism can be further explored from the ICP-OES results. Figure 2 shows the initial elemental composition in 1 g of hydrated binder as solid bars and the calculated proportion of leached elements in the red dashed bars. Leaching of elements in PC is quite severe as compared to other binders in citric acid attack. However, Ca amount in PC exposure solution is slightly lesser than that of CSA(HY). This was due to the consumption of Ca ions in the formation of the expansive calcium citrate salt in case of PC and its absence in CSA(HY). The Fe ion leaching in PC was higher than that of CAC and CSA(HY), explaining the characteristic green colour of exposure solution of PC. The alkali metal leaching was higher in CSA(HY) than PC. This might be due to the absence of portlandite in CSA(HY) causing alkali constituents to leach fast.

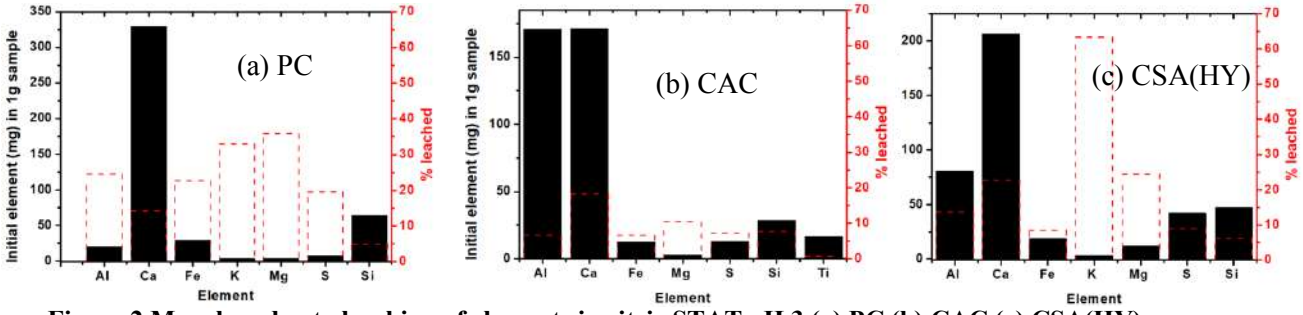


Figure 2 Mass loss due to leaching of elements in citric STAT pH 3 (a) PC (b) CAC (c) CSA(HY)

4. Conclusions

The relative performance of binders in sulfuric (pH 1) and citric (pH 3) acid as observed earlier in (Damion and Chaunsali 2022) found to be similar in case of the leaching behaviour in these acids. The main conclusion of this article is summarised below:

- The binders can be arranged based on mass loss due to leaching. In case of constant pH 1 sulfuric acid attack: CAC>CSA(HY)>PC and in case of constant pH 3 citric acid attack: PC>CSA(HY)>CAC.
- Acid anion independent mechanism of acid attack of CSA(HY) was proved by the negligible consumption of sulfate ions from the exposure solution.
- The extensive leaching in citric acid led to complexolysis. The rate of leaching was higher in PC.

Acknowledgements

The first author would like to acknowledge the doctoral scholarship received from the Ministry of Education, India. The last author is also grateful for the financial support from the New Faculty Seed Grant by ICSR at IIT Madras. The Institute of Eminence Research Initiative project grant on Technologies for Low Carbon and Lean Construction from IIT Madras is also gratefully acknowledged.

References

Albino, V., Cioffi, R., Marroccoli, M., and Santoro, L. (1996). "Potential application of ettringite generating systems for hazardous waste stabilization." *Journal of Hazardous Materials*, 51(1–3), 241–252.

Bakera, A. T., and Alexander, M. G. (2022). "Sewer concrete subjected to biogenic acid corrosion: analysis of concrete deterioration phases using QEMSCAN." *MATEC Web of Conferences, International Conference on Concrete Repair, Rehabilitation and Retrofitting (ICCRRR 2022)*, 03012.

Berardi, R., Cioffi, R., and Santoro, L. (1997). "Matrix stability and leaching behaviour in ettringite-based stabilization systems doped with heavy metals." *Waste Management*, 17(8), 535–540.

Cao, R., Yang, J., Li, G., Liu, F., Niu, M., and Wang, W. (2022). "Resistance of the composite cementitious system of ordinary Portland/calcium sulfoaluminate cement to sulfuric acid attack." *Construction and Building Materials*, Elsevier Ltd, 329(January), 127171.

Damion, T., Cepuritis, R., and Chaunsali, P. (2022). "Sulfuric acid and citric acid attack of calcium sulfoaluminate-based binders." *Cement and Concrete Composites*, Elsevier Ltd, 130(April), 104524.

Damion, T., and Chaunsali, P. (2022). "Evaluating Acid Resistance of Portland Cement, Calcium Aluminate Cement, and Calcium Sulfoaluminate Based Cement Using Acid Neutralisation." *Cement and Concrete Research*, Elsevier Ltd, 162, 1–17.

Dyer, T. (2017). *Biodeterioration of Concrete*. *Taylor and Francis group*.

Irico, S., Meyst, L. De, Qvaeschning, D., Alonso, M. C., Villar, K., and Belie, N. De. (2020). "Severe sulfuric acid attack on self-compacting concrete with granulometrically optimized blast-furnace slag-comparison of different test methods." *Materials*, 13(6).

Min, H., and Song, Z. (2018). "Investigation on the Sulfuric Acid Corrosion Mechanism for Concrete in Soaking Environment." *Advances in Materials Science and Engineering*, 2018, 1–10.

Onuaguluchi, O., and Banthia, N. (2022). "The Influence of CaCl2-Blended Acrylic Polymer on Steel Rebar Corrosion and Acid Attack Resistance of Mortar." *Corrosion and Materials Degradation*, 3(1), 160–177.

Sharma, A., Basavaraj, A. S., Chaunsali, P., and Gettu, R. (2021). "75th RILEM Week-2021 International Conferences on Advances in Sustainable Construc- tion Materials and Structures Environmental Impact of Calcium Sulfoaluminate Cement Manufacturing : An Indian Case Study." *75th RILEM Week-2021, International Conferences on Advances in Sustainable Construc- tion Materials and Structures*, 1–10.

The 16th International Congress on the Chemistry of Cement 2023 (ICCC2023)
"Further Reduction of CO_2 -Emissions and Circularity in the Cement and Concrete Industry"
September 18–22, 2023, Bangkok, Thailand

Reactivity of novel artificial precursors for alkali-activated materials made from industrial residues

R. Firdous[1*], T. Hirsch[1], G. Hovestadt[2], B. Friedrich[2], C. Kemper[3], T. Schür[3], D. Stephan[1] and A. Buchwald[4]

[1] *Technische Universität Berlin, Berlin, Germany*
Email: rafia.firdous@tu-berlin.de
Email: t.hirsch@tu-berlin.de
Email: stephan@tu-berlin.de
[2] *RWTH Aachen University, Aachen, Germany*
Email: GHovestadt@metallurgie.rwth-aachen.de
Email: BFriedrich@metallurgie.rwth-aachen.de
[3] *Elektrowerk Weisweiler GmbH, Eschweiler, Germany*
Email: kemper@elektrowerk.de
Email: schuer@elektrowerk.de
[4] *ASCEM B.V., Rheden, Netherlands*
Email: a.buchwald@ascem.nl

ABSTRACT

Industrial and urban residues, energy usage and natural resources are a few factors that obstacle reaching the current environmental and economic goals. Building material production alone accounts for appr. 10% of the anthropogenic CO_2 emissions. Efforts have been made to reduce these emissions by incorporating several pozzolanic materials in Portland cement. However, aluminosilicate-rich materials can also be used as precursors for alkali-activated binders. But not all aluminosilicate-rich wastes can be directly used because of low reactivity. This study uses ferro-chrome slag (FCS) and municipal solid waste incineration ash (MSWIA) to target alkali-activated binder production. Both show poor reactivity in their original form; therefore, both are molten in a lab furnace, followed by granulation and milling. 5 glass samples with different ratios of FCS and MSWIA were produced. The glasses are milled to comparable fineness in a vibratory disc mill. Moreover, the chemical composition is determined by X-ray fluorescence analysis. The reactivity of all the samples for alkali activation is tested by using NaOH solutions and sodium silicate solutions. The prepared alkali-activated glasses were sealed and cured at 20 °C. Isothermal conduction calorimetry and X-ray diffraction analysis are performed to determine the reactivity and phase composition before and after the reaction. Compressive strength was determined at the age of 28 d. The results show that the MSWIA-based glass shows lower heat development with the used alkaline solutions compared to the glasses containing more FCS indicating their lower reactivity. The glasses molten from a higher proportion of FCS exhibited higher 28 d compressive strength upon their reaction with sodium silicate solutions.

KEYWORDS: *Alkali-activated material, artificial precursor, re-melting, municipal solid waste incineration ash, ferro-chrome slag*

1. Introduction

The EU regulations aim to achieve a circular economy where less waste is generated and as few as possible primary resources are used (European Commission, 2018). This requires better waste management, innovation in recycling technologies and reduced land fillings. To achieve these circular economy goals, the wastes of one industry must be used as feeding material for another industry. Such a circular use of materials will not only help in saving the natural resources and reducing the environmental burden of storage of these wastes but can also help in reducing greenhouse gas emissions. In this regard, this paper deals with the use of two waste streams to produce building materials such that overall less CO_2 is emitted in comparison to clinker production for ordinary Portland cement (OPC), which is alone responsible for up to 8% of anthropogenic CO_2 emissions (Andrew, 2018). Many of these industrial, agricultural, or urban wastes are rich in silica, alumina and alkalis, thus making them suitable for use as a precursor for alkali-activated materials.

Alkali-activated materials and/or geopolymers are prepared by reaction of aluminosilicate raw material with an alkaline solution (Provis and van Deventer, 2014). The aggressive alkaline environment helps dissolve the reactive part which upon condensation builds a strength-carrying reaction product (Provis and van Deventer, 2014). Much research focuses on determining the reactivity of several such waste streams as solid or liquid precursors for alkali-activation (Provis and van Deventer, 2014). However, several wastes show poor reactivity and cannot be used directly or alone for alkali-activation (Silva et al., 2017). Studies dealing with various types of waste streams propose different methods or treatments to enable the reuse/recycling of these materials. The current study investigates the reuse potential of ferro-chrome slag (FCS) and municipal solid waste incineration ash (MSWIA). Both wastes exhibit poor reactivity in their parent form. Therefore, the wastes are remolten in varying proportions to form a novel artificial precursor for alkali-activated materials.

2. Materials and Methods

Two waste streams, including ferro-chrome slag (FCS) and municipal solid waste incineration ash (MSWIA) were used to obtain the precursor for alkali-activation. 5 glass samples are produced with the following weight rations of FCS:MSWIA 100:0, 75:25, 50:50, 25:75 and 0:100 (termed P1 to P5, respectively). The selected materials were heated up and melted in a resistant-heated chamber furnace and granulated to form the artificial precursor.

The heating rate of the furnace was set to 200 °C/h and 1600 °C as the final temperature for 30 min. Sintered Al_2O_3 was used as crucible material showing good resistance against refractory wear, nevertheless some alumina was dissolved in the molten phase. After melting, the crucible was taken out from the hot furnace, and the melt was quenched into water. The mass ratio was 1.5:100 (melt to water). The obtained materials were metal and glassy slag. The metal phase was separated before the glasses were ground in a laboratory disk mill to comparable particle size distributions, such that the average d_{90} and d_{50} is < 90 µm and < 46 µm, respectively. The chemical composition of each glass was analyzed by X-ray fluorescence analysis (XRF, Malvern-Panalytical, UK) and is provided in Table 1.

Table 1. Chemical composition of all glasses measured via XRF (from molten tablets).

Name	Al_2O_3	CaO	Cr_2O_3	Fe_2O_3	MgO	SiO_2	TiO_2	Sum
P1	8.2	39.9	3.0	0.1	7.2	20.0	0.1	79.5
P2	6.9	36.8	2.7	1.8	6.2	24.8	0.4	79.6
P3	7.1	30.9	2.2	3.5	4.9	28.7	0.6	78.0
P4	7.1	25.3	1.16	5.3	3.6	34.2	0.9	77.6
P5	8.1	18.9	0.2	6.2	1.9	40.8	1.3	83.9

The produced artificial precursors were reacted with various NaOH and sodium silicate solutions. For NaOH, the concentrations of 5, 15 and 25 wt.% were taken. Whereas sodium silicate solutions of SiO_2/Na_2O (mol/mol) = 0.9, 1.1, 1.4 and H_2O/Na_2O (mol/mol) = 14 were used. The isothermal calorimetric

measurements were performed ex-situ in a MC-CAL 100P, C3 Prozess- und Analysentechnik GmbH, Germany, for 72 h at 20 °C. The solutions and powders were mixed for 1 min. For compressive strength, the samples were mixed for 3 min, moulded as 2 cm cubes, sealed and cured at 20 °C till test age. The mineralogical composition was examined using an Empyrean XRD device from PANalytical.

3. Results and Discussion

Fig. 1 shows the calorimetric results of the five prepared precursor glass materials with the six chosen alkaline solutions. The results indicate that P1 and P2 show higher reactivity compared to the other precursors with all the used solutions. However, the reaction appears to be fastest with a 15 wt.% NaOH solution. The second exothermic reaction peak is observed earliest and strongest for these combinations. The precursor glasses P3 to P5 show nearly no reactivity with NaOH and sodium silicate solutions. P1 and P2 are glasses formed via melting of higher proportions of FCS than MSWIA and contain, therefore, higher amounts of CaO which appears to be the decisive factor for the reactivity. A higher fraction of MSWIA in the melts introduced a higher amount of SiO_2 to the glass, which slowed down the reaction.

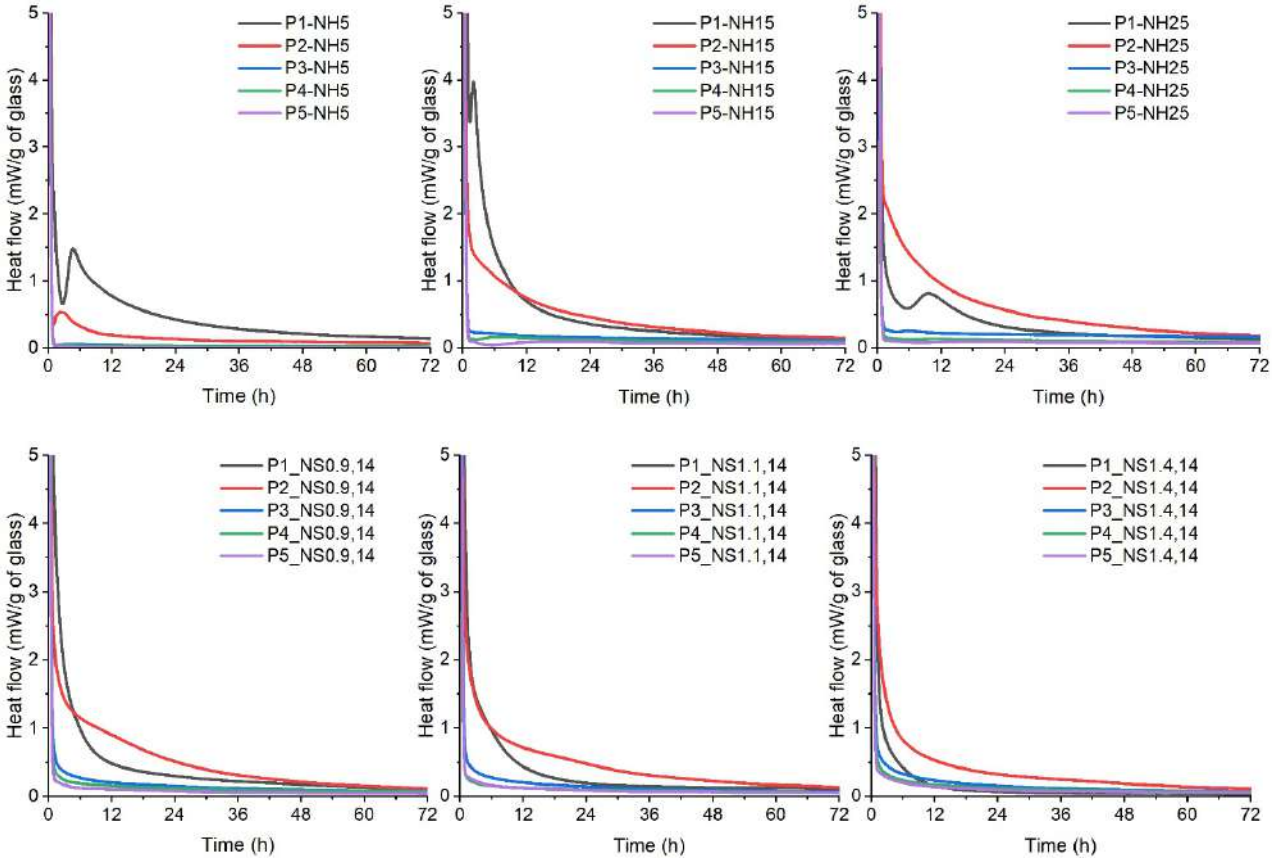


Fig. 1. Calorimetric heat release curves for all precursors with chosen solutions as a function of time.

The compressive strength determined after 28 d of reaction for all precursors with 3 selected sodium silicate solutions is shown in Fig. 2. The compressive strength results are in good agreement with those of calorimetry. The precursor glasses P1 and P2 exhibited higher strengths compared to the other precursors. The higher reactivity of P1 and P2 promoted the development of strength-bearing phases, thus exhibiting higher strengths. However, with the variation of the activators, the strength of the same precursor varied. P1 exhibited higher strength by use of sodium silicate solution with silica modulus of 1.1, whereas P2 exhibited higher strength by use of a 1.4 silica modulus solution, indicating that a higher amount of SiO_2 provided from the solution was helpful in gaining higher strength for P2. The precursor glass P5 exhibited low or no compressive strength even after 28 d of reaction. Therefore, no value is provided in Fig. 2, as the strengths were below the detection limit of the device.

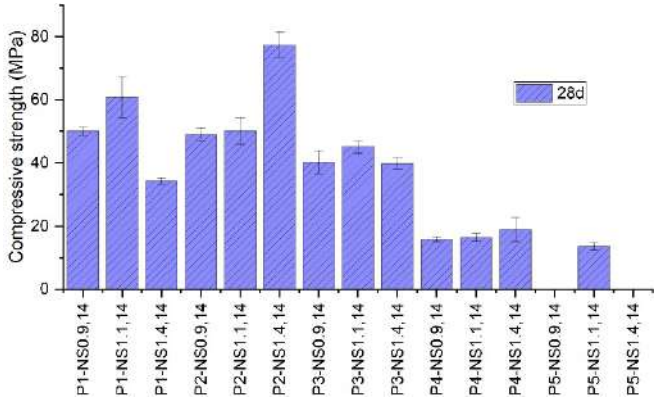


Fig. 2. Compressive strength of all samples after 28 d.

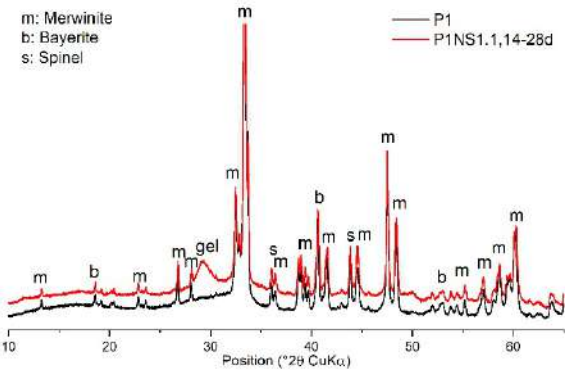


Fig. 3. Crystalline phase of P1 and 28 d reacted P1

The crystalline phase composition determined by XRD for P1 and its reaction product with sodium silicate solution of Ms=1.1 are presented in Fig. 3. The results show that even after quenching, a few crystalline phases can be observed in P1. The major crystalline phase observed in P1 is merwinite, a calcium magnesium silicate. Other minor crystalline phases are bayerite and spinel. In the 28 d reacted sample, a semi-crystalline gel phase is observed at ~29.5° 2θ, likely due to the formation of a sodium-containing calcium silicate hydrate type gel, likely responsible for the mechanical strength.

4. Conclusions

The results of this study indicate that less reactive industrial and municipal residues such as ferro-chrome slag and municipal solid waste incineration ash can be reutilized as precursors for a construction material if pretreated by a re-melting process. However, using a higher amount of municipal solid waste incineration ash in precursor glass production was found to be less beneficial for obtaining glasses with higher reactivity. A higher amount of ferro-chrome slag inherently provided a higher CaO content in the glass, thus improving the reactivity and strength development.

Acknowledgements

This study is supported by Bundesministerium für Bildung und Forschung by the Project PHöMixBeton (grant number 01LJ2006C) and the European Union under NextGenerationEU.

References

Andrew, R.M. (2018) “Global CO_2 emissions from cement production”, *Earth System Science Data*, 10(1): 195–217 doi:10.5194/essd-10-195-2018

European Commission (2018) “A Clean Planet for all - A European strategic long-term vision for a prosperous, modern, competitive and climate neutral economy”, Document Nr. COM(2018) 773 final, European Commission Brussels, 25 pp

Provis, J.L. and van Deventer, J.S.J. (2014) “Alkali Activated Materials, State-of-the-Art Report, RILEM TC 224-AAM”, Springer, Dordrecht, Heidelberg, New York, London

Silva, R.V., Brito, J. de, Lynn, C.J. and Dhir, R.K. (2017) “Use of municipal solid waste incineration bottom ashes in alkali-activated materials, ceramics and granular applications: A review”, *Waste Management*, 68, 207–220. doi:10.1016/j.wasman.2017.06.043

The 16th International Congress on the Chemistry of Cement 2023 (ICCC2023)
"Further Reduction of CO_2 -Emissions and Circularity in the Cement and Concrete Industry"
September 18–22, 2023, Bangkok, Thailand

Belitic calcium sulphoaluminate (BCSA) cements and the current durability standards: What are we testing?

J. Ambrose[1], V.K. Shenbagam[1], J.L. Provis[1], and T. Hanein[1*]

[1] *Department of Materials Science and Engineering, University of Sheffield, S1 3JD, United Kingdom*
Email: jambrose1@sheffield.ac.uk, t.hanein@sheffield.ac.uk

ABSTRACT
The service life of concrete is often estimated using parameters attained from durability tests, as corrosion in concrete under natural exposure typically takes several decades. Standardised tests, such several of those outlined in EN 12390, are performed on specimens after 28 days of curing using conditions designed to accelerate natural effects. These tests were originally created for Portland cements (PCs), which at 28 days will have their major phases mostly hydrated, and thus have a durability representative of their lifespan. However, these tests can underestimate the potential of binder systems that chemically evolve beyond 28 days, such as belitic calcium sulphoaluminate (BCSA) cements, which are often reported to underperform under these procedures. BCSAs at 28 days curing would only fully consider the hydration of ye'elimite, which reacts rapidly, whereas belite typically starts to react much later. The hydration products of belite can contribute to the further filling of pores, lowering the porosity in the binder matrix and improving durability. Therefore, this study aims to review (i) the hydration of binders across time, specifically BCSA cements, (ii) reported durability results at these times, and (iii) assess how representative any results are of a hydrated binder. Furthermore, we aim to recommend alterations to testing that result in more representative data, such as incorporating 'equivalent hydration' into testing regimes.

KEYWORDS: *Belitic calcium sulphoaluminate cement, durability testing, standards, testing methods*

Introduction
Calcium sulphoaluminate (CSA) cements have ye'elimite ($C_4A_3\bar{S}$) as the primary reacting phase, alongside other phases such as belite (C_2S), ferrite (C_4AF) and gypsum ($C\bar{S}H_2$). High belite CSA binders, known as BCSA, do not have a fixed composition, but generally have 50-60% belite and 20-30% ye'elimite (Bescher et al., 2019), where the major variable is ferrite and gypsum content. Due to inconsistencies across literature, the following terminology will be used: US BCSA cement as 'BCSA(US)'; series 3 cement as 'BCSA(F)'; and lower belite CSA systems as '(B)CSA'. The main hydration products of BSCAs are ettringite ($C_6A\bar{S}_3H_{32}$, AFt), monosulphate ($C_4A\bar{S}H_{12}$, AFm), amorphous aluminium hydroxide (AH_3), and strätlingite (C_2ASH_8). BCSA cements will set rapidly and achieve greater early strengths than PCs, where the AFt formation from ye'elimite hydration produces expansive stresses that can help prevent shrinkage through equivalent expansion, resulting in a 'volumetrically neutral' cement. BCSAs also act as a low-CO_2 binder, with reductions in the required clinkering temperature and the binder releasing less CO_2 during hydration. A major obstacle within the current implementation of BCSA cements into the UK and Europe is the perceived subpar performance under durability tests, such as EN 12390-10,11. However, these tests are often conducted under accelerated environments to obtain results in a reasonable time. These standards were created based upon the hydration factor of PCs, which achieve a high level of hydration at 28 days. Slower hydrating phases, such as belite or fly-ash, will therefore have insufficient time to hydrate properly when the tests are conducted. As corrosion initiation can take decades, using accelerated tests on binders that would have otherwise achieved close to complete hydration can lead to unrealistic results.

Binder phases and their hydration products
Alite (C_3S) is the major component of many traditional cements. C_3S is reactive at early ages; findings by Cuesta et al., (2021) show an alite paste at 28 days to reach 80% reaction. Aluminate (C_3A) will rapidly produce ettringite; often responsible for 'flash-setting' in concretes and fully hydrating within 28 days. Belite is typically used in small quantities for long term strength, as C_2S only starts to show significant hydration at ~3 months (Bescher et al., 2019). At 28 days only ~20% of the belite phase will have hydrated but at 3 months curing this will be ~48% (Cuberos et al., 2010). Within aluminium rich environments, belite

will preferentially react to form strätlingite (Table.1), yet in environments depleted in AH_3 there will be preferential production of C-S-H and portlandite. For Ye'elimite, XRD analysis of a BCSA(US) determined hydration to be almost complete after 10 hours of setting (Bescher et al., 2019). SEM analysis by Song et al., (2015) suggests the initial reaction of ye'elimite immediately after adding water produces AFt, AFm, AH_3 and hydrogarnet, with small globules of hydrogarnet surrounded by AH_3 (Table.1). After this, the ye'elimite is expected to either produce AFt or AFm, depending on the gypsum content. Ferrite tested in a BCSA(F) by Glasser and Zhang, (2001) was revealed to be mostly inert even after 10 years, with a very slow reaction with water. A typical PC has the major components of ~50-65% wt.% alite, ~10-25 wt.% belite, ~5-10% aluminate, and ~5-10% ferrite, with varying amounts of gypsum, meaning that Portland cements will often have reached ~70-80+% of total feasible hydration, if ferrite is considered inert. For BCSA(US), as the gypsum will have mostly hydrated with the ye'elimite, it is expected that at 28 days curing the binder will have a total hydration degree of ~47-57%. At 3 months of curing, the hydration would account for almost 75% of a BCSA(US), which bridges the gap between PC.

Table.1 The most common hydration reactions of each of the major phases mentioned within this study.

Phase	Typical Hydration Equations	Reference
Alite	$C_3S + 5.3H \rightarrow C\text{-}S\text{-}H + 1.3CH$	Bishnoi and Scrivener, 2009
Aluminate	$C_3A + 3C\bar{S}H_2 + 32H \rightarrow C_6A\bar{S}H_{32}$	Zheng et al., 2021
Belite	$C_2S + AH_3 + 5H \rightarrow C_2ASH_8$	Cuberos et al., 2010
	$C_2S + 43H \rightarrow C\text{-}S\text{-}H + 0.3CH$	Cuberos et al., 2010
Ye'elimite	$4C_4A_3\bar{S} + 80H \rightarrow C_6A\bar{S}H_{32} + C_4A\bar{S}H_{12} + 2C_3AH_6 + 8AH_3$	Song et al., 2015
	$C_4A_3\bar{S} + 2C\bar{S}H_2 + 34H \rightarrow C_6A\bar{S}_3H_{32} + 2AH_3$	Cuberos et al., 2010
	$C_4A_3\bar{S} + 18H \rightarrow C_4A\bar{S}H_{12} + 2AH_3$	Song et al., 2015
Ferrite	$C_4AF + 16H \rightarrow 2C_2(A_{0.5}F_{0.5})H_8$	Cuberos et al., 2010

Durability of different binder systems

Alongside carbonation and Cl ingress tests, service life of a concrete can be estimated from deterioration depth and dissolved calcium content from acid attack. The microstructurally changed zone (i.e. where the concrete has been damage by acid attack) mostly matches with the maximum chloride content, meaning where porosity has been increased the concrete is most vulnerable to further degradation (Fjendbo et al., 2022). The stabilities of the different hydration phases across pH can be seen in Table.2.

Table.2 adapted from Damion and Chaunsali, (2022), showing the lowest pH before destabilisation.

Phase	pH stability	Reference
Portlandite	12.4 – 12.6	De Windt and Badreddine, 2007
Monosulphate	11.6	Gabrisová et al., 1991
Ettringite	11	McCarthy et al., 1992
Hydrogarnet	10	Gabrisová et al., 1991
C-S-H	8.8	Baston et al., 2012
Calcite	4.5 – 6	Khaitan et al., 2009
AH_3	3 – 4	Allahverdi and Škvára, 2000
Ferric phases	1.5 - 2	Allahverdi and Škvára, 2000

Within PCs, portlandite will act to preserve other hydration products, although once fully dissolved the C-S-H phases will begin decalcification. As C-S-H gel is the major pore-filling component in most cements, any complete decalcification will lead to large increases in the porosity. Portlandite is a well-known buffer of acids, achieved through the raising the pH of systems. A study by Afroughsabet et al., (2021) recorded a pH for PC as 13, while CSA was only 9-10. This buffering ability can be seen in Eq.1, where CH will dissolve to neutralise two ions of H^+. This does however mean that CH is exceptionally vulnerable to acid attack with an open system or low enough pH, leading to rapid dissolution and increases in porosity, and then to further attack within the binder (Damion and Chaunsali, 2022; Scrivener et al., 1999).

$$CH + 2H^+ \rightarrow Ca^{2+} + 2H \quad (1)$$

When hydrogarnet dissolves (Eq.2) it can reprecipitate as AH_3, which is stable to significantly lower pH values of 3-4 (Table 2). This reprecipitation means infill of AH_3 in outer layers, reducing pore space in the degraded sections of the cement, and reducing the effects of further ingress (Scrivener et al., 1999). The produced AH_3 can also act to further buffer a solution (Eq.3) leading to reasoning that these hydrates in CSA-based binders could provide a greater buffering potential to a CH based binder (Dyer, 2017).

$$C_3AH_6 + 6H^+ \rightarrow 3Ca^{2+} + 2AH_3 + 6H \quad (2)$$

$$2AH_3 + 6H^+ \rightarrow 2Al^{3+} + 6H \quad (3)$$

A carbonation test after 28 days curing by Afroughsabet et al., (2021) of reinforcement revealed almost no tarnish to the PC steel fibres, whereas the CSA had significant oxidation. Similarly, a study by Alapati et al., (2022) concluded that of the binders tested at 28 days, CSA performed the worst, and a test by Damion and Chaunsali, (2022) showed that in H_2SO_4, PC binders outperform (B)CSA, where PC lost 4% area and CSA 12.4%. A pH 1.5-2 H_2SO_4 test by Damion et al., (2022) had similar results, with PC outperforming the tested (B)CSA. However, after 14 years in the intertidal zone a tested BCSA(F) showed no corrosion of the embedded steel, implying little Cl ingress (Glasser and Zhang, 2001). The carbonation of BCSA(F) in field tests are also comparable to PCs, even with ettringites reported weakness to carbonation (Afroughsabet et al., 2021), and a study by Dyer, (2017) demonstrates CSAs situationally outperforming PC, with a better core strength retention after acid attack testing. A (B)CSA tested by Chi et al., (2021) also showed promise for resistance to sulphide and chloride attack, as well as carbonation. In a pH 2-3 citric acid test (B)CSA outlasted PC by 50%, seemingly due to a severe vulnerability of portlandite to citric acid, and the higher pH leading to extended preservation of AH_3 (Damion et al., 2022). A study by Cuesta et al., (2021) had a PC and a belite cement (BC) tested at 3 months, with the BC outperforming or matching the performance of PC for the three durability tests of 5% $MgCl_2$ solution, 3% Na_2SO_4 solution and 3x ion seawater. This indicates that with a high enough belite content, and time for significant hydration, a BCSA could produce comparable results to a PC. The belite rich BCSA compositions appear to be more durable than any tested low-belite variations, with the reportedly most resistant being the high belite, high ferrite BCSA(F), which are comparable to PCs. This may be due to a reduction in AFt and/or greater pH stability of included phases such as ferrite, Table.2, or the testing environments allowing for increased hydration.
There are several ways in which we could improve the total hydration of binders to meet that seen by tested PCs, such as extended curing periods, accelerated curing methods, and seeding and/or activation of cements. The most definite (albeit slow) way of testing a representative binder would be to introduce 'equivalent hydration' into testing procedures, instead of a set 28 days of curing. This could be achieved through including an earlier step in the standards to test (or model) hydration of alternative binders, and then test at 70-80% total hydration. This may have some issues with binders that use inert components, such as BCSA(F) however, but this can be mitigated by using an equation such as "hydrated product % / hydrated product % after 5 years", where if the value is ≥ 0.7 the binder can be considered representative of its in-service performance. Accelerated curing at 40°C has been shown to produce a similar strength development past 7 days curing that would usually take beyond 28 days in a BCSA (Borštnar et al., 2020). Higher temperature curing has however been shown to decrease average ettringite crystal size, perhaps through slight thermal decomposition, and produce a system with a higher porosity, due to lack of time for C-S-H infill before hydration (Borštnar et al., 2020), so may not provide a representative binder. Certain minor elements such as Na, K, S and B have been shown to stabilise high-T polymorphs of C_2S, although how this affects the hydration of the cements is not adequately understood (Cuberos et al., 2010), (Cuesta et al., 2021). Using 2wt% Borax to activate belite within a BCSA similar in composition to BCSA(F) by Cuberos et al., (2010) resulted in the formation of 54wt% α'_H-C_2S, completely replacing the β-C_2S. The 0wt% borax sample recorded C_2S reaction of 20, 48 % at 1, 3 months and the 2.0 wt% borax sample recorded 49, 62% reaction at 1, 3 months. However, a later study by Álvarez-Pinazo et al., (2013) using the same compositions of BCSA and borax reported at 28 days curing β-C_2S having 47% hydration and α'_H-C_2S having 27% hydration. This leads to an unknown in how activation truly effects the hydration belite.

Conclusions

At 28 days a typical PC will reach $\geq$ 70-80% total hydration, while a BCSA will be closer to 50%. When given 3 months to cure, a BCSA will have closer to 70-80% total hydration. If a BCSA is given enough

time to hydrate, then the reduction in porosity should produce a binder with much greater performances in testing procedures. This can be achieved by testing binders on a 'equivalent hydration' as opposed to a set 28-day curing time, though implementing an earlier step to test or model hydration of alternative binders, and test when they reach hydration representative of their in-service performance. Using 40ºC curing conditions may also provide a more realistic test at 28 days of curing.

References

Afroughsabet, V., Biolzi, L., Monteiro, P.J.M., Gastaldi, M.M., 2021. Investigation of the mechanical and durability properties of sustainable high performance concrete based on calcium sulfoaluminate cement. J. Build. Eng. 43, 102656. https://doi.org/10.1016/j.jobe.2021.102656

Alapati, P., Moradllo, M.K., Berke, N., Ley, M.T., Kurtis, K.E., 2022. Designing corrosion resistant systems with alternative cementitious materials. Cement 8, 100029. https://doi.org/10.1016/j.cement.2022.100029

Allahverdi, A., Škvára, F., 2000. Acidic corrosion of hydrated cement based materials. Part 1. Mechanism of the phenomenon. Ceram. - Silik. 44, 114–120.

Álvarez-Pinazo, G., Santacruz, I., León-Reina, L., Aranda, M.A.G., De la Torre, A.G., 2013. Hydration Reactions and Mechanical Strength Developments of Iron-Rich Sulfobelite Eco-cements. Ind. Eng. Chem. Res. 52, 16606–16614. https://doi.org/10.1021/ie402484e

Baston, G.M.N., Clacher, A.P., Heath, T.G., Hunter, F.M.I., Smith, V., Swanton, S.W., 2012. Calcium silicate hydrate (C-S-H) gel dissolution and pH buffering in a cementitious near field. Mineral. Mag. 76, 3045–3053.

Bescher, E., Vallens, K., Kim, J., 2019. Belitic calcium sulfoaluminate cement: Hydration chemistry, performance, and use in the United States.

Bishnoi, S., Scrivener, K.L., 2009. Studying nucleation and growth kinetics of alite hydration using μic. Cem. Concr. Res. 39, 849–860. https://doi.org/10.1016/j.cemconres.2009.07.004

Borštnar, M., Daneu, N., Dolenec, S., 2020. Phase development and hydration kinetics of belite-calcium sulfoaluminate cements at different curing temperatures. Ceram. Int., Thermophysical Aspects of Functional Ceramics and Surfaces 2019 46, 29421–29428. https://doi.org/10.1016/j.ceramint.2020.05.029

Chi, L., Wang, Z., Lu, S., Wang, H., Liu, K., Liu, W., 2021. Early assessment of hydration and microstructure evolution of belite-calcium sulfoaluminate cement pastes by electrical impedance spectroscopy. Electrochimica Acta 389, 138699. https://doi.org/10.1016/j.electacta.2021.138699

Cuberos, A.J.M., De la Torre, Á.G., Álvarez-Pinazo, G., Martín-Sedeño, M.C., Schollbach, K., Pöllmann, H., Aranda, M.A.G., 2010. Active Iron-Rich Belite Sulfoaluminate Cements: Clinkering and Hydration. Environ. Sci. Technol. 44, 6855–6862. https://doi.org/10.1021/es101785n

Cuesta, A., Ayuela, A., Aranda, M.A.G., 2021. Belite cements and their activation. Cem. Concr. Res. 140, 106319.

Damion, T., Cepuritis, R., Chaunsali, P., 2022. Sulfuric acid and citric acid attack of calcium sulfoaluminate-based binders. Cem. Concr. Compos. 130, 104524. https://doi.org/10.1016/j.cemconcomp.2022.104524

Damion, T., Chaunsali, P., 2022. Evaluating acid resistance of Portland cement, calcium aluminate cement, and calcium sulfoaluminate based cement using acid neutralisation. Cem. Concr. Res. 162, 107000. 0

De Windt, L., Badreddine, R., 2007. Modelling of long-term dynamic leaching tests applied to solidified/stabilised waste. Waste Manag. 27, 1638–1647. https://doi.org/10.1016/j.wasman.2006.07.019

Dyer, T., 2017. Influence of cement type on resistance to attack from two carboxylic acids. Cem. Concr. Compos. 83, 20–35. https://doi.org/10.1016/j.cemconcomp.2017.07.004

Fjendbo, S., Sørensen, H.E., De Weerdt, K., Jakobsen, U.H., Geiker, M.R., 2022. Correlating the development of chloride profiles and microstructural changes in marine concrete up to ten years. Cem. Concr. Compos. 131, 104590. https://doi.org/10.1016/j.cemconcomp.2022.104590

Gabrisová, A., Havlica, J., Sahu, S., 1991. Stability of calcium sulphoaluminate hydrates in water solutions with various pH values. Cem. Concr. Res. 21, 1023–1027. https://doi.org/10.1016/0008-8846(91)90062-M

Glasser, F.P., Zhang, L., 2001. High-performance cement matrices based on calcium sulfoaluminate–belite compositions. Cem. Concr. Res. 31, 1881–1886. https://doi.org/10.1016/S0008-8846(01)00649-4

Khaitan, S., Dzombak, D.A., Lowry, G.V., 2009. Chemistry of the Acid Neutralization Capacity of Bauxite Residue. Environ. Eng. Sci. 26, 873–881. https://doi.org/10.1089/ees.2007.0228

McCarthy, G.J., Hassett, D.J., Bender, J.A., 1992. Synthesis, crystal chemistry and stability of ettringite, a material with potential applications in hazardous waste immobilization. Mater Res Soc Symp Proc 245, 129–140.

Scrivener, K.L., Cabiron, J.-L., Letourneux, R., 1999. High-performance concretes from calcium aluminate cements. Cem. Concr. Res. 29, 1215–1223. https://doi.org/10.1016/S0008-8846(99)00103-9

Song, F., Yu, Z., Yang, F., Lu, Y., Liu, Y., 2015. Microstructure of amorphous aluminum hydroxide in belite-calcium sulfoaluminate cement. Cem. Concr. Res. 71, 1–6. https://doi.org/10.1016/j.cemconres.2015.01.013

Zheng, D., Monasterio, M., Feng, W., Tang, W., Cui, H., Dong, Z., 2021. Hydration Characteristics of Tricalcium Aluminate in the Presence of Nano-Silica. Nanomaterials 11, 199. https://doi.org/10.3390/nano11010199

The 16th International Congress on the Chemistry of Cement 2023 (ICCC2023)
"Further Reduction of CO_2 -Emissions and Circularity in the Cement and Concrete Industry"
September 18–22, 2023, Bangkok, Thailand

Early-Age Hydration Characteristics of Ye'elimite in the Presence of Calcium Sulfate and Alkalis

Bipina Thaivalappil[1], Vaishnav Kumar Shenbagam[2*], and Piyush Chaunsali[1]

[1] *Department of Civil Engineering, IIT Madras, Chennai, India*

Email: pchaunsali@civil.iitm.ac.in, ce20d700@smail.iitm.ac.in

[2] *Department of Materials Science and Engineering, The University of Sheffield, Sheffield, S1 3JD, UK*

Email: v.shenbagam@sheffield.ac.uk

ABSTRACT

Calcium sulfoaluminate-belite (CSAB) cement is a technically adequate low-CO_2 alternative binder to Portland cement (PC). Ye'elimite, the main phase of CSAB cement, hydrates rapidly to form the calcium sulfoaluminate phases such as ettringite or monosulfate. The reactivity of ye'elimite has been reported to be dependent on other phases in CSAB cement such as the amount and the type of calcium sulfate, calcium hydroxide, and alkalis. CSAB cements exhibit several interesting properties such as rapid setting, early-age strength development, and shrinkage compensation depending on their phase compositions. Hence, it is important to understand the hydration characteristics of ye'elimite and the role of other phases on ye'elimite reactivity. This paper aims at studying the influence of sulfate and alkalis on the reactivity of ye'elimite. For the study, laboratory synthesised ye'elimite, reagent grade gypsum, and NaOH were used. The hydration kinetics and hydrate phase evolution were investigated using various characterization techniques. The sulfate in form of gypsum had significant influence in promoting ye'elimite hydration at an early age. The alkali incorporation in the reaction solution in presence of gypsum further enhanced the dissolution-precipitation reactions in the initial hours of hydration.

KEYWORDS: *Calcium Sulfoaluminate-Belite cement, Ye'elimite, Alkalis, Hydration*

1. Introduction

Ye'elimite ($Ca_4(Al_2O_3)_3SO_4$ or $C_4A_3\hat{S}$ in cement chemistry notation), also known as Klein's compound, constitutes the primary component of Calcium Sulfoaluminate-Belite (CSAB) based binders, which are considered to be alternative binders to Portland cement with reduced carbon footprint(Piyush Chaunsali and S. Vaishnav Kumar (2020)). Ye'elimite has a relatively lower CaO content than the Portland cement (PC) phases, reducing the raw material CO_2 emission associated with its formation(Gartner (2004)). The high early-age strength and shrinkage compensating properties of CSAB-based binders are mainly controlled by the hydration of ye'elimite forming ettringite. Ye'elimite hydrates to form monosulphate or ettringite along with aluminium hydroxide depending on the availability of other phases (Eqn 1-3)(V.Kasselouri and P.Tsakiridis (1995)).

$$C_4A_3\hat{S} + 18H \rightarrow C_3A.C\hat{S}.12H + 2AH_3 \quad (1)$$

$$C_4A_3\hat{S} + 2C\hat{S}H_2 + 34H \rightarrow C_3A.3C\hat{S}.32H + 2AH_3 \quad (2)$$

$$C_4A_3\hat{S} + 6CH + 8C\hat{S}H_2 + 74H \rightarrow 3C_3A.3C\hat{S}.32H \quad (3)$$

Apart from the amount of sulfate, other factors such as type of sulfate source, impurity incorporation, compatibility with other phases, and presence of alkalis can influence the reactivity and hydration of ye'elimite. This paper elucidates the influence of calcium sulfate and alkalis on early age hydration of ye'elimite. The alkalis are contained in various amounts in the raw materials used for CSAB cement production. Hence, hydration reactions and kinetics of ye'elimite in presence of alkalis need to be understood for predicting the behaviour of CSAB system under different alkaline condition. The solubility of aluminate phases was reported to be higher in presence of alkalis(Jawed and Skalny 1978), consequently, ye'elimite may show better reactivity in alkaline medium. A few studies (Canbek et al.

(2020); Chen (2009); Ogawa and Roy (1982)) have reported accelerated reaction of ye'elimite when hydrated in presence of alkalis. However, the influence of alkalis on ye'elimite in presence of gypsum and the mechanism of hydration is not clearly understood.

2. Materials and methodology

Ye'elimite synthesized in laboratory scale using reagent grade CaO, Al_2O_3, and $CaSO_4$ (purity >95%) was used for the study. The stoichiometric proportions of the raw materials were taken and wet mixed using water for homogenous mixing. Additional 5% $CaSO_4$ was added to the mix to compensate for the sulfur volatilization during clinkering. The wet mixed raw mix was pelletized after oven drying and further taken for clinkering in a muffle furnace. A maximum temperature of 1400 °C and heating rate of 5 °C/min were used for the synthesis. The sintered pellet was taken out from furnace at 1000 °C and allowed for rapid air cooling to room temperature. The synthesised material had over 90% ye'elimite with other minor aluminate phases (~5% by weight). Further, it was ground in a planetary ball mill to a finer size with D_{50} of ~46 μm. Laboratory grade $CaSO_4.2H_2O$ and NaOH were used as the sources of gypsum and alkali. The proportioning of different mixes with ye'elimite is shown in Table 1.

Table 1: Mixture proportions used for the study

Sample Name	Mix proportion			
	(wt. %)		*(% by weight of binder)*	
	Ye'elimite	**Gypsum**	**NaOH**	**Water**
Y	100	0	0	50
Y+G	64	36	0	50
Y+G+A	64	36	1	50

Characterization techniques including X-ray diffraction (XRD), thermogravimetry (TG), isothermal calorimetry, and scanning electron microscopy (SEM) were used to study the early age hydration of the proportioned mixes. Hydrated samples were preserved in vaccum dessicator after hydration stoppage using isopropanol. The samples were ground using an agate mortar and pestle and passed through 75 μm sieve for XRD and TG analysis. The quantitative XRD was done with Rietveld refinement using PANalytical Xpert High Score Plus Software V.3. TG analysis was carried in a N_2 atmosphere at heating rate of 10 °C/min. Isothermal calorimetry was performed at constant room temperature (23 °C) for assessing the hydration kinetics using a Calmetrix I-Cal HPC 4-channel calorimeter. The 3-day hydrated samples were taken for SEM to study the morphological evolution of the hydrates. The sample surfaces were imaged after gold sputter coating under 5 kV at different magnifications.

3. Results and discussion

Figure 1 shows the XRD of 1-d and 3-d hydrated ye'elimite mixes. Though generally it is difficult to identify monosulfate from XRD due to their poor crystallinity(Gastaldi et al. 2016), monosulfate in the form of crystalline kuzelite was observed in the pure ye'elimite mix (Y). From XRD and TG analysis (Figure 2) it was confirmed that the major hydration products of ye'elimite were monosulfate and amorphous aluminium hydroxide. Whereas in the presence of gypsum (Y+G), ettringite was observed to form instead of monosulfate. As the Y+G mix had a molar ratio of gypsum to ye'elimite as 2 (amount of calcium sulfate required as per stoichiometry), gypsum depletion leading to monosulfate formation could be prevented. Hence, the main hydration products were ettringite and amorphous aluminium hydroxide in presence of gypsum. When 1% of alkalis in the form of NaOH was introduced to ye'elimite-gypsum mix (Y+G+A), no significant difference could be observed from XRD plots, except for the decrease in the gypsum peak at one day. Unreacted ye'elimite in the mixes quantified using Rietveld refinement were 15%, 12%, 18% (% by weight normalized to anhydrous ye'elimite) in the Y, Y+G, and Y+G+A mixes, respectively. This indicated that the unreacted ye'elimite is minimum in Y+G mix, linking to a higher degree of hydration. Further, the higher cumulative mass loss from TG also indicated a higher degree of hydration in the Y+G mix.

To understand the effect of sulfate and alkalis on the hydration kinetics, calorimetry was conducted on the mixes and the results are shown in Figure 3 and Figure 4. As observed from XRD and TG, the presence of gypsum promoted the hydration of ye'elimite, and it was also evident from the heat evolution curves.

The main hydration peak was shifted toward left, resulting in a reduced dormant period in presence of gypsum. A higher cumulative heat was observed in Y mix compared to Y+G, which could be due to the presence of higher proportion of ye'elimite in the Y mix. Interestingly, significant influence on reaction kinetics at very early age was observed when alkali was incorporated in the mix. In the Y+G+A mix, the major peak was observed with significantly higher heat rate and the peak appeared at a very early stage of reaction (before 3 hours). The pronounced increase in heat flow indicates a higher degree of reaction in ye'elimite and early precipitation of ettringite. The shift in peak could be attributed the faster dissolution of constituent(s) in the presence of alkalis promoting this reaction(Tambara et al. (2020)). As this event occurred at very early stages of hydration, it was not well captured by the calorimeter due to external mixing. However, the acceleration of reaction didn't continue in the further stages of hydration; instead, in the presence of alkalis, the heat evolution was almost stabilized beyond 10 hours. Although the cumulative heat evolved before 10 hours is considerably less in the no-alkali mix, the total heat at 3-day is more as the no-alkali mix continued to hydrate further.

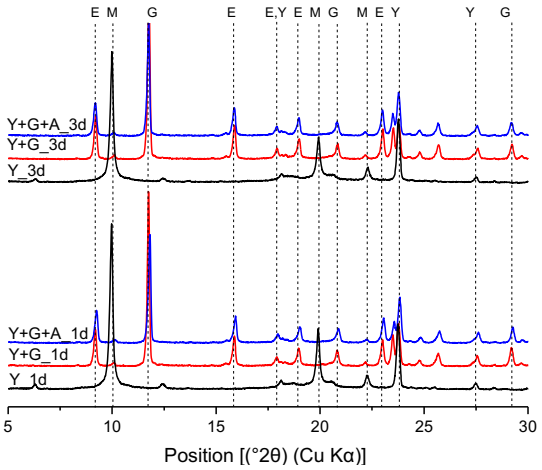


Figure 1: X-ray diffractograms of 1-day and 3-day hydrated ye'elimite *(E: AFt, M: AFm, G: Gyspum, Y: Ye'elimite)*

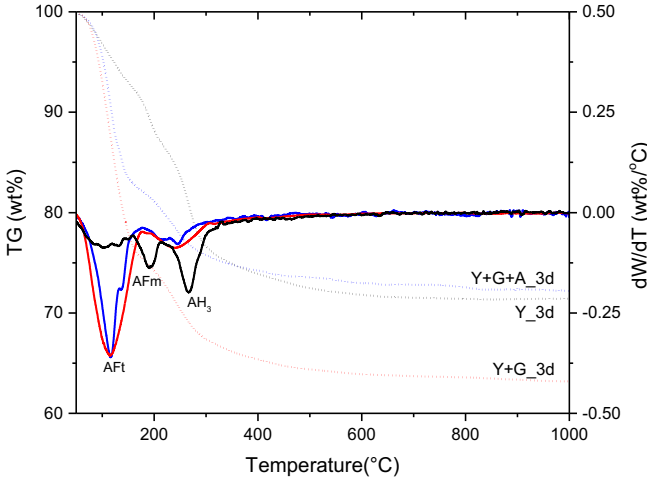


Figure 2: Thermogravimetric analysis of 3-day hydrated ye'elimite

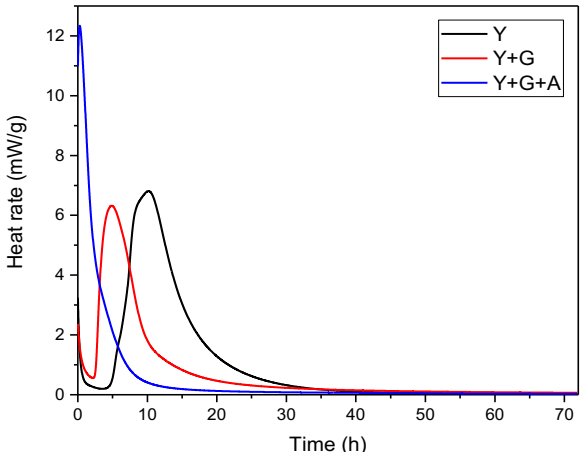


Figure 3: Heat evolution in ye'elimite mixes measured using isothermal calorimetry

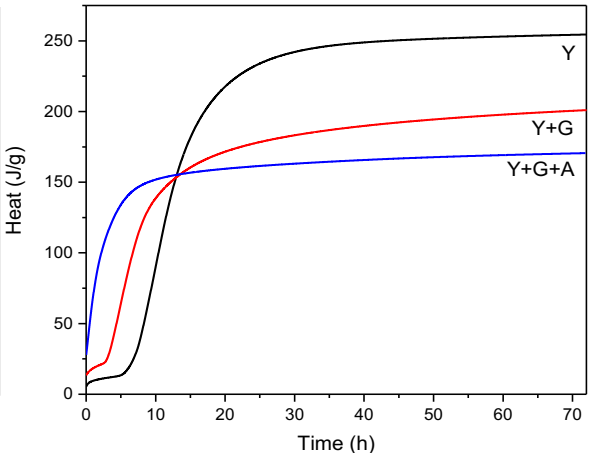


Figure 4: Total heat in ye'elimite mixes measured using isothermal calorimetry

The SEM images of the 3-day hydrated samples are shown in Figure 5. Monosulfate and aluminium hydroxide with grassy-like appearance were identified in the Y mix. Although aluminium hydroxide was observed to form in the Y+G and Y+G+A mixes, the grassy-like appearance could not be observed. Further, the ettringite formed in alkali containing mix was observed to be more slender (higher aspect ratio) compared to that of the no-alkali mix. The slenderness of ettringite is dependent on the pH of the reaction solution; an increase in pH facilitates formation of a greater number of ettringite nuclei leading to precipitation of more fine needle like crystals than columnar crystals (Stark, J and Bollmann (2000)).

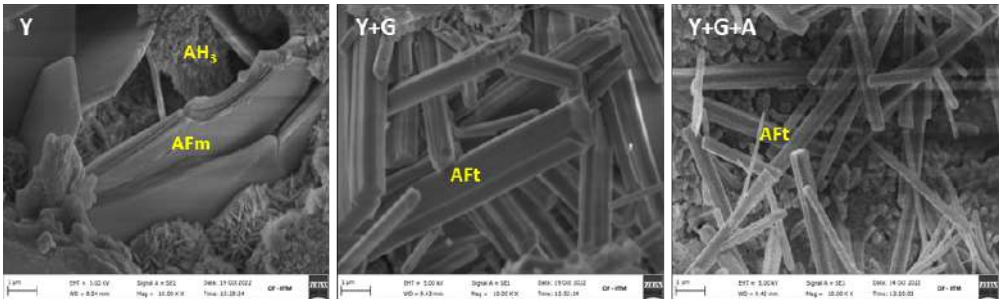


Figure 5: The microstructure of 3-day hydrated ye'elimite captured in secondary electron imaging in SEM

4. Conclusions

In this work, the early age hydration of laboratory synthesized ye'elimite was investigated to understand the influence of sulfate and alkalis. The presence of sulfate in the form of gypsum was found to accelerate the ye'elimite hydration. The alkali incorporation in the reaction solution in presence of gypsum further enhanced the dissolution-precipitation reactions at the initial few hours. A pronounced increase of the major hydration peak was observed in the presence of alkalis. This indicates that the 1% alkali could promote the dissolution of the constituent phases. However, the faster hydration kinetics in presence of alkalis didn't prolong beyond 10 hours of hydration. The progress of hydration was minimal beyond initial 10 hours in the presence of alkalis, resulting in reduced degree of hydration at the end of 3 days. A dissolution study on ye'elimite and gypsum with alkalis could bring more clarity on the effect of alkalis on their solubility. The presence of sulfate and alkali were also found to have an influence on the morphology of hydration products; especially, the morphology of aluminium hydroxide was affected by the presence of sulfate and ettringite morphology was affected by the presence of alkalis.

Acknowledgements

The first author would like to thank Ministry of Education of India for the Prime Minister's Research Fellowship. The authors wish to acknowledge the Institute of Eminence Research Initiative grant on Technologies for Low Carbon and Lean Construction and experimental facilities provided by the Department of Civil Engineering of IIT Madras.

References

Canbek, O., Shakouri, S., and Erdoğan, S. T. (2020). "Laboratory production of calcium sulfoaluminate cements with high industrial waste content." *Cement and Concrete Composites*.

Chen, I. A. (2009). "Synthesis of Portland Cement and Calcium Sulfoaluminate-Belite Cement for Sustainable Development and Performance." *PCA R&D Serial No. SN3130*, 1–216.

Gartner, E. (2004). "Industrially interesting approaches to ' 'low-CO2 ' ' cements." *Cement and Concrete Research*, 34, 1489–1498 Industrially.

Gastaldi, D., Paul, G., Marchese, L., Irico, S., Boccaleri, E., Mutke, S., Buzzi, L., and Canonico, F. (2016). "Hydration products in sulfoaluminate cements: Evaluation of amorphous phases by XRD/solid-state NMR." *Cement and Concrete Research*, Elsevier Ltd, 90, 162–173.

Jawed, I., and Skalny, J. (1978). "Alkalies in Cement: A review II. Effects of Alkalies on Hydration and Performance of Portland Cement." *Cement and Concrete Research*, 9(4), 198–200.

Ogawa, K., and Roy, D. M. (1982). "C4A3S̄ hydration, ettringite formation, and its expansion mechanism: III. Effect of CaO, NaOH and NaCl; conclusions." *Cement and Concrete Research*, 12(2), 247–256.

Piyush Chaunsali; S. Vaishnav Kumar. (2020). "Calcium Sulfoaluminate-Belite Cements: Opportunities and Challenges." *The Indian Concrete Journal*.

Stark, J and Bollmann, K. (2000). "Delayed ettringite formation in concrete structures." *Nordic Concrete Research-Publications*, 23, 4–28.

Tambara, L. U. D., Cheriaf, M., Rocha, J. C., Palomo, A., and Fernández-Jiménez, A. (2020). "Effect of alkalis content on calcium sulfoaluminate (CSA) cement hydration." *Cement and Concrete Research*, Elsevier, 128(August 2019), 105953.

V.Kasselouri, and P.Tsakiridis. (1995). "A study on the hydration products of a non-expansive sulfoaluminate cement V." *Cement and Concrete Research*, 25(8), 1726–1736.

The 16th International Congress on the Chemistry of Cement 2023 (ICCC2023)
"Further Reduction of CO_2 -Emissions and Circularity in the Cement and Concrete Industry"
September 18–22, 2023, Bangkok, Thailand

'A Tale of Two Cations': the influence of interlayer chemistry on the behaviour of montmorillonite clay alkali-activated cements

S.Krishnan[1], A.T.M. Marsh[2], and S.A. Bernal[3*]

Email: S.Krishnan1@leeds.ac.uk
[1] *School of Civil Engineering, University of Leeds, Leeds, United Kingdom*

Email: A.Marsh@leeds.ac.uk
[2] *School of Civil Engineering, University of Leeds, Leeds, United Kingdom*

Email: S.A.BernalLopez@leeds.ac.uk
[3] *School of Civil Engineering, University of Leeds, Leeds, United Kingdom*

ABSTRACT

Common precursors used for alkali-activated cement products such as blast furnace slag, fly ash and high-purity metakaolin are extensively used by the construction industry. In order to future proof this technology, other precursors such as common clays are being considered for such application. Montmorillonite is a 2:1 clay mineral is distinguished by different interlayer cations, which influences its physical and chemical properties. There is a knowledge gap around the role of the interlayer cation on the fresh and hardened state properties of alkali-activated cements produced with such clays. In this study, a comparison was made between two montmorillonites with different interlayer cations: calcium and sodium. Both clays were thermally activated via calcination in a laboratory static furnace and mechano-chemically activated via intensive grinding in a planetary ball mill. Alkali-activated pastes were made using a sodium hydroxide activating solution. The early age reaction kinetics of the pastes were evaluated by isothermal calorimetry, and the microstructural features of hardened pastes were investigated by scanning electron microscopy. The interlayer cation was found to significantly influence the fresh state properties of the alkali-activated cements. Workability was significantly lower for the paste made with activated Ca-montmorillonites, attributed to the higher specific surface arising from its larger basal spacing. These findings highlight the potential pitfalls of using non-kaolinitic clays as precursors and offer potential solutions to overcome them.

KEYWORDS: *alkali-activated cement; interlayer cation; montmorillonite; workability*

1. Introduction

Alkali-activated cements (AACs) show significant potential as low-carbon cements (Palomo et al., 2021); however, the continuous availability of conventional precursors such as fly ash, high-purity metakaolin, and blast furnace slag is uncertain. Common clays are abundant globally and could be a scaleable source of AAC precursors (Khalifa et al., 2020). Montmorillonite is a dioctahedral 2:1 clay mineral and is an important constituent of many clay deposits and soils. The cations (e.g. Na^+, K^+, Cs^+, Ca^{2+}, Sr^{2+}) present in the inter-layer spaces between the 2:1 layers (each consisting of one octahedral sheet between two tetrahedral sheets) of montmorillonite can strongly influence their physical and chemical properties. Ca-montmorillonite and Na-montmorillonite are the two most commonly occurring montmorillonites (Murray, 2006). Recent studies indicate that thermally activated montmorillonitic clays can be a precursor for producing AACs (García-Lodeiro et al., 2014; Valentini et al., 2018); however, no previous study has specifically looked at the effect of the interlayer cation. In this study, a comparison was made between Ca-montmorillonite and Na-montmorillonite alkali-activated cements, to assess the effect of interlayer cation on montmorillonite AACs in the reaction kinetics and microstructural properties of such materials.

2. Materials and Methods

A Na-montmorillonite clay (Na-mont) and a Ca-montmorillonite clay (Ca-mont) sourced from Southern Clay Products (USA) were used in this study. Na-mont had an estimated purity of 61%, as determined by quantitative Rietveld XRD analysis; associated minerals were quartz, albite, biotite and cristobalite. Ca-mont had an estimated purity of 78%; associated minerals were quartz, muscovite, gypsum, K-feldspar, and opal-CT. Two different activation routes, thermal and mechano-chemical, were used to produce the activated clay precursors. The suffix "mech" or "therm" is used with the sample ID to differentiate between the activation routes. For thermal activation, the clays were calcined in a static muffle furnace for 1 hour at 830°C with a soaking time of 1 hour. High-intensity planetary ball milling was used for mechanochemical activation using 2 mm diameter stainless steel balls as grinding media. 10 g of clay was milled with 250 g of grinding media for 1 hour at 500 rpm to produce mechano-chemically activated precursor clays. The activating solution was prepared by dissolving 222 g of NaOH pellets in 500 g of deionized water, having an approximate concentration of 10.2M. The mix designs used to prepare the alkali-activated pastes are shown in Table 1. The mix designs were selected through initial trials to achieve a workable paste using montmorillonite precursors. The higher quantity of activator required for the Ca-Mont systems reflects the poorer workability of the activated Ca-Mont clays compared to the activated Na-Mont clays. This difference was previously observed for blends of Ca-montmorillonite and Na-montmorillonite clays with simulated Portland cement solutions (He et al., 1996). The precursor clays and the activator solutions were mixed for 5 minutes using a high-shear mixer at 1600 rpm to prepare alkali-activated pastes. The pastes were cured at 40°C and analyzed after 28 days. The "-28d" suffix indicates pastes at 28 days of ageing.

Table 1 – Mix designs used for preparing alkali-activated pastes

Sample ID	Mass of Clay (g)	Activation Solution (g)	Mass of Water (g)	Mass of NaOH (g)
Na-mont-mech	100	60	41.5	18.5
Na-mont-therm	100	60	41.5	18.5
Ca-mont-mech	100	100	69.3	30.7
Ca-mont-therm	100	100	69.3	30.7

Isothermal calorimetry was used to monitor the rate of heat evolution for up to 28 days at 40°C using a TAM Air Isothermal Calorimeter. Microstructures of the hardened alkali-activated pastes at 28 days curing were investigated using a Zeiss Evo 15 Scanning Electron Microscope, operating at an accelerating voltage of 20kV. Sections from hardened paste cylinders after 28 days curing were impregnated using an epoxy resin, polished and carbon coated prior to analysis. The compressive strengths of hardened alkali-activated pastes were determined on small cylindrical specimens (diameter = 1.2 cm, height = 2.4 cm) after 90 days of curing.

3. Results and Discussions

The thermally activated clay AAC pastes evolved substantially more heat compared to mechano-chemically activated clay AAC pastes over 28 days, irrespective of the inter-layer cation present in the clay (Figure 1a). A significant portion of the heat release occurred within the first 48 hours, followed by a gradual increase up to 28 days; pastes based on thermally activated clays exhibited a higher rate of heat release beyond 48 hours compared to the mechano-chemically activated clays. Two distinct peaks were observed in the heat flow curves (Figure 1b). Calorimetry studies on metakaolin-based geopolymers suggest that the initial sharp peak is due to the dissolution of metakaolin. The second peak is associated with forming a sodium aluminosilicate hydrate (N-A-S-H) or geopolymer-type gel (Yao et al., 2009). However, the second peak in the Na-mont-therm paste was observed around 12 hours. A third exothermic peak, occurring around 36 hours, have been reported in the calorimetric curves in some NaOH-activated metakaolin system above 35°C (Zhang et al., 2012), indicating the structural reorganization of the N-A-S-H gel or zeolites. For Na-Mont-therm, it is most likely that the late peak is a delayed polycondensation event rather than a

structural transformation event, given that it is much larger and occurs much sooner than any previously reported structural transformation peak. However, the reason for the delayed polycondensation reaction is still unclear.

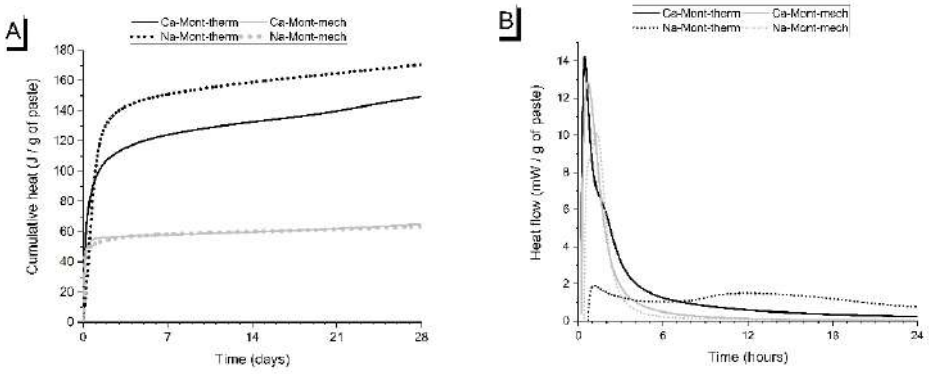


Figure 1 – (a) Cumulative heat for the AAC pastes up to 28 days (b) Rate of heat release up to the first 24 hours.

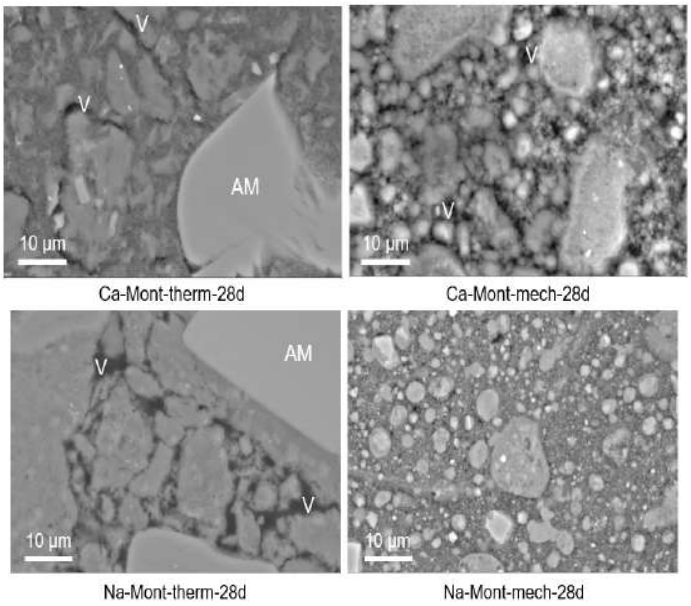


Figure 2- SEM-BSE images of alkali-activated pastes at 28 days. AM denotes large particles of associated minerals, and V indicates voids.

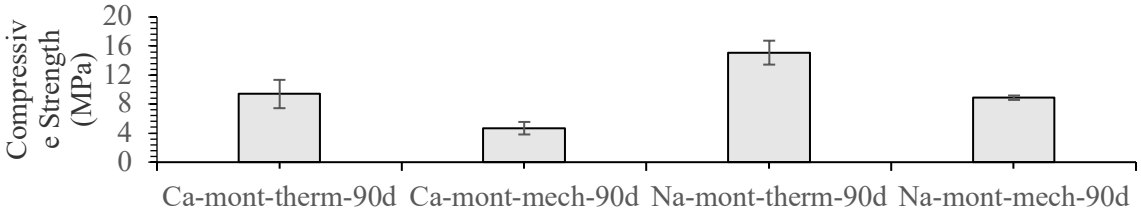


Figure 3 – 90 days compressive strengths of montmorillonite AAC pastes.

Clearly observable features in SEM-BSE images were the voids, associated minerals, loosely connected fine particles (<20 µm) and large patches displaying compositional contrast (Figure 2). Unreacted clay particles and associated minerals were embedded in the binder matrix. A higher amount of voids was observed in Ca-mont-mech-28d compared to Ca-mont-therm-28d, indicating a less dense microstructure in the mechanochemically activated systems. Interestingly, a reverse trend is observed in the case of Na-

montmorillonites, with Na-mont-therm-28d showing distinct voids compared to Na-mont-mech-28d. However, the reason behind this reversal is unclear and requires further investigation. The 90-day compressive strengths of the montmorillonite AACs are shown in Figure 3. Thermally activated sodium montmorillonite displayed the highest compressive strength (nearly 15 MPa) among the four clays investigated by 90 days. Studies (García-Lodeiro et al., 2014) indicate that the curing temperature could also play a critical role in these systems' strength and microstructural development. At 80°C curing temperature, montmorillonitic clays activated with NaOH achieved compressive strengths of nearly 20 MPa after 24 hours, while the samples were cured at 40°C in the present study. The compressive strengths of the Na-mont AAC pastes were higher than that of the Ca-mont AAC pastes, consistent with lower water content in these binders. For the same inter-layer cation, thermal activation appears more effective than mechano-chemical activation regarding compressive strength development for montmorillonite clays. These results differ from what would be expected from 28-day cumulative heat values alone (Figure 1a), in which the activation method has a far more significant influence on the chemical reactivity than the inter-layer cation type present in the clay. This suggests that the differences in microstructure seen in Figure 2 play an important role in determining mechanical properties, alongside the differences in the extent of reaction, as shown through isothermal calorimetry.

4. Conclusion

The results from this study indicate that the inter-layer cation has a strong influence on montmorillonite alkali-activated cements. The type of inter-layer cation appears to affect the workability of the alkali-activated pastes, with the Ca-montmorillonite clay requiring a higher activator dosage to produce workable pastes compared to the Na-montmorillonite clay. This will have practical implications for formulating mix designs. Isothermal calorimetry and compressive strength results indicate that thermal activation may be more effective than mechanochemical activation for producing alkali-activated cements from montmorillonites. However, the precise way in which interlayer cation and activation method affects reaction kinetics and microstructure requires further investigation.

5. Acknowledgements

This study was sponsored by the UK Engineering and Physical Sciences Research Council (EPSRC) via the Early Career Fellowship EP/R001642/1.

REFERENCES

García-Lodeiro, I., Cherfa, N., Zibouche, F., Fernández-Jimenez, A., Palomo, A., 2014. The role of aluminium in alkali-activated bentonites. Mater. Struct. Constr. 48, 585–597.

He, C., Makovicky, E., Osbæck, B., 1996. Thermal treatment and pozzolanic activity of Na- and Ca-montmorillonite. Appl. Clay Sci. 10, 351–368.

Khalifa, A.Z., Cizer, Ö., Pontikes, Y., Heath, A., Patureau, P., Bernal, S.A., Marsh, A.T.M., 2020. Advances in alkali-activation of clay minerals. Cem. Concr. Res. 132, 106050.

Murray, H.H., 2006. Chapter 6 Bentonite Applications. pp. 111–130.

Palomo, A., Maltseva, O., Garcia-Lodeiro, I., Fernández-Jiménez, A., 2021. Portland Versus Alkaline Cement: Continuity or Clean Break: "A Key Decision for Global Sustainability." Front. Chem. 9, 1–28.

Valentini, L., Contessi, S., Dalconi, M.C., Zorzi, F., Garbin, E., 2018. Alkali-activated calcined smectite clay blended with waste calcium carbonate as a low-carbon binder. J. Clean. Prod. 184, 41–49.

Yao, X., Zhang, Z., Zhu, H., Chen, Y., 2009. Geopolymerization process of alkali-metakaolinite characterized by isothermal calorimetry. Thermochim. Acta 493, 49–54.

Zhang, Z., Wang, H., Provis, J.L., Bullen, F., Reid, A., Zhu, Y., 2012. Quantitative kinetic and structural analysis of geopolymers. Part 1. the activation of metakaolin with sodium hydroxide. Thermochim. Acta 539, 23–33.

The 16th International Congress on the Chemistry of Cement 2023 (ICCC2023)
"Further Reduction of CO_2 -Emissions and Circularity in the Cement and Concrete Industry"
September 18–22, 2023, Bangkok, Thailand

Understanding Reaction Mechanisms, Kinetics, and Structural Evolution in Alkali-Activated Slag Cements

E. Cliff[1*], D. A. Geddes[2], J. L. Provis[2] and B. Walkley[1]

[1] *Department of Chemical and Biological Engineering, University of Sheffield, Sheffield, United Kingdom*
Email: ecliff2@sheffield.ac.uk, b.walkley@sheffield.ac.uk
[2] *Department of Materials Science and Engineering, University of Sheffield, Sheffield, United Kingdom*
Email: d.geddes@sheffield.ac.uk, j.provis@sheffield.ac.uk

ABSTRACT

Alkali-activated cements are often noted to have the potential to reduce cement-associated carbon emissions by up to 80%. Despite this, commonly used activators – alkali silicates and hydroxides – have much greater embodied CO_2 emissions compared to less widely used alkali carbonates, which are naturally occurring or produced from CO_2 sequestration, but have lengthy initial setting and hardening times, and poor early strength development. Through use of isothermal calorimetry and infrared spectroscopy, this study explores the reaction mechanisms and kinetics in carbonate- and silicate-activated slag binders. This understanding is essential for driving implementation in industry and minimising the environmental impact from carbon emissions associated with the cement industry.

KEYWORDS: *Alkali-activated slag (AAS), kinetics, reaction mechanisms, structural evolution.*

1. Introduction

A reduction by up to 80% in cement-associated carbon emissions has been proposed to be achievable via the development and use of alkali-activated cements (AACs) (Habert and Ouellet-Plamondon 2016), due to their production from industrial waste and/or by-products, as well as naturally occurring minerals. Despite this, the widely used alkali activators – alkali silicates and hydroxides – have greater embodied CO_2 emissions compared to their less commonly used counterparts, alkali carbonates, which are naturally occurring or can be produced via CO_2 sequestration processes. However, the currently limited use of carbonate activators in AAC production stems from their lengthy initial setting and hardening time, in addition to their poor early strength development. This study, therefore, aims to understand the reaction mechanisms and kinetics of carbonate-activated slag binders in comparison to silicate-activated slag cements, to provide new insight which may then be used to explain their effect on the physical properties of these binders.

2. Materials and Methods

Samples in this study were produced with ground granulated blast furnace slag (GGBFS/BFS), supplied by Ecocem (France), and activated at different dosages with sodium silicate ($Na_2O{\cdot}2SiO_2$), sodium carbonate (Na_2CO_3), or a combination of the two aforementioned activators in a 50:50 mass ratio. These chemical compositions of samples are detailed in Table 1. The initial samples (#1-3) are designed to be comparable with previous studies on the microstructure and nanostructure of AAC made with carbonate-based activators (Bernal et al. 2015, 2016; Walkley et al. 2021). However, it is important to note that the sodium silicate used herein has a modulus (SiO_2/Na_2O) of 2.0, and as such, contains less Na_2O for a given mass than the sodium carbonate activator.

2.1 Isothermal Conduction Calorimetry (ICC)

Isothermal conduction calorimetry was used to study the hydration process of the cement pastes by measuring the rate of their heat production for the first 7 days. For analysis by ICC, samples were prepared directly in glass ampoules, with a total sample mass of 20 g, and mixed for 2 minutes on a vortex mixer. Cement paste samples were assessed against a reference sample of water, and all heat flow data has been normalised for analysis.

Table 1. Chemical formulation of each cement paste tested, where w/s is the water-to-solid ratio of the cement and dosage is defined as mass of activator relative to the mass of anhydrous slag.

Sample #	Activator	$Na_2O{\cdot}2SiO_2$:Na_2CO_3 (wt.%)	w/s	Dosage (wt.%)
1	$Na_2O.2SiO_2$	100:0	0.40	8.0
2	$Na_2O.2SiO_2$ + Na_2CO_3	50:50	0.40	8.0
3	Na_2CO_3	0:100	0.40	8.0
4	$Na_2O.2SiO_2$	100:0	0.40	4.0
5	$Na_2O.2SiO_2$ + Na_2CO_3	50:50	0.40	4.0
6	Na_2CO_3	0:100	0.40	4.0
7	$Na_2O.2SiO_2$	100:0	0.40	12.0
8	$Na_2O.2SiO_2$ + Na_2CO_3	50:50	0.40	12.0
9	Na_2CO_3	0:100	0.40	12.0

2.2 Fourier Transform Infrared Spectroscopy (FTIR)

FTIR was conducted to identify bond environments in the slag samples at points throughout their hydration. Samples were prepared by mixing components (BFS, activator, and water) for 10 minutes using an overhead high-shear mixer at 1200 rpm then sealed and cured at 20°C. At 1, 3, and 7 days, the samples were subjected to solvent exchange with isopropanol to halt the reaction, then dried and ground to a fine powder for analysis.

3. Results and Discussion

3.1 Isothermal Conduction Calorimetry

As can be seen in Figures 1 and 2, the heat evolution shows four distinct stages of reaction. The pre-induction period can be observed as a first peak during the initial few hours of reaction, corresponding to the surface wetting and initial dissolution of slag particles. These data, however, do not capture the heat evolution during the first 2 minutes of reaction after mixing, due to the mixing of samples outside of the calorimeter. The pre-induction period is followed by a dormant (or induction) period where a very low rate of heat is released, associated with a progressive dissolution of slag particles as well as initial condensation and precipitation of reaction products. A second, more significant stage of heat release ensues, consistent with the acceleration period of cementitious binders, which is indicative of the nucleation, growth, and precipitation of a large amount of reaction products. The deceleration period follows as the final stage, where the reaction rate gradually slows after setting (Criado et al. 2018; Ke et al. 2016).

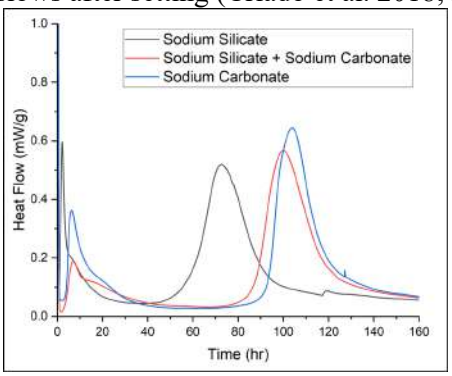


Figure 1. Heat release rate of the alkali-activated slag samples, activated with either sodium silicate, sodium carbonate, or both sodium silicate and sodium carbonate at a dosage of 8 wt.%.

Figure 1 shows that slag binders activated with sodium carbonate have a longer induction period than those activated with sodium silicate, where there is approximately a 30-hour difference between the onset of the respective acceleration periods, consistent with the known slower setting time of carbonate-activated slag cements (Bernal et al. 2015; Ke et al. 2016). The sample produced with the mixed activator appears to react quicker than the solely carbonate-activated sample, which aligns with using combined activators as a compromise between reducing carbon emissions and achieving a desirable setting time. Despite the varying rates of reaction, the length of the induction period is similar for each of the samples.

Additionally, this study investigated the relationship between the dosage of activator with respect to solid precursor and the rate of reaction. For the sodium silicate-activated samples, as seen in Figure 2A, regardless of dosage, the duration of acceleration period is very similar, as is the heat flow during this stage.

However, the rate of reaction varies depending on dosage, with the fastest rate of reaction observed for the sample with 8 wt.% dosage. This is consistent with literature where the optimum dosage of sodium silicate has been found to be up to 7-8 wt.% for stable activation of slag, with higher doses not leading to any significant change in cumulative heat release (Criado et al. 2018). Counterintuitively, the slowest rate of reaction was observed for the sample with 12 wt.% dosage (a trend not observed for the sodium carbonate-activated samples, discussed below). This may result from crystallisaion of the sodium silicate activator at this higher concentration and silicate modulus (Provis and Van Deventer 2014), and appears consistent with ~7 wt. % being the observed upper limit of effectiveness of the activator in silicate-activated slag cements (Criado et al. 2018), however further work is required to fully understand this behaviour.

Sodium carbonate-activated samples (Figure 2B) displayed a much clearer trend with increasing dosage. The rate of reaction increases with activator dosage, as does the heat output, with 12 wt.% dosage displaying a much larger peak for its acceleration period than that of the 4 wt.% dosage. Despite this trend, the optimum dosage of both sodium silicate (8 wt.% dosage) and sodium carbonate (12 wt.% dosage) in this instance appear to give similar setting times according to the calorimetric data in Figure 2, suggesting that the commonly observed slower setting time in alkali carbonate-activated slag cements may be offset by increasing the activator dosage.

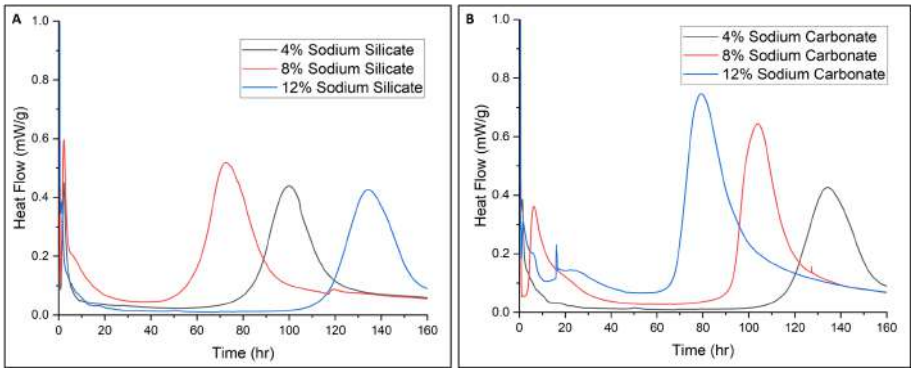


Figure 2. Heat release rate of the alkali-activated slag samples, activated with either (A) sodium silicate or (B) sodium carbonate, at dosages of 4, 8 and 12 wt.%.

3.2 Fourier Transform Infrared Spectroscopy

The FTIR spectra for BFS activated with sodium silicate, sodium carbonate, and a combination of both activators cured for 1, 3, and 7 days can be observed in Figure 3 below. Vibrations at 2970 and 1650 cm^{-1} appear in all samples and are attributed to highly ordered hydroxyl phases, indicative of bound water molecules within hydration phases (Garcia-Lodeiro et al. 2015). The doublet peak at 2325 and 2365 cm^{-1} appears due to attraction of CO_2 from the atmosphere (Berzina-Cimdina and Borodajenko 2012) during data acquisition.

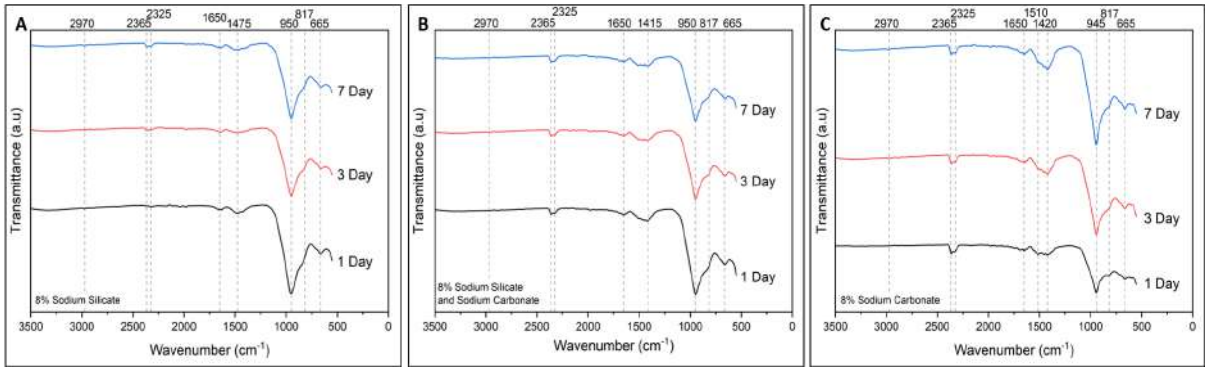


Figure 3. FTIR spectra for slag samples activated with (A) sodium silicate, (B) sodium silicate and sodium carbonate, and (C) sodium carbonate, at a dosage of 8 wt.% and cured for 1, 3, and 7 days as marked.

Bands observed at ~950 and 817 cm^{-1} are assigned to the asymmetric stretching of Si-O-T bonds and the symmetric stretching of T-O-T bonds, respectively, where T represents either Si or Al (Fernandez-Jimenez and Puertas 2003), and appear in the spectra for each sample. These bands are attributed to the aluminosilicate sites in the C-(A)-S-H gel, which is the main hydration and strength-giving phase of alkali-

activated slag cements. Additionally, in each sample, bands at 1475 and 665 cm^{-1} are observed, which correspond to the asymmetric stretching of C-O bonds of carbonate ions (Nguyen et al. 2022), likely attributed to carbonation of the samples.

The slag pastes activated with sodium carbonate display bands at ~1420 and 1510 cm^{-1}, which are also attributed to the asymmetric vibration of C-O bond of carbonate ions (Cao et al. 2020). As these bands do not appear in the sodium silicate-activated samples, it is likely that the precipitation of these carbonates contribute to the slower setting time of slag binders activated with sodium carbonates. Essentially, at early age, the Ca^{2+} ions from the slag preferentially react with the CO_3^{2-} ions of the activator to form calcium carbonates, whilst the aluminosilicate component of the slag likely reacts with the sodium from the activator to form either a sodium aluminosilicate gel (Walkley et al. 2021) or a crystalline zeolite, e.g. zeolite NaA, as observed previously (Bernal et al. 2015). These calcium carbonate phases, in addition to the slow dissolution of slag under moderate pH from the Na_2CO_3 activator, retard the reaction, causing a longer induction period. However, once the CO_3^{2-} is exhausted, the activating reaction continues similarly to an NaOH-activated slag binder (Bernal et al. 2015, 2016)

4. Conclusions

This study investigated the reaction mechanisms and kinetics in sodium carbonate- and sodium silicate-activated slag binders. Analysis of data from both ICC and FTIR show that slag binders activated with sodium carbonate react at a slower rate than those activated with sodium silicate due to the initial formation of calcium carbonates as well as the moderate pH conditions of the activator retarding the reaction. This insight helps to explain the effects of the alkali activator type and dose on the properties of the cements.

Acknowledgements

The study has been funded by the Engineering and Physical Sciences Research Council, through a scholarship to E.C. via a DTP award from the Faculty of Engineering at The University of Sheffield. Additional funding and training is provided through the Grantham Centre for Sustainable Futures.

References

Bernal, S. A., Provis, J. L., Myers, R. J., San Nicolas, R., and Van Deventer, J. S. J. (2015) "Role of Carbonates in the Chemical Evolution of Sodium Carbonate-Activated Slag Binders." *Materials and Structures* 48:517–29.

Bernal, S. A., San Nicolas, R., Van Deventer, J. S. J. and Provis, J. L. (2016) "Alkali-Activated Slag Cements Produced with a Blended Sodium Carbonate/Sodium Silicate Activator." *Advances in Cement Research* 28(4):262–73.

Berzina-Cimdina, L., and Borodajenko, N. (2012) "Research of Calcium Phosphates Using Fourier Transform Infrared Spectroscopy." *Infrared Spectroscopy - Materials Science, Engineering and Technology*. 123-148.

Cao, R., Zhang, S., Banthia, N., Zhang, Y. and Zhang, Z. (2020) "Interpreting the Early-Age Reaction Process of Alkali-Activated Slag by Using Combined Embedded Ultrasonic Measurement, Thermal Analysis, XRD, FTIR and SEM." *Composites Part B* 186:107840.

Criado, M, Walkley, B., Ke, X. and Provis, J. L. (2018) "Slag and Activator Chemistry Control the Reaction Kinetics of Sodium Metasilicate-Activated Slag Cements." *Sustainability* 10:4709.

Fernandez-Jimenez, A., and Puertas, F. (2003) "Structure of Calcium Silicate Hydrates Formed in Alkaline-Activated Slag : Influence of the Type of Alkaline Activator." *Journal of the American Ceramic Society* 86(8):1389–94.

Garcia-Lodeiro, I., Palomo, A. and Fernández-Jiménez, A. (2015) "Crucial Insights on the Mix Design of Alkali-Activated Cement-Based Binders." *Handbook of Alkali-Activated Cements, Mortars and Concretes*. 49-73.

Habert, G. and Ouellet-Plamondon, C. (2016) "Recent Update on the Environmental Impact of Geopolymers." *RILEM Technical Letters* 1:17.

Ke, X., Bernal, S.A. and Provis, J. L. (2016) "Controlling the Reaction Kinetics of Sodium Carbonate-Activated Slag Cements Using Calcined Layered Double Hydroxides." *Cement and Concrete Research* 81:24–37.

Nguyen, T. N., Phung, Q. T., Yu, Z., Frederickx, L., and Jacques, D. (2022) "Alteration in Molecular Structure of Alkali Activated Slag with Various Water to Binder Ratios under Accelerated Carbonation." *Scientific Reports* 1–16.

Provis, J. L., and Van Deventer, J. S. J. (2014). *Alkali Activated Materials: State of The Art Report*.

Walkley, B., Ke, X., Provis, J. L. and Bernal, S. A. (2021) "Activator Anion Influences the Nanostructure of Alkali-Activated Slag Cements." *Journal of Physical Chemistry C* 20727-39.

The 16th International Congress on the Chemistry of Cement 2023 (ICCC2023)
"Further Reduction of CO_2 -Emissions and Circularity in the Cement and Concrete Industry"
September 18–22, 2023, Bangkok, Thailand

Optimization of Hybrid Portland Cement – Metakaolin Binders

C. Monin[1*], L.F.M. Sanchez[2], S.A Bernal[3]

Email: cmoni019@uottawa.ca
[1] *University of Ottawa , Ottawa, Canada*

Email: Leandro.Sanchez@uottawa.ca
[2] *University of Ottawa , Ottawa, Canada*

Email: S.A.BernalLopez@leeds.ac.uk
[3] *University of Leeds, Leeds, United Kingdom*

ABSTRACT

The urgent need to develop sustainable and durable alternatives to Portland cement (PC) concrete has been a major drive for research on alkali-activated materials (AAMs). Amongst AAMs, hybrid alkaline binders appear to be the most industry-ready option, as their manufacturing process is similar to that of PC binders, they use milder doses of alkali-activators compared with other AAMs, and materials produced with those binders can develop excellent mechanical properties and high chemical resistance. However, the added complexity of these binders raises the need for further research to better understand and optimize them on a micro- to macroscale level. This study focuses on the optimization of hybrid alkali-activated metakaolin (MK) paste with varying PC content. The effect of the activator dose, in this case a sodium sulfate (NS) solution, was also evaluated. On a meso-to macroscale, the setting time and compressive strength of the samples were appraised, while conducting XRD and TGA on the hydrated cement pastes allowed for a microscale assessment of the chemical features. This study has shown that setting time may be decreased with NS addition. Improvements in early mechanical performance are also found at higher levels of PC substitution and with moderate amounts of activator, as shown by the strength of the 30%PC-5NS and 50%PC-10NS mixes surpassing that of the 50PC-0NS mix. These findings correlated well with microscale results which indicated greater extent of reaction from the raw precursors in the NS-activated mixes.

KEYWORDS: *Hybrid alkali-activated binders, calcined clay, multi-scale testing*

1. Introduction

The growing cement consumption worldwide is causing the construction industry to face crucial sustainability challenges. Finding sustainable and economical alternatives to traditional PC-based concrete has thus been a major focus of the scientific community in recent years and has driven the research in alkali-activated materials (AAMs) (Duxson et al., 2007; Wu et al., 2019). AAMs are a class of binders comprising amorphous aluminosilicate precursors activated with an alkaline activator solution such as sodium silicate, sodium hydroxide, or sodium sulfate (NS). These materials are promising and more sustainable alternatives to traditional concrete materials (Duxson et al., 2007). However, their most common activator, sodium silicate, is unsustainable with respect to many non-carbon environmental categories (Habert, 2013). Furthermore, both sodium silicate and sodium hydroxide are expensive and highly corrosive, which are major roadblocks on the path to large-scale industrialization of AAMs. Near-neutral salts, such as NS, have emerged as sustainable, user-friendly, and cost-effective alternatives to traditional activators (Bernal, 2016). Research on NS-activated binders remain scarce due to the delayed setting and strength gain that were observed for these materials (Bernal et al., 2014). The addition of PC clinker has however been found to improve the performance of NS-activated AAMs (Dakhane et al., 2017; Nawaz et al., 2020). To better understand the behaviour of this class of binders, this study will discuss the setting time, mechanical performance, and microscopic chemical features (i.e., XRD and TGA) of NS-activated MK-PC paste blends.

2. Experimental methodology

2.1 Materials and sample preparation

In this study, different blends of hybrid NS activated MK–PC paste samples were manufactured. The chemical composition of the raw MK and PC precursors was evaluated by X-ray fluorescence (XRF) and can be found in Table 1. The mix-design follows a 2-level factorial design. The water/binder ratio and binder (MK+PC) content are kept constant for all mixes and their value are fixed at 0.55 and 480 kg/m^3 respectively, while PC content is varied between 10 and 50 wt.% and NS content between 0 to 10 wt.%. NS solutions were made by magnetic stirring of the dry anhydrous NS powder in water at elevated temperature (40° – 80°C) until complete dissolution. The solutions were then left at room temperature to cool down. Prior to batching, the dry precursors were weighted and blended to ensure proper distribution of the MK and PC particles in the cast samples. The solutions were then incorporated gradually to the dry ingredients. After 5 minutes of mixing, the paste samples were cast in 50 mm x 100 mm molds for 24 hours, until demolding. They were then sealed to prevent carbonation and kept at room temperature (21 °C) until testing.

Table 1. Chemical composition of raw materials, determined by X-ray fluorescence (XRF).

Material	CaO	SiO_2	Al_2O_3	Fe_2O_3	MgO	SO_3	K_2O	Na_2O	Others
Metakaolin	0.385	62.5	29.8	1.23	0.42	-	1.75	0.18	0.77
Portland cement	61.5	19.4	4.9	3.7	2.4	3.9	0.95	-	3.25

2.2 Tests conducted

The setting time of the samples was determined following ASTM C191 (ASTM, 2021b) using a manual Vicat needle apparatus. In between measurements, samples were kept under a wet cloth to simulate high relative humidity conditions. Samples at 1 and 6 days of curing were tested in compression after being ground at both ends. 3 samples of each mix were tested each time and the test followed the procedure of ASTM C39 with 50 x 100 mm cylinders and an applied load of 0.25 MPa/s (ASTM, 2021a). At 6 days of curing, a sample from each mix design was crushed in large chunks and their hydration process was arrested with isopropanol. Two filtrations with ethanol were then conducted, 10 minutes apart. The pieces were then dried at 60 °C for 20 minutes and ground in an agate crucible. Before testing, the dried powder were kept in a dessicator to prevent carbonation. Powder X-ray diffraction (XRD) was performed on powdered samples using the Rigaku Ultima IV diffractometer equipped with a copper source and a diffracted beam monochromator. The samples were scanned over a 2θ range between 5º and 50ºC. Thermogravimetric analysis (TGA) was conducted on powdered samples using the Q5000 TGA instrument at a ending temperature of 1000°C and ramping rate of 20°C/min.

3. Results and discussion

3.1 Meso to macroscale analysis

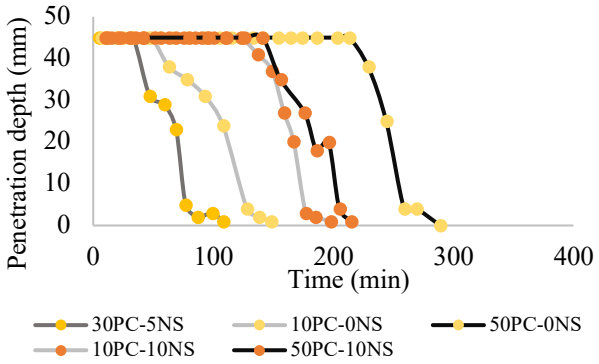


Figure 1. Vicat needle testing measurements

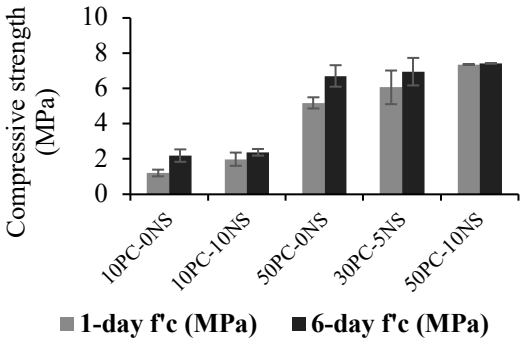


Figure 2. Compressive strength at 1 and 6 days

The results of Vicat needle testing illustrated in Figure 1 show that for mixtures with low PC content (10PC-0NS and 10PC-10NS), the final setting time was slower for the mix with 10NS. This result is surprising, as the incorporation of NS would typically raise the alkalinity of the fresh paste, which in

turn would accelerate the reaction kinetics of cement (Mota et al., 2018). On the other hand, for mixtures with high PC content (50PC-0NS and 50PC-10NS), the effect of NS was as anticipated, with the high NS content mix setting faster than its low NS counterpart. Regarding the impact of PC content, the 50PC mixes took the longest to set, but it is unlikely to be the direct consequence of their higher PC content. Higher calcium AAMs tend to have a shorter setting time, which would explain the faster setting of mix 30PC-5NS in comparison with mixes 10PC-10NS and 10PC-0NS. The longer setting of 50PC-0NS and 50-10NS might be more correlated with the w/b of these mixes. Because the high surface area and plate-like shape of MK significantly reduces the workability of high MK content mixes, the w/b ratio for all mixtures was based on minimal workability of the 10PC mixes (i.e., 10PC-10NS and 10PC-0NS). For the two 50PC mixes, the high w/b chosen led to a very flowable mix which may have artifically prolonged the setting of these mixes.

The compressive strength of the mixes at 1 and 6 days is shown in Figure 2. From this figure, it is possible to see that higher PC and higher NS contents generally provided higher strength to the samples. At low PC, the increase of strength due to NS was more significant after 1 day than at 6 days. Similar results are found for mixes 50PC-10NS and 50PC-0NS: strength is 42% higher for the 10NS mix after 1 day curing, and only 11% higher after 6 days. Those results may indicate that the presence of NS accelerates the early reaction kinetics, but may not have a significant impact on strength at later ages. It is also interesting to observe that the 30PC-5NS mix performed better that the the 50PC-0NS mixture, especially after 1 day of curing. This might indicate that the addition of NS could prevent the loss in mechanical properties typically associated with higher levels of PC replacement.

3.2 Microscale analysis

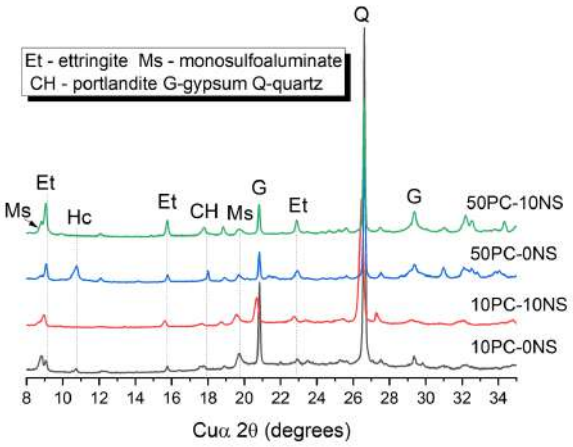


Figure 3. XRD patterns of 6-days samples

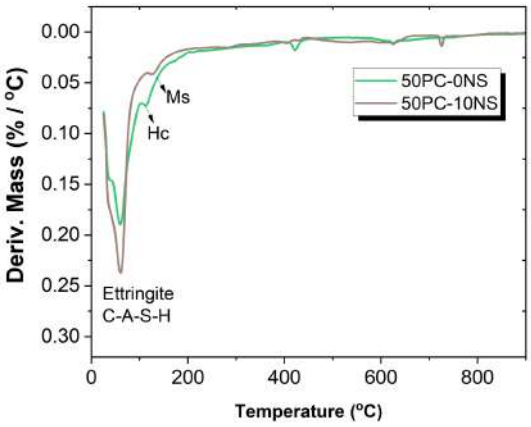


Figure 4. TGA of the 6-days high PC content samples

The diffraction patterns of all mixtures illustrated in Figure 3 reveals that both PC and NS content had a strong impact on the types of crystalline phases found in the binders. Hemicarbonate (HC) appears to be only forming in samples with no NS and is barely distinguisable at low PC (10PC-0NS). Low PC and low NS conditions seemed to favour the formation of monosulfoaluminate (Mc), while ettringite (E) seemed to be preferably formed at high PC and high NS conditions. A small peak due to portlandite (CH) appears in mixes with high PC content only. The presence of a strong quartz peak in all mixes is found to be due to the raw precursors. Finally, all mixes showed traces of gypsum, except for the one with low PC and high NS (10PC-10NS).

Figure 4 illustrates TGA results on the two mixes with the highest PC content (i.e., 50PC-10NS and 50PC-0NS). It is possible to observe that the thermal decomposition peaks vary in location and intensity. The first peak is observed in both samples from 55°C to 200°C. This peak is likely associated with the decomposition of evaporable water and C-S-H, as well as the dehydration of ettringite (Christopher Hall et al., 1996; Myers et al., 2014). The difference in intensity of this peak between the samples could be explained by a higher degree of dissolution of the precursors in the 10NS mix, and because of the greater degree of ettringite formation in sulfate-activated binders. The former hypothesis would correlate with the compressive strength and setting time results reported for the two mixes. Indeed, faster reaction kinetics and improved dissolution of the PC and MK may have occured

due to the addition of NS. The presence of a peak around 450°C for the 50PC-0NS paste only is further supporting this hypothesis. This peak indicates the decomposition of portlandite, but it is not observed in 50PC-10NS due to the consumption of the mineral by MK (Antoni et al., 2012). This suggests that more MK reacted in the sulfate-activated mix.

4. Conclusions

In this work, the properties of hybrid NS-activated MK-PC have been investigated on a micro to macroscale. The fresh state testing revealed that NS could accelerate the setting of cement paste with at least 30% of PC, but may slow setting at low PC contents (i.e., 10%PC). Furthermore, at the same level of PC content, the addition of NS benefited the strength of the samples. For the intermediate mix 30PC-10NS, the strength at 1 and 6 days was superior to that of the 50PC-0NS mix, thereby suggesting that higher levels of cement replacement could potentially be achieved with NS alkali-activation. This finding was correlated by the conduction of chemical analyses which revealed greater amounts of reaction products in NS-activated mixes.

References

Antoni, M., Rossen, J., Martirena, F., & Scrivener, K. (2012). *Cement substitution by a combination of metakaolin and limestone*. https://doi.org/10.1016/j.cemconres.2012.09.006

ASTM. (2021a). ASTM C39/C39M - 21 Standard Test Method for Compressive Strength of Cylindrical Concrete Specimens. In *ASTM International* . ASTM International. https://doi.org/10.1520/C0039_C0039M-21

ASTM. (2021b). ASTM C191 − 21 Standard Test Methods for Time of Setting of Hydraulic Cement by Vicat Needle. In *ASTM International*. ASTM International. https://doi.org/10.1520/C0191-21

Bernal, S. A. (2016). Advances in near-neutral salts activation of blast furnace slags. *RILEM Technical Letters*, *1*, 39. https://doi.org/10.21809/rilemtechlett.v1.8

Bernal, S. A., Provis, J. L., Fernández-Jiménez, A., Krivenko, P. V., Kavalerova, E., Palacios, M., & Shi, C. (2014). Binder chemistry - High-calcium alkali-activated materials. In *RILEM State-of-the-Art Reports* (Vol. 13, pp. 59–91). https://doi.org/10.1007/978-94-007-7672-2_3

Christopher Hall, Paul Barnes, Andrew D. Billimore, Andrew C. Jupeb, & Xavier Turrillasb. (1996). Thermal decomposition of ettringite Ca, [Al(OH)6]2(S04)3 26H2. *Journal of Chemistry Society*, *92*(12).

Dakhane, A., Tweedley, S., Kailas, S., Marzke, R., & Neithalath, N. (2017). Mechanical and microstructural characterization of alkali sulfate activated high volume fly ash binders. *Materials and Design*, *122*, 236–246. https://doi.org/10.1016/j.matdes.2017.03.021

Duxson, P., Fernández-Jiménez, A., Provis, J. L., Lukey, G. C., Palomo, A., & Van Deventer, J. S. J. (2007). Geopolymer technology: The current state of the art. *Journal of Materials Science*, *42*(9), 2917–2933. https://doi.org/10.1007/s10853-006-0637-z

Habert, G. (2013). Environmental impact of Portland cement production. *Eco-Efficient Concrete*, 3–25. https://doi.org/10.1533/9780857098993.1.3

Mota, B., Matschei, T., & Scrivener, K. (2018). Impact of NaOH and Na2SO4 on the kinetics and microstructural development of white cement hydration. *Cement and Concrete Research*, *108*(April), 172–185. https://doi.org/10.1016/j.cemconres.2018.03.017

Myers, R. J., L'hôpital, E., Provis, J. L., & Lothenbach, B. (2014). *Effect of temperature and aluminium on calcium (alumino)silicate hydrate chemistry under equilibrium conditions*. https://doi.org/10.1016/j.cemconres.2014.10.015

Nawaz, M. A., Ali, B., Qureshi, L. A., Usman Aslam, H. M., Hussain, I., Masood, B., & Raza, S. S. (2020). Effect of sulfate activator on mechanical and durability properties of concrete incorporating low calcium fly ash. *Case Studies in Construction Materials*, *13*. https://doi.org/10.1016/j.cscm.2020.e00407

Wu, Y., Lu, B., Bai, T., Wang, H., Du, F., Zhang, Y., Cai, L., Jiang, C., & Wang, W. (2019). Geopolymer, green alkali activated cementitious material: Synthesis, applications and challenges. *Construction and Building Materials*, *224*(206), 930–949. https://doi.org/10.1016/j.conbuildmat.2019.07.112

The 16th International Congress on the Chemistry of Cement 2023 (ICCC2023)
"Further Reduction of CO_2 -Emissions and Circularity in the Cement and Concrete Industry"
September 18–22, 2023, Bangkok, Thailand

Evaluation of the properties of completely recyclable mortar

Y.P. Liu[1,*], Y.Y. Cui[2], C. Yang[3] and M. Zhu[4]

[1] *State Key Laboratory of Silicate Materials for Architectures, Wuhan University of Technology, Wuhan, China*
Email: liuyunpeng@whut.edu.cn
[2] *State Key Laboratory of Silicate Materials for Architectures, Wuhan University of Technology, Wuhan, China*
Email: cuiyy2021@163.com
[3] *State Key Laboratory of Silicate Materials for Architectures, Wuhan University of Technology, Wuhan, China;*
Beijing Triumph International Engineering Co., Ltd, Beijing, China
Email: yangchao1996@whut.edu.cn
[4] *State Key Laboratory of Silicate Materials for Architectures, Wuhan University of Technology, Wuhan, China*
Email: mingz99@163.com

ABSTRACT

A completely recyclable concrete (CRC) was prepared based on the composition of raw cement meal. It was directly used as raw cement meal or incorporated with minor correction admixtures to prepare Portland cement clinker after demolition. Then, recycled cement could be used to prepare another CRC and further recycled. The authors' previous studies have studied the burnability, XRD patterns, free calcium oxide content, and mechanical strength of the recycled clinker after each cycle. In this study, the properties of a completely recyclable mortar have been investigated. The results showed that compared to control cement mortar, CRM showed a reduced early compressive strength but increased later strength growth rate. Moreover, its pore structure was refined, and its late-age impermeability improved. Adding steel slag and fly ash reduces the standard consistency water demand, and the setting time is prolonged considerably. At the same time, the addition of steel slag powder in the recycled concrete (23.9wt.% of the cementitious material) does not affect the volume stability of the concrete.

KEYWORDS: Completely recyclable concrete, regenerated cement clinker, compressive strength, impermeability

1. Introduction

Completely recyclable concrete (CRC) is designed according to the chemical compositions of cement clinker, whose chemical compositions are similar to those of raw cement meal (De Schepper et al.(2013; Schepper(2014)). Therefore, after being abandoned, it could be used as raw cement material to calcine cement clinker or added with minimal correction material. Furthermore, the obtained cement clinker can continue preparing another CRC and regenerating cement. In previous research, we investigated the incorporation of completely recyclable concrete as raw cement meal on the burnability of Portland clinker and conducted four recycles (Liu et al.(2021a); Liu et al.(2021b)). As a result, the CRC mix proportions differ from common concretes to meet the requirements of raw cement meal. However, the properties of CRC have yet to be investigated. Therefore, this study mainly compares the performance of CRC and ordinary cement concrete, which sheds some light on the design of CRC.

2. Materials and Methods

2.1 Materials

The cement used is P. I 42.5 Portland cement produced by QuFu ZhongLian Cement Co., Ltd. The coarse aggregates are gravel limestone with a 5 – 25 mm continuous grading. The fine aggregate consists of river sand with an apparent density of 2640 kg/m^3 and a fineness modulus of 2.77, as well as machine-made limestone sand with a powder content of 6.2 wt.% and a fineness modulus of 3.15. The steel slag has a 3.1 g/cm^3 density and a specific surface area of 352 kg/m^2. The fly ash is class II fly ash with a 2.9 g/cm^3 density. The chemical compositions of each raw material are shown in Table 1.

Table 1 Chemical compositions of raw materials (wt.%)

	SiO_2	Al_2O_3	Fe_2O_3	CaO	MgO	SO_3	Na_2O	K_2O	Loss
P·I 42.5	23.089	6.496	2.907	60.494	2.075	2.367	0.155	0.725	1.190
Coarse aggregate	3.217	0.123	0.047	52.13	2.661	0.109	0	0.016	40.970
River sand	69.57	13.314	4.088	3.082	1.133	0.034	4.055	2.925	0.770
Machine-made sand	3.412	0.407	0.366	53.615	1.711	0.12	0	0.074	40.150
Steel slag	17.884	4.382	21.749	42.855	3.137	0.564	0.079	0.216	4.768
Fly ash	54.699	30.093	4.326	3.436	0.569	0.357	0.5	1.029	3.21

1# in Table 2 is the reference mix proportion for C40 concrete, 2# concrete replaces 56.8 wt.% of river sand with machine-made sand based on 1#, and 3# concrete is a CRC obtained by replacing 40 wt.% of cement with steel slag and fly ash based on 2#. The designed oxide contents and rate values of the raw material for CRC are Fe_2O_3: 3.12%, Al_2O_3: 5.30%, SiO_2: 22.73%, CaO: 65.85%; KH = 0.88, SM = 2.7, and IM = 1.7.

Table 2 Mix proportions of CRC and reference concrete (kg/m^3)

	P.I 42.5	Steel slag	Fly ash	Coarse aggregate	River sand	Machine-made sand	Water
1#	477	0	0	1125	579	0	215
2#	477	0	0	1125	250	329	215
3#	287	114	76	1125	250	329	215

2.2 Methods

After mixing and molding, the three concretes were covered with plastic film and cured for one day before being molded. Afterward, they were cured in a standard curing room until the corresponding age. The compressive strength was conducted following GB/T 50081-2002. The chloride ion diffusion coefficient was determined following GB/T 50082-2009. The water absorption test was conducted following ASTM C1585. The mercury intrusion porosimetry test was conducted to measure the pore structure of cement mortar. The standard consistency water content, setting time, and cement stability were tested per GB/T1346-2011.

3. Results and discussion

Figure 1 shows the compressive strength and compressive strength growth rate of concretes. With the increase of age, the strength of each concrete group has significantly increased. After replacing river sand, the compressive strength of 2# concrete is improved. This improvement is because the surface of the machine-manufactured sand is rough and contains sharp corners and some stone powder. The CRC had lower early strength but showed good strength development potential in later stages. This last age increment could be attributed to adding fly ash and steel slag as correction materials, which increased late age strength due to their pozzolanic reaction.

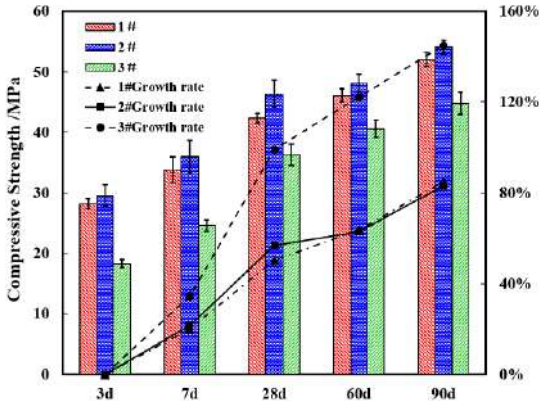


Figure 1 Compressive strength of concretes in each group.

Figures 2 and 3 show the chloride ion diffusion coefficient and capillary water absorption rate of concretes. Again, 2# concrete showed the best impermeability. However, when the curing age increased from 28 days to 90 days, each concrete's chloride ion permeability coefficients decreased by 33.24%, 38.72%, and 42.18%, respectively. This indicates that although the incorporation of steel slag and fly ash had lower hydration ability in the early stages, they produced more hydration products in the later stages. The capillary water absorption test results shown in Figure 3 are consistent with Fig.2.

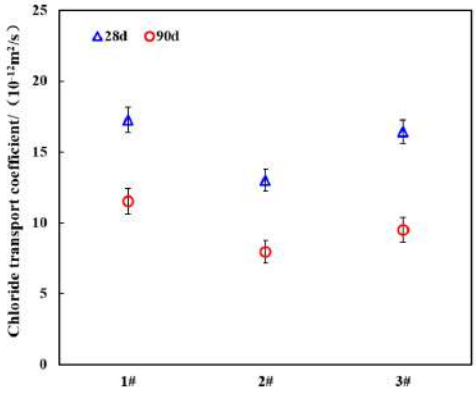


Figure 2 Chloride ion permeability coefficients of concrete samples

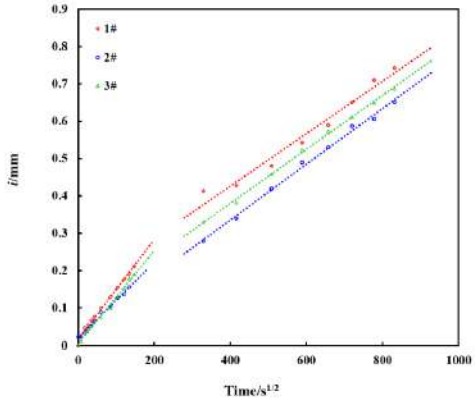


Figure 3 Capillary water absorption rate of concrete samples

Fig.4 shows the pore structure of different concrete samples. Compared with 1#, the gel pores smaller than 10 nm and the transition pores of 10-100 nm in mortar 2# are significantly reduced. Compared with 2# mortar, the number of gel pores in mortar 3# increases. This is because steel slag and fly ash showed poor cementitious performance, which generated insufficient hydration products.

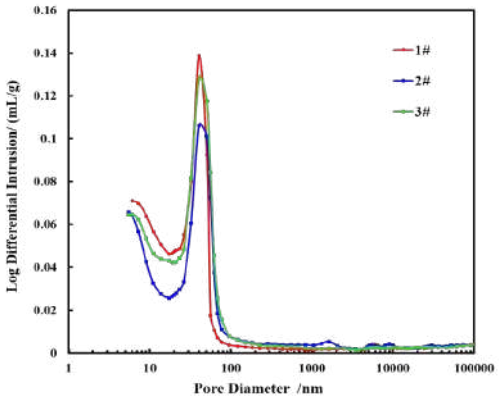


Figure 4 Pore structure of mortar samples

Table 3 shows the standard consistency water quantity of the pure cement paste and "cement-steel slag and -fly ash paste." Adding steel slag and fly ash reduces the standard consistency water demand by

5.74% compared to pure cement paste. This is because the hydration activity of steel slag is low, and more particles can fill the gaps, replacing the water space between the original cement particles. Fly ash could play a "Rolling ball effect" and "Filling effect," reducing the water demand. Meanwhile, the low hydration activity of steel slag and fly ash increases the setting time compared to the pure cement paste.

Table 3 Influence of steel slag and fly ash on standard consistency water quantity and setting time

	Standard consistency water quantity/%	Setting time/min	
		Initial setting	Final setting
Cement	29.6	104	188
Cement-Steel slag-Fly ash	27.9	165	257

A cement-steel slag-fly ash paste was conducted on volume stability by Le Chatelier boiling methods. The changes in the specimens before and after the test are shown in Figure 5. There is almost no change in the samples before and after boiling, which indicates that adding steel slag (23.9 wt.% of the cementitious material) in the recycled concrete does not affect the volume stability of the concrete.



(a) before boiling (b) after boiling

Figure 5 Change of specimens before and after boiling

4. Conclusion

(1) Adding low-reactivity steel slag and fly ash reduces the early-age compressive strength but increases the later strength growth rate. Moreover, the physical filling and chemical effects of steel slag and fly ash refined the pore structure and improved the late-age impermeability.
(2) Adding steel slag and fly ash significantly reduces the standard consistency water demand, but the setting time is prolonged considerably. At the same time, the addition of steel slag powder in the recycled concrete (23.9 wt.% of the cementitious material) does not affect the volume stability of the system.
(3) When designing a CRC, supplemental cementitious materials rich in Al and Fe were usually incorporated. Therefore, the mix proportions need to be carefully evaluated according to the chemical compositions of raw cement meals and the requirements of standards.

Acknowledgments

This work was supported by the National Natural Science Foundation of China (No. 51872216).

References

De Schepper, M., De Buysser, K., Van Driessche, I., & De Belie, N. (2013). "The regeneration of cement out of Completely Recyclable Concrete: Clinker production evaluation". *Construction and Building Materials*, 38: 1001-1009.

Liu, Y., Yang, C., Wang, F., Hu, S., Zhu, M., Hu, C., & Lu, L. (2021a). "Performance evaluation of regenerated clinker from completely recyclable mortar". *Construction and Building Materials*, 309.

Liu, Y., Yang, C., Wang, F., Hu, S., Zhu, M., Hu, C., Lu, L., & Liu, Z. (2021b). "Evaluation on recycled clinker production and properties from regeneration of completely recycle concrete". *Construction and Building Materials*, 301.

Schepper, M. D. (2014). "Completely recyclable concrete for a more environment-friendly construction". *Faculty of Engineering and Architecture Ghent University*, Ghent, Belgium.

The 16th International Congress on the Chemistry of Cement 2023 (ICCC2023)
"Further Reduction of CO_2 -Emissions and Circularity in the Cement and Concrete Industry"
September 18–22, 2023, Bangkok, Thailand

Synthesis, characterization and solubility of sodium aluminosilicate hydrate (N-A-S-H) gel

Yun Chen[1,4*], Luiz Miranda de Lima[1], Zhenming Li[1], Bin Ma[2], Barbara Lothenbach[3], Suhong Yin[4], Qijun Yu[4], Guang Ye[1]

1 Faculty of Civil Engineering and Geosciences, Delft University of Technology, Delft, The Netherlands

E-mail: Y. Chen-9@tudelft.nl, L.MirandadeLima@tudelft.nl, zhenming.li@sheffield.ac.uk, G.Ye@tudelft.nl

2 Laboratory for Waste Management, Paul Scherrer Institute (PSI), Switzerland

E-mail: bin.ma@psi.ch

3 Laboratory for Concrete & Construction Chemistry, Empa, Switzerland

E-mail: barbara.lothenbach@empa.ch

4 School of Materials Science and Engineering, South China University of Technology, Guangzhou, China

E-mail: imshyin@scut.edu.cn, concyuq@scut.edu.cn

ABSTRACT

Sodium aluminosilicate hydrate (N-A-S-H) gels with various Si/Al ratios are the dominant reaction products of geopolymer. However, their solubility products have not yet been fully determined, which hinders further investigation of thermodynamic modelling of geopolymer system. In this work, N-A-S-H gels with Si/Al ratios ranging from 1 to 3 were synthesized using the sol-gel method. The chemical composition of the synthesized N-A-S-H gels was determined by X-ray spectroscopy (XRF) and thermogravimetric analysis (TGA). The gel structure was characterized by X-ray diffraction (XRD). Dissolution experiments were further performed using the synthesized N-A-S-H gels to determine their solubility products. After dissolution, the aqueous concentrations of Na, Al, and Si were quantified by inductively coupled plasma-optical emission spectroscopy (ICP-OES) and the solution pH was measured. It has been shown that N-A-S-H gels with various Si/Al ratios differ in atomistic structures and solubility products. The thermodynamic properties of N-A-S-H gels can be determined from the experimentally derived solubility products at different temperature, which are expected to complement the thermodynamic database.

KEYWORDS: *N-A-S-H gel, Si/Al ratio, Solubility product, Sol-gel method, Thermodynamics*

1. Introduction

The primary reaction product formed in geopolymer is sodium aluminosilicate hydrate (N-A-S-H) gel. The chemical composition of N-A-S-H gel can be expressed as $Na^{+}[AlO_2 \cdot nSiO_2]^{-} \cdot mH_2O$, where n stands for Si/Al ratio and mainly varies from 1 to 3, depending on the raw materials and the curing regime (Pacheco-Torgal, Castro-Gomes, and Jalali 2008). As the principal phases, N-A-S-H gels with different thermodynamic properties are expected to control the geopolymerization reaction.

Several previous studies have reported the solubility product of synthesized N-A-S-H gel. Gomez-Zamorano et al. synthesized N-A-S-H gel with Si/Al ratios of 1 and 2 by sol-gel method and performed solubility test at 20 ℃ and 50 ℃ (Gomez-Zamorano et al. 2017). A similar route was adopted in Williamson's work to study the solubility of N-A-S-H gel (Williamson et al. 2019, 2020). However, N-A-S-H gels with high Si/Al were rarely synthesized in his study. As a result, only the solubility of N-A-S-H gel with a Si/Al of around 1 has been measured. In addition, Walkley et al. determined the solubility of

N-A-S-H gel obtained by alkali activation of synthesized aluminosilicate glass (Walkley et al. 2021). Again, the Si/Al ratio was below 2, which did not cover the domainant Si/Al ratios of the N-A-S-H gel formed in the geopolymer. To date, no solubility products of N-A-S-H with Si/Al above 2 have been reported. In addition, more data on the solubility of N-A-S-H gel at various temperatures are needed to build an accurate thermodynamic database of N-A-S-H gels.
This study aims to determine the solubility products of N-A-S-H gels with Si/Al ranging from 1 to 3 at different temperatures. First, N-A-S-H gels with various Si/Al compositions were synthesized using the sol-gel method. Next, the chemical composition of the N-A-S-H gel was determined by XRF and TGA, while the structural information of the N-A-S-H gel was obtained from XRD. Finally, dissolution experiments were performed at different temperatures to determine the solubility product of the N-A-S-H gel.

2. Experimental method

2.1 Synthesis of N-A-S-H gels

1M sodium silicate solution and 1M aluminum nitrate solution were used as the raw materials for the synthesis of the N-A-S-H gels. A 10 M NaOH solution and a HNO_3 solution (>65%) were used to maintain the pH when necessary. The sodium silicate solution was first mixed with a pH regulator and stirred for 30 minutes. A solution of aluminum nitrate was then added slowly to the stirring solution. The detailed synthesis conditions are given in Table 1 for all samples. The above procedure was performed in an N_2 filled glove box. After stirring for 1 day, the gel was obtained from the suspension by centrifugation and subjected to triple washing with deionized water. After that, the gel was dried in a vacuum desiccator for 14 days.

Table 1 Synthesis mixtures and conditions

Samples	Na_2SiO_3	$Al(NO_3)_3$	pH regulator	Target Si/Al	pH[(a)]
G1	50ml	50ml	20ml 10M NaOH	1	13.64
G2	280ml	100ml	-	2	13.46
G3	200ml	40ml	10ml HNO_3	3	13.40

(a) pH of filtrate referring to 25°C.

2.2 Characterization of synthesized N-A-S-H gels

XRF, XRD and TGA were used to characterize the gel. XRF measurement was performed with a Panalytical Axios Max WD-XRF spectrometer. XRD analysis was carried out at 45 KV and 40 mA using CuKα radiation, scanning from 8° to 60° 2θ at a rate of 2 seconds per step and a step size of 0.02° 2θ. TGA data were recorded at a heating rate of 10 ℃/min from 40 ℃-1000 ℃, except in the middle stage staying at 105 ℃ for 6h in order to determine the amount of non-evaporable water in N-A-S-H gel.

2.3 Solubility measurements

The resulting N-A-S-H gel was dispersed into deionized water with a solid-to-solution ratio of 20 g/L. The dissolution test was conducted in a shaker at 25 ℃ for 2 months, at 40 and 60 ℃ for 1 month, respectively. After equilibrium time, the suspension was filtered to obtain the aqueous phase. The pH of the filtrate was measured with a pH meter. Concentrations of Si, Al and Na in the filtrate were measured with an ICP-OES spectrometer. According to the element concentration and pH, the activities of the aqueous species, i.e., $\{Na^+\}$, $\{AlO_2^-\}$, $\{SiO_2^0\}$ and $\{OH^-\}$, were calculated out in GEMS (Kulik et al. 2013). Depending on the chemical composition of the N-A-S-H gels, their solubility products can be calculated. Note that the results in this work represent the average of three measurements.

3. Results and Discussion

3.1 Overview of the synthesized N-A-S-H gel

The chemical composition of the three types of synthesized N-A-S-H gels was determined by XRF. As shown in Table 2, the target Si/Al ratios, namely 1, 2 and 3, were successfully obtained. The amount of non-evaporable water was also determined, i.e. the amount of water that cannot be removed by D-drying or equivalent procedures, e.g. drying at 105 ℃. In this work, drying at 105 ℃ was selected to determine the dry weight and calculate the amount of non-evaporable water based on TGA tests. According to TGA results, the amount of non-evaporable water, indicated by the weight loss between 105 ℃ to 1000 ℃, was 5.59 %, 4.84 % and 4.90 % in G1, G2 and G3 respectively. Combining the XRF and TGA results, the chemical formula of the synthesized N-A-S-H gel can be determined, as summarized in Table 2.

Table 2 Chemical composition of synthesized N-A-S-H gel

Samples	Si/Al	Chemical composition
G1	1.10±0.01	$(Na_2O)_{0.46}(Al_2O_3)_{0.46}(SiO_2)_1(H_2O)_{0.48}$
G2	1.95±0.02	$(Na_2O)_{0.25}(Al_2O_3)_{0.25}(SiO_2)_1(H_2O)_{0.29}$
G3	2.81±0.02	$(Na_2O)_{0.18}(Al_2O_3)_{0.18}(SiO_2)_1(H_2O)_{0.26}$

The XRD patterns of N-A-S-H gels with various Si/Al ratios exhibit a single amorphous hump, as shown in Fig. 1. The hump was observed to shift towards lower angles as Si/Al increased, which aligns with previous observations in geopolymer pastes (Lee et al. 2017). This is the first time that such a shift towards lower 2θ with increasing Si/Al has been reported for N-A-S-H gels, indicating a difference in their chemical compositions.

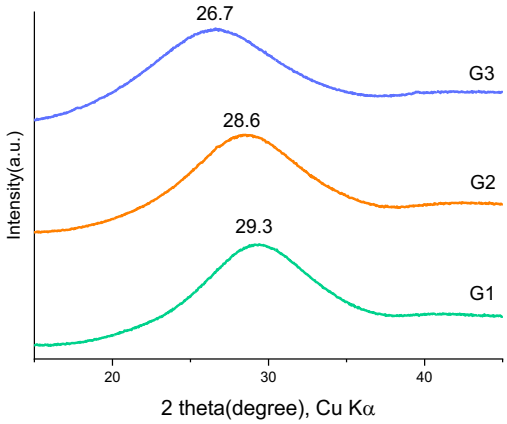


Fig. 1 XRD patterns for synthesized N-A-S-H gels with Si/Al from 1 to 3

3.2 Solubility products of N-A-S-H gels

The solubility product is defined based on the dissolution reaction. Using the dissolution reactions as listed in Table 3, the log K_{sp} values of the synthesized N-A-S-H gel at different temperatures were calculated, as shown in Fig. 2(a). The log K_{sp} values for each type of N-A-S-H gel increase with temperature. The log K_{sp} values of N-A-S-H gels with Si/Al of 1 and 2 are found consistent with (Gomez-Zamorano et al. 2017). N-A-S-H gels with different Si/Al ratios also show different solubility properties. In order to study the effect of Si/Al on the solubility, the log K_{sp} values were normalized by the sum of Si and Al as shown in Fig. 2(b). It can be seen that the log K_{sp} values increase with increasing Si/Al, especially from 2 - 3. Consistent trending was found in (Gomez-Zamorano et al. 2017). This indicates that N-A-S-H gel with higher Si/Al (e.g. up to 3) is less likely to form, which is in agreement with simulation result in (Chen et al. 2022). This may be one of the reasons why the synthesis of N-A-S-H gel with Si/Al of 3 has not been reported in the literature.

Table 3 The dissolution reactions used to calculate solubility products

Samples	Dissolution reactions
G1	$(Na_2O)_{0.46}(Al_2O_3)_{0.46}(SiO_2)_1(H_2O)_{0.48} \rightarrow 0.92\ Na^+ + 0.92\ AlO_2^- + SiO_2^0 + 0.48\ H_2O$
G2	$(Na_2O)_{0.25}(Al_2O_3)_{0.25}(SiO_2)_1(H_2O)_{0.29} \rightarrow 0.5\ Na^+ + 0.5\ AlO_2^- + SiO_2^0 + 0.29H_2O$
G3	$(Na_2O)_{0.18}(Al_2O_3)_{0.18}(SiO_2)_1(H_2O)_{0.26} \rightarrow 0.36\ Na^+ + 0.36\ AlO_2^- + SiO_2^0 + 0.36H_2O$

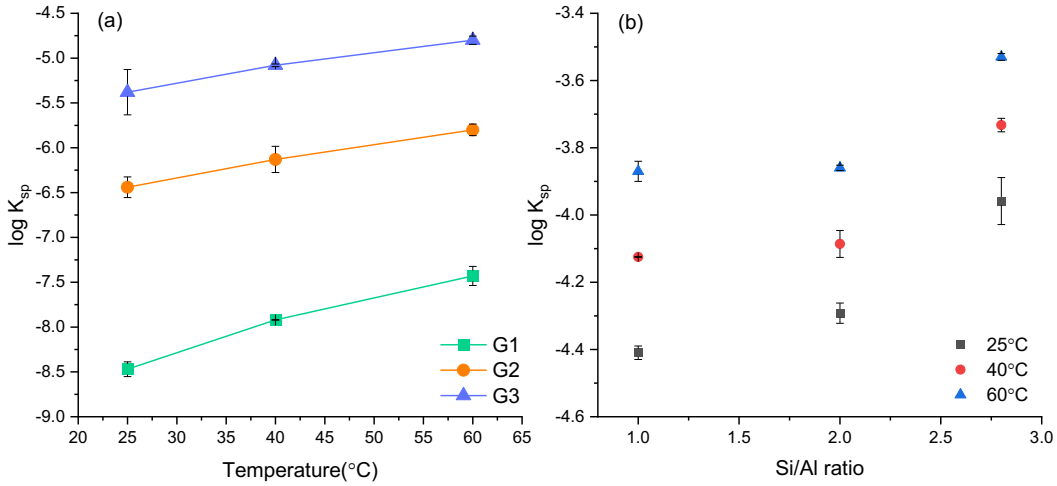


Fig. 2 Solubility products (log K_{sp}) of N-A-S-H gels with various Si/Al ratios at different temperatures

4. Conclusions

In this work, N-A-S-H gels with Si/Al ratios of 1, 2 and 3 were synthesized using the sol-gel method. XRF and TGA were used to determine the chemical composition of the N-A-S-H gel. XRD results also confirm the high purity of all the amorphous N-A-S-H gels. To the best of our knowledge, this is the first synthesis of N-A-S-H gels with high Si/Al ratios.

The solubility products of N-A-S-H gel with various Si/Al ratios were determined at 25, 40 and 60 ℃ and showed consistency with some literature values. Overall, this work has enriched and extended the solubility of N-A-S-H gels for a wide range of Si/Al ratios at various temperatures. The experimentally derived solubility products can be used to further calculate thermodynamic data for N-A-S-H gels, which are essential inputs for thermodynamic modelling to study chemical reactions in geopolymers.

Acknowledgements

The first author would like to acknowledge China Scholarship Council (Grant No. 201906150022) for financial support in this work.

References

Chen, Yun, Jorge S Dolado, Suhong Yin, and Qijun Yu. 2022. "A Molecular Dynamics Study of N–A–S–H Gel with Various Si/Al Ratios." *Journal of American Ceramic Society*: 1–13.

Gomez-Zamorano, Lauren et al. 2017. "C–(N)–S–H and N–A–S–H Gels: Compositions and Solubility Data at 25°C and 50°C." *Journal of the American Ceramic Society* 100(6): 2700–2711.

Kulik, Dmitrii A. et al. 2013. "GEM-Selektor Geochemical Modeling Package: Revised Algorithm and GEMS3K Numerical Kernel for Coupled Simulation Codes." *Computational Geosciences* 17(1): 1–24.

Lee, Bokyeong et al. 2017. "Strength Development Properties of Geopolymer Paste and Mortar with Respect to Amorphous Si/Al Ratio of Fly Ash." *Construction and Building Materials* 151: 512–19.

Pacheco-Torgal, Fernando, João Castro-Gomes, and Said Jalali. 2008. "Alkali-Activated Binders: A Review: Part 1. Historical Background, Terminology, Reaction Mechanisms and Hydration Products." *Construction and Building Materials* 22(7): 1305–14.

Walkley, Brant, Xinyuan Ke, Oday Hussein, and John L Provis. 2021. "Thermodynamic Properties of Sodium Aluminosilicate Hydrate (N-A-S-H)." *Dalton Transactions*.

Williamson, Trevor et al. 2019. "Method for Experimentally Determining N-A-S-(H) Solubility." *RILEM Technical Letters* 3(2018): 104–13.

Williamson, Trevor et al. 2020. "Relationship between Aqueous Chemistry and Composition, Structure, and Solubility of Sodium Aluminosilicate Hydrates." *Journal of the American Ceramic Society* 103(3): 2160–72.

The 16th International Congress on the Chemistry of Cement 2023 (ICCC2023)
"Further Reduction of CO_2 -Emissions and Circularity in the Cement and Concrete Industry"
September 18–22, 2023, Bangkok, Thailand

Investigation of the effects of supplementary cementitious materials in mitigating alkali-silica reaction using thermodynamic modelling

Haoliang Jin[1], Sam Ghazizadeh[2], and John L. Provis[1*]

[1] *Department of Materials Science and Engineering, The University of Sheffield, Sheffield, United Kingdom*
Email: hjin15@sheffield.ac.uk, j.provis@sheffield.ac.uk

[2] *Special Services, Mott MacDonald, London, United Kingdom*
Email sam.ghazizadeh@mottmac.com

ABSTRACT

Supplementary cementitious materials mitigate the risk of alkali-silica reaction (ASR) in cement blends. The thermodynamic reasoning behind this is not yet fully explained at standard temperature (25 °C) as the thermodynamic properties of some important ASR products at this temperature are unknown. This study enriches the thermodynamic database of two main ASR products that have been found in field concretes and models ASR in systems representing Portland cement blends. To do this, the phase assemblage resulting from cement hydration is obtained first, then extra silica is added to the system to model the process by which aggregate participates in ASR. Al-rich SCMs such as fly ash and metakaolin are discussed to highlight the role of Al. Consistent with previously published observations, the results of thermodynamic modelling indicate that incorporating SCMs does control ASR formation and their roles are various, such as controlling calcium hydroxide, limiting the amount of Na and/or K alkali ions in the pore solution and slowing the dissolution of reactive aggregate.

KEYWORDS: *Alkali-silica reaction, mitigation, supplementary cementitious materials, thermodynamic modeling.*

1. Introduction

Incorporation of supplementary cementitious materials (SCMs) into Portland cement is considered the most efficient and economic method to alleviate the swelling and expansion caused by alkali-silica reaction (ASR) in concretes, which is attributable to swelling of products that precipitate from a series of reactions between alkalis (mainly from cement) and reactive silica from reactive aggregates. Thermodynamic modelling is not yet a fully mature method for the simulation of ASR due to the lack of fundamental data for some important alkali-silica reaction products. In this study, we develop the temperature-dependent thermodynamic properties of Na- and K-shlykovite, which have previously been found to form during alkali-silica reaction in concrete (Shi et al., 2019). Other types of ASR products may be observed, both stable and metastable, but the focus of this work is specifically on the shlykovite family. A modelling approach was then developed to predict ASR in blended cement systems with four different SCMs (ground granulated blast furnace slag, fly ash, metakaolin, or silica fume) using this extended database, at ambient temperature, to investigate the roles of different SCMs compared with the current literature.

2. Methodology

2.1 Estimation of thermodynamic parameters of ASR products

In order to estimate the thermodynamic parameters of the two shlykovite-type ASR products at ambient temperature, standard molar entropy and molar heat capacity are estimated by Eq. 1 and Eq. 2 respectively, where V_m is the volume per formula unit, in nm^3:

$$S° = 1579 \cdot V_m + 6 \quad (1)$$

$$Cp° = 1388.1 \cdot V_m + 4.58 \quad (2)$$

Gibbs free energy of formation is related to solubility products ($\log_{10}K$) at 25 °C. Eqs. 3-6 are used to obtain a temperature-dependent $\log_{10}K_T$ from the $\log_{10}K$ values determined at 80 °C by Shi et al. (Shi et al., (2019)) converted to values applicable at 25°C.

$$\log K_T = A_0 + A_2 T^{-1} + A_3 \ln T \quad (3)$$

$$A_0 = \frac{0.4343}{R} \cdot \left[\Delta_r S^0_{T_0} - \Delta_r Cp^0_{T_0}(1 + \ln T_0)\right] \quad (4)$$

$$A_2 = \frac{0.4343}{R} \cdot \left(\Delta_r H^0_{T_0} - \Delta_r Cp^0_{T_0} T_0\right) \quad (5)$$

$$A_3 = \frac{0.4343}{R} \cdot \Delta_r Cp^0_{T_0} \quad (6)$$

Where A_0, A_2, and A_3 are empirical coefficients. Here T_0 is 298.15 K (25 °C) and T is the calculation temperature of interest. Enthalpy ($\Delta_r H^\circ$) in Eq.5 is the only parameter that is unknown due to lack of enthalpy data for the two ASR products, and is determined iteratively by fitting $\log_{10}K_T$ at 80 °C using the value in Shi's paper (Shi et al., (2019)).

2.2 Software and database

The GEM-Selektor software (http://gems.web.psi.ch/GEMS3/) was used to predict ionic activities and phase assemblages by minimisation of Gibbs free energy with mass balance constraints. The activity coefficients of aqueous species are calculated by the Truesdell-Jones form of the extended Debye-Hückel equation, which is shown in Eq. (7):

$$\log_{10}\gamma_i = \frac{-A_\gamma z_i^2 \sqrt{I}}{1 + aB_\gamma \sqrt{I}} + b_\gamma I \quad (7)$$

where the coefficients A_γ and B_γ are related to the temperature and pressure of the system, z_i is the charge of species i, and I is the effective molal ionic strength, which is calculated by Eq. (8):

$$I = \frac{1}{2}\sum_{i=1}^{n} c_i z_i^2 \quad (8)$$

where c_i is the concentration of the i^{th} ionic species. In Eq. (1), a and b_γ are solution-dependent parameters. Assuming that in Portland cement or a blended system,the aqueous phase is dominated by KOH, a and b_γ are set to 3.67 Å and 0.123 kg/mol respectively (Lothenbach et al., (2019)).

The Cemdata18 database (Lothenbach et al., (2019)) covers the majority of phases used in this study, along with the additional data for ASR products as described above (Jin et al. (2023)).

2.3 Modelling method

In this study, we deliberately separated the reaction process into two parts; the hydration process is assumed to be relatively rapid and the ASR process relatively slow, so they can be separated in time. Firstly, we simulated (blended) cement hydration with or without SCMs to obtain a mature cement paste phase assemblage at w/c = 0.48 (Ramlochan et al., 2003). Then, an additional 50 g of silica source representing the dissolution of silica from the aggregate was added based on previous confirmatory simulation, and allowed to participate in the reaction system by reacting with all of the portlandite and pore solution obtained from the previous hydration calculation, with all other hydrate products treated as unable to further react during this stage. This two-step method was intended to avoid the direct incorporation of the added silica into hydrate phases via pozzolanic reactions; it is acknowledged that there may be some minor changes in the main hydrate phases during ASR, but given that the most damaging formation of ASR products is likely to take place in cracks in the aggregate particles, the assumption that only the pore fluid and portlandite are available for reaction seems a reasonable approximation.

3. Results and discussion

3.1 Thermodynamic parameter estimation

The thermodynamic parameters of two ASR products are summarized in table 1. Here, we obtained the solubility products associated with the error bars to -31.4±1.2 for K-shlykovite and -34.8±0.4 for Na-shlykovite, respectively (Jin et al. (2023)) based on the previous research (Shi and Lothenbach (2019)). The rest of the thermodynamic parameters of ASR products then were calculated based on these newly-estimated solubility products.

Table 1. Thermodynamic properties for ASR products at 25°C (Jin et al. (2023))

Products	$\log_{10}K$	$\Delta_fH°$ (kJ/mol)	$\Delta_fG°$ (kJ/mol)	S° (J/mol·K)	Cp° (J/mol·K)
K-shlykovite: $KCaSi_4O_8(OH)_3 \cdot 2H_2O$	-31.4±1.2	-5739.5	-5294.4	479.8	421.8
Na-shlykovite: $NaCaSi_4O_8(OH)_3 \cdot 2.3H_2O$	-34.8±0.4	-5841.4	-5364.4	429.9	377.9

3.2 Thermodynamic modelling of ASR in blended cement

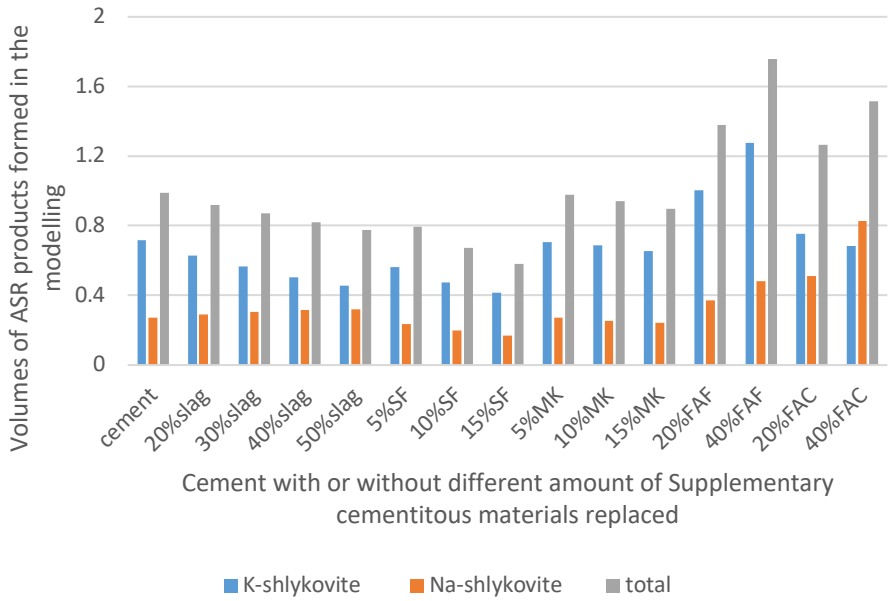


Fig. 1. The volumes of ASR products formed in the cements blended with different SCMs; hydration of cements of the specified compositions was simulated at w/c = 0.48, then 50 g of SiO_2 per 100 g of hydrated paste was allowed to react with the pore fluid and portlandite that was in each case calculated to be present.

In order to investigate the role of different SCMs in mitigating the ASR damage, Fig. 1 illustrates the volumes of each of the shlykovite-type ASR products precipitated, and the total of these, in each blended cement. It can be seen that the total volume shows a reduced trend in the presence of SCMs, and the degree of reduction increased with the increase of SCMs replaced, apart from fly ash which results in an increase in the volume. The results indicated that although the formation of ASR products seems to be inevitable in the presence of SCMs, the decreased formation supported the idea that SCMs can mitigate ASR.

Alkali sources are considered as the main factor triggering ASR, which requires both alkali metal ions and a Ca source. For slag, its role is to dilute the amount of alkali metal ions in the pore solution and reduce presence of portlandite in blended cements, which restricts the supply of the necessary constituents for ASR

product formation. Thermodyamic modelling of blended cement performed by Lothenbach also supports this idea (Lothenbach et al., (2011)). Considering silica fume, binding more alkalis is the main reason for the reduction of ASR product formation. However, Al-rich SCMs (metakaolin and fly ash) seem to be relatively weak in terms of inhibiting ASR, which may support another hypothesis regarding the well-known effectiveness of these SCMs, which is that the main role of Al is to slow down the dissolution of reactive silica from reactive aggregate.

4. Conclusions

The first aim of this study has been to further develop the thermodynamic database for ASR products. Then we applied thermodynamic modelling into alkali silica reaction simulation where considering blending four types of supplementary cementitious materials. A new two-step modelling method was used to investigate the volumes of ASR products formed in the cement with or without SCMs. Limiting the alkali source is considered as the main reason to explain the role of SCMs on reducing the volume of K- and Na-shlykovite products formed, as this approach does not show a strong influence from Al content as is observed experimentally. However, different SCMs have different effects on reducing alkalis in the pore solution. Overall, this study provides new insight into ASR processes and a modelling approach that may be extended and applied to further interrogate the effects of different parameters on ASR processes.

References

Jin, H., Ghazizadeh, S., Provis, J.L. 2023, Assessment of the thermodynamics of Na,K-shlykovite as potential alkali-silica reaction products in the $(Na,K)_2O$-CaO–SiO_2-H_2O system. Under Review

Lothenbach, B., Kulik, D.A., Matschei, T., Balonis, M., Baquerizo, L., Dilnesa, B., Miron, G.D., Myers, R.J., 2019. Cemdata18: A chemical thermodynamic database for hydrated Portland cements and alkali-activated materials. Cement and Concrete Research 115, 472–506. https://doi.org/10.1016/j.cemconres.2018.04.018

Lothenbach, B., Scrivener, K., Hooton, R.D., 2011. Supplementary cementitious materials. Cement and Concrete Research, 41, 1244–1256. https://doi.org/10.1016/j.cemconres.2010.12.001

Ramlochan, T., Zacarias, P., Thomas, M.D.A., Hooton, R.D., 2003. The effect of pozzolans and slag on the expansion of mortars cured at elevated temperature: Part I: Expansive behaviour. Cement and Concrete Research 33, 807–814. https://doi.org/10.1016/S0008-8846(02)01066-9

Shi, Z., Geng, G., Leemann, A., Lothenbach, B., 2019. Synthesis, characterization, and water uptake property of alkali-silica reaction products. Cement and Concrete Research 121, 58–71. https://doi.org/10.1016/j.cemconres.2019.04.009

Shi, Z., Lothenbach, B., 2019. The role of calcium on the formation of alkali-silica reaction products. Cement and Concrete Research 126, 105898. https://doi.org/10.1016/j.cemconres.2019.105898

Utilization of Dolomitic Limestone Waste for manufacturing of Limestone Calcined Clay Cement

A. Sadangi[1*] and P. Desai[2]

[1]Nuvoco Vistas Corporation Ltd, Mumbai, India
arunachala.sadangi@nuvoco.com

[2]Nuvoco Vistas Corporation Ltd, Mumbai, India
pranav.desai@nuvoco.com

ABSTRACT

The quantities of waste rocks and tailings generated from the limestone mines have been increased in the last decades. The accumulation and the surface storage of these mine wastes represents a real challenge in terms of environmental and sustainability point of view for the cement industry. Thus, the recycling and valorization of these mine wastes is one of the most effective ways of reducing their volume and mitigating their negative environmental impact. In India most of the cement plants are operating on heterogeneous intricate limestone deposits with the result that mine reject generation is high. Besides low grade its variability is extremely high due to intercalation of dolomite, clay, pegmatite, schist etc.

Recently, Indian Bureau of Mines issued a notification for implementation for thresh hold value of minerals. "Threshold Value of Minerals" means limit prescribed by Indian Bureau of Mines based on the chemical composition of Limestone. The limestone having CaO 34% (Min.) and MgO 5% (Max) are incorporated as beneficiable/marketable, below which a mineral/material obtained after mining can be discarded as waste. The aim and objective of this paper is to study the suitability of reject grade limestone i.e. dolomitic - limestone as supplementary cementitious material with calcined clay and clinker for manufacturing of Limestone Calcined Clay Cement. Around 10 Tons of Cement produced in commercial scale and evaluated their mechanical and chemical properties. From the study it is found that up to 7% MgO bearing dolomitic limestone can be used for manufacturing of Limestone Calcined Clay Cement.

KEYWORDS: *Dolomitic Limestone, Calcined Clay, LC^3 Cement, Concrete*

Introduction

Limestone is the basic raw materials for cement manufacture and the growth of the cement industry depends on the availability of right grade cement grade limestone. India is having huge limestone deposits distributed throughout the geological stratigraphic horizon starting from archaean to tertiary formations. The quality variation of limestone from deposit to deposit is very wide in India. The geographical distribution of limestone deposits in India is also not uniform. Some states do not have any limestone deposits. In India, limestone is basically a sedimentary rock composed mainly calcium carbonate ($CaCO_3$) in the form of calcite and secondary minerals like quartz, feldspar, mica and clay present as accessories. About 90% of the Indian limestones are sedimentary origin and 10% is partial metamorphic origin. The two most important constituents of limestone are calcite and dolomite. Limestone often contains magnesium carbonate either as dolomite $CaMg(CO_3)_2$ or magnesite ($MgCO_3$) mixed with calcite. Such rocks are termed as dolomitic or magnesian limestone. Limestone is altered by dynamic or contact metamorphisms become coarsely crystalline and are referred to as marble or crystalline limestone. The present study was conducted in one of plant located in Northern part of India having around 20 MT dolomitic limestones having present and not in use for clinker manufacturing.

Experimental Work

Representative raw materials like clinker, kaolinite clay, dolomitic limestone and mineral gypsum has collected for this study. To ensure representative sampling, the dolomitic limestone samples were collected from 10-12 locations in one of mine located at North region (Figure1&2). The quantity of reject grade sample collected from each location was about 300 kg. Further, the 300 Kgs of sample was reduced to about 100 kg by coning and quartering and the same was used for preparation of LC^3cement. Clay calcinations were carried out in the rotary kiln having capacity of 50 TPD. Three sets of LC^3 blend prepared in the laboratory scale with dolomitic limestone having composition of 65% clinker, 20% calcined clay, 10% dolomitic limestone (MgO content varies from 4.93 -10.62%) and 5% natural gypsum. LC^3:Set1 having MgO content 4.93%, LC^3:Set2: 7.73% and LC^3: Set 3 is 10.62% (Table-1). The dolomitic limestone used in this study is rejected grade and presently not in use for clinker manufacturing. Table 2 shows, physical, chemical and heat of hydration of LC^3 Cement was analyzed as per IS 4031. The microstructure analysis of cement paste was investigated by Scanning Electron Microscope. The concrete analysis were done as per IS 456-2000 & 10262-2019. Table 3 shows the durability properties like RCPT, water permeability, shrinkage & MOE of LC^3 concrete.



Figure 1: Dolomitic limestone Waste dump at mines site



Figure2: MgO content varies from 4-10%

Table 1: Chemical Composition of raw materials by XRF method (Wt %)

Sample	LOI	CaO	SiO_2	Al_2O_3	Fe_2O_3	MgO	SO_3	Na_2O	K_2O
Dolo LSt- Set1	15.6	28.5	43.2	4.44	3.13	4.93	0.3	0.11	0.23
Dolo Lst- Set2	34.6	32.44	19	3.23	1.59	7.73	0.45	0.25	0.31
Dolo Lst – Set3	37.8	33.9	13.07	2.41	1.29	10.62	0.52	0.36	0.14
Calcined Clay	0.49	1.69	60.65	32.68	1.67	0.11	0.07	0.07	0.05
Clinker	0.26	62.87	21.29	5.82	4.29	4.56	0.30	0.153	0.220

From the table 1, it indicates the reject grade limestone having high SiO_2 content ranges from 13-43.2% and MgO content varies from 4.93 – 10.62% suggest the limestone classification is falling under dolomitic limestone category and which is not useful for cement manufacturing as per IBM policy. The calcined clay having kaolinite content varies from 50-60%.

Results and Discussion

The initial and final setting time of three sets of LC^3 cement varies from 60 – 75 minutes and final is 125 – 145 minutes, indicates no impact of high MgO limestone in the setting time (Table 2). The Autoclave and

Lechatlier expansion varies from 0.7-0.8% & 0.9 -1mm also with in limit as per IS 4031-1988. The significant impact observed in the strength parameters. At 4.93% MgO level, latter strength is drastically decreasing. At .7.73% MgO level, both early and latter strength is encouraging and satisfactory (Table 2). When MgO content increases up to 10%, both early and latter strength have decreasing trend. The heat of hydration is marginally high, may be due to presence of higher content of dolomite in the mix.

Table 2: Physical, Chemical and Mechanical Properties of LC^3 and OPC Cement

		Setting Time (Minutes)			Expansion		Strength (MPa)			
Trial	NC (%)	Initial	Final	SSA(m^2/Kg)	LC, mm	Auto,%	1D	3 D	7 D	28 D
OPC	28.5	110	185	320	0.8	0.5	17.0	29.5	37.5	56.0
LC^3: Set1: MgO-4.93	31.3	63	145	348	0.9	0.7	11.37	27.81	37.98	41.2
LC^3:Set2: MgO – 7.73	30	75	125	367	1	0.8	12.7	34.1	37.98	51.9
LC^3: Set3: MgO – 10.62	30	60	125	354	1	0.8	9.8	26..9	35.4	43.4
Chemical Composition of (LC^3Set 2 Sample by XRF)							**Heat of Hydration (KJ/Kg) – LC^3 Set2**			
LOI	MgO	SO_3	IR	Na_2O	K_2O	Cl	1Day	3Days	7Days	28Days
4.09	4.33	3.27	8.57	0.27	0.29	0.041	133	202	293	373

Microsturcuture

The microstructure analysis of LC^3 –Set2 cement was studied using Environmental Scanning Electron Microscope. The morphology was observed at different intervals of hydration i.e. 1d, 3d, 7d and 28 days. The samples were studied in both fractured surface and polished section using SE and BSD at variable pressure mode. The hydration product such as calcium silicate hydrate (C-S-H), Calcium hydroxide (CH), ettringilte (AFt), monosulfate (AFm), C-S-A-H, Carbo Aluminates (Dudi etal 2022), limestone particles and deleterious material like quartz and feldspar were observed (Figure 3). The initial products (1day) of hydration are amorphous looking like fibrous shape. These products mainly appear on the surface of the un-hydrated grains, filling in void space as they grow. During the first 7 days of hydration, the surface of the C_3S grain covered by the radiating fibrous particles of C-S-H, honeycomb structure and interlocking space between the grains (Figure 4). As time of hydration increased, the fibrous structure developed in to needle like C-S-H at 28 days. At 28 days hydration, the paste displayed a massive tabular structure with platy with occasionally fibrous hydration products. The morphology of C-S-H is similar at 3 and 7days. Both type I & II C-S-H were observed in all the hydration period. The size of C-S-H increased form 200nm to 1.5 micron as hydration period increases from 1 to 28 days. The morphology of ettringite also changes from needle to rod like structure as the hydration period increases. At 28days, the microstructure becomes dense indicates dolomitic limestone acts as a filler.

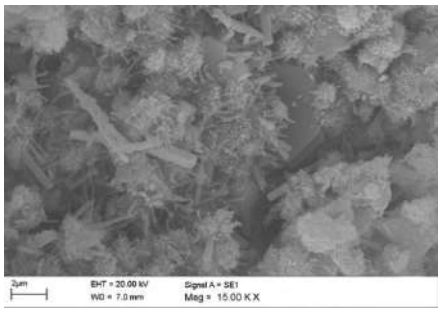


Figure 3: Microstructure of cement paste at 28 days

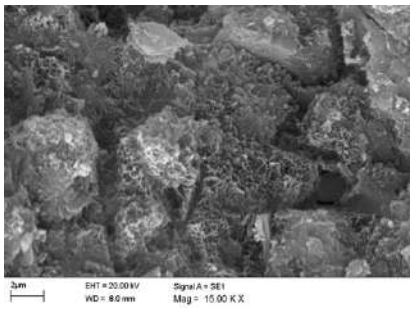


Figure 4: Fibrous & Dense Microstructure

Concrete Analysis

M25 Grade concrete mix has been made with LC^3- Set2 cement. Durability parameters were evaluated as per standard procedure and listed in the table 3. The strength parameters like compression and flexural results are satisfactory. The durability of LC^3 is good for tested grade i.e. comparable with conventional concrete (Table 3).

Table 3: Durability parameters of concrete made with LC^3 – Set2 Cement

7D (N/mm2)	28 D (N/mm2)	RCPT (Coloumbs)	Water Perm.(mm)	Shrinkage (%)	Flex. Strength (Mpa)	MOE (Gpa)
32.3	40	3164	19	0.0348	4.25	28

The porosity analysis of concrete specimen was investigated using fluorescent microscope for both OPC concrete and LC^3- Set2 concrete. Left hand side micrograph is showing high porosity made with OPC concrete (Figure 5). Right hand side micrograph showing less porous made with LC^3 – Set2 Cement (Figure 6), indicates dolomite limestone acts as filler.

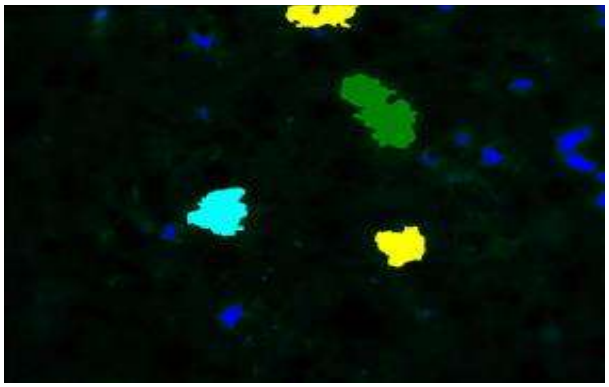


Figure 5: High Porosity concrete made with OPC

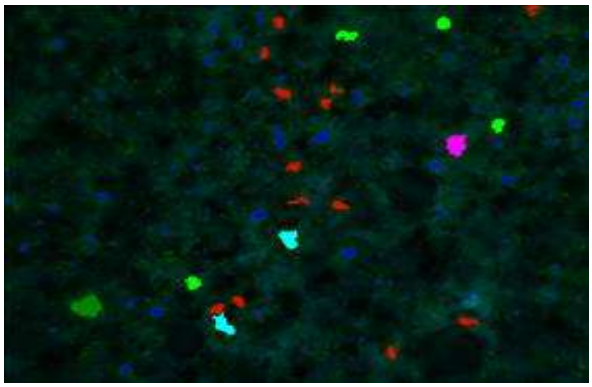


Figure 6: Low porosity concrete made with LC^3- Set2

Conclusions

Present study concludes that utilization of dolomitic limestone having MgO content up-to 7% will not impact on the physical, chemical and microstructural properties of the cement and concrete. The dolomite particles act as filler and the structure becomes dense with increasing in ages. There is significant improvement in strength parameters and durability factors equivalent to conventional concrete.

References

1. Dudi, L., Satapathy, A., Bishnoi, S (2022), "Low grade limestone suitability for Limestone Calcined Clay (LC^3) Production" 17th NCB International Conference on Cement and Building Material, 1-4
2. Chundawat,D,Mansoori,G,Sharma,D(2021), "Experimental study on utilizing mine's waste as a source of blended cement concrete" Materials Today proceedings 38, 1222- 1228
3. Indian Standard (456: 2000), "Plain and Reinforced Concrete – Code of Practice, 15-23
4. Indian Standard (10262 : 2019)," Concrete Mix Proportioning" – Guidelines, 2-35

The 16th International Congress on the Chemistry of Cement 2023 (ICCC2023)
"Further Reduction of CO_2 -Emissions and Circularity in the Cement and Concrete Industry"
September 18–22, 2023, Bangkok, Thailand

High-efficient Solidification and Stabilization by Low Carbon Supersulfated Cement

J.X. Ban [1,2], Jian-Xin Lu [2,3*], and C.S. Poon [2,3]

[1] *School of Water Resource and Environmental, Research Center of Environmental Science and Engineering, China University of Geosciences (Beijing), Beijing, China*
Email: jiaxing.ban@cugb.edu.cn
[2] *Department of Civil and Environmental Engineering, The Hong Kong Polytechnic University, Hung Hom, Kowloon, Hong Kong, China*
Email: jianxin.lu@polyu.edu.hk
[3] *Research Centre for Resources Engineering towards Carbon Neutrality, The Hong Kong Polytechnic University*
Email: cecspoon@polyu.edu.hk

ABSTRACT

This study developed a novel low-carbon supersulfated cement (SSC) mortar prepared with multiple types of solid waste, including phosphogypsum and cathode ray tube (CRT) panel glass for realizing carbon neutrality. In this present research, the mechanical (compressive strength) and durable (drying shrinkage) properties of the SSC system after incorporating the CRT glass aggregate is discussed. And the environmental impacts including toxic characteristic leaching procedure (TCLP) and carbon emission are clarified. A detailed stabilization mechanism for the heavy metals in the SSC system is proposed. The results show that the compressive strength witnesses a slight increase after replacing river sand with CRT glass. In terms of the drying shrinkage, it falls gradually with the addition of the CRT glass. Even when 100% CRT glass is used as aggregate, the leaching concentration of the heavy metals is still within the limit of the standard using the SW-846 Method 1311. Most of the heavy metals are trapped in the structure of the ettringite by replacing the place of the Al atom. Compared with ordinary Portlandite cement (OPC), the production of SSC can decrease 80% of carbon emissions resulting from incineration. In conclusion, the recycling of the waste CRT glass and waste phosphogypsum in the SSC system can not only obtain ideal mechanical and durable performance but also realize the stabilization of the heavy metals.

KEYWORDS: *Supersulfated cement; Pozzolanic reaction; CRT glass; Solidification and stabilization; Carbon emissions*

1. Introduction

Carbon dioxide emissions have been an urgent environmental problem across the world. The production of Ordinary Portland Cement (OPC) contributed to the major proportion of the carbon emissions in the construction industry (Cristelo et al., 2015). When producing one-ton clinker, there will be 0.8 tons of CO_2 released into the atmosphere (Turner and Collins, 2013). Besides, the energy-intensive manufacture of OPC can also emit hazardous gases such as NOx and SO_2 (Zhang et al., 2020). Therefore, it is urgent to look for a novel low-carbon cementitious material.

Super-sulfated cement (SSC) is a promising low-carbon cement prepared with sustainable raw materials without incineration, which includes gypsum and slag (Da Luz and Hooton, 2015). During the production procedure, there is no carbon emission, because it does not need any high-temperature clinkering process ,which could decrease by about 90% carbon emissions compared to OPC according to (Niu and Zhang, 2015). Due to its lower hydration heat and superior durability performance in terms of chemical resistance, it has the potential to be used as an alternative to OPC to some extent, (Juenger et al., 2011).

It is estimated that there is about 6 billion tons phosphogypsum generated around the world. And it still increases at a rate of 150 million tons/per year (Du et al., 2022), while only 15% of which is recycled (Silva et al., 2022). Besides, the hazardous waste cathode ray tubes (CRT) glass is gradually being replaced by liquid crystal displays and light-emitting resulting in much CRT glass abandoned in the world (Gao et al., 2022). If there is no appropriate treatment for the CRT glass, it would threaten the surrounding environment by heavy metals leaching (Elshkaki et al., 2005; Long et al., 2022).

Based on these solid waste, the present study recycle CRT glass as aggregate in replace of the river sand and use phosphogypsum to replace natural gypsum to conduct the mechanical and durable research.

2. Materials and Methods

2.1 Materials

The slag was collocted from a steel plant (Guangdong Shaoguan Steel Company Ltd.). The CRT glass (panel part) was collected from a waste electronic equipment recyclor. The phosphofypsum was recycled from a phosphoric acid production factory in Guizhou province (China).

2.2 Methods

The compressive strength of the SSC system mortar cubes (40 mm × 40 mm × 40 mm) was obtained using the compression machine at 3, 7, 28 d based on BS EN 12390-3. The loading speed was 0.6 MPa/s. After demolded, the mortar bars are first immersed in a water bath at 25 °C for 5 d. Hereafter, the lengths of the mortar bars are measured as the initial length. The length of the mortar bars from 0 d to 28 d are measured by using a length comparator (0.001 mm accuracy) according to ASTM C490. Then the TCLP test was conducted for exploring whether the recycled CRTGS can be applied to the SSC system in terms of environmental impact. Mortars after curing for 28d is smashed into small particles with the size of 9 mm. Then the particles are immersed in the glacial acetic acid with the pH of 2.88 ± 0.05 (EPA, 1992). The extract solution is set at a liquid-to-solid ratio of 20:1. The reactor is rotated at 30 rpm for 18 h. After tumbling, the supernatant was filtered through a 0.45 μm membrane filter and digested with concentrated nitric acid. The heavy metals in the leachate are determined by an inductively coupled plasma emission spectrometer (Spectro Blue).

3 Results and discussions

With the replacement of river sand by CRT glass, the crack propagation of the cement mortars was inhibited during the drying shrinkage period due to the irregular shape of the CRT glass (Fig. 1). The drying shrinkage was reduced with the increased content of the CRT sand (Fig. 2). The dense interfacial transition zone (ITZ) was found due to the pozzolanic reaction between the CRT glass and SSC matrix.

Simultaneously, during the pozzolanic reaction, the heavy metal ions in CRT glass were dissolved and released into the pore solution. These heavy metal ions reacted with sulfate ions dissolved in gypsum and precipitate as a form of insoluble sulfate substance around the aggregates and further improved ITZ. This can not only realize the bonding improvement between the aggregate and the paste, but also achieve a superior solidification and stabilization (S/S) effect for the heavy metals in the CRT glass (Fig. 3). The special reaction can not be observed in OPC-river sand based cementitious materials.

In addition, the larger amount of the ettringite crystals in the SSC also contributed to achieving S/S through the isomorphous replacement effects (Figs. 4 and 5) of the ettringite. The special cementitious products, dense ITZ, and high concentration of sulfate ions in the pore solution make it a promising construction material, which can be used for stabilizing hazardous wastes. The prepared SSC was able to reduce carbon emissions up to 80% compared to the OPC system (Fig. 6).

Overall, the joint use of low-carbon SSC and CRT glass can reduce carbon emissions by realizing the valorization of multiple types of solid wastes and achieve better solidification and stabilization, and durability performance.

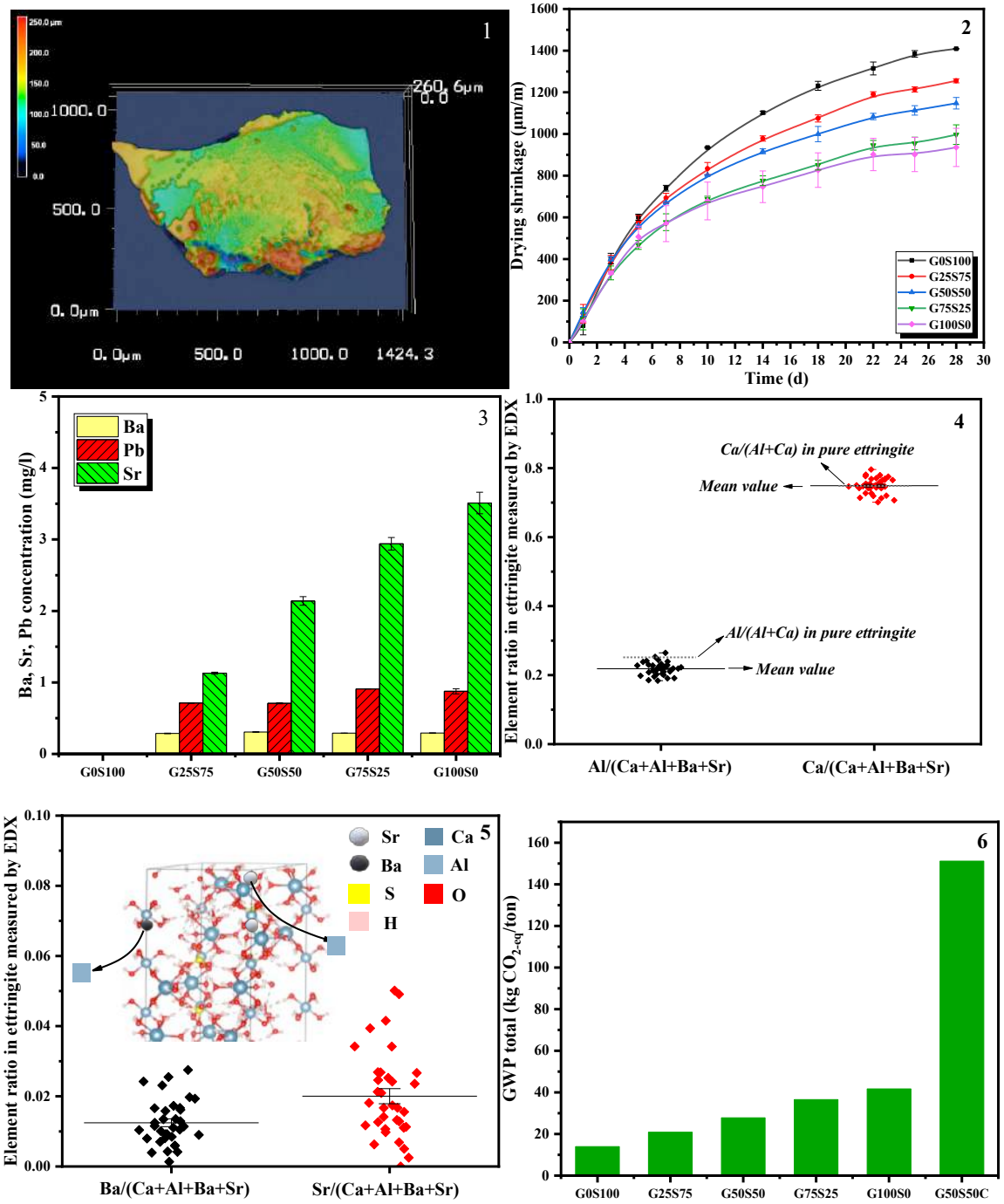


Fig. 1 3D microscope image of the CRT glass; **Fig. 2** Drying shrinkage of the SSC mortars with various CRT glass sand; **Fig. 3** TCLP test results after incorporating CRT glass; **Fig. 4** EDX statistical analysis (Al, Ca) on ettringite; **Fig. 5** EDX statistical analysis (Ba, Sr) on ettringite; **Fig. 6** GWP of SSC mortars with various CRT sand (/ton mortar)

Conclusions

The new low-carbon cementitious material provides a promising recycling approach for these two wastes. CRT glass in this cementitious system not only realizes the efficient immobilization of heavy metals but

also optimizes the SSC in terms of durable performance. This work can act as a reference to extend the application of hazardous CRT glass and phosphogypsum in engineering.

Acknowledgments

The authors would like to acknowledge the funding support from the General Research Fund from the Hong Kong Research Grants Council (Q80K) and Green Technology Fund (GTF202110180).

References

Cristelo, N., Miranda, T., Oliveira, D.V., Rosa, I., Soares, E., Coelho, P., Fernandes, L., 2015. Assessing the production of jet mix columns using alkali activated waste based on mechanical and financial performance and CO_2 (eq) emissions. J. Clean. Prod. 102, 447-460.

Da Luz, C.A., Hooton, R., 2015. Influence of curing temperature on the process of hydration of supersulfated cements at early age. Cem. Concr. Res. 77, 69-75.

Du, M., Wang, J., Dong, F., Wang, Z., Yang, F., Tan, H., Fu, K., Wang, W., 2022. The study on the effect of flotation purification on the performance of α-hemihydrate gypsum prepared from phosphogypsum. Sci. Rep. 12(1), 1-16.

Elshkaki, A., van der Voet, E., Timmermans, V., Van Holderbeke, M., 2005. Dynamic stock modelling: A method for the identification and estimation of future waste streams and emissions based on past production and product stock characteristics. Energy 30(8), 1353-1363.

EPA, U., 1992. Method 1311 Toxicity characteristic leaching procedure (TCLP). Agency EP, editor. Washington DC, USA1992.

Gao, X., Yao, X., Xie, R., Li, X., Cheng, J., Yang, T., 2022. Performance of fly ash-based geopolymer mortars with waste cathode ray tubes glass fine aggregate: A comparative study with cement mortars. Constr. Build. Mater. 344, 128243.

Juenger, M., Winnefeld, F., Provis, J.L., Ideker, J., 2011. Advances in alternative cementitious binders. Cem. Concr. Res. 41(12), 1232-1243.

Long, W.-J., Zhang, X., Xie, J., Kou, S., Luo, Q., Wei, J., Lin, C., Feng, G.-L., 2022. Recycling of waste cathode ray tube glass through fly ash-slag geopolymer mortar. Constr. Build. Mater. 322, 126454.

Niu, Q., Zhang, R., 2015. Experimental study on some properties of a low-carbon cement, 2015 3rd International Conference on Advances in Energy and Environmental Science. Atlantis Press, pp. 1440-1443.

Silva, L.F., Oliveira, M.L., Crissien, T.J., Santosh, M., Bolivar, J., Shao, L., Dotto, G.L., Gasparotto, J., Schindler, M., 2022. A review on the environmental impact of phosphogypsum and potential health impacts through the release of nanoparticles. Chemosphere 286, 131513.

Turner, L.K., Collins, F.G., 2013. Carbon dioxide equivalent (CO_2-e) emissions: A comparison between geopolymer and OPC cement concrete. Constr. Build. Mater. 43, 125-130.

Zhang, J., Ye, C., Tan, H., Liu, X., 2020. Potential application of Portland cement-sulfoaluminate cement system in precast concrete cured under ambient temperature. Constr. Build. Mater. 251, 118869.

The 16th International Congress on the Chemistry of Cement 2023 (ICCC2023)
"Further Reduction of CO_2 -Emissions and Circularity in the Cement and Concrete Industry"
September 18–22, 2023, Bangkok, Thailand

Comparison of set retarders in CSA and blended CSA/OPC systems

E. Kapeluszna[1*], I. Buchała[1,2], W. Szudek[1,3] and P. Szołdra[1,4]

[1] AGH University of Krakow, Faculty of Materials Science and Ceramics, Department of Building Materials Technology, Krakow, Poland

Email: ewak@agh.edu.pl

[2] Email:ilona.buchala1@gmail.com
[3] Email: szudek@agh.edu.pl
[4] Email: szoldra@agh.edu.pl

ABSTRACT

The aim of the presented work was to determine the influence of CSA on the properties of CSA/OPC blended binder. Moreover, the impact of four set retarders (citric acid, tartaric acid, sodium gluconate and borax) on the hydration and performance of such cement was investigated. DTA/TG and microcalorimetric analyses were carried out on cement pastes, followed by consistency, setting time and compressive strength measurements. DTA/TG method allowed for a qualitative and quantitative characterization of the phase composition of pastes after 24 hours of hydration. In the case of neat CSA, a correlation was found between the amount of water chemically bound in the samples and their compressive strength. All of the selected set retarders had a different effect on the hydration and properties of pure CSA, not only increasing its setting time but also affecting the amount of products formed during the hydration. In the case of CSA, the most efficient set retarders were sodium gluconate and borax while for the blended cement, the set-retarding effect was not observed.

KEYWORDS: *: calcium sulfoaluminate cement, hydration, set retarder, borax, sodium gluconate*

1. Introduction

In recent years, calcium sulfoaluminate cements (CSA) have attracted the attention of both scientists and cement industry. Compared to OPC, the reaction of CSA cements is much faster and a greater fraction of their hydration heat is generated within the first 12 h. The early-age hydration products include ettringite, monosulfate and amorphous aluminum hydroxide. Due to the fast reaction of CSA cements, the use of a retarder is often required in order to obtain a sufficient open time. Citric, tartaric and gluconic acids and their salts are powerful set retarders in calcium sulfoaluminate cements. Moreover, borax proved to be an effective CSA retarder by preventing (to a certain extent) the dissolution of ye'elimite and lowering the initial pH. However, little is known about their performance in binary CSA/OPC systems. Therefore, the goal of the presented study was to compare the effectiveness of various set retarders in pure CSA and blended CSA/OPC systems.

2. Experimental

2.1 Methods

Chemical composition of the materials used in the experiments was determined with a PANAnalytical WDXRF Axios Max spectrophotometer. Their phase composition was analyzed using a Philips PW 1050/70 diffractometer. Patterns were collected in the range of 5-65 °2θ, with a 0.05° 2θ step. The heat of hydration of cement pastes was measured at 25°C using a differential heat-conduction microcalorimeter. DTA/TG measurements were carried out in the temperature range of 25-1000°C using

a Netzsch STA 449F3 Jupiter thermoanalyzer in a synthetic air atmosphere. Grain size distribution was determined with a Malvern Mastersizer 2000 laser diffractometer. Consistency of mortars was investigated with a flow table according to PN-EN 1015-3. Setting time of cement pastes was measured according to PN-EN 196-3. The compressive strength of cement mortars was determined on 25 x 25 x 100 mm bar samples using a Controls Automax 5 hydraulic press.

2.2 Materials

Calcium sulfoaluminate cement (CSA) and ordinary Portland cement (OPC) were used in the investigations. Their chemical compositions are presented in Table 1. Their phase composition was examined by X-ray diffractometry. Fig. 1 shows the X-ray patterns of both types of cement.

Table 1. Chemical composition of cements.

Oxide		CaO	SiO_2	Al_2O_3	MgO	SO_3	Fe_2O_3	Na_2O	K_2O	Na_2O	Cl
Cement [%]	CSA	39.8	5.5	23.2	2.6	23.9	1.1	1.2	0.5	1.2	0.2
	OPC	64.7	18.7	4.6	1.7	4.7	3.7	0.4	0.4	0.4	0.1

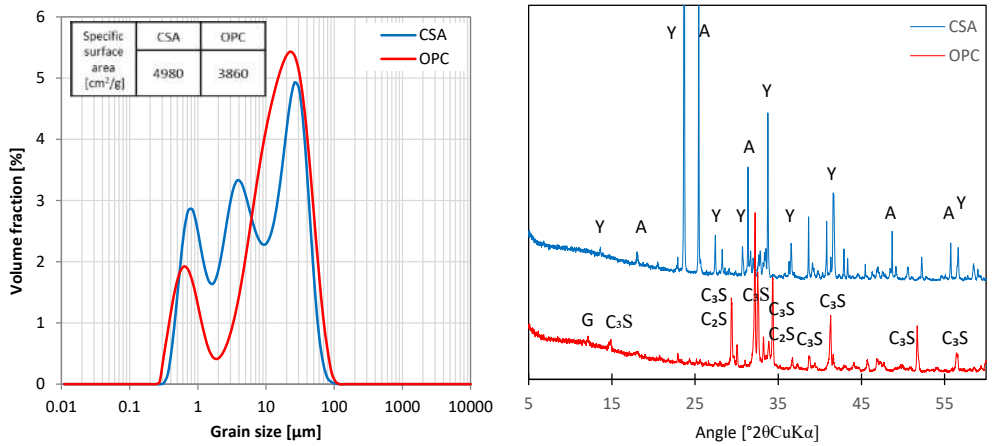


Fig 1. Grain size distribution and phase composition of CSA and OPC; C_3S-Alite, C_2S-Belite, Y-Ye'elimite, A-Anhydrite, G-Gypsum.

The effect of various set retarders (citric acid, tartaric acid, sodium gluconate and borax) on the properties of calcium sulfoaluminate cement (CSA100) and CSA/OPC blend (CSA20 - 80% of OPC and 20% of CSA) was investigated. For this purpose, heat evolution, consistency and compressive strength were examined as a function of time. Moreover, phase composition of CSA and OPC pastes with various set retarders was determined after 24 hours of hydration in order to compare the differences in the amount of the hydration products.

3. Results

The admixtures affect the kinetics of hydration (Fig 2). The analysis of the amount and rate of heat released during the reaction shows that sodium gluconate and borax most effectively prolonged the induction period and extended the setting time of CSA cement pastes, while the most effective set retarders of CSA20 were citric acid, borax and sodium gluconate. According to the literature, borax prevents the dissolution of ye'elimite, which was confirmed by the calorimetric analysis – the introduction of borax lead to the greatest extension of the induction period. The different shape of the calorimetric curves shows that the admixtures might have various action mechanisms. The presence of sulfates in CSA cement probably delayed the hydration of Portland clinker phases, resulting in a lower heat of hydration. All admixtures increased the setting time of CSA, as determined by Vicat apparatus (Table 2). At the same time, admixtures used in the amount of 0.2% did not effectively delay the setting of the blended binder. In its case, the rate of ettringite formation is very high; therefore, the effect of the admixtures may be decreased due to their incorporation into the structure of the hydration products.

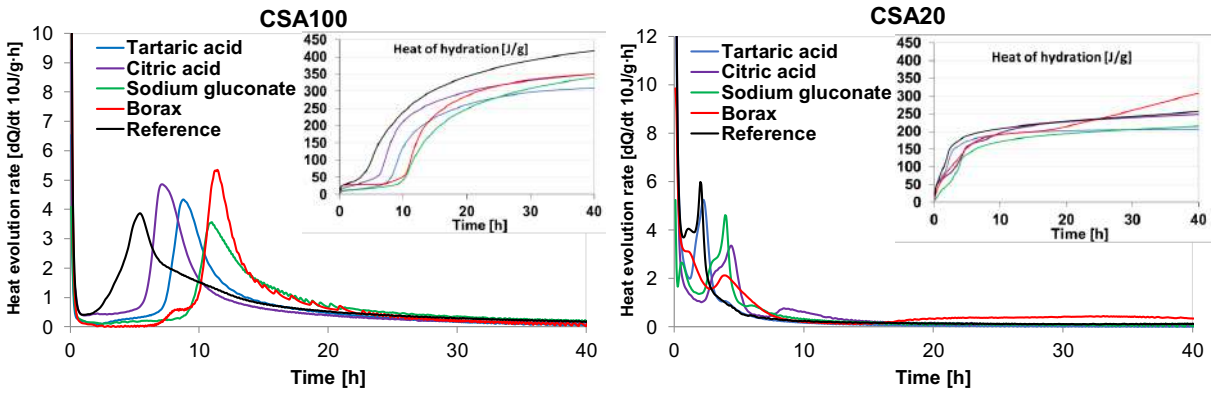


Fig 2. Heat of hydration of CSA and blended CSA/OPC pastes.

Table 2. Setting time determined by Vicat apparatus.

Setting time [min]	CSA100					CSA20				
	Ref	Citric acid	Sodium gluconate	Borax	Tartaric acid	Ref	Citric acid	Sodium gluconate	Borax	Tartaric acid
	105	154	228	360	230	30	38	32	28	31

In general, sodium gluconate and citric acid increased the consistency of mortars containing neat CSA cement, while borax and tartaric acid caused a decrease in their flow. On the other hand, in the case of CSA20 mortars, the consistency was increased by all of the admixtures except for borax (Fig. 3).

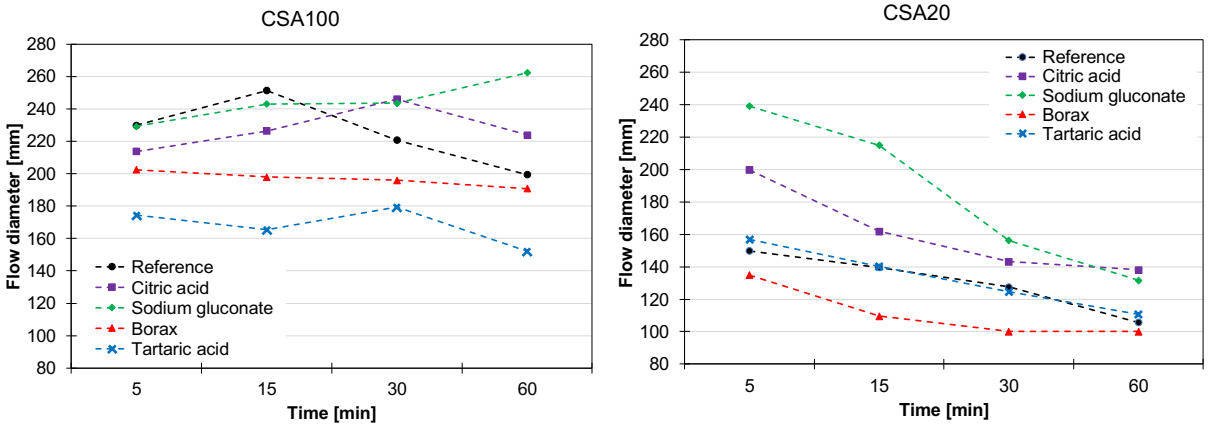


Fig 3. Consistency vs time of CSA and blended CSA/OPC mortars.

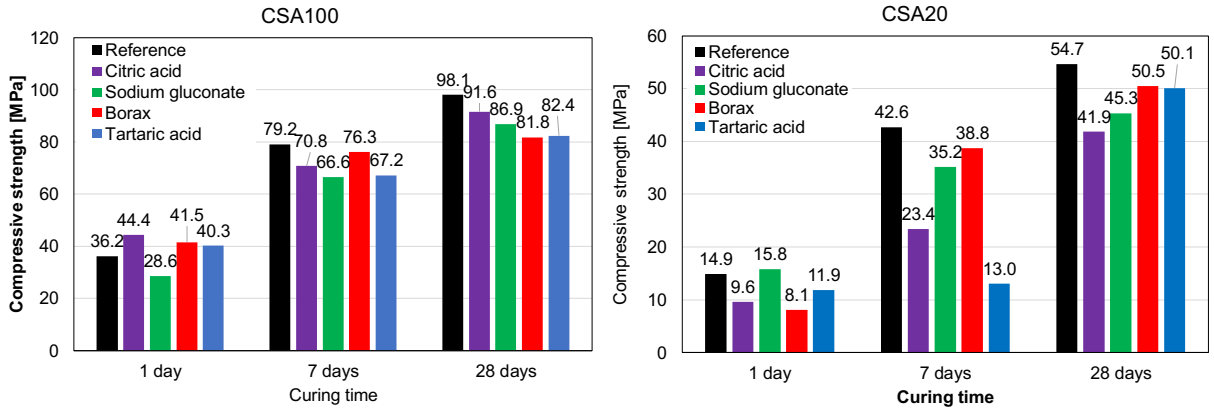


Fig 4. Compressive strengths of CSA and blended CSA/OPC mortars.

After 1 day of curing, citric acid, tartaric acid and borax increased the strength of CSA mortar by 11 to 23%, while sodium gluconate deteriorated its mechanical properties. Such outcome corresponds to the

results of the calorimetric measurements. After 7 and 28 days of curing, all admixtures caused a decrease in strength of the CSA100 mortars (Fig. 4). For blended cement, in general, a decrease in compressive strength was observed after the addition of all of the set retarders.
The differences in the compressive strength are related to the content and probably the morphology of ettringite, which was proven by the DTA/TG analysis. The increase in compressive strength after 1 day of curing may result from a different morphology of the ettringite formed and thus, a different contribution of chemically bound water. The amount of ettringite was the highest for CSA100 with the addition of citric acid (Fig 5). Tartaric acid probably affects the morphology of ettringite, which may result from the high affinity of tartrate ions towards aluminate phases and their incorporation into the forming hydration products. The DTA/TG results indicate that in the case of OPC with the addition of tartaric acid, after 24 hours, the amount of hydration products - AFt, C-S-H and $Ca(OH)_2$ was the lowest out of all admixtures.

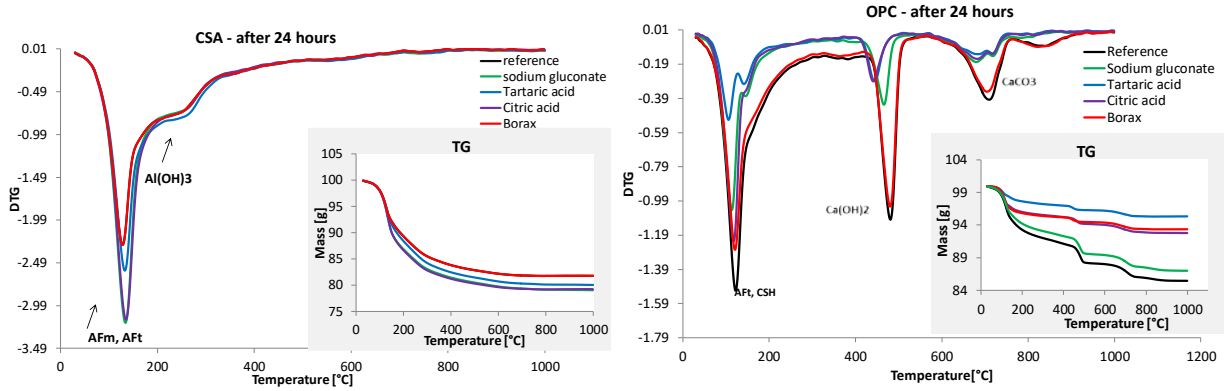


Fig 5. DTA curves of CSA and OPC pastes after 24 hour of hydration.

3. Conclusions

1. The addition of CSA to Portland cement significantly accelerates its early hydration and increases the amount of heat released after approx. 15 hours. However, the heat released after 40 hours is lower, most likely due to a delay in the hydration of Portland clinker phases resulting from the presence of sulfates.
2. In the case of CSA, the addition of borax results in the greatest extension of setting time and the most significant prolongation of the induction period. However, it leads to an increase in the compressive strength after 1 day and a decrease after 7 and 28 days of curing, compared to the reference sample.
3. Citric acid extended the setting time of CSA by approx. 50 minutes, making it the least effective among all tested admixtures. In the microcalorimetric curves of the samples containing citric acid, the shortest induction period was observed, compared to pastes with other admixtures.
4. The DTA/TG analysis showed that after 24 hours of hydration, the sample with citric acid contained a higher amount of ettringite, which explains the greatest increase in the strength of CSA100 mortars.
5. All admixtures influence the hydration of CSA/OPC blend, however, they are ineffective in retarding the setting of such binders.

Acknowledgements

This research was partially funded by the National Science Centre, Poland, project no. 2021/43/D/ST8/02603

References

Ben Haha, M., Winnefeld, F. and Pisch, A. (2019) "Advanced in understanding ye'elimite-rich cements", *Cement and Concrete Research*, 123(105778): 1-20

Bullerjahn, F., Zając, M., Skocek, J. and Ben Haha, M. (2019) "The role of boron during the early hydration of belite ye'elimite ferrite cements", *Construction and Building Materials*, 215: 252-263

El Khessaimi, Y., El Hafiane, Y. and Smith, A. (2020) "Effect of fineness and citric acid addition on the hydration of ye'elimite", *Construction and Building Materials*, 258(119686): 1-12

Zając M,, Skocek J., Bullerjahn F. and Ben Haha, M. (2016) "Effect of retarders on the early hydration of calcium-sulpho-aluminate (CSA) type cements", *Cement and Concrete Research*, 84: 62-75

The 16th International Congress on the Chemistry of Cement 2023 (ICCC2023)
"Further Reduction of CO_2 -Emissions and Circularity in the Cement and Concrete Industry"
September 18–22, 2023, Bangkok, Thailand

CO_2 mineralization in the limestone calcined clay cement

Q. Liu[1], S. Hu[2], Y.C. Hu[3], and G.Q. Geng[4*]

[1] *Department of Civil and Environmental Engineering, National University of Singapore, 117576, Singapore*
Email: liuqing@nus.edu.sg
[2] *Department of Civil and Environmental Engineering, National University of Singapore, 117576, Singapore*
Email: e0920941@u.nus.edu
[3] *Department of Civil and Environmental Engineering, National University of Singapore, 117576, Singapore*
Email: yc_hu@nus.edu.sg
4 Department of Civil and Environmental Engineering, National University of Singapore, 117576, Singapore
Email: ceegg@nus.edu.sg

ABSTRACT

In ready-mixed concrete plants, producing concrete inevitably generates waste cement paste which will pollute the environment if disposed of randomly. Herein, we carbonated the waste cement paste by aqueous carbonation to replace the limestone to develop a novel limestone calcined clay cement (LC^3). Carbonation not only reactivates the waste cement paste but also fixes the CO_2 in the cement matrix. The results showed that the waste cement paste could be carbonated quickly within 8.5 h with the formation of the carbonated products, mainly calcium carbonates and amorphous silica gel. By tuning the substitution ratio of carbonated waste cement paste, the compressive strength of LC^3 with carbonated waste cement paste is higher than the OPC and LC^3 due to the high activity and specific surface area of carbonated waste cement paste. The pore structure of LC^3 with carbonated waste cement paste was refined. Hopefully, our work may pave a new way to develop a novel LC^3 by replacing limestone with carbonated waste cement paste, accompanied by permanently realizing the sequestration of CO_2 in the cement matrix.

KEYWORDS: *Carbonation, Waste cement paste, LC^3, Mechanical strength*

1. Introduction

With the rapid development of the economy and society, concrete is extensively used to carry out infrastructure construction, leading to a huge demand for cement. It is well known that producing cement releases a large amount of CO_2, which abets global warming. Furthermore, the thriving concrete industry produces a mass of hardened cement and concrete waste, which is harmful to protecting the environment and achieving the sustainable development of society. Therefore, reusing hardened cement and concrete waste is becoming urgent.

The recycled coarse aggregate (RCA) can be extracted from the hardened concrete and was applied in concrete blocks and road construction (Zuo et al (2018) and Gupta et al (2018)). However, recycled concrete fines (RCF) have a rough surface texture, a high-water absorption ratio and inferior properties, restricting their application in new concrete. To expand the application of RCF, recently, researchers have focused on improving the properties of RCF by carbonation (Mehdizadeh et al (2021), Qin et al (2019) and Wu et al (2022)). Aqueous carbonation as an indirect method has been employed to improve the activity of RCF due to their high efficiency in producing calcium carbonate ($CaCO_3$) and amorphous silica gel (Zajac et al (2020) and Shen et al (2021)). The hydrated cement paste in RCF is eliminated via the leaching-carbonation process, where RCF is converted to $CaCO_3$ and silica-rich gel that can be used in concrete as supplementary cementitious materials.

LC^3 as a new cement has attracted a lot of attention from researchers due to its low carbon footprint and low cost. Clays with a kaolinite content of approximately 40% or above were calcined to prepare LC^3-50 which displayed a comparable compressive strength with the cement mortar for 7 days (Alujas et al (2015) and Avet et al (2016)). Although limestone is widely used in LC^3 due to its low price, high availability, and filling effect, its main component is $CaCO_3$ which has low activity, limiting the strength development of LC^3. To address this issue, here, the concrete slurry waste is carbonated by aqueous carbonation to produce $CaCO_3$ and amorphous silica gel to replace limestone.

In this study, we aim to fabricate a novel LC^3 whose limestone is replaced by carbonated products produced by carbonation of waste cement paste. The waste cement paste was carbonated first to obtain the carbonated products. The pH of the solution with waste cement paste was monitored during carbonation. X-ray diffraction (XRD) and thermogravimetric analysis (TGA) were used to characterize the carbonated waste cement paste. Finally, the compressive strength was measured to evaluate the effect of carbonated waste cement paste on the LC^3 mortar.

2. Materials and methods

2.1 Materials

Ordinary Portland cement (OPC) Type I is used to prepare LC^3. A combination of Singapore marine clay and kaolin is calcined at 800 °C to obtain the calcined clay. Limestone (98% $CaCO_3$ content) and gypsum with a purity of more than 99% were purchased from Singapore. The fine aggregate is river sand, and the fineness modulus is 2.4. The water-reducing (WR) agent is a high-performance polycarboxylate liquid water reducer with water reducing rate of 27%.

Cement pastes with a water-cement ratio of 0.4 were used to represent waste cement paste. After 21 days of standard curing, samples were taken out for drying, crushing, and ball milling, and finally obtained the waste cement waste powder with a diameter of less than 75μm. The component of LC^3 was listed in Table 1. The mix proportion was presented in Table 2. The WR agent was used to control the workability of the mortar. The preparation and curing of mortar specimens referred to the requirements of ASTM-C305. In this experiment, three kinds of mortars are prepared, namely OPC, LC^3 using limestone powder (LC^3), and LC^3 using carbonated waste cement paste (LC^3-waste).

Table 1 Components of LC^3

OPC	Calcined clay	Limestone or Waste cement slurry	Gypsum
70%	19%	9%	2%

Table 2 Mix proportion of mortar

LC^3 or Cement	Sand	Water	Water reducing agent
1	2.75	0.485	0.013

2.2 Methods

2.2.1 Carbonation test

The experiment was carried out using a self-made rapid carbonation device (in a liquid environment), as shown in Fig. 1. The raw material was waste cement paste powder with a particle size below 75 μm. The flow rate of carbon dioxide was 0.5 L/min, and the liquid-solid ratio was 2 with a mixing speed of 200 r/min. Samples were taken every 1 h from 0.5 h until 8.5 h. After carbonation, waste cement paste was taken out and dried to obtain carbonated waste cement paste powder for preparing LC^3.



Fig. 1 Carbonation of waste cement paste

2.3.2 XRD and TGA

After drying, the sample was ground into powder and mixed with 1-part CaF_2 in a mass ratio of 4:1. Finally, the D8 Advance X-ray Diffractometer was employed to characterize the phase composition quantitatively. The scanning angle was 5–60°, and the speed was 1°/ min. DTG-60H thermogravimetric

analyzer was conducted to study the thermal stability. The temperature range was from 30 °C to 950 °C at a rate of 20 °C/min.

2.3.3 Compressive strength test

The pressure testing machine was carried out to measure the compressive strength of cube specimens (40mm) according to ASTM-C109. The test loading rate was 144 kN/min. Three parallel specimens were tested to calculate the average value.

3. Rseults and discussion

3.1 Carbonation of waste cement paste

With the increase of carbonation time, the pH value of the cement slurry decreases continuously, showing a trend of rapid decline first and then slow decline (Fig. 2(a)). Through the test results of XRD and TGA, the time-history curves of calcium hydroxide ($Ca(OH)_2$) and $CaCO_3$ content can be calculated. The content of both $Ca(OH)_2$ and $CaCO_3$ increases rapidly in the first 4.5h and slows down in the next 4h.

After the 8.5h carbonation test, the content of $CaCO_3$ was calculated to be 55.97% in the carbonated waste paste by XRD (Fig. 2(c)), and that by TGA was calculated to be 59.42% (Fig. 2(d)). This indicates that the carbonation test can generate more than 55% $CaCO_3$ in the carbonated waste paste within 8.5h, which is because, under the high alkaline environment, the introduction of carbon dioxide rapidly converts the $Ca(OH)_2$ in the cement waste slurry to $CaCO_3$. However, as the carbonation time increases, the amount of $Ca(OH)_2$ decreases, resulting in a reduction in the conversion rate.

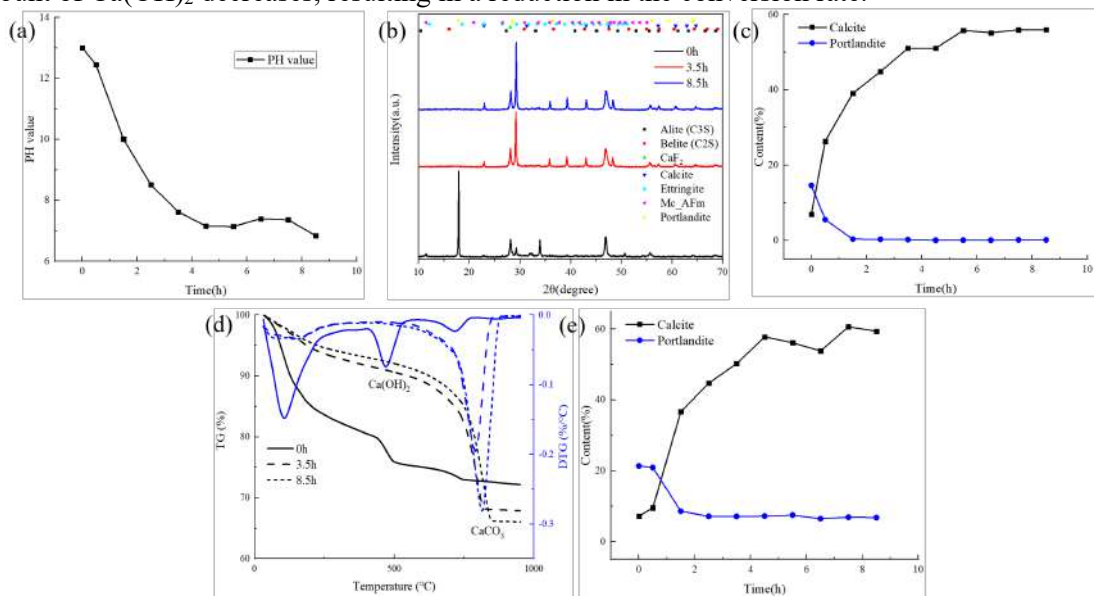


Fig. 2 Carbonation of waste cement paste. (a) pH of waste cement slurry after carbon dioxide injection. (b) XRD spectra; (c) Content of portlandite and calcite calculated from XRD; (d) TGA curves; (e) Content of portlandite and calcite calculated from TGA.

3.2 Compressive strength

Fig.3 depicts the compressive strength of mortars with different curing ages. The compressive strength of OPC is the highest at 3 days and 28 days among the three mixtures, whereas LC^3 shows the lowest compressive strength regardless of the curing age. LC^3-waste has a higher compressive strength than the counterpart of LC^3, indicating that carbonated waste cement paste promotes cement hydration. It is worth noting that the 7-day compressive strength of LC^3-waste is slightly higher than that of OPC, which may be due to the nucleation effect of calcium carbonate and the pozzolanic reaction of silica gel. The particle size of the limestone and the carbonated waste paste is at the same level, which means that the filling effect of the carbonated waste cement paste also contributes to the increased strength. The low compressive strength of LC^3-waste and LC^3 is attributed to their poor fluidity due to the presence of marine clay, which entraps some air bubbles in the matrix and thus deteriorates the compressive strength. The marine clay was found to increase the total porosity of cement mortar, resulting in a low mechanical strength (Dang et al (2020)). Moreover, the dilution effect reduces the compressive strength as well.

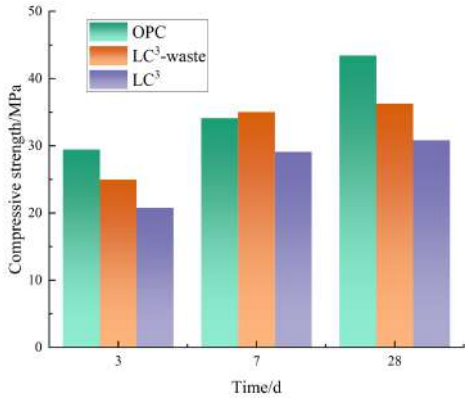


Fig. 3 Compressive strength of mortars with different curing ages. The dosage of WR is 1.3% for LC^3-waste and LC^3.

4. Conclusions

This work carbonated the waste cement paste by aqueous carbonation to produce carbonated products and amorphous silica gel and used the carbonated products to replace limestone to prepare LC^3. Through the self-made rapid carbonation device, more than 55% content of $CaCO_3$ can be generated within 8.5h. The compressive strength of LC^3-waste is slightly higher than the OPC and LC^3 at 7 days, while the 28-day strength of LC^3-waste and LC^3 is lower in comparison to the control mixture. Although the recycling of waste cement paste can be achieved by carbonation, the reduction in compressive strength of LC^3-waste is bad for the application of the carbonated waste cement paste. Therefore, it is essential to optimize the formula of LC^3 or use other chemical additives to increase the compressive strength and thus realize the application of this novel LC^3 in the construction industry.

References

Alujas, A., Fernández, R., Quintana, R., Scrivener, K.L. and Martirena, F. (2015) "Pozzolanic reactivity of low grade kaolinitic clays: Influence of calcination temperature and impact of calcination products on OPC hydration", *Applied Clay Science*, 108: 94-101

Avet, F., Snellings, R., Diaz, A.A., Haha, M.B. and Scrivener, K. (2016) "Development of a new rapid, relevant and reliable (R3) test method to evaluate the pozzolanic reactivity of calcined kaolinitic clays", *Cement and Concrete Research*, 85: 1-11

Dang, J., Du, H.J., and Pang, D.S. (2020) "Hydration, strength and microstructure evaluation of eco-friendly mortar containing waste marine clay", *Journal of Cleaner Production*, 272: 122784

Guo, Z., Tu, A., Chen, C. and Lehman, D.E. (2018) "Mechanical properties, durability, and life-cycle assessment of concrete building blocks incorporating recycled concrete aggregates", *Journal of Cleaner Production*, 199: 136-149

Gupta, N., Kluge, M., Chadik, P.A. and Townsend, T.G. (2018) "Recycled concrete aggregate as road base: Leaching constituents and neutralization by soil Interactions and dilution", *Waste Management*, 72: 354-361

Mehdizadeh, H., Jia, X., Mo, K.H. and Ling, T.C. (2021) "Effect of water-to-cement ratio induced hydration on the accelerated carbonation of cement pastes", *Environmental Pollution*, 280: 116914

Qin, L. and Gao, X. (2019) "Recycling of waste autoclaved aerated concrete powder in Portland cement by accelerated carbonation", *Waste Management*, 89: 254-264

Shen, P., Sun, Y., Liu, S., Jiang, Y., Zheng, H., Xuan, D., Lu J.X. and Poon, C.S. (2021) "Synthesis of amorphous nano-silica from recycled concrete fines by two-step wet carbonation", *Cement and Concrete Research*, 147: 106526

Wu, Y., Mehdizadeh, H., Mo, K.H. andLing, T.C. (2022) "High-temperature CO_2 for accelerating the carbonation of recycled concrete fines", Journal of Building Engineering, 52: 104526

Zajac, M., Skibsted, J., Skocek, J., Durdzinski, P., Bullerjahn, F. and Haha, M.B. (2020) "Phase assemblage and microstructure of cement paste subjected to enforced, wet carbonation", *Cement and Concrete Research*, 130: 105990

Zhang, J., Leung, C.K.Y. and Xu, S. (2010) "Evaluation of Fracture Parameters of Concrete from Bending Test using Inverse Analysis Approach", *RILEM Materials and Structures*, 43(6): 857-874

The 16th International Congress on the Chemistry of Cement 2023 (ICCC2023)
"Further Reduction of CO_2 -Emissions and Circularity in the Cement and Concrete Industry"
September 18–22, 2023, Bangkok, Thailand

Influence of slaked lime on hydration kinetics of Portland cement

Y. Zeng[1*], G.S. Munhoz[2], and G. Ye[3*]

[1] *Faculty of Civil Engineering and Geosciences, TU Delft, Delft, The Netherlands*
Email: Y.Zeng-4@tudelft.nl
[2] *Faculty of Civil Engineering and Geosciences, TU Delft, Delft, The Netherlands*
Email: G.daSilvaMunhoz-1@tudelft.nl
[3] *Faculty of Civil Engineering and Geosciences, TU Delft, Delft, The Netherlands*
Email: G.Ye@tudelft.nl

ABSTRACT

Due to the lower calcification temperature and better carbon sequestration performance, calcium lime binders are accepted as sustainable alternatives to conventional Portland cement in masonry structures. However, calcium lime binders mainly get hardened through long-term carbonation, and the strength development is slow. To overcome this drawback and ensure the mechanical performance at early ages, mixtures of slaked lime (i.e., $Ca(OH)_2$) and Portland cement are preferred in engineering practice. To investigate the hydration kinetics of lime-cement binders, especially to clarify the influence of lime-to-cement ratio (*l*/*c* ratio), calorimetry tests, X-ray diffraction (XRD) and thermogravimetric analyses (TGA) were carried out on binders with four different lime-to-cement ratios (*l*/*c*=0.0, 0.5, 1.0, and 2.0). Compared to pure cement paste, earlier occurrence of the main hydration peak (i.e., formation of C-S-H) and shorter induction period were observed in lime-cement binders, suggesting that the hydration is facilitated by additional slaked lime. The acceleration effect was further proved by quantitative analyses of XRD results and TGA, as the consumption rates of all four major phases (i.e., C_3S, C_2S, C_3A and C_4AF) increased with *l*/*c* ratio, and quicker transformation from Ettringite to AFm phases were observed in lime-cement binders. Further comparisons with inert SiO_2 fillers suggest that the acceleration effect is attributed to both physical and chemical influences, and detailed influence mechanisms will be investigated in future research.

KEYWORDS: *Slaked lime, Portland cement, hydration kinetics*

1. Introduction

Compared to Portland cement, calcium lime is calcined at lower temperatures, and the material itself could absorb CO_2 during the hardening process. Therefore, it is believed to be an ideal alternative to conventional cementitious materials in applications like plastering materials and joint materials between masonry blocks (Alvarez et al. 2021). However, one significant drawback of calcium lime binders is the poor early-age mechanical performance. Instead of gaining strength through hydration, calcium lime binders get hardened through carbonation, which may take months or even years. Therefore, in engineering practice, the mixture of calcium lime and conventional Portland cement is preferred to keep the balance between sustainability and mechanical properties (Gulbe et al. 2017).

Several previous studies have investigated the hydration process of lime-cement binders. For example, Cizer (2009) observed that the induction period could be greatly shortened by additional slaked lime. Fourmentin et al. (2015) observed similar results in their tests. However, neither of these investigations discussed the influence during the whole hydration process, and the detailed influence of slaked lime on cement hydration is still unclear.

Therefore, in this research, hydration process of four different lime-cement binders were investigated through the combined use of thermogravimetric analyses (TGA), X-ray diffraction (XRD) and

calorimetry. Based on these test results, hydration kinetics of lime-cement binders, as well as related influence mechanisms, will be discussed.

2. Materials and Methods

CEM I 42.5N cement from ENCI and CL-90S slaked lime from Lhoist were used in this research. Properties of these raw materials are summarized in Table 1.

Table 1 Raw material properties

Categories	Properties (Units)	Cement	Lime	Methods
Physical properties	Density (g/cm^3)	3.15	2.30	Pycnometer
	Specific surface area (m^2/g)	0.86	13.46	Nitrogen sorption (BET)
	Mean particle size D_{43} (μm)	29.41	15.56	Laser diffraction
Chemical composition	Alite C_3S (%)	62.90	N/A	XRD
	Belite C_2S (%)	10.26	N/A	XRD
	Alumina C_3A (%)	5.70	N/A	XRD
	Ferrite C_4AF (%)	10.37	N/A	XRD
	Portlandite CH (%)	N/A	96.30	XRD/TG
	Calcite CĈ (%)	N/A	3.70	XRD/TG
	Sulfates (%)	5.95	N/A	XRD

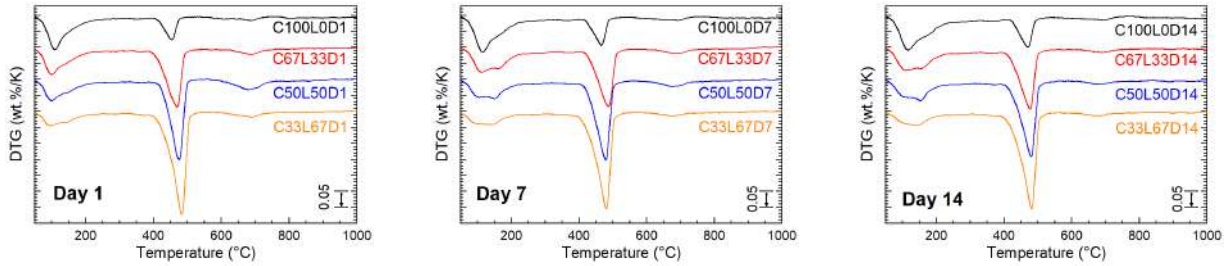
In order to investigate the influence of *l/c* ratio, three groups of lime-cement binders were considered in this research, and one group of pure cement paste was prepared for comparisons. Detailed mixture designs are presented in Table 2. It should be noted that, due to the large specific surface area of lime, a higher *w/b* ratio (0.8) was designed for all lime-cement binders to keep the consistency at a similar level.

Table 2 Mixture designs

Groups	Lime-to-cement (*l/c*) ratio	Water-to-binder (*w/b*) ratio
C100L0	0.0	0.6
C67L33	0.5	0.8
C50L50	1.0	
C33L67	2.0	

Following procedures recommended by Snellings et al. (2018), powder samples were collected after 6 hours, 1 day, 3 days, 7 days and 14 days for TGA and XRD. In the former test, around 30mg sample was heated to 1200℃ at a rate of 10K/min. In the latter analysis, 10% silicon powder was added as the internal standard, and the sample was scanned from 5° 2θ to 75° 2θ, with a stepwise of 0.02° 2θ.
Meanwhile, hydration heat release during the first 7 days (at 20℃) were measured through isothermal calorimetry. For comparisons, inert SiO_2 fillers with a similar specific surface area (11.94m^2/g) were also used to reflect the filler effect. All test results will be presented and discussed in the following section.

3.Results and Discussions

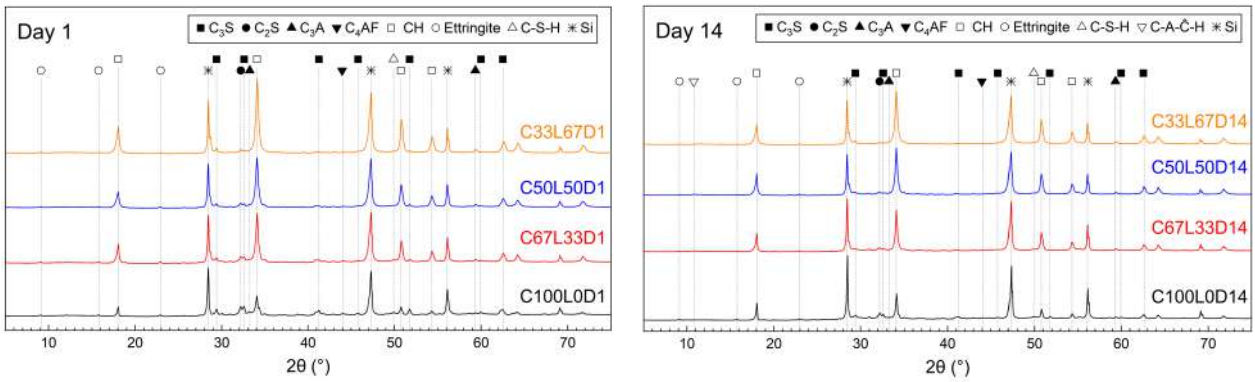


(a) Day 1 (b) Day 7 (c) Day 14

Figure 1 Representative DTG curves of hydration products

As shown in Figure 1, with the increase of lime content, the dehydration peak of $Ca(OH)_2$ at around 480℃ becomes more significant. Meanwhile, due to the inevitable existence of $CaCO_3$ in slaked lime (shown in Table 1), decarbonation peaks at around 700℃ were observed in lime-cement binders. However, after several days, these peaks become less obvious, indicating that $CaCO_3$ was consumed during the hydration process. As a result, calcium carboaluminate hydrate (C-A-Ĉ-H) was found in XRD tests (shown in Figure 2).

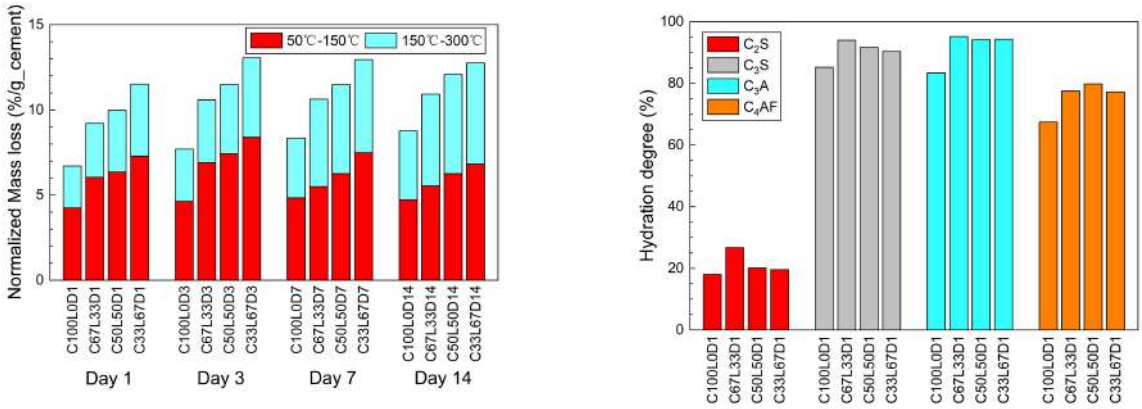
Regarding dehydration of other products, two peaks were observed between 50℃ and 300℃. The peak at around 100℃ appears right within the first day. This is mainly attributed to the rapid formation of ettringite and C-S-H. With the development of hydration, AFm phases are formed through continuous reactions between ettringite and cement clinkers. Therefore, the first peak gradually gets lower, and a new peak at around 170℃ grows with time. Other Afm phases, like C-A-Ĉ-H, should also contribute to the second peak, but their contributions should be marginal, as there is no obvious peak detected after 200℃. After 14 days, the second peak become dominant in lime-cement binders, while the first peak is still more obvious in pure cement paste. Therefore, it can be concluded that the additional slaked lime could facilitate the formation of AFm.



(a) Day 1 (b) Day 14

Figure 2 Typical XRD patterns of hydration products

Such acceleration effect could be better reflected through quantitative analyses of tests mentioned above. By calculating mass losses between 50℃ and 300℃, and normalizing them with cement proportion, it is obvious that the normalized mass loss increases with the lime content. Even though the mass loss cannot be clearly attributed to the dehydration of one single phase, this indicator can still prove that the total amount of hydration products is greater in groups with more slaked lime inside (shown in Figure 3a).



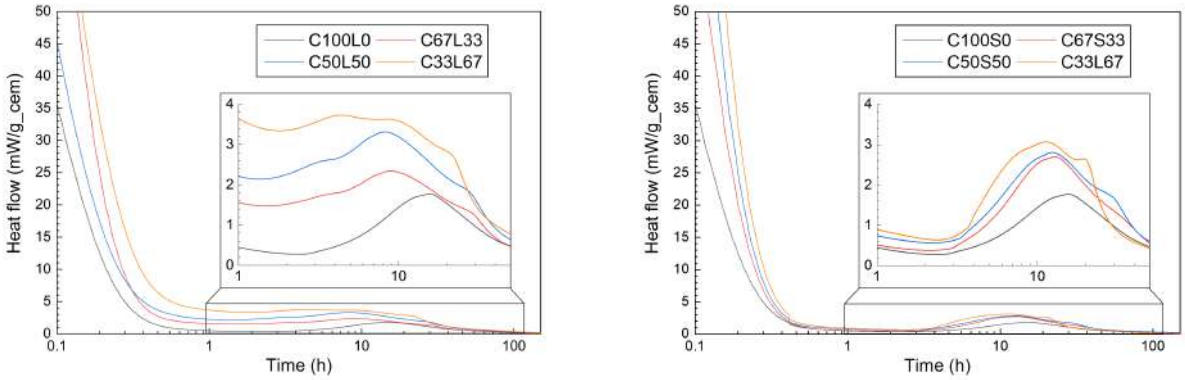
(a) Normalized mass losses observed in TGA (b) Hydration degrees of four major phases after 14 days

Figure 3 Quantitative analyses of TGA and XRD results

Through Rietveld refinements of XRD results, hydration degrees of four major hydraulic phases (i.e., C_3S, C_2S, C_3A, C_4AF) could be assessed (shown in Figure 3b). Despite the semi-quantitative nature of the analysis method, the accelerated hydration of all four phases is still obvious. However, the acceleration effect seems less relevant to the lime content, but vary significantly among different phases. For C_3S, C_3A and C_4AF, hydration degrees were increased by 8%-12%, while for C_2S, the increment is less obvious. A possible explanation to these phenomena is that the rapid hydration in early ages. Due to the growth of hydration products, further hydration reactions, especially the hydration of C_2S, could be greatly hindered, so the influence of slaked lime becomes less significant.

Several possible explanations to the acceleration effect have been proposed in previous investigations (e.g., Cizer 2009, Fourmentin et al. 2015), and among them the most reasonable one is the filler effect.

Due to the limited solubility of $Ca(OH)_2$, most of the slaked lime will not dissolve during the mixing process, and therefore could provide additional precipitation surface for hydration products. However, through comparisons with inert SiO_2 fillers (shown in Figure 4), it is clear that the induction period is significantly shorter in lime-cement binders, and the peak heat flow is also greater. Given that the surface area of inert SiO_2 fillers is similar to that of slaked lime particles, the decrease in the induction period should be more likely attributed to chemical effects, like higher affinity to hydration products and higher calcium concentration in pore solution systems. The detailed influence mechanism will be further investigated through ICP-OES tests and microscopy observations.



(a) Lime-cement binders (b) Cement pastes with SiO2 fillers

Figure 4 Heat release during the hydration process

4. Conclusions

In this research, hydration process of four typical lime-cement binders has been investigated, and related influence mechanisms have been briefly discussed. Within the scope of this research, the following conclusions could be drawn:

(1) The additional slaked lime could facilitate the formation of ettringite and C-S-H, as well as the formation of AFm.

(2) Hydration of all four hydraulic phases could be accelerated by slaked lime, but the acceleration effect is less significant on C_2S. This phenomenon may be related to the rapid formation of hydration products.

(3) The acceleration effect should be not only attributed to physical filler effect, but also related to chemical effects, which will be investigated in future research.

Acknowledgements

This project has received funding from the European Union's Horizon 2020 research and innovation programme under Marie Sklodowska-Curie project SUBLime [Grant Agreement no. 955986]

References

Alvarez, J., Veiga, R., Martinez-Ramirez, S., Secco, M., Faria, P., Maravelaki, P.N., Ramesh, M., Papayianni, I., and Valek, J. (2021) "RILEM TC 277-LHS report: a review on the mechanisms of setting and hardening of lime-based binding systems." *Materials and Structures*, 54, 63.

Cizer, O. (2009). "Competition between Carbonation and Hydration on the Hardening of Calcium Hydroxide and Calcium Silicate Binders." KU Leuven.

Fourmentin, M., Faure, P., Gauffinet, S., Peter, U., Lesueur, D., Daviller, D., Ovarlez, G., and Coussot, P. (2015). "Porous structure and mechanical strength of cement-lime pastes during setting." *Cement and Concrete Research*, 77, 1-8.

Gulbe, L., Vitina, I., and Setina, J. (2017). "The influence of cment on properties of lime mortars." *Procedia Engineering*, 172, 325-332.

Snellings, R., Chwast, J., Cizer, Ö., De Belie, N., Dhandapani, Y., Durdzinski, P., Elsen, J., Haufe, J., Hooton, D., Patapy, C., Santhanam, M., Scrivener, K., Snoeck, D., Steger, L., Tongbo, S., Vollpracht, A., Winnefeld, F., and Lothenbach, B. (2018). "RILEM TC-238 SCM recommendation on hydration stoppage by solvent exchange for the study of hydrate assemblages." *Materials and Structures*, 51(6), 172.